Physics of the Solid State, Vol. 46, No. 9, 2004, pp. 1583–1590. Translated from Fizika Tverdogo Tela, Vol. 46, No. 9, 2004, pp. 1537–1543.
Original Russian Text Copyright © 2004 by Moliver.

METALS AND SUPERCONDUCTORS

Auger-Spectroscopic Appearance of Electron Correlation at the Fermi Surface of Graphite

S. S. Moliver

Ul'yanovsk State University, ul. L'va Tolstogo 42, Ul'yanovsk, 432700 Russia

e-mail: moliver@sv.uven.ru

Received October 8, 2003

Abstract—It is shown that, in Auger-electron spectra of three-dimensional semimetal graphite and two-dimensional graphite (a zero band-gap semiconductor), an energy gap should be observed between the thresholds (edges) of the forward and inverse processes (threshold gap). In the one-electron approximation, this gap is zero, since the threshold for the Auger spectrum of the forward process is the minimum hole energy in the valence band, while the threshold for the spectrum of the inverse process is the minimum energy of conduction electrons. Inclusion of the electron correlation at the Fermi surface within the quantum-chemical approximation of a single open electron shell for multiplet structures of the restricted Hartree–Fock method makes it possible to determine the threshold gap as 1.5 eV for a 48-atom cyclic model of three-dimensional graphite and as 2.0 eV for a 24-atom model of two-dimensional graphite. The threshold gap does not contain the Fermi energy, in contrast to the Auger spectrum thresholds, where $\frac{1}{2}(4.0\text{ eV} - \varepsilon_F)$ for the forward Auger spectrum (holes) and $\frac{1}{2}(-1.1\text{ eV} + \varepsilon_F)$ for the inverse spectrum (conduction electrons), the sum of which gives this gap. The results of calculations for the forward Auger spectra of three-dimensional graphite (including the conclusion that electron correlation of holes in the top valence bands is weak in the Auger process) are shown to agree with the experimental data. © *2004 MAIK "Nauka/Interperiodica".*

1. INTRODUCTION

Auger electron spectroscopy (AES) and inverse AES (iAES) are of particular importance in developing the electronic theory of three-dimensional (3D) semimetal graphite, since these methods carry information on the electron correlation. In the one-electron approximation, the Auger electron spectrum describes the process that yields two holes in the valence band below the Fermi level ε_F. In other words, one valence electron transfers from the level ε_{v1} to the level $\varepsilon_{\text{core}}$ of a preliminarily generated deep core hole (the state close to the atomic orbital *C*1*s* in the case of graphite) and another valence electron transfers from the level ε_{v2} to a free state with kinetic energy ε_{kin}. In the same approximation, the inverse Auger spectrum describes the process resulting in the formation of two conduction electrons. More specifically, a probe-beam electron with kinetic energy ε_{kin} is captured into the vacant conduction level ε_{c1} and another electron transfers from the core level to another conduction level ε_{c2}. We note that the abbreviation iAES is not conventional; it was introduced to associate various electron spectroscopy versions with the inverse Auger process, e.g., appearance-potential spectroscopy (APS).

In what follows, we are interested only in systems with metal filling and spectrum edges (thresholds) caused by the lowest excitations of holes (AES) and conduction electrons (iAES) at the Fermi surface. In the one-electron approximation, the spectra are double convolutions of the density of states with a matrix element of the Coulomb interaction of two final particles. The energy dependence of the matrix element can be found within the one-electron approximation, whereas the many-electron approximation radically changes the transition probability and includes correlation corrections of the following types:

(i) The interaction of valence electrons with a deep hole. This component has almost no effect on the shape of the spectra and reduces to a constant, which is included in the empirical parameter $\varepsilon_{\text{core}} = 284.35 \pm 0.05$ eV [1]. This parameter is directly measured as the threshold for internal photoelectron emission in the x-ray absorption spectrum.

(ii) The "direct" correlation associated with the interaction of two final particles, i.e., holes (AES) or conduction electrons (iAES). In the case of an insulator (semiconductor) with delocalized carriers, this correlation is small and is considered using the representation of large-radius excitons. In particular, this correction contains the static permittivity and, in effect, takes into account the "indirect" correlation of all the crystal electrons. The opposite extreme case of strong localization (e.g., narrow 3*d* bands of transition metals) under conditions of completely filled bands is also convenient for analytical consideration in the Hubbard approximation.

1063-7834/04/4609-1583$26.00 © 2004 MAIK "Nauka/Interperiodica"

(iii) The indirect correlation associated with all valence electrons. It is impossible to strictly distinguish between this and the previous contribution. However, in the case where we have metal filling of bands and spectrum edges associated with shallow delocalized excitations near the Fermi level, exactly this type of correlation becomes dominant. In this study, we perform numerical simulation of this correlation.

The kinetic energy of primary (in forward AES) or secondary electrons (in iAES) is involved in the binding energy,

$$\begin{aligned} \varepsilon_v &= \frac{1}{2}(\varepsilon_{\text{core}} - \varepsilon_{\text{kin}}^{\text{AES}} - \varepsilon_{\text{F}}), \\ \varepsilon_c &= \frac{1}{2}(\varepsilon_{\text{kin}}^{\text{iAES}} - \varepsilon_{\text{core}} + \varepsilon_{\text{F}}), \end{aligned} \quad (1)$$

where all the energy parameters are positive: ε_F is measured downwards from the zero potential, at which $\varepsilon_{kin} = 0$; i.e., the Fermi energy is numerically equal to the work function. The particle energies (in the approximation of independent electrons) are also taken positive: ε_v and ε_c are measured downwards and upwards from the Fermi level, respectively.

The first Auger spectrum in (1) was recently measured for 3D semimetal graphite under the same conditions as a photoelectron emission spectrum (PES) (a single sample in the same chamber without loss of vacuum and a single detector of electrons) [1]. Although each measured electron spectrum coincided with x-ray [2, 3] and Auger electron [4] spectra previously obtained for graphite, accurate fixing of the contact potential with the detector [1] allowed the authors to conclude that the critical points of the AES and PES spectra coincide (double differentiation was used, since the spectra strongly differed in shape). Since the photoemission spectrum is one-electron and its features coincide with the high-symmetry points of the band structure $\varepsilon_v(\mathbf{k}) = 2.3, 4.8, 7.8$ eV, …, their coincidence with critical points (1) was interpreted as being due to weakness of the direct correlation of final holes from the upper valence bands in the Auger process.

However, the shapes of the AES and PES spectrum edges differ significantly over the range from the Fermi level to the first critical point [1]. The difference in the spectrum shapes is evident, and differentiation reveals an additional critical point in the Auger electron spectrum. This point cannot be interpreted as belonging to a band. Referencing the Auger electron spectra to the Fermi level is always characterized by an error of no less than 0.1 eV. Therefore, it is reasonable to say that the electron correlation of the states at the Fermi surface (including the direct correlation of two final particles at this surface) is the main effect that controls the position of the Auger spectrum threshold of semimetal graphite. Such an interpretation is also applicable to the threshold for the inverse Auger spectrum, for which no experimental data have yet been obtained.

We note that, for correlation with a core hole [see item (i)], the edge shape of the AES spectrum of graphite is affected by the Auger process with an initial state consisting of an exciton formed by a core hole and a valence electron. This contribution to the resulting Auger spectrum was studied using convolution of the one-electron density of graphite valence bands with a model delta-shaped density of states of the exciton under the assumption that the exciton binding energy is small and is identical to the Auger spectrum threshold [4]. In fact, there is a satellite of the basic Auger process whose threshold is shifted by the binding energy of the core-hole exciton. The spectrum narrows since the exciton band is substituted for one of the valence densities of states in the convolution integral for the probability of the Auger process. The contribution of the exciton satellite can be experimentally separated, since the lifetime of the free core hole is significantly longer than the lifetime of an excitonic hole. The influence of the electron correlation on the spectrum threshold energies for this satellite is the same as in the case of the basic Auger process.

The approach that is developed in this paper is also completely applicable to 2D graphite (zero band-gap semiconductor), i.e., to a system with the Fermi surface degenerated into a point. The thresholds of the Auger spectra calculated in this work and their comparison with experimental data for 2D (plane) and 3D hexagonal graphite show that these parameters can be important experimental characteristics of the electronic properties of cluster carbon materials.

2. AUGER PROCESSES AND QUANTUM-CHEMICAL MODELS

Quantum-chemical calculation yields the total energy of a crystal model consisting of a certain number of atomic cores and valence electrons (or bare nuclei and all electrons). Let the crystal model contain N valence electrons. The total energy $E(N)$ of the ground state is at least a self-consistent Hartree–Fock approximation, which is more or less accurate depending on the calculation method (semiempirical or nonempirical, *ab initio* method for calculating the matrix elements of the electron–electron interaction). The total energy can also account for the electron correlation if the configuration interaction or perturbation theory is applied to the self-consistent many-electron wave function [5].

The final states of the forward and inverse Auger processes correspond to the energies $E(N \pm 2)$, which can be calculated by changing the number of model electrons by two. In this case, the problem of a nonzero total charge of the model arises. For example, if the model is a building block of an infinite crystal and the calculation method takes into account only the valence

electrons, then a small compensating charge should be placed on the cores. Let $\Delta(N \pm 1)$ be the correction to the total model energy associated with the difference between the electron charge of the model containing only valence electrons and the charge of a separated crystal volume involved in the Auger process. This correction is introduced with the following purpose. The correction itself can be determined in quantum-chemical calculations, whereas direct calculations of $E(N \pm 1)$ can be meaningless, e.g., because of the odd total spin of the model.

In the forward Auger process, the initial energy is $E(N) - \Delta(N-1) + \varepsilon_{core}$ and the final energy is $E(N-2) + \varepsilon_{kin}$. The charge correction takes into account that the charge of the separated crystal volume changes by +1 in the Auger process, while the charge of valence electrons of the model changes by +2. Substituting these energies into Eq. (1), we obtain a theoretical formula for the absolute position of the AES spectrum edge,

$$\varepsilon_v = \frac{1}{2}[E(N-2) - E(N) + \Delta(N-1) - \varepsilon_F]. \quad (2)$$

In the inverse Auger process, the initial energy is $E(N) + \varepsilon_{kin}$ and the final energy is $E(N+2) - \Delta(N+1) + \varepsilon_{core}$; thus, we obtain a theoretical formula for the absolute position of the iAES spectrum edge,

$$\varepsilon_c = \frac{1}{2}[E(N+2) - E(N) - \Delta(N+1) + \varepsilon_F]. \quad (3)$$

The charge corrections make up a fixed fraction of the energy of electrostatic interaction of cores with each other and with all electrons; both corrections are independent of the electron correlation and are approximately equal. Therefore, summing Eqs. (2) and (3), we obtain

$$U_F = \varepsilon_v + \varepsilon_c = \frac{1}{2}(\varepsilon_{kin}^{iAES} - \varepsilon_{kin}^{AES}) = \frac{1}{2}[E(N+2) + E(N-2) - 2E(N)]. \quad (4)$$

In a system with metal filling, the energies of holes and conduction electrons are very close to the Fermi energy in the one-electron approximation. Hence, the energy gap between the thresholds of the forward and inverse Auger spectra (see Eq. (4)) is the characteristic energy of the electron correlation and can be measured experimentally. To this end, it is necessary not only to measure the forward and inverse Auger spectra but also to determine their threshold energy involved in relation (4), which is a complex problem. Its solution is facilitated by the fact that one does not have to determine the absolute position of the Fermi level but rather maintain a constant contact potential between the sample and the electron spectrometer.

Finally, if $E(N \pm 2)$ are taken to be energies of excited (rather than ground) states selected in a certain way, then Eqs. (2) and (3) can be used to determine not only thresholds but also specific features of Auger spectra.

3. OPEN-SHELL METHOD FOR 2D AND 3D GRAPHITE

Although the above conclusion relates to an arbitrary many-electron system with an open shell, an adequate quantum-chemical model for calculating the total energies can be constructed only in a few cases. Due to the fact that the Fermi surface of semimetal graphite encloses a small phase volume, the electronic structure of graphite can be adequately described by a cyclic model based on an extended unit cell (EUC) of the crystal, which allows one to calculate the wave functions at several high-symmetry points of the Brillouin zone, including points close to the Fermi surface, e.g., inside electron pockets. In 2D graphite, the Fermi surface degenerates into a single high-symmetry point of the Brillouin zone (zero band-gap semiconductor); therefore, the model of a single open shell is adequate for 2D graphite. This model and the method for calculating its electronic properties [6] are characterized by the following features:

(i) The crystal is modeled by a quasi-molecular EUC characterized by the $\mathbf{D}_{3h}$ point symmetry and by the k set $\{\Gamma + 6T + 3M(Q) + 2K(P)\}$ and consists of two crystal planes, with 24 carbon atoms in each. The model of 2D graphite ($\mathbf{D}_{6h}$ symmetry) consists of a single plane; however, its k set is much the same. Therefore, all group-theoretic constructions remain valid due to simple doubling of the irreducible representations. The prefix "quasi" in the model title means that periodic boundary conditions are imposed on molecular orbitals (MOs); i.e., the entire set of Bloch states of the crystal is reduced to the k set indicated above (widely used alternative designations of the high-symmetry points of the Brillouin zone of hexagonal graphite are given in parentheses). Thus, the number of valence electrons in the models of the initial states of Auger processes is $N = 192$ and 96 in the cases of 3D and 2D graphite, respectively [see Eqs. (2)–(4)].

(ii) The open electron shell of such a quasi-molecular EUC models the Fermi surface of an infinite 3D crystal according to the following scheme. The graphite band states nearest to the Fermi surface are π-type, i.e., are composed of p_z atomic orbitals (AOs). In turn, at the point K, which is at the center of the main electron pocket of the Fermi surface, the upper band π state of the model is doubly degenerate and corresponds to the bottom of the partially filled conduction band and the valence band top of the crystal. As indicated in the k set of the model, the Brillouin zone of graphite contains two points K, which cannot be transferred to one another by translation through a reciprocal lattice vec-

tor; hereafter, they are designated as K' and K''. The open shell formed by MOs with these quasimomenta includes four degenerate MOs grouped into two subshells with different wave vectors. Each subshell is a spatial MO doublet, which transforms according to the 2D representation E' or E'' of the $\mathbf{D}_{3h}$ point group. Three spinless configurations of the type $(K')^m(K'')^{n-m} = (2K)^n$ with an even number of electrons $n = 2, 4, 6$ can be formed from the MOs of the open shell. All the above also relates to the model of the "Fermi surface" of 2D graphite, which degenerated into the points K; only the designations of irreducible representations should be changed in the group-theoretic formulas.

The tables given in [6] list all terms of every configuration, i.e., spectroscopic combinations of the Slater determinants, whose group-theoretic selection and designations correspond to (a) a certain wave vector, Γ or K, which is determined by summing the wave vectors of n electrons settled over four MOs of the open shell; (b) irreducible representations of the $\mathbf{D}_{3h}$ point group (which is the point group of hexagonal semimetal graphite and of a 48-atom EUC); and (c) the type of filling of the open-shell MOs: χ is the pairing type (the open shell contains only doubly filled MOs), ψ is the exchange type (the open shell contains only singly filled MOs), and φ is the mixed type.

For example, according to a self-consistent calculation, the model ground state with energy $E(N)$ at the beginning of the Auger process is represented by a term with configuration $(K')^2(K'')^2$, whose wave function is composed of four Slater determinants differing in the filling of four MOs of the open shell [see Eq. (5)].

In fact, the group-theoretic analysis of the multiplet structure of the open electron shell of the cyclic model of semimetal graphite [6] is the basis of the proposed theoretical description of Auger processes; the remainder relates to calculation of the electronic properties.

(iii) The construction of the model of semimetal graphite described above predetermined the method for calculating its properties: the restricted open-shell Hartree–Fock–Roothaan method. Although the abbreviation ROHF (restricted open-shell Hartree–Fock) is used for this method as in quantum chemistry [5], an open shell with any degeneracy (orbital and/or with respect to the wave vector), rather than the simplest version with half-filling of the upper MO as in conventional software packages, is meant in the case under consideration. Such an extended interpretation of the ROHF necessitated the development of the McWeeney projection method by using electron density matrices to calculate Fock matrices and by introducing a system of open-shell coefficients [6] and a symmetrization procedure (in the presence of subshells in crystal models). As a result of these modifications, the self-consistency cycle takes into account the electron correlation associated with the open shell (the calculated terms involve several determinants). The high spatial symmetry of the model is also used in full (for example, when selecting molecular orbitals for an initial approximation and for calculating transition energies with allowance for the selection rules).

(iv) The other features of the calculation are methodical and are associated with the AO basis (semiempirical Slater AOs C2*s*2*p*), parametrization of matrix elements of the electron–electron interaction [intermediate neglect of differential overlap (INDO)], techniques for summing over an infinite lattice, etc. The restrictions used on the basis size and Coulomb integrals are associated exclusively with the potential of the computer equipment employed and the experience gained in the study of solid-state carbon systems (diamond, its surface, and its structural defects; fullerene, its crystals and chemical compounds).

We emphasize that the cyclic model and its electronic structure representation within the approximation of one open shell (ROHF) are not related to semiempirical calculations and are quite feasible in *ab initio* quantum chemistry. For this reason, details of the geometrical parametrization of graphite and its properties are hereafter omitted.

4. CALCULATION OF AUGER PROCESS THRESHOLDS

It should be emphasized once again that the above-stated method for calculating the Auger process thresholds can be feasible at any level of quantum chemistry with MOs (*ab initio*, semiempirical, tight-binding approximation). However, since numerical results are considered below, we first of all discuss the quantum-chemical formalism of the software developed by the author. These data were published in parts (semiempirical implementations of the conventional Hartree–Fock–Roothaan method always differ in some details associated with the class of problems to be solved): the Fock matrix construction for the self-consistency cycle [7]; implementation of the self-consistent field (ΔSCF) method for electron excitations [8]; the procedure of orthogonal transformation of MOs of a degenerate electron shell, which is necessary to relate these MOs to equivalent wave vectors, i.e., subshells [9]; and the calculation features associated with the cyclic model of the crystal, which are important in estimating charge corrections in the Auger process models described by Eqs. (2) and (3) [9].

To demonstrate the quality of the semiempirical parametrization, Fig. 1 shows the MO energy spectra obtained using self-consistent ROHF calculations of the diagonal Slater sum of the configuration $(2K)^4(\Gamma + K)$ of two cyclic models of the initial Auger-process states: (i) 2D graphite (graphene), a zero band-gap semiconductor whose Fermi surface collapses into the point K of the Brillouin zone (a 24-atom EUC), and (ii) 3D hexagonal graphite, a semimetal with a small Fermi surface (a 48-atom EUC).

The optimum basis interatomic distances are $d = 2.90a_B = 1.53$ Å (experimental value, 1.42 Å) and $c = 6.79a_B = 3.59$ Å (3.35 Å). Both spectra confirm the reliability of the calculation by showing small splitting (doubling) of the graphene bands as the interplane interaction in 3D graphite is included, except for the π bands at the Brillouin zone center Γ [10].

The orbital energy of the open shell is designated by diamonds (*1*) in Fig. 1; the dash-dotted line shows that the conduction band begins at this energy. This energy does not obey the Koopmans' theorem [7]; therefore, in contrast to the case of orbital energies of closed and virtual shells, this theorem cannot be applied to estimate the energy of one-electron excitations, in particular, to determine the Fermi level. By decreasing or increasing the number of electrons of the EUC by two, we obtain quantum-chemical models of the final states of Auger processes, namely, diagonal Slater sums of the configurations $(2K)^2(\Gamma + K)$ and $(2K)^6(\Gamma + K)$ with open-shell coefficients [6]. As a result, the following terms or Slater sums of almost degenerate terms turned out to be ground states:

$$E(N) = A'_{1\chi}(\Gamma) = \frac{\alpha\beta\alpha\beta}{\sqrt{4}} \sum_{i=1,2} \sum_{j=1,2} K'_i K'_i K''_j K''_j = -5657.65 \text{ eV } (-2828.53 \text{ eV}), \quad (5)$$

$$E(N-2) = \frac{1}{4}[A'_{1\psi}(\Gamma) + A'_{2\psi}(\Gamma) + 2E'_{\psi}(\Gamma)] = -5658.67 \text{ eV } (-2829.02 \text{ eV}), \quad (6)$$

$$E(N+2) = \frac{1}{4}[A'_{1\varphi}(\Gamma) + A'_{2\varphi}(\Gamma) + 2E'_{\varphi}(\Gamma)] = -5653.65 \text{ eV } (-2823.96 \text{ eV}), \quad (7)$$

where only the states of the open shell are given, α and β are the spin basis functions, and the numerical values for the 24-atom model of 2D graphite are parenthesized.

Spectroscopic combinations of the Slater determinants for the terms entering in diagonal Slater sums (6) and (7) and their open-shell coefficients are given by

$$A'_{1\psi}(\Gamma) = \frac{1}{\sqrt{4}}(\psi_{11} + \psi_{22})(\alpha\beta - \beta\alpha),$$

$$A'_{2\psi}(\Gamma) = \frac{1}{\sqrt{4}}(\psi_{12} - \psi_{21})(\alpha\beta - \beta\alpha),$$

$$E'_{\psi}(\Gamma) = \frac{1}{\sqrt{8}}[(\psi_{11} - \psi_{22}) \pm (\psi_{12} + \psi_{21})](\alpha\beta - \beta\alpha),$$

$$\psi_{ij} = K'_i K''_j$$

and are tabulated in [6].

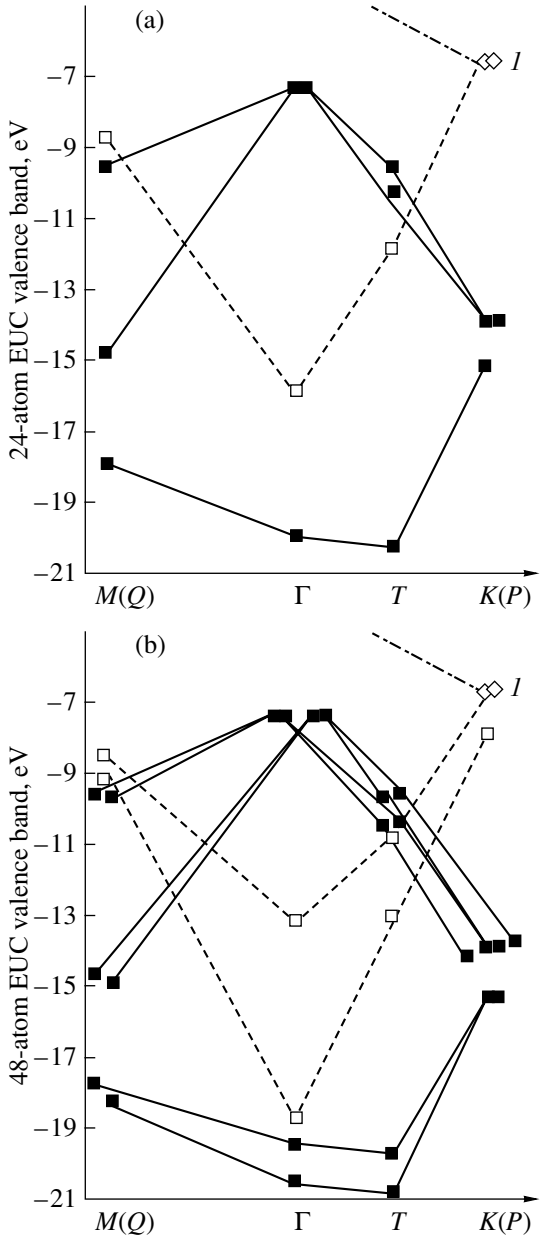

Fig. 1. Spectra of molecular orbitals of cyclic models of (a) 2D and (b) 3D graphite. Closed squares and solid lines are σ bands, and open squares and dashed lines are π bands; numeral *1* indicates the open-shell states.

Analogous terms of the mixed-filling type (with subscript φ) entering into Eq. (7) have other open-shell coefficients and can be determined using the same formulas with the substitutions

$$\psi \longrightarrow \varphi, \quad (\alpha\beta - \beta\alpha) \longrightarrow \alpha\beta\alpha\beta(\alpha\beta - \beta\alpha),$$

$$\varphi_{ij} = (\bar{K}'_i \bar{K}'_i)(\bar{K}''_i \bar{K}''_j) K'_i K''_j.$$

Formally, these terms should be split by combinations of three non-Hartree–Fock Coulomb integrals, which

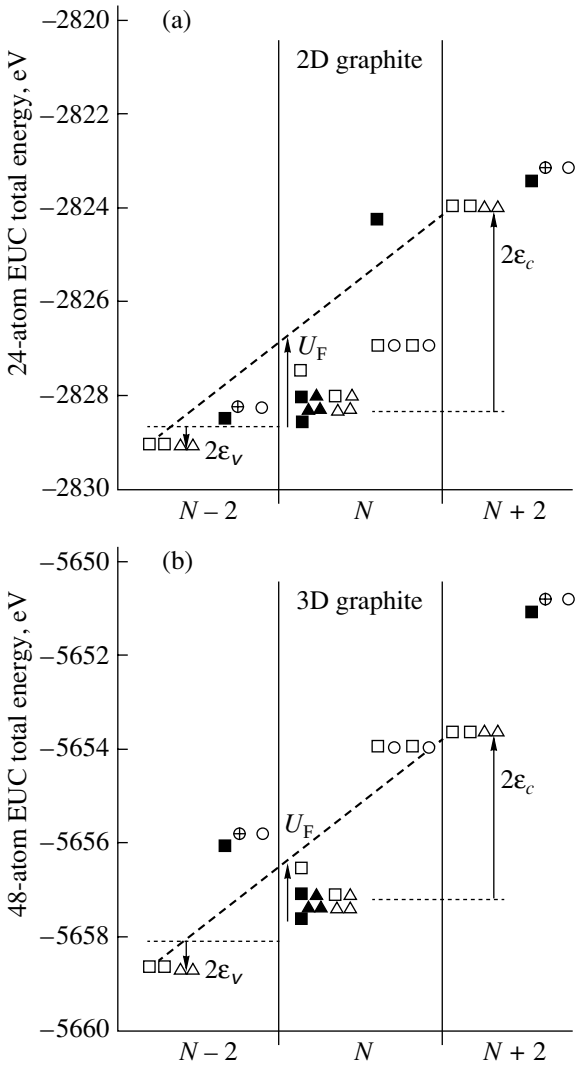

Fig. 2. Determination of the Auger process thresholds for cyclic models of (a) 2D and (b) 3D graphite. The terms of the three multiplets are separated by vertical lines and grouped in column pairs. The left-hand and right-hand columns contain the wave vectors Γ and *K*, respectively. Squares, triangles (symbols are paired in the case of double degeneracy), and circles designate the terms belonging to the representations *A*', *E*', and (*E*', *i*), respectively. Closed symbols show the pairing type of filling χ. The notations allow one to determine the term type using the tables from [6].

involve all four MOs of the open shell [6]. In fact, all these integrals strictly vanish. It is not necessary to perform a group-theoretic analysis, since direct calculation with a symmetrization procedure yields zero values for all three integrals at all values of the parameters (which is another argument in favor of a maximum complete consideration of the symmetry in quantum-chemical calculations).

Figure 2 shows the self-consistently calculated complete multiplet structures of the models of the initial and final states of Auger processes. For convenience, in the tables from [6], the terms are designated by different symbols [see (a–c) in item (ii) of Section 3]. Applying definition (4) to energies (5)–(7), we immediately obtain a numerical estimate of the observed effective electron correlation at the Fermi surface of 3D (2D in parentheses) graphite,

$$U_F = 1.5 \text{ eV } (2.0 \text{ eV}). \tag{8}$$

We estimate Auger process thresholds (2) and (3) by determining the charge corrections. According to their definition, we need to estimate the change in the total energy of the model caused by a change in the total charge of cores at a fixed state of the system of valence electrons. The total energy terms containing the charge correction are involved in any quantum-chemical calculation. In the model we proposed, this term is the "Madelung" energy E^{M} defined as the energy of atomic cores in their field (repulsion) and in the self-consistent field of the valence electrons (attraction). This total energy component should be calculated to control convergence of lattice sums [11]; specific implementations [9] are not of principle importance. Since this part of the total energy is proportional to the squared charge of the atomic core (all cores of the model are identical) and since an identical extra charge is placed on each core (to retain the entire model neutrality) as the number of valence electrons changes by *i*, we have the simple proportionality

$$E^{\mathrm{M}}(N \pm i) \sim \left(1 \pm \frac{i}{N}\right)^2.$$

It follows from this relation (and it is confirmed by calculations) that the Madelung energies for the sequence of states (6), (5), and (7) with a gradually increasing number of electrons form a uniform series. Hence, simple averaging is sufficient to estimate the charge corrections (in electronvolts):

$$\Delta(N \pm 1) \approx \pm\frac{1}{2}[E^{\mathrm{M}}(N \pm 2) - E^{\mathrm{M}}(N)] = \begin{matrix} 5.047\ (4.697), \\ 5.052\ (4.798) \end{matrix}$$

(the values for 2D graphite are in parentheses). The error in linearity is of the same order of smallness as the difference in the determined charge corrections. Graphic subtraction for determining the Auger process thresholds, carried out at a Fermi energy of 4.6 eV [2] (the work function of semimetal 3D graphite), is shown in Fig. 2: the level $E(N)$ is shifted by $\pm[\Delta(N \pm 1) - \varepsilon_F]$. Half differences between the obtained levels and the final-state energies $E(N \pm 2)$ yield the sought thresholds according to Eqs. (2) and (3). For 3D graphite (Fig. 2b), we get

$$\begin{aligned} \varepsilon_v &= \frac{1}{2}(4.0 \text{ eV} - \varepsilon_F) = -0.3 \text{ eV}, \\ \varepsilon_c &= \frac{1}{2}(-1.1 \text{ eV} + \varepsilon_F) = +1.8 \text{ eV}. \end{aligned} \tag{9}$$

These formulas correspond to the performed calculation, within which ε_F cannot be accurately determined; these numerical estimations are carried out with an experimental value of 4.6 eV for the Fermi energy [2]. The same value was also substituted into the formulas for the thresholds for 2D graphite (Fig. 2a),

$$\varepsilon_v = \frac{1}{2}(4.2\ \text{eV} - \varepsilon_F) = -0.2\ \text{eV},$$
$$\varepsilon_c = \frac{1}{2}(-0.2\ \text{eV} + \varepsilon_F) = +2.2\ \text{eV}, \quad (10)$$

although the Fermi energy in graphene apparently differs from that in 3D graphite. We note that the indicated numerical estimates of the thresholds and of the effective correlation depend only weakly on the conditions for summing the exchange matrix elements, in contrast to other model properties (upper levels of the valence band, the elastic moduli, the multiplet levels of the open shell in the ground state) [9]. Moreover, the determined values of the Auger process thresholds are size-consistent; i.e., they do not contain a proportional dependence on the model size, as seen from Fig. 2, where the same energy range (10 eV) is shown for the 24- and 48-atom models. This independence shows that the calculation procedure is reliable and that the results reflect the real properties of open-shell electrons rather than artifacts depending on quantum-chemical parameters.

The first of the thresholds (9) determined for holes agrees with the conclusion (based on experimental data [1]) that the correlation correction to the forward Auger process is small; at least, this correction is of the order of the experimental error in determining the Fermi energy. There is also other experimental verification. The negative effective correlation ε_v can be compared to the negative critical energy of the forward Auger spectrum [1]. Its exact value is not given in [1], since this spectral region cannot be explained using the one-electron approximation and other explanations (exciton satellite of the initial core hole, correlation of final holes) were not considered. This value was determined within a unified technique for all critical points and, judging from the presented spectra, is approximately –0.8 eV.

We can see that the electron correlation at the Fermi surface of graphite should most significantly manifest itself in the inverse Auger process. The sum of the calculated thresholds does not contain the uncertainty associated with the calculated values of the charge correction and the Fermi energy in Eq. (9); therefore, it is the value (8) of the observed quantity (4) that is the main numerical prediction in this study.

5. CONCLUSIONS

The quantum-chemical method for calculating the thresholds of Auger electron spectra proposed in this paper is intended to analyze the effects of the electron correlation of final particles generated at the Fermi surface of semimetal graphite, namely, two holes in the forward Auger process or two conduction electrons in the inverse process. Since it is oriented toward a specific electron system, i.e., is conceptually a materials-science approach, this method loses in generality in comparison with analytical methods based on approximations, such as the Hubbard model [12–15]. However, this approach has certain advantages.

(i) No special approximations are required to describe the "direct" correlation of final particles in the Auger process. Within a quantum-chemical model, this Coulomb interaction is necessarily included in the self-consistent Hartree–Fock approximation and in the correlation calculated in the open-shell approximation.

(ii) The range of application of our method is dictated by the feasibility of constructing a quantum-chemical model rather than by restrictions on the effective Hamiltonian (because an accurate description can be made for closed shells, for atomic spectra of adsorbates or impurities weakly affected by band electrons).

The difference in the calculated thresholds for the Auger electron spectra between 2D and 3D graphite [see Eqs. (9), (10)], as well as their relation to the Fermi energy, shows that the experimental technique based on measuring the threshold energies is promising in the spectroscopy of materials based on 2D graphite, where the substrate and/or adsorbate can change the Fermi energy.

ACKNOWLEDGMENTS

This study was supported by the federal program "Controlled Synthesis of Fullerenes and Other Atomic Clusters."

REFERENCES

1. L. Calliari, G. Speranza, J. C. Lascovich, and A. Santoni, Surf. Sci. **501** (3), 253 (2002).
2. F. R. McFeely, S. P. Kowalczyk, L. Ley, R. G. Cavell, R. A. Pollak, and D. A. Shirley, Phys. Rev. B **9** (12), 5268 (1974).
3. P. Skytt, P. Glans, D. C. Mancini, J.-H. Guo, N. Wassdahl, J. Nordgren, and Y. Ma, Phys. Rev. B **50** (15), 10457 (1994).
4. J. E. Houston, J. W. Rogers, Jr., R. R. Rye, F. L. Hutson, and D. E. Ramaker, Phys. Rev. B **34** (2), 1215 (1986).
5. J. A. Pople, *Nobel Prize Lecture* (Stockholm, 1998); Usp. Fiz. Nauk **172** (3), 349 (2002).
6. S. S. Moliver, Fiz. Tverd. Tela (St. Petersburg) **42** (8), 1518 (2000) [Phys. Solid State **42**, 1561 (2000)].

7. S. S. Moliver, Fiz. Tverd. Tela (St. Petersburg) **41** (3), 404 (1999) [Phys. Solid State **41**, 362 (1999)].
8. S. S. Moliver and Yu. F. Biryulin, Fiz. Tverd. Tela (St. Petersburg) **43** (5), 944 (2001) [Phys. Solid State **43**, 982 (2001)].
9. S. S. Moliver, Doctoral Dissertation (Ul'yanovsk State Univ., Ul'yanovsk, 2001).
10. M. S. Dresselhaus, G. Dresselhaus, K. Sugihara, I. L. Spain, and H. A. Goldberg, *Graphite Fibers and Filaments* (Springer, Berlin, 1988).
11. A. Shluger and E. Stefanovich, Phys. Rev. B **42** (15), 9664 (1990).
12. M. Cini and C. Verdozzi, J. Phys.: Condens. Matter **1** (40), 7457 (1989).
13. C. Verdozzi, M. Cini, J. A. Evans, R. J. Cole, A. D. Laine, P. S. Fowles, L. Duo, and P. Weightman, Europhys. Lett. **16** (8), 743 (1991).
14. G. A. Zawatzky and A. Lanselink, Phys. Rev. B **21** (5), 1790 (1980).
15. W. Nolting, G. Geipel, and K. Ertl, Phys. Rev. B **45** (11), 5790 (1992).

Translated by A. Kazantsev

Physics of the Solid State, Vol. 46, No. 9, 2004, pp. 1591–1603. Translated from Fizika Tverdogo Tela, Vol. 46, No. 9, 2004, pp. 1544–1556.
Original Russian Text Copyright © 2004 by Malishevskiĭ, Silin, Uryupin, Uspenskiĭ.

METALS AND SUPERCONDUCTORS

Vortices in a Josephson Junction Sandwiched between Two Superconducting Waveguides

A. S. Malishevskiĭ, V. P. Silin, S. A. Uryupin, and S. G. Uspenskiĭ

Lebedev Physical Institute, Russian Academy of Sciences, Leninskiĭ pr. 53, Moscow, 119991 Russia

e-mail: malish@sci.lebedev.ru

Received December 23, 2003

Abstract—For a Josephson junction magnetically coupled to the superconducting waveguides enclosing it, solutions to the equation for the difference of the Cooper pair phases over the Josephson junction are found and the corresponding magnetic field values are calculated. Two gaps imposing an upper limit for the vortex velocity are found for free vortices (moving without dissipation). Existence conditions are found for fast vortices in the two high-velocity allowed regions. The dependence of the transport current on vortex velocity is established in cases where the current flows through the Josephson junction only or through the entire structure. A reverse current phenomenon is discovered in which vortices inside allowed velocity regions move opposite to the usual direction. © *2004 MAIK "Nauka/Interperiodica".*

1. INTRODUCTION

Vortices in layered Josephson structures have attracted the attention of researchers for a long time (see, i.e., [1–3]). The interest in them is due primarily to the fact that high-temperature superconductors can be regarded as layered structures consisting of conducting layers separated by insulators, with Cooper pairs being able to tunnel through the latter [4]. Also, the properties of vortices in layered structures differ significantly from those in a single Josephson junction (JJ) [5, 6]. The reason for the appearance of these new characteristics is not only the changed spatial distribution of the magnetic field of the vortices [5] but also the possible generation of electromagnetic fields outside the JJ by moving vortices [7, 8]. In particular, changes in the properties of vortices in a JJ coupled magnetically to a planar waveguide were studied in [8]. It was shown that vortices could propagate with a velocity much higher than the Swihart velocity of the JJ. The perturbation of the phase difference between the wave functions of the superconductors in the waveguide that is generated by such a fast vortex and produces a certain electromagnetic field was also calculated in [8].

To further study the possibility of governing the vortex properties by varying the parameters of a layered structure, we consider in the present paper a vortex moving in a more complex structure consisting of a JJ coupled to two planar waveguides located on both sides of the JJ. In the case where the Swihart velocities of the waveguides V_{s1} and V_{s2} exceed the Swihart velocity V_s of the JJ, it is found that two additional allowed velocity ranges appear due to the presence of the two waveguides; in these ranges, fast vortices can move at a speed $v > V_s$. If $V_{s2} > V_s > V_{s1}$, there is only one velocity range for fast vortices, and a velocity gap appears at $v < V_s$ because of the influence of the waveguide with the Swihart velocity V_{s1}. If $V_s > V_{s1}, V_{s2}$, then the influence of the two waveguides gives rise to two velocity gaps in the region $v < V_s$. We find a relation between the transport current flowing through the JJ and the vortex velocities for all these cases. We demonstrate that, for all allowed velocities, the current sustaining vortex motion is small compared to the critical Josephson current j_c if dissipation is low both in the JJ and in the waveguides and if the vortex velocity is not too close to the boundaries of the allowed regions. The $j(v)$ dependence is found for two paths of current flow through the layered structure. In the case of a current flowing through the JJ only, induced motion of a vortex is maintained by the Lorentz force, which is due to the interaction of the current with the portion of the vortex magnetic field localized in the JJ and superconductors adjacent to it. If a current flows through the entire layered structure, then the zone of effective interaction between the current and the magnetic field becomes wider and the main contribution to the Lorentz force arises from the parts of the structure where the magnetic field is the highest. For example, the magnetic field of fast vortices is mainly concentrated in the waveguides and the superconductors bordering them. Consequently, the current flowing through these parts contributes most to the Lorentz force, which leads to a lower value of the current required to sustain induced vortex motion as compared to the case of the current flowing through the JJ only.

Another unusual phenomenon arises if at least one of the Swihart velocities, for example, V_{s1}, is smaller than V_s. In this case, the magnetic field of the vortex with a Swihart velocity just below V_{s1} in the vicinity of the waveguide is directed opposite to the magnetic field

in the JJ. As a result, as shown below, the net Lorentz force changes sign and vortices with these velocities move opposite to the direction in which vortices move at velocities far from V_{s1}. In the case when the Swihart velocities of both waveguides are smaller than V_s, there are two velocity ranges, close to V_{s1} and V_{s2}, where vortices move opposite to the direction in which vortices move at speeds far from V_{s1} and V_{s2}.

2. EQUATIONS FOR THE PHASE DIFFERENCE

Let us consider a layered structure consisting of a thin nonsuperconducting layer with dielectric constant ε and conductivity σ, located in the region $-d < x < d$, and two nonsuperconducting waveguides with dielectric constants ε_1 and ε_2 and conductivities σ_1 and σ_2, located in the regions $-L_1 - d - 2d_1 < x < -L_1 - d$ and $L_2 + d < x < L_2 + d + 2d_2$, respectively. Superconductors with thicknesses L_1 and L_2 and London penetration depths λ_1 and λ_2 separate the nonsuperconducting layers. The regions $x < -L_1 - d - 2d_1$ and $x > L_2 + d + 2d_2$ are filled by superconductors with London penetration depths λ_0 and λ_3. The waveguides are presumed to be thick enough to neglect the tunneling current of superconducting pairs through them. In this case, the structure can be considered a JJ sandwiched between two waveguides.

We assume that electromagnetic fields are independent of y and that the superconducting layers are thin enough for the magnetic field inside them to be independent of x.

The condition for the x component of the generalized current to be continuous at the interfaces between the superconducting and nonsuperconducting layers gives equations that relate the wave-function phase differences $\varphi(z, t)$, $\varphi_{w1}(z, t)$, and $\varphi_{w2}(z, t)$ for the superconductors separated by the corresponding nonsuperconducting layers to the y components of the magnetic fields $H(z, t)$, $H_1(z, t)$, and $H_2(z, t)$ in these layers:

$$\begin{aligned}
&\frac{\partial^2\varphi_{w1}(z,t)}{\partial t^2} + \beta_1\frac{\partial\varphi_{w1}(z,t)}{\partial t} = -\frac{4|e|c}{\hbar}\frac{d_1}{\varepsilon_1}\frac{\partial}{\partial z}H_1(z,t),\\
&\frac{\partial^2\varphi_{w2}(z,t)}{\partial t^2} + \beta_2\frac{\partial\varphi_{w2}(z,t)}{\partial t} = -\frac{4|e|c}{\hbar}\frac{d_1}{\varepsilon_2}\frac{\partial}{\partial z}H_2(z,t),\\
&\omega_j^2\sin\varphi(z,t) + \beta\frac{\partial\varphi(z,t)}{\partial t} + \frac{\partial^2\varphi(z,t)}{\partial t^2}\\
&\qquad = -\frac{4|e|c}{\hbar}\frac{d}{\varepsilon}\frac{\partial}{\partial z}H(z,t).
\end{aligned} \tag{1}$$

Here, $\beta = 4\pi\sigma/\varepsilon$; $\beta_i = 4\pi\sigma_i/\varepsilon_i$, $i = 1, 2$; and ω_j is the Josephson frequency ($\omega_j^2 = 16\pi|e|j_c d/\hbar\varepsilon$).

Another set of equations relating the fields to the phase differences follows from the Maxwell equations and the continuity of the magnetic field and the z component of the electric field at the interfaces [9]:

$$\begin{aligned}
a_1H(z,t) - B_1H_1(z,t) &= \frac{\hbar c}{2|e|}\frac{\partial}{\partial z}\varphi_{w1}(z,t),\\
a_2H(z,t) - B_2H_2(z,t) &= \frac{\hbar c}{2|e|}\frac{\partial}{\partial z}\varphi_{w2}(z,t),\\
a_2H_2(z,t) - B_0H(z,t) + a_1H_1(z,t) &= \frac{\hbar c}{2|e|}\frac{\partial}{\partial z}\varphi(z,t).
\end{aligned} \tag{2}$$

Here, we used the following notation:

$$\begin{aligned}
B_0 &= 2d + \lambda_1\coth(L_1/\lambda_1) + \lambda_2\coth(L_2/\lambda_2),\\
B_1 &= 2d_1 + \lambda_0 + \lambda_1\coth(L_1/\lambda_1),\\
B_2 &= 2d_2 + \lambda_3 + \lambda_2\coth(L_2/\lambda_2),\\
a_i &= \lambda_i/\sinh(L_i/\lambda_i), \quad i = 1, 2.
\end{aligned}$$

Solving the set of equations (2) for the magnetic field components, we obtain

$$\begin{aligned}
H(z,t) &= -\frac{\phi_0}{2\pi}\frac{1}{\Delta}\frac{\partial}{\partial z}[a_1B_2\varphi_{w1}(z,t)\\
&\quad + B_1B_2\varphi(z,t) + a_2B_1\varphi_{w2}(z,t)],\\
H_1(z,t) &= -\frac{\phi_0}{2\pi}\frac{1}{\Delta}\frac{\partial}{\partial z}[(B_0B_2 - a_2^2)\varphi_{w1}(z,t)\\
&\quad + a_1B_2\varphi(z,t) + a_1a_2\varphi_{w2}(z,t)],\\
H_2(z,t) &= -\frac{\phi_0}{2\pi}\frac{1}{\Delta}\frac{\partial}{\partial z}[a_1a_2\varphi_{w1}(z,t)\\
&\quad + a_2B_1\varphi(z,t) + (B_0B_1 - a_1^2)\varphi_{w2}(z,t)],
\end{aligned} \tag{3}$$

where $\Delta = B_0B_1B_2 - a_2^2B_1 - a_1^2B_2$ and $\phi_0 = \pi\hbar c/|e|$ is the magnetic flux quantum. Substituting these magnetic fields into the first and second equations in set (1), which describe the waveguides, we get

$$\begin{aligned}
\frac{\partial^2\varphi_{w1}(z,t)}{\partial t^2} + \beta_1\frac{\partial\varphi_{w1}(z,t)}{\partial t} &= V_{s1}^2\frac{\partial^2\varphi_{w1}(z,t)}{\partial z^2}\\
&\quad + S_{10}V_{s1}^2\frac{\partial^2\varphi(z,t)}{\partial z^2} + S_{10}S_{02}V_{s1}^2\frac{\partial^2\varphi_{w2}(z,t)}{\partial z^2},\\
\frac{\partial^2\varphi_{w2}(z,t)}{\partial t^2} + \beta_2\frac{\partial\varphi_{w2}(z,t)}{\partial t} &= V_{s2}^2\frac{\partial^2\varphi_{w2}(z,t)}{\partial z^2}\\
&\quad + S_{20}V_{s2}^2\frac{\partial^2\varphi(z,t)}{\partial z^2} + S_{01}S_{20}V_{s2}^2\frac{\partial^2\varphi_{w1}(z,t)}{\partial z^2}.
\end{aligned} \tag{4}$$

From the third equation in set (1), which describes the JJ, we get

$$\omega_j^2 \sin\varphi(z,t) + \beta\frac{\partial\varphi(z,t)}{\partial t} + \frac{\partial^2\varphi(z,t)}{\partial t^2} = V_s^2\frac{\partial^2\varphi(z,t)}{\partial z^2} + S_{01}V_s^2\frac{\partial^2\varphi_{w1}(z,t)}{\partial z^2} + S_{02}V_s^2\frac{\partial^2\varphi_{w2}(z,t)}{\partial z^2}. \quad (5)$$

Equations (4) and (5) constitute a closed set of equations for the phase differences. Here, V_s, V_{s1}, and V_{s2} are the Swihart velocities of the JJ and the waveguides magnetically coupled to each other,

$$V_s^2 = c^2\frac{2d}{\varepsilon}\frac{B_1B_2}{\Delta}, \quad V_{s1}^2 = c^2\frac{2d_1}{\varepsilon_1}\frac{B_0B_2 - a_2^2}{\Delta},$$

$$V_{s2}^2 = c^2\frac{2d_2}{\varepsilon_2}\frac{B_0B_1 - a_1^2}{\Delta},$$

S_{10} and S_{20} are the coupling constants describing the influence of the JJ on the first and second waveguides, respectively,

$$S_{10} = \frac{a_1B_2}{B_0B_2 - a_2^2}, \quad S_{20} = \frac{a_2B_1}{B_0B_1 - a_1^2},$$

and S_{01} and S_{02} are the coupling constants describing the influence of the waveguides on the JJ, $S_{01} = a_1/B_1$ and $S_{02} = a_2/B_2$. It should be stressed that the Swihart velocities V_s, V_{s1}, and V_{s2} are defined with allowance for the interaction between the JJ and the waveguides. Clearly, in the limit of large distances between the nonsuperconducting layers, all coupling constants vanish and the quantities V_s, V_{s1}, and V_{s2} approach the Swihart velocities of the isolated JJ and waveguides.

3. FREE-MOVING JOSEPHSON VORTICES

Let us consider vortices in free motion at constant speed v along the z axis. Such motion is possible, in particular, if dissipation in the nonsuperconducting layers is negligible. Dropping β, β_1, and β_2 from Eqs. (4) and (5), we obtain

$$\begin{aligned}
&(V_{s1}^2 - v^2)\psi_{w1}''(\zeta) + S_{10}V_{s1}^2\psi''(\zeta) + S_{10}S_{02}V_{s1}^2\psi_{w2}''(\zeta) = 0,\\
&(V_{s2}^2 - v^2)\psi_{w2}''(\zeta) + S_{20}V_{s2}^2\psi''(\zeta) + S_{01}S_{20}V_{s2}^2\psi_{w1}''(\zeta) = 0,\\
&S_{01}V_s^2\psi_{w1}''(\zeta) + S_{02}V_s^2\psi_{w2}''(\zeta) + (V_s^2 - v^2)\psi''(\zeta) = \omega_j^2\sin\psi(\zeta).
\end{aligned} \quad (6)$$

Here, $\psi(\zeta) = \varphi(z,t)$, $\psi_{w1}(\zeta) = \varphi_{w1}(z,t)$, and $\psi_{w2}(\zeta) = \varphi_{w2}(z,t)$, with $\zeta = z - vt$. From the first two equations in set (6), we find

$$\begin{aligned}
\psi_{w1}''(\zeta) &= S_{10}V_{s1}^2\\
&\times\frac{v^2 - (1 - S_{20}S_{02})V_{s2}^2}{(V_{s1}^2 - v^2)(V_{s2}^2 - v^2) - S_{01}S_{10}S_{02}S_{20}V_{s1}^2V_{s2}^2}\psi''(\zeta),\\
\psi_{w2}''(\zeta) &= S_{20}V_{s2}^2\\
&\times\frac{v^2 - (1 - S_{10}S_{01})V_{s1}^2}{(V_{s1}^2 - v^2)(V_{s2}^2 - v^2) - S_{01}S_{10}S_{02}S_{20}V_{s1}^2V_{s2}^2}\psi''(\zeta).
\end{aligned} \quad (7)$$

Substituting Eqs. (7) into the third equation in set (6), we get an equation for $\psi(\zeta)$,

$$\sin\psi(\zeta) = k_j^{-2}(v)\psi''(\zeta), \quad (8)$$

where $k_j(v)$ is defined as

$$\omega_j^2k_j^{-2}(v) = \frac{(v_0^2 - v^2)(v_1^2 - v^2)(v_2^2 - v^2)}{(\tilde{v}_1^2 - v^2)(\tilde{v}_2^2 - v^2)}. \quad (9)$$

Here, v_0, v_1, and v_2 are the roots of the equation

$$\begin{aligned}
&(V_s^2 - v^2)(V_{s1}^2 - v^2)(V_{s2}^2 - v^2)\\
&- S_{01}S_{10}V_s^2V_{s1}^2(V_{s2}^2 - v^2) - S_{02}S_{20}V_s^2V_{s2}^2(V_{s1}^2 - v^2)\\
&+ S_{01}S_{10}S_{02}S_{20}V_{s1}^2V_{s2}^2(V_s^2 + v^2) = 0,
\end{aligned} \quad (10)$$

and the positive quantities given by

$$\tilde{v}_n^2 = \frac{V_{s1}^2 + V_{s2}^2}{2} + \frac{(-1)^n}{2}\sqrt{(V_{s1}^2 - V_{s2}^2)^2 + 4S_{01}S_{10}S_{02}S_{20}V_{s1}^2V_{s2}^2}, \quad n = 1, 2,$$

are the roots of the equation

$$(V_{s1}^2 - v^2)(V_{s2}^2 - v^2) - S_{01}S_{10}S_{02}S_{20}V_{s1}^2V_{s2}^2 = 0. \quad (11)$$

The solution to Eq. (8) that corresponds to a stable elementary vortex (2π kink) moving at constant velocity v is given by

$$\psi(\zeta) = 4\arctan\{\exp(k_j(v)\zeta)\}. \quad (12)$$

This solution describes a vortex only if $k_j(v)$, defined by Eq. (9), is real. For example, if the coupling constants S_{10}, S_{20}, S_{01}, and S_{02} are sufficiently small, an elementary vortex can move in one of three velocity ranges: (1) from zero to the smallest root of Eq. (10), (2) from the smallest root of Eq. (11) to the middle of the three roots of Eq. (10), and (3) from the largest root of Eq. (11) to the largest root of Eq. (10).

If the coupling constants S_{10}, S_{20}, S_{01}, and S_{02} are small and the Swihart velocities V_s, V_{s1}, and V_{s2} do not coincide with each other ($V_{s2} > V_{s1}$), the roots of Eq. (11) are given by

$$\begin{aligned}\tilde{v}_1 &= V_{s1} + O(S_{01}S_{10}S_{02}S_{20}),\\ \tilde{v}_2 &= V_{s2} + O(S_{01}S_{10}S_{02}S_{20}),\end{aligned} \tag{13}$$

and the roots of Eq. (10) are approximately equal to

$$\begin{aligned}v_0 &\approx V_s\left(1 + \frac{1}{2}S_{01}S_{10}\frac{V_{s1}^2}{V_s^2 - V_{s1}^2} + \frac{1}{2}S_{02}S_{20}\frac{V_{s2}^2}{V_s^2 - V_{s2}^2}\right),\\ v_1 &\approx V_{s1}\left(1 + \frac{1}{2}S_{01}S_{10}\frac{V_s^2}{V_{s1}^2 - V_s^2}\right),\\ v_2 &\approx V_{s2}\left(1 + \frac{1}{2}S_{02}S_{20}\frac{V_s^2}{V_{s2}^2 - V_s^2}\right).\end{aligned} \tag{14}$$

When the Swihart velocity of the JJ is small compared to the Swihart velocities of the waveguides ($V_s \ll V_{s1} < V_{s2}$), the roots of Eq. (10) are given by the simple expressions

$$\begin{aligned}v_0 &\approx V_s[1 - (S_{01}S_{10} + S_{02}S_{20})/2],\\ v_1 &\approx V_{s1}\left(1 + \frac{1}{2}S_{01}S_{10}\frac{V_s^2}{V_{s1}^2}\right),\\ v_2 &\approx V_{s2}\left(1 + \frac{1}{2}S_{02}S_{20}\frac{V_s^2}{V_{s2}^2}\right).\end{aligned}$$

In this case, there are two relatively narrow velocity ranges ($\tilde{v}_1$, v_1) and ($\tilde{v}_2$, v_2) where the 2π kink can move at a speed much higher than the Swihart velocity in the JJ. As in [8], we can assume that there are fast Josephson vortices whose velocity lies in these ranges and significantly exceeds the Swihart velocity in the JJ, the limiting speed for a vortex moving in a solitary JJ. In contrast to [8], in the structure under study here, consisting of a JJ and two waveguides magnetically coupled to it, there are two (rather than one) ranges in which the velocity of fast vortices lie; therefore, we can refer to them as the first and second fast vortices.

Let us consider another simple limiting case of $V_{s1} \ll V_s < V_{s2}$. This case takes place, for example, if the London penetration depths of superconductors are close in value, $\lambda_0 \approx \lambda_1 \approx \lambda_2 \approx \lambda_3 \approx \lambda$, and $\varepsilon_1(d_1 + \lambda)/d_1 \gg \varepsilon(d_1 + \lambda)/d > \varepsilon_2(d_2 + \lambda)/d_2$. In this case, the roots of Eq. (10) are

$$\begin{aligned}v_0 &\approx V_s\left(1 - \frac{1}{2}S_{02}S_{20}\frac{V_{s2}^2}{V_{s2}^2 - V_s^2}\right),\\ v_1 &\approx V_{s1}(1 - S_{01}S_{10}/2),\\ v_2 &\approx V_{s2}\left(1 + \frac{1}{2}S_{02}S_{20}\frac{V_s^2}{V_{s2}^2 - V_s^2}\right).\end{aligned}$$

Let us compare these results to the data from [8], where a structure consisting of a JJ magnetically coupled to one waveguide was considered. It is evident that the addition of a second waveguide with a relatively small Swihart velocity V_{s1} leads to a narrow gap near V_{s1}, where an allowed velocity range was before. However, if a waveguide with a Swihart velocity V_{s2} higher than the Swihart velocity of the JJ is added, a narrow velocity range of allowed vortex motion arises. In the latter case, if the Swihart velocity of the second waveguide is much higher than that of the JJ ($V_s \ll V_{s2}$), we can say that a fast Josephson vortex appears.

If the Swihart velocities of both waveguides are smaller than the Swihart velocity of the JJ ($V_{s1} < V_{s2} < V_s$), the effect of the waveguides is that a vortex can move with velocities $v < V_s$ lying in three ranges separated by two relatively narrow gaps located near the Swihart velocities of the waveguides.

Let us discuss now three special cases that are outside the field of application of Eqs. (13) and (14). One of them is the case where all three Swihart velocities coincide ($V_s = V_{s1} = V_{s2}$); the solutions to Eq. (11) are given by

$$\begin{aligned}\tilde{v}_1 &\approx V_{s1}\left(1 - \frac{1}{2}\sqrt{S_{01}S_{10}S_{02}S_{20}}\right),\\ \tilde{v}_2 &\approx V_{s1}\left(1 + \frac{1}{2}\sqrt{S_{01}S_{10}S_{02}S_{20}}\right),\end{aligned}$$

and the roots of Eq. (10) are

$$\begin{aligned}v_0 &= V_s + O(S_{01}S_{10} + S_{02}S_{20}),\\ v_1 &\approx V_s\left(1 - \frac{1}{2}\sqrt{S_{01}S_{10} + S_{02}S_{20}}\right),\\ v_2 &\approx V_s\left(1 + \frac{1}{2}\sqrt{S_{01}S_{10} + S_{02}S_{20}}\right).\end{aligned}$$

In this case, there are two relatively narrow gaps (in the vicinity of the Swihart velocity) for the velocity of an elementary vortex.

In the other case, the Swihart velocities of the JJ and one of the waveguides are equal ($V_s = V_{s1} \neq V_{s2}$); the solutions to Eq. (11) are still given by Eqs. (13), while the solutions to Eq. (10) are described by the approximate expressions

$$v_0 \approx V_s\left(1 - \frac{1}{2}\sqrt{S_{01}S_{10}}\right), \quad v_1 \approx V_s\left(1 + \frac{1}{2}\sqrt{S_{01}S_{10}}\right),$$

$$v_2 \approx V_{s2}\left(1 + \frac{1}{2}S_{02}S_{20}\frac{V_s^2}{V_{s2}^2 - V_s^2}\right).$$

If, in addition, $V_s < V_{s2}$, then there is a relatively narrow gap close to the Swihart velocity V_s and a narrow allowed velocity range near the gap. Another narrow region of allowed motion of an elementary vortex is close to V_{s2}. If $V_s \ll V_{s2}$, fast vortex motion is possible in this region. However, if $V_{s2} < V_s$, then there are relatively narrow gaps close to each of the Swihart velocities.

In the third special case, the Swihart velocities of the waveguides are equal and much higher than the Swihart velocity of the JJ ($V_s \ll V_{s1} = V_{s2}$) and the motion of an elementary vortex is possible at a speed (much higher than the Swihart velocity of the JJ) inside two narrow ranges close to $V_{s1} = V_{s2}$ and separated by a relatively narrow gap. The width of the allowed ranges in this case is $\sim(S_{01}S_{10} + S_{02}S_{20})V_s^2/V_{s1}$. It should be stressed that the same pattern of allowed velocity ranges and gaps for vortex motion takes place for $v < 0$.

4. MAGNETIC FIELD OF A FREE-MOVING VORTEX

A vortex moving through the layered structure is characterized by a certain spatial distribution of the magnetic field. The fields inside the nonsuperconducting layers are given by Eqs. (3), (7), and (12), and the magnetic field inside the superconductors is related to the field inside the JJ and waveguides by

$$\begin{aligned}
&H(x < -L_1 - d - 2d_1, z, t)\\
&= H_1(z, t)\exp[(x + L_1 + d + 2d_1)/\lambda_0],\\
&H(-L_1 - d < x < -d, z, t)\\
&= H(z, t)\frac{\sinh[(x + L_1 + d)/\lambda_1]}{\sinh(L_1/\lambda_1)}\\
&- H_1(z, t)\frac{\sinh[(x + d)/\lambda_1]}{\sinh(L_1/\lambda_1)},\\
&H(d < x < d + L_2, z, t)\\
&= H_2(z, t)\frac{\sinh[(x - d)/\lambda_2]}{\sinh(L_2/\lambda_2)}\\
&- H(z, t)\frac{\sinh[(x - d - L_2)/\lambda_2]}{\sinh(L_2/\lambda_2)},\\
&H(x > d + L_2 + 2d_2, z, t)\\
&= H_2(z, t)\exp[-(x - L_2 - d - 2d_2)/\lambda_2].
\end{aligned} \tag{15}$$

It follows from Eq. (12) that the characteristic scale of the variations of the vortex magnetic field along the z axis is determined by $k_j^{-1}(v)$, which depends on vortex velocity and is given by Eq. (9). It is clear from Eq. (9) that the field variation scale along the z axis decreases with the vortex velocity v approaching one of the roots of Eq. (10) and increases as v approaches roots of Eq. (11).

The distribution of the vortex magnetic field along the x axis is described in full by formulas (15). It is evident that the London penetration depths of the superconductors are characteristic scales of field variations along this axis. However, the magnetic field distribution depends on both the vortex speed and the proportion between the Swihart velocities of the JJ and waveguides.

The magnetic field distributions are presented in Fig. 1 for all cases studied. The graphs are plotted according to Eqs. (3), (7), (12), and (15) for $t = 0$ for the case where $\lambda_0 = \lambda_1 = \lambda_2 = \lambda_3 = \lambda$ and $L_1 = L_2 = \lambda$. We also assumed that the widths of the waveguides are significantly less than λ. This kind of relation between L_1, L_2 and the London penetration depths corresponds to the coupling constants $S_{01} = S_{10} = S_{02} = S_{20} \approx 0.4$. All the graphs have a common maximum of the magnetic field as a function of z at the point $z = 0$ and confinement of the field along the x axis to layers of thickness λ near the boundaries of the superconductors, which is a manifestation of the Meissner effect. Therefore, we will assume that the magnetic field is concentrated near a nonsuperconducting layer.

Let us consider the case of $V_{s2} = 2V_{s1} = 6V_s$. With such a relation between the Swihart velocities of the JJ and the waveguides, the motion of an elementary vortex is possible inside the wide velocity range $v < v_0 \sim V_s$ and in two narrow velocity ranges close to V_{s1} and V_{s2}. The magnetic field of a vortex has a specific distribution in each of the allowed ranges. The distribution of the magnetic field of a slow vortex with speed $v = 0.6V_s < v_0 \sim V_s$ is shown in Fig. 1a. It is seen that the field of such a vortex is mainly concentrated close to the JJ, which is positioned in the $x = 0$ plane in Fig. 1a. The magnetic field distribution of the first fast vortex is shown in Fig. 1b. Unlike the slow vortex, the magnetic field in this case is concentrated close to the first waveguide, which is positioned in the $x = -\lambda$ plane in the figure. The magnetic field of the second fast vortex is mainly concentrated close to the second waveguide, which is in the $x = \lambda$ plane. The field distribution of this vortex is similar to that shown in Fig. 1b, but the field is concentrated near the second waveguide.

Let us consider now the case of $V_{s2} = 4V_s/3 = 2V_{s1}$. In this case, there are two relatively wide and one narrow velocity range allowed for the motion of an elementary vortex. The magnetic field of a slow vortex moving at speed $v < v_1 \sim V_{s1}$ is shown in Figs. 1c and 1d. The magnetic field is concentrated mainly near the JJ, as can be seen from Fig. 1c, which shows the field of a vortex moving at a speed $v = 0.5V_{s1}$ corresponding to

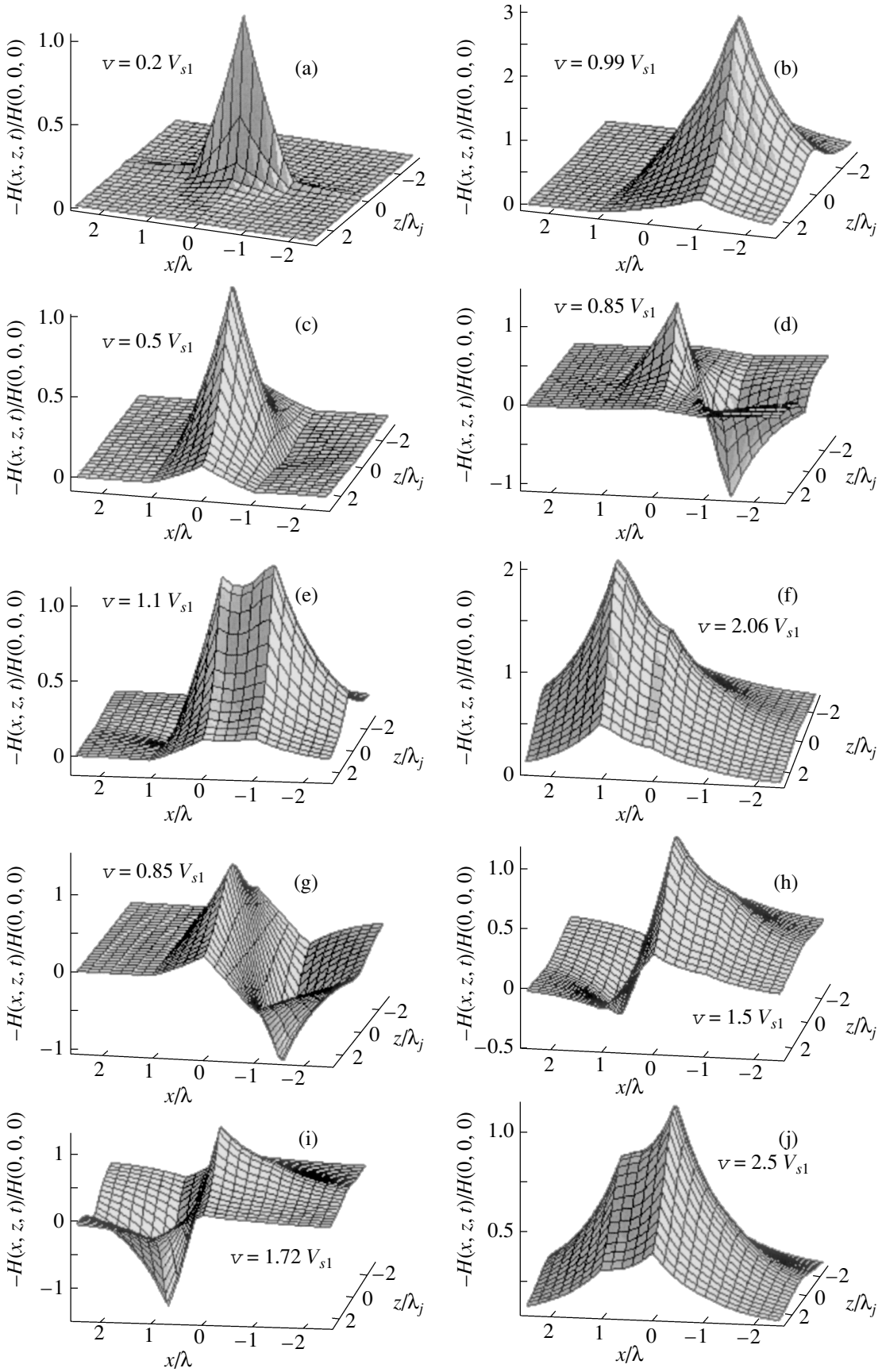

Fig. 1. Magnetic field distribution of a vortex for (a, b) $V_s = V_{s1}/3$, $V_{s2} = 2V_{s1}$; (c–f) $V_s = 3V_{s1}/2$, $V_{s2} = 2V_{s1}$; and (g–j) $V_s = 3V_{s1}$, $V_{s2} = 2V_{s1}$.

the middle of the allowed range. It is also seen that the magnetic field near the first waveguide changes sign. The influence of a slow vortex on the field distribution intensifies as the vortex velocity increases and approaches the Swihart velocity of the first waveguide. The magnetic field distribution of a slow vortex in the part of the allowed range adjacent to the Swihart velocity of the first waveguide is shown in Fig. 1d. In this case, the magnetic field in the structure, for the most part, reverses sign under the influence of the waveguide. Figure 1e shows the magnetic field distribution of a vortex moving at speed $v = 1.1V_{s1}$, which corresponds to the middle of the wide allowed range $\tilde{v}_1 \approx V_{s1} < v < v_0 \sim V_s$. In this case, the magnetic field is concentrated in the superconductors close to the first waveguide and the JJ. The magnetic field distribution of a fast vortex moving with a speed in the narrow allowed range near the Swihart velocity of the second waveguide is shown in Fig. 1f. Similar to the fast vortex presented in Fig. 1b, the field is mainly concentrated close to this waveguide, whose influence gives rise to the narrow allowed range.

Finally, let us discuss the spatial distribution of the magnetic field of vortices in the case where $V_s = 3V_{s2}/2 = 3V_{s1}$. In this case, vortex motion is allowed in three wide velocity ranges separated by two narrow gaps. The magnetic field of a vortex moving at a speed in the middle of the allowed range $v < v_1 \sim V_{s1}$ is similar to that shown in Fig. 1a.

The magnetic field distribution of a vortex moving with a speed in the range $v < v_1 \sim V_{s1}$ but closer to $v_1 \sim V_{s1}$ is shown in Fig. 1g. Similar to the vortex presented in Fig. 1d, the magnetic field reversed sign in the superconductors in the regions near the first waveguide. Figures 1h and 1i show the magnetic field distribution of vortices moving with speeds in the allowed range $\tilde{v} \approx V_{s1} < v < v_2 \sim V_{s2}$. A vortex moving at speed $v = 1.5V_{s1}$, which corresponds to the middle of this allowed range, is presented in Fig. 1h. It is seen that near the second waveguide the magnetic field changes sign. Similar to the previous cases (Figs. 1c, 1d), the influence of the second waveguide intensifies as the speed of the vortex approaches $v_2 \sim V_{s2}$. If the vortex moves at a speed close to $v_2 \sim V_{s2}$, most of its magnetic flux reverses sign (Fig. 1i). The magnetic field distribution of a vortex moving at a speed in the middle of the third wide allowed range $\tilde{v}_2 \approx V_{s2} < v < v_0 \sim V_s$ is shown in Fig. 1j. The magnetic field of this vortex is concentrated in the superconductors adjacent to the JJ and to the second waveguide.

The graphs shown in Fig. 1 present the entire variety of magnetic field distributions of elementary vortices that can move in the structure consisting of a JJ and two waveguides coupled to it. The data on the magnetic field of vortices discussed in this section are important for the development of various methods for sustaining induced motion of vortices by passing a current through layered structures.

5. INDUCED VORTEX MOTION

Let us examine vortex motion induced by a transport current with density j flowing through the JJ along the x axis. In this case, the phase differences are described by the two equations in (4) and Eq. (5), in which the current density is introduced:

$$\omega_j^2 \sin\varphi(z,t) + \frac{\partial^2\varphi(z,t)}{\partial t^2} + \omega_j^2\frac{j}{j_c} + \beta\frac{\partial\varphi(z,t)}{\partial t} = V_s^2\frac{\partial^2\varphi(z,t)}{\partial z^2} + S_{01}V_s^2\frac{\partial^2\varphi_{w1}(z,t)}{\partial z^2} + S_{02}V_s^2\frac{\partial^2\varphi_{w2}(z,t)}{\partial z^2}. \quad (16)$$

Similar to the previous section, we only consider vortices moving at a constant speed. With the help of an approximate solution to Eqs. (4) for the case of negligible dissipation in the nonsuperconducting layers (see Appendix), we represent Eq. (16) in the form (cf. Eq. (8))

$$\sin\psi(\zeta) - k_j^{-2}(v)\psi''(\zeta) + \frac{j}{j_c} = \frac{v\beta(v)}{\omega_j^2}\psi'(\zeta), \quad (17)$$

where we introduced the notation

$$\beta(v) = \beta + \beta_1 V_s^2 V_{s1}^2 S_{01}S_{10}\frac{(V_{s2}^2 - v^2 - S_{02}S_{20}V_{s2}^2)^2}{(\tilde{v}_1^2 - v^2)^2(\tilde{v}_2^2 - v^2)^2} + \beta_2 V_s^2 V_{s2}^2 S_{02}S_{20}\frac{(V_{s1}^2 - v^2 - S_{01}S_{10}V_{s1}^2)^2}{(\tilde{v}_1^2 - v^2)^2(\tilde{v}_2^2 - v^2)^2}.$$

In the limit of small coupling constants S_{10}, S_{20}, S_{01}, and S_{02}, we obtain from Eq. (17) (cf. [8])

$$\beta(v) \approx \beta + \beta_1 S_{01}S_{10}\frac{V_s^2 V_{s1}^2}{(V_{s1}^2 - v^2)^2} + \beta_2 S_{02}S_{20}\frac{V_s^2 V_{s2}^2}{(V_{s2}^2 - v^2)^2}. \quad (18)$$

This expression holds when the coupling between the waveguides can be completely disregarded.

Using the formal similarity between Eq. (17) and the equation describing uniform motion of a vortex in a solitary JJ, we can obtain, following [10], a relation between the transport current density and vortex velocity,

$$\left[\frac{j(v)}{j_c}\right]_{JJ} = \frac{4}{\pi}\frac{\beta(v)vk_j(v)}{\omega_j^2}. \quad (19)$$

Let us discuss Eq. (19) for a structure consisting of a JJ and two waveguides magnetically coupled to it with

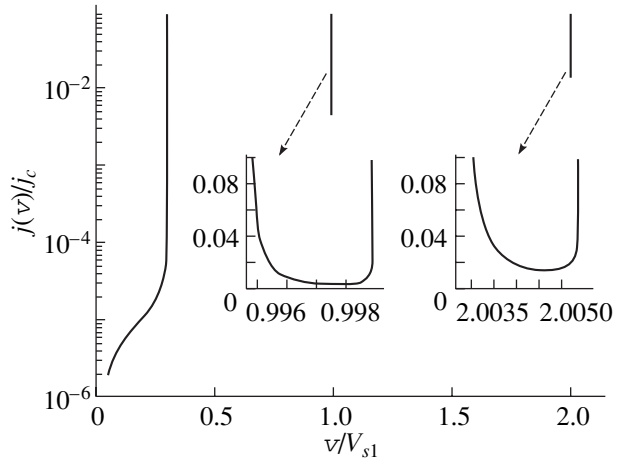

Fig. 2. Transport current density as a function of the vortex velocity for $V_s = V_{s1}/3$ and $V_{s2} = 2V_{s1}$.

small coupling constants S_{10}, S_{20}, S_{01}, S_{02}, and $\beta_1 \sim \beta_2$ in the case where $V_s \ll V_{s1} \ll V_{s2}$. In this case, the layered structure has a wide velocity range for a slow vortex and two narrow fast-vortex velocity ranges. Inside the wide slow-vortex velocity range $0 < v < v_0 \approx V_s[1 - (S_{01}S_{10} + S_{02}S_{20})/2]$, Eq. (19) can be approximated as

$$\left[\frac{j(v)}{j_c}\right]_{JJ} \approx \frac{4}{\pi}\left(\beta + \beta_1 S_{01}S_{10}\frac{V_s^2}{V_{s1}^2} + \beta_2 S_{02}S_{20}\frac{V_s^2}{V_{s2}^2}\right) \times \frac{v}{\omega_j}\frac{1}{\sqrt{v_0^2 - v^2}}. \quad (20)$$

Equation (20) differs from the known expression for a single junction [10] by, first, the additional terms related to dissipation in the waveguides and, second, the replacement of the Swihart velocity of the JJ by a smaller quantity v_0 under the radical sign.

Inside the two narrow ranges $\tilde{v}_i \approx V_{si} < v < v_i \approx V_{si}(1 + S_{0i}S_{i0}V_s^2/2V_{si}^2)$ for the motion of the first and second fast vortices, we get

$$\left[\frac{j(v)}{j_c}\right]_{JJ} \approx \frac{4}{\pi}\left[\beta + \beta_i S_{0i}S_{i0}\frac{V_s^2 V_{si}^2}{(v^2 - V_{si}^2)^2}\right]\frac{v}{\omega_j}\sqrt{\frac{v - V_{si}}{v_i - v}}. \quad (21)$$

Here, $i = 1, 2$ for the first and second fast vortices, respectively. It follows from Eq. (21) that, for each of the fast vortices, the $j(v)$ dependence has a minimum inside the corresponding allowed range. Note that, in the case of fast vortex motion in a JJ magnetically coupled to one waveguide, the current also has a local minimum inside the velocity range where a fast vortex exists. If $\beta \ll \beta_1 V_{s1}^2/(S_{01}S_{10}V_s^2) \sim \beta_2 V_{s2}^2/(S_{02}S_{20}V_s^2)$, which corresponds to the case where dissipation in the waveguides is significant as compared to that in the JJ, we can find the minimum value of the transport current in these regions:

$$\min\left[\frac{j(v)}{j_c}\right]_{JJ} \approx \frac{64}{3\sqrt{3}\pi}\frac{\beta_i V_{si}^2}{\omega_j V_s^2}\frac{1}{S_{0i}S_{i0}}.$$

It is seen that it is the parameters of the waveguide associated with the particular fast vortex that determine the minimum value of the transport current needed to sustain fast vortex motion. The minimum value is reached at a quarter of the width of the allowed range away from its upper limit. Figure 2 shows the $j(v)$ dependence plotted according to Eq. (19) for all allowed velocity ranges of an elementary vortex. The plot corresponds to the following values of parameters: $V_s = V_{s1}/3$, $V_{s2} = 2V_{s1}$, $S_{01} = S_{10} = S_{02} = S_{20} = 0.3$, and $\beta = \beta_1 = \beta_2 = 10^{-5}\omega_j$. It is clear from Fig. 2 that, in the region of the slowest vortex, the transport current grows steadily up to the edge of the allowed velocity range. In the narrow ranges for the fast vortex, the transport current has a local minimum, which is significantly lower than the critical current j_c. According to Eq. (21) and Fig. 2, the derivative of $j(v)$ is negative when the vortex velocity is just slightly lower than the value corresponding to the minimum of the current. By drawing on the analogy between $j(v)$ and the current–voltage characteristic of a conductor, we will call the range of $j'(v) < 0$ the region of negative differential conductivity. The presence of such a region in the $j(v)$ curve suggests that a system of a JJ magnetically coupled to a waveguide (or waveguides) can be used to generate electromagnetic radiation.

Let us now examine the case where the Swihart velocity of one of the waveguides is much smaller than the Swihart velocity of the JJ, $V_{s1} \ll V_s \ll V_{s2}$. In this case, for the velocity range $0 < v < v_1 \approx V_{s1}(1 - S_{01}S_{10}/2)$, we obtain from Eq. (19) that

$$\left[\frac{j(v)}{j_c}\right]_{JJ} \approx \frac{4}{\pi}\left[\beta + \beta_1 S_{01}S_{10}\frac{V_s^2 V_{s1}^2}{(V_{s1}^2 - v^2)^2}\right] \times \frac{v}{v_0\omega_j}\sqrt{\frac{V_{s1} - v}{v_1 - v}}. \quad (22)$$

Inside the second wide range $\tilde{v}_1 \approx V_{s1} < v < v_0 \approx V_s(1 - S_{02}S_{20}/2)$, the current is given by

$$\left[\frac{j(v)}{j_c}\right]_{JJ} \approx \frac{4}{\pi}\left[\beta + \beta_2 S_{02}S_{20}\frac{V_s^2}{V_{s2}^2}\frac{(V_{s1}^2 - v^2 - S_{01}S_{10}V_{s1}^2)^2}{(V_{s1}^2 - v^2)^2} + \beta_1 S_{01}S_{10}\frac{V_s^2 V_{s1}^2}{(V_{s1}^2 - v^2)^2}\right]\frac{v}{\omega_j}\sqrt{\frac{v^2 - V_{s1}^2}{(v_0^2 - v^2)(v^2 - v_1^2)}}. \quad (23)$$

In the relatively narrow range $\tilde{v}_2 \approx V_{s2} < v < v_2 \approx V_{s2}(1 + S_{02}S_{20}V_s^2/2V_{s2}^2)$, where fast vortex motion is possible, approximate expression (21) follows from Eq. (19).

The current density is given in Fig. 3a as a function of the vortex velocity for the case $V_{s1} < V_s < V_{s2}$. This $j(v)$ graph is plotted for the following parameter values: $V_s = 3V_{s1}/2$, $V_{s2} = 2V_{s1}$, $S_{01} = S_{10} = S_{02} = S_{20} = 0.3$, and $\beta = \beta_1 = \beta_2 = 10^{-5}\omega_j$. It is seen that, in the region of the slowest vortex, the function $j(v)$ grows steadily, while inside the two other (narrow and wide) allowed ranges of vortex motion this function has a local minimum. As the vortex velocity approaches the lower boundary of each of these ranges, we have $j'(v) < 0$.

Finally, let us consider the case where the Swihart velocities of both waveguides are smaller than the Swihart velocity of the JJ, $V_{s1} \ll V_{s2} \ll V_s$. In the region $0 < v < v_1 \approx V_{s1}(1 - S_{01}S_{10}/2)$, the current is described by Eq. (22). Note that the transport current is a monotonically increasing function of velocity in the region of the slowest vortex regardless of the relation between the Swihart velocities.

Inside the second wide velocity range $v_1 < \tilde{v}_1 \approx V_{s1} < v < v_2 \approx V_{s2}(1 - S_{01}S_{10}/2)$, it follows from Eq. (19) that

$$\left[\frac{j(v)}{j_c}\right]_{JJ} \approx \frac{4}{\pi}\left[\beta + \beta_1 S_{01}S_{10}\frac{V_s^2V_{s1}^2(V_{s2}^2 - v^2 - S_{02}S_{20}V_{s2}^2)^2}{(V_{s1}^2 - v^2)^2(V_{s2}^2 - v^2)^2} + \beta_2 S_{02}S_{20}\frac{V_s^2V_{s2}^2(V_{s1}^2 - v^2 - S_{01}S_{10}V_{s1}^2)^2}{(V_{s1}^2 - v^2)^2(V_{s2}^2 - v^2)^2}\right] \times \frac{v}{V_s\omega_j}\sqrt{\frac{(v^2 - V_{s1}^2)(V_{s2}^2 - v^2)}{(v^2 - v_1^2)(v_2^2 - v^2)}}. \quad (24)$$

For the third wide velocity region $v_2 < \tilde{v}_2 \approx V_{s2} < v < v_0 \approx V_s$, it follows from Eq. (19) that

$$\left[\frac{j(v)}{j_c}\right]_{JJ} \approx \frac{4}{\pi}\left[\beta + \beta_1 S_{01}S_{10}\frac{V_s^2V_{s1}^2(V_{s2}^2 - v^2 - S_{02}S_{20}V_{s2}^2)^2}{v^4(V_{s2}^2 - v^2)^2} + \beta_2 S_{02}S_{20}\frac{V_s^2V_{s2}^2}{(V_{s2}^2 - v^2)^2}\right]\frac{1}{\omega_j}\sqrt{\frac{v^2 - V_{s2}^2}{(v_0^2 - v^2)(v^2 - v_2^2)}}. \quad (25)$$

The function $j(v)$ for the case where vortex motion is possible in three relatively wide allowed ranges sepa-

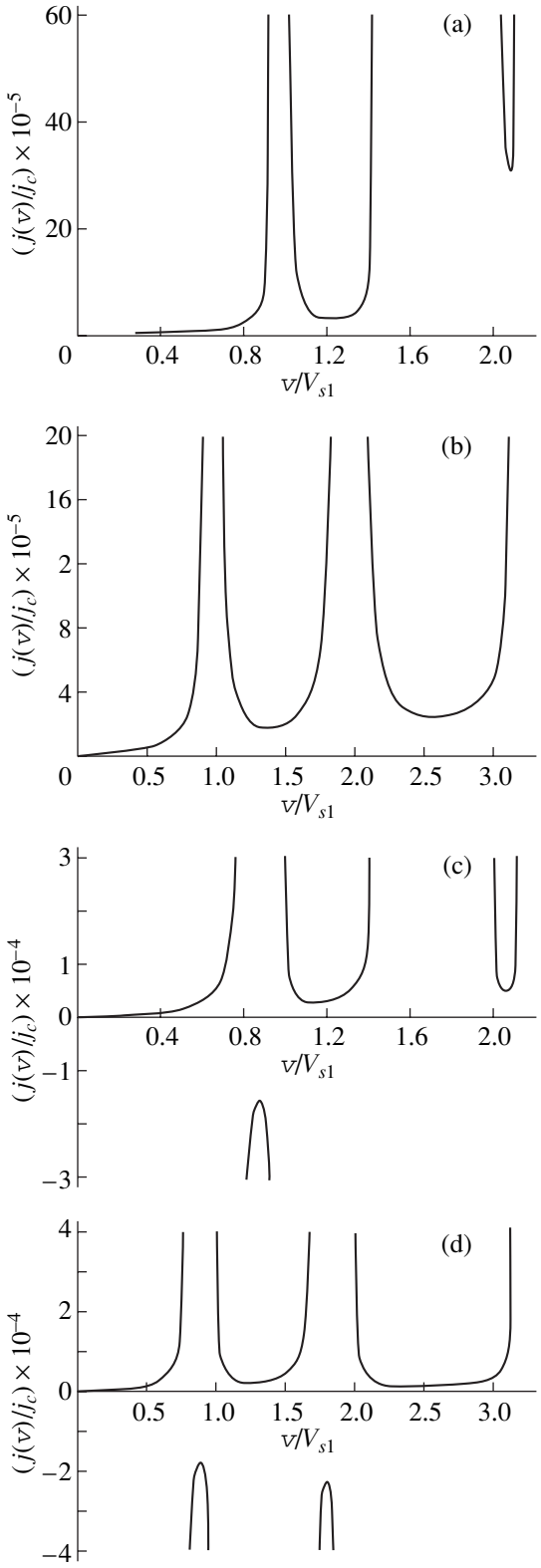

Fig. 3. Transport current density as a function of the vortex velocity for (a, c) $V_s = 3V_{s1}/2$, $V_{s2} = 2V_{s1}$ and (b, d) $V_s = 3V_{s1}$, $V_{s2} = 2V_{s1}$. Panels (c) and (d) correspond to the case where the current flows through both the JJ and the waveguides.

rated by two narrow gaps is plotted in Fig. 3b for $V_s = 3V_{s1}$, $V_{s2} = 2V_{s1}$, and the same values of the coupling constants and parameters β/ω_j and β_i/ω_j as before. It follows from Fig. 3b that the current grows steadily inside the first allowed region, while in each of the two wide ranges the current has a local minimum and there is a region where $j'(v) < 0$.

6. INDUCED VORTEX MOTION IN THE CASE WHERE A CURRENT FLOWS THROUGH THE ENTIRE STRUCTURE

Let us consider vortex motion induced by a current of density j flowing along the x axis not only through the JJ but also through both waveguides. In this case, the phase differences are described by Eq. (16) and the two equations in (4) with inclusion of the current:

$$\begin{aligned}
&\frac{\partial^2\varphi_{w1}(z,t)}{\partial t^2} + \frac{16\pi|e|d_1}{\hbar\varepsilon_1}j + \beta_1\frac{\partial\varphi_{w1}(z,t)}{\partial t} \\
&= V_{s1}^2\frac{\partial^2\varphi_{w1}(z,t)}{\partial z^2} + S_{10}V_{s1}^2\frac{\partial^2\varphi(z,t)}{\partial z^2} \\
&\quad + S_{10}S_{02}V_{s1}^2\frac{\partial^2\varphi_{w2}(z,t)}{\partial z^2}, \\
&\frac{\partial^2\varphi_{w2}(z,t)}{\partial t^2} + \frac{16\pi|e|d_2}{\hbar\varepsilon_2}j + \beta_2\frac{\partial\varphi_{w2}(z,t)}{\partial t} \\
&= V_{s2}^2\frac{\partial^2\varphi_{w2}(z,t)}{\partial z^2} + S_{20}V_{s2}^2\frac{\partial^2\varphi(z,t)}{\partial z^2} \\
&\quad + S_{20}S_{01}V_{s2}^2\frac{\partial^2\varphi_{w1}(z,t)}{\partial z^2}.
\end{aligned} \tag{26}$$

If the current and dissipation in the JJ and the waveguides are small, the quantities ψ_{w1} and ψ_{w2} can be found (approximately) from Eq. (26) in the same way as in Section 5. By using approximate expressions for ψ_{w1} and ψ_{w2}, we get the following equation instead of Eq. (17):

$$\sin\psi(\zeta) - k_j^{-2}(v)\psi''(\zeta) + \frac{j}{j_c}\frac{1}{I(v)} = \frac{v\beta(v)}{\omega_j^2}\psi'(\zeta), \tag{27}$$

where we used the notation

$$\begin{aligned}
I(v) &= \left\{1 - \frac{V_s^2}{(\tilde{v}_1^2 - v^2)(\tilde{v}_2^2 - v^2)}\right. \\
&\times\left[S_{01}\frac{d_1}{\varepsilon_1}\frac{\varepsilon}{d}(V_{s2}^2(1 - S_{02}S_{20}) - v^2)\right. \\
&\left.\left. + S_{02}\frac{d_2}{\varepsilon_2}\frac{\varepsilon}{d}(V_{s1}^2(1 - S_{01}S_{10}) - v^2)\right]\right\}^{-1}.
\end{aligned} \tag{28}$$

With the help of the data from Section 5 and [10], we obtain from Eq. (27) that

$$\frac{j(v)}{j_c} = \frac{4}{\pi}\frac{\beta(v)vk_j(v)}{\omega_j^2}I(v). \tag{29}$$

Equation (29) differs from Eq. (19) by a factor $I(v)$. This velocity-dependent factor appeared because of the current flowing not only through the JJ but also through the waveguides.

As in the previous section, let us examine the relation between the transport current density and vortex velocity in the case of small coupling constants of the JJ and waveguides. In the case of $V_s \ll V_{s1} \ll V_{s2}$, where two fast-vortex regions exist, for the low-velocity allowed range $0 < v < v_0 \approx V_s[1 - (S_{01}S_{10} + S_{02}S_{20})/2]$ we get

$$\frac{j(v)}{j_c} \approx \left[\frac{j(v)}{j_c}\right]_{JJ}\frac{1}{1 - S_{10} - S_{20}}. \tag{30}$$

Here and henceforth, $[j(v)/j_c]_{JJ}$ is the dependence of the transport current on velocity in the case where the current flows through the JJ only. In this particular case, this dependence is given by Eq. (20). Equation (30) differs from Eq. (20) by a constant factor greater than unity. This means that, in the case where the current flows through the entire structure, a higher current is required to sustain the motion of a slow vortex as compared to the case where the current flows through the JJ only. A different situation occurs inside the two narrow velocity regions where fast vortices can move. In the narrow velocity ranges $\tilde{v}_i \approx V_{si} < v < v_i \approx V_{si}(1 + S_{0i}S_{i0}V_s^2/2V_{si}^2)$, where the first ($i = 1$) and the second ($i = 2$) fast vortex can move, the relation between the current and velocity is given by

$$\frac{j(v)}{j_c} \approx \left[\frac{j(v)}{j_c}\right]_{JJ}\left(1 + S_{i0}\frac{V_{si}^2}{v^2 - V_{si}^2}\right)^{-1}. \tag{31}$$

Recall that, in the case where the current flows through the JJ only, the dependence of the current on the fast vortex velocity is given by Eq. (21). It is evident from Eq. (31) that the current flowing through the waveguides causes a relative reduction of $j(v)$ in value by $\sim S_{0i}V_s^2/V_{si}^2$ for the first (i =1) and the second ($i = 2$) fast vortex.

Let us comment on these results. To understand the peculiarities of the interaction of a moving vortex and the current in cases that differ in the way in which the current flows through the layered structure, it is necessary to know where the magnetic field of the vortex is concentrated. When a transport current flows through the layered structure, the vortex is subjected to a

Lorentz force, whose amplitude per unit vortex length along the y axis is given by

$$F_z = -\int dxdz\frac{jH(x, z, t)}{c}, \tag{32}$$

where $H(x, z, t)$ is the vortex magnetic field. Integration in Eq. (32) should be performed over all regions where the transport current flows. If the current flows through the entire layered structure, we substitute Eq. (15) into Eq. (32) and obtain

$$F_z = -\frac{j}{c}\int dz[(B_1 - a_1)H_1(z, t) + (B_0 - a_1 - a_2)H(z, t) + (B_2 - a_2)H_2(z, t)]. \tag{33}$$

By substituting the magnetic field of the slowest vortex obtained from Eqs. (3) and (7) into Eq. (33), we find the Lorentz force acting on a slow vortex:

$$F_z \approx \frac{j}{c}\phi_0(1 - S_{10} - S_{20}). \tag{34}$$

If the transport current flows through the JJ only, we get, instead of Eq. (33),

$$F_z = -\frac{j}{c}\int dz[B_0H(z, t) - a_1H_1(z, t) - a_2H_2(z, t)]. \tag{35}$$

Hence, using explicit expressions for the magnetic fields, we obtain

$$F_z \approx \frac{j}{c}\phi_0. \tag{36}$$

By comparing Eq. (34) to Eq. (36), we find that, when the current flows through the entire structure, the Lorentz force is smaller than in the case when the current flows through the JJ only. Resistance to vortex motion in the layered structure is due to energy dissipation in the nonsuperconducting layers. The change in the energy of the system due to ohmic losses is given by

$$\frac{dW}{dt} = -\int dxdz\sigma E_x^2, \tag{37}$$

where integration is performed over the nonsuperconducting layers. With the help of the time-dependent Josephson relation and Eqs. (7) and (12), from Eq. (37) we obtain

$$\frac{dW}{dt} = -\frac{4}{\pi}\frac{\phi_0 j_c}{\omega_j^2}\frac{v^2k_j(v)\beta(v)}{c} \equiv -vF_{\text{diss}}. \tag{38}$$

Relation (38) defines the dissipative force F_{diss} acting on a vortex moving at speed v.

It follows from Eq. (38) that the friction force acting on an elementary vortex is

$$F_{\text{diss}} = \frac{4}{\pi}\frac{\phi_0 j_c}{\omega_j^2}\frac{vk_j(v)\beta(v)}{c}. \tag{39}$$

According to Eqs. (37)–(39), the friction force is independent of the way in which the current flows through the layered structure. The value of the transport current required to sustain the induced vortex motion is determined by equating the Lorentz force, which supports the vortex motion, to the friction force, which opposes it. Comparing Eqs. (34) and (36) with Eq. (39) shows that the flow of current through the entire layered structure causes a reduction in the Lorentz force and, therefore, increases the transport current required to sustain the vortex motion.

Let us now explain Eq. (31). The magnetic field of the first fast vortex, as follows from Fig. 1b, is mainly concentrated near the first waveguide, which is positioned in the plane $x = -\lambda$ in this figure. In the same way, the field of the second fast vortex is mainly concentrated near the second waveguide, which is positioned in the plane $x = \lambda$. If the current flows through the JJ only, it does not pass through the regions where the main part of the magnetic field of the fast vortex is concentrated. Therefore, these regions do not contribute to the Lorentz force (32). In the case where the transport current of the same density flows through the entire layered structure, the contributions from the main part of the magnetic field, concentrated near the waveguide, significantly enhance the Lorentz force acting on the fast vortex. Since the friction force (39) does not change, a smaller transport current density is required to sustain the vortex motion at the same speed, which follows from Eq. (31).

Let us examine the vortex motion induced by a transport current in the case where the Swihart velocity of one of the waveguides is much lower than V_s, $V_{s1} \ll V_s \ll V_{s2}$. In Fig. 3c, the function $j(v)$ is plotted in all allowed velocity ranges for the parameter values $V_s = 3V_{s1}/2$, $V_{s2} = 2V_{s1}$, $S_{01} = S_{10} = S_{02} = S_{20} = 0.3$, and $\beta = \beta_1 = \beta_2 = 10^{-5}\omega_j$. It can be seen that a region of negative current appears in the velocity range of allowed motion of a slow vortex $0 < v < v_1 \approx V_{s1}(1 - S_{01}S_{10}/2))$. Let us examine this phenomenon more closely. Near the right-hand boundary of the allowed range $v < v_1$, most of the magnetic flux of the slow vortex changes sign under the influence of the waveguide, as seen from Fig. 1d. Therefore, the Lorentz force (32) acting on the vortex also changes sign. There is no such effect inside the other two allowed regions, as can be seen from Figs. 1e and 1f. In the case where $V_{s1} \ll V_s \ll V_{s2}$ and there is weak coupling between the waveguides and the JJ, Eq. (29) reduces to the following expression in the velocity range $0 < v < v_1 \approx V_{s1}(1 - S_{01}S_{10}/2)$:

$$\frac{j(v)}{j_c} \approx \left[\frac{j(v)}{j_c}\right]_{\text{JJ}}\left(1 - S_{10}\frac{V_{s1}^2}{V_{s1}^2 - v^2} - S_{20}\frac{V_{s1}^2 - v^2 - V_{s1}^2S_{01}S_{10}}{V_{s1}^2 - v^2}\right)^{-1}. \tag{40}$$

According to Eq. (40), the current can reverse sign in the allowed region $0 < v < v_1 \approx V_{s1}(1 - S_{01}S_{10}/2)$. The sign reverses in Eq. (40) because of the change in sign of the factor $I(v)$ given by Eq. (28); the change in sign of the current is due to the transport current flowing through the waveguides. It follows from Eq. (40) that the current is negative in the velocity range

$$V_{s1}\sqrt{1 - S_{10}} \approx V_{s1}(1 - S_{10}/2) < v < v_1. \quad (41)$$

From Eqs. (3) and (7), it follows that in this velocity region the magnetic fields inside the nonsuperconducting layers are given by

$$H(z, t) \approx -\frac{\phi_0}{2\pi}\frac{1}{B_0}\frac{\partial}{\partial z}\varphi(z, t),$$
$$H_1(z, t) \approx \frac{\phi_0}{2\pi}\frac{1}{B_1}\frac{S_{10}V_{s1}^2}{V_{s1}^2 - v^2}\frac{\partial}{\partial z}\varphi(z, t), \quad (42)$$
$$H_2(z, t) \approx 0.$$

Here, we keep only the main terms not containing small coupling constants S_{10}, S_{20}, S_{01}, and S_{02}. It can be seen from Eq. (42) that, in this approximation inside the velocity range (41), the magnetic fields in the first waveguide and the JJ are in opposite directions, which is in full agreement with Fig. 1d. After substituting Eq. (42) into Eq. (32) and performing integration, we get

$$F_z \approx \frac{j}{c}\phi_0\left(1 - S_{10}\frac{V_{s1}^2}{V_{s1}^2 - v^2}\right). \quad (43)$$

It could be seen from Eq. (43) that, in the velocity range (41), the force acting on the vortex changes sign, which means that vortex motion is induced in the opposite direction. Hence, a waveguide with a Swihart velocity smaller than that of the JJ can provide conditions for vortex motion in the reverse direction.

Inside the second wide allowed region $\tilde{v}_1 \approx V_{s1} < v < v_0 \approx V_s(1 - S_{02}S_{20}/2)$, the current is given by Eq. (40). The magnetic field of the vortex in this range, as can be seen from Fig. 1e, is concentrated in the JJ and the first waveguide, and the vortex magnetic flux that reverses sign in the vicinity of the second waveguide is negligibly small.

Inside the narrow velocity range of the fast vortex $\tilde{v}_2 \approx V_{s2} < v < v_2 \approx V_{s2}(1 + S_{02}S_{20}V_s^2/2V_{s2}^2)$, the current is given by

$$\frac{j(v)}{j_c} \approx \left[\frac{j(v)}{j_c}\right]_{JJ}\left(1 + S_{20}\frac{V_{s2}^2}{v^2 - V_{s2}^2}\right)^{-1}. \quad (44)$$

It follows from Fig. 3c and Eqs. (40) and (44) that, in both the wide and narrow allowed ranges, the current has a local minimum and there are regions where $j'(v) < 0$.

Figure 3d plots the function $j(v)$ for a system containing two waveguides with Swihart velocities lower than the Swihart velocity of the JJ, $V_{s1} \ll V_{s2} \ll V_s$; the calculation is performed for $V_s = 3V_{s1}$ and $V_{s2} = 2V_{s1}$ (the values of the other parameters are the same as before). Two ranges of negative current appear on the $j(v)$ graph near each of the Swihart velocities of the waveguides. In this case, Eq. (40) can be used to describe the dependence of the transport current on velocity in the first velocity range $0 < v < v_1 \approx V_{s1}(1 - S_{01}S_{10}/2)$. In the next allowed range, $\tilde{v}_1 \approx V_{s1} < v < v_2 \approx V_{s2}(1 - S_{01}S_{10}/2)$, we get

$$\frac{j(v)}{j_c} \approx \left[\frac{j(v)}{j_c}\right]_{JJ}\left[1 + S_{10}V_{s1}^2\frac{V_{s2}^2 - v^2 - S_{02}S_{20}V_{s2}^2}{(v^2 - V_{s1}^2)(V_{s2}^2 - v^2)} + S_{20}V_{s2}^2\frac{V_{s1}^2 - v^2 - S_{01}S_{10}V_{s1}^2}{(v^2 - V_{s1}^2)(V_{s2}^2 - v_2^2)}\right]^{-1}. \quad (45)$$

It follows from Eq. (45), in particular, that the second region of negative current appears inside the allowed velocity range. It can be seen from Fig. 1i that most of the magnetic flux also changes sign near the Swihart velocity of the second waveguide, which is the reason for the reversed direction of vortex motion.

Finally, in the third range $\tilde{v}_2 \approx V_{s2} < v < v_0 \approx V_s$, from Eq. (29) we get

$$\frac{j(v)}{j_c} \approx \left[\frac{j(v)}{j_c}\right]_{JJ} \times \left[1 + S_{10}V_{s1}^2\frac{V_{s2}^2 - v^2 - S_{02}S_{20}V_{s2}^2}{v^2(V_{s2}^2 - v^2)} + \frac{S_{20}V_{s2}^2}{V_{s2}^2 - v^2}\right]^{-1}. \quad (46)$$

In this case, the magnetic field is concentrated near the JJ and the second waveguide, as can be seen from Fig. 1j. The field concentrated near the waveguide (which does not contribute to the Lorentz force (32) when the current flows through the JJ only) causes the current to change when the current flows through the entire structure. Thus, we examined all possible cases of induced vortex motion in a layered structure.

7. CONCLUSIONS

A set of equations for the Cooper pair phase differences has been considered for a layered structure consisting of a JJ magnetically coupled to two waveguides, with the mutual influence of the waveguides and the JJ being taken into account. The possible existence of an elementary vortex moving at a constant velocity in such a structure was studied in the dissipation-free limit. Such a vortex was found to exist inside three finite velocity ranges. This is the difference between our system and a system with one waveguide, where there are only two allowed velocity ranges. Possible vortex

motion in two narrow velocity ranges at a speed much higher than the Swihart velocity of the JJ was demonstrated for the case where the Swihart velocity of the JJ is much lower than the Swihart velocities of the waveguides. The existence of the second range for the fast vortex is due to the presence of a second waveguide with a relatively high Swihart velocity. The motion of an elementary vortex can be induced inside the allowed velocity ranges by a current flowing through the JJ; the required value of the current is small as compared to the critical Josephson current. A qualitatively new phenomenon of induced motion of an elementary vortex opposite to the regular direction has been predicted in the case where the Swihart velocity of a waveguide is much smaller than the Swihart velocity of the JJ.

ACKNOWLEDGMENTS

This work was supported by the President of the Russian Federation (project nos. NSh-1985.2003.2, MK-1800.2003.02) and the Ministry of Industry, Science, and Technology of the Russian Federation (contract no. 40.012.11.1357).

APPENDIX

Let us consider in detail the derivation of Eq. (17). For vortices moving at a uniform speed v, the set of equations (4) and (16) takes the form (cf. Eq. (6))

$$\begin{aligned}
&(V_{s1}^2 - v^2)\psi''_{w1}(\zeta) + \beta_1 v\psi'_{w1}(\zeta) + S_{10}V_{s1}^2\psi''(\zeta) \\
&\quad + S_{10}S_{02}V_{s1}^2\psi''_{w2}(\zeta) = 0, \\
&(V_{s2}^2 - v^2)\psi''_{w2}(\zeta) + \beta_2 v\psi'_{w2}(\zeta) + S_{20}V_{s2}^2\psi''(\zeta) \\
&\quad + S_{01}S_{20}V_{s2}^2\psi''_{w1}(\zeta) = 0, \\
&S_{01}V_s^2\psi''_{w1}(\zeta) + S_{02}V_s^2\psi''_{w2}(\zeta) + (V_s^2 - v^2)\psi''(\zeta) \\
&\quad + \beta_2 v\psi'_{w2}(\zeta) = \omega_j^2 \sin\psi(\zeta) + \omega_j^2 \frac{j}{j_c}.
\end{aligned} \tag{A1}$$

Let us express the second derivatives of the functions $\psi_{w1}(\zeta)$ and $\psi_{w2}(\zeta)$ with the help of the first of equations (A1):

$$\begin{aligned}
&\psi''_{w1}(\zeta) \\
&= \{(S_{10}S_{20}S_{02}V_{s1}^2V_{s2}^2 - S_{10}V_{s1}^2(V_{s2}^2 - v^2))\psi''(\zeta) \\
&- \beta_1 v(V_{s2}^2 - v^2)\psi'_{w1}(\zeta) + \beta_2 S_{10}S_{02}vV_{s1}^2\psi'_{w2}(\zeta)\} \\
&\times [(\tilde{v}_1^2 - v^2)(\tilde{v}_2^2 - v^2)]^{-1}, \\
&\psi''_{w2}(\zeta) \\
&= \{(S_{01}S_{10}S_{20}V_{s1}^2V_{s2}^2 - S_{20}V_{s2}^2(V_{s1}^2 - v^2))\psi''(\zeta) \\
&- \beta_2 v(V_{s1}^2 - v^2)\psi'_{w2}(\zeta) + \beta_1 S_{01}S_{20}vV_{s2}^2\psi'_{w1}(\zeta)\} \\
&\times [(\tilde{v}_1^2 - v^2)(\tilde{v}_2^2 - v^2)]^{-1}.
\end{aligned} \tag{A2}$$

We will limit ourselves to the case of low dissipation in the nonsuperconducting layers. In the linear approximation for β_1 and β_2, we substitute the first derivatives of $\psi_{w1}(\zeta)$ and $\psi_{w2}(\zeta)$ obtained from Eqs. (7) (which neglect dissipation) into the terms containing β_1 and β_2 in the right-hand side of Eqs. (A2). The derivatives are found by integrating Eqs. (7) and taking into account that functions ψ'_{w1} and ψ'_{w2} vanish as $\zeta \longrightarrow \pm\infty$. As a result, Eqs. (A2) allow us to obtain approximate expressions for the second derivatives of the phase differences on both waveguides in terms of the phase difference on the JJ. By substituting these explicit expressions for the second derivatives into the last equation in set (A1), we obtain Eq. (17).

REFERENCES

1. Yu. S. Kivshar and B. A. Malomed, Phys. Rev. B **37** (16), 9325 (1988).
2. N. G. Grønbech-Jensen, M. R. Samuelsen, P. S. Lomdahl, and J. A. Blackburn, Phys. Rev. B **42** (7), 3976 (1990).
3. E. Goldobin, A. Wallraff, N. Thussen, and A. V. Ustinov, Phys. Rev. B **57** (1), 130 (1998).
4. L. N. Bulaevskii, D. Dominguez, M. P. Maley, A. R. Bishop, O. K. C. Tsui, and N. P. Ong, Phys. Rev. B **54** (10), 7521 (1996).
5. S. Sakai, P. Bodin, and N. F. Pedersen, J. Appl. Phys. **73** (5), 2411 (1993).
6. S. Sakai, A. V. Ustinov, H. Kohlstedt, A. Petraglia, and N. F. Pedersen, Phys. Rev. B **50** (17), 12905 (1994).
7. V. V. Kurin and A. V. Yulin, Phys. Rev. B **55** (17), 11659 (1997).
8. A. S. Malishevskii, V. P. Silin, and S. A. Uryupin, Phys. Lett. A **306** (2–3), 153 (2002).
9. Yu. M. Aliev, K. N. Ovchinnikov, V. P. Silin, and S. A. Uryupin, Zh. Éksp. Teor. Fiz. **107** (3), 972 (1995) [JETP **80**, 551 (1995)].
10. D. W. McLaughlin and A. C. Scott, Phys. Rev. A **18** (4), 1652 (1978).

Translated by G. Tsydynzhapov

Physics of the Solid State, Vol. 46, No. 9, 2004, pp. 1604–1612. Translated from Fizika Tverdogo Tela, Vol. 46, No. 9, 2004, pp. 1557–1565.
Original Russian Text Copyright © 2004 by Kuleeva, Kuchinskiĭ.

METALS AND SUPERCONDUCTORS

Pseudogap-State Superconductivity in a "Hot-Point" Model: Gor'kov Equations

N. A. Kuleeva and É. Z. Kuchinskiĭ

Institute of Electrophysics, Ural Division, Russian Academy of Sciences, ul. Komsomol'skaya 34, Yekaterinburg, 620016 Russia

e-mail:strigina@iep.uran.ru, kuchinsk@iep.uran.ru

Received November 24, 2003; in final form, January 26, 2004

Abstract—The specific features of the superconducting state (with *s* and *d* pairing) are considered in terms of a pseudogap state caused by short-range order fluctuations of the "dielectric" type, namely, antiferromagnetic (spin density wave) or charge density wave fluctuations, in a model of the Fermi surface with "hot points." A set of recurrent Gor'kov equations is derived with inclusion of all Feynman diagrams of a perturbation expansion in the interaction between an electron and short-range order fluctuations causing strong scattering near hot points. The influence of nonmagnetic impurities on superconductivity in such a pseudogap state is analyzed. The critical temperature for the superconducting transition is determined, and the effect of the effective pseudogap width, correlation length of short-range-order fluctuations, and impurity scattering frequency on the temperature dependence of the energy gap is investigated. © *2004 MAIK "Nauka/Interperiodica".*

1. INTRODUCTION

The pseudogap state, existing in a wide region on the phase diagram of high-T_c superconducting (HTSC) cuprates, gives rise to various anomalies in their properties in both the normal and superconducting states [1, 2]. The preferable scenario for formation of the pseudogap state in HTSC oxides is believed to be based on the fact that, in this region of the phase diagram, there is strong scattering of carriers by short-range-order fluctuations of the "dielectric" type, namely, antiferromagnetic (AFM) [spin-density-wave (SDW)] or charge-density-wave (CDW) fluctuations [2]. In momentum space, this scattering occurs in the vicinity of the antiferromagnetism vector $\mathbf{Q} = (\pi/a, \pi/a)$ (a is the two-dimensional lattice parameter) and affects the electronic spectrum, thereby causing it to exhibit a clearly defined non-Fermi-liquid behavior in the neighborhood of the so-called "hot points" on the Fermi surface [2]. Recent experiments have provided fairly convincing evidence in favor of this scenario of pseudogap formation [3–5]. Based on these concepts, a simplified model of the pseudogap state has been proposed, which describes the main features of this state [2] and includes the contributions from all Feynman diagrams of a perturbation expansion in scattering by (Gaussian) short-range-order fluctuations with a characteristic scattering momentum lying in the region of the vector $\mathbf{Q}$ (this region is determined by the corresponding correlation length ξ) [6, 7].

Up to now, most of the relevant theoretical studies have been dedicated to models of the pseudogap state in the normal phase (at $T > T_c$). In [8–11], we considered superconductivity using a simplified pseudogap-state model in which hot flat sections were assumed to exist on the Fermi surface. In the framework of this model, a Ginzburg–Landau expansion was obtained for different types of Cooper pairs [8, 10] and the superconducting state at temperatures $T < T_c$ was studied using solutions to the Gor'kov equations [9–11].

Analysis of the superconducting properties in terms of the Ginzburg–Landau expansion in the immediate vicinity of the superconducting transition temperature T_c was performed in [12] using a more realistic model of hot points on the Fermi surface. In this paper, we analyze, in terms of this model, the main properties of the superconducting state (for various types of pairing) in a wide range of temperatures $T < T_c$ and investigate the influence of scattering by nonmagnetic impurities on superconductivity in this case.

2. HOT-POINT MODEL AND PAIRING

In the "nearly antiferromagnetic" Fermi liquid model, which is extensively used to explain the microscopic mechanism of high-T_c superconductivity [13, 14], an effective interaction between electrons and spin fluctuations is introduced and described by a dynamic susceptibility depending on the spin-fluctuation correlation length ξ, the antiferromagnetism vector in the insulating phase $\mathbf{Q} = (\pi/a, \pi/a)$, and the characteristic spin-fluctuation frequency ω_{sf} [6]. The dynamic susceptibility and, hence, the effective interaction reach a maximum in the region of $\mathbf{q} \sim \mathbf{Q}$. Therefore, quasiparticles whose momenta are in the vicinity of the hot points on the Fermi surface (Fig. 1) are strongly scattered by spin fluctuations, with the scattering vector

being of the order of **Q**. The effective interaction for quasiparticles whose momenta are far from the hot points is fairly weak.

At sufficiently high temperatures, $2\pi T \gg \omega_{sf}$, we can ignore the spin dynamics [6] and restrict our consideration to the static approximation. Calculations are substantially simplified and the contributions from higher order terms in a perturbation expansion can be analyzed if the interaction between electrons and spin (or charge) fluctuations is approximately described by [7]

$$V_{\text{eff}}(\mathbf{q}) = W^2 \frac{2\xi^{-1}}{\xi^{-2} + (q_x - Q_x)^2} \frac{2\xi^{-1}}{\xi^{-2} + (q_y - Q_y)^2}, \quad (1)$$

where W is an effective parameter with energy dimensions. In what follows, W and ξ are treated as phenomenological parameters to be determined from experiment. Equation (1) is qualitatively analogous to the interaction in the static limit, considered in [13, 14], and, for the appropriate values of the parameters, differs from it only slightly in the most interesting region of $|\mathbf{q} - \mathbf{Q}| < \xi^{-1}$, which determines scattering in the vicinity of the hot points. In effect, the actual interaction with short-range-order fluctuations is replaced in this case by the interaction of the electrons with the static random (Gaussian) field of these fluctuations. The assumption of the static (and Gaussian) character of fluctuations is physically least justified and is applicable only at sufficiently high temperatures [6, 7]. At low temperatures, and in the superconducting phase in particular, the spin dynamics and non-Gaussian character of fluctuations can significantly affect the microscopic mechanism of formation of Cooper pairs described in terms of the nearly antiferromagnetic Fermi liquid model [13, 14]. We believe, however, that the static Gaussian approximation will suffice to qualitatively investigate the effect of the pseudogap formation on superconductivity.

The spectrum of the original (free) quasiparticles is taken in the form [6]

$$\xi_p = -2t(\cos p_x a + \cos p_y a) - 4t' \cos p_x a \cos p_y a - \mu, \quad (2)$$

where t is the transfer integral between the nearest neighbors on the square lattice, t' is the transfer integral between the second-to-nearest neighbors, a is the lattice parameter, and μ is the chemical potential. This expression is fairly close to that given by band calculations performed for real HTSC systems. For example, for $YBa_2Cu_3O_{6+\delta}$, we have $t = 0.25$ eV and $t' = -0.45t$ [6]. The chemical potential is determined by the carrier density.

In the limit of an infinitely long correlation length, $\xi \longrightarrow \infty$, the short-range-order fluctuation scattering model under study can be solved exactly [15]. For finite values of ξ, an approximate solution can be found [6, 7] by generalizing the one-dimensional consideration carried out in [16]. In this case, all diagrams of the perturbation expansion of the one-particle electron Green's function can be approximately summed.

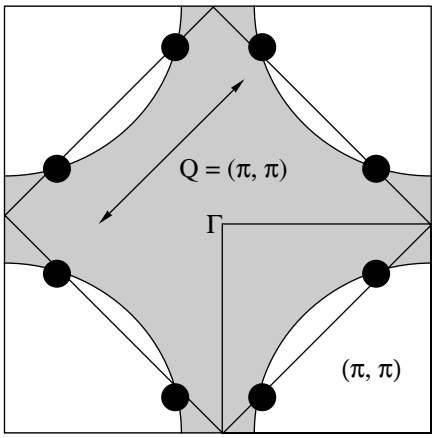

Fig. 1. Fermi surface with "hot points" connected by the scattering momentum vector $\mathbf{Q} = (\pi/a, \pi/a)$.

3. GOR'KOV EQUATIONS FOR A PSEUDOGAP SUPERCONDUCTOR

In studying superconductivity in the system in question undergoing developed short-range-order fluctuations, we assume that superconducting pairing occurs due to an attracting potential of the simplest (BCS) type,

$$V_{\text{sc}}(\mathbf{p}, \mathbf{p}') = -Ve(\mathbf{p})e(\mathbf{p}'), \quad (3)$$

where $e(\mathbf{p})$ is taken to be

$$e(\mathbf{p}) = \begin{cases} 1 & (s \text{ pairing}), \\ \cos(p_x a) - \cos(p_y a) & (d_{x^2-y^2} \text{ pairing}). \end{cases} \quad (4)$$

The constant V, as is usually assumed, is nonzero in a layer $2\omega_c$ thick in the vicinity of the Fermi level (ω_c is the characteristic frequency of phonons responsible for attraction between electrons). In general, the superconducting energy gap is anisotropic and can be written as $\Delta(\mathbf{p}) = \Delta e(\mathbf{p})$. In what follows, we will write $\Delta(\mathbf{p})$ as Δ to simplify the notation and will indicate the momentum dependence only where necessary.

In the subsequent consideration, the energy gap of the superconductor is assumed to be self-averaging over short-range-order fluctuations, which allows us to employ a standard method from the theory of disordered superconductors [17, 18]. In the case where the short-range-order correlation length satisfies the inequality $\xi \ll \xi_0$, where $\xi_0 \sim v_F/\Delta_0$ is the BCS coherence length (i.e., fluctuations are correlated over distances shorter than the characteristic Cooper pair size), the assumption of self-averaging Δ must be valid; this assumption ceases to be true only for $\xi > \xi_0$ [9–11].[1]

For the superconducting state, a perturbation expansion in the interaction with AFM fluctuations described by Eq. (1) is performed using the "unperturbed" normal and anomalous Green's functions:

$$G_{00}(\varepsilon_n \mathbf{p}) = -\frac{i\varepsilon_n + \xi_\mathbf{p}}{\varepsilon_n^2 + \xi_\mathbf{p}^2 + |\Delta|^2},$$
$$F_{00}^+(\varepsilon_n \mathbf{p}) = \frac{\Delta^*}{\varepsilon_n^2 + \xi_\mathbf{p}^2 + |\Delta|^2}, \quad (5)$$

where $\varepsilon_n = 2\pi T(n + 1/2)$.

Following paper [10], we can write a set of recurrent Gor'kov equations taking into account short-range-order fluctuation scattering to all orders in the perturbation expansion. The contribution from an Nth-order diagram in interaction (1) to the full normal or anomalous Green's function is the product of $N + 1$ unperturbed normal (G_{0k_j}) and anomalous ($F_{0k_j}^+$) Green's functions characterized by specially renormalized frequencies and energy gaps (see below). Here, k_j is the number of interaction lines covering the jth (counted from the ingoing line of the diagram) electron line. As in the normal state, the contribution from any diagram is characterized by a set of integers k_j and each diagram with crossed interaction lines is equivalent to a certain diagram of the same order without these lines crossed. Therefore, we can consider only diagrams without crossed interaction lines and take into account the contribution from the other diagrams by introducing combinatorial factors $s(k)$, which are assigned to the interaction lines.

In what follows, we consider commensurate fluctuations with $\mathbf{Q} = (\pi/a, \pi/a)$ [16] without regard for their spin structure (i.e., the CDW type of fluctuations). In this case, the combinatorial factor is [6]

$$s(k) = k. \quad (6)$$

If the spin structure of the interaction is taken into account in the framework of the nearly antiferromagnetic Fermi liquid model (spin-fermion model [6]), the combinatorial analysis of the diagrams becomes more complicated. In particular, in this model, the spin and charge two-particle vertices are radically different. In [6], the spin interaction was described in terms of the isotropic Heisenberg model. If this interaction is described within the Ising model, then only spin-preserving scattering processes will retain, for which the diagrams for commensurate fluctuations are characterized by combinatorial factor (6) for both the one-particle Green's function and the spin and charge vertices. Therefore, we will consider only the case of commensurate "Ising" spin AFM (SDW) fluctuations characterized by Eq. (6) and commensurate charge fluctuations (CDWs). Detailed consideration of the case of incommensurate CDW-type fluctuations can be found in [7, 15, 16].

Charge fluctuation scattering is insensitive to the electron spin, and the interaction sign is independent of whether the vertex closing the interaction line is a charge vertex or a spin vertex, changing the electron spin. In the case of spin fluctuations, an extra factor of (–1) should be assigned to an interaction line with longitudinal spin component S^z closed by a spin vertex changing the spin direction [6]. Therefore, this factor should also be assigned to an interaction line covering an anomalous Green's function in the case of spin fluctuations.

As a result, we obtain the Gor'kov equations [19] shown in diagrammatic notation in Fig. 2a. Here and henceforth, the upper sign corresponds to the case of charge fluctuations and the lower sign to that of spin fluctuations. The corresponding two coupled recurrent equations for the normal and anomalous Green's functions have the form

$$G_k = G_{0k} + G_{0k}\tilde{G}G_k - G_{0k}\tilde{F}F_k^+ - F_{0k}\tilde{G}^*F_k^+ - F_{0k}\tilde{F}^+G_k,$$
$$F_k^+ = F_{0k}^+ + F_{0k}^+\tilde{G}G_k - F_{0k}^+\tilde{F}F_k^+ + G_{0k}^*\tilde{G}^*F_k^+ + G_{0k}^*\tilde{F}^+G_k, \quad (7)$$

where

$$\tilde{G} = W^2 s(k+1) G_{k+1}, \quad \tilde{F}^+ = \pm W^2 s(k+1) F_{k+1}^+, \quad (8)$$

$$G_{0k}(\varepsilon_n \mathbf{p}) = -\frac{i\tilde{\varepsilon}_n + \xi_k}{\tilde{\varepsilon}_n^2 + \xi_k^2 + |\tilde{\Delta}|^2},$$
$$F_{0k}^+(\varepsilon_n \mathbf{p}) = \frac{\tilde{\Delta}^*}{\tilde{\varepsilon}_n^2 + \xi_k^2 + |\tilde{\Delta}|^2}. \quad (9)$$

Here,

$$\xi_k = \begin{cases} \xi_{\mathbf{p}+\mathbf{Q}} & \text{for odd } k \\ \xi_\mathbf{p} & \text{for even } k \end{cases} \quad (10)$$

and the renormalized frequency $\tilde{\varepsilon}$ and energy gap $\tilde{\Delta}$, given by

$$\tilde{\varepsilon}_n = \eta_k \varepsilon_n, \quad \tilde{\Delta} = \eta_k \Delta_k, \quad \eta_k = 1 + \frac{k v_k \kappa}{\sqrt{\varepsilon_n^2 + |\Delta_k|^2}}, \quad (11)$$

are analogous to those that appear when considering superconductors with impurities [19]. Here, $\kappa = \xi^{-1}$,

$$v_k = \begin{cases} |v_x(\mathbf{p}+\mathbf{Q})| + |v_y(\mathbf{p}+\mathbf{Q})| & \text{for odd } k \\ |v_x(\mathbf{p})| + |v_y(\mathbf{p})| & \text{for even } k, \end{cases} \quad (12)$$

[1] The result obtained in [11] according to which the superconducting energy gap is not self-averaging even for $\xi < \xi_0$ is likely due to the specific features of the short-range-order model used in that work.

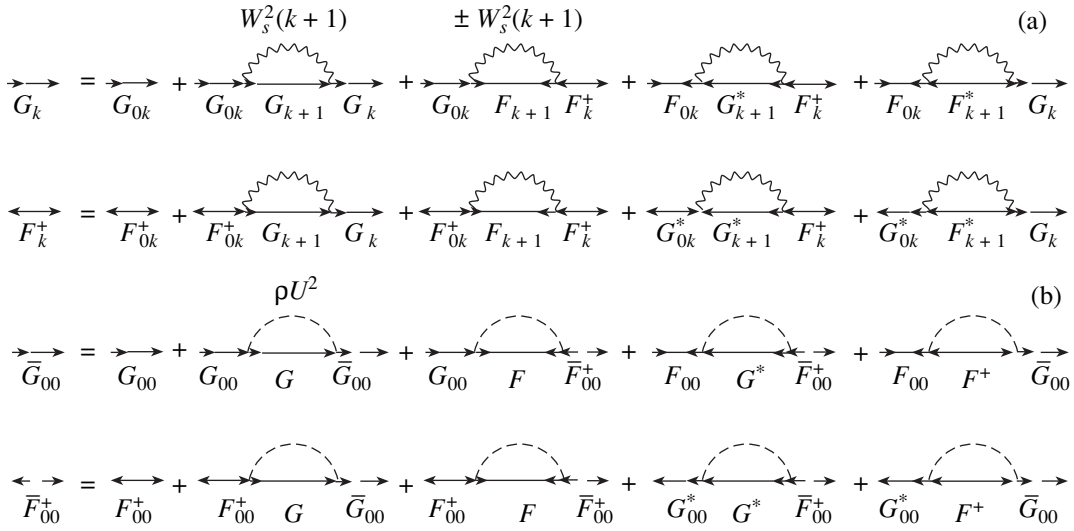

Fig. 2. Diagrammatic representation of (a) the recurrent Gor'kov equations and (b) equations for the Green's functions $\bar{G}_{00}$ and $\bar{F}_{00}$.

where $\mathbf{v}(\mathbf{p}) = \partial\xi_\mathbf{p}/\partial\mathbf{p}$ is the velocity of a free quasiparticle, and the bare energy gap is

$$\Delta_k = \begin{cases} \Delta e(\mathbf{p}+\mathbf{Q}) & \text{for odd } k \\ \Delta e(\mathbf{p}) & \text{for even } k. \end{cases} \quad (13)$$

A set of recursion relations for the real and imaginary parts of the normal Green's function and for the anomalous Green's function can easily be derived from Eq. (7)–(11). Introducing the notation

$$\mathrm{Im}\, G_k = -\varepsilon_n J_k, \quad \mathrm{Re}\, G_k = R_k, \quad F_k^+ = \Delta_k^* f_k, \quad (14)$$

we obtain the following set of recursion relations for J_k, R_k, and f_k:

$$J_k = \frac{\eta_k + W^2 s(k+1) J_{k+1}}{d_k},$$

$$R_k = -\frac{\xi_k + W^2 s(k+1) R_{k+1}}{d_k}, \quad (15)$$

$$f_k = \frac{\eta_k \pm W^2 s(k+1)(\Delta_{k+1}^*/\Delta_k^*) f_{k+1}}{d_k},$$

where $d_k = \varepsilon_n^2(\eta_k + W^2 s(k+1)J_{k+1})^2 + (\xi_k + W^2 s(k+1)R_{k+1})^2 + |\Delta_k|^2(\eta_k \pm W^2 s(k+1)(\Delta_{k+1}^*/\Delta_k^*) f_{k+1})^2$.

The normal and anomalous Green's functions of interest to us are expressed in terms of J_0, R_0, and f_0 as

$$\mathrm{Im}\, G = -\varepsilon_n J_0, \quad \mathrm{Re}\, G = R_0, \quad F^+ = \Delta^* e(\mathbf{p}) f_0 \quad (16)$$

and are obtained by completely summing the perturbation expansion in the interaction between an electron and short-range-order dielectric fluctuations in the superconductor.

Let us consider the case of charge fluctuations. For *s* pairing, the superconducting energy gap remains unchanged as the vector **Q** is added to the momentum; i.e., $e(\mathbf{p}+\mathbf{Q}) = e(\mathbf{p})$, as is the case in the model where hot flat sections are assumed to exist on the Fermi surface [10]. In this case, it turns out that $\Delta_{k+1} = \Delta_k$ and the recursion relations for J_k and f_k are identical, so $J_k = f_k$. For $d_{x^2-y^2}$ pairing, the superconducting energy gap changes sign as the vector **Q** is added to the momentum, ($e(\mathbf{p}+\mathbf{Q}) = -e(\mathbf{p})$); therefore, $\Delta_{k+1} = -\Delta_k$ and the second terms in the recursion relations for f_k and J_k differ in sign.

Thus, the reversal in sign of the superconducting energy gap upon adding the vector **Q** to the momentum is equivalent to a sign reversal of the second term in the recursion relation for the anomalous Green's function [the last expression in Eqs. (15)], i.e., is equivalent to passing over to the case of spin fluctuations. Therefore, in the case of spin fluctuations, the types of pairing are interchanged; namely, for *s* pairing, the gap does not change upon adding the vector **Q** to the momentum and the recursion relations for J_k and f_k differ in sign, while for $d_{x^2-y^2}$ the recursion relations for these quantities are identical and, hence, $J_k = f_k$.

Thus, the recursion relation for the anomalous Green's function takes the form

$$f_k = \frac{\eta_k \pm W^2 s(k+1) f_{k+1}}{d_k}, \quad (17)$$

where the plus sign corresponds to *s* pairing in the case of charge (CDW) fluctuations and to $d_{x^2-y^2}$ pairing in the case of spin (SDW) fluctuations and the minus sign corresponds to *s* pairing for spin fluctuations and to $d_{x^2-y^2}$ pairing for charge fluctuations.

Two qualitatively different types (corresponding to the upper and lower signs in Eq. (17)) of models of the influence of the pseudogap on superconductivity also arise when analyzing the superconducting properties of such systems in the vicinity of the critical temperature ($T \sim T_c$) on the basis of the Ginzburg–Landau expansion [12]. The case of spin fluctuation scattering and $d_{x^2-y^2}$ pairing (corresponding to the plus sign in Eq. (17)) is most likely to take place in copper oxide–based high-T_c superconductors. Therefore, we primarily consider this case in what follows.

4. SUPERCONDUCTOR WITH IMPURITIES

In considering a superconductor in the pseudogap state with impurities, we assume that the disorder is fairly weak and restrict our consideration to diagrams in which (dashed) lines corresponding to impurity scattering do not cross one another and wavy lines representing dielectric-fluctuation scattering.[2]

Let us consider the normal ($\bar{G}_{00}$) and anomalous ($\bar{F}_{00}$) Green's functions given by the diagrammatic equations in Fig. 2b, where the full (dressed) normal (G) and anomalous (F) Green's functions taking into account scattering by impurities and dielectric fluctuations are indicated below the impurity lines. In explicit form, these equations can be written as

$$\begin{aligned}\bar{G}_{00} &= G_{00} + G_{00}\bar{G}\bar{G}_{00} - G_{00}\bar{F}\bar{F}^{+}_{00} \\ &\quad - F_{00}\bar{G}^{*}\bar{F}^{+}_{00} - F_{00}\bar{F}^{+}\bar{G}_{00}, \\ \bar{F}^{+}_{00} &= F^{+}_{00} + F^{+}_{00}\bar{G}\bar{G}_{00} - F^{+}_{00}\bar{F}\bar{F}^{+}_{00} \\ &\quad + G^{*}_{00}\bar{G}^{*}\bar{F}^{+}_{00} + G^{*}_{00}\bar{F}^{+}\bar{G}_{00},\end{aligned} \tag{18}$$

where

$$\bar{G} = \rho U^2 \sum_{\mathbf{p}} G, \quad \bar{F}^{+} = \rho U^2 \sum_{\mathbf{p}} F^{+}, \tag{19}$$

ρ is the concentration of impurities, and U is their potential.

In the absence of dielectric fluctuations, we have $G = \bar{G}_{00}$ and $F = \bar{F}_{00}$ and the diagrammatic equations in Fig. 2b and Eqs. (18) go over to the conventional Gor'kov equations for a superconductor with impurities [19].

The normal, $\bar{G}_{00}$, and anomalous, $\bar{F}_{00}$, Green's functions defined by Eqs. (18) have the form of unperturbed Green's functions (5) with impurity-renormalized frequency and gap[3]:

$$\bar{G}_{00} = -\frac{i\bar{\varepsilon}_n + \xi_{\mathbf{p}}}{\bar{\varepsilon}_n^2 + \xi_{\mathbf{p}}^2 + |\bar{\Delta}|^2}, \quad \bar{F}^{+}_{00} = \frac{\bar{\Delta}^*}{\bar{\varepsilon}_n^2 + \xi_{\mathbf{p}}^2 + |\bar{\Delta}|^2}, \tag{20}$$

where

$$\begin{aligned}\bar{\varepsilon}_n &= \varepsilon_n - \rho U^2 \sum_{\mathbf{p}} \mathrm{Im}\, G \equiv \eta_\varepsilon \varepsilon_n, \\ \bar{\Delta}^* &= \Delta^* + \rho U^2 \sum_{\mathbf{p}} F^{+} \equiv \eta_\Delta \Delta^*.\end{aligned} \tag{21}$$

The frequency- and gap-renormalization factors η_ε and η_Δ defined by Eqs. (21) depend on dielectric-fluctuation scattering, i.e., on W, but are momentum-independent. Therefore, we can construct perturbation theory with respect to interaction with dielectric fluctuations starting with the dressed normal and anomalous Green's functions $\bar{G}_{00}$ and $\bar{F}_{00}$ (taking into account impurity scattering) in much the same way as was done in the absence of impurities starting with unperturbed Green's functions (5). The results obtained in this case coincide with those from Section 3 after the substitutions $\varepsilon_n \longrightarrow \eta_\varepsilon \varepsilon_n$ and $\Delta \longrightarrow \eta_\Delta \Delta$. The recursion relations for the quantities J_k, R_k, and f_k defined by Eqs. (14) coincide with Eqs. (15), derived for a superconductor without impurities, if in them one makes the substitutions

$$\eta_k \longrightarrow \eta_{\varepsilon k} = \left(1 + \frac{k v_k \kappa}{\sqrt{\eta_\varepsilon^2 \varepsilon_n^2 + \eta_\Delta^2 |\Delta_k|^2}}\right)\eta_\varepsilon \tag{22}$$

in the equation for the imaginary part of the normal Green's function, J_k, and

$$\eta_k \longrightarrow \eta_{\Delta k} = \left(1 + \frac{k v_k \kappa}{\sqrt{\eta_\varepsilon^2 \varepsilon_n^2 + \eta_\Delta^2 |\Delta_k|^2}}\right)\eta_\Delta \tag{23}$$

in the equation for the anomalous Green's function f_k. The normal and anomalous Green's functions in this case are expressed in terms of R_0, J_0, and f_0 through Eqs. (16) as before.

The recursion relation for the anomalous Green's function in the presence of impurity scattering coin-

[2] In effect, this approximation corresponds to the assumption that the density of states and the superconducting energy gap are self-averaging in the random field of impurities and dielectric fluctuations.

[3] There is also a renormalization of the spectrum, $\bar{\xi}_{\mathbf{p}} = \xi_{\mathbf{p}} + \rho U^2 \sum_{\mathbf{p}} \mathrm{Re}\, G$, which reduces to an insignificant (as numerical estimations show) renormalization of the chemical potential and which is neglected in what follows.

cides with Eq. (17) after substitution (23). As mentioned above, we will consider only the cases corresponding to the plus sign in Eq. (17), i.e., the case of *s* pairing for charge fluctuations and the case of *d* pairing for spin fluctuations.

For *s* pairing and charge fluctuations, we have $\eta_\varepsilon = \eta_\Delta$ and

$$\eta_{\varepsilon k} = \eta_{\Delta k} = \eta_\varepsilon + \frac{kv_k\kappa}{\sqrt{\varepsilon_n^2 + |\Delta_k|^2}}. \quad (24)$$

In this case, as in the absence of impurities, the recursion relations for J_k and f_k are identical and, hence, $J_k = f_k$.

For *d* pairing and spin fluctuations, because of anisotropy of the superconducting energy gap, we have $\sum_{\mathbf{p}} F = 0$ and $\eta_\Delta = 1$ and Eqs. (22) and (23) take the form

$$\eta_{\varepsilon k} = \left(1 + \frac{kv_k\kappa}{\sqrt{\eta_\varepsilon^2\varepsilon_n^2 + |\Delta_k|^2}}\right)\eta_\varepsilon,$$
$$\eta_{\Delta k} = 1 + \frac{kv_k\kappa}{\sqrt{\eta_\varepsilon^2\varepsilon_n^2 + |\Delta_k|^2}}. \quad (25)$$

The renormalization factors η_ε and η_Δ should be determined self-consistently in the recurrent procedure; therefore, from Eqs. (21), we obtain

$$\eta_\varepsilon = 1 + \rho U^2 \sum_{\mathbf{p}} J_0, \quad \eta_\Delta = 1 + \rho U^2 \sum_{\mathbf{p}} e(\mathbf{p}) f_0. \quad (26)$$

This self-consistent calculation of the renormalization factors in recurrent procedure (15) need to be carried out for each Matsubara frequency, which greatly increases the computational effort. For this reason, in addition to the above self-consistent scheme for including impurity and dielectric-fluctuation scattering, we will also use a simpler, non-self-consistent approximation, in which the impurity lines in the diagrammatic equations in Fig. 2b represent the unperturbed Green's functions G_{00} and F_{00}.[4] In this approximation, the frequency- and gap-renormalization factors are calculated from simple equations

$$\eta_\varepsilon = \eta_\Delta = 1 + \frac{\gamma_0}{\sqrt{\varepsilon_n^2 + |\Delta_k|^2}} \quad (s \text{ pairing}),$$
$$\eta_\varepsilon = 1 + \frac{\gamma_0}{\sqrt{\varepsilon_n^2 + |\Delta_k|^2}}, \quad \eta_\Delta = 1 \quad (d \text{ pairing}), \quad (27)$$

where $\gamma_0 = \pi\rho U^2 N_0(0)$ is the impurity scattering frequency and $N_0(0)$ is the density of states at the Fermi level in the absence of impurities and a pseudogap.

5. CRITICAL TEMPERATURE AND THE TEMPERATURE DEPENDENCE OF THE SUPERCONDUCTING ENERGY GAP

The energy gap of a superconductor is given by

$$\Delta(\mathbf{p}) = -T\sum_{\mathbf{p}'}\sum_{\varepsilon_n} V_{sc}(\mathbf{p}, \mathbf{p}')F(\varepsilon_n\mathbf{p}'). \quad (28)$$

The anomalous Green's function can be found from Eq. (16) using recurrent procedure (15). With regard for Eq. (4), Eq. (28) can be written as

$$1 = VT \sum_{|\varepsilon_n| < \omega_c} \sum_{\mathbf{p}} f_0(\varepsilon_n\mathbf{p})e^2(\mathbf{p}). \quad (29)$$

From Eq. (29), we obtain an equation for the superconducting transition temperature T_c by setting $\Delta \longrightarrow 0$

$$1 = VT_c \sum_{|\varepsilon_n| < \omega_c} \sum_{\mathbf{p}} \lim_{\Delta \to 0} f_0(\varepsilon_n\mathbf{p})e^2(\mathbf{p}). \quad (30)$$

To perform numerical calculations, we choose an energy (temperature) scale characterizing the superconducting state in our model in the absence of pseudogap-state fluctuations ($W = 0$). In this case, the equation for the corresponding superconducting transition temperature T_{c0} has the conventional BCS form (in the general case of anisotropic pairing):

$$1 = \frac{2VT}{\pi^2}\sum_{n=0}^{\bar{m}}\int_0^\pi dp_x \int_0^\pi dp_y \frac{e^2(\mathbf{p})}{\xi_p^2 + \varepsilon_n^2}, \quad (31)$$

where $\bar{m} = \omega_c/2\pi T_{c0}$ is a dimensionless frequency cutoff of the sum over Matsubara frequencies. All calculations are performed for quasiparticle spectrum (2), which is typical of high-T_c superconductors, with $\mu = -1.3t$ and $t'/t = -0.4$. For (arbitrarily chosen) $\omega_c = 0.4t$ and $T_{c0} = 0.01t$, we can easily find the value of the pairing parameter V in Eq. (31) for which the temperature T_{c0} is equal to the chosen value for the different types of pairing indicated in Eq. (4). For *s* and $d_{x^2-y^2}$ pairing, we obtain $V/ta^2 = 1$ and 0.55, respectively [12].

Typical values of the superconducting transition temperature T_c calculated numerically directly from Eq. (30), based on recursion relations (15) for a superconductor with a pseudogap in the absence of impurities, are shown in the inset to Fig. 3. Pseudogap-state (dielectric) fluctuations are seen to cause a significant decrease in the superconducting transition temperature, with $d_{x^2-y^2}$ pairing being suppressed to a noticeably

[4] This approximation was used in [20] to analyze the influence of impurities on superconductivity in terms of an extremely simplified version of the pseudogap-state model with a infinite correlation length and the Fermi surface exhibiting a complete "nesting."

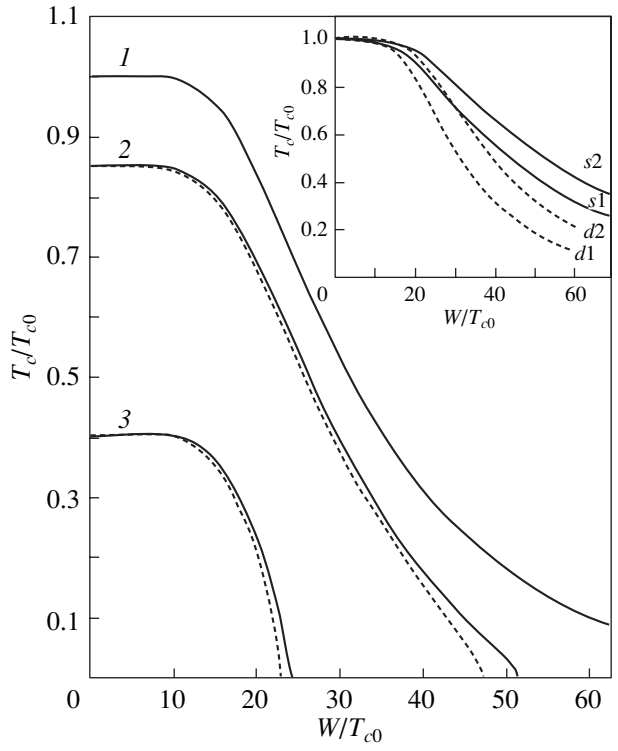

Fig. 3. Dependence of the superconducting transition temperature on the effective pseudogap width in the case of *d* pairing for $\kappa a = 0.2$ and different values of the impurity scattering frequency γ_0/T_{c0}: (*1*) 0, (*2*) 0.18, and (*3*) 0.64. Solid lines are self-consistent solutions, and dashed lines are non-self-consistent solutions. The inset is the dependence of the superconducting transition temperature on the effective pseudogap width in the case of *s* pairing and charge (CDW) fluctuation scattering (curves *s1*, *s2*) and in the case of *d* pairing and spin AFM (SDW) fluctuation scattering (curves *d1*, *d2*). The inverse correlation length is $\kappa a =$ 0.2 (curves *s1*, *d1*) and 0.5 (curves *s2*, *d2*).

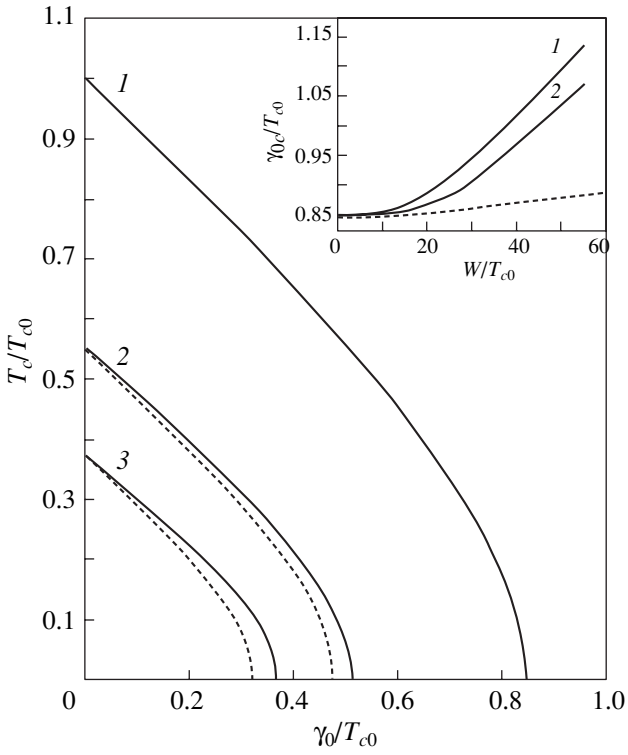

Fig. 4. Dependence of the superconducting transition temperature on the impurity scattering frequency in the case of *d* pairing for various values of the effective pseudogap width and inverse correlation length: (*1*) $W/T_{c0} = 0$ and (*2*) 37 and (*1*, *2*) $\kappa a = 0.5$ and (*3*) $W/T_{c0} = 37$ and $\kappa a = 0.2$. Solid curves are self-consistent solutions, and dashed curves are non-self-consistent solutions. The inset is the dependence of the ratio of the critical impurity scattering frequency to the superconducting transition temperature on the effective pseudogap width for (*1*) $\kappa a = 0.2$ and (*2*) 0.5. Dotted curve is a non-self-consistent solution for $\kappa a = 0.2$.

greater extent than *s* pairing. In contrast, a decrease in the correlation length ξ (i.e., an increase in parameter κ) of pseudogap-state fluctuations causes T_c to increase. These results are in complete agreement with those obtained by analyzing the Cooper instability of the normal phase in terms of the same pseudogap-state model [12] and are qualitatively similar to the results obtained earlier within the hot-section model [8, 10]. However, in the latter case, there are significant distinctions; namely, the dependence of T_c on the pseudogap width W exhibits a characteristic "shelf" in the region of $W < 10T_{c0}$ and T_c is significantly decreased over the range of $W \sim 50T_{c0}$.

Figures 3 and 4 show data on the superconducting transition temperature for *d* pairing calculated with inclusion of nonmagnetic-impurity scattering from Eq. (30) [based on recursion relations (15)], with the coefficients η_ε and η_Δ being determined either self-consistently in the recurrent procedure using Eqs. (26) (solid curves) or non-self-consistently from Eqs. (27) (dashed curves).

In the presence of impurity scattering, dielectric fluctuations suppress superconductivity to a greater extent and a critical value of the effective pseudogap width appears at which the superconducting transition temperature T_c vanishes (Fig. 3).

In the presence of pseudogap-state fluctuations, nonmagnetic impurities also strongly suppress *d*-pairing superconductivity [20]. The dependence of the superconducting transition temperature on the impurity-scattering frequency (Fig. 4) fairly closely follows the conventional Abrikosov–Gor'kov curve [21, 22] in the absence of a pseudogap (curve *1*). As the pseudogap increases, the critical value of the scattering frequency increases only slightly (inset to Fig. 4), from the conventional value given by the Abrikosov–Gor'kov theory $\gamma_{0c}/T_c = \pi/2\gamma$ in the absence of a pseudogap to the value $\gamma_{0c}/T_c \approx 1.0$–$1.1$ near the critical value of the

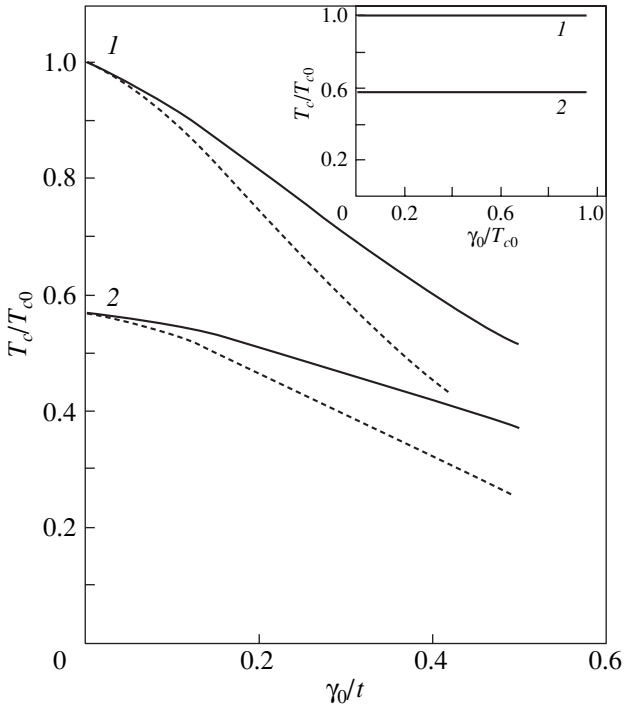

Fig. 5. Dependence of the superconducting transition temperature on the impurity scattering frequency in the case of *s* pairing for various values of the effective pseudogap width: (*1*) $W/T_{c0} = 0$ and (*2*) 37; $\kappa a = 0.2$. Solid curves are self-consistent solutions, and dashed curves are non-self-consistent solutions.

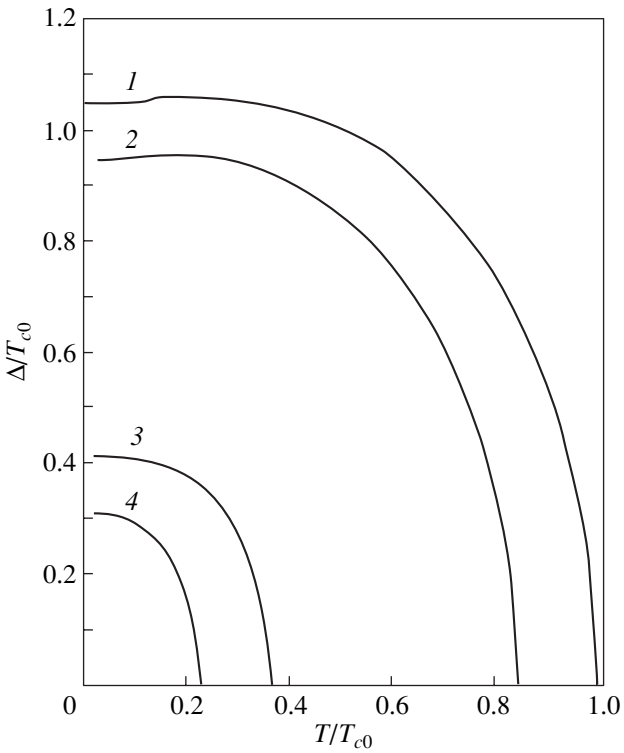

Fig. 6. Temperature dependence of the superconducting energy gap in the case of *d* pairing for $\kappa a = 0.2$ and various values of the effective pseudogap width W/T_{c0} and the impurity scattering frequency γ_0/T_{c0}: (*1*) 0, 0; (*2*) 0, 0.18; (*3*) 37, 0; and (*4*) 37, 0.18, respectively.

pseudogap width at which superconductivity is completely suppressed.

In the case of *s* pairing, nonmagnetic-impurity scattering affects superconductivity only slightly (inset to Fig. 5). The small decrease in T_c at $\gamma_0 \sim t$ (Fig. 5) is due mainly to the general decrease in the density of states resulting from the band broadening produced by such strong impurity scattering.

Figure 6 shows the temperature dependence of the *d*-type superconducting energy gap calculated from Eq. (29) using the recurrent procedure. This dependence is qualitatively similar to that given by the BCS theory (curve *1* in Fig. 6). However, there are distinctions; in particular, for the impurity scattering frequency corresponding to curves *2* and *4* in Fig. 6 ($\gamma_0 = 0.18T_{c0}$), the ratio $2\Delta(T = 0)/T_c$ increases twofold as the pseudogap width *W* increases from zero to the critical value at which superconductivity is completely suppressed. In the case of *s*-pairing superconductivity, the ratio $2\Delta(T = 0)/T_c$ is virtually independent of both the impurity scattering frequency and pseudogap width.

It should be noted that all of the above results concerning the superconducting energy gap are valid if the superconducting order parameter (gap width) is self-averaging with respect to AFM fluctuations (mean-field approximation [9]). This condition is satisfied if the correlation length is not very long: $\xi < \xi_0$, where ξ_0 is the coherence length of the superconductor (the Cooper pair size at $T = 0$). For $\xi \gg \xi_0$, the absence of self-averaging leads to significant effects, which manifest themselves in the appearance of characteristic "tails" in the temperature dependence of the averaged energy gap in the range $T_c < T < T_{c0}$ [9, 11].

In studying the pseudogap state of real HTSC systems, it is important to analyze the dependence of the physical characteristics on carrier density. In our model, this dependence is due to the carrier density dependences of the effective pseudogap width *W* and the correlation length ξ, which, unfortunately, are experimentally determined only indirectly and are to a poor extent [1, 2]. The analogous dependence of the temperature T_{c0} (on which there is no information) can also be of importance. According to very rough estimates, the correlation length ξ varies only moderately over a fairly wide range of carrier densities and the pseudogap width *W* decreases linearly with increasing carrier density from a value of the order of 10^3 K near the region of the dielectric phase down to a value of the order of the superconducting transition temperature (as the optimum doping level is approached) and then vanishes at somewhat higher densities (see [2, Fig. 6], based on [3, Fig. 4], where the corresponding data for

the YBCO system are presented). Using this dependence, one can easily transform the dependences on W presented in this paper into the corresponding carrier density dependences. Assuming a linear dependence of T_{c0} on carrier density, such a consideration was recently given in [20] in terms of an extremely simplified version of our model in which the correlation length is infinite and the Fermi surface exhibits a complete nesting. It was shown that this model qualitatively describes the typical phase diagram of HTSC cuprates. However, attempts at "improving" these qualitative results are not worthwhile because of the obvious roughness of the model and the absence of reliable experimental data on the carrier density dependences of W, ξ, and T_{c0}.

ACKNOWLEDGMENTS

The authors are grateful to M.V. Sadovskiĭ for his collaboration and many helpful discussions.

This study was supported in part by the Russian Foundation for Basic Research (project no. 02-02-16031), the basic research program of the Presidium of the Russian Academy of Sciences "Strongly Correlated Electrons in Semiconductors, Metals, Superconductors, and Magnetic Materials," and the Ministry of Industry and Science of the Russian Federation (program "Study of Collective and Quantum Effects in Condensed Media").

REFERENCES

1. T. Timusk and B. Statt, Rep. Prog. Phys. **62** (1), 61 (1999).
2. M. V. Sadovskiĭ, Usp. Fiz. Nauk **171** (5), 539 (2001) [Phys. Usp. **44**, 515 (2001)].
3. J. L. Tallon and J. W. Loram, Physica C (Amsterdam) **349** (1–2), 53 (2000).
4. V. M. Krasnov, A. Yurgens, D. Winkler, P. Delsing, and T. Claeson, Phys. Rev. Lett. **84** (25), 5860 (2000).
5. N. P. Armitage, D. H. Lu, C. Kim, A. Damascelli, K. M. Shen, F. Ronning, D. L. Feng, B. Bogdanov, and Z.-X. Shen, Phys. Rev. Lett. **87**, 147003 (2001).
6. J. Schmalian, D. Pines, and B. Stojkovic, Phys. Rev. Lett. **80** (17), 3839 (1998); Phys. Rev. B **60** (1), 667 (1999).
7. É. Z. Kuchinskiĭ and M. V. Sadovskiĭ, Zh. Éksp. Teor. Fiz. **115** (5), 1765 (1999) [JETP **88**, 968 (1999)].
8. A. I. Posazhennikova and M. V. Sadovskiĭ, Zh. Éksp. Teor. Fiz. **115** (2), 632 (1999) [JETP **88**, 347 (1999)].
9. É. Z. Kuchinskiĭ and M. V. Sadovskiĭ, Zh. Éksp. Teor. Fiz. **117** (3), 613 (2000) [JETP **90**, 535 (2000)].
10. É. Z. Kuchinskiĭ and M. V. Sadovskiĭ, Zh. Éksp. Teor. Fiz. **119** (3), 553 (2001) [JETP **92**, 480 (2001)].
11. É. Z. Kuchinskiĭ and M. V. Sadovskiĭ, Zh. Éksp. Teor. Fiz. **121** (3), 758 (2002) [JETP **94**, 654 (2002)].
12. É. Z. Kuchinskiĭ, M. V. Sadovskiĭ, and N. A. Strigina, Zh. Éksp. Teor. Fiz. (in press).
13. P. Monthoux, A. V. Balatsky, and D. Pines, Phys. Rev. B **46** (22), 14803 (1992).
14. P. Monthoux and D. Pines, Phys. Rev. B **47** (10), 6069 (1993); Phys. Rev. B **49** (6), 4261 (1994).
15. M. V. Sadovskiĭ, Zh. Éksp. Teor. Fiz. **66** (6), 1720 (1974) [Sov. Phys. JETP **39**, 845 (1974)]; Fiz. Tverd. Tela (Leningrad) **16** (10), 2504 (1974) [Sov. Phys. Solid State **16**, 1632 (1974)].
16. M. V. Sadovskiĭ, Zh. Éksp. Teor. Fiz. **77** (5), 2070 (1979) [Sov. Phys. JETP **50**, 989 (1979)].
17. L. P. Gor'kov, Zh. Éksp. Teor. Fiz. **37** (5), 1407 (1959) [Sov. Phys. JETP **10**, 998 (1959)].
18. P. G. de Gennes, *Superconductivity of Metals and Alloys* (Benjamin, New York, 1966; Mir, Moscow, 1968).
19. A. A. Abrikosov, L. P. Gor'kov, and I. E. Dzyaloshinskiĭ, *Methods of Quantum Field Theory in Statistical Physics* (Fizmatgiz, Moscow, 1962; Prentice Hall, Englewood Cliffs, N.J., 1963).
20. A. Posazhennikova and P. Coleman, Phys. Rev. B **67** (16), 165109 (2003).
21. A. A. Abrikosov and L. P. Gor'kov, Zh. Éksp. Teor. Fiz. **39** (6), 1781 (1960) [Sov. Phys. JETP **12**, 1243 (1960)].
22. A. I. Larkin, Pis'ma Zh. Éksp. Teor. Fiz. **2** (3), 205 (1965) [JETP Lett. **2**, 130 (1965)].

Translated by Yu. Epifanov

Physics of the Solid State, Vol. 46, No. 9, 2004, pp. 1613–1621. Translated from Fizika Tverdogo Tela, Vol. 46, No. 9, 2004, pp. 1566–1573.
Original Russian Text Copyright © 2004 by Bryksin, Kleinert, Petrov.

SEMICONDUCTORS AND DIELECTRICS

Rectification of Space-Charge Waves upon Optical and Electrical Excitation

V. V. Bryksin*, P. Kleinert, and M. P. Petrov***

** Ioffe Physicotechnical Institute, Russian Academy of Sciences, Politekhnicheskaya ul. 26, St. Petersburg, 194021 Russia*
e-mail: vvb@mail.ioffe.ru
e-mail: mpetr.shuv@pop.ioffe.rssi.ru
*** Paul-Drude-Institut für Ferstkörperelektronik, Berlin, 10117 Germany*
e-mail: kl@pdi-berlin.de
Received January 26, 2004

Abstract—A comparative analysis is performed for three optical and electrical methods of exciting space-charge waves in photosemiconductors: (i) excitation by an external ac electric field combined with a static interference pattern, (ii) excitation by a moving interference grating, and (iii) excitation by an oscillating interference grating. It is shown that, in the case when space-charge waves are excited using a combination of all three methods, the dependence of the direct current passing through a sample on the excitation frequency exhibits two peaks that correspond to the resonant excitation of two modes of space-charge oscillations, namely, drift waves and trap recharging waves. It is noted that experimental observation of the peak attributed to the excitation of trap recharging waves should not pose any problems, whereas observation of the second peak associated with the excitation of drift waves is significantly complicated because of the small magnitude of the effect, especially for materials with a low electrical conductivity (or a long Maxwell relaxation time). © *2004 MAIK "Nauka/Interperiodica".*

1. INTRODUCTION

In recent years, particular interest has been expressed by researchers in experimental and theoretical investigations into the properties of space-charge waves in semiconductors. These waves are considered eigenmodes of electron density oscillations occurring in semiconductors in an external electric field. There exist two eigenmodes of space-charge waves. One eigenmode is associated with

the transfer of electron density fluctuations of free carriers in an external electric field. This mode is described by the dispersion law $\omega_1 = q\mu E_0$, where q is the wave vector, μ is the mobility of charge carriers, and E_0 is the strength of the external electric field. For brevity, waves of this mode will be referred to as drift waves. The second eigenmode of space-charge waves is associated with the capture of electrons in traps. Waves of this mode are termed trap recharging waves. For the second mode, the dispersion law has the form $\omega_2 = -(q\mu E_0\tau\tau_M)^{-1}$, where τ is the electron lifetime in the conduction band and τ_M is the Maxwell relaxation time. The phase velocities of these two modes have opposite directions, whereas the group velocities coincide in direction. The lifetime of space-charge waves depends on the relaxation times τ and τ_M, the trap concentration, and the carrier diffusion. Under actual experimental conditions, there can occur situations where the relaxation processes play the dominant role in damping of space-charge waves. Consequently, in a sufficiently strong electric field (under the conditions $q\mu E_0 \gg \tau^{-1}$, τ_M^{-1}), the high Q factor of space-charge waves is ensured and the inequalities $\omega_1 \gg \tau^{-1}$, $\tau_M^{-1} > \omega_2$, and $\omega_1 > \omega_2$ are satisfied. The theory of drift waves was described, for example, in [1–3], and the drift waves themselves were experimentally investigated by various methods in [4–7].

The first theoretical studies of trap recharging waves were published in [2, 3]. These waves were first experimentally observed using electrical [8] and optical [9] methods.

Space-charge waves have been attracting increasing research interest since the advent of optical methods for their excitation and detection. At present, the excitation of space-charge waves with the use of oscillating [10] and moving [9, 11] interference patterns is the most universally employed method. If a crystal is illuminated with the use of an interference pattern oscillating about its equilibrium position, the space-charge waves are resonantly excited under the condition that their spatial period and eigenmode coincide with the spatial period and frequency of oscillations of the interference pattern. In this case, the excitation conditions do not depend on the direction of the applied electric field. In the other method (upon illumination of a sample with an interference grating moving in one direction), the resonant excitation occurs when the period of the interference pattern and the velocity of its motion coincide

with the spatial period and phase velocity of the space-charge waves. In this method, it is necessary to ensure the appropriate direction of the applied electric field (or the appropriate direction of motion of the interference pattern). The excited space-charge waves can be detected by measuring either the Bragg diffraction of light (for photorefractive materials) or the electric current passing through the sample. In the latter case, it is necessary to provide conditions for effective nonlinear interactions of space-charge waves.

The nonlinear effects responsible for changes in the electric current under excitation of space-charge waves involve spatial [12, 13] and complete [14, 15] rectification of space-charge waves. For spatial rectification, a traveling space-charge wave interacts with a static charge grating (which always arises in the oscillating interference pattern). This interaction generates a spatially homogeneous but time-oscillating current both in the crystal and in the external circuit.

Complete rectification occurs upon the interaction of a moving charge grating with a moving field grating if the phase shift between these gratings is not equal to $\pi/2$. This interaction leads to a change in the direct current passing through the sample. Until now, complete rectification had been observed only using the oscillating-pattern method and only for trap recharging waves. Spatial rectification has been detected both for trap recharging waves [13] and, most likely, for drift waves [6, 7]. The complete and spatial rectification of these two modes upon excitation with an oscillating interference pattern (under standard conditions [14] and in crystals with negative differential conductivity [16]) has been theoretically investigated in sufficient detail. There are also works concerned with effects that are similar to complete rectification but are observed in the case of forced relaxation charge-density oscillations excited by a moving interference pattern rather than by trap recharging waves (see, for example, [17]). In the present work, we performed a theoretical investigation of the following effects: (i) the complete rectification of space-charge waves of both modes in the case of a moving interference pattern and (ii) the complete and spatial rectification upon combined (optical and electrical) excitation of space-charge waves when the sample is illuminated with a static interference pattern under the joint action of dc and ac electric fields.

The analysis performed in this work revealed that the effects of rectification of space-charge waves upon excitation with different methods are characterized by specific features. In particular, these effects depend on the carrier sign, excitation frequency, and other factors.

2. EXCITATION OF SPACE-CHARGE WAVES IN AN ALTERNATING-CURRENT ELECTRIC FIELD

As was noted above, the rectification of space-charge waves brings about the appearance of an alternating-current component in the circuit and a change in the direct-current component upon excitation of space-charge waves. Let us calculate the electric current passing through a sample that is placed in an electric field with the electric potential $U(t) = U_0 + U_{ac}\cos(\Omega t)$ and illuminated using a static interference pattern with the intensity $W(x) = W_0[1 + m\cos(K_g x)]$, where m is the contrast of the interference pattern and K_g is the wave vector of the pattern. In this calculation, we use a standard system of nonlinear equations [16] for the density $n(x, t)$ of free electrons and the electric field $E(x, t)$, that is,

$$\frac{\partial n(x,t)}{\partial t} + \frac{n(x,t) - \tilde{n}_0}{\tau} = g_0[1 + h(x)] + \frac{\varepsilon}{4\pi e}\frac{\partial^2 E(x,t)}{\partial x \partial t}, \quad (1)$$

$$\frac{\varepsilon}{4\pi}\frac{\partial E(x,t)}{\partial t} + j(x,t) = I(t), \quad (2)$$

$$j(x,t) = en(x,t)v[E(x,t)] - eD[E(x,t)]\frac{\partial n(x,t)}{\partial x}. \quad (3)$$

Here, $\tilde{n}_0$ is the equilibrium electron density, τ is the electron lifetime in the conduction band, ε is the permittivity of the crystal, $j(x, t)$ is the density of the electron current, $I(t)$ is the density of the total current, $v(E)$ is the drift velocity, and $D(E)$ is the diffusion coefficient. As in our previous work [16], we will consider the general case of a nonlinear current–voltage characteristic. This approach, in particular, makes it possible to examine space-charge waves in the vicinity of the instability point associated with the formation of either domain structures in superlattices or Gunn-type domain structures (see the discussion of this problem in [16]). In a weak electric field, when the Ohm law holds, the drift velocity has the form $v(E) = \mu E$, where μ is the mobility of charge carriers. In this case, the diffusion coefficient obeys the Einstein relation $D = kT\mu/e$ and does not depend on the external electric field E. Note also that, here, e is the carrier charge: $e > 0$ for hole conduction and $e < 0$ for electron conduction. Correspondingly, we have the mobility $\mu > 0$ for holes and $\mu < 0$ for electrons. Therefore, when comparing with the results obtained in [16], it is necessary to make the changes $e \longrightarrow -e$ and $v(E) \longrightarrow -v(E)$, because, in [16], e is the charge of electrons whose mobility was assumed to be positive. In the present work, the appropriate replacement is used to simplify the changeover from electrons to holes. The inclusion of holes is of considerable interest, especially in the study of a moving grating, when the important role is also played by particle fluxes rather than only by electric currents, as is the case with an oscillating grating. It should be noted that the rectification effects are associated with the nonlinear contribution from the product $en(x, t)v[E(x, t)]$ in Eq. (3).

Equations (1)–(3) differ from the relationships used in [16] only in that the rate of electron photogeneration

$$g(x) = g_0[1 + h(x)], \quad h(x) = m\cos(K_g x) \qquad (4)$$

does not depend on time. However, in the problem under consideration, the alternating component of the external electric field leads to a more complex boundary condition,

$$\frac{1}{L}\int_0^L dx E(x, t) + \rho I(t) = \Xi_0 + \Xi_{ac}\cos(\Omega t), \qquad (5)$$

where L is the length of the sample, $\Xi_0 = U_0/L$, $\Xi_{ac} = U_{ac}/L$, $\rho = RS/L$, R is the external resistance, and S is the cross section of the sample.

Since the equations used in this work and in [16] are similar to each other, they can be solved according to the same scheme. The sought quantities can be represented in the following form:

$$\begin{gathered} E(x, t) = E_0 + \delta E(x, t), \quad n(x, t) = n_0 + \delta n(x, t), \\ I(t) = I_0 + \delta I(t), \end{gathered} \qquad (6)$$

where E_0, n_0, and I_0 are the electric field, the electron density, and the total current under uniform illumination (i.e., at $m = 0$), respectively. In the absence of the alternating component of the external electric field (i.e., at $U_{ac} = 0$), we have

$$\begin{gathered} n_0 = \tilde{n}_0 + g_0\tau, \quad I_0 = en_0 v(E_0), \\ E_0 + \rho en_0 v(E_0) = \Xi_0. \end{gathered} \qquad (7)$$

The last of these relationships implicitly specifies the position of the operating point E_0 (for more detail, see [16]) as a function of the external voltage U_0. The corrections δE, δn, and δI at a sufficiently small value of the contrast m (or, more precisely, the effective parameter $mg_0\tau/n_0 < m$) and a small ac field amplitude U_{ac} are insignificant. Hence, we can use the expansion in the vicinity of the operating point E_0:

$$v(E_0 + \delta E) \cong v_0 + v_0'\delta E + \frac{1}{2}v_0''\delta E^2,$$

$$D(E_0 + \delta E) \cong D_0 + D_0'\delta E.$$

As a result, from Eqs. (1)–(3), we obtain a system of nonlinear equations for the dimensionless quantities,

$$\begin{gathered} \Omega\tau_M\frac{\partial Y}{\partial T} + Y + \lambda - \Lambda\frac{\partial\lambda}{\partial z} + \lambda Y + cY^2 - \Lambda' Y\frac{\partial\lambda}{\partial z} \\ = f(T), \end{gathered} \qquad (8)$$

$$\Omega\tau\frac{\partial\lambda}{\partial T} + \lambda = \frac{g_0\tau}{n_0}h(z) + \Omega\tau_M d\frac{\partial^2 Y}{\partial z\partial T}. \qquad (9)$$

Here,

$$\begin{gathered} z = K_g x, \quad T = \Omega t, \quad Y = \delta E\frac{v_0'}{v_0}, \quad \lambda = \frac{\delta n}{n_0}, \\ f = \frac{\delta I}{en_0 v_0}, \quad d = v_0 K_g\tau, \quad \Lambda = \frac{D_0 K_g}{v_0}, \\ \Lambda' = \frac{D_0' K_g}{v_0'}, \quad c = \frac{v_0'' v_0}{2v_0'^2} \end{gathered} \qquad (10)$$

and $\tau_M^{-1} = 4\pi e v_0' n_0/\varepsilon$ is the reciprocal of the Maxwell relaxation time generalized to the case where the conditions are nonlinear in the electric field. Recall that, for comparison with the results obtained in [16], it is necessary to carry out the changes $d \longrightarrow -d$, $\Lambda \longrightarrow -\Lambda$, and $\Lambda' \longrightarrow -\Lambda'$.

In Eqs. (8) and (9), we change over to the Fourier transform with respect to the coordinate and time

$$Y(z, T) = \sum_{p, l = -\infty}^{\infty} Y_{p, l}\exp(ipz + ilT). \qquad (11)$$

After simple manipulations, we obtain a closed equation for the Fourier components of the dimensionless electric field (compare with Eq. (19) in [16]):

$$\begin{aligned} f_l\delta_{p,0} &= Y_{p,l}\left(1 + i\Omega\tau_M l - \Omega\tau_M dpl\frac{1 - i\Lambda p}{1 + i\Omega\tau l}\right) \\ &+ \frac{g_0\tau}{n_0}(1 - i\Lambda p)h_p\delta_{l,0} + \frac{g_0\tau}{n_0}\sum_{p'}Y_{p-p',l}(1 - i\Lambda' p')h_{p'} \\ &- \sum_{p', l'}Y_{p-p', l-l'}Y_{p', l'}\left(\Omega\tau_M dp'l'\frac{1 - i\Lambda' p'}{1 + i\Omega\tau l'} - c\right), \end{aligned} \qquad (12)$$

where

$$h_p = \frac{m}{2}(\delta_{p,1} + \delta_{p,-1}). \qquad (13)$$

Equation (12) should be completed by the expression relating the electric current to the homogeneous electric field inside the sample. This expression can be derived from relationship (5) in the following form:

$$Y_{0,l} + \rho\sigma_d f_l = Y_{ac}\frac{1}{2}(\delta_{l,1} + \delta_{l,-1}), \qquad (14)$$

where $Y_{ac} = \Xi_{ac}v_0'/v_0$ and $\sigma_d = en_0 v_0'$ is the differential conductivity of a material at the operating point E_0.

By solving Eq. (12), we initially find the Fourier components $Y_{p,l}$ of the electric field with $p \neq 0$ (i.e., the spatially inhomogeneous components). These compo-

nents at $m = 0$ become zero. In the approximation lowest (linear) with respect to m, we have

$$Y_{p,l} = -\frac{g_0\tau}{n_0}h_p\Big[(1-i\Lambda p)\delta_{l,0} + \frac{(1-i\Lambda' p)Y_{0,l}}{1+i\Omega\tau_M l-\Omega\tau_M dlp(1-i\Lambda p)(1+i\Omega\tau l)^{-1}}\Big]. \quad (15)$$

When deriving relationship (15) from Eq. (12), we set $p \neq 0$, drop all contributions proportional to m^2 (the last term on the right-hand side), and take into account only the term with $p' = p$ in the penultimate term.

Now, we turn to the determination of the spatially homogeneous components $Y_{0,l}$ of the electric field. Setting $p = 0$ in Eq. (12) and using condition (14), we obtain

$$\frac{Y_{ac}}{2\rho\sigma_d}(\delta_{l,1}+\delta_{l,-1}) - \Big(1+i\Omega\tau_M l+\frac{1}{\rho\sigma_d}\Big)Y_{0,l} - c\sum_{l'}Y_{0,l-l'}Y_{0,l'} = \frac{g_0\tau}{n_0}\sum_{p\neq 0}h_pY_{-p,l}(1-i\Lambda' p) - \sum_{l',\,p\neq 0}Y_{-p,l-l'}Y_{p,l'}\Big(\Omega\tau_M dpl'\frac{1-ip\Lambda'}{1+il'\Omega\tau}-c\Big). \quad (16)$$

Since the calculations are performed to the lowest order in m, the spatially inhomogeneous components $Y_{p,l'}$ of the electric field in relationship (15) can be obtain from the homogeneous components in the zeroth order in m. By designating the homogeneous electric field components at $m = 0$ through $Y^{(0)}_{0,l}$, from expression (16), we derive the following equation for these quantities:

$$\frac{Y_{ac}}{2\rho\sigma_d}(\delta_{l,1}+\delta_{l,-1}) - \Big(1+i\Omega\tau_M l+\frac{1}{\rho\sigma_d}\Big)Y^{(0)}_{0,l} = c\sum_{l'}Y^{(0)}_{0,l-l'}Y^{(0)}_{0,l'}. \quad (17)$$

Thus, we derived the electric-circuit equation for a sample with a nonlinear current–voltage characteristic in the presence of an external resistance ρ. For a sufficiently small amplitude Y_{ac} of the ac electric signal, Eq. (17) can be solved by the iteration method. As a result, within a factor Y^2_{ac}, we obtain

$$Y^{(0)}_{0,l} \cong \frac{1}{1+\rho\sigma_d(1+i\Omega\tau_M l)}\Big\{\frac{Y_{ac}}{2}(\delta_{l,1}+\delta_{l,-1}) - \frac{c}{4}\rho\sigma_d Y^2_{ac}\Big[\frac{2\delta_{l,0}}{(1+\rho\sigma_d)^2+(\rho\sigma_d\Omega\tau_M)^2} + \frac{\delta_{l,2}}{(1+\rho\sigma_d(1+i\Omega\tau_M))^2}+\frac{\delta_{l,-2}}{(1+\rho\sigma_d(1-i\Omega\tau_M))^2}\Big]\Big\}. \quad (18)$$

Hereinafter, our interest will be only in the zeroth and first electric field components with $l = 0, \pm 1$.

After rather cumbersome but simple calculations, the expression for the first Fourier component of the electric current can be determined accurate to within the contributions $\propto m^2 Y_{ac}$; that is,

$$I_1 = \frac{1}{2}\frac{en_0v_0'\Xi_{ac}}{1+\rho\sigma_d(1+i\Omega\tau_M)}\Big\{1+i\Omega\tau_M + \frac{(g_0\tau m/n_0)^2}{1+\rho\sigma_d(1+i\Omega\tau_M)}\Big[\frac{c\rho\sigma_d[1+\Lambda\Lambda'-c(1+\Lambda^2)]}{(1+\rho\sigma_d)} - \frac{1+i\Omega\tau}{4\tau\tau_M}\Big(\frac{C(\Omega)}{(\Omega+\Omega_1)(\Omega+\Omega_2)} + \frac{C^*(-\Omega)}{(\Omega-\Omega_1^*)(\Omega-\Omega_2^*)}\Big)\Big]\Big\}, \quad (19)$$

where

$$C(\Omega) = 2c(1+i\Lambda)(1-i\Lambda') - (1+\Lambda'^2) - (1+\Lambda^2)\Big(\frac{1-i\Lambda'}{1-i\Lambda}\Big)^2(1+i\Omega\tau_M), \quad (20)$$

$$\Omega_{1,2} = \frac{1}{2}\Big[K_g v_0 - i\Big(\frac{1}{\tau}+\frac{1}{\tau_M}+K_g^2D_0\Big)\Big] \pm \sqrt{\frac{1}{4}\Big[K_g v_0 - i\Big(\frac{1}{\tau}+\frac{1}{\tau_M}+K_g^2D_0\Big)\Big]^2+\frac{1}{\tau\tau_M}}. \quad (21)$$

Formulas (21) for the frequencies $\Omega_{1,2}$ are the dispersion relations for the aforementioned two eigenmodes of space-charge waves and can be conveniently represented by the approximate expressions (see also [16])

$$\Omega_1 = K_g v_0 - i\Big(\frac{1}{\tau}+\frac{1}{\tau_M}+K_g^2D_0\Big), \quad (22)$$

$$\Omega_2 = -\frac{1}{\tau\tau_M}\frac{1}{K_g v_0 - i(\tau^{-1}+\tau_M^{-1}+K_g^2D_0)}. \quad (23)$$

Therefore, as in the case of an oscillating interference pattern, the frequency dependence of the first Fourier component of the electric current for a static grating and in the presence of the ac component of an external electric field exhibits two peaks at $\Omega = |\mathrm{Re}\,\Omega_{1,2}|$, which have a distinct resonant character under the condition $\mathrm{Re}\,\Omega_{1,2} > \mathrm{Im}\,\Omega_{1,2}$.

In the general case, the determination of the dc electric field component appears to be a rather laborious problem and the solution found for the direct current I_0 is represented by a very cumbersome relationship. The point is that the resonant contribution to the electric current I_0 is proportional to the term $m^2Y^2_{ac}$ and, hence,

the calculations have to be performed with the appropriate accuracy. The calculations of the dc component $Y_{0,0}$ of the electric field in the sample become cumbersome because of the last term on the left-hand side of Eq. (16). This term describes a combination of two nonlinear contributions, namely, the current–voltage characteristic (if $c \neq 0$) and the interaction of space-charge waves with the charge grating ($\propto m^2$). The calculations are significantly simplified when the Ohm law is valid ($c = 0$) or the voltage source with zero external resistance ($\rho = 0$) is used. In the latter case, there is no need to apply Eq. (16), because the voltage across the sample for this source according to relationship (14) is equal to the external voltage,

$$Y_{0,l} = \frac{1}{2}Y_{ac}(\delta_{l,1} + \delta_{l,-1}). \quad (24)$$

Then, setting $p = 0$ and $l = 0$ in Eq. (12), from expression (15) for the spatially inhomogeneous field components $Y_{p,l}$ and the boundary condition (24) for the spatially homogeneous field components, we find that the direct current passing through the sample can be determined from the relationship

$$I_0 = en_0v_0\left\{1 - 2\left(\frac{g_0\tau m}{2n_0}\right)^2[1 + \Lambda\Lambda' - c(1 + \Lambda^2)]\right.$$
$$+ \frac{c}{2}\left(\frac{\Xi_{ac}v_0'}{v_0}\right)^2 + \left(\frac{g_0 m\Xi_{ac}v_0'}{2n_0v_0}\right)^2\frac{1 + \Lambda'^2}{2\tau_M^2} \quad (25)$$
$$\left.\times\left[\frac{B(\Omega)}{|\Omega + \Omega_1|^2|\Omega + \Omega_2|^2} + \frac{B(-\Omega)}{|\Omega - \Omega_1|^2|\Omega - \Omega_2|^2}\right]\right\},$$

where

$$B(\Omega) = -\Omega\tau_M d(1 - \Omega\tau\Lambda') + c(1 + \Omega^2\tau^2). \quad (26)$$

The inclusion of the external resistance ρ does not radically change relationship (25) for the direct current but substantially complicates the form of the coefficient $B(\Omega)$. It should be kept in mind that the inclusion of the external resistance can turn out to be of fundamental importance in two cases: (i) in measurements of the voltage across the sample rather than the current in the circuit (see, for example, [15]) and (ii) in measurements with a falling current–voltage characteristic in the vicinity of the instability threshold where the behavior of the system significantly changes after the crossover from the current source mode to the voltage source mode [2].

The expression for the direct current is also considerably simplified for linear current–voltage characteristics when $c = \Lambda' = 0$ and $v_0 = \mu E_0$. In this case, with allowance made for the external resistance ρ, we have

$$\frac{\delta I_0}{\sigma E_0} = \left(\frac{g_0\tau m}{n_0\sqrt{2}}\right)^2\left\{\frac{\Omega K_g\mu E_0(\Xi_{ac}/2E_0)^2}{(\rho\sigma + 1)^2 + (\rho\sigma\Omega\tau_M)^2}\right.$$
$$\left.\times\left[\frac{(\tau\tau_M)^{-1}}{|\Omega - \Omega_1|^2|\Omega - \Omega_2|^2} - \frac{(\tau\tau_M)^{-1}}{|\Omega + \Omega_1|^2|\Omega + \Omega_2|^2}\right] - 1\right\}. \quad (27)$$

If the Ohm law is valid, the following equality is satisfied: $\sigma_d \equiv \sigma = en_0\mu$. From Eq. (7), the relationship between the electric field Ξ_0 of the external voltage source and the electric field E_0 in the sample can be derived in the explicit form $E_0 = \Xi_0/(1 + \rho\sigma)$.

Therefore, the dependence of the direct current on the frequency of the ac electric field component has two extrema, namely, a minimum at the frequency $-\mathrm{Re}\Omega_2 \cong (K_g\mu E_0\tau\tau_M)^{-1} = 4\pi en_0/(\varepsilon K_g\tau E_0)$ and a maximum at the frequency $\mathrm{Re}\Omega_1 = K_g\mu E_0$. This inference remains the same with a changeover from hole conduction to electron conduction (i.e., after changing $e \longrightarrow -e$, $\mu \longrightarrow -\mu$, $\Omega_{1,2} \longrightarrow -\Omega_{1,2}^*$).

3. MOVING GRATING

Both modes of space-charge waves can also be observed upon excitation with a moving interference grating in an external dc electric field. The nonlinear system under consideration, as before, is described by Eqs. (8) and (9). However, in Eq. (9), it is necessary to make the change $h(z) \longrightarrow h(z, T)$. Here, the function $h(z, T)$ has the form

$$h(z, T) = m\cos(z - T). \quad (28)$$

For a moving grating, the frequency Ω and the velocity of motion u are related by the expression $\Omega = K_g u$. The Fourier components are also described by Eq. (12), in which we need to make the change $h_p\delta_{l,0} \longrightarrow h_{p,l}$. Here, the quantity $h_{p,l}$ can be written as

$$h_{p,l} = \frac{m}{2}(\delta_{p,1}\delta_{l,-1} + \delta_{p,-1}\delta_{l,1}). \quad (29)$$

Thus, the equation for the Fourier components coincides with Eq. (19) in [16]. However, the changeover from the vibrating grating to the moving grating requires the use of expression (29) for the quantity $h_{p,l}$. Therefore, relationship (23) from [16] with the appropriate changes can be used for the Fourier components of the electric field with $p \neq 0$; that is,

$$Y_{p,l} = \frac{g_0\tau}{n_0}h_{p,l}\left[\Omega\tau_M dpl - \frac{(1 + i\Omega\tau_M l)(1 + i\Omega\tau l)}{1 - i\Lambda p}\right]^{-1}. \quad (30)$$

Here, one additional essential remark needs to be made. For the moving grating, only the electric field compo-

nents $Y_{p,l}$ with $p = -l$ are nonzero. This implies that the system of partial differential equations (8) and (9) is reduced to ordinary differential equations through the substitution $Y(z, T) = Y(z - T)$, because $h(z, T) = h(z - T) = m\cos(z - T)$ [see relationship (28)]. In this case, the electric current $f(T)$ through the sample does not depend on the time T. Consequently, only the direct current passes through the sample in the system with the moving grating. This situation radically differs from both the case with an oscillating grating and the case with an external ac electric field component. Physically, the absence of an alternating current for the moving grating can be explained by the absence of a static charge grating, because it is this interaction of the moving grating with the static grating that is responsible for the passage of the alternating current through the sample. The alternating current in the system with a moving grating can be generated, for example, through additional illumination of the sample with a static grating. However, analysis of this situation does not enter into the scope of the present paper. The possibility of reducing the problem under consideration to ordinary differential equations, in principle, enables us to examine the stability of the system within the framework of classical mechanics (see, for example, [2]).

With the use of the equation for the electric current (21) taken from [16] (compare with Eq. (12) in the present work) and simple transformations, we obtain the relationship between the direct current passing through the sample and the grating velocity u in the form

$$I_0 = en_0v_0\left\{1 - \frac{1}{2(1+\rho\sigma_d)}\left(\frac{g_0 m}{n_0\tau_M}\right)^2 \times \frac{1 + \Lambda\Lambda' + \Omega\tau_M(\Lambda - \Lambda') - c(1+\Lambda^2)}{|\Omega - \Omega_1|^2|\Omega - \Omega_2|^2}\right\}. \quad (31)$$

In the limiting case of a linear current–voltage characteristic, from expression (31), we have

$$\frac{\delta I_0}{\sigma E_0} = -\frac{1}{2(1+\rho\sigma)}\left(\frac{g_0 m}{n_0\tau_M}\right)^2 \frac{1_0 + \Omega_0\tau_M E_D/E_0}{|\Omega - \Omega_1|^2|\Omega - \Omega_2|^2}, \quad (32)$$

where $E_D = K_g D_0/\mu$ is the effective diffusion electric field. Therefore, the dependence of the direct current on the grating velocity u exhibits two resonant minima either at $u = v_0$ and $u = -(\tau\tau_M K_g^2 v_0)^{-1}$ or at $u = \mu E_0$ and $u = -4\pi en_0/(K_g^2\varepsilon\tau E_0)$ for the linear current–voltage characteristic. This makes it possible to observe both modes of space-charge waves in experiments with a moving grating. However, there is a fundamental difference between these experiments and the variant with an oscillating grating or excitation of the modes in an external ac electric field. In the experiments with a moving lattice, the result of observation depends on the direction of motion of the grating with respect to the direction of the dc electric field and the type of conductivity of the sample. For definiteness, we assume that the positive potential of the external electric field is applied to the left electrode; i.e., $E_0 > 0$. In materials with hole conductivity ($e > 0$, $\mu > 0$), the minimum current is observed for the high-frequency mode Ω_1 of space-charge waves at $u = \mu E_0$ for the grating motion from left to right ($u > 0$) and for the low-frequency mode Ω_2 at $u = -4\pi en_0/(K_g^2\varepsilon\tau E_0)$ for the grating motion from right to left ($u < 0$). By contrast, in the case of electron conductivity ($e < 0$, $\mu < 0$), the electric current should be minimum for the low-frequency mode Ω_2 when the grating moves from left to right and for the high-frequency mode Ω_1 when the grating moves from right to left. This circumstance is associated with the fact that the resonance occurs when the grating velocity coincides with the phase velocity of elementary excitations and the phase velocity reverses sign with a change in the conductivity type. As regards the experiments with an oscillating grating or an external ac electric field component, their results do not depend on the type of material conductivity, because the preferred direction of grating motion is absent in these cases.

A somewhat different situation arises with a sufficiently high grating velocity, i.e., under the condition $|u|K_g^2 D_0\tau_M > |\mu E_0|$. In this range of grating velocities, the current gain δI_0 reverses sign and becomes positive at $u < 0$ for holes or $u > 0$ for electrons. This can be explained by the fact that the total current (32) involves two components: the ohmic component proportional to μE_0 and the diffusion component proportional to $uK_g^2 D_0\tau_M$. If the quantities u and μ are opposite in sign, the above components of the current are oppositely directed and, consequently, the total current δI_0 at a sufficiently high grating velocity changes sign.

The diffusion contribution to the electric current stems from fact that, in the experiments with a moving grating, there exists a preferred direction of motion. This leads to the passage of the direct current through the sample in the absence of external electric fields. Substituting $E_0 = 0$ into expression (32) gives the diffusion component of the electric current:

$$I_0 = -\frac{en_0 u}{2(1+\rho\sigma_d)}\left(\frac{g_0 m}{n_0 K_g}\right)^2 \frac{D_0}{\tau_M(u^2 + u_1^2)(u^2 + u_2^2)}. \quad (33)$$

In the absence of external electric fields, the field grating is formed according to the pure diffusion mechanism and no resonant interaction of space-charge waves occurs. At $v_0 = 0$, the frequencies $\Omega_{1,2}$ in the denomi-

nator of formula (32) become strictly imaginary: $\Omega_{1,2} = iK_g u_{1,2}$. In this relationship,

$$K_g u_{1,2} = -\frac{1}{2}\left(\frac{1}{\tau} + \frac{1}{\tau_M} + K_g^2 D_0\right) \pm \sqrt{\frac{1}{4}\left(\frac{1}{\tau} + \frac{1}{\tau_M} + K_g^2 D_0\right)^2 - \frac{1}{\tau\tau_M}}. \quad (34)$$

A relationship similar to expression (33) for the direct current in the absence of an external electric field upon excitation with a moving interference pattern is given in [16]. A similar relationship was also derived in [17] for materials with a mixed electron–hole conductivity. It is worth noting that the electric current defined by formula (33) reverses sign upon crossover from the hole mechanism to the electron mechanism of conduction (i.e., after changing $e \longrightarrow -e$). The dependence of the electric current $I_0(u)$ on the grating velocity is antisymmetric, and the current vanishes at $u = 0, \pm\infty$. This dependence at particular velocities exhibits an extremum (see also [16]). The dependence of the quantity $I_0 u$ on u^2 is described by the expression $x(x + u_1^2)^{-1}(x + u_2^2)^{-1}$ (where $x = u^2$) and exhibits a maximum at $x = x_{max} = (u^2)_{max} = u_1 u_2 = (K_g^2 \tau\tau_M)^{-1}$. This feature of the dependence of the electric current on the grating velocity makes it possible to measure the parameter $\tau\tau_M$ in the experiment at a specified wave vector of the grating K_g. Moreover, additional measurements of the electrical conductivity σ of the system provide information on the Maxwell relaxation time $\tau_M = \varepsilon/(4\pi\sigma)$. Therefore, the important microscopic parameter, namely, the electron lifetime τ in the band, can be determined from the measured dependence $I_0(u)$.

When comparing the aforementioned theoretical results with experimental data, it is necessary to take into account the following circumstance. As was noted above, the frequency Ω_1 of the high-frequency mode can be of the order of tens or hundreds of megahertz (because there is a very large uncertainty in the mobilities). On the other hand, measurements have been often performed using materials with a high content of impurities. In these materials, charge transfer occurs through electron trapping rather than through free band electrons. The former mechanism (which is referred to as dispersion transport) is characterized by a considerable frequency dispersion of the electrical conductivity [18]. Moreover, the electrical conductivity cannot be uniquely represented in the traditional form as the product of the mobility and the concentration $\sigma = en\mu$. Consequently, the problem is substantially complicated, especially in a nonlinear case. Some aspects of this problem are discussed in [19, 20]. Note also that the above results are valid in the absence of saturation of impurity centers when the concentration N_A of compensating acceptor impurities is sufficiently high to satisfy the inequalities $E_q \gg E_0$ and $E_q \gg E_D$, where $E_q = 4\pi e N_a/(\varepsilon K_g)$ (this restriction was considered in more detail in [16]).

4. DISCUSSION

Let us consider the three main methods for optical excitation of space-charge waves: (1) excitation by an external ac electric field combined with a static interference pattern, (2) excitation by a moving interference pattern, and (3) excitation by an oscillating interference pattern. The first two methods were analyzed above, and the dependences of the direct current through the sample on the excitation frequency (when the Ohm law holds) are described by formulas (27) and (32) for the external ac electric field and the moving grating, respectively. In our previous work [16], we analyzed the third method for exciting space-charge waves with an oscillating interference pattern, when electrons are photogenerated according to the law [compare with relationship (4)]

$$g(x, t) = g_0[1 + m\cos(K_g x + \Theta\cos\Omega t)], \quad (35)$$

where Θ is the oscillation amplitude. In [16], we considered the general case of a nonlinear current–voltage characteristic. In the present work, we will disregard the instability processes occurring in the vicinity of the threshold of the domain structure formation (this problem was thoroughly discussed in [16]) and restrict our consideration to the special case of linear characteristics. Under these conditions, the dependence of the direct current on the frequency Ω of grating oscillations can be obtained from relationship (26) derived in [16]; that is,

$$\frac{\delta I_0}{\sigma E_0} = -\frac{1}{1 + \rho\sigma}\left(\frac{g_0\tau m}{2n_0}\right)^2\left[2 - \Theta^2 + \frac{\Theta^2}{2\tau^2\tau_M^2} \times\left(\frac{1 + \Omega\tau_M E_D/E_0}{|\Omega - \Omega_1|^2|\Omega - \Omega_2|^2} + \frac{1 - \Omega\tau_M E_D/E_0}{|\Omega + \Omega_1|^2|\Omega + \Omega_2|^2}\right)\right]. \quad (36)$$

A comparison of expressions (27), (32), and (36) shows that all three excitation methods have specific features. First and foremost, it should be noted that long-lived space-charge waves in a sample can be excited only in sufficiently strong external dc electric fields E_0. In the absence of a dc electric field E_0, no resonant excitation of space-charge waves occurs and we are dealing here with relaxation processes. In sufficiently strong electric fields $E_0 > \Omega\tau_M|E_D|$, only the method for exciting space-charge waves with a moving grating is sensitive to the type of conductivity of the material (the electric current reverses sign when changing over from electrons to holes). Upon excitation in an external ac electric field, the results of measurements never depend on the conductivity type. In this case, the frequency dependence of the direct current always exhibits a maximum

at the high frequency Ω_1 and a minimum at the low frequency Ω_2. Upon excitation of space-charge waves with an oscillating interference pattern at $E_0 > \Omega\tau_M|E_D|$, the frequency dependence of the direct current is characterized by minima at both frequencies. In the case of a moving grating at $E_0 > \Omega\tau_M|E_D|$, the electric current increases in magnitude for electrons and holes at both resonant frequencies, but the quantity δI_0 reverses sign with a change in the conductivity type. In the reversed situation (at $E_0 < \Omega\tau_M|E_D|$), the dependence of the direct current upon excitation with an oscillating grating has a minimum at one of the resonant frequencies and a maximum at the other resonant frequency depending on the conductivity type.

One more specific feature of the methods used for exciting space-charge waves in an external ac electric field and with an oscillating grating is that the direct current passes through the sample simultaneously with the alternating current at frequencies $n\Omega$ (where n is an integer). The dependence of the amplitude of the alternating current components on the excitation frequency also exhibit a resonant behavior. This can be seen from both relationship (19) for the frequency dependence of the alternating current amplitude upon excitation of space-charge waves in an external ac electric field and expression (29) derived [13] for an oscillating grating (these formulas describe the alternating current with $n = 1$). Upon excitation of space-charge waves with a moving grating, the direct current alone passes through the sample. In this method, the alternating current can be generated under additional illumination of the sample with a static interference pattern characterized by a wave vector K_g identical to that of the moving grating. Such an additional illumination induces a static grating of the internal electric field, whereas the electric fields of the moving and static gratings generate an alternating current in the system due to the interaction between the harmonics of the internal electric field. These harmonics are proportional to $\exp(iK_g x - i\Omega t)$ and $\exp(-K_g x)$. Even greater possibilities for measurements exist when the second interference pattern with a wave vector K_g identical to that of the first interference pattern also moves in the sample at a velocity differing from the velocity of the first pattern. In this case, there are two different frequencies of excitation of space-charge waves in the system. As a result, an alternating current with frequencies equal to different combinations of these excitation frequencies passes through the sample due to nonlinear interactions.

In conclusion, we calculate the relative change in the direct current at resonant frequencies. The magnitude of this current determines the possibility of observing the above effects in experiments. Let us first consider the resonance of the low-frequency mode at $\Omega = \Omega_2$ [the resonant frequencies Ω_1 and Ω_2 are given by relationships (22) and (23), respectively]. Upon excitation of the modes in an ac electric field, from expression (27) at the resonant frequency, we have

$$\frac{\delta I_0}{\sigma E_0} = \frac{m'^2}{8}\left(\frac{\Xi_{ac}}{E_0}\right)^2 \frac{d^2}{[1-\tau/(d^2\tau_M)]^2} \approx \frac{m'^2}{8}\left(\frac{\Xi_{ac}}{E_0}\right)^2 d^2. \quad (37)$$

Here, $m' = mg_0\tau/n_0$ is the effective contrast of the interference pattern ($m' \le m$ also for insulators with $\tilde{n}_0 = 0$, $m' = m$). In what follows, we will analyze the situation where the external resistance is absent, i.e., where $\rho = 0$. For estimates, it should be remembered that the inequality $d \gg 1$ always holds under experimental conditions. As a consequence, the Q factor has a rather large value and the reciprocal of the eigenmode lifetime is less than the eigenmode frequency.

Upon excitation with an oscillating interference pattern, from relationship (36), we obtain

$$\frac{\delta I_0}{I_0} = \frac{m'^2\Theta^2 d^2(1 + d^{-1}E_D/E_0)}{2(1-\tau/(d^2\tau_M))^2} \approx \frac{m'^2\Theta^2 d^2}{2}. \quad (38)$$

Finally, for the moving interference pattern, from formula (32), we have

$$\frac{\delta I_0}{I_0} = \frac{m'^2 d^2[1 + d^{-1}E_D/E_0]}{2(1-\tau/(d^2\tau_M))^2} \approx \frac{m'^2 d^2}{2}. \quad (39)$$

The above estimates indicate that observation of the resonance for the low-frequency mode of space-charge waves with the use of all three methods should not pose any problems. For this purpose, it is only necessary to satisfy the condition $d = K_g\mu E_0\tau > 1$, which ensures a small reciprocal of the eigenmode lifetime as compared to the eigenmode frequency.

Now, we turn to the resonance of the high-frequency drift mode at frequency Ω_1. Upon excitation in an external ac electric field, according to expression (27), we obtain

$$\frac{\delta I_0}{\sigma E_0} = \frac{m'^2}{8}\left(\frac{\Xi_{ac}}{E_0}\right)^2 \frac{\tau}{\tau_M}\frac{1}{[1-\tau/(d^2\tau_M)]^2} \approx \frac{m'^2}{8}\left(\frac{\Xi_{ac}}{E_0}\right)^2 \frac{\tau}{\tau_M}. \quad (40)$$

From formula (36), the resonant amplitude in the case of excitation with an oscillating grating is determined by the relationship

$$\frac{\delta I_0}{I_0} = \frac{m'^2\Theta^2}{2(1-\tau/(d^2\tau_M))^2}\left(\frac{\tau}{\tau_M} + d\frac{E_D}{E_0}\right) \approx \frac{m'^2\Theta^2}{2}\left(\frac{\tau}{\tau_M} + d\frac{E_D}{E_0}\right). \quad (41)$$

For a moving grating, from formula (32), we have

$$\frac{\delta I_0}{I_0} = \frac{m'^2}{2(1-\tau/(d^2\tau_M))^2}\left(\frac{\tau}{\tau_M} + d\frac{E_D}{E_0}\right) \approx \frac{m'^2 d^2}{2}\left(\frac{\tau}{\tau_M} + d\frac{E_D}{E_0}\right). \quad (42)$$

It can be seen from these relationships that the relative resonant amplitude for the high-frequency mode is considerably less than the amplitude upon interaction with space-charge waves and involves the additional small parameter $\tau/(d^2\tau_M)$ This parameter is rather small, especially for semi-insulating materials with $\tau/\tau_M \ll 1$. This can be corrected for by measuring the diffusion contribution using the method with an oscillating or moving grating. If $\tau/\tau_M < dE_D/E_0$, the signal amplitude upon interaction with the high-frequency mode is small compared to that upon interaction with the low-frequency mode according to the parameter $E_D/(dE_0) = d^{-2}(K_g l_D)^2$, where $l_D = \sqrt{D_0\tau}$ is the diffusion length. The magnitude of this parameter in experiments can be chosen larger than the parameter $\tau/(d^2\tau_M)$ when the grating wave vector is not overly small and $(K_g l_D)^2 > \tau/\tau_M$.

ACKNOWLEDGMENTS

This work was supported by the Deutsches Zentrum für Luft- und Raumfahrt and the Russian Foundation for Basic Research (project no. 02-02-17603).

REFERENCES

1. B. K. Ridley, Proc. Phys. Soc. London **86**, 637 (1965).
2. A. F. Volkov and Sh. M. Kogan, Usp. Fiz. Nauk **96** (4), 633 (1968) [Sov. Phys. Usp. **11**, 881 (1968)].
3. R. F. Kazarinov, R. A. Suris, and B. I. Fuks, Fiz. Tekh. Poluprovodn. (Leningrad) **7** (1), 102 (1972) [Sov. Phys. Semicond. **7**, 68 (1973)]; Fiz. Tekh. Poluprovodn. (Leningrad) **7**, 688 (1972) [Sov. Phys. Semicond. **7**, 480 (1972)].
4. G. Pauliat, A. Villing, J. C. Launay, and G. Roosen, J. Opt. Soc. Am. B **7**, 1481 (1990).
5. J. P. Partanen, J. M. Jonathan, and R. W. Hellwarth, Appl. Phys. Lett. **57**, 2404 (1990).
6. I. A. Sokolov and S. I. Stepanov, J. Opt. Soc. Am. B **10** (8), 1483 (1993).
7. M. Brushinin, V. Kulikov, and I. Sokolov, Phys. Rev. B **67** (7), 075202 (2003).
8. B. I. Fuks, M. S. Kagan, R. A. Suris, and N. G. Zhdanova, Phys. Status Solidi A **40**, k61 (1977).
9. S. I. Stepanov, V. V. Kulikov, and M. P. Petrov, Opt. Commun. **44**, 19 (1982).
10. M. P. Petrov, V. V. Bryksin, V. M. Petrov, S. Wevering, and E. Kraetzig, Phys. Rev. A **60** (3), 2413 (1999).
11. J. P. Huignard and A. Marrakchi, Opt. Commun. **38** (8), 249 (1981).
12. V. V. Bryksin and M. P. Petrov, Fiz. Tverd. Tela (St. Petersburg) **42** (10), 1808 (2000) [Phys. Solid State **42**, 1854 (2000)].
13. M. P. Petrov, A. P. Paugurt, V. V. Bryksin, S. Wevering, and E. Krätzig, Phys. Rev. Lett. **84**, 5114 (2000).
14. V. V. Bryksin and M. P. Petrov, Fiz. Tverd. Tela (St. Petersburg) **44** (10), 1785 (2002) [Phys. Solid State **44**, 1869 (2002)].
15. M. P. Petrov, V. V. Bryksin, H. Vogt, F. Rahe, and E. Krätzig, Phys. Rev. B **66** (8), 085107 (2002).
16. V. V. Bryksin, P. Kleinert, and M. P. Petrov, Fiz. Tverd. Tela (Leningrad) **45** (11), 1947 (2003) [Phys. Solid State **45**, 2044 (2003)].
17. U. Haken, M. Hundhausen, and L. Ley, Phys. Rev. B **51** (16), 10579 (1995).
18. H. Boettger and V. V. Bryksin, *Hopping Conduction in Solids* (Akademie, Berlin, 1985).
19. N. Korneev, S. Mansurova, P. Rodriguez, and S. Stepanov, J. Opt. Soc. Am. B **12**, 615 (1995).
20. N. A. Korneev, J. J. Sanchez Mondragon, and S. I. Stepanov, Opt. Commun. **133**, 109 (1997).

Translated by O. Borovik-Romanova

Physics of the Solid State, Vol. 46, No. 9, 2004, pp. 1622–1626. Translated from Fizika Tverdogo Tela, Vol. 46, No. 9, 2004, pp. 1574–1577.
Original Russian Text Copyright © 2004 by Kazanskiĭ.

SEMICONDUCTORS AND DIELECTRICS

Microwave Measurements of Electrical Conductivity of CdF_2 Semiconductor Crystals

S. A. Kazanskiĭ

Vavilov State Optical Institute, All-Russia Research Center, Birzhevaya liniya 12, St. Petersburg, 199034 Russia
e-mail: Kazanski@SK7936.spb.edu

Received January 29, 2004

Abstract—The electrical conductivity of CdF_2 semiconductor crystals is measured using the microwave intracavity technique at a frequency of ~35 GHz. The crystals are activated with yttrium donor impurities and indium and gallium ions forming bistable one-electron donor impurity and two-electron *DX* centers. The conclusion is drawn that the concentration of electrons in the conduction band of CdF_2 : Ga crystals has an anomalously high value. This confirms the results obtained in earlier NMR investigations of CdF_2 semiconductor crystals at room temperature. *© 2004 MAIK "Nauka/Interperiodica".*

1. INTRODUCTION

A fluorite-type dielectric crystal CdF_2 can be transformed into a semiconducting state through doping with Group III elements of the periodic table with subsequent annealing in a reducing atmosphere [1]. During this process (which is referred to as additive coloring), F^- interstitial ions that compensate for an excess charge +1 of activator ions diffuse from the bulk toward the surface of the crystal. This is attended by an injection of electrons into the crystal bulk, which provides charge neutralization of the crystal. The injected electrons either can remain in the conduction band of the crystal or can be localized at hydrogen-like donor orbitals of trivalent impurity ions. In CdF_2 crystals, donor impurities are characterized by a binding energy of ~100 meV and bring about the appearance of a photoionization IR absorption band with a maximum at wavelength $\lambda_{max} \approx 7$ μm, which is also observed in the visible spectral range [2, 3]. At room temperature, the electronic conductivity of CdF_2 semiconductor crystals can be as high as 10 Ω^{-1} cm^{-1}. However, all attempts to achieve an electron concentration exceeding ~10^{19} cm^{-3} in these crystals have not been successful [1, 2, 4].

Among the donor impurity ions introduced in CdF_2 crystals, gallium and indium ions play a special role. These impurity ions are considered an analog of *DX* centers in III–V and II–VI semiconductors [5] and can reside not only in a shallow-lying hydrogen-like state but also in a deep-lying strongly localized two-electron state accompanied by an enhanced lattice relaxation [6]. Owing to this relaxation, the two aforementioned states of the impurity center are separated by an energy barrier, which leads to an increase in the time required to occupy a deep-lying level and to attain thermal equilibrium, especially at low temperatures [7–9]. The impurity level of a *DX* center is located at an energy of ~0.25 eV for indium and ~0.7 eV for gallium [5].

Earlier [8–10], CdF_2 semiconductor crystals containing *DX* centers and exhibiting photochromic properties were studied using optical and spectroscopic methods. It was found that, in "better" CdF_2 : Ga crystals, the concentration of active centers and the total concentration of electrons injected into the crystals during additive coloring are several times lower than those in CdF_2 : In crystals. However, indirect estimates obtained for the concentration of electrons in the conduction band of these crystals from data on the ^{113}Cd nuclear spin–lattice relaxation [11] led to inverse ratios (at room temperature). Moreover, the temperature dependence of the concentration of electrons in the conduction band was examined using the ^{113}Cd NMR technique. It was shown that the activation energy for the CdF_2 : In crystal agrees with the theoretical value calculated with due regard for the population of the deep-level *DX* centers in this crystal [12] but is substantially less than the theoretical activation energy calculated for the CdF_2 : Ga crystal.

The main objective of the present work was to obtain additional information on CdF_2 semiconductor crystals. With this aim in view, I developed a simple noncontact microwave method for measuring the electrical conductivity and compared the experimental results obtained by this method for the above crystals and CdF_2 : Y semiconductor crystals containing no *DX* centers.

2. EXPERIMENTAL TECHNIQUE

The crystals used in microwave measurements were grown from a melt. The concentration N_M of activator ions introduced into the crystal (see table) was con-

Experimental and calculated parameters of the CdF_2 semiconductor crystals

Crystal	N_M^a, 10^{17} cm^{-3}	$n_\Sigma^{a,b}$, 10^{17} cm^{-3}	$n_D^{a,b}$, 10^{17} cm^{-3}	σ^a, Ω^{-1} cm^{-1}	n_c, 10^{17} cm^{-3}
CdF_2 : In	100	30	3.0	0.15	0.6
CdF_2 : Ga	100	6	0.7	0.22	0.9
CdF_2 : Ga[c]			~3.6[d]	0.6	2.4
CdF_2 : Y	500	40	25	2.9	12

[a] The accuracy in determining the parameters presented in the table is equal to ±20%.
[b] Data obtained from the experimental IR spectra of the crystal.
[c] Data obtained upon exposure of the crystal to high-power UV radiation.
[d] Difference $n_\Sigma - n_c$.

trolled using mass spectrometric analysis. Additive coloring was performed at a temperature of ~500°C in vapors of a potassium–cadmium mixture. The total concentration n_Σ of electrons injected into the crystal in the course of additive coloring and the concentration n_D of electrons localized at shallow-lying donor levels were determined from the intensity of the IR absorption band ($\lambda_{max} \approx 7$ μm) at different temperatures upon illumination of CdF_2 : In and CdF_2 : Ga crystals in the photoionization IR absorption bands of deep-level *DX* centers [9].

In the experiments, the complex permittivity of the samples, i.e., $\varepsilon = \varepsilon_1 - i\varepsilon_2$, was determined using the microwave intracavity technique. The changes in the frequency and loaded-Q factor of the microwave cavity operating in the 8-mm band were examined upon insertion of the sample at $T = 300$ K. Without a sample present, the TE_{011}-type cylindrical reflection cavity (diameter $b \approx 12$ mm, height $H \approx 8$ mm) had a loaded-Q factor $Q_{LS} \approx 1000$ and was matched to a waveguide. As a consequence, the microwave power from a Gunn-diode oscillator with electric frequency tuning provided by a varactor almost completely dissipated in the TE_{011}-type cavity at the resonance frequency. The oscillation frequency was swept by a sawtooth voltage on the varactor in the range 34.5–35.7 GHz, and the curve of the cavity was observed on an oscilloscope [13]. Indications from a wave meter were used as frequency markers. For microwave intracavity measurements, cylindrical samples (diameter ~2.5 mm, height ~2.5 mm) were inserted into the cavity precisely along the cavity axis through a hole (diameter, 3.0 mm) at the center of the upper cavity piston with the use of a fine adjustment screw. (Note that the presence of a through hole in the cavity piston does not affect the distribution pattern of the electromagnetic field in the cavity [13].) The curve of the cavity with a sample was measured in steps of 0.1 mm. From analyzing this curve (see [13, 14]) on a computer, we determined the frequency shift δf_c and the change (degradation) in the Q factor of the cavity δQ_{LS}^{-1} upon insertion of the sample as a function of the parameter x (x is the length of the part of the sample inserted into the cavity. The experimental dependences $\delta Q_{LS}^{-1}(x)$ and $\delta f_c(x)$ thus obtained were compared with the family of theoretical curves constructed for different values of the complex permittivity. In this way, we determined the complex permittivity for the studied sample. It should be noted that these measurements were performed with samples of relatively large volume. Hence, the complex permittivity ε could not be calculated within the approximation of an infinitely small sample [14–16]. Therefore, we sought an approximate solution to the wave equation for the distribution of the electromagnetic field in the cavity with a sample.

3. COMPUTATIONAL TECHNIQUE

The equation for the electric component E_φ of the electromagnetic field of the TE_{011} mode in the cylindrical coordinates (z, r, φ) for a cylindrical cavity with a dielectric sample has the form [13]

$$\frac{\partial}{\partial r}\left(\frac{1}{r}\frac{\partial}{\partial r}(rE_\varphi)\right) + \frac{\partial^2 E_\varphi}{\partial z^2} + \omega^2 \frac{\varepsilon(z, r, \varphi)}{c^2} E_\varphi = 0, \quad (1)$$

where c is the velocity of light, $E_\varphi \equiv E_\varphi(z, r)$, $\varepsilon(z, r, \varphi) = 1$ for the cavity without a sample, and $\varepsilon(z, r, \varphi) = \varepsilon$ for the cavity with a dielectric sample. For the complex permittivity $\varepsilon = \varepsilon_1 - i\varepsilon_2$, Eq. (1) has solutions only at characteristic (resonance) values of the complex circular frequency ω of a perturbed cavity. The complex circular frequency ω is related to the frequency and the Q factor of the cavity with a dielectric sample through the relationship [14]

$$\omega = 2\pi(f_c + \delta f_c)\left(1 - \frac{i}{2}\delta Q_{LS}^{-1}\right). \quad (2)$$

The solutions to Eq. (1) under the boundary condition $E_\varphi \equiv 0$ at the cavity walls can be obtained in the form of a series expansion:

$$E(r, z) = \sum_{i=1}^{L}\sum_{j=1}^{L} C_{ij} J_1(X_i r/b)\sin(\pi z j/H), \quad (3)$$

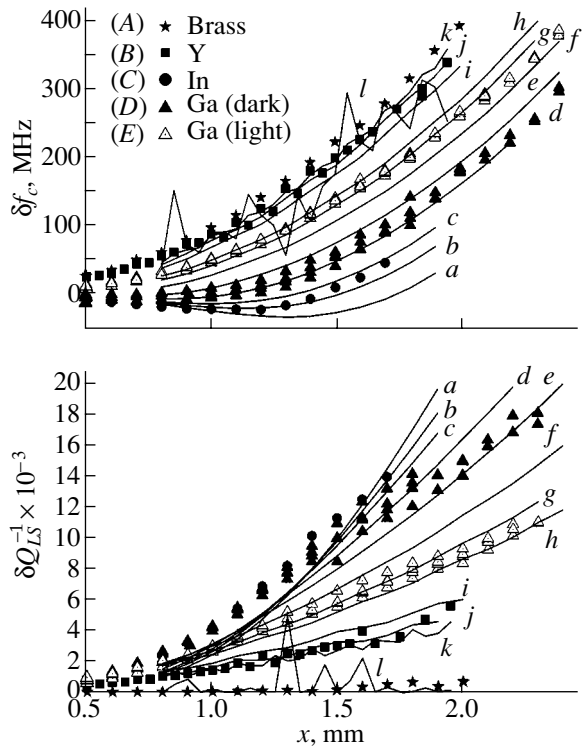

Experimental (symbols) and calculated (solid lines) dependences $\delta Q_{LS}^{-1}(x)$ and $\delta f_c(x)$ for samples of (*A*) metal (brass) and CdF_2 crystals doped with (*B*) yttrium, (*C*) indium, (*D*) gallium (in the dark), and (*E*) gallium (upon exposure of the crystal to high-power UV radiation). The dependences are calculated under the assumption that the permittivity ε_1 is equal to 8.49 [17] for the dielectric loss ε_2 = (*a*) 6, (*b*) 7, (*c*) 8, (*d*) 10, (*e*) 13, (*f*) 20, (*g*) 30, (*h*) 40, (*i*) 100, (*j*) 200, (*k*) 400, and (*l*) 10 000. Sample diameter $d = 2.53 \pm 0.02$ mm.

where X_i is the *i*th root of the Bessel function of the first kind J_1. With the use of expansion (3), Eq. (1) can be transformed into a system of linear equations with unknown coefficients C_{ij}. By solving this system, we determined the complex frequencies $\omega/2\pi$ for the perturbed cavity, which were close in magnitude to the frequency of the unperturbed cavity at different values of the complex permittivity of the sample and the length of the part of the sample inserted into the cavity. The number of sought expansion coefficients C_{ij} (where $i, j = 1 \ldots L$) was equal to $L \times L = 60 \times 60$. Note that this number was limited by the memory capacity of the computer used in our calculations. (In these calculations, we determined the eigenvalues of the matrix of 3600×3600 complex numbers.)

4. RESULTS AND DISCUSSION

The figure shows the experimental dependences $\delta f_c(x)$ and $\delta Q_{LS}^{-1}(x)$ (symbols) for all the crystals studied and the approximating curves (solid lines) calculated at different values of the dielectric loss ε_2. Since the impurity concentration in the doped crystals was not very high, the calculations were performed under the assumption that the permittivity of the samples is equal to the permittivity of undoped CdF_2, i.e., $\varepsilon_1 = 8.49$ [17]. Moreover, the CdF_2 : Ga crystal was studied upon exposure to high-power radiation (up to 30 mW) from a nitrogen laser ($\lambda = 335$ nm) in the absorption band of deep-level *DX* centers. The characteristic time τ required to attain equilibrium between the shallow and deep Ga impurity centers at room temperature was rather long and approximately equal to 10 s. As a result, the irradiation of the sample led to a complete depletion of deep-level centers in the CdF_2 : Ga crystal. It should be noted that, in the CdF_2 : In crystal, the characteristic time τ is approximately equal to 10^{-7} s and, hence, the photobleaching of deep-level centers becomes impossible in the stationary mode at room temperature. The time taken to achieve thermal equilibrium between electrons in the conduction band and electrons localized at donor levels is most likely shorter than 10^{-9} s.

The measurements performed in this work demonstrated that the dielectric losses in all the studied samples are relatively large, i.e., $\varepsilon_2 \gg 1$. Since the uncolored crystal CdF_2 contained only cubic impurity centers, it was assumed that this crystal should not exhibit dielectric losses through the relaxation reorientation of low-symmetry centers in an oscillating electromagnetic field [18]. This assumption was confirmed in the study of uncolored crystals CdF_2. It was revealed that the uncolored crystals CdF_2 have no appreciable dielectric losses, including those due to ionic conduction. In colored crystals CdF_2 : In and CdF_2 : Ga, the *DX* centers at a concentration $N_{DX} < n_\Sigma/2$ possess a dipole moment $p_{DX} < 3D$ (this estimate was obtained in the electrostatic approximation). However, at room temperature, the contribution of the *DX* centers to the dielectric loss, apparently, should not exceed the limiting value determined by the relationship [19]

$$(\varepsilon_2)_{DX}^{\lim} \le 2\pi \frac{\varepsilon_1 + 2}{3} N_{DX} \frac{p_{DX}^2}{kT} < 0.1, \qquad (4)$$

where *k* is the Boltzmann constant. Therefore, the contribution of the *DX* centers to the dielectric loss ε_2 can be ignored.

In CdF_2 semiconductor crystals, dielectric losses are due to electronic conduction. It should be noted that, at room temperature, the dominant contribution to the dielectric loss is most likely made by electrons in the conduction band [4]. As can be seen from the figure, the cavity frequency considerably increases when the conducting samples are inserted into the cavity to a depth $x > 1$ mm. These findings can be explained by the fact

that the electromagnetic field penetrates into a conducting sample only to the skin depth [14]

$$\delta = \frac{c}{\pi f_c \sqrt{2\varepsilon_2}} \quad (5)$$

and is "suppressed" in the rest of the volume of the conducting sample. This leads to a decrease in the effective size of the cavity, and, consequently, the frequency of the cavity increases. For comparison, the figure shows the experimental dependences for a sample having the same shape and size but prepared from a "good" metal (brass). It should be noted that, in the case when the samples inserted into the cavity are characterized by small (or moderate) dielectric losses, the cavity frequency, on the contrary, decreases [13]. In our case, as the length x of the part of the sample inserted into the cavity increases from 0 to ~2δ, the shift in the cavity frequency is first negative in sign and then begins to increase. As a result, the dependence $\delta f_c(x)$ exhibits a minimum at $x \sim 2\delta$. This minimum is clearly seen both in the experimental dependence (closed circles *C*) for the CdF_2 : In crystal characterized by a skin depth $\delta \sim$ 0.6 mm and in calculated curves *a–c* (see figure). On this basis, it is possible in principle to determine the permittivity ε_1 of the studied sample more exactly; however, to accomplish this refinement, the measurements must be performed with a higher accuracy.

When analyzing the experimental dependences $\delta Q_{LS}^{-1}(x)$ and $\delta f_c(x)$, it should be remembered that the accuracy in determining the values of $\delta f_c(x)$ is higher than that of $\delta Q_{LS}^{-1}(x)$. The errors in calculating the theoretical (approximating) curves were estimated from a comparison with exact solutions of Eq. (1). The exact solutions were obtained for two specific cases: (i) a thin disk with a diameter equal to the diameter of the cavity and (ii) a long cylindrical rod passing through the cavity [16]. It was established that the calculated dependences agree with the exact solutions within an error approximately equal to the spread of the values (the amplitude of oscillations) of the corresponding calculated dependence. It can be seen from the figure that the spread in the values becomes appreciable at dielectric losses $\varepsilon_2 \sim 200$ and that it is impossible to obtain the calculated dependence for a good metal (for example, at $\varepsilon_2 = 10000$). This restriction is associated with the fact that, at large values of ε_2, the skin depth is substantially less than the period of spatial oscillations of the terms in expansion (3). Consequently, approximating the electromagnetic field in the cavity with the use of expansion (3) becomes unsatisfactory.

The experimental and calculated parameters of the studied crystals are presented in the table. It should be noted that the total concentration of electrons in the CdF_2 : Ga crystals is approximately five times less than that in the CdF_2 : In crystals, and the impurity levels of *DX* centers in the former crystals are located at a considerably lower energy than those in the latter crystals (see above). Therefore, according to the theoretical estimates obtained in [12], it can be assumed that the electronic conductivity of the CdF_2 : In crystal should be at least one order of magnitude higher than that of the CdF_2 : Ga crystal. However, the tabulated values of the microwave conductivity

$$\sigma = \frac{\varepsilon_2 f_c}{2}\ [\mathrm{s}^{-1}] = \frac{\varepsilon_2 f_c}{2}\frac{10^9}{c^2}\ [\Omega^{-1}\ \mathrm{cm}^{-1}] \quad (6)$$

indicate that, on the contrary, the conductivity of the CdF_2 : Ga crystals is ~1.5 times higher than that of the crystals doped with indium ions. It is unlikely that the above differences are associated with the large difference between the electron mobilities in these crystals. The CdF_2 semiconductor crystals studied in this work are characterized by a high optical quality, are grown and colored using the same methods under identical conditions, and contain activator ions at a relatively low concentration. Therefore, as was done in [18], we can assume that, in these crystals, the electron mobility in the conduction band is typical of CdF_2 semiconductor crystals [1, 2, 4]: $\mu = 15\ \mathrm{cm}^2/(\mathrm{V\ s})$. Hence, the electron concentration n_c can be estimated from the microwave conductivity. This estimate (see the last column in the table) suggests a substantially higher relative concentration of electrons in the conduction band of the CdF_2 : Ga crystal as compared to that of the CdF_2 : In crystal.

It is of interest to note that, within the limits of experimental error, the concentration ratio between the electrons localized at the donor levels and in the conduction band of the CdF_2 : Ga crystal approximately coincides with the corresponding ratio for the CdF_2 : Y crystal free of *DX* centers. The same ratio is completely retained upon photobleaching of the CdF_2 : Ga crystal with light from a nitrogen laser. Exposure of the crystal to high-power laser illumination leads to a complete release of electrons from the deep-level centers. Therefore, we can exclude the deep-level centers from our consideration. As a result, the CdF_2 : Ga crystal becomes similar to the CdF_2 : Y crystal with a lower total electron concentration. In both cases, the electrons are localized at the donor levels and in the conduction band.

5. CONCLUSIONS

Thus, the electrical conductivities of CdF_2 semiconductor crystals were measured using the microwave intracavity technique. The results obtained confirm the conclusion drawn in earlier NMR investigations [11] that the concentration of free electrons in the conduction band of CdF_2 : Ga crystals at room temperature has an anomalously high value. It was assumed that, in the CdF_2 : Ga crystal, the equilibrium population of shallow- and deep-lying levels is disturbed through an

unknown mechanism. In order to solve this problem conclusively, it is necessary to "count" the electrons localized at the donor levels, at the *DX* centers, and in the conduction band. In turn, this calls for an investigation of the Hall effect in CdF_2 semiconductor crystals exhibiting photochromic properties. Note that, until now, these investigations had been performed only for CdF_2 semiconductor crystals not containing any *DX* centers [1, 2, 4].

ACKNOWLEDGMENTS

The author would like to thank A.I. Ryskin, A.S. Shcheulin, A.I. Ritus, and A.A. Volkov for their participation in discussions of the results and helpful remarks.

This work was supported by the International Research and Technical Center, project no. 2136.

REFERENCES

1. P. F. Weller, Inorg. Chem. **4** (11), 1545 (1966); Inorg. Chem. **5** (5), 739 (1966).
2. F. Moser, D. Matz, and S. Lyu, Phys. Rev. **182** (3), 808 (1969).
3. T. H. Lee and F. Moser, Phys. Rev. B **3**, 347 (1971).
4. R. P. Khosla, Phys. Rev. **183** (3), 695 (1969).
5. C. H. Park and D. J. Chadi, Phys. Rev. Lett. **82**, 113 (1999).
6. D. J. Chadi and K. J. Chang, Phys. Rev. B **39**, 10063 (1989).
7. I. Kunze and W. Ulrici, Phys. Status Solidi B **55**, 567 (1973).
8. J. M. Langer, Rev. Solid State Sci. **4**, 297 (1990).
9. A. S. Shcheulin, A. I. Ryskin, K. Swiatek, and J. M. Langer, Phys. Lett. A **222**, 107 (1996).
10. A. I. Ryskin, A. S. Shcheulin, and D. E. Onopko, Phys. Rev. Lett. **80**, 2949 (1998); A. S. Shcheulin, D. E. Onopko, and A. I. Ryskin, Fiz. Tverd. Tela (St. Petersburg) **39**, 2130 (1997) [Phys. Solid State **39**, 1906 (1997)].
11. D. Hilger, S. A. Kazanskii, A. I. Ryskin, and W. W. Warren, Physica B (Amsterdam) **308–310**, 1020 (2001).
12. A. S. Shcheulin, A. K. Kupchikov, A. E. Angervaks, D. E. Onopko, A. I. Ryskin, A. I. Ritus, A. V. Pronin, A. A. Volkov, P. Lunkenheimer, and A. Loidl, Phys. Rev. B **63**, 205207 (2001).
13. Ch. P. Poole, *Electron Spin Resonance: A Comprehensive Treatise on Experimental Techniques* (Interscience, New York, 1966).
14. O. Klein, S. Donovan, M. Dressel, and G. Gruner, Int. J. Infrared Millim. Waves **14** (12), 2423 (1993); S. Donovan, O. Klein, M. Dressel, K. Holczer, and G. Gruner, Int. J. Infrared Millim. Waves **14** (12), 2459 (1993); M. Dressel, O. Klein, S. Donovan, and G. Gruner, Int. J. Infrared Millim. Waves **14** (12), 2489 (1993).
15. H. M. Altshuller, in *Handbook of Microwave Measurements*, Ed. by M. Suchner and J. Fox (Interscience, New York, 1963), Vol. 2, Chap. 9.
16. A. A. Brandt, *Microwave Studies of Dielectrics* (Fizmatgiz, Moscow, 1963) [in Russian].
17. D. R. Bosomworth, Phys. Rev. **157**, 709 (1967).
18. A. I. Ritus, A. V. Pronin, A. A. Volkov, P. Lunkenheimer, A. Loidl, A. S. Shcheulin, and A. I. Ryskin, Phys. Rev. B **65**, 165209 (2002).
19. C. Kittel, *Introduction to Solid State Physics*, 3rd ed. (Wiley, New York, 1966; Fizmatgiz, Moscow, 1963).

Translated by O. Borovik-Romanova

Physics of the Solid State, Vol. 46, No. 9, 2004, pp. 1627–1630. From Fizika Tverdogo Tela, Vol. 46, No. 9, 2004, pp. 1578–1580.
Original English Text Copyright © 2004 by Tien, Charnaya, Sherman.

SEMICONDUCTORS AND DIELECTRICS

Fluorine Mobility in an Aluminum-Doped CeF_3 Crystal: NMR and Conductivity Studies*

C. Tien[1], E. V. Charnaya[1, 2], and A. B. Sherman[3]

[1] *Department of Physics, National Cheng Kung University, Tainan, 70101 Taiwan*
[2] *Institute of Physics, St. Petersburg State University, St. Petersburg, 198904 Russia*
[3] *Ioffe Physicotechnical Institute, Russian Academy of Sciences, St. Petersburg, 194021 Russia*
e-mail: charnaya@mail.ru

Received February 11, 2004

Abstract—Electrical conductivity and NMR measurements were carried out for an aluminum-doped CeF_3 crystal to study the influence of substitutional impurities on the superionic fluorine mobility. Activation enthalpy was found to remain constant from low temperatures to about 325 K and to increase as compared to that of a pure CeF_3 crystal. Above about 325 K, a trend towards gradual conductivity saturation was observed. This change was ascribed to a superionic phase transition not accompanied by structural transformations. NMR also revealed some alterations in the local fluorine dynamics as compared to that reported for a pure CeF_3 crystal. According to NMR measurements, the superionic phase transition near 325 K results in acceleration of the exchange between rigid or slow fluorine in the F_1, F_2, and F_3 sublattices, while highly mobile F_1 fluorine ions move independently at least until 400 K. © *2004 MAIK "Nauka/Interperiodica".*

1. INTRODUCTION

Cerium fluoride, CeF_3, belongs to the group of trifluoride crystals with tysonite-type structure, which evince high ionic mobility already at room temperature (see [1–4] and references therein). The space group is $P\bar{3}c1$ [5]. The pure CeF_3 crystal has three nonequivalent fluorine sublattices with different dynamics (see [2–4, 6] and references therein). It was found from electrical conductivity measurements [7] that CeF_3, like other fluorides LnF_3 (*Ln* = La and Nd) [2, 7], at about 435 K exhibits strong alterations in the character of the fluorine mobility, which manifest themselves as an abrupt change in the activation enthalpy but are not accompanied with a structural phase transition. A much weaker change in the activation enthalpy was also observed near 290 K [2, 8]. For neodymium fluoride, the temperatures of similar changes in the activation enthalpy were associated with bends on the temperature dependences of the tysonite lattice parameters *a* and *c* [2]. Doping the fluoride crystals strongly influences not only the activation enthalpy but also the local dynamics of fluorine ions [2–4]. This provides additional information on the mechanisms of superionic mobility in trifluoride crystals. In this paper, we present results of studies on fluorine mobility in mixed $Ce_{0.95}Al_{0.05}F_3$ crystals on the basis of electrical conductivity and ^{19}F NMR.

2. SAMPLES AND EXPERIMENT

A mixed cerium aluminum fluoride single crystal with composition $Ce_{0.95}Al_{0.05}F_3$ was grown by the Bridgman–Stockbarger method. According to x-ray powder diffraction, the crystal structure is tysonite-like and the crystal is single-phase. The lattice parameters are a = 7.177 Å and c = 7.277 Å. The composition of the crystal was checked by inductively coupled plasma (ICP) optical emission spectrometry and chemical analysis.

The sample for conductivity measurements had the form of a parallelepiped with dimensions of $10.5 \times 8 \times 5$ mm cut along the crystallographic axes. The temperature dependence of the conductivity was recorded using an immitance meter E7-14 operating at four fixed frequencies 0.1, 1, and 10 kHz and 1 MHz. Gold film electrodes were made on the sample faces perpendicular and parallel to the *c* axis. During the measurements, the temperature was gradually varied within the range 110–510 K at a rate of 1 K/min.

NMR measurements were carried out using a Bruker Avance400 NMR spectrometer within the temperature range 290–400 K. The ^{19}F NMR line for the $Ce_{0.95}Al_{0.05}F_3$ powder sample was observed as the Fourier transform of the free-induction signal after a 90° pulse. The rate of the change in temperature was no more than 1 K/min. Prior to each measurement, the sample was kept at a fixed temperature for about 10 min. The accuracy of temperature control was better than 1 K.

* This article was submitted by the authors in English.

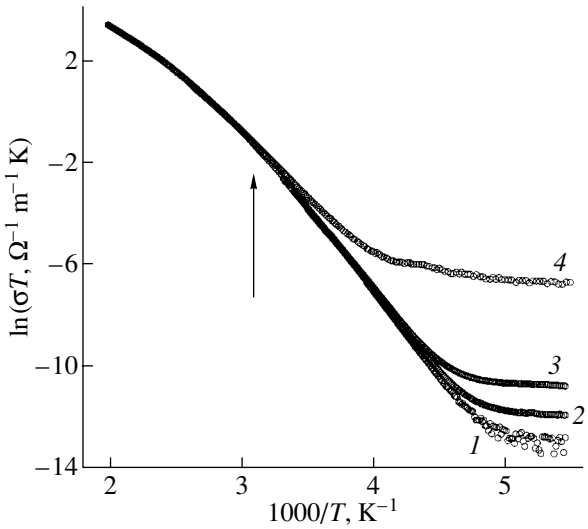

Fig. 1. Logarithm of electrical conductivity parallel to the *c* axis measured at (*1*) 0.1, (*2*) 1, and (*3*) 10 kHz, and 1 MHz (*4*) multiplied by temperature versus inverse temperature. The arrow marks a temperature of the onset of curve deviation from the linear dependence.

3. RESULTS AND DISCUSSION

Figure 1 shows the results of the conductivity measurements along the *c* axis at four different frequencies. Above about 230 K, the sample displays high ionic conductivity, which does not depend on frequency at higher temperatures, in agreement with the delocalized nature of fluorine mobility. The logarithmic curves are straight lines for lower frequencies between about 230 and 325 K. The activation enthalpy calculated from these curves is equal to 0.54 eV. This enthalpy is somewhat higher than that found within the corresponding temperature range for the pressed polycrystalline pure CeF_3 sample (0.45 eV) [2]. At about 325 K, the curves exhibit noticeable changes in the slope. Contrary to pure CeF_3 [2], the logarithmic curves for the sample under study cannot be approximated by straight lines above 325 K but rather indicate a gradual saturation of the conductivity with increasing temperature up to 510 K. Note that the conductivity in the mixed fluoride under study is slightly less than in the pure cerium fluoride [2]. The behavior of the conductivity in the direction perpendicular to the *c* axis for the sample under study was very similar to that along the *c* axis for a weak anisotropy of ionic mobility in fluorides with a tysonite-like structure [9, 10]. Nevertheless, the activation enthalpy evaluated below 325 K was a little higher for conductivity perpendicular to the *c* axis than for that parallel to the *c* axis and equal to 0.56 eV.

^{19}F NMR studies showed strong changes in the line shape with increasing temperature from 190 K, reflecting alterations in the fluorine mobility. Some NMR spectra are depicted in Fig. 2. Near room temperature, the line shape is very similar to that observed in the pure cerium fluoride crystal near and below room temperature [11]. According to [2–4, 6, 11], in crystals with a tysonite-like structure, there are three different fluorine sublattices, usually referred to as F_1, F_2, and F_3. Fluorine ions in the F_1 sublattice were found to be mobile even at low temperatures, while the F_2 and F_3 sublattices (often referred to as the F_{23} sublattice) remained rigid. Fluorine ions in the second and third rigid sublattices have about the same surroundings and chemical shift, so their NMR lines overlap. The amount of fluorine in the F_1 sublattice is about twice as much as in the F_{23} sublattice. Thus, below room temperature, in pure tysonite-like crystals one can normally see two distinct peaks ascribed to fluorine in the F_1 and F_{23} sublattices with positive and negative chemical shifts, respectively [2, 4]. With and increase in temperature up to room temperature, an additional peak may appear [2] because of the increasing partial exchange of fluorine

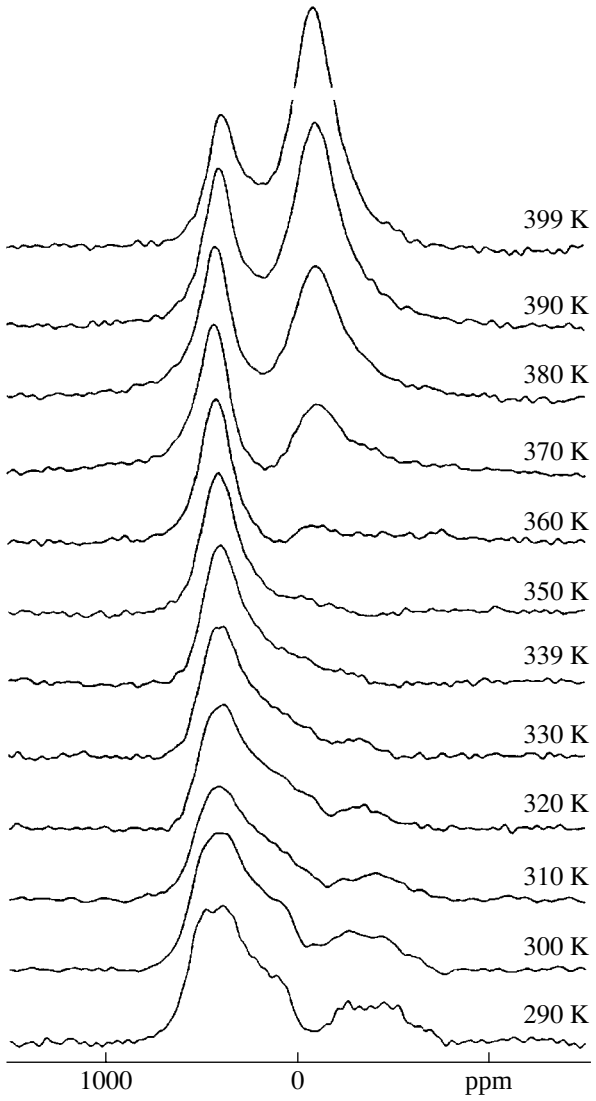

Fig. 2. ^{19}F NMR spectra at several temperatures from 290 to 399 K.

between the F_1 and F_{23} sublattices. Which of the two sublattices, F_2 or F_3, first starts exchanging with the F_1 sublattice and becomes mobile remains a subject of debate [2, 12]. In [12], the additional peak was not observed. Instead of this, the F_1 peak slightly shifted and intensified when the F_1–F_{23} exchange became faster, which was explained in terms of fast interchange within the F_1 sublattice.

Thus, two distinct peaks with chemical shifts of about 450 and –400 ppm that were seen in the sample under study near room temperature (where ionic conductivity is still moderate) can be mainly attributed to fluorine in the F_1 and F_{23} sublattices, respectively. The integral intensity of the F_{23} peak is noticeably less than half of that of the F_1 peak. This means that only part of the fluorine in the F_{23} sublattice remains rigid. Another part participates in the exchange between the F_1 and the F_{23} sublattices. Mobile ions that originated from the F_{23} sublattice might form the right shoulder of the high-frequency peak.

Above room temperature, the position and the intensity of the main peak with a positive chemical shift remain practically constant, while drastic alterations occur in the NMR line in the lower frequency region. First, with increasing temperature, the F_{23} peak vanishes completely by 340 K and the low frequency shoulder of the main peak smoothes away. At 350 K, one can actually see only a rather symmetric single NMR line with a chemical shift of about 400 ppm. Above about 360 K, a new peak appears with a chemical shift of about –100 ppm whose intensity gradually increases with increasing temperature. The shape of this peak can be fitted well by a Lorentzian function, contrary to the shape of the higher frequency peak, which is simulated well by a Gaussian function, as can be seen in Fig. 3 for 393 K. At about 400 K, the new peak dominates the ^{19}F NMR spectrum.

On the whole, the obtained results differ drastically from the temperature dependences of NMR spectra in pure CeF_3 that were reported in [2]. The appearance of the new peak above 360 K can hardly be explained by fast exchange between mobile fluorine in the F_1 sublattice and fluorine in the F_{23} sublattice, as was done for the pure CeF_3 and some other trifluoride crystals in [2, 4, 12]. In fact, when this peak starts to rise, the intensity and position of the F_1 peak do not change noticeably. Another supposition seems to be more credible. One can assume that the single peak at 350 K, which remains stable from room temperature up to at least 399 K, originates from mobile fluorine in the F_1 sublattice. Jumps of these fluorine atoms are mainly responsible for the conductivity near and below room temperature with a constant activation enthalpy. Above room temperature, acceleration in the ion exchange between slow or rigid fluorine in the F_2, F_3, and F_1 sublattices leads first to smearing of the relevant resonance lines and then to a rise in the new peak. Since the integral intensity of the new peak at, for instance, 390 K is higher than that of the high-frequency peak, one can suggest that the number of fluorine ions in the F_1 sublattice that remain slow or rigid near room temperature is at least comparable to the number of mobile F_1 fluorine ions. Note that the Lorentzian shape of the new peak corresponds to a high mobility of collective fluorine ions.

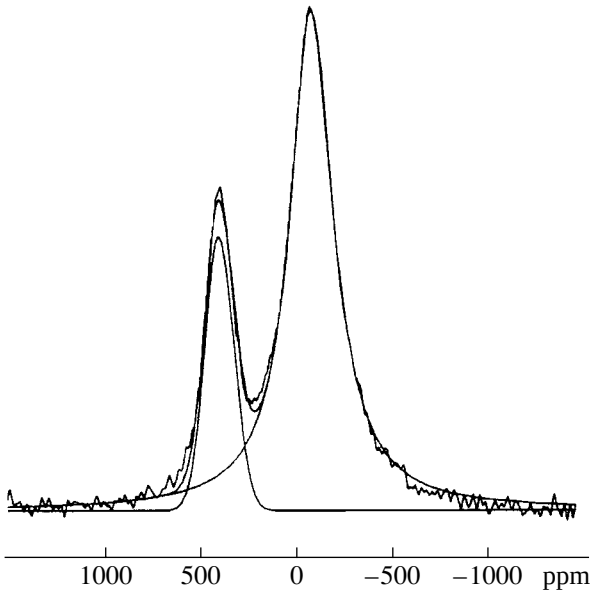

Fig. 3. Deconvolution of the ^{19}F NMR spectrum at 393 K.

The change in the character of fluorine mobility could be treated as a superionic phase transition in type-II ionic conductors [1]. Such superionic phase transitions are accompanied by a saturation of conductivity [1], in agreement with the results shown in Fig. 1. According to Fig. 1, the onset of the saturation of conductivity starts at about 325 K and this agrees with the changes in the NMR spectra shown in Fig. 2. The slight step in the lattice parameters and changes in the activation enthalpy seen near room temperature for some rare-earth trifluorides [2] support the existence of such a phase transition.

4. CONCLUSIONS

The conductivity and ^{19}F NMR spectra measurements in the $Ce_{0.95}Al_{0.05}F_3$ superionic crystal revealed noticeable distinctions from the results for pure CeF_3. The activation enthalpy near room temperature evaluated from the conductivity was higher than in the pure crystal. A gradual saturation of conductivity was observed at elevated temperatures, contrary to the sharp bend reported for pure CeF_3. Detailed observations of the evolution of the NMR spectra with changes in the temperature showed that the simple picture of fast exchange between the whole F_1 and F_{23} sublattices used

to treat the high-temperature spectra in a pure CeF_3 crystal is no longer valid for the doped crystal under study. The measurements also revealed a superionic phase transition near 325 K that is not accompanied by structural transformations.

ACKNOWLEDGMENTS

This work was supported by the National Science Council of Taiwan under grant 92-2811-M-006-014.

REFERENCES

1. J. B. Boyce and B. A. Huberman, Phys. Rep. **51**, 189 (1979).
2. M. E. Omari, J. Sénégas, and J.-M. Réau, Solid State Ionics **107**, 281 (1998).
3. N. I. Sorokin and B. P. Sobolev, Kristallografiya **39**, 837 (1994) [Crystallogr. Rep. **39**, 810 (1994)].
4. A. F. Privalov, H.-M. Vieth, and I. V. Murin, J. Phys.: Condens. Matter **6**, 8237 (1994).
5. *PCPDFWIN*, *JCPDS-International Center for Diffraction Data* (1999), No. 860967.
6. G. A. Jaroszkiewiez and J. H. Strange, J. Phys. C **18**, 2331 (1985).
7. L. E. Nagel and M. O. Keeffe, in *Fast Ionic Transport in Solids, Solid State Batteries and Devices*, Ed. by W. van Gool (North-Holland, Amsterdam, 1973), p. 165.
8. I. V. Murin, O. V. Glumov, and Yu. V. Amelin, Zh. Prikl. Khim. (Leningrad) **53**, 1474 (1980).
9. A. Roos, F. C. M. van de Pol, R. Keim, and J. Schoonman, Solid State Ionics **13**, 191 (1984).
10. C. Hoff, H.-D. Wiemhöfer, O. Glumov, and I. V. Murin, Solid State Ionics **101–103**, 445 (1997).
11. M. E. Omari, J. Sénégas, and J.-M. Réau, Solid State Ionics **107**, 293 (1998).
12. F. Wang and C. P. Grey, Chem. Mater. **9**, 1068 (1997).

Physics of the Solid State, Vol. 46, No. 9, 2004, pp. 1631–1636. Translated from Fizika Tverdogo Tela, Vol. 46, No. 9, 2004, pp. 1581–1585.
Original Russian Text Copyright © 2004 by Fedoruk.

SEMICONDUCTORS AND DIELECTRICS

Transient Nutation of Dressed Spin States of E_1' Centers in a Quartz Crystal

G. G. Fedoruk

Institute of Physics, University of Szczecin, Szczecin, 70-451 Poland
Institute of Applied Physical Problems, ul. Kurchatova 7, Minsk, 220064 Belarus
e-mail: fedaruk@wmf.univ.szczecin.pl

Received December 23, 2003

Abstract—The transient nutation of states dressed by a microwave field in a two-level system (E_1' centers in a quartz crystal) is observed in pulsed electron paramagnetic resonance (EPR) in the course of an additional pulse of a linearly polarized radio-frequency (rf) field that has an amplitude $2B_2$ and is applied parallel to the static magnetic field. It is shown that, when the frequency of the rf field coincides with the frequency of nutation of the bare spin system, the signal of this nutation is modulated by the nutation of dressed states at the frequency $\omega_2 = \gamma B_2$, where γ is the electron gyromagnetic ratio. The decay time of nutation of dressed states is considerably (no less than four times) longer than that of bare states of E_1' centers due to spin–spin relaxation and correlates with the spin–lattice relaxation time in the rotating coordinate system. © *2004 MAIK "Nauka/Interperiodica".*

1. INTRODUCTION

Eigenstates of a quantum system in a strong electromagnetic field with a frequency close to the frequency of quantum transitions of the system differ substantially from the eigenstates in the absence of an external electromagnetic field. States of this quantum system, which is dressed by the electromagnetic field, are often referred to as dressed states, in contrast to the states of an unperturbed bare system. The properties of the dressed quantum system are determined by both the properties of the bare quantum system and the parameters of the external electromagnetic field. Most frequently, the properties of dressed quantum systems have been investigated using stationary methods in optical resonance [1]. The resonance of nuclear spin states dressed by a resonant radio-frequency (rf) field was observed in stationary nuclear magnetic resonance and was termed the rotary saturation [2].

In recent years, the use of pulsed methods has made it possible to study the dynamics of quantum transitions between dressed states and to observe transient nutations of these states in optical [3, 4] and electron paramagnetic [5] resonances. The interaction of dressed states of a spin system with an electromagnetic field depends on the matrix element of the transition dipole moment, whereas the interaction of these states with the environment occurs under conditions that differ significantly from a similar interaction for a bare system. In this respect, investigation into the dynamics of dressed states can provide information that would be useful for extending the capabilities of coherent spectroscopy as an efficient tool for studying complex multilevel systems [5].

In this work, the transient nutation of dressed states was investigated in the electron paramagnetic resonance of E_1' centers in a quartz crystal. As was done by Jeschke [5], the transient nutation was induced by an additional pulse of a linearly polarized rf magnetic field aligned parallel to the static magnetic field. However, in our experiments, we observed transient nutation of dressed states in the course of the exciting rf pulse which modulated the transient nutation of a bare spin system, whereas Jeschke [5] recorded nutation after the termination of the exciting pulse indirectly with the use of a spin echo signal from a bare system.

2. THEORETICAL BACKGROUND

Let us consider an electron spin system with spin $S = 1/2$ in a static magnetic field $\mathbf{B}_0$, which is oriented parallel to the z axis of the laboratory coordinate system, and a linearly polarized electromagnetic field $2\mathbf{B}_1\cos(\omega t)$, which is aligned with the x axis. In this case, the Hamiltonian (in frequency units) can be represented in the form

$$H_1 = \omega_0 S_z + 2\omega_1 \cos(\omega t) S_x, \qquad (1)$$

where $\omega_0 = \gamma B_0$ is the Larmor frequency (resonant frequency of spin transitions), $\gamma = g\beta_e/\hbar$ is the electron gyromagnetic ratio, g is the electron g factor, β_e is the Bohr magneton, and $\omega_1 = \gamma B_1$. The linearly polarized electromagnetic field can be decomposed into two circularly polarized components that have the amplitude B_1 and rotate in opposite directions about the z axis in the xy plane at frequencies $\pm\omega$. In the rotary-wave

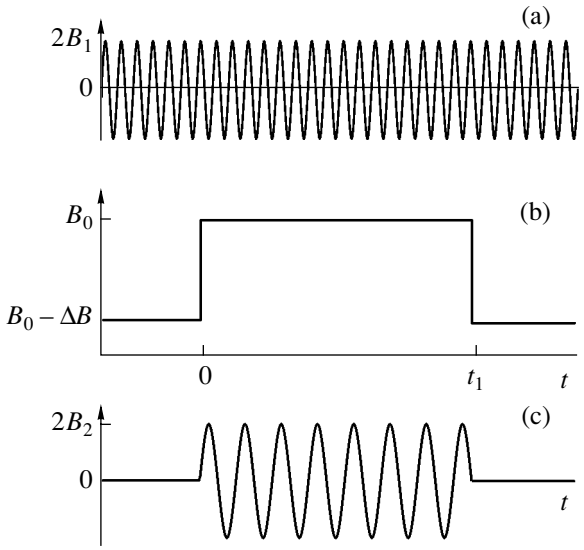

Fig. 1. Scheme of generating transient nutations of bare and dressed spin states in electron paramagnetic resonance with (a) transverse continuous microwave radiation, (b) a pulse of the magnetic field, and (c) a pulse of the linearly polarized rf field (the fields are applied along the static magnetic field).

approximation, under the conditions of magnetic resonance ($\omega \approx \omega_0$), only one component of the linearly polarized electromagnetic field, which rotates in the direction of the Larmor spin precession, efficiently induces resonant spin transitions. The frequency of the second component of the electromagnetic field differs significantly from the resonant frequency and the effect of this component at $B_1 \ll B_0$ can be ignored with a high accuracy. In the rotary-wave approximation, the Hamiltonian in the coordinate system rotating about the z axis at the frequency ω has the form

$$\tilde{H}_1 = (\omega_0 - \omega)S_z + \omega_1 S_x. \quad (2)$$

In the presence of an additional linearly polarized electromagnetic field $2B_2\cos(\omega_{rf}t)$ aligned parallel to the z axis, the Hamiltonian in the rotating coordinate system takes the following form [5]:

$$\tilde{H}_2 = (\omega_0 - \omega)S_z + \omega_1 S_x + 2\omega_2\cos(\omega_{rf}t)S_z, \quad (3)$$

where $\omega_2 = \gamma B_2$.

It follows from relationship (3) that, under the conditions of magnetic resonance with the first electromagnetic field ($\omega = \omega_0$), the Hamiltonians $\tilde{H}_2$ and H_1 have the same form, except for the difference in the coordinate axes. Consequently, the effect of the additional electromagnetic field on states of the spin system dressed by the first electromagnetic field is identical to the effect exerted by the first electromagnetic field on states of the bare system in the static magnetic field.

As is known, transient nutation is the simplest effect that arises upon exposure of a bare quantum system to a pulsed resonant electromagnetic field and which directly reflects the dynamics of quantum transitions [6]. In the case of magnetic resonance under the condition $\omega_1 \gg 1/T_2 \gg 1/T_1$, the transient nutation signal along the y axis (absorption signal) for a spin system, which is in thermal equilibrium prior to excitation, can be described by the relationship [7]

$$S_y \propto \frac{\omega_1}{\sqrt{\omega_1^2 + \delta^2}}\sin[\sqrt{(\omega_1^2 + \delta^2)}t] \times \exp\left[-\frac{t}{T_2}\left(1 - \frac{1}{2}\frac{\omega_1^2}{\omega_1^2 + \delta^2}\right)\right], \quad (4)$$

where $\delta = \omega_0 - \omega$ is the detuning from resonance and T_1 and T_2 are the spin–lattice and spin–spin relaxation times, respectively. It can be seen from expression (4) that, at exact resonance, the transient nutation of the bare spin system has the frequency $\omega_1 = \gamma B_1$. It follows from relationship (3) that, for zero detuning ($\delta = 0$) under the condition of nutation resonance (the frequency of the additional field B_2 is equal to the frequency of nutation of the bare system, i.e., $\omega_{rf} = \omega_1$), the nutation of the dressed system should have the frequency $\omega_2 = \gamma B_2$.

Despite the similarity of the $\tilde{H}_2$ and H_1 Hamiltonians, the transitions between the states of the dressed and bare spin systems occur under different physical conditions, in particular, due to a substantial difference in the static and alternating magnetic fields (as a rule, $B_1 \ll B_0$). This leads to a difference in the interaction of the spins systems with the environment and brings about a change in the relaxation processes. On the other hand, in the case of transitions between the states of the dressed system, there can readily arise a situation where $B_2 \sim B_1$. As a result, the rotary-wave approximation becomes invalid and the effect of the second circularly polarized component of the electromagnetic field B_2 must be taken into account. It is known that, upon transitions between the states of a bare spin system, the oppositely rotating component of the electromagnetic field leads both to a shift in the resonant frequency of one-photon transitions with respect to the frequency ω_0 (the Bloch–Siegert shift) and to multiphoton transitions at frequencies $\omega_0/(2n + 1)$ [8]. A similar effect of the oppositely rotating component should be expected upon transitions between the states of the dressed spin system, which, in turn, initiate nutation.

3. EXPERIMENTAL TECHNIQUE

The pulse sequence used to observe the transient nutations of bare and dressed spin states in electron paramagnetic resonance is shown in Fig. 1.

The nutations of bare spin states were induced by continuous microwave radiation (Fig. 1a) and a longitudinal magnetic-field pulse (Fig. 1b) [9, 10]. Initially, the spin system was exposed to an off-resonant static magnetic field $B = B_0 - \Delta B$ and a perpendicular microwave field $\gamma B_1 > 1/T_2, 1/T_1$) for a time long enough for a stationary state of the system to be reached. In this case, no absorption of microwave radiation occurred. Then, the magnetic field amplitude was jumpwise changed to the resonant value B_0. The time required to attain the resonance conditions was chosen shorter than the spin–spin relaxation time T_2, and the rate of change in the magnetic field amplitude satisfied the inequality $|dB/dt| > \gamma B_1^2$. The magnetic-field pulse (Fig. 1b) was applied at the instant of time $t = 0$. With a jump in the magnetic field $\Delta B = |B - B_0|$ due to the Zeeman effect, the frequency ω_0' of the quantum transition in the spin system at the instant $t = 0$ changed to ω_0 and became equal to the frequency ω of the microwave field (Fig. 1a). Under these conditions, the magnetic-field pulse was attended by a resonant interaction of the microwave field with the spin system, which, in turn, induced transient nutation.

The nutation of dressed spin states was generated by a pulse of a linearly polarized rf field aligned with the field B_0. This pulse had an amplitude $2B_2$ and was applied simultaneously with the magnetic-field pulse ΔB (Fig. 1c). As was already noted, the effect of the additional alternating magnetic field (with an amplitude B_2 of the circularly polarized component and a frequency ω_{rf}) applied along the field B_0 on the dressed spin states is similar to that of the microwave field on the bare system. As a result, a resonance is observed for the dressed spin states at $\omega_{rf} = \omega_1$. Upon pulsed excitation of these states at resonance, there arises a transient nutation with frequency $\omega_2 = \gamma B_2$. Technically, both magnetic-field pulses were produced by passing the electric current through the same modulation unit. The measurement of the current made it possible to calibrate the amplitude B_2 of the rf field in the region of the sample against the known amplitude ΔB of the magnetic-field pulse. The amplitude ΔB was determined from the beat frequency (equal to $\Delta B/\gamma$) of the free-induction signal observed after the termination of the magnetic-field pulse [11].

The above technique was used to generate nutation signals on a modified pulsed EPR spectrometer operating in the X band ($\omega/2\pi = 10.1$ GHz) [11]. The maximum amplitude B_1 of the magnetic field in an H_{102}-type rectangular cavity with the sample was approximately equal to 0.054 mT and provided the generation of nutation signals at a frequency up to $\omega_1/2\pi = 1.5$ MHz for two-level systems with spin $S = 1/2$. Multichannel digital summation of the signals was used in order to improve the signal-to-noise ratio. The phase of the rf field was not locked to the onset of the magnetic-field pulse or, hence, to the nutation of the bare spin system.

Owing to the narrow EPR line and long relaxation times, E_1' centers in quartz crystals are convenient objects for investigating nutation [5, 10, 11]. The ground state of E_1' centers is represented by a Kramers doublet with spin $S = 1/2$ and a weak anisotropy of the spectroscopic splitting factor ($\Delta g = 9 \times 10^{-4}$). When the magnetic field is parallel to the optic axis of the crystal, the EPR spectrum of these centers in the X band consists of a single line with the width $\Delta B_{pp} = 0.016$ mT and $g = 2.0008$. The relaxation times for E_1' centers are relatively long even at room temperature: $T_1 \approx 0.2$ ms [12, 13] and T_2 is determined by the dipole–dipole interaction [12] and is approximately equal to 12 μs when the concentration of E_1' centers is 10^{17} cm^{-3}.

The E_1' centers were generated under exposure of a quartz single crystal ($1.5 \times 1.5 \times 2$ mm) to reactor neutrons at a neutron fluence of approximately 10^{18} cm^{-2}. The concentration of E_1' centers was estimated by comparing their stationary spectra with the spectra of a reference sample and amounted to approximately $(3 \pm 0.8) \times 10^{17}$ cm^{-3}.

4. RESULTS AND DISCUSSION

The measurements were performed at room temperature in a resonant static magnetic field in the course of the pulse. These conditions ensured the strongest absorption signal of nutations of the bare spin system at the frequency $\omega_1 = \gamma B_1$. The static magnetic field was aligned parallel to the optic axis of the crystal. The duration of magnetic-field pulses t_1 was equal to 10 μs, the magnetic-field pulse amplitude ΔB amounted to 0.12 mT, and the pulse repetition period was 1.25 ms.

Figure 2 depicts the nutation signals of E_1' centers in the quartz crystal at different amplitudes B_2 of the resonant rf field ($\omega_{rf} = \omega_1$). It can be seen from oscillogram *a* in Fig. 2 that, under resonant excitation ($\omega = \omega_0$) by the field B_1 in the absence of the field B_2, the nutation of the bare spin system in accordance with relationship (4) is observed at the frequency $\omega_1/2\pi i = 1.34$ MHz. At the same time, the interaction with the resonant rf field B_2 leads to modulation of the nutation signal of the bare spin system (oscillograms *b–d* in Fig. 2). Note that the frequency of this modulation increases proportionally to the amplitude B_2, as could be expected from expression (3) for the transient nutation of the dressed spin states.

The nutation EPR signals of E_1' centers at nutation resonance ($\omega_{rf} = \omega_1$) for the same rf field amplitude B_2 and different amplitudes B_1 of the microwave field (and, correspondingly, different frequencies ω_{rf} of the rf

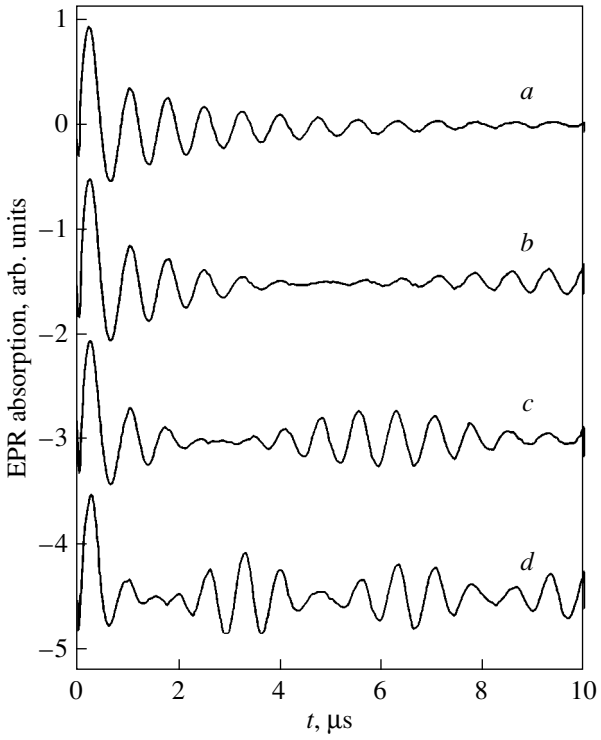

Fig. 2. Nutation EPR signals of E_1' centers in a quartz crystal at different amplitudes B_2 of the resonant rf field (ω_{rf} = ω_1 = 2π × 1.34 MHz). B_2 = (*a*) 0, (*b*) 2.8, (*c*) 5.6, and (*d*) 11.2 μT.

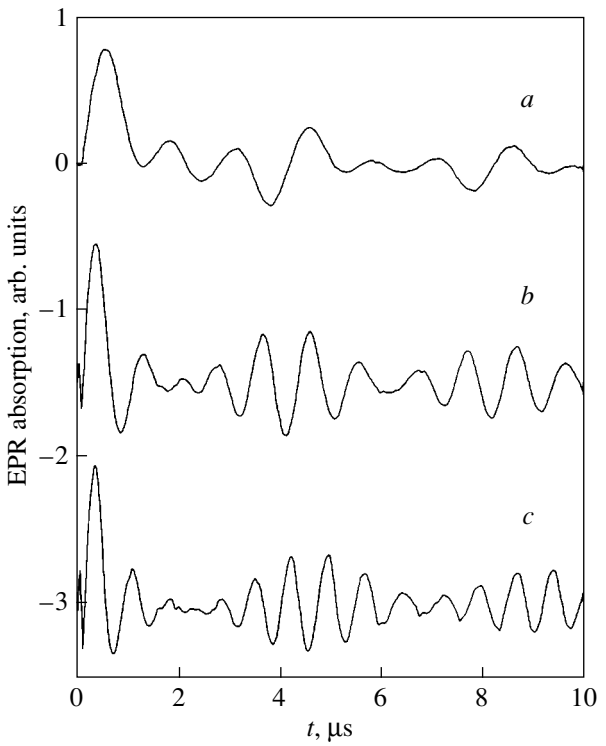

Fig. 3. Nutation EPR signals of E_1' centers at a constant amplitude of the rf field B_2 = 8.0 μT and different frequencies (ω_{rf} = ω_1) of nutation resonance: (*a*) 0.52, (*b*) 0.97, and (*c*) 1.34 MHz.

field) are shown in Fig. 3. These signals indicate that the modulation frequency (nutation frequency of the dressed spin states) remains constant with a change in the frequency of the nutation resonance.

In the case of nutation of the dressed spin states under conditions of resonant excitation (ω_{rf} = ω_1), the observed signal can be described in the rotary-wave approximation by the relationship

$$V \propto [1 + \cos(\omega_2 t)]\sin(\omega_1 t)\exp\left(-\frac{t}{T_{mp}}\right), \qquad (5)$$

where $\omega_2 = \gamma B_2$ is the nutation frequency of the dressed spin states at $\omega_{rf} = \omega_1$ and T_{mp} is the relaxation time characterizing the decay of nutation of the dressed spin states.

The possibility of calibrating the amplitude B_2 in our experiments provides a means for quantitative analysis of the nutation frequency ω_2 as a function of the amplitude B_2 (Fig. 4). It can be seen from Fig. 4 that the obtained dependence is in good agreement with the theoretically predicted linear dependence of the nutation frequency of the dressed spin states $\omega_2 = \gamma B_2$.

The interaction of the dressed spin states with the environment is accompanied by relaxation processes and the decay of nutations with frequency ω_2. In this case, the microwave field B_1 plays the role of a static magnetic field B_0 in the relaxation of the bare spin states. This relaxation brings about the decay of nutations with frequency ω_1 and is characterized by the relaxation times T_1 and T_2. Since $B_1 \ll B_0$, the relaxation of the dressed spin states at resonance $\omega_{rf} = \omega_1$ can exhibit specific behavior. A comparison of the decay rates of the nutations depicted in Fig. 2 shows that the interaction of the dressed spin states with the environment (oscillograms *b*–*d*) is considerably weaker than the interaction of the bare spin states (oscillogram *a*). According to the estimates made from relationships (4) and (5), we have $T_2 = 3.6 \pm 0.4$ μs and $T_{mp} = 16 \pm 2$ μs.

On the other hand, the relaxation time T_2 for E_1' centers in the case of the dipole–dipole interaction and a random arrangement of these centers in the lattice can be represented in the form [12]

$$T_2 = \frac{9\sqrt{3}}{4\pi^2\gamma^2\hbar C} = \frac{1}{8.1 \times 10^{-13} C}. \qquad (6)$$

The relaxation time T_2 determined from this formula at a concentration of E_1' centers $C = 3 \times 10^{17}$ cm^{-3} for the studied sample is equal to 4.1 μs. It can be seen that the relaxation time T_2 estimated from the nutation decay is

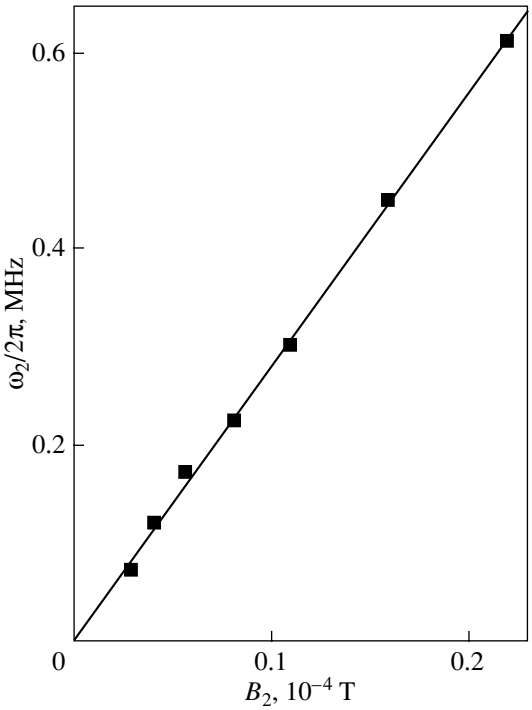

Fig. 4. Dependence of the nutation frequency of the dressed spin states under resonant excitation ($\omega_{rf} = \omega_1$) on the amplitude B_2 of the rf field.

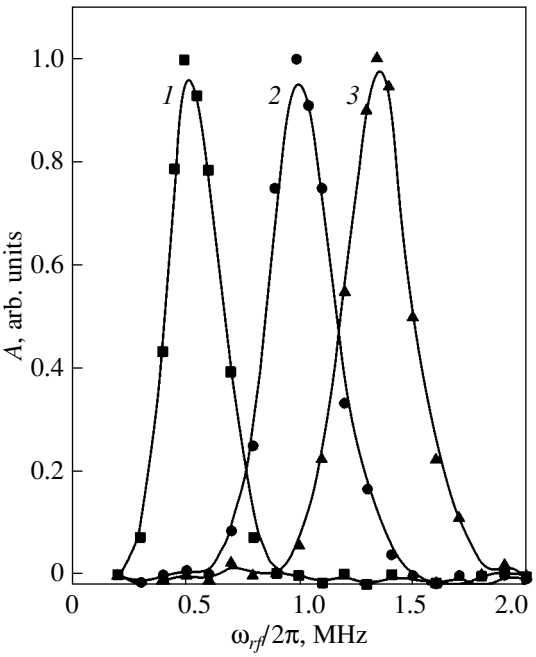

Fig. 5. Spectra of states dressed by the microwave field in E_1' centers at $\omega_2/2\pi = 0.078$ MHz and different nutation frequencies $\omega_1/2\pi$ of bare states. $\omega_1/2\pi$ = (*1*) 0.52, (*2*) 0.97, and (*3*) 1.34 MHz.

close to the relaxation time T_2 determined from the concentration of E_1' centers. This indicates that the inhomogeneity of the field B_1 has a weak effect in our experiments.

The relaxation time T_{mp} agrees both with the estimate ($T_{mp} > 10$ μs) obtained in [5] from data on the decay of the spin echo signal of the dressed spin states and with the measured time $T_{1\rho} = 14$ μs. As a result, we have $T_{m\rho} \approx T_{1\rho}$, where $T_{1\rho}$ is the spin–lattice relaxation time in the rotating coordinate system. Moreover, although the phase memory time for E_1' centers in the sample studied in [5] is longer than that in our sample by a factor of 1.8, the decay time of nutations of the dressed spin states in our case turned out to be significantly (by a factor of 16) longer than that obtained in [5]. This difference can be associated with the inhomogeneities of exciting fields, which more clearly manifest themselves due to the stronger fields used in [5].

The spectrum of the dressed spin states can be obtained by measuring both the frequency of the rf field ω_{rf} (when the other parameters of excitation of the spin system are fixed) and the change in the nutation amplitude due to the difference between the decay rates of nutations of the bare and dressed spin states. It is seen from Fig. 2 that, at $t > 5$ μs, the nutation amplitudes of the bare spin system differ significantly from those of the dressed spin system. This difference (A) was used to construct the spectrum of the dressed spin states (Fig. 5). The exciting rf field was taken to be substantially weaker than the microwave field in order to avoid a noticeable Bloch–Siegert shift for the resonance line of the dressed spin states. It can be seen from Fig. 5 that, according to expression (3), the maximum of the nutation signal from the dressed spin system is observed when the frequency of the rf field coincides with the frequency ω_1. The amplitude of the rf field ($B_2 = 2.8$ μT) was also considerably less than the width of the EPR line of E_1' centers (the peak-to-peak derivative width $\Delta B_{pp} = 16$ μT). In this case, the spectrum of the dressed spin states can be similar to a usual EPR spectrum. Indeed, the width of the resonance line of the dressed spin states at half-maximum is determined to be $\Delta B_{1/2} = 11$ μT.

5. CONCLUSIONS

Thus, it was demonstrated that the nutation of dressed spin states of E_1' centers in quartz crystals can be directly measured in electron paramagnetic resonance. The nutation was observed upon exposure to continuous microwave radiation and polarizing magnetic-field pulses with amplitudes modulated by an rf field. Since the decay time of this nutation is close to the spin–lattice relaxation time $T_{1\rho}$ in the rotating coordinate system and this time in solids, as a rule, is longer than the decay time of nutation of bare spin states

(which is associated with the spin–spin relaxation time T_2), the use of dressed spin states provides information that cannot be obtained for dynamic processes from measurements of the relaxation times T_1 and T_2. Moreover, pulsed experiments with dressed spin states and, in particular, two-dimensional correlation experiments make it possible to extend the capabilities of nutation EPR spectroscopy as an efficient tool for studying complex multilevel systems with overlapping spectra [5].

ACKNOWLEDGMENTS

The author is grateful to I.Z. Rutkovskiĭ for his assistance in performing the experiments.

REFERENCES

1. C. Cohen-Tannoudji, J. Dupont-Roc, and G. Grynberg, *Atom–Photon Interaction: Basic Processes and Application* (Wiley, New York, 1992).
2. A. G. Redfield, Phys. Rev. **98**, 1787 (1955).
3. C. Wei, N. B. Manson, and J. P. D. Martin, Phys. Rev. Lett. **74** (7), 1083 (1995).
4. C. Wei, S. A. Holmstrom, A. D. Greentree, and N. B. Manson, J. Opt. B: Quantum Semiclassic. Opt. **1**, 289 (1999).
5. G. Jeschke, Chem. Phys. Lett. **301** (5–6), 524 (1999).
6. H. C. Torrey, Phys. Rev. **76** (8), 1059 (1949).
7. S. Stoll, G. Jeschke, M. Willer, and A. Schweiger, J. Magn. Reson. **130** (1), 86 (1998).
8. U. Haeberlen, *High-Resolution NMR in Solids* (Academic, New York, 1976; Mir, Moscow, 1980).
9. I. Z. Rutkovskiĭ and G. G. Fedoruk, Zh. Éksp. Teor. Fiz. **78** (3), 1237 (1980) [Sov. Phys. JETP **51**, 623 (1980)].
10. G. G. Fedoruk, Zh. Prikl. Spektrosk. **69** (2), 141 (2002).
11. V. S. Kuz'min and G. G. Fedoruk, *Nonstationary Coherent Phenomena in Paramagnetic Spin Systems* (Beloruss. Gos. Univ., Minsk, 2001) [in Russian].
12. K. M. Salikhov, A. G. Semenov, and Yu. D. Tsvetkov, *Electron Spin Echo and Its Application* (Nauka, Novosibirsk, 1976) [in Russian].
13. L. K. Aminov, I. N. Kurkin, D. A. Lukoyanov, and K. P. Chernov, Fiz. Tverd. Tela (St. Petersburg) **39** (8), 1335 (1997) [Phys. Solid State **39**, 1184 (1997)].

Translated by O. Borovik-Romanova

Physics of the Solid State, Vol. 46, No. 9, 2004, pp. 1637–1638. Translated from Fizika Tverdogo Tela, Vol. 46, No. 9, 2004, pp. 1586–1587.
Original Russian Text Copyright © 2004 by Aleksandrov, Zamkov, Zaĭtsev, Turchin, Sysoev, Parfenov.

SEMICONDUCTORS AND DIELECTRICS

Acoustical and Acoustooptical Properties of Lead Tetraborate Single Crystals

K. S. Aleksandrov[1, 2], A. V. Zamkov[1], A. I. Zaĭtsev[1], P. P. Turchin[2], A. M. Sysoev[1], and A. A. Parfenov[2]

[1] *Kirensky Institute of Physics, Siberian Division, Russian Academy of Sciences, Akademgorodok, Krasnoyarsk, 660036 Russia*

[2] *Krasnoyarsk State University, Svobodnyĭ pr. 79, Krasnoyarsk, 660062 Russia*

e-mail: az@iph.krasn.ru

Received January 29, 2004

Abstract—The velocities of bulk acoustic waves and the acoustooptical Q factors M_2 are measured. The results of these measurements are used for calculating the photoelastic coefficients of a lead tetraborate single crystal.
© 2004 MAIK "Nauka/Interperiodica".

1. INTRODUCTION

Although single crystals of lead tetraborate PbB_4O_7 have long been known [1], these materials hold considerable promise for acoustical and acoustooptical applications. Owing to their point symmetry ($mm2$), PbB_4O_7 single crystals can also be used as pyroelectric or piezoelectric materials. To date, the structure, nonlinear optical and electrooptical properties [1–3], and other macro- and microscopic characteristics of lead tetraborate have been investigated. The dependence of the velocity of sound in lead tetraborate crystals on the ratio of the melting temperature to the average atomic weight for oxides, which was reconstructed from the values of the microhardness, deviates from the well-known ("linear") dependence of the velocity of elastic waves [4]. Moreover, this compound is transparent in the ultraviolet range (up to 250 nm) [2], which is not typical of lead compounds. The above properties of PbB_4O_7 single crystals and prospects for their practical application call for more comprehensive study of the acoustic and acoustooptical properties of this material.

2. SAMPLE PREPARATION AND EXPERIMENTAL TECHNIQUE

The initial batch used for growing lead tetraborate crystals was prepared from basic lead carbonate (reagent grade) and boric acid (special-purity grade) according to the reaction

$$Pb(OH)_2 \cdot 2PbCO_3 + 12H_3BO_3 = 3PbB_4O_7 + 2CO_2\uparrow + 19H_2O\uparrow.$$

Single crystals of lead tetraborate were grown by the Czochralski technique along the b axis at a rate of 2 mm/day. The crystals grown had a length of 20 mm and a diameter of 20 mm. These crystals were used to obtain the oriented samples. Crystallographic setting of the samples was carried out according to the technique described in [2] (space group $Pnm2_1$). The single crystals of lead tetraborate are transparent in the ultraviolet range up to 250 nm. The unit cell parameters of lead tetraborate single crystals are as follows: a = 4.4547(7) Å, b = 10.839(2) Å, c = 4.2437(8) Å, and ρ = 5.852 g/cm^3 [2]. The samples prepared are characterized by a high degree of homogeneity.

The velocities of bulk acoustic waves in the single-crystal samples were measured by a pulsed ultrasonic method at a frequency of 30 MHz in the crystallographic directions [100], [010], and [001].

The acoustooptical measurements were performed using the extended Dixon–Cohen method (Bragg diffraction of light by an ultrasonic wave). The measurement accuracy was no less than 10%. The experimental setup was described earlier in [5]. The measurements were carried out at an ultrasonic frequency of 105 MHz for longitudinal acoustic waves with the use of emissions from a helium–neon laser (λ = 632.8 nm). Fused silica was used as a reference substance.

The measured velocities of propagation of bulk acoustic waves in lead tetraborate single crystals are presented in Table 1. The acoustooptical Q factors M_2 and the photoelastic constants $P_{\lambda\mu}$, which were calculated from the M_2 values and the velocities of bulk acoustic waves, are given in Table 2.

3. RESULTS

The measured velocities of bulk acoustic waves (the highest velocity $V_L[001] \sim 8$ km/s) are in excellent agreement with the predicted high values. It was found that the material under investigation is characterized by very small values of the acoustooptical Q factors (max-

Table 1. Velocities of propagation of bulk acoustic waves in the PbB_4O_7 single crystal

No.	*N*	*U*	Mode	*V*, m/s
1	[100]	[100]	*L*	7637.6 ± 0.5
2		[010]	*S*	4684.5 ± 0.5
3		[001]	*S*	4442.6 ± 0.5
4	[010]	[010]	*L*	7070.0 ± 0.5
5		[100]	*S*	4684.3 ± 0.5
6		[001]	*S*	4807.5 ± 0.5
7	[001]	[001]	*L*	7897.9 ± 0.5
8		[100]	*S*	4421.9 ± 0.5
9		[010]	*S*	4776.9 ± 0.5

Note: *N* is the direction of propagation of bulk acoustic waves, and *U* is the direction of oscillations in bulk acoustic waves.

Table 2. Acoustooptical and photoelastic characteristics of the PbB_4O_7 single crystal

Direction of propagation of the longitudinal acoustic wave	Velocity *V*, m/s	Direction of light polarization	*n*	M_2, 10^{-18} s^3/g	$P_{\lambda\mu}$
[100]	7637.6	[100]	1.9325	0.03	0.0387
[010]	7070.0	[100]	1.9325	0.29	0.1073
[001]	7897.9	[100]	1.9325	0.24	0.1152
[100]	7637.6	[010]	1.9183	0.15	0.0885
[010]	7070.0	[010]	1.9183	0.07	0.0177
[100]	7637.6	[001]	1.9269	0.23	0.1082
[010]	7070.0	[001]	1.9269	0.66	0.1632
[001]	7897.9	[001]	1.9269	0.04	0.0474

Note: *n* is the refractive index for the specified direction of light polarization.

imum value $M_2 = 0.66 \times 10^{-18}$ s^3/g) and photoelastic constants. This makes lead tetraborate crystals unsuitable for use in acoustooptical devices.

Such unusual acoustical and acoustooptical characteristics of lead tetraborate single crystals can be explained by the high density, which is unique for borates, and the character of packing of this structural type [6].

ACKNOWLEDGMENTS

This work was supported by the Russian Foundation for Basic Research (project no. 02-02-16428), the Division of Physical Sciences of the Russian Academy of Sciences (project no. 2.2.6.1), and the Ministry of Industry and Science of the Russian Federation (project NSh 939.2003.2).

REFERENCES

1. A. Perloff and S. Block, Acta Crystallogr. **20**, 274 (1966).
2. Y. S. Oseledchik, A. L. Prosvirnin, A. I. Pisarevskiy, V. V. Starshenko, V. V. Osadchuk, S. P. Belokrys, N. V. Svitanko, A. S. Korol, S. A. Krikunov, and A. F. Selevich, Opt. Mater. **4**, 669 (1995).
3. F. Pan, G. Shen, R. Wang, X. Wang, and D. Shen, Cryst. Growth **241**, 108 (2002).
4. A. A. Blistanov, V. S. Bondarenko, N. V. Perelomova, F. N. Strizhevskaya, V. V. Chkalova, and M. P. Shaskol'skaya, *Acoustical Crystals*, Ed. by M. P. Shaskol'skaya (Nauka, Moscow, 1982) [in Russian].
5. A. V. Zamkov, Candidate's Dissertation (Krasnoyarsk, 1986).
6. N. I. Leonyuk and L. I. Leonyuk, *Crystal Chemistry of Anhydrous Borates* (Mosk. Gos. Univ., Moscow, 1983) [in Russian].

Translated by N. Korovin

Physics of the Solid State, Vol. 46, No. 9, 2004, pp. 1639–1643. Translated from Fizika Tverdogo Tela, Vol. 46, No. 9, 2004, pp. 1588–1592.
Original Russian Text Copyright © 2004 by Nikiforov, Zakharov, Chernyshev.

SEMICONDUCTORS AND DIELECTRICS

Local Structure of Gd^{3+} and Eu^{2+} Impurity Centers in a CdF_2 Crystal

A. E. Nikiforov, A. Yu. Zakharov, and V. A. Chernyshev

Ural State University, pr. Lenina 51, Yekaterinburg, 620083 Russia

Received February 17, 2004

Abstract—The local crystal structure of Gd^{3+} and Eu^{2+} cubic impurity centers in cadmium fluoride is calculated within the shell model in the pair potential approximation. The local compressibility of the cationic and anionic sublattices of the host lattice is determined in the vicinity of the Gd^{3+} (Eu^{2+}) impurity ion. © *2004 MAIK "Nauka/Interperiodica".*

1. INTRODUCTION

Fluorite crystals doped with rare-earth ions are widely used as detectors of ionizing radiation and scintillators [1, 2]. Upon doping of a fluorite crystal, a rare-earth ion substitutes for an Me^{2+} cation in the crystal lattice. In the case of heterovalent substitution, charge compensation can occur either locally or nonlocally with the formation of impurity centers of different symmetry. The energy spectrum of an impurity center is governed by the interaction of 4*f*, 5*s*, and 5*p* electrons of the rare-earth ion with the nearest neighbor ions in the crystal lattice. The sensitivity of transitions between sublevels of the $4f^n$ configuration to a local environment of the rare-earth ion makes it possible to use rare-earth ions as a probe in studying local distortions of the host lattice [3]. In this respect, investigating the local structure of impurity centers is of considerable interest.

Experimental ENDOR and EPR studies of Gd^{3+} and Eu^{2+} impurity centers in cadmium fluoride CdF_2 [4, 5] have demonstrated that these centers have cubic symmetry (Fig. 1). Moreover, the ENDOR and EPR experiments revealed the location of the second, third, and fourth anionic coordination shells in the vicinity of the impurity ion. However, the positions of F^- ligands surrounding the impurity ion and the positions of ions with zero nuclear spin (Cd^{2+} cations) cannot be determined to sufficient accuracy by the ENDOR and EPR techniques. Since other methods have also not provided reliable information on the local structure of Gd^{3+} and Eu^{2+} impurity centers in cadmium fluoride, it is expedient to investigate the local crystal structure of these centers in the framework of the shell model.

2. MODEL CALCULATION OF THE ENERGY OF A CRYSTAL

The equilibrium positions of ions in a crystal can be determined by minimizing the energy of the crystal lattice.

Within the shell model in the pair potential approximation, the lattice energy can be represented in the form

$$U_{\text{lat}} = \frac{1}{2}\sum_i \sum_{k(\neq i)} V_{ik} + \frac{1}{2}\sum_i k_i \boldsymbol{\delta}_i^2, \qquad (1)$$

where $k_i\boldsymbol{\delta}_i^2$ is the energy of the core–shell interaction for the *i*th ion, $\boldsymbol{\delta}_i$ is the displacement of the shell with respect to the core, and V_{ik} is the energy of the interac-

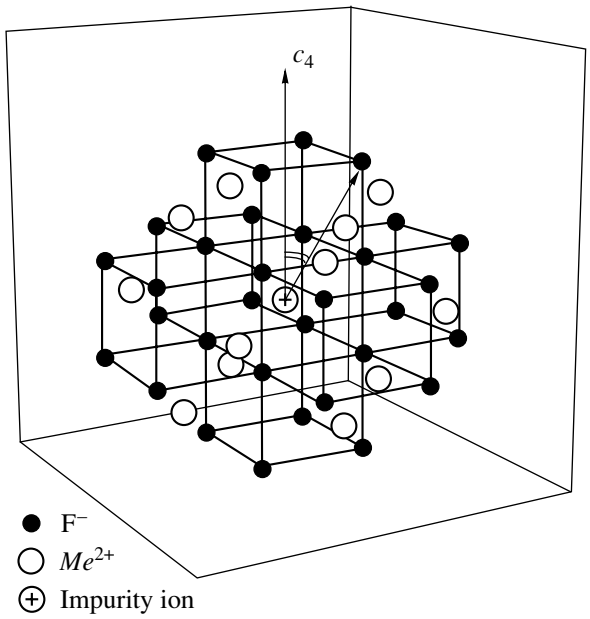

Fig. 1. Local structure of a Gd^{3+} (Eu^{2+}) cubic impurity center in the CdF_2 crystal.

1063-7834/04/4609-1639$26.00 © 2004 MAIK "Nauka/Interperiodica"

Table 1. Parameters of the pair interactions between ions (in au)

Ions	A_{ij}	B_{ij}	C_{ij}	D_{ij}	λ_{ij}
F^-–F^-	36.456	1.3778	157.083	1.8927	69.5469
Cd^{2+}–F^-	68.207	1.5453	268.940	2.0342	0.0
Cd^{3+}–F^-	0.0	0.0	267.283	2.058	0.0
Eu^{2+}–F^-	0.0	0.0	268.291	1.921	0.0

Note: $K_{Cd} = 8.2402$ and $K_F = 4.1797$.

tion between the *i*th and *k*th ions. This energy can be written in the form

$$V_{ik} = \frac{X_i X_k}{|\mathbf{r}_i - \mathbf{r}_k|} + \frac{Y_i X_k}{|\mathbf{r}_i - \mathbf{r}_k + \boldsymbol{\delta}_i|} + \frac{X_i Y_k}{|\mathbf{r}_i - \mathbf{r}_k - \boldsymbol{\delta}_k|} + \frac{Y_i Y_k}{|\mathbf{r}_i - \mathbf{r}_k + \boldsymbol{\delta}_i - \boldsymbol{\delta}_k|} + f_{ik}(|\mathbf{r}_i - \mathbf{r}_k|) + g_{ik}(|\mathbf{r}_i - \mathbf{r}_k + \boldsymbol{\delta}_i - \boldsymbol{\delta}_k|). \quad (2)$$

Here, X_i and Y_i are the charges of the core and the shell of the *i*th ion, respectively; $\mathbf{r}_i$ is the vector specifying the position of the core of the *i*th ion; the function

$$f_{ik}(r) = -A_{ik}\exp(-B_{ik}r)/r \quad (3)$$

characterizes the short-range screening of the electrostatic interaction of the ion cores; and the function

$$g_{ik}(r) = C_{ik}\exp(-D_{ik}r) - \lambda_{ik}/r^6 \quad (4)$$

describes the short-range repulsion between the ion shells in the form of the Born–Mayer potential and the van der Waals interaction. In this work, we used the following charges of the ion cores: $X_F = +5$, $X_{Cd} = +8$, $X_{Eu} = +10$, and $X_{Gd} = +11$. The charges of the ion shells were calculated from the condition $Z_i = X_i + Y_i$, where Z_i is the charge of the ion in the compound under investigation. The energy of the Coulomb interaction of ions [the first four terms in relationship (2)] was calculated using the Ewald method. The short-range interaction of metal ions with each other was ignored, because these ions are separated by a large distance. The parameters of the F^-–F^- interaction were calculated within the *ab initio* Hartree–Fock approach and the configuration interaction method [6]. When calculating the Me^{2+}–F^- short-range interaction, the contribution of the van der Waals interaction was disregarded and the parameters of the Cd^{2+}–F^- electrostatic screening were determined by numerical integration of the interaction between the electron densities of free ions; in these calculations, the charge distribution was specified by the wave functions [7, 8]. The parameters of the Cd^{2+}–F^- short-range interaction and the parameter k_i of the core–shell interaction for the Cd^{2+} ion were determined from the best fit of the calculated characteristics of the CdF_2 crystal to the available experimental data, such as the lattice constant [9]; the permittivities ε_0 and ε_∞ [10]; the elastic constants C_{11}, C_{12}, and C_{44} [9]; and the frequencies of fundamental vibrations ω_{TO} [10] and ω_R [11]. Therefore, three empirical parameters were determined with the use of eight experimental quantities.

Upon incorporation of an impurity ion, the crystal lattice is polarized in the vicinity of this ion. Within the shell model, the polarization is taken into account through the displacement of the ion shells with respect to the ion cores. In a cubic impurity center, the displacements of the shells of the ions belonging to the host lattice are symmetry-allowed, whereas the displacement of the shell of the impurity ion is forbidden. The Gd^{3+}–F^- and Eu^{2+}–F^- short-range interactions were calculated without regard for the short-range screening. In this case, the parameters *C* and *D* of the short-range repulsion were determined from the best fit of the calculated data to the radial displacements of the second, third, fourth, and fifth anion orbits, which were determined in the cubic centers of these rare-earth ions in MeF_2 (*Me* = Ca, Sr, Ba) compounds from the ENDOR experiments [12, 13].

The parameters of the pair interactions used in our calculations are presented in Table 1. For the given accuracy in determining the parameters of the pair interactions, the interionic distances within the shell model can be calculated accurate to 0.01 au.

The local crystal structure of an impurity center was calculated using the embedded-cluster method. According to this method, the crystal is divided into two regions, namely, a defect region and the rest of the host crystal. The defect region contains an impurity ion and nearest neighbor ions belonging to the host lattice that can relax within a specified symmetry. The ions of the rest of the crystal are assumed to be fixed. The size of the defect region is chosen so that a further increase in the size of this region will not result in substantial changes in the ion positions in the nearest environment of the impurity ion. In our calculations, the defect region involved ten coordination shells around the impurity ion. The energy of the crystal lattice of the doped crystal was calculated by the same methods and under the same assumptions as those used for a pure crystal [see relationships (1)–(4)]. The lattice constant of the CdF_2 crystal, which was necessary for calculating the local crystal structure of the impurity center, was preliminarily determined in the framework of the same model ($a_{calcd} = 554.7$ pm, $a_{exp} = 535.6$ pm [9]).

3. LOCAL DISTORTIONS OF THE CRYSTAL LATTICE IN THE VICINITY OF IMPURITY IONS

The results of calculating the local structure of the $CdF_2 : Gd^{3+}$ and $CdF_2 : Eu^{2+}$ crystals are presented in Tables 2 and 3. In this work, we used the notion of an orbit, which, according to [14], is taken to mean a group of ions capable of transforming into each other through any symmetry operation of the point group of a doped crystal. In cubic impurity centers, each coordination

shell is considered an orbit. The sole exception is the seventh coordination shell, which involves two orbits. The radial displacements of ions in the vicinity of the Gd^{3+} and Eu^{2+} impurity centers in the CdF_2 crystal (Table 2) are expressed in terms of fractions of the lattice constant (calculated or determined in the experiment). The results of calculating the radial displacements agree well with the experimental data. It should be noted that the calculated radial displacements of the second anionic shell coincide, to within the limits of error, with the experimental data for both $CdF_2 : Gd^{3+}$ and $CdF_2 : Eu^{2+}$ crystals. The coincidence of the radial displacements for the second anionic shell is particularly important because, in this case, the radial displacement can be determined in the experiment to the highest accuracy. The error in the experimental determination of the radial displacements of more distant anionic shells increases severalfold and even exceeds the displacements themselves in the $CdF_2 : Eu^{2+}$ crystal (Table 2). For this reason, the experimental data should be used with care.

The calculations demonstrated that the distance between the Gd^{3+} impurity ion and the F^- ligand in the $CdF_2 : Gd^{3+}$ crystal is 3.4 pm shorter than the Me^{2+}–F^- distance in the pure lattice, whereas the distance between the Eu^{2+} impurity ion and the F^- ligand in the $CdF_2 : Eu^{2+}$ crystal is 20.6 pm longer than the Me^{2+}–F^- distance in the pure lattice. Our results for the $CdF_2 : Eu^{2+}$ crystal are in agreement with the empirical calculations performed by Baker [15], according to which the distance between the Eu^{2+} impurity ion and the F^- ligand is 12.6 pm longer than the corresponding distance in the pure lattice. As follows from our calculations, the incorporation of the Eu^{2+} impurity ion brings about a considerable expansion of the crystal lattice. However, the lattice distortions rapidly decay and, already in the fourth coordination shell, decrease by one order of magnitude. This behavior of the lattice distortions is consistent with the concept that the lattice ion is isovalently replaced by a larger sized impurity ion (R_{Cd} = 1.10 Å, R_{Eu} = 1.25 Å [16]). The lattice distortions in the vicinity of the Gd^{3+} impurity ion exhibit an oscillatory behavior and decrease more slowly than those in the vicinity of the Eu^{2+} impurity ion. This can be explained by the fact that the excess charge of the impurity ion affects the cationic and anionic coordination shells in different ways. The calculated angular coordinates of the lattice ions in the vicinity of the Gd^{3+} and Eu^{2+} impurity ions in the CdF_2 crystal are listed in Table 3. The angular displacements decrease drastically. In particular, the angular displacements in the fifth and sixth coordination shells are one order of magnitude smaller than those in the third coordination shell and are almost completely absent in the seventh coordination shell. In the CdF_2 crystal, the angular coordinates decrease in the vicinity of the Eu^{2+} impurity center and increase in the vicinity of the Gd^{3+} center (except for the sixth coordination shell formed by cations).

Table 2. Radial displacements of ions in the vicinity of the Gd^{3+} and Eu^{2+} impurity centers in the CdF_2 crystal (in fractions of the lattice constant calculated or determined in the experiment)

Orbit number (ion type)		$CdF_2 : Gd^{3+}$	$CdF_2 : Eu^{2+}$
1	Calculation	0.0062	−0.040
(F)	Experiment	–	–
2	Calculation	−0.0097	−0.013
(Cd)	Experiment	–	–
3	Calculation	0.0034	−0.0061
(F)	Experiment	0.0032(7)	−0.0067(20)
4	Calculation	−0.00096	−0.0040
(Cd)	Experiment	–	–
5	Calculation	−0.0011	−0.0038
(F)	Experiment	0.0028(20)	−0.0017(50)
6	Calculation	−0.0026	−0.0015
(Cd)	Experiment	–	–
7	Calculation	0.0012	0.00049
(F)	Experiment	0.00085(39)	−0.0020(102)
8	Calculation	0.0018	−0.0035
(F)	Experiment		
9	Calculation	−0.0032	−0.0022
(Cd)	Experiment		–

Note: Numbers in parentheses denote the error in units of the last decimal place. The positive sign corresponds to a displacement toward the impurity ion (lattice contraction). The experimental data for the $CdF_2 : Gd^{3+}$ and $CdF_2 : Eu^{2+}$ crystals are taken from [5] and [4], respectively.

Table 3. Changes in the angular coordinates of ions (in degrees) in the vicinity of the Gd^{3+} and Eu^{2+} impurity centers in the CdF_2 crystal (the positive sign corresponds to an increase in the angle)

Pure crystal	Orbit number			
	3	5	6	8
	25.24	76.74	35.26	15.79
$CdF_2 : Gd^{3+}$ (calculation)	0.20	0.01	−0.02	0.00
$CdF_2 : Eu^{2+}$ (calculation)	−0.22	−0.02	−0.06	0.00

4. LOCAL COMPRESSIBILITY OF THE CRYSTAL LATTICE IN THE VICINITY OF IMPURITY IONS

Studying the local elastic properties of a crystal lattice in the vicinity of an impurity ion is of particular interest, because information on the local compressibil-

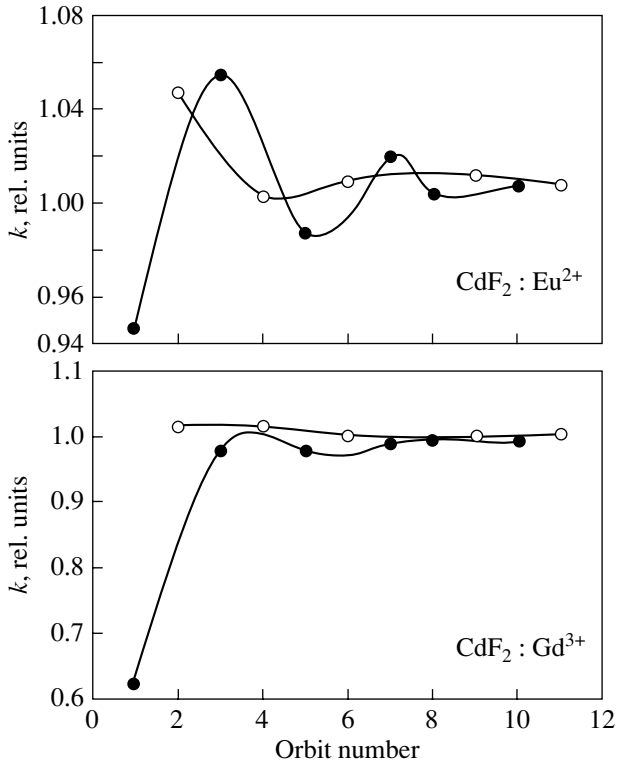

Fig. 2. Volume compressibilities of the orbits in the vicinity of the Gd^{3+} and Eu^{2+} impurity ions in the CdF_2 crystal. Closed and open circles correspond to the orbits of anions and cations, respectively. The compressibilities are given in fractions of the volume compressibility of a pure CdF_2 crystal.

ity of the studied crystal can be used to interpret the results of piezospectroscopic experiments and to determine the distance between an impurity ion and the F^- ligand from the experimental dependence db_4/dP of the crystal field parameter b_4 on the external hydrostatic pressure [15].

For cubic symmetry, the local compressibility of the crystal can be determined as follows. All ions of a particular orbit are arranged on the same spherical surface. Under compression of the crystal, the volume of the sphere decreases. In this case, we deal with a decrease in the volume of this sphere under pressure and introduce the local compressibility for the given orbit:

$$k_i = -\frac{1}{V_i(0)}\frac{V_i(P) - V_i(0)}{P}, \qquad (5)$$

where V_i is the volume of the sphere and P is the pressure. Since $V_i \sim r_i^3$ (where r_i is the distance to the ions of the orbit), we have

$$k_i = -\frac{1}{r_i^3(0)}\frac{r_i^3(P) - r_i^3(0)}{P}. \qquad (6)$$

By calculating the distortions of the crystal lattice in the vicinity of an impurity ion under hydrostatic pressure, we can determine the local compressibility k_i for each orbit. The effect of pressure on the doped crystal was taken into account through the lattice constant calculated for the pure crystal as a function of the hydrostatic pressure. The dependence of the lattice constant on the external hydrostatic pressure was obtained by minimizing the Gibbs thermodynamic potential at zero temperature:

$$G = E + PV, \qquad (7)$$

where E is the static energy (1) of the crystal, P is the hydrostatic pressure, and V is the volume of the crystal.

The local distortions of the crystal structure of the Eu^{2+} and Gd^{3+} impurity centers were calculated at external hydrostatic pressures of 1, 2, and 3 GPa. The local compressibility k_i was determined for each orbit. It was found that the local compressibilities calculated at different pressures differ insignificantly. The mean local compressibilities expressed in fractions of the volume compressibility of the pure CdF_2 crystal are presented in Fig. 2. According to our calculations, the local compressibility of the anionic sublattice considerably decreases (by more than 30%) in the vicinity of the Gd^{3+} impurity ion, whereas the local compressibility of the cationic sublattice remains approximately equal to that of the pure crystal (its value increases by no more than 2%). The results obtained suggest a higher mobility of the anionic sublattice. This type of behavior is characteristic of fluorites. In the vicinity of the Eu^{2+} impurity ion, the local compressibility of the anionic sublattice also decreases, whereas the local compressibility of the cationic sublattice increases; however, these changes are close in magnitude and do not exceed 5–6%. Therefore, we can conclude that the incorporation of an Eu^{2+} impurity ion into a CdF_2 crystal only slightly affects the local compressibility of the crystal lattice.

The results of our calculations indicate that, upon incorporation of an impurity ion into the host lattice, the nearest environment of the Eu^{2+} impurity ion (8 F^- ions) expands, whereas the nearest environment of the Gd^{3+} impurity ion undergoes contraction (Table 2). In order to elucidate how the excess charge affects the lattice distortions, we calculated the local distortions in the vicinity of the gadolinium impurity ion for the same potentials of the short-range interaction but with an ion charge of +2 instead of +3. These calculations demonstrated that the short-range interaction of gadolinium impurity ions, like the short-range interaction of europium impurity ions, brings about an expansion of the crystal lattice. This result is consistent with the fact that Eu^{2+} and Gd^{3+} ions have the same electron configuration. The excess positive charge induces an additional Coulomb interaction, which, in turn, affects the orbits of cations and anions in different ways. Accord-

ing to the calculation, this leads to a contraction of the nearest environment of the Gd^{3+} impurity ion.

Moreover, we calculated the energy of the crystal lattice under compression and extension of the nearest environment of the Cd^{2+} cation, which is replaced by a rare-earth ion in the doped crystal. It was found that the increase in the energy of the crystal lattice under compression of the nearest environment of the Cd^{2+} cation is greater than the increase in the lattice energy under extension. This is in agreement with the fact that the decrease in the local compressibility of the anionic sublattice in the vicinity of the gadolinium impurity ion, whose incorporation into the host lattice is attended by a contraction of its own nearest environment, substantially exceeds the decrease in the local compressibility of the anionic sublattice in the vicinity of the europium impurity ion; consequently, the crystal lattice undergoes expansion in the region of the nearest environment of the europium ion (Fig. 2).

5. CONCLUSIONS

Thus, the shell model used in our calculations adequately describes the local structure of Gd^{3+} and Eu^{2+} impurity centers in a CdF_2 crystal. The local compressibility of the crystal lattice of cadmium fluoride was calculated in the vicinity of the Gd^{3+} and Eu^{2+} impurity ions. This calculation predicted an insignificant change in the compressibility of the cationic and anionic sublattices upon isovalent substitution of an Eu^{2+} impurity ion for a lattice cation and a considerable decrease in the compressibility of the anionic sublattice in the vicinity of a Gd^{3+} impurity ion with excess positive charge. The results obtained can be used in further investigations of the local dynamics of Gd^{3+} and Eu^{2+} impurity ions in cadmium fluoride and in studying excitons localized near the impurity ions.

ACKNOWLEDGMENTS

This work was supported by the US Civilian Research and Development Foundation for the Independent States of the Former Soviet Union (CRDF), grant no. REC 005.

REFERENCES

1. M. Kobayashi, M. Isshi, B. P. Sobolev, Z. I. Zhmurova, and E. A. Krivandina, in *Solid-State Detectors of Ionizing Radiation* (Ural. Gos. Tekh. Univ., Yekaterinburg, 1997), p. 197 [in Russian].
2. A. A. Kozlov, B. M. Shapiro, L. V. Viktorov, V. L. Petrov, and S. I. Gorkunova, in *Scintillators and Their Application* (Ural. Gos. Tekh. Univ., Yekaterinburg, 1996), p. 23 [in Russian].
3. C. S. Yoo, H. B. Radousky, N. C. Holmes, and N. M. Edelstein, Phys. Rev. B **44** (2), 830 (1991).
4. R. H. Borcherts, T. Cole, and T. Horn, J. Chem. Phys. **49** (11), 4880 (1968).
5. R. Valentin, Phys. Lett. A **30** (6), 344 (1969).
6. A. E. Nikiforov and S. Yu. Shashkin, *Spectroscopy of Crystals* (Nauka, Leningrad, 1989), p. 274 [in Russian].
7. E. Clementi and C. Roetti, At. Data Nucl. Data Tables **14** (3–4), 177 (1974).
8. A. D. McLean and R. S. McLean, At. Data Nucl. Data Tables **26** (3–4), 197 (1981).
9. D. O. Pederson and J. A. Brewer, Phys. Rev. B **16** (10), 4546 (1977).
10. D. R. Bosomworth, Phys. Rev. **157** (3), 709 (1967).
11. P. Denham, G. R. Field, and P. L. R. Morse, Proc. R. Soc. London, Ser. A **317**, 55 (1970).
12. J. M. Baker and L. J. C. Bluck, J. Phys.: Condens. Matter **2** (21), 7537 (1990).
13. V. A. Chernyshev, A. D. Gorlov, A. A. Mekhonoshin, A. E. Nikiforov, A. I. Rokeakh, S. Yu. Shashkin, and A. Yu. Zaharov, Appl. Magn. Reson. **14** (1), 37 (1998).
14. Yu. A. Izyumov and V. N. Syromyatnikov, *Phase Transitions and Crystal Symmetry* (Nauka, Moscow, 1984), p. 248 [in Russian].
15. J. M. Baker, J. Phys. C **12**, 4039 (1979).
16. R. D. Shannon, Acta Crystallogr. A **32**, 751 (1976).

Translated by O. Borovik-Romanova

Physics of the Solid State, Vol. 46, No. 9, 2004, pp. 1644–1648. Translated from Fizika Tverdogo Tela, Vol. 46, No. 9, 2004, pp. 1593–1598.
Original Russian Text Copyright © 2004 by Kolesnikova, Romanov.

DEFECTS, DISLOCATIONS, AND PHYSICS OF STRENGTH

Generation of Dislocation Loops in Strained Quantum Dots Embedded in a Heterolayer

A. L. Kolesnikova* and A. E. Romanov**

** Institute for Problems of Mechanical Engineering, Russian Academy of Sciences, Bol'shoĭ pr. 61, Vasil'evskiĭ Ostrov, St. Petersburg, 199178 Russia*

*** Ioffe Physicotechnical Institute, Russian Academy of Sciences, Politekhnicheskaya ul. 26, St. Petersburg, 194021 Russia*

e-mail: aer@mail.ioffe.ru

Received February 5, 2004

Abstract—The generation of prismatic dislocation loops in strained quantum dots is investigated. The quantum dots are embedded in a film–substrate heterostructure with mechanical stresses caused by the difference between the lattice parameters of the film (heterolayer) and the substrate. The intrinsic plastic strain ε_m of a quantum dot arises from the misfit between the lattice parameters of the materials of the quantum dot and the surrounding matrix. The interface between the heterolayer and the substrate is characterized by a misfit parameter f. The critical radius of a quantum dot R_c at which the generation of a dislocation loop in the quantum dot becomes energetically favorable is analyzed as a function of the intrinsic plastic strain ε_m and the misfit parameter f. *© 2004 MAIK "Nauka/Interperiodica".*

1. INTRODUCTION

Investigation of the heterostructures containing quantum dots and quantum wires is of considerable interest. Elastic strains of semiconductor heterostructures substantially affect their electronic and optoelectronic properties [1–3]. The lattice parameters of the materials of quantum dots and quantum wires, as a rule, differ from those of the surrounding matrix. Owing to this circumstance, quantum dots (quantum wires) can be simulated by inclusions with an intrinsic plastic strain ε_m caused by the misfit between the lattice parameters. The energy of elastic strains introduced by such inclusions is proportional to their volume [4] and hypothetically can reach infinitely large values. It is obvious that there exist mechanisms that provide dissipation of the elastic energy by these inclusions. Particular interest has been expressed by researchers in the mechanisms associated with the following processes: (i) the generation of a prismatic misfit dislocation loop at the interface between an inclusion and the surrounding matrix [5], as is the case with the generation of dislocations at the interface between the film and the substrate (see, for example, [6, 7]), and (ii) the ejection of a prismatic dislocation loop from an inclusion into the surrounding matrix [8–10]. Since an elastically strained film in contact with a substrate is a typical heterostructure, it is necessary to analyze the above mechanisms providing dissipation of the elastic energy by quantum dots embedded in the heterostructure.

In this work, we determined the conditions of generation of prismatic misfit dislocation loops in quantum dots and analyzed how the lattice misfit between the film and the substrate affects the dependence of the critical radius of a quantum dot (at which the generation of a dislocation loop becomes energetically favorable) on the intrinsic plastic strain of this inclusion. This study continues our investigation of the problem concerning the generation of a misfit dislocation loop at the interface between an inclusion and an unstrained surrounding matrix [5].

Among the studies devoted to similar problems with quantum wires, mention should be made of the works concerned with the generation of misfit dislocations aligned parallel to the axis of a quantum wire with a triangular, circular, or rectangular cross section [11–13]. In particular, Gutkin *et al.* [13] considered the generation of a rectangular dislocation loop in a quantum wire near a free surface. Special interest has also been expressed in the related problems regarding the generation of misfit dislocations at the interface between a film and a substrate in spherical [14] and cylindrical [15] solids. A number of models describing the generation of misfit dislocations in strained islands located in a substrate were proposed in [16–18].

2. THEORETICAL ANALYSIS

In our case, a spheroidal inclusion of radius R_{sp} simulates a quantum dot embedded in a film–substrate heterostructure (Fig. 1). The lattice parameter of the film a_{film} differs from the lattice parameter of the substrate a_{sub}. This difference is characterized by the misfit parameter $f = (a_{sub} - a_{film})/a_{film}$ and gives rise to mechanical stresses in the heterostructure. Under the assump-

tion that the substrate is semi-infinite and the film has a finite thickness t, the stresses are constant and arise only in the film:

$$\sigma_{xx}^{\text{misf}} = \sigma_{yy}^{\text{misf}} = \frac{2G(1+\nu)f}{(1-\nu)}, \quad 0 \le z \le t. \qquad (1)$$

We consider the generation of a prismatic misfit dislocation loop in an inclusion located well away from a free surface. This assumption substantially simplifies the calculation and analysis of the influence of the strained film on the generation of a prismatic dislocation loop at the interface between the inclusion and the surrounding matrix. The free surface has a profound effect on both the elastic fields and the energies of the inclusion and dislocation loop and, consequently, on the relaxation processes occurring in the inclusion, provided this defect is located in the surface layer with a thickness of the order of the defect radius. This influence of the free surface will be taken into account in a more detailed analysis.

For a spheroidal inclusion, the plastic distortion β_{ij}^* caused by the misfit between the lattice parameters of the materials of the spheroid a_{sp} and the film a_{film} can be represented by the relationship

$$\beta_{xx}^* = \beta_{yy}^* = \beta_{zz}^* = \varepsilon_m \delta(\Omega_{\text{sp}}), \qquad (2)$$

where $\varepsilon_m = (a_{\text{sp}} - a_{\text{film}})/a_{\text{film}}$ and $\delta(\Omega_{\text{sp}})$ is the Dirac delta function for a region Ω_{sp} occupied by the spheroid. The Dirac delta function is defined by the following expression:

$$\delta(\Omega_{\text{sp}}) = \begin{cases} 1, & \mathbf{r} \in \Omega_{\text{sp}} \\ 0, & \mathbf{r} \notin \Omega_{\text{sp}}. \end{cases}$$

The sign of the parameter ε_m corresponds to the character of dilatation: $\varepsilon_m > 0$ for expansion and $\varepsilon_m < 0$ for compression.

The stresses ${}^{\infty}\sigma_{ij}$ inside a spherical inclusion located in an infinite medium have the form [4]

$$\sigma_{xx}^{(\text{in})} = \sigma_{yy}^{(\text{in})} = \sigma_{zz}^{(\text{in})} = -\frac{4G\varepsilon_m(1+\nu)}{3(1-\nu)}, \qquad (3)$$

where G is the shear modulus and ν is the Poisson ratio.

The condition of generating a dislocation loop at the surface of the inclusion can be represented by the inequality

$$E_{\text{loop}} + W_{\text{sp–loop}} + W_{\text{loop–film}} \le 0, \qquad (4)$$

where E_{loop} is the elastic energy of the prismatic dislocation loop, $W_{\text{sp–loop}}$ is the energy of the elastic interaction between the spheroid and the dislocation loop, and $W_{\text{loop–film}}$ is the energy of the elastic interaction between the dislocation loop and the field of stresses in the film.

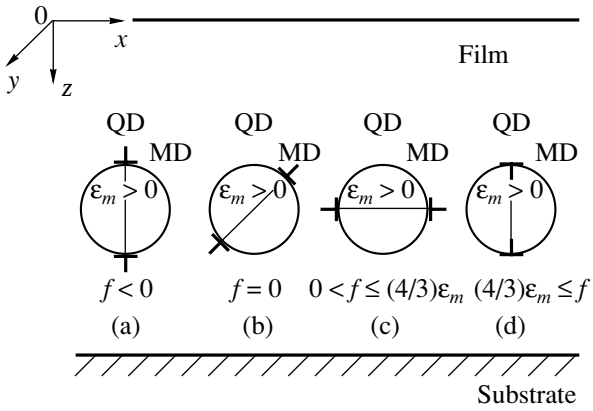

Fig. 1. Schematic diagram illustrating (*a–d*) the orientations and types of a prismatic misfit dislocation loop (MD) in a quantum dot (QD) embedded in a heterolayer. Designations: ε_m is the intrinsic plastic dilatation of the quantum dot, and f is the misfit parameter of the crystal lattices of the film and the substrate.

The elastic energy of a circular prismatic dislocation loop has the form [9]

$$E_{\text{loop}} = \frac{Gb^2 r_{\text{loop}}}{2(1-\nu)}\left(\ln\frac{8r_{\text{loop}}}{r_{\text{core}}} - 2\right). \qquad (5)$$

Here, b is the magnitude of the Burgers vector of the dislocation loop, r_{loop} is the radius of the dislocation loop, and r_{core} is the radius of the dislocation core. In relationship (5), the energy of the dislocation core can be included by putting $r_{\text{core}} = b/\alpha$ (where α is an empirical constant dependent on the material; for example, for nonmetals, $\alpha = 4$) [20]:

$$E_{\text{loop}} = \frac{Gb^2 r_{\text{loop}}}{2(1-\nu)}\ln\left(\frac{1.08\alpha r_{\text{loop}}}{b}\right). \qquad (6)$$

The energy of the interaction of the dislocation loop with the inclusion $W_{\text{sp–loop}}$ and the energy of the interaction of the dislocation loop with the stress field of the film $W_{\text{loop–film}}$ are determined as the work expended on generating a dislocation loop in the stress fields of the inclusion and the film, respectively. Let us now consider a situation where a vacancy prismatic dislocation loop is generated at the boundary of an inclusion with an intrinsic plastic strain $\varepsilon_m > 0$. This generation is energetically favorable [see condition (4)] when the misfit parameter f takes on negative or small positive values:

$$W_{\text{sp–loop}} = -\int_{V_{\text{loop}}} \beta_{ij}^{*\text{loop}} \sigma_{ij}^{(\text{in})} dV = -\int_{S_{\text{loop}}} (-b)\sigma_{jj}^{(\text{in})} dS = -\frac{4\pi G(1+\nu)\varepsilon_m}{3(1-\nu)} b r_{\text{loop}}^2, \qquad (7)$$

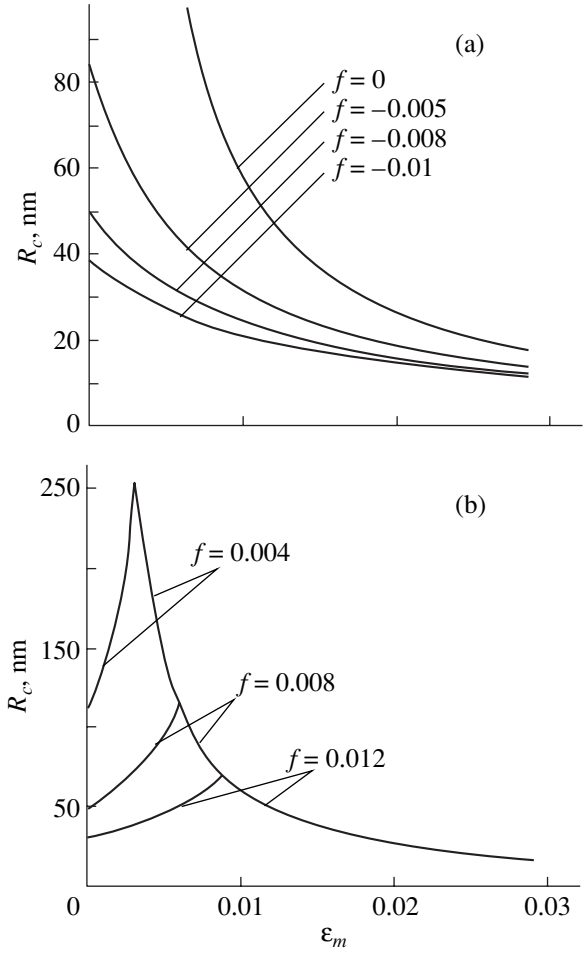

Fig. 2. Dependences of the critical radius of the quantum dot R_c on the intrinsic plastic dilatation ε_m at different misfit parameters f for the Burgers vector of the dislocation loop b = 0.3 nm, the constant characterizing the contribution from the energy of the dislocation core $\alpha = 4$, and the Poisson ratio $\nu = 0.3$.

$$W_{\text{loop–film}} = -\int_{V_{\text{loop}}} \beta_{ij}^{*\text{loop}} \sigma_{ij}^{\text{misf}} dV$$

$$= \begin{cases} 0, \quad \beta_{zz}^{*\text{loop}} = -b\delta(z - z_0)H(1 - \gamma_1), & (8) \\ +\dfrac{2\pi G b(1+\nu) f}{(1-\nu)} b r_{\text{loop}}^2, & \\ \beta_{xx}^{*\text{loop}} = -b\delta(x - x_0)H(1 - \gamma_2). & (9) \end{cases}$$

Here, $\delta(z - z_0)$ and $\delta(x - x_0)$ are the Dirac delta functions, $H(1 - \gamma_1)$ and $H(1 - \gamma_2)$ are the Heaviside functions, $\gamma_1 = \sqrt{(x - x_0)^2 + (y - y_0)^2}/r_{\text{loop}}$, $\gamma_2 = \sqrt{(z - z_0)^2 + (y - y_0)^2}/r_{\text{loop}}$, and (x_0, y_0, z_0) are the coordinates of the center of the dislocation loop.

It should be noted that the radius of the nucleated dislocation loop is equal to the radius of the inclusion: $r_{\text{loop}} = R_{\text{sp}}$. The energy of the interaction between the dislocation loop and the field of stresses in the film is analyzed in two cases: (a) the plane of the dislocation loop is aligned parallel to the plane of the boundary between the film and the substrate (the interface plane) [see expression (8)], and (b) the plane of the dislocation loop is perpendicular to the interface plane [see expression (9)] (Fig. 1).

From expressions (4) and (6)–(9) and the equality $r_{\text{loop}} = R_{\text{sp}}$, we obtain the following equation for the critical radius of the inclusion R_c at which the generation of a prismatic misfit dislocation loop is energetically favorable:

$$R_c = \frac{3b}{4\pi(1+\nu)(2\varepsilon_m - 3f^*)} \ln\left(\frac{1.08\alpha R_c}{b}\right). \quad (10)$$

Here, $f^* = 0$ for a dislocation loop plane aligned parallel to the interface plane and $f^* = f$ for a dislocation loop plane oriented perpendicular to the interface plane. It follows from relationship (10) that the generation of a misfit dislocation loop perpendicular to the interface plane is energetically favorable at $f < 0$. In this case, the fields of stresses in the film (at $f < 0$, these stresses are compressive) are favorable for the formation of a local inhomogeneity in the form of a misfit dislocation loop at the boundary of the inclusion (at $\varepsilon_m > 0$, the stresses inside the inclusion are also compressive). An inclusion located in this film takes a misfit dislocation loop with smaller radii in comparison with an inclusion located in the unstrained matrix ($f = 0$) (Fig. 2a). It should be noted that, in the framework of the elastic continuous model, when no stresses are induced in the film ($f = 0$), the misfit dislocation loop involved in an inclusion can be arbitrarily oriented in space. The situation with a misfit parameter $f > 0$ is of particular interest. According to relationship (10), the only possibility exists of locating a dislocation loop parallel to the interface plane ($f^* = 0$). However, for sufficiently large positive stresses in the film, the generation of an interstitial dislocation loop is energetically more favorable, because it is this interstitial dislocation loop that decreases the total elastic energy of the system [see condition (4)]. In this case, the equation for the critical radius of the inclusion takes the form

$$R_c = \frac{3b}{4\pi(1+\nu)(3f - 2\varepsilon_m)} \ln\left(\frac{1.08\alpha R_c}{b}\right). \quad (11)$$

The criterion for the generation of an interstitial dislocation loop is determined as $3f > 4\varepsilon_m$ ($\varepsilon_m > 0$).

3. RESULTS AND DISCUSSION

The above analysis revealed the following variants of the formation of a misfit dislocation loop in an inclu-

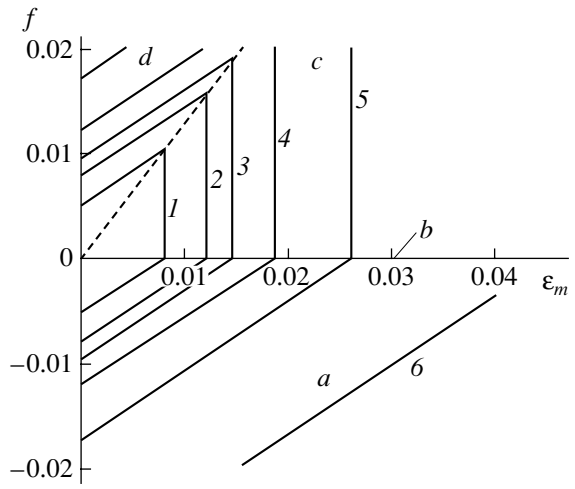

Fig. 3. Isolines of the critical radius of the inclusion R_c as a function of the intrinsic plastic dilatation ε_m and the misfit parameter f for the Burgers vector of the dislocation loop b = 0.3 nm, the constant characterizing the contribution from the energy of the dislocation core α = 4, and the Poisson ratio ν = 0.3. R_c, nm: (*1*) 80, (*2*) 50, (*3*) 40, (*4*) 30, (*5*) 20, and (*6*) 10. Regions *a*–*d* correspond to the orientations of the misfit dislocation loop depicted in Fig. 1.

sion with an intrinsic plastic dilatation $\varepsilon_m > 0$ in a film deposited on a substrate.

(1) For a negative parameter of the lattice misfit between the film and the substrate ($f < 0$), a vacancy prismatic dislocation loop is formed in the inclusion in a plane perpendicular to the interface (Fig. 1a). The critical radius of the inclusion is determined from condition (10) (Fig. 2a).

(2) For $f = 0$, a vacancy prismatic dislocation loop is formed in the inclusion in a plane arbitrarily oriented in space (Fig. 1b). The critical radius of the inclusion is also determined from condition (10) (Fig. 2a).

(3) For $0 < f < 4/3\varepsilon_m$, a vacancy prismatic dislocation loop is formed in the inclusion in a plane aligned parallel to the interface (Fig. 1c). The critical radius of the inclusion is determined from the condition

$$R_c = \frac{3b}{8\pi(1+\nu)\varepsilon_m}\ln\left(\frac{1.08\alpha R_c}{b}\right). \qquad (12)$$

The dependence $R_c(\varepsilon_m)$ is depicted by the curve at $f = 0$ in Fig. 2a.

(4) For $f = 4/3\varepsilon_m$, there can exist two variants: either a vacancy prismatic dislocation loop is formed in the inclusion in a plane parallel to the interface (Fig. 1c), or an interstitial prismatic dislocation loop is formed in the inclusion in a plane perpendicular to the interface (Fig. 1d). The critical radius of the inclusion is determined from condition (12) (Fig. 2a).

(5) For $f > 4/3\varepsilon_m$, an interstitial prismatic dislocation loop is formed in the inclusion in a plane perpendicular to the interface (Fig. 1d). The critical radius of the inclusion is determined from condition (11) (Fig. 2b).

Figure 3 presents the isolines of the critical radius in the ε_m–f coordinates. The regions *a*–*d* correspond to the positions of the misfit dislocation loop in Fig. 1.

The analysis of the generation of a misfit dislocation loop for inclusions with an intrinsic plastic dilatation $\varepsilon_m < 0$ is similar to that presented above and leads to a mirrored result.

4. CONCLUSIONS

The theoretical analysis performed in this work allowed us to conclude that the stresses induced in the film due to the lattice misfit between the film and the substrate have a noticeable effect not only on the critical radius of the quantum dot (at which the generation of a misfit dislocation loop is energetically favorable) but also on the orientation of the dislocation loop with respect to the interface and on the dislocation loop type (a vacancy dislocation loop or an interstitial dislocation loop).

ACKNOWLEDGMENTS

This work was performed in the framework of the program of the Russian Ministry of Industry “Physics of Solid-State Nanostructures.”

REFERENCES

1. A. D. Andreev and E. P. O’Reilly, Phys. Rev. B **62**, 15851 (2000).
2. P. Waltereit, A. E. Romanov, and J. S. Speck, Appl. Phys. Lett. **81**, 4754 (2002).
3. N. Usami, T. Ichitsubo, T. Ujihara, T. Takanashi, K. Fujiwara, G. Sazaki, and K. Nakajima, J. Appl. Phys. **94**, 916 (2003).
4. T. Mura, *Mircomechanics of Defects in Solids* (Martinus Nijhoff, Boston, 1987).
5. A. L. Kolesnikova and A. E. Romanov, Pis’ma Zh. Tekh. Fiz. **30**, 89 (2004) [Tech. Phys. Lett. **30**, 126 (2004)].
6. V. I. Vladimirov, M. Yu. Gutkin, and A. E. Romanov, Fiz. Tverd. Tela (Leningrad) **29**, 2750 (1987) [Sov. Phys. Solid State **29**, 1581 (1987)].
7. R. Beanland, D. J. Dunstan, and P. J. Goodhew, Adv. Phys. **45**, 87 (1996).
8. N. D. Zakharov, V. N. Rozhanskiĭ, and R. L. Korchazhkina, Fiz. Tverd. Tela (Leningrad) **16**, 1444 (1974) [Sov. Phys. Solid State **16**, 926 (1974)].
9. V. V. Chaldyshev, N. A. Bert, A. E. Romanov, A. A. Suvorova, A. L. Kolesnikova, V. V. Preobrazhenskii, M. A. Putyato, B. R. Semyagin, P. Werner, N. D. Zakharov, and A. Claverie, Appl. Phys. Lett. **80**, 377 (2002).

10. N. A. Bert, A. L. Kolesnikova, A. E. Romanov, and V. V. Chaldyshev, Fiz. Tverd. Tela (St. Petersburg) **44** (12), 2139 (2002) [Phys. Solid State **44**, 2240 (2002)].
11. T. J. Gosling and L. B. Freund, Acta Mater. **44**, 1 (1996).
12. J. Colin and J. Grihle, Philos. Mag. Lett. **82**, 125 (2002).
13. M. Yu. Gutkin, I. A. Ovid'ko, and A. G. Sheinerman, J. Phys.: Condens. Matter **15**, 3539 (2003).
14. L. I. Trusov, M. Yu. Tanakov, V. G. Gryasnov, A. M. Kaprelov, and A. E. Romanov, J. Cryst. Growth **114**, 133 (1991).
15. M. Yu. Gutkin and A. G. Sheinerman, Phys. Status Solidi A **184**, 485 (2001).
16. E. Pehlke, N. Moll, A. Kley, and M. Scheffler, Appl. Phys. A **65**, 525 (1997).
17. K. Tillmann and A. Foster, Thin Solid Films **368**, 93 (2000).
18. I. A. Ovid'ko, Phys. Rev. Lett. **88**, 046103 (2002).
19. J. Dundurs and N. J. Salamon, J. Phys. C **50**, 125 (1972).
20. J. Hirth and J. Lothe, *Theory of Dislocations*, 2nd ed. (Wiley, New York, 1982; Atomizdat, Moscow, 1972).

Translated by O. Moskalev

Physics of the Solid State, Vol. 46, No. 9, 2004, pp. 1649–1654. Translated from Fizika Tverdogo Tela, Vol. 46, No. 9, 2004, pp. 1597–1602.
Original Russian Text Copyright © 2004 by Borisenko, Gnesin.

DEFECTS, DISLOCATIONS, AND PHYSICS OF STRENGTH

Effect of Humidity and Holding Temperature (in the Range from –13 to +60°C) on the Recrystallization and Aging of Strontium-Doped KCl Crystals after Plastic Deformation

E. B. Borisenko and B. A. Gnesin

Institute of Solid-State Physics, Russian Academy of Sciences, Chernogolovka, Moscow oblast, 142432 Russia

e-mail: borisenk@issp.ac.ru

Received January 27, 2004

Abstract—The effect of humidity and temperature in the range from –13 to + 60°C on the processes of recrystallization and aging is studied upon holding of KCl crystals doped with 0.06 wt % Sr after plastic deformation. The crystals initially consist of a supersaturated solid solution. The presence of water is found to increase the rates of nucleation and growth of grains with twinned orientations with respect to the initial single crystal. Upon aging of these crystals in the presence of water vapor, strontium chloride crystalline-hydrate $SrCl_2 \cdot 6H_2O$ forms along the boundaries of recrystallized grains and crack edges. This results not only in a decreased plastic deformation–induced increment in the hardness but also in decomposition of the crystals. It is found that varying the temperature in the range from –13 to +25°C affects the recrystallization rate and aging processes much more weakly than does the presence of excess moisture. The most stable structure and properties are observed in the case where deformed crystals that are held at temperatures from –13 to +25°C remain in a solid-solution state. The possible long-term conservation of the high hardness of deformed crystals owing to an additional postdeformation treatment is discussed. © *2004 MAIK "Nauka/Interperiodica".*

1. INTRODUCTION

In [1–7], it was found that recrystallization kinetics and aging processes in alkali halide crystals (AHCs) doped with salts of bivalent metals depend strongly on the dopant concentration, doping conditions, deformation, and high-pressure treatment. The high strength caused by plastic deformation of strontium-doped KCl single crystals was shown to be retained for more than a year; this ability is substantially determined by the ratio of the aging rate to the grain-boundary migration rate during recrystallization [4, 7]. It should be noted that the high strength of AHCs usually deteriorates in two to three months after plastic deformation.

Apart from grain growth during recrystallization, which decreases the strength, there are other factors that hinder the long-term application of AHC materials in laser optics. One of the most destructive factors is the hygroscopicity of most AHCs [8].

Moisture adsorption from the environment leads to an increase in the absorption coefficient (measured at an IR-laser wavelength λ = 10.6 μm) in the deformed surface layer of KCl crystals [9] because of the contribution of hydroxyl ions, which are often present in AHCs in a complex that contains OH^- (in the anion lattice position), a cation, and vacancies [10]. Contact with water can deteriorate not only optical but also mechanical properties, to the point of decomposition of the crystals. In this work, we consider how the water of a gas phase interacts with deformed AHCs and whether it is possible to avoid its harmful influence on the properties of these crystals or, at least, to decrease it.

We also study the effect of the temperature of postdeformation holding on the structure and properties of deformed crystals. More specifically, we analyze the effect of varying the holding temperature from +60 to –13°C on the processes of aging and grain growth and on the microhardness of strontium-doped KCl crystals.

2. EXPERIMENTAL

We used Czochralski-grown KCl single crystals for the study. The results of chemical analysis of the samples are given in [4]; they indicate that the level of each controlled impurity in them is lower than 10^{-4} wt %. For tests, we used $3 \times 3 \times 8$-mm specimens cleaved along the {100} cleavage planes. Upsetting deformation was performed on an Instron machine at a rate of 0.1 mm/min to 70% reduction at 250°C; then, the specimens were furnace-cooled to room temperature. Pole figures (PFs) and diffuse scattering patterns were recorded by the techniques described in [3, 4]. Pole figures were recorded according to the Schulz method with a computer-assisted texture diffractometer at a maximum tilt angle of 65°. Diffuse scattering patterns

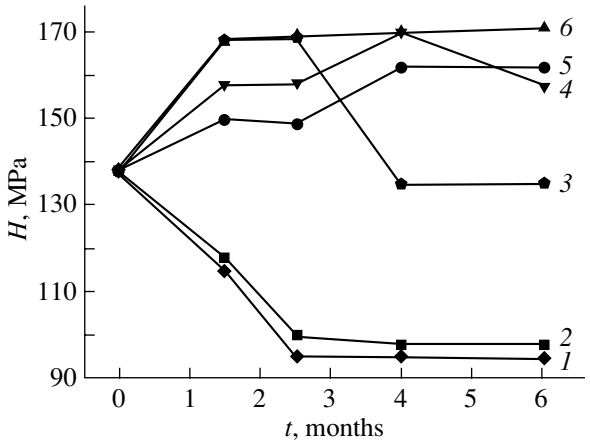

Fig. 1. Dependence of the microhardness on the holding time at various temperatures and humidity: (*1*) $T = -13°C$, high humidity; (2) $T = +20°C$, high humidity; (*3*) $T = +20°C$, normal humidity (relative air humidity 50%); (*4*) annealing at $T = +60°C$ for 30 min followed by storage at $T = +20°C$ under normal humidity; (*5*) holding at $T = -13°C$ in an ampoule at a pressure $P = 10^{-2}$ mbar for two months followed by storage at $T = +20°C$ under normal humidity; and (*6*) storage at $T = +20°C$, $P = 10^{-2}$ mbar for two months followed by storage at $T = +20°C$ under normal humidity.

and PFs were recorded under the same conditions, with the sole exception that, in the former case, the counter was rotated 1°–2° with respect to the exact position of the diffraction peak. X-ray diffraction patterns of the specimens were recorded using the technique designed for phase analysis of lightly doped single crystals [7]. The main difference between this technique and the standard one is that the x-ray diffraction patterns are recorded at different positions of a sample with respect to the diffraction vector (the sample surface is not normal to the diffraction vector). Phases were identified using several lines recorded at different orientations of the sample, provided that the position of the line deviated from the tabulated position by less than 0.4° and that the line intensity met the criterion $(I_{max} - I_{back}) \geq 3(I_{back})^{1/2}$, where I_{max} is the line maximum and I_{back} is the local background. To hold specimens in vacuum, they were placed in quartz ampoules and the ampoules were pumped out with a roughing pump to a pressure of 10^{-2} mbar and then sealed. To create an atmosphere of saturated water vapor, specimens were placed in a tightly sealed vessel near a glass of water at a temperature of +25°C or in a closed chamber with ice at –13°C. The fraction of recrystallized grains and their sizes were measured using standard metallographic techniques [3, 4].

3. RESULTS AND DISCUSSION

Before analyzing the time dependence of the microhardness under various conditions of postdeformation holding, we note that the microhardness of as-grown single crystals and of single crystals after deformation strongly depends on the cooling rate of the deformed specimens. This behavior is related to the different states of impurities depending on the heat treatment conditions [11]. After growing and air quenching, the hardness of KCl : 0.06 wt % Sr crystals is 173 MPa and subsequent storage of the single crystals at room temperature does not change this value. If a single crystal is furnace-cooled after annealing at 250°C, its hardness decreases to 130 MPa. If a single crystal of this chemical composition is then deformed and air-quenched, its hardness increases to 193 MPa [13]. If single crystals of this chemical composition are deformed and furnace-cooled without exposure to air, their hardness is slightly higher than that of the single crystal annealed at 250°C (Fig. 1). All the specimens studied in this work are deformed at 250°C and then furnace-cooled to room temperature.

Figure 1 shows the variation of the microhardness of deformed specimens upon subsequent holding at various temperatures and humidity. It is seen that, under the conditions of reduced humidity (the as-deformed crystal was placed in an ampoule pumped out to a pressure of 10^{-2} mbar), the microhardness of the specimens increases during postdeformation holding. Increasing the temperature from –13 to +25°C has an effect on the microhardness: the microhardness of the single crystals held at +25°C is found to be about 5% higher. The microhardness of the crystals that are annealed at $T = +60°C$ for half an hour after deformation and then exposed to air at +25°C also increases with the holding time. In the crystals held at room temperature under the conditions of only atmospheric moisture without additional treatments, the increase in the microhardness is not as stable: the microhardness increases to about 170 MPa then, decreases after a 2.5-month holding and reaches the values characteristic of the initial single crystals with the same strontium content in the next 1.5-month holding. When the crystals are held under the conditions of high air humidity at temperatures from +25 to –13°C, the microhardness begins to decrease noticeably even in the first days of postdeformation holding and decreases down to the value characteristic of a pure KCl single crystal in four months. It should be noted that the microhardness of reference undeformed single-crystal specimens having the same strontium content does not change at these temperatures during holding either in air, vacuum, or under high humidity. Thus, the experimental data indicate that the effect of moisture on the microhardness of deformed strontium-containing potassium chloride single crystals is stronger than that of the temperature varying in a wide temperature range (from –13 to +60°C). The lower the humidity, the higher the hardness and the longer the time over which the hardness is at a higher level (this level is 30% higher than the hardness of the as-deformed crystals; see Fig. 1). In our previous studies, we used a specific technique for taking x-ray dif-

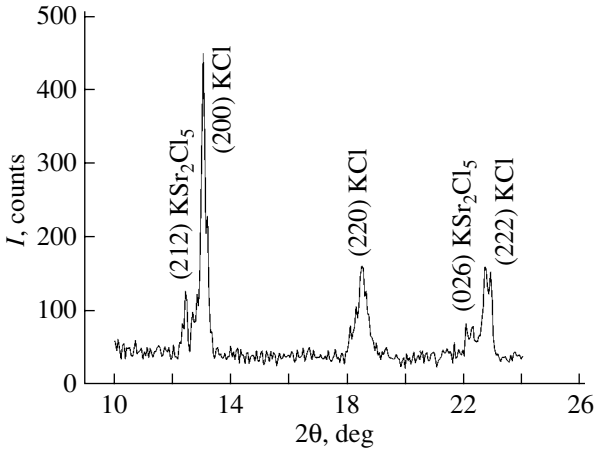

Fig. 2. X-ray diffraction pattern of a KCl : 0.06 wt % Sr crystal taken after 70% plastic deformation at T = 250°C and subsequent holding at T = +3°C for six months.

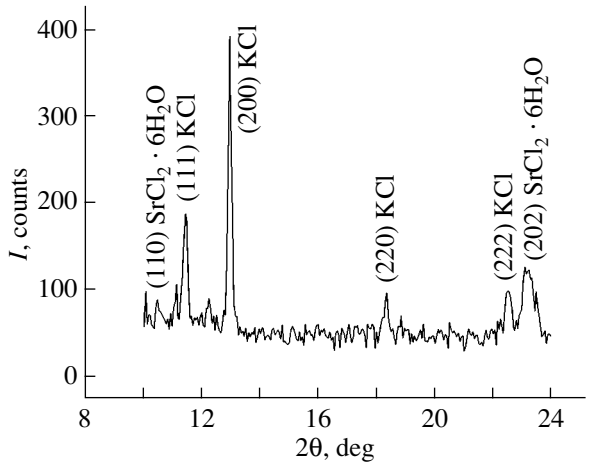

Fig. 3. X-ray diffraction pattern of a KCl : 0.06 wt % Sr crystal taken after 70% plastic deformation at T = 250°C and subsequent holding at T = –13°C for three months under high humidity.

fraction patterns [7] in order to track the change in the phase composition of samples after a polymorphic transformation under pressure or after plastic deformation. We found that KSr_2Cl_5 particles precipitated at room temperature in plastically deformed (at 250°C) potassium chloride samples containing 0.02–0.06 wt % Sr [4]. In this work, we also used this technique to study the effect of varying the holding temperature in the range from –13 to +25°C and of the humidity on the aging of KCl : 0.06 wt % Sr specimens after plastic deformation at 250°C followed by slow cooling in a furnace. We revealed that, upon holding of the specimens at temperatures of +3 to +25°C and normal humidity, particles of complex potassium–strontium chloride form in them; diffraction lines of this chloride appear in the x-ray diffraction patterns of the specimens after holding for 2.5–3 months (Fig. 2). Furthermore, 2–3 μm particles arranged along the boundaries of recrystallized grains become visible in polarized light in a polished section cut parallel to the (100) plane. In crystals held under the conditions of high humidity at –13 or +25°C, particles precipitate upon aging; the diffraction lines of these particles most likely belong to strontium chloride crystalline hydrate $SrCl_2 \cdot 6H_2O$ (Fig. 3). The interplanar spacings were calculated using the data from [12] on the structure and lattice parameters of this crystalline hydrate. The volume fraction of this phase, which was estimated from the condition that the amount of strontium in this phase not exceed the amount introduced in the specimen in the form of $SrCl_2$, is ≃0.25%. This value is in agreement with the measured volume fraction of the particles in the polished section, which are visible under the microscope in polarized light (≅0.22%). According to [13, 14], crystalline hydrate in the $SrCl_2$–H_2O system in the temperature range from –18 to +60°C can exist in the form of $SrCl_2 \cdot 6H_2O$ and, at temperatures from +64 to 114°C, strontium chloride crystalline hydrate has the formula $SrCl_2 \cdot 2H_2O$. The x-ray diffraction patterns of specimens held under the conditions of saturated water vapor at temperatures of –13 and +25°C contain the lines of $SrCl_2 \cdot 6H_2O$ (Fig. 3). However, upon holding under these conditions, the lines of the crystalline hydrate disappear when the holding time exceeds 12 months. Apparently, water condensate, whose amount increases with the holding time, dissolves fine crystalline-hydrate particles arranged along grain and pore boundaries. Therefore, a liquid layer of a salt solution or a layer consisting of ice and a salt solution forms at different temperatures. According to [14], the latter layer exists in the pseudobinary KCl–H_2O and KCl–$SrCl_2$ systems in the absence of solid-state solubility up to temperatures $T \cong -10.6$ and –18.7°C, respectively. There is good reason to believe that the point of the ternary eutectic is at lower temperatures. X-ray diffraction patterns of crystals placed in a vacuum after deformation (in an ampoule pumped out to a pressure of 10^{-2} mbar and then sealed) at temperatures of –13 and +25°C contain only the KCl lines. X-ray diffraction patterns of crystals subjected to postdeformation annealing at 60°C for 30–60 min and then stored at room temperature for 12 months exhibit no additional lines; weak lines, which are likely to belong to α-$SrCl_2$, are observed only after longer storage (Fig. 4). The manifestation of these lines is preceded by a 5–6% decrease in the microhardness of these specimens (Fig. 1). The x-ray diffraction data indicate that the presence of water exerts a key effect on the aging rate and phase composition of deformed KCl : 0.06 wt % Sr single crystals. As is known [15], the presence of steam can cause decomposition of solid solutions (e.g., in the system of KCl–KBr continuous solid solutions and in the NaCl–NaBr system). After being stored at room temperature for one year, nonstoichiometric crystalline

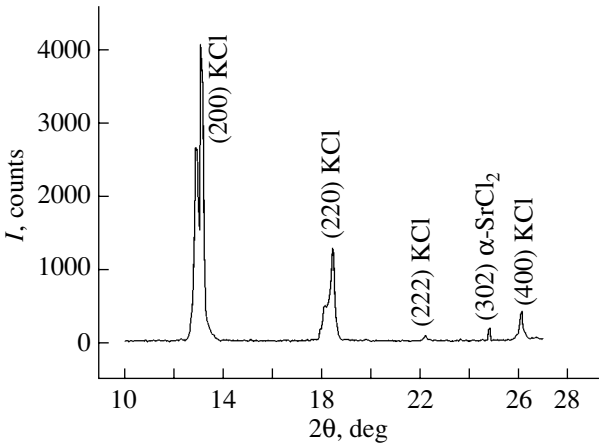

Fig. 4. X-ray diffraction pattern of a KCl : 0.06 wt % Sr crystal taken after 70% plastic deformation at $T = 250$°C, annealing at $T = +60$°C for 30 min, and storage at $T = +20$°C under normal humidity for eight months.

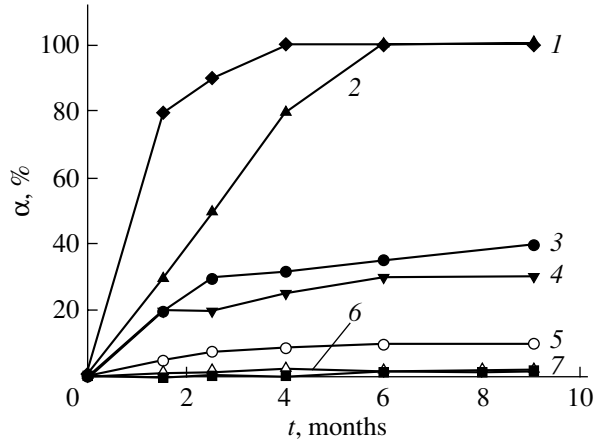

Fig. 5. Dependence of the volume fraction of the recrystallized material on the holding time: (*1*) $T = -13$°C, high humidity; (*2*) $T = +20$°C, high humidity; (*3*) $T = +20$°C, normal humidity (relative air humidity 50%); (*4*) $T = +3$°C, normal humidity; (*5*) $T = -13$°C, storage in an ampoule at a pressure $P = 10^{-2}$ mbar for two months and subsequent storage at $T = +20$°C under normal humidity; (*6*) $T = +20$°C, normal humidity (measurements are performed after annealing at $T = +60$°C for 30 min); and (*7*) $T = +20$°C, normal humidity (before measurements, the sample is stored at +20°C under a pressure $P = 10^{-2}$ mbar for two months).

hydrates form in KCl–KBr crystals (according to electron diffraction data) and stoichiometric crystalline hydrates form in the NaCl–NaBr system (according to x-ray diffraction data). In single crystals, the decomposition of the solid solution into potassium or sodium salts and crystalline hydrate occurs in a near-surface layer less than 0.04 μm thick that contains sorbed water [15]. When the deformed single crystals studied in this work are stored, the presence of subgrain and recrystallized-grain boundaries stimulates the penetration of water from the surface into the bulk and its chemical interaction with the strontium-containing KCl crystal throughout the entire volume. Thus, an undeformed single crystal is destroyed from the surface through dissolution of the alkali halide crystal in water, whereas in a deformed single crystal the water penetrates into the crystal (in the form of crystalline hydrate or of a liquid layer of a salt solution) along grain and subgrain boundaries, thereby breaking the integrity of the crystal and destroying it. It is very important to avoid contact with water, especially at an early stage of storage. Annealing at relatively low temperatures (from +60 to +120°C) immediately after plastic deformation (where grain boundaries do not transform in relatively short annealing times [1] and the mechanical properties do not deteriorate due to a change in the state of bivalent additions with increasing temperature [11]) makes it possible to fix the deformed structure and the state of the supersaturated solid solution (in particular, due to the drying of crystals upon annealing). With storage under conditions of atmospheric moisture, as a result of aging, particles of the complex potassium–strontium chloride appear and, under high humidity, particles of strontium chloride crystalline hydrate precipitate. The precipitation of the water-containing phases upon aging (which is detected by x-ray diffraction) is accompanied by a significant decrease in the microhardness of the deformed single crystals of strontium-containing potassium chloride.

The change in the properties of the deformed crystals during postdeformation holding is obviously caused by the processes of aging, recovery, and recrystallization, which proceed at different rates and affect each other at various temperatures and humidity. For example, the maximum grain-growth rate in the crystals studied was detected in the crystals held under conditions of high humidity at a temperature of –13°C. In this case, twinned grains rapidly grow to reach 1000 μm in diameter within the first month of storage and then a slower stage of migration of high-angle boundaries sets in. The related changes in the grain structure affect the PFs. In time, intensity maxima associated with new grains and differing from {110} appear in {220} PFs. However, the crystal orientation remains $\{100\}\langle 001\rangle$, which is typical of deformed single crystals [3]. Under conditions of high humidity at room temperature, twinned-grain sizes in the crystals reach the same values but in two months; that is, the boundary migration rate in the stage of twin growth is smaller by a factor of 2–2.5. Recrystallized-grain growth under normal humidity at temperatures of +3 and +25°C occurs at similar rates. As seen from Fig. 5, the grain growth decelerates after a 2.5-month holding, because particles of the complex potassium–strontium chloride (detected by x-ray diffraction) precipitate along the boundaries of growing grains and begin to hinder their growth. The mean grain size by this time is about 50 μm. Figure 5 also demonstrates that recrystalliza-

tion in the crystals under the conditions of low humidity is much less pronounced than under conditions of normal or high humidity. In PFs of crystals held under conditions of low humidity, the {100}<001> orientation remains stable for the whole holding time and the number of reflections from grains of other orientations is found to be substantially smaller than in the case of crystals under conditions of high humidity at a temperature of –13 or +25°C. A comparison of these data with the x-ray diffraction data shows that the recrystallization rate is minimum in the specimens consisting of a supersaturated solid solution. As follows from Figs. 1 and 5 and the x-ray diffraction data, the microhardness increases and remains high for a long time after deformation in crystals in the state of a solid solution. In this case, when the recrystallization and precipitation rates upon aging are similar (as in the case of the crystals stored at room temperature and normal humidity), precipitated particles of complex potassium–strontium chloride hinder grain growth and provide a relatively high microhardness, which is, however, lower than that of the deformed crystals in the solid-solution state. In the deformed crystals that are under high humidity over the whole temperature range under study (from –13 to +25°C), the grain growth is faster than the aging-induced processes; therefore, the microhardness decreases from the very beginning of holding and reaches values characteristic of a pure KCl single crystal. Moreover, the precipitation of crystalline hydrates and the subsequent formation of a liquid layer along boundaries can result in decomposition of the specimens along the boundaries of recrystallized grains (Fig. 6). It should be noted that the straight-line boundaries of twinned grains retained after holding are etched by the liquid phase much less than high-angle boundaries.

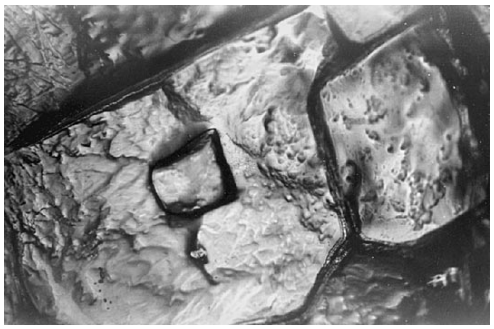

Fig. 6. Microstructure of a KCl : 0.06 wt % Sr crystal after 70% plastic deformation at $T = 250$°C and subsequent storage at $T = +20$°C for three months under high humidity (×50).

Alkali halide materials are known to be very hygroscopic [8, 9]. When crystals are grown from melts, their interaction with water causes contamination of the melts with hydroxyl ions and compounds that form due to the water interacting with the material of the crucible, e.g., platinum [9]. By applying vacuum drying, we can reduce the amount of sorbed water in KCl to 10^{-6}% [9], and treatment of the melt with an HCl-halide gas flow allows us to reduce the concentration of OH^- ions. These measures helped us to grow crystals with a low content of impurities, including oxides that form as a result of interaction with water. However, our experimental data show that, when plastic deformation is applied to increase the mechanical strength of an AHC, water interacts with the deformed crystal and deteriorates its properties. The water is adsorbed on the surface and penetrates into the bulk of the crystal in the presence of grain and subgrain boundaries. Moreover, as is seen from the experimental results, water favors accelerated growth of recrystallized grains (especially in the initial stage of the growth of grains with twinned orientations with respect to the initial single crystal). Simultaneously, the water from the vapor phase interacts chemically with doping components; as a result, crystalline-hydrate particles and then a liquid layer of a salt solution form along the boundaries of recrystallized grains, which causes failure of these boundaries. A decrease in the moisture content at the initial stage of holding deformed crystals by any means (e.g., by their postdeformation annealing at a temperature in the range from +60 to +120°C or by placing them in a vacuum for two to three months after deformation) makes it possible to conserve the deformation-induced structure and the solid-solution state in the deformed doped single crystals. Thus, one can conserve, for a long time, the high microhardness that is achieved by deformation of single crystals and their postdeformation holding. Decreasing the temperature from +25 to –13°C does not decrease either the boundary migration rate or the diffusion of the doping component.

ACKNOWLEDGMENTS

This work was supported by the Russian Foundation for Basic Research, project no. 01-02-16476.

REFERENCES

1. E. B. Borisenko, B. A. Gnesin, O. O. Likhanova, and I. B. Savchenko, Fiz. Tverd. Tela (St. Petersburg) **37** (7), 2029 (1995) [Phys. Solid State **37**, 1105 (1995)].
2. E. B. Borisenko and B. A. Gnesin, Textures Microstruct. **26–27**, 369 (1996).
3. E. B. Borisenko and B. A. Gnesin, Fiz. Tverd. Tela (St. Petersburg) **41** (2), 259 (1999) [Phys. Solid State **41**, 230 (1999)].
4. E. B. Borisenko and B. A. Gnesin, Fiz. Tverd. Tela (St. Petersburg) **42** (7), 1261 (2000) [Phys. Solid State **42**, 1299 (2000)].
5. E. B. Borisenko and B. A. Gnesin, in *Proceedings of the 1st Joint International Conference on Recrystallization and Grain Growth*, Ed. G. Gottstein and D. A. Molodov (Springer, Berlin, 2001), p. 1391.
6. E. B. Borisenko and B. A. Gnesin, Scr. Mater. **44**, 923 (2001).

7. E. B. Borisenko and B. A. Gnesin, Fiz. Tverd. Tela (St. Petersburg) **45** (5), 826 (2003) [Phys. Solid State **45**, 868 (2003)].
8. Yu. R. Zakis, Izv. Akad. Nauk SSSR, Ser. Fiz. **29** (2), 441 (1965).
9. S. V. Val'kovskiĭ, A. V. Gorbunov, and V. N. Erofeev, Preprint (Chernogolovka, 1983).
10. T. G. Stoebe, J. Phys. Chem. Solids **31** (6), 1291 (1970).
11. P. L. Pratt, R. P. Harrison, and C. W. A. Newey, Discuss. Faraday Soc. **38**, 211 (1964).
12. P. A. Agron and W. R. Busing, Acta Crystallogr. C **42**, 141 (1986).
13. A. B. Zdanovskiĭ, E. F. Solov'eva, and L. L. Ézrokhi, *Handbook on the Solubility of Salt Systems* (Goskhimizdat, Leningrad, 1963), Vol. 4 [in Russian].
14. A. I. Kirgintsev, L. N. Trushnikova, and V. G. Lavrent'ev, *Solubility of Inorganic Substances in Water* (Khimiya, Leningrad, 1972) [in Russian].
15. L. D. Grigor'eva, Dokl. Akad. Nauk **362** (3), 327 (1998) [Dokl. Phys. **43**, 556 (1998)].

Translated by K. Shakhlevich

Physics of the Solid State, Vol. 46, No. 9, 2004, pp. 1655–1657. Translated from Fizika Tverdogo Tela, Vol. 46, No. 9, 2004, pp. 1603–1606.
Original Russian Text Copyright © 2004 by Pinchuk, Shavreĭ.

DEFECTS, DISLOCATIONS, AND PHYSICS OF STRENGTH

Threshold Character of the Magnetoplastic Effect in Twinning of Bismuth Crystals

A. I. Pinchuk and S. D. Shavreĭ

Mozyr' State Pedagogical University, Mozyr', 247760 Belarus

e-mail: apinchook@tut.by

Received October 31, 2003; in final form, December 29, 2003

Abstract—It is found that, when a bismuth crystal is subjected simultaneously to concentrated loading and a dc magnetic field, the magnetoplastic effect manifests itself as an abrupt decrease in the average length of wedge twins on the (111) cleavage plane (and, hence, as a decrease in the total twinned volume of the crystal) as a threshold value of the magnetic field is reached. However, the magnetic field stimulates glide deformation, which is indicated by an increase in the size of dislocation rosettes. The microhardness of a crystal varies smoothly and tends to increase with increasing magnetic field. The last phenomenon is accounted for by hardening of the crystal under the indenter in the presence of a magnetic field, because several slip systems become operative. © *2004 MAIK "Nauka/Interperiodica".*

Magnetoplastic effects (MPEs) that accompany glide deformation are well known (see, e.g., [1, 2]). It was found in [3] that the application of a dc magnetic field (MF) decreases the size and number of wedge twins. In [4, 5], it was predicted and experimentally observed that there is a threshold field B_c above which an MPE occurs. The objective of this work is to answer the following questions:

(1) Does a threshold field B_c exist at which the average length L of wedge twins decreases in a jump in the case of twinning of bismuth crystals?

(2) Is the abrupt decrease in L accompanied by an increase in the size of dislocation rosettes?

(3) How does the microhardness H of samples vary with increasing magnetic field?

In the study, we used bismuth single crystals grown, following the Bridgman technique, from a 99.97 wt % pure raw material (with a Pb impurity). Measurements were performed on the (111) cleavage plane of as-cleaved bismuth crystals. Samples were rectangular prisms $10 \times 5 \times 5$ mm in size. Measurements were carried out using a PMT-3 microhardness tester, with a diamond pyramid applying a concentrated load. All components of the experimental setup with which a sample was mounted and loaded were made from nonmagnetic materials to exclude instrumental effects. The absence of artifacts was confirmed by a special check experiment. The dimensions of indentations in the absence of a load on the indenter rod did not change when a magnetic field was turned on or off. A sample was placed in the center of the electromagnet core gap. Measurements performed with a Hall probe showed that the relative field variations along the sample did not exceed 2–3%. Loading of a sample was performed concurrently with exposure to a magnetic field. The magnetic field B was varied in the range from 0 to 0.9 T. The time of the sample exposure to a magnetic field was 5 min. The force applied to the indenter rod was P = 0.14 N. Direct measurements were made of the diagonals of the pyramid indentations, the length and width of wedge twins at the mouth, and the number of wedge twins. Averaging was performed over measurements of twenty indentations. The measurement error did not exceed 3%.

The degree of plastic deformation in twinning can be characterized by the total twinned volume $\sum V_{tw}$ [6, 7]. The volume of a wedge twin with a thickness h at the mouth can be found using a formula for the volume of a sphere segment. Since the volume of a twin V_{tw} is half of the sphere segment volume and $r \approx L$ (r is the radius of the segment base), we have $V_{tw} = \frac{1}{24}\pi h^2\left(3L - \frac{h}{2}\right)$. The total twinned volume is $\sum V_{tw} = V_{tw}N$, where N is the number of twins.

To determine the sizes of the crystal surface areas that were glide-hardened in the presence and in the absence of a magnetic field, the ratio $\frac{\Delta H}{H}$ (which is the measure of strain hardening [8]) was plotted against the distance l from the center of a prick. Here, $\Delta H = H' - H$ is the difference between the microhardness of the deformed area (H') and that of the undeformed area (H) of the crystal surface. In this case, we were interested in the $\frac{\Delta H}{H}(l)$ dependence (rather than in the exact values of microhardness), which allowed us to compare the sizes of hardened areas in the presence and in the absence of a magnetic field. Since it is difficult to cor-

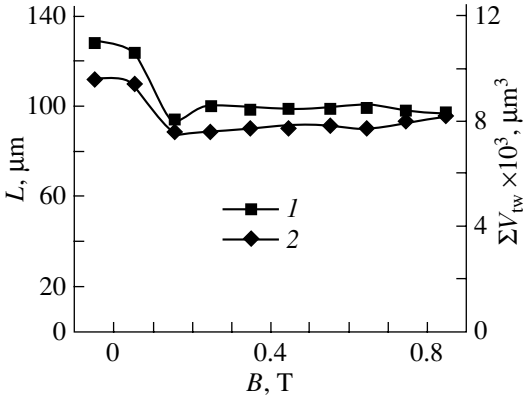

Fig. 1. Dependences (*1*) of the average length L of wedge twins formed on the cleavage plane of a bismuth crystal and (*2*) of the total twinned volume $\sum V_{tw}$ on magnetic field B.

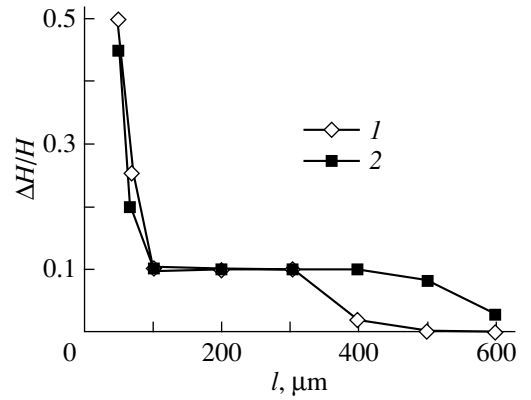

Fig. 2. Dependence of the ratio $\Delta H/H$ on the distance l from the center of a prick (*1*) in the absence and (*2*) in the presence of a magnetic field.

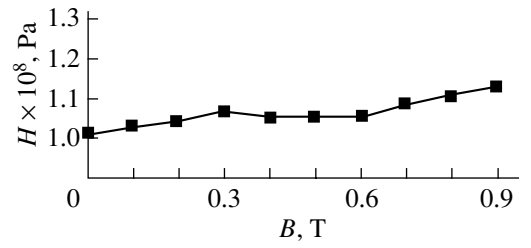

Fig. 3. Dependence of the microhardness H of a bismuth crystal on magnetic field B.

rectly determine the size of a hardened area in the case of a small applied load, we made a prior prick by applying a comparatively large load (P = 0.8 N) to the indenter. The values of H' and H were measured in the absence of an MF using a small load (P = 0.01 N).

It is seen from Fig. 1 (curve *1*) that, for bismuth crystals, there is a threshold magnetic field ($B \sim 0.2$ T) at which the average length L of wedge twins on the (111) cleavage plane decreases abruptly. Therefore, there is a threshold for the MPE in twinned bismuth crystals at which the average path length of twinning dislocations $\lambda = \sum_i L_i/2N$ decreases in a jump. Since the average thickness h of wedge twins at the mouth is the same to within experimental error, the number of twinning dislocations at the twin–matrix boundary (which is equal to h/a) also remains unchanged.

It was established that the decrease in L is the chief cause of the abrupt decrease in the total twinned volume $\sum V_{tw}$ at $B \sim 0.2$ T (curve *2* in Fig. 1), because the number of twins N does not change to within experimental error.

From comparison of the dependence of $\Delta H/H$ on the distance from the center of prick l in the presence of an MF with that measured in the absence of an MF (Fig. 2, curves *2*, *1*, respectively), it follows that the MF causes the hardened area of the crystal surface to increase significantly in size. As the MF reaches the value $B \sim 0.2$ T, the ratio $\Delta H/H$ decreases to zero at large values of l, which indicates that the size of the dislocation rosette increases in a jump.

However, the microhardness H varies smoothly and tends to increase in high fields B (Fig. 3). The experimental dependence observed by us can be explained as follows. It was conjectured in [9] that the strain-hardening coefficient of the region beneath the indenter is due to all crossing slip systems being operative. In order to elucidate the question as to whether the MF causes all slip systems to operate, we performed a special experiment. It is known [10] that a dislocation rosette on the (111) cleavage plane of a bismuth crystal consists of etching pits forming two equilateral triangles. The vertices of one of these triangles lie on the $\langle \bar{1}\bar{1}2 \rangle$ axes, and the vertices of the other lie on the $\langle 11\bar{2} \rangle$ axes. The first triangle consists of dislocation rows lying in the $\{11\bar{1}\}$ planes making an obtuse angle with the direction of the applied force. The other triangle consists of dislocation rows lying in the $\{11\bar{1}\}$ planes making an acute angle with the direction of the applied force. At room temperature, only the first type of triangles forms around indents in the absence of an MF, because twins prevent the formation of dislocation rows of the second type [10]. Our investigation of the $\frac{\Delta H}{H}(l)$ dependence for the $\langle \bar{1}\bar{1}2 \rangle$ and $\langle 11\bar{2} \rangle$ directions showed that in both cases this dependence follows curve *2* in Fig. 2 to within experimental error. Therefore, our experimental data suggest that the MF causes all slip systems to operate. As a result, strain hardening occurs, which accounts for the fact that the microhardness does not decrease in spite of the plasticizing effect of the magnetic field.

ACKNOWLEDGMENTS

This study was supported by the Belarussian Foundation for Basic Research, project no. F03-105.

REFERENCES

1. N. A. Tyapunina, V. L. Krasnikov, and É. P. Belozerova, Fiz. Tverd. Tela (St. Petersburg) **41** (6), 1035 (1999) [Phys. Solid State **41**, 942 (1999)].
2. A. A. Skvortsov, A. M. Orlov, and L. I. Gonchar, Zh. Éksp. Teor. Fiz. **120** (1), 134 (2001) [JETP **93**, 117 (2001)].
3. A. I. Pinchuk and S. D. Shavreĭ, Fiz. Tverd. Tela (St. Petersburg) **43** (1), 39 (2001) [Phys. Solid State **43**, 39 (2001)].
4. V. I. Al'shits, E. V. Darinskaya, O. L. Kazakova, E. Yu. Mikhina, and E. A. Petrzhik, Pis'ma Zh. Éksp. Teor. Fiz. **63** (8), 628 (1996) [JETP Lett. **63**, 668 (1996)].
5. V. I. Al'shits, E. V. Darinskaya, and O. L. Kazakova, Fiz. Tverd. Tela (St. Petersburg) **40** (1), 81 (1998) [Phys. Solid State **40**, 70 (1998)].
6. A. I. Pinchuk, Metallofiz. Noveishie Tekhnol. **22** (3), 88 (2000).
7. A. I. Pinchuk and S. D. Shavreĭ, Metallofiz. Noveishie Tekhnol. **22** (12), 43 (2000).
8. Yu. S. Boyarskaya, D. Z. Grabko, and M. S. Kats, *Physics of Microindentation* (Shtiintsa, Chisinau, 1986) [in Russian].
9. Z. K. Saralidze, M. V. Galustashvili, and D. G. Driyaev, Fiz. Tverd. Tela (St. Petersburg) **41** (11), 1999 (1999) [Phys. Solid State **41**, 1834 (1999)].
10. D. Z. Grabko, Yu. S. Boyarskaya, and N. P. Dyntu, *Mechanical Properties of Bismuth-Type Semimetals* (Shtiintsa, Chisinau, 1982) [in Russian].

Translated by Yu. Epifanov

Physics of the Solid State, Vol. 46, No. 9, 2004, pp. 1658–1666. Translated from Fizika Tverdogo Tela, Vol. 46, No. 9, 2004, pp. 1606–1613.
Original Russian Text Copyright © 2004 by Slutsker.

DEFECTS, DISLOCATIONS, AND PHYSICS OF STRENGTH

Characteristics of Elementary Acts in the Kinetics of Metal Fracture

A. I. Slutsker

Ioffe Physicotechnical Institute, Russian Academy of Sciences, Politekhnicheskaya ul. 26, St. Petersburg, 194021 Russia
e-mail: Alexander.Slutsker@mail.ioffe.ru

Received January 15, 2004

Abstract—Experimental studies of the fracture kinetics of polycrystalline metals have led to the problem of the barrier and activation volume of elementary fracture acts. A model is proposed where the field binding one atom to its environment in a metal is represented by equivalent bonds directed along three orthogonal axes. These bonds are described using the Morse potential, whose parameters are found from the values of the Young's modulus and the linear thermal expansion coefficient for metals. The validity of the model is checked by comparing the results obtained with metal sublimation data. The values of the barrier and activation volume of elementary fracture acts are determined for 15 polycrystalline metals. The levels of local overstresses are estimated. The theoretical breaking strengths of the metals are calculated. © *2004 MAIK "Nauka/Interperiodica".*

1. INTRODUCTION

The concept of elementary fracture acts of solids, including metals, entered fracture physics when the kinetic nature of mechanical fracture was established. Numerous systematic studies have shown that the fracture of a loaded body cannot be considered a critical event occurring under a certain load or deformation of a body. Fracture was found to be a kinetic phenomenon: a sufficiently long process develops from the instant of loading and terminates in macroscopic fracture of the body [1, 2].

The integrated characteristic of the rate of the processes resulting in fracture is the life τ, namely, the time from the instant of loading to the instant of fracture. This time is inversely proportional to the mean fracture rate. There is a wide scatter in the values of the life for various bodies; experimentally determined values vary from 10^{-3} to 10^{7} s [2]. This means that the mean fracture rate (if, e.g., the fracture rate is measured as the rate of decrease in the bearing cross section of a body) is well below (by orders of magnitude) the acoustic-wave velocity in solids. Therefore, it follows that the process of fracture consists of a sequence of certain elementary acts. If the appearance of these acts has a probabilistic character, then the life of a body under a load should be logarithmically close to the mean expectation time for one act [2].

The life of metals (just as other solids) was found to exponentially depend on stress σ and temperature T [1–4]. This dependence made it possible to reveal the mechanism of the elementary acts of the process resulting in fracture.

Dependences of the life of metals on temperature and applied stress, i.e., the $\tau(\sigma, T)$ dependences, are shown in Fig. 1. The results are given for cases where a uniaxial tensile stress is maintained constant when measuring the life of each sample. Similar dependences were also obtained for many other metals [5–8]. In a wide range, but not at very low and very high values of σ and T, the $\tau(\sigma, T)$ dependences are described by the Zhurkov formula [1–8]

$$\tau(\sigma, T) \cong \tau_0 \exp\frac{U(\sigma)}{kT}, \quad (1)$$

where k is the Boltzmann constant. An important feature of Eq. (1) is the common value of the preexponential factor ($\tau_0 \approx 10^{-13}$–10^{-12} s) for all solids, which is close to the mean period of atomic vibrations in solids (or the period of maximum-frequency oscillations in a Debye spectrum) [2].

Equation (1) can be is compared with the fundamental Frenkel formula for the mean expectation time of a local energy fluctuation E_{fl} [9]:

$$\tau_{\text{fl}} \cong \tau_0 \exp\frac{E_{\text{fl}}}{kT}, \quad (2)$$

where τ_0 is the same as in Eq. (1). The correspondence between Eqs. (1) and (2) (under the condition $U(\sigma) = E_{\text{fl}}$) and the interpretation of the life $\tau(\sigma, T)$ as the mean expectation time for elementary fracture acts allow us to conclude that these acts have a thermal fluctuation nature, i.e., that the potential barrier $U(\sigma)$ is overcome due to local energy fluctuations [1–8]. Therefore, the barrier $U(\sigma)$, which is often called the fracture activation energy, is the most important characteristic of an elementary act of fracture.

1063-7834/04/4609-1658$26.00 © 2004 MAIK "Nauka/Interperiodica"

Experimental data similar to those shown in Fig. 1 were used to obtain the $U(\sigma)$ dependences for many metals. Examples of such dependences are given in Fig. 2. The $U(\sigma)$ dependences are seen to be close to linear, which allows us to describe them by the expression

$$U(\sigma) \cong U_0 - \gamma\sigma. \quad (3)$$

Equation (3) shows that the elementary act of metal fracture is characterized by an initial barrier U_0 and that the barrier decreases with increasing tensile stress σ applied to a body.

In Eq. (3), the coefficient γ has the dimensions of volume and its value determines the degree to which the applied stress decreases the barrier. Thus, when analyzing the elementary act of metal fracture, one has to reveal the physical meaning of both U_0 and γ.

The properties of U_0 and γ have been found to be different. The barrier U_0 was established to be a stable characteristic of a metal. When the structural state of a metal is changed (by annealing, quenching, or alloying), the value of U_0 remains virtually constant (although it is different for different metals) [4–8, 10]. Unlike U_0, the coefficient γ varies strongly with the structural state of a metal (up to an order of magnitude) [4–7]. As an example, Fig. 3 shows the $U(\sigma)$ dependences for zinc; it is seen that $U_0 \approx$ const and the coefficient γ (the slope of the $U(\sigma)$ curve) changes by several times.

The basic characteristics of metal fracture kinetics (U_0 and γ) were analyzed earlier, and a basis for their interpretation was developed in [1–8].

The purpose of this work is to comprehensively study the initial barrier U_0 and the stress dependence of the barrier $U(\sigma)$, characterized by the coefficient γ, in elementary acts of metal fracture.

2. ANALYSIS OF THE INITIAL BARRIER U_0 IN ELEMENTARY ACTS OF METAL FRACTURE

Table 1 gives the values of U_0 that were determined in studying the fracture kinetics of a number of polycrystalline metals having various lattice types and brittle–plastic properties. It is seen that the values of U_0 for the metals vary in the range 1–7 eV.

To reveal the physical meaning of U_0, it is useful to compare the values of U_0 with a characteristic of metal destruction, such as the sublimation (evaporation) energy D_s [1–8, 11]. The values of D_s are given in Table 1 in the column next to that of U_0. The values of U_0 and D_s are seen to be close to each other. Taking the ratios

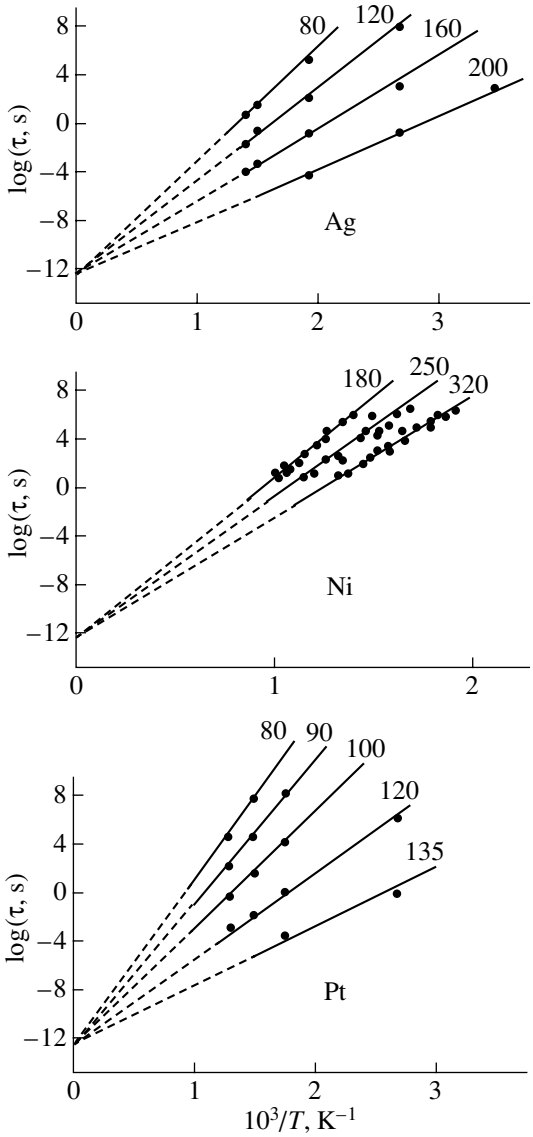

Fig. 1. Dependences of the life on temperature and applied uniaxial tensile stress for polycrystalline metals: silver (99.96%) [6], nickel (99.80%) [8], and platinum (99.94%) [3]. Numerals on the curves show the stresses in MPa.

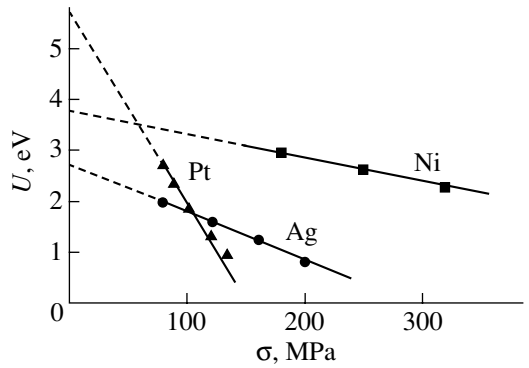

Fig. 2. Force dependences of the barrier in elementary acts of metal fracture (data from Fig. 1).

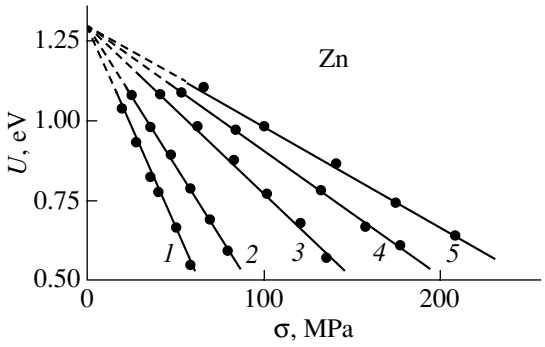

Fig. 3. Force dependences of the barrier in elementary acts of the fracture of polycrystalline zinc (99.94%) annealed at different temperatures [4]: (*1*) 630, (*2*) 530, (*3*) 490, (*4*) 450, and (*5*) 370 K.

U_0/D_s for all 15 metals, we calculate the average ratio U_0/D_s and the average scatter to be

$$\left\langle \frac{U_0}{D_s} \right\rangle = 1.01 \pm 0.07.$$

It should be noted that the values of U_0, as determined from experimental studies of the fracture kinetics, are accurate to within ~10% [2]. The values of D_s given in various sources [12–15] have a scatter that reaches ~20% in some cases. Table 1 gives values of D_s that are either the most stable or averaged over the data from [12–15].

Making allowance for these circumstances, the authors of [1–8, 10, 11] concluded that, actually, the barrier U_0 for the elementary act of metal fracture coincides with the sublimation energy D_s. The process of sublimation, which consists in the transition of an atom from the surface of a metallic body to a gaseous monatomic state, is related to bond breaking in the metallic body. The sublimation energy is half the energy of binding an atom to its environment in the body [16, 17]. The actual equality between U_0 and D_s means that interatomic bonds also break in the elementary act of metal fracture.

Interatomic bonds in metals have specific features. Indeed, cohesion in nonmetallic bodies is due to binary and directed bonds, such as covalent, van der Waals, and hydrogen bonds. The elastic and anharmonic characteristics of such bonds are measured by various spectroscopic methods. The strength of a nonmetallic body and its fracture are comparable to the strength and breaking of real binary bonds. In metals, there are no analogous individual interatomic bonds. A metal consists of an ionic lattice embedded into an electron plasma, and the binding of an atom to its environment has a specific "diffuse" character. Therefore, we believe that destruction processes in metals, such as sublimation or fracture, can be analyzed using a specific

Table 1. Metal characteristics. Estimates of the theoretical strength and activation volume in an elementary act of metal fracture

Metal	U_0, eV	D_s, eV	$\frac{U_0}{D_s}$	V_a, 10^{-2} nm^{-3}	E, GPa	α, 10^5 K^{-1}	D_e, eV	$\frac{D_e}{D_s}$	σ_m, GPa	V_A^e, 10^{-2} nm^3	$\frac{V_A^e}{V_a}$	V_A^F, 10^{-2} nm^3	
												$V_A^e \frac{U_0}{D_e}$	$3V_a$
Ag	2.7 [6]	2.8	0.97	1.7	77	1.9	0.7	0.25	8.5	1.4	0.8	5.3	5.1
B	5.7 [11]	5.5	1.04	0.8	345	0.8	2.0	0.36	43	0.8	1.0	2.3	2.4
Cd	1.2 [7]	1.2	1.00	2.2	52	~3	0.3	0.25	4	1.3	0.6	5.2	6.6
Cu	3.6 [8]	3.5	1.03	1.2	120	1.7	0.8	0.23	13	1.0	0.8	4.5	3.6
Fe	4.4 [7]	4.2	1.05	1.2	200	1.2	1.0	0.24	19	0.9	0.8	4.0	3.6
Mg	1.5 [7]	1.5	1.00	2.3	44	2.5	0.5	0.33	4.5	1.9	0.8	5.7	6.9
Mo	7.5 [7]	6.9	1.09	1.6	315	0.53	2.4	0.35	31	1.2	0.8	3.7	4.8
Nb	6.6 [7]	7.1	0.93	1.8	150	0.7	2.4	0.34	20	2.0	1.1	5.6	5.4
Ni	3.8 [8]	3.9	0.97	1.1	210	1.3	0.9	0.23	19	0.8	0.7	3.4	3.3
Pb	1.9 [7]	2.0	0.95	3.1	16	~2.8	0.8	0.40	3	4.6	1.5	11	9.3
Pt	5.7 [3]	5.5	1.04	1.5	162	0.9	1.7	0.31	19	1.4	0.9	4.6	4.5
Ti	5.3 [7]	4.9	1.08	1.8	110	0.83	2.4	0.49	17	2.3	1.3	5.1	5.4
V	5.7 [7]	5.3	1.08	1.4	155	0.8	2.4	0.45	24	1.7	1.2	4.1	4.2
Zn	1.3 [4]	1.2	1.08	1.5	115	~3	0.2	0.17	5.7	0.6	0.4	3.9	4.5
Zr	5.3 [7]	6.1	0.87	2.4	90	0.74	2.8	0.46	15	3.1	1.3	5.9	7.2
Average			1.01					0.32			0.9		

approach to obtain quantitative characteristics of the elementary acts of these processes.

Note the following essential circumstance. All studies of the fracture kinetics of metals whose results (the values of U_0 and γ) are given in Tables 1 and 2 were performed on polycrystalline samples. The values of sublimation energy in Table 1 also correspond to polycrystalline metals. In what follows, we will use values of the Young's modulus and linear thermal expansion coefficient that are also related to polycrystalline metals.

Naturally, the properties of crystalline cells of a metal, such as the interatomic distances, elasticity, strength, and thermal expansion, are anisotropic. In polycrystalline metals, these characteristics are averaged (in the absence of texture); the metals are considered to be macroscopically isotropic. Thus, a polycrystalline structure is characterized by averaged values of U_0 and D_s, which leads us to use averaged quantities for further analysis of U_0 and D_s.

We assume that the field binding an atom to its environment in a metal is represented by six identical equivalent bonds directed along three orthogonal axes. In this case, we can try to determine the dissociation energy, fracture activation volume, and theoretical strength of the equivalent bonds by using the measured values of the Young's modulus E and linear thermal expansion coefficient α in metals. To find out whether the calculations are reliable, we will compare the calculated equivalent-bond dissociation energy D_e with the sublimation energy D_s; the value of D_e should be close to $(1/3)D_s$.

To determine the characteristics of the equivalent metallic bond, we assume that the dependence of the atomic interaction potential W on the distance r between atomic centers is described by the Morse function [18], which is widely applied to describe interatomic bonds [19–23]:

$$W(r) = D\{\exp[-2a(r-d_0)] - 2\exp[-a(r-d_0)]\}, \quad (4)$$

where d_0 is the equilibrium interatomic distance, D is the dissociation energy, and a is a parameter. Expression (4) corresponds to an asymmetric potential well with depth $-D$ and a minimum of $W(r)$ at d_0.

Let us introduce $x = r - d_0$ and expand $W(r)$ in a power series in x up to a cubic term near the minimum $x = 0$:

$$W(x) = -D + Da^2x^2 - Da^3x^3. \quad (5)$$

Expression (5) corresponds to the general form of the cubic potential of binary interatomic interaction:

$$W(x) = -D + \frac{1}{2}fx^2 - \frac{1}{3}gx^3, \quad (6)$$

where f is the coefficient of linear bond elasticity (stiffness) and g is the first-order anharmonicity coefficient.

Comparing Eqs. (5) and (6), we obtain

$$f = 2Da^2; \quad g = 3Da^3. \quad (7)$$

Table 2. Estimates of the local overstresses in metals

Metal	Annealing T, K	γ, nm^3	$V_A^F = 3V_a$, 10^{-2} nm^3	$q = \dfrac{\gamma}{V_A^F}$
Ag	800	1.3 [6]	5.1	~25
B		0.22 [11]	2.4	~10
Cu	900	1.6 [8]	3.6	~45
Ni	1060	0.7 [8]	3.3	~20
Pt	1250	5.2 [3]	4.5	~110
	370	0.8 [4]		~18
	450	1.0 [4]		~22
Zn	490	1.3 [4]	4.5	~30
	530	2.1 [4]		~50
	630	3.2 [4]		~70

Then, it follows that

$$a = \frac{2}{3}\frac{g}{f}; \quad D = \frac{9}{8}f\left(\frac{f}{g}\right)^2. \quad (8)$$

Thus, given the coefficients f and g, we can find the bond dissociation energy D. To estimate the coefficients f and g as characteristics of equivalent bonds in metals, we use the values of the Young's modulus and linear thermal expansion coefficient (TEC) of polycrystalline metals.

The elasticity of an isotropic body during uniaxial tension and the thermal expansion of the body along the same axis are considered to be determined by the elastic and anharmonic characteristics (i.e., f and g) of one equivalent interatomic bond operating along this axis.

Then, the Young's modulus is

$$E \cong \frac{f}{d_0}; \quad (9)$$

and the linear TEC (in the classic region) is

$$\alpha \cong \left(\frac{g}{f}\right)\frac{k}{2fd_0}, \quad [9, 17]. \quad (10)$$

Using Eq. (8) combined with Eqs. (9) and (10), the equivalent-bond dissociation energy D_e is found to be

$$D_e \cong \frac{9}{32}\frac{k^2}{E\alpha^2 d_0^3} \cong \frac{9}{32}\frac{k^2}{E\alpha^2 V_a}, \quad (11)$$

where $V_a = d_0^3$ is the mean volume per atom in the metal.

Thus, to calculate D_e, we need to know V_a, E, and α. The value of V_a can be found from the relation $V_a \cong A/\rho N_A$, where A is the atomic weight, ρ is the density, and N_A is Avogadro's number. The values of E and α for polycrystalline metals at temperature $T = 300$ K (for boron, α was taken at 650 K) were borrowed from [15].

The temperature of 300 K for all metals under analysis (excluding boron) corresponds to a classic region, since the Debye temperatures of these metals fall in the range from 88 K (Pb) to 420 K (Fe). This justifies the application of Eqs. (10) and (11) for the calculation of D_e.

The values of V_a, E, and α for the metals under study and the dissociation energies of the equivalent interatomic bonds calculated from Eq. (11) are given in Table 1.

As noted above, it is important to compare the calculated values of D_e with the sublimation energies D_s of the metals. As follows from Table 1, $D_e < D_s$; that is, D_e is a fraction of D_s. This fraction is $D_e/D_s \equiv \beta$ and is given in Table 1 for each metal. The values of β are rather uniformly distributed over the range 0.2–0.5. The mean value and scatter of β are found to be $\langle\beta\rangle = 0.32 \pm 0.08$.

Thus, the dissociation energy of one equivalent interatomic bond (for the metals under study) is, on average, one-third of the sublimation energy (or one-sixth of the total energy of binding an atom to its environment inside the metallic body). The scatter in the values of β with respect to one-third can be due to the assumptions and approximations made to calculate D_e; nevertheless, it can reflect the specific structural features of different metals to some extent.

The closeness of the calculated dissociation energies of the equivalent interatomic bonds to one-third of the sublimation energy supports the validity of the model of the division of the interaction field of an atom with its environment into six components (equivalent bonds) and the validity of applying the Morse potential. Therefore, an elementary sublimation act, namely, evaporation of an atom from the surface of a metallic body, can be considered an act of breaking three (in average) equivalent bonds.

Since the barriers in the elementary acts of fracture and sublimation are virtually the same ($U_0 \cong D_s$), the elementary act of metal fracture can also be considered an act of breaking three (in average) equivalent interatomic bonds, with each of them having the dissociation energy D_e.

Of course, the elementary act of metal fracture differs from the sublimation act, i.e., from the removal of one atom from a metallic surface. Our next problem is to develop a model for an elementary act of metal fracture that includes the breaking of three equivalent bonds (e.g., in crack growth kinetics).

3. COEFFICIENT γ INVOLVED IN THE FORCE DEPENDENCE OF THE BARRIER $U(\sigma)$ IN THE ELEMENTARY ACT OF METAL FRACTURE

According to Eq. (3), the coefficient γ is determined as the derivative $\gamma = \dfrac{dU(\sigma)}{d\sigma}$. Note that σ is the average stress applied to a sample. The characteristic values of γ for metals lie in the range 1–10 nm^3 [2]. In [24–27], the derivative $\dfrac{dU(\sigma)}{d\sigma}$ was called the activation volume.

Upon fluctuation-induced breaking of a stressed interatomic bond, the required energy, which is equal to the bond dissociation energy D, consists of two components, more specifically, the tensile stress energy $\Delta A = \sigma_{loc} V_A$ (where σ_{loc} is the stress applied to the bond) and the fluctuation energy E_{fl}:

$$D = E_{fl} + V_A \sigma_{loc}. \quad (12)$$

Therefore, the fluctuation energy required for breaking a stressed bond is

$$E_{fl}(\sigma_{loc}) = D - V_A \sigma_{loc}. \quad (13)$$

Note that Eq. (13) has the same structure and, in general, the same meaning as Eq. (3), which follows from analysis of the metal fracture kinetics. The quantity V_A involved in Eqs. (12) and (13) is the activation volume of breaking an interatomic bond, that is, the increment in the volume at which the work of the applied stress σ_{loc} provides the removal of an atom from a potential well with depth D. At the moment the interatomic bonds break, the characteristic values of V_A are close to the atomic volumes (in order of magnitude) and fall in the range 0.01–0.03 nm^3 [7, 9]. Thus, the coefficient γ of metals is well above (by orders of magnitude) the values of V_A, which calls into question the meaning of γ as the activation volume in elementary acts of metal fracture.

The interpretation of the coefficient γ proposed in [2, 4] is based on the fact that local stresses σ_{loc} operating at the "point" of an elementary act can significantly exceed the average stress σ in a body. The concept of stress concentrators (local overstresses), which are caused by structural heterogeneity and defects in real solids, was proposed a long time ago [28–30] and confirmed experimentally. Therefore, we can introduce the coefficient (index) of local overstresses q by assuming that σ_{loc} is proportional to the average stress σ:

$$\sigma_{loc} = q\sigma.$$

Assuming that the barrier decreases because of local stresses, we obtain from Eq. (3)

$$U(\sigma) = U_0 - \gamma\sigma = U_0 - \gamma'\sigma_{loc} = U_0 - \gamma' q\sigma. \quad (14)$$

Comparison of Eqs. (14) and (13) shows that we can call γ' the activation volume of the elementary act of metal fracture V_A^F:

$$\gamma = qV_A^F. \quad (15)$$

In this case, the scatter in the values of γ is explained by a change in the index of local overstresses q due to changes in the structure of the metal (at a constant activation volume V_A^F). Therefore, we should determine the activation volume V_A^F in the elementary act of metal fracture, which has not been analyzed earlier in detail. Note that the estimation of V_A^F will allow us to more accurately estimate the level of local overstresses q from the experimental values of $\gamma\left(q = \frac{\gamma}{V_A^F}\right)$.

The method for determining the activation volume V_A of the elementary act of metal fracture is based on the same model for equivalent bonds. Let us calculate the activation volume of breaking one equivalent bond V_A^e. To this end, we need the dependence of the bond dissociation barrier on the tensile stress (or tensile force) applied to the bond.

We again use the Morse potential. From Eq. (4), we derive the force that induce bond deformation (this force is equal to the restoring elastic force during bond deformation):

$$F(x) = \frac{dW(x)}{dx} = 2aD[\exp(-ax) - \exp(-2ax)].$$

The force $F(x)$ starts from $F = 0$ at $x = 0$, goes through a maximum F_m as x increases, and then decreases. From the condition $\frac{dF(x)}{dx} = 0$, F_m is found to be

$$F_m = \frac{1}{2}aD.$$

We go from the force to the stress

$$\sigma_m = \frac{F_m}{d_0^2} = \frac{aD}{2d_0^2}, \qquad (16)$$

where d_0^2 is the cross section of an atom. The authors of [31–34] used the Morse potential to find the dependence of the bond dissociation barrier $D(\sigma_{loc})$ on the stress. This dependence is nonlinear and rather complex. However, in the range ~(0.2–1.0)σ_m, this dependence can be approximated as

$$D(\sigma_{loc}) \cong D\left(1 - \sqrt{\frac{\sigma_{loc}}{\sigma_m}}\right) \cong D - \frac{D}{\sigma_m}\sqrt{\frac{\sigma_m}{\sigma_{loc}}}\sigma_{loc}. \qquad (17)$$

Equation (17) shows that the application of the maximum stress σ_m for a bond decreases the bond dissociation barrier to zero.

Upon breaking, the barrier $D(\sigma_{loc})$ is overcome because of a fluctuation in energy (i.e., $E_{fl} = D(\sigma_{loc})$). Therefore, by comparing Eqs. (17) and (13), we find the activation volume of bond breaking:

$$V_A \cong \frac{D}{\sigma_m}\sqrt{\frac{\sigma_m}{\sigma_{loc}}}. \qquad (18)$$

Expression (18) shows that V_A is not constant but rather depends on the applied stress σ_{loc}. This dependence is weak; for example, in the range σ_{loc} = (0.2–1.0)σ_m, the quantity V_A changes only by two times.

As follows from the analysis of the experimental data on the kinetics of metal fracture, the stress dependence of the barrier is close to the linear dependence given by Eq. (3), where $\gamma = qV_A^F \cong$ const. In the case where $q \approx$ const, we have $V_A^F \approx$ const. This difference between the experimental linear $U(\sigma)$ dependence and the calculated $D(\sigma_{loc})$ nonlinear dependence can be caused by the conditions for deriving the $D(\sigma_{loc})$ dependence. In this derivation, the stress σ_{loc} was assumed to be constant in the act of bond breaking. In a real loaded body, however, the stress applied to a bond is determined by the tensile stresses of the neighboring bonds; the elongation of this bond in a breaking act leads to contraction of the neighboring stretched bonds and, thus, to a decrease in the stress applied to a given bond. This effect decreases the nonlinearity of the $D(\sigma_{loc})$ dependence, and the factor $\sqrt{\sigma_m/\sigma_{loc}}$ approaches unity [35–37].

The simulation of the kinetics of fluctuation-induced breaking of a stressed atom chain performed in [38] using the Morse potential to describe the interatomic bond in the chain showed that the $D(\sigma_{loc})$ dependence is linear, with $V_A \cong D/\sigma_m$.

Based on the considerations given above, we think that the activation volume of breaking an equivalent interatomic bond can be calculated from the relation

$$V_A^e \cong \frac{D_e}{\sigma_m}. \qquad (19)$$

The values of D_e are determined above (Table 1). From Eq. (16) combined with Eqs. (7)–(11), we obtain

$$\sigma_m = \frac{aD_e}{2d_0^2} = \frac{3}{8}f\left(\frac{f}{g}\right)\frac{1}{d_0^2} \cong \frac{3}{16}\frac{k}{\alpha V_a}. \qquad (20)$$

The calculated values of σ_m for the metals under study are given in Table 1. The maximum stress is commonly called the theoretical bond strength. Table 1 indicates that the theoretical strengths of the equivalent bonds of the metals lie in a wide range, from 4 to 43 GPa.

From the ratio of D_e to σ_m, we find the activation volumes of breaking equivalent interatomic bonds V_A^e for the metals under study (Table 1).

The values of V_A^e can be compared with the values of V_a (which is the volume per atom in the metallic body), i.e., with the atomic volumes (Table 1). The mean ratio V_A^e/V_a and the mean scatter are

$$\left\langle \frac{V_A^e}{V_a} \right\rangle \approx 0.9 \pm 0.2.$$

Thus, the activation volume of breaking an equivalent bond in metals is, on average, close to the atomic volume in them.

Now, we estimate the activation volume V_A^F in the elementary act of metal fracture by assuming that this volume is the sum of the activation volumes of breaking equivalent bonds in an elementary act of fracture. We estimate V_A^F using two methods.

When calculating each metal individually, we get

$$V_A^F \cong V_A^e \frac{U_0}{D_e}.$$

Here, U_0/D_e is the number of equivalent bonds broken in an elementary act of fracture (or sublimation, since $U_0 \approx D_s$) of a given metal.

For calculating the average, we assume that $V_A^e \cong V_a$ and that the number of broken equivalent bonds is equal to three (since the average ratio $U_0/D_e \approx 3$). In this case, $V_A^F \cong 3V_a$. The values of V_A^F found using the two methods are also given in Table 1.

The values of V_A^F calculated by the different methods are seen to be rather similar. Taking into account that our calculations are only approximate, it is wise to take a simpler relation for the activation volume of the elementary act of metal fracture, namely, $V_A^F \cong 3V_a$.

Estimating the activation volume of the elementary act of metal fracture makes it possible to estimate the level of local overstresses q in polycrystalline metals from Eq. (15):

$$q \cong \frac{\gamma}{V_A^F} \cong \frac{\gamma}{3V_a}.$$

Examples of such estimates for a number of metals are given in Table 2. These estimates indicate that local overstresses as high as 10–100 appear under loading of real metallic bodies. Such stress concentrations have been detected (using spectroscopic methods) in polymer bodies [39] and follow from the analysis of the luminescence of loaded crystals [40, 41], observations of pinned dislocation pileups [42], and force-induced bending of single dislocations [43]. Therefore, the obtained estimates of the local overstresses in loaded polycrystalline metals seem realistic.

Note again that, unlike the barrier U_0 of an elementary act of fracture (which is constant for a given metal), the overstress index varies depending on the structural state of the metal. This fact is seen from the data for zinc (Fig. 3, Table 2).

Local overstresses that appear due to structural defects and initiate elementary fracture acts do cause smaller breaking strengths of real bodies than their theoretical strengths. The real breaking strength σ_r can be estimated from the ratio $\sigma_r \approx \frac{1}{q}\sigma_m$ (see below).

The calculated characteristics related to elementary acts of metal fracture (D_e, V_A^F, q, σ_m) are of course averaged; they are averaged due to the polycrystalline structure of metals, the model of equivalent bonds, and the use of the average values of α and E. The results obtained can be supported by the calculated theoretical strengths of equivalent bonds.

In the model of equivalent bonds, the theoretical breaking strength σ_{th} of a polycrystalline metallic body is equal to the theoretical strength σ_m of one equivalent bond. Indeed, two neighboring atomic layers are bonded by only the equivalent bonds normal to the layer plane. Breaking a layer off the neighboring layer occurs upon breaking of a number of equivalent bonds equal to the number of atoms in the layer. Therefore, the interlayer strength (the breaking force per layer area) is equal to the strength of one equivalent bond. Thus, the values of the theoretical strength σ_m of equivalent bonds given in Table 2 can be treated as the theoretical breaking strengths σ_{th} of polycrystalline metals.

In the literature, the theoretical strength of metals has been estimated using various methods. These estimates led to an approximate relation between the theoretical strength and Young's modulus, $\sigma_{th} \cong (0.05–0.2)E$ [17, 44]. The calculated values of σ_m (Table 1) also demonstrate general correlation with the Young's modulus of polycrystalline metals (Fig. 4). The averaged line in Fig. 4 has a slope close to 0.1. This finding allows us to conclude that the calculated values of σ_m are reasonable quantitatively. However, as is seen from Eq. (20), the theoretical strength is not related to the Young's modulus explicitly. Nevertheless, the correlation between σ_m and E manifests itself, since the coefficient of linear bond elasticity f enters into Eq. (10) for TEC and α is approximately inversely proportional to f.

Many researchers [44] have studied the micromechanics of metal fracture and revealed the conditions of both brittle and ductile fracture by using dislocation and diffusion processes and by considering crack nucleation and growth. However, many questions remain in the complex process of fracture at a microscopic level regarding both the micromechanics of the process and the relationship between the macro- and microfracture characteristics. It is important for the physics of metal strength to consider the kinetics of

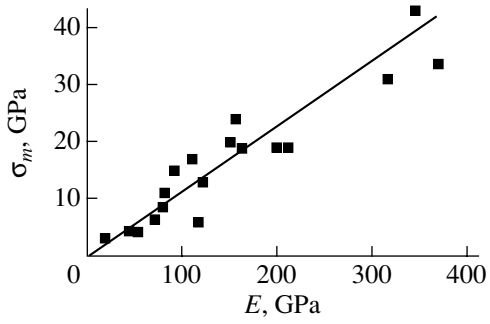

Fig. 4. Correlation between the calculated theoretical breaking strength and Young's modulus for polycrystalline metals.

metal fracture, since data on the life (macroscopic characteristic of fracture) and characteristics, such as the elastic modulus and thermal expansion coefficient, can give information on the microscopic characteristics of fracture (the characteristics of the elementary act of metal fracture). The data obtained (though strongly averaged over elementary acts of the process resulting in fracture of a metallic body) can serve as reference points. Of course, it is still necessary to study the micromechanics of fracture (including elementary acts of metal fracture) in more detail.

REFERENCES

1. S. N. Zhurkov, Vestn. Akad. Nauk SSSR, No. 11, 78 (1957).
2. V. R. Regel', A. I. Slutsker, and É. E. Tomashevskiĭ, *Kinetic Nature of the Strength of Solids* (Nauka, Moscow, 1974) [in Russian].
3. S. N. Zhurkov and T. P. Sanfirova, Zh. Tekh. Fiz. **28** (8), 1720 (1958) [Sov. Phys. Tech. Phys. **3**, 1586 (1959)].
4. S. N. Zhurkov and T. P. Sanfirova, Fiz. Tverd. Tela (Leningrad) **2** (6), 1033 (1960) [Sov. Phys. Solid State **2**, 933 (1960)].
5. T. P. Sanfirova, Candidate's Dissertation (Leningrad, 1961).
6. V. I. Betekhtin, S. N. Zhurkov, and A. V. Savitskiĭ, Fiz. Met. Metalloved. **10** (3), 453 (1960).
7. S. N. Zhurkov and V. I. Betekhtin, Fiz. Met. Metalloved. **25** (5), 940 (1967).
8. V. M. Ilyasov and V. I. Betekhtin, Fiz. Met. Metalloved. **31** (4), 765 (1971).
9. J. Frenkel, *Kinetic Theory of Liquids*, 2nd ed. (Nauka, Leningrad, 1975; Dover, New York, 1955).
10. A. V. Savitskiĭ, Candidate's Dissertation (Physicotechnical Inst., USSR Academy of Sciences, Leningrad, 1966).
11. A. I. Slutsker and Kh. Aĭdarov, Fiz. Tverd. Tela (Leningrad) **25** (3), 777 (1983) [Sov. Phys. Solid State **25**, 444 (1983)].
12. F. R. Bichowsky and F. D. Rossini, *The Thermochemistry of the Chemical Substances* (Reinhold, New York, 1936).
13. A. N. Nesmeyanov, *Vapor Pressure of the Chemical Elements* (Akad. Nauk SSSR, Moscow, 1961; Elsevier, New York, 1963).
14. G. I. Nikolaev and A. M. Nemets, *Atom-Absorption Spectroscopy in Investigations of Metal Evaporation* (Metallurgiya, Moscow, 1982) [in Russian].
15. *Physical Quantities. Handbook*, Ed. by I. S. Grigor'ev and E. Z. Meĭlikhov (Énergoatomizdat, Moscow, 1991) [in Russian].
16. M. Born and M. Goppert-Mayer, in *Handbuch der Physik*, Ed. by H. Geiger and K. Scheel (Springer, Berlin, 1933), Vol. 24, Part 2, p. 623 [*The Theory of Solids* (ONTI, Moscow, 1938)].
17. Ya. I. Frenkel', *Introduction to the Theory of Metals* (GITTL, Moscow, 1948) [in Russian].
18. P. M. Morse, Phys. Rev. **34**, 57 (1929).
19. J. H. de Boer, Trans. Faraday Soc. **32**, 10 (1936).
20. P. P. Kobeko, *Amorphous Substances* (Akad. Nauk SSSR, Moscow, 1952) [in Russian].
21. J. C. Dugdale and D. K. C. MacDonald, Phys. Rev. **96**, 57 (1954).
22. A. G. Gaydon, *Dissociation Energies and Spectra of Diatomic Molecules* (Chapman and Hall, London, 1947; Akad. Nauk SSSR, Moscow, 1949).
23. H. Eyring, S. H. Lin, and S. M. Lin, *Basic Chemical Kinetics* (Wiley, New York, 1980; Mir, Moscow, 1983).
24. Ya. S. Umanskiĭ, B. N. Finkel'shteĭn, M. E. Blanter, S. T. Kishkin, N. S. Fastov, and S. S. Gorelik, *Physical Metallurgy* (Metallurgiya, Moscow, 1955) [in Russian].
25. A. H. Cottrell, *Dislocations and Plastic Flow in Crystals* (Clarendon, Oxford, 1953; Metallurgizdat, Moscow, 1958).
26. R. Berner and H. Kronmüller, *Plastische Verformung von Einkristallen* (Springer, Berlin, 1965; Mir, Moscow, 1968).
27. G. M. Bartenev and Yu. S. Zuev, *Strength and Destruction of Hyperelastic Materials* (Khimiya, Moscow, 1964) [in Russian].
28. A. A. Griffith, Philos. Trans. R. Soc. London, Ser. A **221**, 163 (1921).
29. A. F. Ioffe, M. V. Kirpicheva, and M. A. Levitskaya, Zh. Russ. Fiz.–Khim. O-va, Chast Fiz. **56**, 489 (1924).
30. A. F. Ioffe, *Physics of Crystals* (Gosizdat, Moscow, 1929) [in Russian].
31. E. Poncelet, Colloid Chem. **6**, 77 (1946).
32. A. I. Gubanov and A. D. Chevychelov, Fiz. Tverd. Tela (Leningrad) **4** (5), 928 (1962) [Sov. Phys. Solid State **4**, 681 (1962)].
33. A. D. Chevychelov, Fiz. Tverd. Tela (Leningrad) **5** (8), 1394 (1963) [Sov. Phys. Solid State **5**, 1013 (1963)].
34. W. Kauzmann and H. Eyring, J. Am. Chem. Soc. **62** (7), 3113 (1940).
35. A. N. Orlov, Yu. M. Plishkin, and M. M. Shepeleva, Fiz. Met. Metalloved. **4** (3), 540 (1957).
36. Yu. M. Plishkin, Tr. Inst. Fiz. Met. (Sverdlovsk), No. 22, 13 (1959).

37. É. E. Tomashevskiĭ, Fiz. Tverd. Tela (Leningrad) **12**, 3202 (1970) [Sov. Phys. Solid State **12**, 2588 (1970)].
38. A. I. Mel'ker and A. I. Mikhaĭlin, Fiz. Tverd. Tela (Leningrad) **26** (4), 1236 (1984) [Sov. Phys. Solid State **26**, 753 (1984)].
39. S. N. Zhurkov, V. I. Vettegren', V. E. Korsukov, and I. I. Novak, Fiz. Tverd. Tela (Leningrad) **11** (2), 290 (1969) [Sov. Phys. Solid State **11**, 233 (1969)].
40. V. A. Zakrevskii and A. V. Shuldiner, Philos. Mag. B **71** (2), 127 (1995).
41. A. V. Shuldiner and V. A. Zakrevskii, J. Phys.: Condens. Matter **14**, 9555 (2002).
42. I. I. Afanas'ev, O. L. Volkova, K. V. Naumov, and B. I. Smirnov, Fiz. Tverd. Tela (Leningrad) **27** (10), 2826 (1985) [Sov. Phys. Solid State **27**, 1704 (1985)].
43. F. Appel, H. Bethge, and U. Messercshmidt, Phys. Status Solidi A **38**, 103 (1976).
44. *Atomic Mechanism of Destruction: Proceedings of International Conference on Problems of Destruction* (USA, 1959; Moscow, 1963).

Translated by K. Shakhlevich

Physics of the Solid State, Vol. 46, No. 9, 2004, pp. 1667–1670. Translated from Fizika Tverdogo Tela, Vol. 46, No. 9, 2004, pp. 1614–1617.
Original Russian Text Copyright © 2004 by Tyalin, Tyalina, Fedorov, Chemerkina, Butyagin.

DEFECTS, DISLOCATIONS, AND PHYSICS OF STRENGTH

Healing of Cracks in Alkali Halide Crystals

Yu. I. Tyalin, V. A. Tyalina, V. A. Fedorov, M. V. Chemerkina, and A. A. Butyagin

Tambov State University, Internatsional'naya ul. 33, Tambov, 392622 Russia

e-mail: feodorov@tsu.tmb.ru

Received January 23, 2004

Abstract—The healing of micro- and macrocracks under local heating and x-ray irradiation of LiF single crystals is studied. The main features revealed in crack healing due to local actions are described. The contribution of the plastic zone formed upon the arrest and healing of a crack to the strength of the crystal is estimated. *© 2004 MAIK "Nauka/Interperiodica".*

1. INTRODUCTION

At present, there are many publications concerned with the crack healing predominantly observed in ionic crystals with clearly defined cleavage planes [1]. In particular, Grdina and Neverov [2] described the main features revealed in the healing of cracks under compression loads. Finkel' and Sergeeva [3] and Fedorov *et al.* [4] investigated the crack self-healing upon the arrest of a crack and fast unloading of the sample, for example, through lateral chipping off the crystal. Special attention was paid to the influence exerted by external factors (heating, electric field) on the recovery of the continuity of crystals and their strength properties [5].

In this work, we analyzed the possibility of healing a crack in LiF crystals under conditions where the crack tip is subjected to a local mechanical load. The local load was applied to the crack tip by way of heating or x-ray irradiation of the material in the immediate vicinity of the crack tip. In the loaded region, there arise compressive stresses, which can be used to recover the continuity disturbed under the load. The difference between these schemes of loading the samples lies in the fact that heat stresses disappear upon cooling of the sample, whereas the stresses induced during irradiation can persist in the crystal over a long period of time and keep the crack closed even in the case when the continuity of the material remains disturbed.

In this respect, the main objectives of the present work were (i) to choose the regimes and schemes of local action on a crack tip in such as way as to ensure recovery of the continuity of the material at the crack tip and (ii) to develop an appropriate method for directly measuring the strength of the samples with a healed crack and to perform these measurements.

2. SAMPLE PREPARATION AND EXPERIMENTAL TECHNIQUE

Prismatic samples $3 \times 8 \times 40$ mm in size were cleaved from large blocks of LiF single crystals along the cleavage planes. An incipient crack of length L = 20–30 mm was formed in the (001) plane. The crack was symmetric with respect to the larger face of the sample.

The dislocation structure of the tip of the arrested crack was revealed by chemical etching of the sample in an aqueous solution of ferric chloride $FeCl_3$. For chemical etching, we used only the freshly cleaved surfaces of the sample. For this purpose, the initial sample was split into two parts along the (100) plane: one part of the sample was used to observe the initial dislocation structure at the crack tip, and the other part was used to reveal a structure formed at the crack tip after healing.

The required length of the crack to be studied was attained through intermittent propagation of the crack under a small impact load. A single jump of the crack was equal to 2–3 mm. This character of crack propagation provided the formation of slip lines in the form of a specific dislocation cross at points where the crack was arrested.

Crack healing was accomplished using three schemes: local heating, irradiation, and compression. For local heating of the samples, we used a copper rod 4 mm in diameter. The temperature of the copper rod was varied in the range from 100 to 350°C. This scheme provided one-sided and two-sided heating of the samples. In the second scheme, the samples were irradiated on a DRON-2 diffractometer at a tube voltage of 25–30 kV and a current of 8–10 mA. These parameters of the irradiation correspond to a dose of 0.05 R/s. In the third scheme, the samples were compressed under a load of up to 20 N either with the use of a prism or in a cramp. In some experiments, the action on the sample was combined: a slightly compressed sample was locally heated in the region of the crack tip.

A number of experiments were carried out with microcracks formed upon indentation on the surface of the crystals [6]. Such microcracks are penny-shaped and lie in the (110) planes. In these experiments, the length of cracks was measured by the optical method before and after the indentation.

1063-7834/04/4609-1667$26.00 © 2004 MAIK "Nauka/Interperiodica"

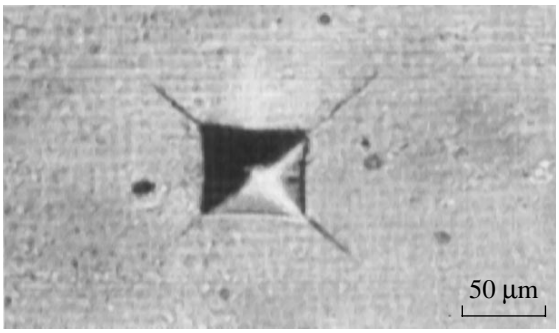

Fig. 1. Microcracks formed under indentation with a Vickers pyramid.

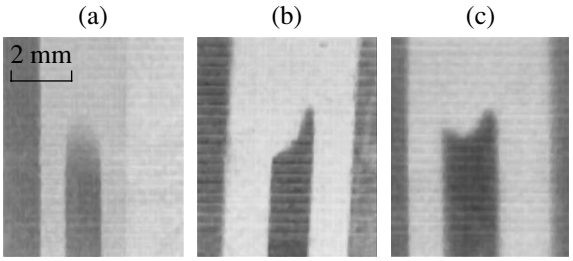

Fig. 2. Fronts of the initial and healed cracks: (a) the initial crack, (b) the crack after one-sided heating, and (c) the crack after two-sided heating.

The quality of the healing of macrocracks was evaluated by mechanical testing of the samples with initial and healed cracks. In this case, first, we measured the crack length L and the critical breaking load F. Then, these data were used to determine the intensity factor of crack tip stresses from the relationship [7]

$$K_1 = \frac{2\sqrt{3}LF}{wh\sqrt{h}},$$

where h is the half-width of the sample and w is the thickness of the sample.

3. RESULTS AND DISCUSSION

3.1. Healing of Microcracks

Microcracks were formed upon indentation with loads of 0.5, 1.0, and 2.0 N. At these loads, the characteristic size of the cracks was equal to 20–60 μm (Fig. 1). Initially, there were only a few incipient microcracks in a small region. Then, this region was subjected to either heating or x-ray irradiation through a lead mask with an aperture 2 mm in diameter. The crack sizes were measured before and after the exposure. We did not observe a variation in the length of microcracks upon local heating. However, under x-ray irradiation, the sizes of microcracks slightly decreased (see table).

The samples were irradiated for 2 h. No effect was observed at shorter exposures (of the order of 10^3 s). Therefore, the healing should be enhanced with an increase in the irradiation dose. Since no crack healing was revealed upon local heating, the microcracks formed upon indentation are fairly stable. This can be associated with the geometry of the {110} surface of the cracks, which is not a cleavage plane. The cracks in these planes have a well-developed surface relief inhibiting the healing. Chemical etching of the irradiated samples did not reveal grooves typical of regions with healed cracks. This suggests that, in the case under consideration, there occurs only a visual decrease in the crack size (optical contact is regained).

Changes in the microcrack size (μm) under local irradiation

a	91	77	79	65	42	103	112	78	161	148	124	192
b	82	70	79	65	39	91	108	75	155	140	123	184

Note: *a* is the size of the microcrack before irradiation, and *b* is the size of the microcrack after irradiation.

3.2. Healing of Macrocracks

As a rule, upon single-stage heating of a sample, the initial crack closes within a segment with a size of the order of the loaded region (2–3 mm). Most frequently, the crack is completely healed along the whole length of this segment. The front of the initial crack is not rectilinear but is slightly concave toward the crack propagation. As the thickness of the sample increases, the front of the crack straightens out but the oval form is retained for crystals of all sizes used in our experiments (Fig. 2a).

In some experiments, the samples were subjected to one-sided heating. The specific features of the crack healing upon one-sided heating are illustrated in Fig. 2b. It can be seen that the crack is not uniformly healed in the bulk of the sample.

The healed crack segment adjacent to the heating rod is longer than that located deep in the bulk or at the opposite end of the sample. As the thickness of the sample increases, the healing of cracks becomes more nonuniform. More effective healing is provided by two-sided heating of the sample (Fig. 2c). In this case, the sample is more uniformly heated in the bulk and the whole tip of the crack occurs in the zone of compressive stresses. It should be noted that the front of the crack healing is concave away from the initial crack. This can be associated with the fact that the contours of the opposite edges of the crack at the center of the sample coincide with each other more closely than those at the periphery of the sample. Microcleavages that are more frequently observed at the periphery of the sample can inhibit the edges of the crack from approaching each other and, thus, prevent crack healing.

An attempt was made to heal a crack in a large region. To accomplish this, the heating area was gradu-

ally shifted toward the origin of the crack during healing. A fragment of the healed crack is shown in Fig. 3. It can be seen that the healing is not as perfect as in the first case. The quality of the healing is reduced away from the crack tip. It is worth noting that unhealed segments of the crack are observed both at the periphery and at the center of the sample.

When the temperatures of heating are not very high and in the case of "hard" crystals, the crack closes as a result of the reversible slip along the same bands and lines that are formed at the arrest of the crack. This is not attended by the formation of new zones of plastic deformation. In "soft" crystals and at high temperatures of heating, the heated regions undergo a severe deformation. This is accompanied not only by an increase in the size of the slip bands at the tip of the initial crack but also by a plastic deformation in the region of thermal contact along the other slip planes.

Analysis of the etch patterns of the samples with healed cracks demonstrates that, in the majority of the studied samples, crack healing restores not only the optical contact but also the adhesion between the opposite edges of the crack. The quality of the healing in the regions adjacent to the tip of the crack is higher than that in the regions away from it. In some cases, chemical etching revealed only a few pits on the track of the healed crack (Fig. 4). It is assumed that these pits are formed through local plastic compression of asperities of subatomic size (Fig. 5).

The number of asperities increases away from the crack tip. There arise groups of etch pits and single etch grooves. As a result, the total number of relief macroasperities so large that their healing necessitates substantially increased stresses in the loaded region. However, these stresses will give rise to strains not only in the vicinity of the crack but also in the whole volume of the crystal. In our experiments, we did not reach such large loads and restricted our measurements to the range of stresses that did not cause an appreciable strain of the sample as a whole.

It is of interest to evaluate the degree to which the strength properties of the crystals can be recovered. For this purpose, samples with a healed crack were broken according to the scheme of a normal rupture. In this case, we measured the critical breaking load F for a sample with a crack of specified length. The results of these experiments for two sets of samples with initial and healed cracks are presented in Fig. 6.

It should be noted that the breaking load for a sample with a healed crack is larger than that for a sample with an unhealed crack. Figure 6 shows the dependences of the breaking load on the length of the initial healed and unhealed cracks. The main and obvious factor behind the above difference between the breaking loads is the decrease in the length of the crack upon healing. This is associated with the fact that, in some cases, the length L of a healed crack cannot be determined precisely because the front of this crack is far from rectilinear.

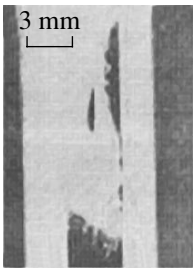

Fig. 3. Surface of the healed crack after repeated local heating.

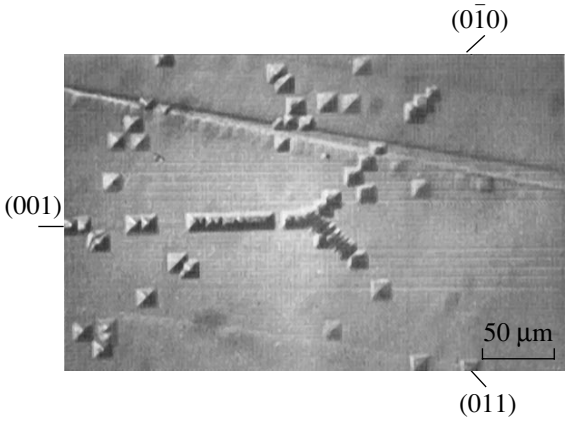

Fig. 4. Dislocation structure of the tip of the healed crack.

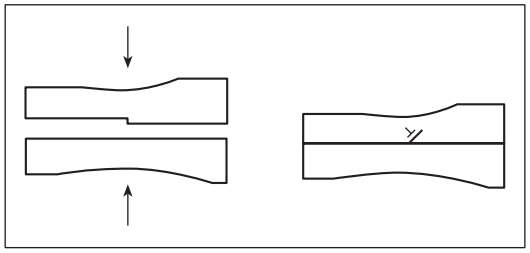

Fig. 5. Schematic diagram illustrating the formation of etch pits along the trajectory of the healed crack.

However, the effective healing length ΔL, which is determined from the change in the critical breaking load, as a rule, somewhat exceeds the mean value of ΔL obtained in the experiment. In other words, apart from the decrease in the length of the crack, there is another factor that causes a certain hardening of the samples with a healed crack. In particular, this hardening can be caused by the interaction of the crack with a plastic zone formed upon the arrest and healing of this crack.

The plastic zone can be represented in the form of two slip lines in the $(0\bar{1}1)$ and (011) half-planes (facing

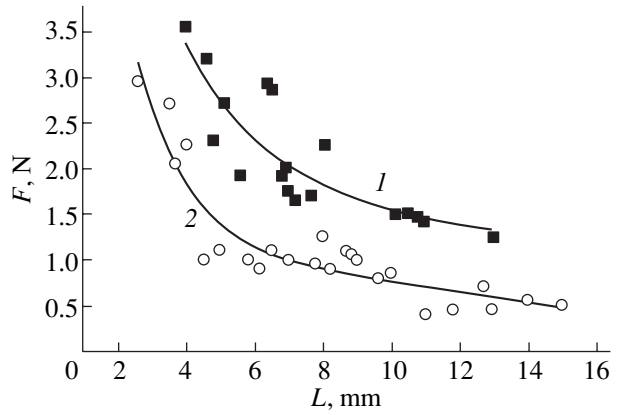

Fig. 6. Critical breaking load F for samples with (*1*) a healed crack and (*2*) an unhealed crack.

the origin of the crack) and a disclination dipole at the tip of the healed crack in the (001) plane. Then, the change in the intensity factor of crack tip stresses ΔK_1 due to elastic stresses in the plastic zone can be written in the form

$$\Delta K_1 = \frac{2\sqrt{3}L}{wh\sqrt{h}} \int_{\Delta L}^{\Delta L + L} \sigma_{xx}(x)dx,$$

where σ_{xx} are the stresses at the edges of the crack and ΔL is the length of the healed region. Under the condition $l < \Delta L\sqrt{2}$ (l is the length of the slip line), which is satisfied almost without exception in the case of spontaneous arrest of the crack [8], the stresses σ_{xx} are compressive stresses. The change in the factor ΔK_1 can be represented in the form

$$\Delta K_1 = \frac{2\sqrt{6}LAn}{wh\sqrt{h}} \ln\left(1 + \frac{L}{\Delta L}\right)\alpha,$$

where $A = Gb/2\pi(1 - \nu)$, G is the shear modulus, b is the Burgers vector of dislocations, ν is the Poisson ratio, n is the number of dislocations in the slip line, and α is the numerical coefficient determined by the geometry of the plastic zone ($\alpha < 1$).

For a sufficiently large number of dislocations in the slip line ($n > 100$), the change in the intensity factor of crack tip stresses ΔK_1 can be as great as several tens of percent. The hardening effect can give way to the softening effect in the case of other modes of crack arrest when the plastic flow is more pronounced in the $(0\bar{1}1)$ and (011) half-planes lying in front of the crack tip.

ACKNOWLEDGMENTS

This work was supported by the Russian Foundation for Basic Research, project no. 02-01-01173.

REFERENCES

1. M. P. Shaskol'skaya, Van-Yan-En, and Gu-Ju-Jao, Kristallografiya **6** (4), 605 (1961) [Sov. Phys. Crystallogr. **6**, 483 (1962)].
2. Yu. V. Grdina and V. V. Neverov, Kristallografiya **12** (3), 493 (1967) [Sov. Phys. Crystallogr. **12**, 421 (1967)].
3. V. M. Finkel' and O. G. Sergeeva, Fiz. Tverd. Tela (Leningrad) **29** (3), 857 (1987) [Sov. Phys. Solid State **29**, 489 (1987)].
4. V. A. Fedorov, T. N. Pluzhnikova, and Yu. I. Tyalin, Fiz. Tverd. Tela (St. Petersburg) **42** (4), 685 (2000) [Phys. Solid State **42**, 703 (2000)].
5. V. A. Fedorov, L. G. Karyev, A. M. Nikolyukin, and V. P. Ivanov, Fiz. Tverd. Tela (St. Petersburg) **38** (2), 664 (1996) [Phys. Solid State **38**, 370 (1996)].
6. V. A. Fedorov and L. G. Karyev, in *Abstracts of XIV International Conference on Physics of the Strength and Plasticity of Materials* (Samara, 1995), p. 72.
7. G. P. Cherepanov, *Mechanics of Brittle Fracture* (Nauka, Moscow, 1974; McGraw-Hill, New York, 1979).
8. Yu. I. Tyalin, V. A. Fedorov, T. N. Pluzhnikova, and V. A. Kuranova, Fiz. Tverd. Tela (St. Petersburg) **42** (7), 1253 (2000) [Phys. Solid State **42**, 1290 (2000)].

Translated by O. Moskalev

Physics of the Solid State, Vol. 46, No. 9, 2004, pp. 1671–1673. Translated from Fizika Tverdogo Tela, Vol. 46, No. 9, 2004, pp. 1618–1620.
Original Russian Text Copyright © 2004 by Golovin, Ivolgin, Lebedkin, Sergunin.

DEFECTS, DISLOCATIONS, AND PHYSICS OF STRENGTH

Regions of the Portevin–Le Chatelier Effect Existing under the Conditions of Continuous Room-Temperature Indentation of an Al–2.7% Mg Alloy

Yu. I. Golovin*, V. I. Ivolgin*, M. A. Lebedkin, and D. A. Sergunin***

** Tambov State University, Internatsional'naya ul. 33, Tambov, 392622 Russia*

e-mail: golovin@tsu.tmb.ru

*** Institute of Solid-State Physics, Russian Academy of Sciences, Chernogolovka, Moscow oblast, 142432 Russia*

Received January 27, 2004

Abstract—Dynamic indentation is used to study the character of a plastic flow during room-temperature deformation of an Al–2.7% Mg alloy in micro- and submicrovolumes (the indentation depth is varied from 50 nm to 15 μm) at strain rates varying in the range 0.0005–1 s^{-1}. In this region of parameters, the boundaries of stable deformation and two modes of unstable deformation have been found. © *2004 MAIK "Nauka/Interperiodica".*

INTRODUCTION

Aluminum–magnesium alloys are classic examples of materials that can exhibit various plastic-flow instability modes [in particular, the Portevin–Le Chatelier (PLC) effect] during deformation [1–8]. The processes of self-organization in dislocation ensembles, which are still poorly understood, are of fundamental interest, since the macroscopic properties of materials can be predicted using extensive knowledge on the dynamics of isolated defects.

From the practical standpoint, it is important that the PLC effect causes deformation localization and a large number of deformation bands (Lüders bands); as a result, a smooth surface becomes rough. Al–Mg alloys are widely applied as materials for disposable food packaging (cans, tubes, etc.) and are promising materials for use in the automotive industry (car bodies and internal and external coverings) [9], where rough surfaces of manufactured parts are unacceptable. Therefore, the problem of determining the boundaries of deformation modes that separate the regions of stable and unstable plastic flows is of particular importance. These boundaries are usually found by testing macroscopic samples at various temperatures and strain rates [2–5]. Such tests, however, are labor- and material-consuming.

The method of mechanical testing where a small, continuously increasing load is applied to a well-certified diamond indenter (nanoindentation, or depth-sensing testing) has recently attracted considerable interest. It consists in continuous recording of the load $P(t)$ applied to the indenter and of the indentation depth $h(t)$ with a resolution of ~1 nm. These data are used to plot a P–h loading diagram (which is an analog of a σ–ε diagram for uniaxial testing), which is then analyzed [10–12]. It is very tempting to substitute nondestructive tests for macroscopic tests of destructive samples using only local deformation.

Unlike tension/compression, nanoindentation makes it possible to localize plastic deformation in a submicron or micron zone and to vary its dimension R (R is usually taken to be equal to h) and the strain rate $\dot{\varepsilon} = dh/hdt$ by several orders of magnitude within one test cycle. The modern methods of dynamic nanoindentation can vary the deformed zone from virtually atomic to macroscopic sizes in one cycle by applying a load that is continuously varied from zero. Because of this specific feature, mechanical properties are automatically scanned through the plastically deformed zone, which substantially increases the efficiency and accuracy of mechanical tests. Moreover, multiple tests of the same sample make it possible, if necessary, to accumulate huge statistical experimental data (e.g., on serrated deformation) and to analyze them by modern processing methods (multifractal, spectral, and other methods of analysis).

However, it is unclear how the substitution of nanoindentation for mechanical macroscopic tests affects the physical mechanisms and phenomenology of the development of flow instabilities. In particular, various plastic-flow instabilities, which reflect the self-organization and collective behavior of a large number of structural defects, will inevitably change character as the characteristic sizes of the deformation zone decrease to values that can be comparable, e.g., to the conventional sizes of dislocation pileups.

In this work, we studied the regions of various modes of plastic-flow instabilities, including the PLC effect, depending on the size of the deformed zone and the strain rate in an Al–2.7% Mg alloy (comprehensively studied by mechanical macroscopic tests) under

1063-7834/04/4609-1671$26.00 © 2004 MAIK "Nauka/Interperiodica"

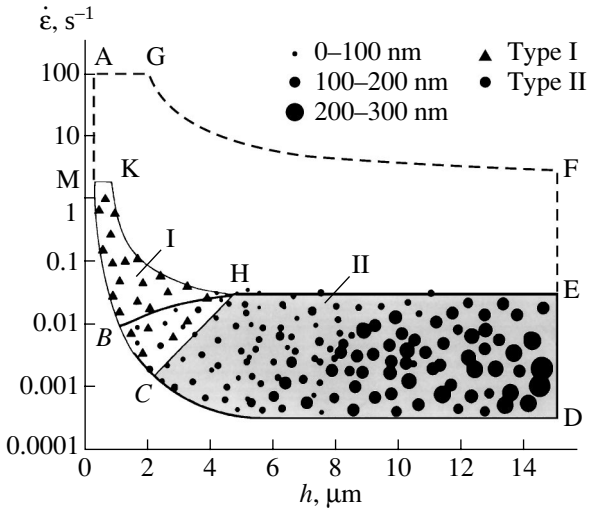

Fig. 1. Regions of jumps of types I and II with an amplitude Δh observed during indentation of the Al–2.7% Mg alloy.

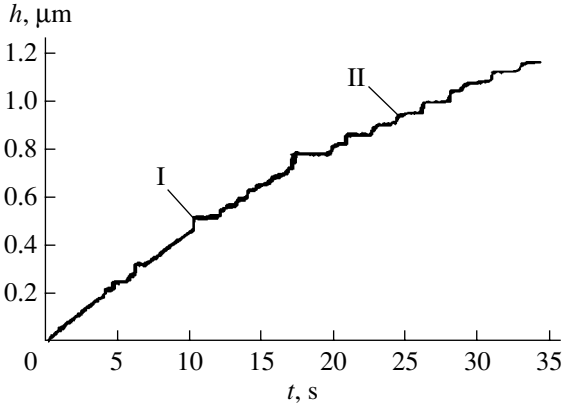

Fig. 2. Instabilities of types I and II in the transition region observed under a linearly increased load.

a load that linearly increases with time at room temperature.

Indentation measurements were performed on a unique device, which allowed us to record a *P*–*h* diagram with a *P* resolution of ~1 mN, an *h* resolution of ~1 nm, and a time resolution of $t \sim 50$ μs. Samples of the Al–2.7% Mg alloy 8 × 5 × 40 mm in size were spark-cut from rolled sheets. The samples were mechanically polished with a paste having a grain size of 3–5 μm, annealed at 450°C for 2 h, and then water-quenched. In our previous work [13], we found that deformation jumps during nanoindentation of the Al–3% Mg alloy can be divided into two types: irregular jumps with steep edges (<50 μs) (type I) and regular slow jumps with edges >10–100 ms (type II). The results of this work allowed us to determine kinematic conditions of the appearance of instabilities and to refine the boundaries of their regions (Fig. 1). The diagram in Fig. 1 was plotted after processing more than 400 measurements performed on the same sample in a wide range of loading rates (about four orders of magnitude) at indentation depths of 0.05–15 μm with Berkovich and Vickers indenters. Contour ABCDEFGA shows the region of variables *h* and $\dot{\varepsilon}$ studied by us.

In most cases, the unstable type-I plastic flow (MKHBM region) is detected at small indentation depths (from ~0.05 to 2–4 μm). As a rule, the number of such jumps is small (from several to several dozen) and their coordinates in the h–$\dot{\varepsilon}$ pseudophase diagram are strongly scattered. Ordinarily, a substantial portion of the curve in this mode corresponds to stable deformation.

The type-II instability, which is characterized by a linear dependence of the deformation-jump height on the indentation depth [13], is limited by contour EHBCDE. This region is bounded from above on $\dot{\varepsilon}$ by curve BE, which becomes virtually horizontal at $h > 4$–5 μm. In segment EH, the critical strain rate corresponding to a change of the plastic-flow modes is $\dot{\varepsilon}_c \cong 0.05\ \text{s}^{-1}$. At $h < 3$–4 μm, the value of $\dot{\varepsilon}_c$ decreases smoothly. Since the region below curve ABCD cannot be reached experimentally, the position of point B is dictated by the technical capabilities of the equipment; this point is likely to move below 1 μm when the strain rate decreases at these depths.

In intermediate region BCH, jumps of both types occur; as *h* increases, instabilities of type II substituted for type-I jumps (Fig. 2).

It should be noted that nanoindentation did not reveal a noticeable dependence of the results, including the positions of the instability boundaries, on the type of pyramid indenter employed (Berkovich or Vickers indenter).

The results obtained allow us to make some conclusions regarding the nature of instabilities observed during dynamic indentation. Instabilities of types I and II are most likely controlled by different microscopic mechanisms. A type-I instability may be due to static pinning of dislocations. This conclusion is supported by the presence of steep jump edges and a horizontal plateaus (Fig. 2), which can be related to the action of a system of obstacles hindering dislocation motion under certain conditions (depth *h* does not increase) until a certain critical stress is reached. This stress should be determined by the strength and volume distribution of the obstacles that appear in the Al–Mg alloy upon rolling and subsequent quenching. We can use this conclusion to explain the random appearance of this type of instability, which manifests itself in both the indentation-depth jump and the related increase in the load.

An instability of type II is most likely determined by dynamic strain aging due to the interaction of dislocations with impurity Mg atoms (Cottrell atmospheres). This conclusion is supported by the change in the jump shapes. The rise time of the jumps is much longer than

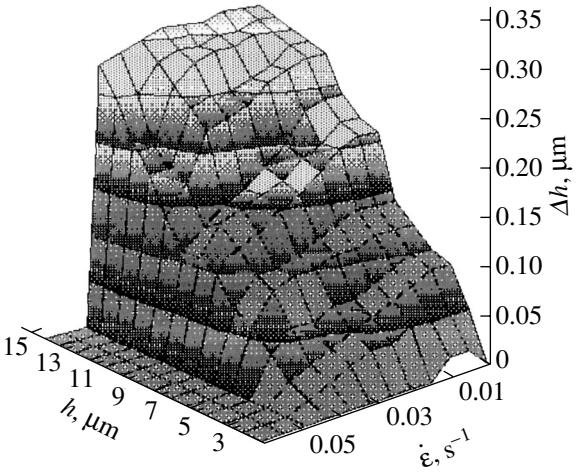

Fig. 3. Three-dimensional region of type-II jumps observed during continuous indentation of the Al–2.7% Mg alloy.

the rise time of type-I jumps and corresponds to the time of motion of dislocations with impurity clouds, and the flat segments of the slow increase in h correspond to the breakaway of dislocations from impurity clouds (which causes more rapid dislocation motion). An additional argument for the mechanism of strain aging is the presence of a critical strain rate determining the upper limit of this mode ($\dot{\varepsilon}_c \approx 0.05\ s^{-1}$). This value virtually coincides with the analogous value measured upon uniaxial tension of macroscopic samples of the Al–Mg alloy in "soft" tension testing machines [14–16], where this mechanism is believed to be most probable. In terms of this model of the PLC effect, the regularity of the instability is due to a uniform impurity distribution, which is provided by proper heat treatment of the alloy. The independence of $\dot{\varepsilon}_c$ from h in the greater part of the h range under study, as well as the almost linear increase in Δh with h (Fig. 3), indicates that the critical quantity for the formation of a jump is a certain overstress at the jump leading edge: $\Delta\sigma \approx \Delta P/24.5h^2 \approx 0.05\Delta P/24.5h^2 \approx 0.05\langle\sigma\rangle$, where $\langle\sigma\rangle$ is the average contact pressure at the indentation surface or, what is the same, the microhardness HV [17].

The character of the plastic flow in the transition region is determined by the competition between these two types of instability. As the average rate $\dot{\varepsilon}$ decreases (with increasing indentation depth h in the case of a linear increase in the load), a type-II instability becomes dominant.

Thus, using continuous indentation, we have found the boundaries of various plastic-flow modes that occur during local deformation of the Al–Mg alloy. The fact that the critical value $\dot{\varepsilon}_c$ (characterizing the transition from an unstable to a stable flow) for a local test at $h >$ 3–4 μm coincides with the analogous critical value as determined upon uniaxial macroscopic tests indicates that the nature of the instability in both cases is caused by internal microscopic factors rather than by the scheme of loading. This finding gives grounds to hope that, if necessary, it will be possible to replace labor- and material-consuming macroscopic tests with dynamic microindentation in order to measure structural characteristics of such alloys and the boundaries of instabilities of the PLC type.

ACKNOWLEDGMENTS

This work was supported by the Russian Foundation for Basic Research (project nos. 01-02-16573, 00-15-96703) and the Ministry of Education of the Russian Federation (project no. E02-3.4-263).

REFERENCES

1. L. P. Kubin and Y. Estrin, Acta Metall. **33** (3), 397 (1985).
2. M. Lebyodkin, Y. Brechet, Y. Estrin, and L. Kubin, Acta Mater. **44**, 4531 (1996).
3. B. J. Brindley and P. J. Worthington, Metall. Rev. **15**, 101 (1970).
4. A. W. McReinolds, Met. Trans. **32** (1949).
5. L. P. Kubin and Y. Estrin, Acta Metall. Mater. **38** (5), 697 (1990).
6. R. B. Schwarz and L. L. Funk, Acta Metall. **33** (2), 295 (1985).
7. P. R. Cetlin, A. S. Gulec, and A. R. Reed-Hill, Metall. Trans. **4** (2), 513 (1973).
8. G. Berges, N. Q. Chinh, A. Juhash, and J. Lendvai, Acta Mater. **46** (6), 2026 (1998).
9. I. N. Fridlyander, V. G. Sister, O. E. Grushko, V. V. Berestenev, L. M. Sheveleva, and L. A. Ivanova, Metalloved. Term. Obrab. Met., No. 9, 3 (2002).
10. Yu. I. Golovin, A. I. Tyurin, V. I. Ivolgin, and V. V. Korenkov, Zh. Tekh. Fiz. **70** (5), 82 (2000) [Tech. Phys. **45**, 605 (2000)].
11. W. C. Oliver and G. M. Pharr, J. Mater. Res. **7** (6), 1564 (1992).
12. N. X. Randall, C. Julia-Schmutz, J. M. Soro, *et al.*, Thin Solid Films **308–309**, 297 (1997).
13. Yu. I. Golovin, V. I. Ivolgin, and M. A. Lebedkin, Fiz. Tverd. Tela (St. Petersburg) **44** (7), 1254 (2002) [Phys. Solid State **44**, 1310 (2002)].
14. A. Zeghloul, M. Mliha-Touati, and S. Bakir, J. Phys. **3** (6), 1467 (1966).
15. M. M. Krishtal, Fiz. Met. Metalloved. **80** (12), 140 (1990).
16. M. M. Krishtal, Zavod. Lab. **65** (1), 35 (1999).
17. S. I. Bulychev and V. P. Alekhin, *Testing Materials Under Continuous Indentation* (Mashinostroenie, Moscow, 1990) [in Russian].

Translated by K. Shakhlevich

Physics of the Solid State, Vol. 46, No. 9, 2004, pp. 1674–1680. Translated from Fizika Tverdogo Tela, Vol. 46, No. 9, 2004, pp. 1621–1627.
Original Russian Text Copyright © 2004 by Filippov, Bichurin, Petrov, Laletin, Srinivasan.

MAGNETISM AND FERROELECTRICITY

Resonant Amplification of the Magnetoelectric Effect in Ferrite–Piezoelectric Composites

D. A. Filippov*, M. I. Bichurin*, V. M. Petrov*, V. M. Laletin, and G. Srinivasan*****

**Novgorod State University, ul. Sankt-Peterburgskaya 41, Novgorod, 173003 Russia*

***Institute of Technical Acoustics, Belarussian Academy of Sciences, pr. Lyudnikova 13, Vitebsk, 210717 Belarus*

****Physics Department, Oakland University Rochester, Michigan, 48309 USA*

Received October 28, 2003; in final form, December 16, 2003

Abstract—The magnetoelectric effect in ferrite–piezoelectric composites is considered. A theory of the magnetoelectric effect in the electromechanical-resonance region for disk-shaped samples is presented. The magnetooptical coefficient is calculated for longitudinal and transverse orientations of electric and magnetic fields. It is shown that the effect increases by a few orders of magnitude at the electromechanical-resonance frequency. The frequency dependence of the effect is experimentally studied for a ferrite-nickel spinel–PZT composite. A resonant increase in the effect is observed (in agreement with the theory); the highest value of the magnetoelectric coefficient was 15 V/(cm Oe). © *2004 MAIK "Nauka/Interperiodica".*

1. INTRODUCTION

The magnetoelectric (ME) effect consists in the initiation of polarization under a magnetic field and, vice versa, in the initiation of magnetization under an electric field. In magnetoelectric crystals, the mechanism of this effect is the joint action of the spin–orbit coupling and the interaction of a magnetoactive ion with the antisymmetric part of the crystalline potential and the external electric field [1, 2]. In ferrite–piezoelectric composites, the ME effect can be absent in individual ferrite and piezoelectric components and appears due to mechanical interaction between the ferrite and piezoelectric subsystems. In a magnetic field, mechanical stresses arise in the magnetic subsystem due to magnetostriction and are transferred to the piezoelectric phase, where they produce an electric field due to the inverse piezoelectric effect. The ME effect in such composites is a secondary effect or a so-called "product property" [3].

Macroscopically, composite materials can be characterized by effective parameters, such as the effective elastic moduli, piezoelectric effect, and magnetostriction. It is clear that these effective parameters can be defined in terms of the parameters of the ferrite and piezoelectric components, their proportions, and the degree of connectivity. The effective parameters characterizing a material can be used if the characteristic scales of changes in external influences are much larger than the sizes of the building blocks. For the layered materials in question, these sizes are the thicknesses of the ferrite and piezoelectric layers. Since these sizes for layered and bulk composite materials are typically ~10 μm, the effective parameters can be used to describe the propagation of mechanical vibrations up to frequencies of the order of hundreds of megahertz.

In ferrite–piezoelectric composites, the ME effect is associated with the mechanical interaction of the subsystems; therefore, a significant increase in the magnetoelectric coefficient will be observed in the vicinity of electromechanical resonance. This effect was indicated for the first time in [4, 5]. The magnetoelectric coefficient was measured in bulk rod-shaped composite materials at the resonant frequency in [6]; however, the resonance was used in [6] only as a method for separating the signal from the background; neither a theoretical nor a detailed experimental study was carried out. The frequency dependence of the effect in the region of the electromechanical resonance was experimentally studied in [7]. Rectangular samples based on terphenol and lead zirconate-titanate (PZT) were studied. At a frequency of 59.8 kHz, the magnetoelectric coefficient was as large as 8.7 V/(cm Oe) in a dc magnetic field of 0.7 kOe. In [8], the frequency dependence of the ME effect for plate-shaped samples in the range of sonic frequencies was theoretically described for the first time and experimental results for ferrite-nickel spinel–PZT composites were presented. The magnetoelectric coefficient was calculated for transverse and longitudinal electric and magnetic fields in terms of the effective parameters of the composite. It was shown that the magnetoelectric coefficient increases more than tenfold at the antiresonance frequency. However, disk-shaped (rather than plate-shaped) samples are more often used in practice. The theory of the ME effect in ferrite–piezoelectric composites for disk-shaped samples is briefly presented in [9]. However, the magnetoelectric coefficient is calculated only for longitudinal electric and magnetic fields. In practice, the effect under transverse fields is generally tenfold stronger than under longitudinal fields. Currently, there is no theoretical

description of the ME effect in the region of the electromechanical resonance under transverse fields.

In this paper, we initially give a detailed theoretical description of the ME effect in the range of sonic frequencies in terms of effective parameters. The case of longitudinal and transverse magnetic fields is considered for disk-shaped samples. The frequency dependence of the magnetoelectric coefficient is found theoretically in the region of the electromechanical resonance. For specific samples of ferrite-nickel spinel–PZT composites, the frequency dependence of the magnetoelectric coefficient is calculated and compared with experimental results.

2. MODEL AND BASIC EQUATIONS

Let us consider a ferrite–piezoelectric composite sample shaped as a thin disk of radius R and thickness d with thin metal contacts deposited onto its bottom and top surfaces (Fig. 1).

Let the sample be polarized along the normal to the contact planes (z axis). A dc (bias) and an ac magnetic field can be directed either along the normal to the contact plane or in the contact plane. Therefore, we will consider the cases of longitudinal and transverse fields. Due to magnetostriction, the ac magnetic field causes vibrations to propagate over the sample thickness and radius (thickness and radial vibrations, respectively). In what follows, we will restrict our consideration to the lowest frequency radial vibrations, since they are the easiest to observe. Thickness vibrations have higher frequencies and are more difficult to separate from higher harmonics of radial vibrations.

Let the disk be thin, i.e., $d \ll R$. Since the disk surfaces are free, the normal components of the stress tensor are zero. For a thin disk, the component T_3 of the stress tensor can be considered to be zero not only at the surface but also in the entire volume. Moreover, the top and bottom disk surfaces are equipotential; therefore, only the z component of the electric field will be nonzero. Thus, in the case of longitudinal fields, the strain tensor S_i and the z component D_z of the electric induction vector satisfy the equations

$$\begin{aligned} S_1 &= s_{11}T_1 + s_{12}T_2 + d_{31}E_3 + q_{31}H_3, \\ S_2 &= s_{12}T_1 + s_{22}T_2 + d_{31}E_3 + q_{31}H_3, \\ D_3 &= \varepsilon_{33}E_3 + d_{31}(T_1 + T_2) + m_{33}H_3, \end{aligned} \tag{1}$$

where s_{ij} are the effective compliances of the composite; d_{ij} and q_{ij} are the effective piezoelectric and piezomagnetic moduli, respectively; ε_{ij} is the effective permittivity; and E_i and H_i are the components of the electric and magnetic field vectors. The procedure for calculating the effective parameters of a composite is given in [10].

In the case of transverse electric and magnetic fields, we choose the coordinate system such that the x axis coincides with the magnetic field direction. Therefore, the equations for the strain tensor and the electric induction vector are

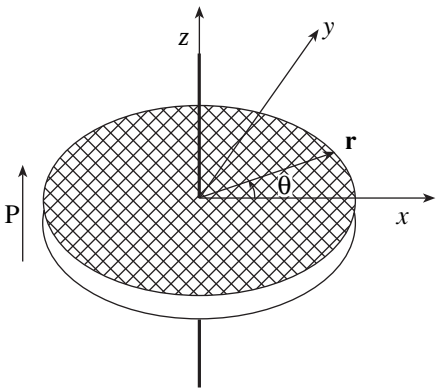

Fig. 1. Sample configuration.

$$\begin{aligned} S_1 &= s_{11}T_1 + s_{12}T_2 + d_{31}E_3 + q_{11}H_1, \\ S_2 &= s_{12}T_1 + s_{22}T_2 + d_{31}E_3 + q_{12}H_1, \\ D_3 &= \varepsilon_{33}E_3 + d_{31}(T_1 + T_2) + m_{31}H_1. \end{aligned} \tag{2}$$

For further calculations, it is convenient to use the symmetry of the problem and to pass over to cylindrical coordinates z, r, and θ. In going to the new coordinate system, the components of the strain and stress tensors are transformed as [11]

$$\begin{aligned} S_1 &= S_{rr}\cos^2\theta - 2S_{r\theta}\sin\theta\cos\theta + S_{\theta\theta}\sin^2\theta, \\ S_2 &= S_{rr}\sin^2\theta + 2S_{r\theta}\sin\theta\cos\theta + S_{\theta\theta}\cos^2\theta, \\ T_{rr} &= T_1\cos^2\theta + 2T_5\sin\theta\cos\theta + T_2\sin^2\theta, \\ T_{\theta\theta} &= T_1\sin^2\theta - 2T_5\sin\theta\cos\theta + T_2\cos^2\theta. \end{aligned} \tag{3}$$

The strain tensor components in the cylindrical coordinate system are expressed in terms of the medium displacement vector **u** as

$$\begin{aligned} S_{rr} &= \partial u_r/\partial r, \\ S_{\theta\theta} &= (1/r)\partial u_\theta/\partial\theta + u_r/r, \\ S_{r\theta} &= \partial u_\theta/\partial r - u_\theta/r + (1/r)\partial u_r/\partial\theta. \end{aligned} \tag{4}$$

By substituting the expressions for the stress tensor into the equation of motion of the medium, we obtain an equation of radial displacements, from which we can find the strains. However, the form of the equation for medium displacements depends on the electric and magnetic field orientations; therefore, we next consider the cases of longitudinal and transverse fields separately.

3. LONGITUDINAL ELECTRIC AND MAGNETIC FIELDS (THEORY)

In the case of longitudinal fields, the dc bias and ac magnetic fields are aligned with the polarization vector. The longitudinal magnetic field causes mechanical vibrations of the medium due to magnetostriction. These vibrations, in turn, produce an electric field due to the piezoelectric effect. In order to determine the strength of the induced electric field and the magnetoelectric coefficient, we first solve the equations of medium motion to determine the arising strains and then solve the electrostatic equations to determine the strength of the arising electric field.

Due to the axial symmetry, the nonzero components of the stress and strain tensors in the cylindrical coordinate system are T_{rr}, $T_{\theta\theta}$, S_{rr}, and $S_{\theta\theta}$. The other components of the stress and strain tensors are zero. From the axial symmetry, it also follows that the displacement component u_θ is zero. Therefore, Eqs. (1) take on the form

$$\begin{aligned} S_{rr} &= s_{11}T_{rr} + s_{12}T_{\theta\theta} + d_{31}E_3 + q_{31}H_3, \\ S_{\theta\theta} &= s_{12}T_{rr} + s_{11}T_{\theta\theta} + d_{31}E_3 + q_{31}H_3. \end{aligned} \tag{5}$$

The equation of motion for radial vibrations of the disk is

$$\frac{\partial T_{rr}}{\partial r} + \frac{1}{r}(T_{rr} - T_{\theta\theta}) + \rho\omega^2 u_r = 0, \tag{6}$$

where ρ is the composite density and ω is the circular frequency.

Let us express the stress components from Eqs. (5) in terms of the strain components:

$$\begin{aligned} T_{rr} &= \frac{1}{s_{11}(1-\nu^2)}(S_{rr} + \nu S_{\theta\theta} - (1+\nu)(d_{31}E_3 + q_{31}H_3)), \\ T_{\theta\theta r} &= \frac{1}{s_{11}(1-\nu^2)}(\nu S_{rr} + S_{\theta\theta} - (1+\nu)(d_{31}E_3 + q_{31}H_3)), \end{aligned} \tag{7}$$

where $\nu = -s_{12}/s_{11}$ is the Poisson ratio.

To derive an equation for radial displacements, we substitute Eqs. (7) into Eq. (6). After transformations, Eq. (6) reduces to the Bessel equation

$$\frac{\partial^2 u_r}{\partial r^2} + \frac{1}{r}\frac{\partial u_r}{\partial r} - \frac{u_r}{r^2} + k^2 u_r = 0, \tag{8}$$

where $k = \omega\sqrt{\rho s_{11}(1-\nu^2)}$. The general solution to Eq. (8) is a linear combination of the first- and second-order Bessel functions,

$$u_r = c_1 J_1(kr) + c_2 Y_1(kr). \tag{9}$$

The integration constants c_1 and c_2 are determined from the boundary conditions: at $r = 0$, the displacement $u_r = 0$, and at $r = R$, the stress $T_{rr} = 0$. This yields

$$\begin{aligned} c_2 &= 0, \\ c_1 &= \frac{(1+\nu)R}{\kappa J_0(\kappa) - (1-\nu)J_1(\kappa)}(q_{31}H_3 + d_{31}E_3), \end{aligned} \tag{10}$$

where we introduced a dimensionless variable $\kappa = kR$, which depends on the frequency, disk radius, and the propagation velocity of elastic vibrations.

Substituting Eqs. (10) for the integration constants c_1 and c_2 into Eq. (9) and expressing the stress components in terms of strains, we obtain

$$\begin{aligned} T_{rr} &= \frac{1}{s_{11}(1-\nu)}\left[\frac{\kappa J_0(kr) - (1-\nu)\frac{R}{r}J_1(kr)}{\kappa J_0(\kappa) - (1-\nu)J_1(\kappa)} - 1\right] \\ &\quad \times (q_{31}H_3 + d_{31}E_3), \\ T_{\theta\theta} &= \frac{1}{s_{11}(1-\nu)}\left[\frac{\nu\kappa J_0(kr) + (1-\nu)\frac{R}{r}J_1(kr)}{\kappa J_0(\kappa) - (1-\nu)J_1(\kappa)} - 1\right] \\ &\quad \times (q_{31}H_3 + d_{31}E_3). \end{aligned} \tag{11}$$

The electric field can be found from the equation for the normal component of the electric induction vector:

$$D_3 = d_{31}(T_{rr} + T_{\theta\theta}) + \varepsilon_{33}E_3 + m_{33}H_3. \tag{12}$$

Under open-circuit conditions (as in experiment), we have

$$\int_0^R r dr \int_0^{2\pi} d\theta D_3 = 0. \tag{13}$$

Substituting Eq. (12) into Eq. (13) and using Eqs. (11), we obtain (after some mathematical manipulation) the induced electric field:

$$E_3 = -\frac{1}{\Delta_a}\left[\frac{2d_{31}q_{31}}{\varepsilon_{33}s_{11}(1-\nu)}\left(\frac{(1+\nu)J_1(\kappa)}{\Delta_r} - 1\right) + \frac{m_{33}}{\varepsilon_{33}}\right]H_3, \tag{14}$$

where

$$\Delta_r = \kappa J_0(\kappa) - (1-\nu)J_1(\kappa), \tag{15}$$

$$\Delta_a = 1 - K_p^2 + K_p^2(1+\nu)J_1(\kappa)/\Delta_r. \tag{16}$$

Here, $K_p^2 = \dfrac{2d_{31}^2}{\varepsilon_{33}s_{11}(1-\nu)}$ is the electromechanical coupling coefficient for radial vibrations.

For longitudinal electric and magnetic fields, the magnetoelectric coefficient is defined as $E_3 = \alpha_{E,L}H_3$ and can be found to be

$$\alpha_{E,L} = \frac{1}{\Delta_a}\left[\frac{2d_{31}q_{31}}{\varepsilon_{33}s_{11}(1-\nu)}\left(1-\frac{(1+\nu)J_1(\kappa)}{\Delta_r}\right)-\frac{m_{33}}{\varepsilon_{33}}\right]. \quad (17)$$

Expression (17) for the magnetoelectric coefficient has a resonant frequency dependence. The roots of Eq. (15) define the resonance frequencies, and the roots of Eq. (16) give the antiresonance frequencies for the piezoelectric effect. Thus, under open-circuit conditions, a sharp increase in the magnetoelectric coefficient is observed at the antiresonance frequency. The resonance frequency, as in the case of the piezoelectric resonance, is controlled primarily by the disk radius R and compliance s_{11}. For ferrospinel–PZT composite samples ~1 cm in radius, the lower value of the resonant frequency is near 300 kHz. For longitudinal fields, the magnetoelectric coefficient is directly proportional to the product of piezoelectric (d_{31}) and piezomagnetic (q_{31}) moduli and is inversely proportional to the permittivity ε_{33} and compliance s_{11} of the material. In fact, such structures are always characterized by losses, primarily in contacts. These losses control the resonance linewidth and limit the peak value of the magnetoelectric coefficient. The losses can be taken into account in the damping coefficient by considering either k or ω to be a complex quantity [12]. We will use the latter method, representing the circular frequency as $\omega = \omega' + i\chi$, where χ is a parameter characterizing damping, which can be determined experimentally from the resonance linewidth.

4. TRANSVERSE ORIENTATION OF THE ELECTRIC AND MAGNETIC FIELDS (THEORY)

Now, we consider the case where the dc bias and ac magnetic fields lie in the disk plane and are perpendicular to the electric field (which is directed along the z axis). Using Eqs. (3) to pass to the cylindrical coordinate system, we represent Eqs. (2) in the form

$$\begin{aligned} S_{rr} &= s_{11}T_{rr} + s_{12}T_{\theta\theta} + d_{31}E_3 \\ &+ (q_{11}\cos^2\theta + q_{12}\sin^2\theta)H_1, \\ S_{\theta\theta} &= s_{12}T_{rr} + s_{11}T_{\theta\theta} + d_{31}E_3 \\ &+ (q_{11}\sin^2\theta + q_{12}\cos^2\theta)H_1. \end{aligned} \quad (18)$$

In this case, the equations for the strain tensor become more complicated and, in addition to the radial dependence, there appears an angular dependence because of the magnetic field breaking the axial symmetry of the problem. Let us express the stress components T_{rr} and $T_{\theta\theta}$ from Eqs. (18). After simple algebra, we obtain

$$\begin{aligned} T_{rr} &= \frac{1}{s_{11}(1-\nu^2)}[S_{rr} + \nu S_{\theta\theta} - (1+\nu)d_{31}E_3 \\ &- ((\cos^2\theta + \nu\sin^2\theta)q_{11} + (\sin^2\theta + \nu\cos^2\theta)q_{12})H_1], \\ T_{\theta\theta} &= \frac{1}{s_{11}(1-\nu^2)}[\nu S_{rr} + S_{\theta\theta} - (1+\nu)d_{31}E_3 \\ &- ((\nu\cos^2\theta + \sin^2\theta)q_{11} + (\nu\sin^2\theta + \cos^2\theta)q_{12})H_1]. \end{aligned} \quad (19)$$

Substituting Eqs. (19) into the equation of motion (6), we arrive at an equation for radial vibrations for the transverse field orientation,

$$\frac{\partial^2 u_r}{\partial r^2} + \frac{1}{r}\frac{\partial u_r}{\partial r} - \frac{u_r}{r^2} + k^2 u_r - \frac{D(\theta)}{r} = 0, \quad (20)$$

where we introduced the notation $D(\theta) = (q_{11} - q_{12})(1 - \nu)(\cos^2\theta - \sin^2\theta)H_1$.

The solution to Eq. (20) is

$$u_r = c_1 J_1(kr) + c_2 Y_1(kr) + D(\theta)/(k^2 r), \quad (21)$$

where $J_1(kr)$ and $Y_1(kr)$ are the first- and second-order Bessel functions, respectively, and $k = \omega\sqrt{\rho s_{11}(1-\nu^2)}$.

The integration constants c_1 and c_2 are determined from the same boundary conditions as in the case of longitudinal fields. To satisfy the boundary condition at $r = 0$, we take into account that the second-order Bessel function at small values of the argument can be written as

$$Y_1(z) \approx -2/(\pi z). \quad (22)$$

Using this property of the Bessel function, the integration constant c_2 is found to be

$$c_2 = \pi D(\theta)/(2k). \quad (23)$$

From the boundary condition that the radial component of the stress tensor vanish at the lateral surface of the disk, we find the integration constant c_1 to be

$$\begin{aligned} c_1 &= R\{(1+\nu)d_{31}E_3 \\ &+ (q_{11}(\cos^2\theta + \nu\sin^2\theta) + q_{12}(\nu\cos^2\theta + \sin^2\theta))H_1 \\ &+ D(\theta)(1-\nu)(\pi Y_1(\kappa)/(2\kappa) + 1/\kappa^2 - \pi Y_0/2)\}/\Delta_r. \end{aligned} \quad (24)$$

As follows from Eq. (21) combined with Eqs. (23) and (24), the amplitude of radial vibrations for transverse field orientations depends not only on the radial variable r but also on the angular variable θ. Indeed, the excitation of elastic vibrations along the magnetic field

(x axis, $\theta = 0$) and perpendicular to it (y axis, $\theta = \pi/2$) is determined by different coefficients, q_{11} and q_{12}, respectively. Since these coefficients differ in value, the amplitude of radial vibrations depends on the angular variable. The spatial frequency of radial vibrations is controlled by the properties of the medium and is independent of the excitation method applied; therefore, the parameter k is the same for longitudinal and transverse field orientations.

Using solution (21), we express the components of the stress tensor from Eqs. (19) combined with Eqs. (4). The calculations yield

$$\begin{aligned}
T_{rr} &= \frac{1}{s_{11}(1-\nu^2)}\left(c_1\left(kJ_0(kr) - (1-\nu)\frac{J_1(kr)}{r}\right)\right.\\
&+ D(\theta)\left(\frac{\pi}{2}Y_0(kr) - (1-\nu)\frac{\pi}{2}\frac{Y_1(kr)}{kr} - (1-\nu)\frac{1}{k^2r^2}\right)\\
&- (1+\nu)d_{31}E_3 - ((\cos^2\theta + \nu\sin^2\theta)q_{11}\\
&\left.+ (\sin^2\theta + \nu\cos^2\theta)q_{12})H_1\right),\\
T_{\theta\theta r} &= \frac{1}{s_{11}(1-\nu^2)}\left(c_1\left(\nu kJ_0(kr) + (1-\nu)\frac{J_1(kr)}{r}\right)\right.\\
&+ D(\theta)\left(\nu\frac{\pi}{2}Y_0(kr) + (1-\nu)\frac{\pi}{2}\frac{Y_1(kr)}{kr} + (1-\nu)\frac{1}{k^2r^2}\right)\\
&- (1+\nu)d_{31}E_3 - ((\nu\cos^2\theta + \sin^2\theta)q_{11}\\
&\left.+ (\nu\sin^2\theta + \cos^2\theta)q_{12})H_1\right).
\end{aligned} \tag{25}$$

As in the case of the longitudinal field orientation, the electric field can be found from Eq. (12) for the normal component of the electric induction combined with the open-circuit condition (13). Substituting Eqs. (25) into Eq. (12) and the result into Eq. (13), we obtain, after integration and simple algebra,

$$\begin{aligned}
E_3 = \frac{1}{\Delta_a}\left[\frac{d_{31}(q_{11}+q_{12})}{\varepsilon_{33}s_{11}(1-\nu)}\left(1 - \frac{(1+\nu)J_1(\kappa)}{\Delta_r}\right)\right.\\
\left. - \frac{m_{31}}{\varepsilon_{33}}\right]H_1.
\end{aligned} \tag{26}$$

In the case of transverse field orientations, the magnetoelectric coefficient is defined as $\alpha_{E,T} = E_3/H_1$. Using this definition and Eq. (26), we obtain

$$\begin{aligned}
\alpha_{E,T} &= \frac{1}{\Delta_a}\left[\frac{d_{31}(q_{11}+q_{12})}{\varepsilon_{33}s_{11}(1-\nu)}\left(1 - \frac{(1+\nu)J_1(\kappa)}{\Delta_r}\right) - \frac{m_{31}}{\varepsilon_{33}}\right].
\end{aligned} \tag{27}$$

As follows from Eq. (27), in the case of transverse orientation of the electric and magnetic fields, as well as for longitudinal orientation, the magnetoelectric coefficient is proportional to the product of the piezoelectric and piezomagnetic moduli. For the longitudinal orientation, this coefficient is proportional to the double product $d_{31}q_{31}$, and for the transverse orientation, it is proportional to the product $d_{31}(q_{11} + q_{12})$. Since q_{11} and q_{12} are almost tenfold larger than q_{31} because of the absence of demagnetization, it might be expected that the effect will be several times stronger for transverse field orientations than for the longitudinal orientation. The frequency dependence of the coefficient $\alpha_{E,T}$ is completely identical to the frequency dependence of the coefficient $\alpha_{E,L}$. This identity is explained by the fact that the same radial modes of vibrations are excited both for longitudinal and transverse orientations of the electric and magnetic fields; only the excitation methods are different.

5. EXPERIMENT

The magnetoelectric effect was studied experimentally on multilayer composite samples consisting of eleven nickel ferrospinel layers 13 μm thick each and ten piezoelectric PZT ceramic layers 26 μm thick each. The samples were disk-shaped with a radius R = 9.5 mm. Before measurements, the samples were polarized in an electric field of 4 kV/mm for three hours at a temperature of 80°C. The ME effect was studied by measuring the ac voltage induced across a sample under an ac and a slowly varying bias magnetic field. First, the field dependence of the low-frequency ME effect was studied at a fixed amplitude of the ac magnetic field of 1 Oe; the ME coefficient was measured as a function of the bias field strength. Then, for the bias magnetic field strength corresponding to the maximum ME coefficient, the frequency dependence of this coefficient was measured in the region of the electromechanical resonance. The measurements were carried out for longitudinal and transverse orientations of electric and magnetic fields. The open-circuit condition in the measurements was satisfied satisfactorily. The input impedance (active and capacitive resistances) of the preamplifier and contact wires exceeded the sample impedance more than tenfold.

The experimental results and the dependences calculated using formulas (17) and (27) are shown in Figs. 2 and 3, respectively. The calculations were carried out using the parameters of nickel spinel ${}^m s_{11} = 6.5 \times 10^{-12}$ m^2/N, ${}^m s_{12} = -2.4 \times 10^{-12}$ m^2/N, ${}^m q_{31} = 70 \times$

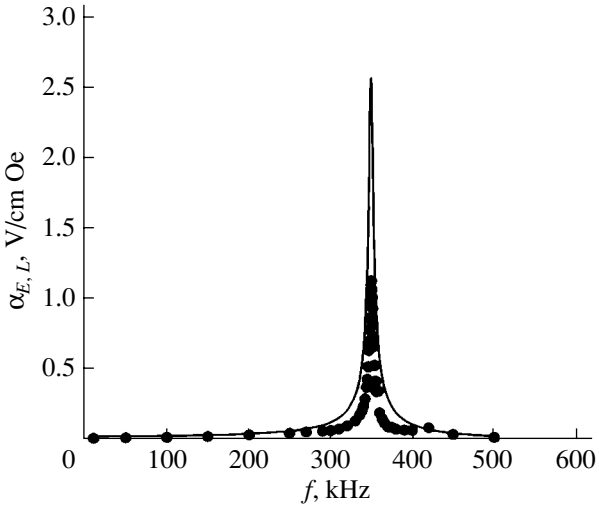

Fig. 2. Theoretical (solid curve) and experimental (dots) frequency dependences of the magnetoelectric coefficient for the longitudinal field orientation. Damping coefficient $\chi = 15000$ rad/s.

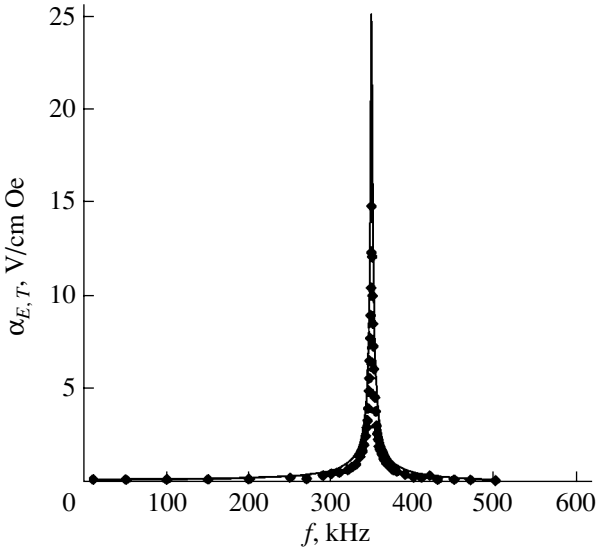

Fig. 3. The same as in Fig. 1, but for transverse field orientations. Damping coefficient $\chi = 7500$ rad/s.

10^{-12} m/A, ${}^{m}q_{11} = -430 \times 10^{-12}$ m/A, ${}^{m}q_{12} = 125 \times 10^{-12}$ m/A, and ${}^{m}\varepsilon_{33}/\varepsilon_0 = 10$ and the parameters of PZT ${}^{p}s_{11} = 15.3 \times 10^{-12}$ m^2/N, ${}^{p}s_{12} = -5 \times 10^{-12}$ m^2/N, ${}^{p}d_{31} = -175 \times 10^{-12}$ m/V, and ${}^{p}\varepsilon_{33}/\varepsilon_0 = 1750$. The effective parameters of the composite were calculated (using the technique described in [7]) to be $s_{11} = 10 \times 10^{-12}$ m^2/N, $s_{12} = -3.9 \times 10^{-12}$ m^2/N, $q_{31} = 60 \times 10^{-12}$ m/A, $q_{11} = -320 \times 10^{-12}$ m/A, $q_{12} = 84 \times 10^{-12}$ m/A, and ${}^{m}\varepsilon_{33}/\varepsilon_0 = 28$; the damping parameter was determined from the electromechanical resonance linewidth.

6. DISCUSSION

It can be seen from Figs. 2 and 3 that there is good agreement between the theory and the experimental results. A resonant increase in the effect is observed at a frequency near 350 kHz. The highest magnetoelectric coefficient (almost 15 V/cm Oe) is observed in the disk for transverse field orientations, while at a frequency of 100 Hz this coefficient is 0.16 V/cm Oe. The damping coefficient was determined from the resonance linewidth. For transverse orientations of electric and magnetic fields, this coefficient was found to be smaller than for the longitudinal orientation. In our opinion, this result is due to the fact that the currents excited in metal contacts (and leading to losses) are smaller in the case of in-plane magnetic fields.

In the case of transverse orientations of magnetic and electric fields, the effect is tenfold stronger than for the longitudinal orientation, because, as indicated above, the demagnetizing fields that arise for longitudinal field orientation decrease the effective piezomagnetic modulus.

Quantitative discrepancies in the values of the magnetoelectric coefficient are observed in both the low-frequency range and the region of the electromechanical resonance. The reason for these discrepancies is that the effective parameters were calculated for a composite characterized by ideal connectivity and uniform composition over the sample. Meanwhile, imperfections of layers always occur when multilayer composite materials are prepared, with the result that the composition is not uniform over the sample. It should be noted that the effective parameters exhibit a strong dependence on concentration.

The theory developed in this paper is applicable to both multilayer and bulk composites. The effective parameters of composite materials will be different for these two cases.

ACKNOWLEDGMENTS

This study was supported in part by the Ministry of Education of the Russian Federation (project no. E02-3.4-278), the federal program "Universities of Russia" (project no. UR 01.01.007), and the National Science Foundation (project no. DMR-0322254).

REFERENCES

1. G. T. Rado, Phys. Rev. **128**, 2546 (1962).
2. L. É. Gurevich and D. A. Filippov, Fiz. Tverd. Tela (Leningrad) **28**, 2696 (1986) [Sov. Phys. Solid State **28**, 1510 (1986)].
3. J. van Suchtelen, Philips Res. Rep. **27**, 28 (1972).
4. M. I. Bichurin, D. A. Filippov, V. M. Petrov, and G. Srinivasan, in *Proceedings of International Conference on Physics of Electron Materials* (Kaluga, 2002), p. 309.

5. D. A. Filippov, M. I. Bichurin, V. M. Petrov, and G. Srinivasan, Bull. Am. Phys. Soc. **48**, 214 (2003).
6. A. M. J. G. van Run, D. R. Terrell, and J. H. Scholing, J. Mater. Sci. **9**, 1710 (1974).
7. J. G. Wan, J.-M. Liu, H. L. W. Chand, C. L. Choy, G. H. Wang, and C. W. Nan, J. Appl. Phys. **93** (12), 9916 (2003).
8. D. A. Filippov, M. I. Bichurin, V. M. Petrov, V. M. Laletin, N. N. Poddubnaya, and G. Srinivasan, Pis'ma Zh. Tekh. Fiz. **30** (1), 15 (2004) [Tech. Phys. Lett. **30**, 6 (2004)].
9. M. I. Bichurin, D. A. Filippov, V. M. Petrov, V. M. Laletsin, N. Paddubnaya, and G. Srinivasan, Phys. Rev. B **68**, 132408 (2003).
10. M. I. Bichurin, V. M. Petrov, and G. Srinivasan, Phys. Rev. B **68**, 054402 (2003).
11. W. P. Mason, Phys. Rev. **74** (9), 1134 (1948).
12. R. Truell, Ch. Elbaum, and Br. Chick, *Ultrasonic Methods in Solid State Physics* (Academic, New York, 1969; Mir, Moscow, 1972).

Translated by A. Kazantsev

Physics of the Solid State, Vol. 46, No. 9, 2004, pp. 1681–1685. Translated from Fizika Tverdogo Tela, Vol. 46, No. 9, 2004, pp. 1628–1632.
Original Russian Text Copyright © 2004 by Titov, Yarmoshenko, Neumann, Pleshchev, Titova.

MAGNETISM AND FERROELECTRICITY

Hierarchy of Percolation Thresholds and the Mechanism for Reduction of Magnetic Moments of Transition Metals Intercalated into $TiSe_2$

A. N. Titov*, Yu. M. Yarmoshenko*, M. Neumann, V. G. Pleshchev***, and S. G. Titova******

** Institute of Metal Physics, Ural Division, Russian Academy of Sciences, ul. S. Kovalevskoĭ 18, Yekaterinburg, 620219 Russia*

e-mail: alexander.titov@usu.ru

*** Universität Osnabrück, Fachbereich Physik, Osnabrück, 49069 Germany*

**** Ural State University, pr. Lenina 51, Yekaterinburg, 620089 Russia*

***** Institute of Metallurgy, Ural Division, Russian Academy of Sciences, Yekaterinburg, 620016 Russia*

Received December 1, 2003

Abstract—The concentration dependences of the effective magnetic moment of transition metal atoms intercalated into $TiSe_2$ are analyzed in the framework of the percolation theory. It is shown that, depending on the degree of localization of impurity states, the effective magnetic moment is determined by the overlap of 3*d* orbitals of transition metals or orbitals of titanium atoms coordinated by impurity atoms. © *2004 MAIK "Nauka/Interperiodica".*

1. INTRODUCTION

Intercalated materials based on titanium dichalcogenides are formed through the intercalation of atoms of different metals into the interlayer space of the host lattice. Earlier investigations [1–4] revealed that the intercalation of transition metals and silver into $TiSe_2$ brings about the formation of Ti–*Me*–Ti covalent centers, where *Me* is an intercalated metal (Ti, Cr, Fe, Co, Ni, Ag). The formation of covalent centers can be judged from the distortion of the host lattice. In the case when impurity atoms are ionized with electron transfer to the conduction band of the initial compound, the lattice parameter c_0 increases with an increase in the impurity content x. At the same time, the formation of covalent centers is accompanied by a decrease in the lattice parameter c_0 with an increase in the impurity content x. Electrons transferred with intercalant atoms are localized at these centers. Such centers serve as traps of free charge carriers, on the one hand, and as strain centers of the lattice, on the other hand. Consequently, these centers can be treated as polarons. Upon the formation of polarons in the lattice, the influence of an intercalated impurity atom is localized in the vicinity of the site occupied by this atom. As a result, the dependences of the electrical and magnetic properties of intercalation materials on the intercalant content exhibit a pronounced nonmonotonic behavior. Therefore, the concentration dependences of the physical parameters of intercalation materials can be described in terms of the percolation theory.

Earlier [3–5], we demonstrated that, for $TiSe_2$-based intercalation compounds, the concentration dependences of the kinetic properties and the host-lattice strain arising upon intercalation of transition metals are adequately described within the percolation theory. The characteristic concentrations are in close agreement with the percolation threshold analytically calculated by Sykes and Essam [6], who solved the site problem for a triangular lattice with sites occupied by intercalated atoms. However, the question as to which physical quantity plays the role of the percolation parameter remains open. In our opinion, it is reasonable to consider at least three possible mechanisms of percolation: (1) the overlap of lattice distortion fields in the vicinity of each intercalated atom, (2) the overlap of orbitals of impurity atoms, and (3) the overlap of orbitals of titanium atoms coordinated by impurity atoms (the overlap of orbitals of Ti–*Me*–Ti centers). At the same time, elucidation of the nature of the percolation thresholds is of considerable importance in interpreting the observed concentration dependence of the effective magnetic moment μ_{eff} of intercalated atoms. As was shown in our previous work [7], the difference between the effective magnetic moment μ_{eff} and the spin moment of a free ion is directly proportional to the lattice strain. The reduction of magnetic moments of impurity atoms can be explained in the framework of the Anderson impurity model for magnetic ions with an unfilled *d*(*f*) shell [8]. According to this model, the magnetic moment of an atom is determined by the difference in the occupancies of spin-polarized *d*(*f*) orbitals. The hybridization of the orbitals with the environment leads to their broadening and, hence, to a decrease in the difference between the occupancies of these orbitals, which, in turn, results in

a decrease in the magnetic moment. Consequently, the dominant role in the reduction of the magnetic moment is played by the concentration (temperature, etc.) dependence of the *d* subband of impurity atoms. However, it is clear that the hybridization is only one of the possible mechanisms of band broadening. This broadening can also be caused by the increase in the overlap of orbitals as the impurity atoms approach each other with an increase in their concentration. Therefore, the identification of percolation features with points of anomalies in the concentration dependence of the effective magnetic moment μ_{eff} will make it possible to reveal the mechanism responsible for the reduction of the magnetic moments of impurity atoms intercalated into titanium dichalcogenides.

Since the impurity atoms occupy octahedral positions forming a triangular lattice, the impurity concentration corresponding to the percolation threshold in the case of mechanism (2) is easily determined to be $x = 0.5$ [6] (where x is the dimensionless impurity concentration per unit cell containing only one octahedral position that can be occupied by an impurity atom). For mechanisms (1) and (3), the critical impurity concentration is equal to $x = 0.25$. This follows from the structural features of the materials under investigation. Actually, if an octahedral position in the structure of these materials is occupied, the octahedral positions nearest to this occupied position along the normal to the basal plane of the crystal cannot be occupied by impurity atoms [9]. Consequently, the intercalation of each impurity metal atom leads to the formation of a Ti–*Me*–Ti center with two titanium atoms coordinated by the impurity atom. Therefore, at the impurity concentration $x = 0.25$, the concentration of titanium atoms coordinated by impurity atoms coincides with the percolation threshold in the triangular lattice. Since the density of octahedral positions that cannot be occupied upon intercalation is equal to $2x$ (taking into account that each blocked position belongs to two unit cells), the impurity concentration corresponding to the critical value $x = 0.5$ also amounts to $x = 0.25$.

2. SAMPLE PREPARATION AND EXPERIMENTAL TECHNIQUE

The concentration dependences of the lattice parameters will be discussed using the data obtained earlier in [2, 5, 9]. The effective magnetic moments of impurity atoms were determined from the temperature dependence of the magnetic susceptibility in the paramagnetic temperature range. The measurements were performed by the Faraday method according to the technique described in [4].

The x-ray photoelectron spectra of Cr_xTiSe_2 single crystals were recorded on a Perkin-Elmer spectrometer with an energy resolution of 0.4 eV. The spectra were excited with monochromated AlK_α radiation. Samples were applied on an adhesive conducting substrate. In order to reduce undesirable effects of adsorbed atmospheric gases and carbon on the spectra, the sample surface was mechanically cleaned directly in the measuring chamber of the spectrometer under vacuum (at a residual pressure of 10^{-8} Torr).

Single-crystal samples were used to improve the resolution. On the one hand, this approach restricted detailed analysis of the influence of the impurity content on the electronic structure to the compositions with $x = 0.10$ and 0.33 for which we succeeded in growing the single crystals. On the other hand, the use of single-crystal samples with a juvenile surface, which was prepared by cleaving directly in the spectrometer chamber under high vacuum, made it possible to obtain conclusive results. The crystals were grown by the gas-transport reaction method with the use of I_2 as a gas carrier. The growth procedure was described in detail in [7].

3. RESULTS AND DISCUSSION

The concentration dependences of the lattice parameters for Me_xTiSe_2 (*Me* = Cr, Fe, Co, Ni) compounds exhibit anomalies in the form of kinks at $x = 0.25$. It is obvious that these anomalies can be associated with the percolation. However, the question as to whether mechanism (1) or mechanism (3) is dominant remains unclear. The contributions from the mechanisms of percolation due to the overlap of lattice distortion fields and the overlap of orbitals can be separated using different degrees of localization of Ti–*Me* hybrid orbitals for different metals. As was shown in our earlier work [5], the degree of localization is governed by the lattice strain arising upon intercalation of impurity atoms. It is clear that, if the localization is sufficiently strong, the percolation through mechanism (3) can be completely absent. This situation can occur when the spatial extension of the orbitals of titanium atoms coordinated by impurity atoms is less than half the distance between the nearest localization centers. In turn, this distance cannot be less than the lattice parameter a_0. The strain reaches a maximum in Co_xTiSe_2 compounds. Hence, we can expect that, in these compounds, the percolation through mechanism (3) is absent. In this case, the anomaly at $x = 0.25$ should be assigned solely to the overlap of distortion fields. Indeed, an increase in the cobalt impurity content above the critical value $x = 0.25$ results only in a decrease in the slope of the concentration dependence of the lattice parameter $c_0(x)$ for Co_xTiSe_2 compounds. This can be explained by the interaction of strain centers due to the overlap of their distortion fields. Therefore, an increase in the cobalt impurity content $x > 0.25$ leads to an increase in the concentration of strain centers with a simultaneous decrease in the strain per intercalated atom. This inference is consistent with the data obtained in our work [4], in which we observed linear concentration dependences of the electrical conductivity and the Seebeck coefficient in the cobalt concentration range $x = 0$–0.33.

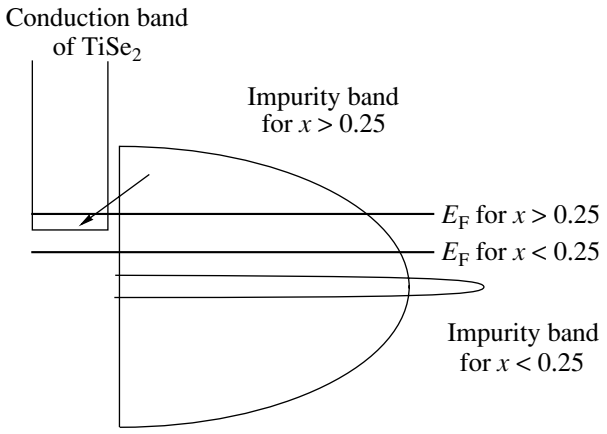

Fig. 1. A schematic diagram illustrating the shift of the Fermi level upon broadening of the impurity band due to the overlap of orbitals of localization centers. The arrow indicates the electron transfer from the polaron band to the conduction band of the host lattice with an increase in the energy at the top of the polaron band.

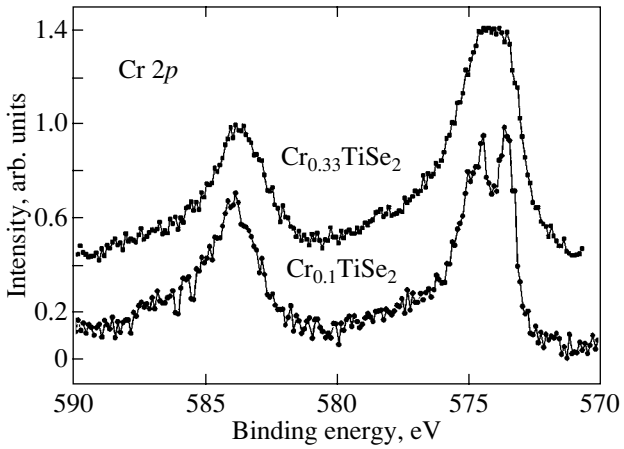

Fig. 2. Cr 2p photoemission spectra of Cr_xTiSe_2 compounds with intercalant concentrations below ($x = 0.1$) and above ($x = 0.33$) the percolation threshold in the sublattice of Ti–Cr–Ti centers. The splitting of the line at an energy of 574 eV (Cr $2p_{3/2}$) in the spectrum of $Cr_{0.1}TiSe_2$ is caused by the spin polarization of states at the Fermi level.

Consequently, the intercalation of each cobalt atom at a cobalt content below and above $x = 0.25$ does not change the localization of charge carriers.

The above dependence differs substantially from the concentration dependence of the lattice parameter $c_0(x)$ for Cr_xTiSe_2 compounds, in which the strain is minimum and, hence, the extension of orbitals of Ti–Cr–Ti centers is maximum. In these compounds, an increase in the chromium content $x > 0.25$ results in an increase in the lattice parameter c_0 [10]. Apparently, this difference should be caused by the additional contribution from the overlap of orbitals of Ti–Cr–Ti centers. An increase in the concentration of strain centers cannot be attended by a decrease in the total strain. Such a behavior can be explained solely by the decrease in the number of strain centers in the chromium concentration range $x > 0.25$. Physically, this situation can be interpreted as follows (Fig. 1): the impurity band can be broadened to an extent that the impurity band top appears to be higher than the conduction band bottom of $TiSe_2$. As a consequence, electrons partially transfer to the conduction band of $TiSe_2$. In the impurity band, the states between the impurity band top and the Fermi level turn out to be empty, which, in essence, corresponds to a partial decay of localization centers.

Thus, the overlap of distortion fields around intercalated impurity atoms results in a decrease in the strain induced upon intercalation. A decrease in the contraction of the lattice parameter c_0 can be provided only by an overlap of orbitals of localization centers. Relevant direct experimental evidence can be obtained by analyzing the electronic structure of the compounds under investigation in the chromium concentration ranges $x < 0.25$ and $x > 0.25$.

Figure 2 shows the Cr 2p core-level photoemission spectra of the $Cr_{0.1}TiSe_2$ and $Cr_{0.33}TiSe_2$ compounds. In the spectrum of the $Cr_{0.1}TiSe_2$ compound, the Cr $2p_{3/2}$ line is split as a result of a strong exchange magnetic interaction between Cr $2p_{3/2}$ holes and spin-polarized Cr d electrons [7]. This is in agreement with the band calculations performed in [11], according to which the exchange splitting of this line is approximately equal to 0.9 eV. On the other hand, no splitting is observed in the spectrum of the $Cr_{0.33}TiSe_2$ compound. However, the maximum of this line appears to be flattened; i.e., it retains indications of the splitting observed in the concentration range $x < 0.25$. Such a situation can occur when the broadening of the Cr 3d spin subbands is larger than the splitting. In turn, this can be interpreted as resulting from the increase in the overlap of the wave functions of chromium atoms due to the percolation in the sublattice of the Ti–Cr–Ti centers.

Moreover, the width of the Ti 2p line in the spectrum of the $Cr_{0.33}TiSe_2$ compound is considerably larger than that in the spectrum of the $Cr_{0.1}TiSe_2$ compound, whereas the energy positions of these lines coincide with each other (Fig. 3). This can be explained by the fact that the latter compound contains only identical isolated Ti–Cr–Ti centers. As the impurity concentration increases above the percolation threshold, the existence of both isolated and closely spaced centers becomes quite possible.

Therefore, the extension of orbitals of Ti–Cr–Ti centers in Cr_xTiSe_2 compounds can be estimated to be approximately equal to the lattice parameter a_0.

Upon intercalation, the lattice distortion of Fe_xTiSe_2 compounds is somewhat greater that of Cr_xTiSe_2 compounds (0.135 and 0.133 Å, respectively) [5]. Conse-

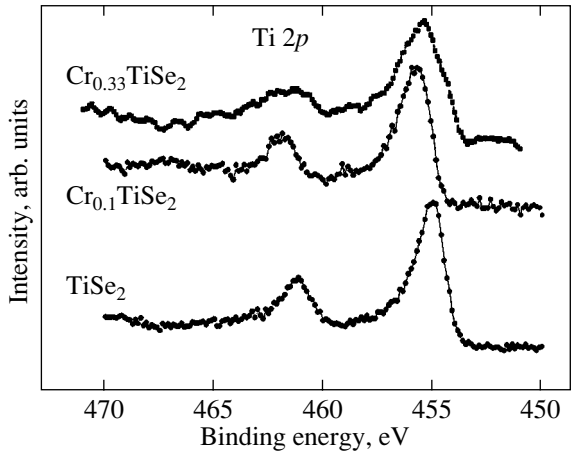

Fig. 3. Ti 2*p* photoemission spectra of the $Cr_{0.1}TiSe_2$ and $Cr_{0.33}TiSe_2$ compounds. The Ti 2*p* photoemission spectrum of the $TiSe_2$ initial compound is shown for comparison.

quently, it can be expected that the degree of localization of electrons in Fe_xTiSe_2 compounds should be slightly higher than the degree of their localization in Cr_xTiSe_2 compounds. Actually, an increase in the impurity content $x > 0.25$ manifests itself only in a kink in the dependence $c_0(x)$. At the same time, an increase in the lattice parameter c_0 is observed in the concentration range at $x = 0.5$, which corresponds to the percolation in the intercalant sublattice rather than in the sublattice of Ti–Fe–Ti centers. This can also be explained by the broadening of the impurity band, as is the case in the Cr_xTiSe_2 compounds. However, in the Fe_xTiSe_2 compounds, this broadening can be caused by the direct overlap of orbitals of iron atoms. Since the lattice parameter c_0 begins to increase at an impurity content slightly less than $x = 0.5$, the extension of iron orbitals most likely exceeds the lattice parameter a_0. It should also be noted that, when the impurity content x approaches 0.5, the concentration of Ti–Fe–Ti centers tends to unity. None of the known types of plane lattices has a percolation threshold corresponding to such a concentration of localization centers. Therefore, the direct overlap of the iron orbitals is the sole possible explanation for the concentration dependence $c_0(x)$ of the Fe_xTiSe_2 compounds. The orbitals of Ti–Fe–Ti centers do not overlap in any of the cases. Hence, the extension of these orbitals is considerably smaller than the lattice parameter a_0.

It is evident that, in materials with a greater lattice strain, such as Ni_xTiSe_2 compounds, the orbitals of Ti–*Me*–Ti centers should not overlap. Indeed, the lattice parameter c_0 for these compounds decreases in the intercalant concentration range $0 < x < 0.5$ [9].

The concentration dependence of the lattice parameter $c_0(x)$ for the Co_xTiSe_2 compounds exhibits only an insignificant kink. This suggests that the percolation

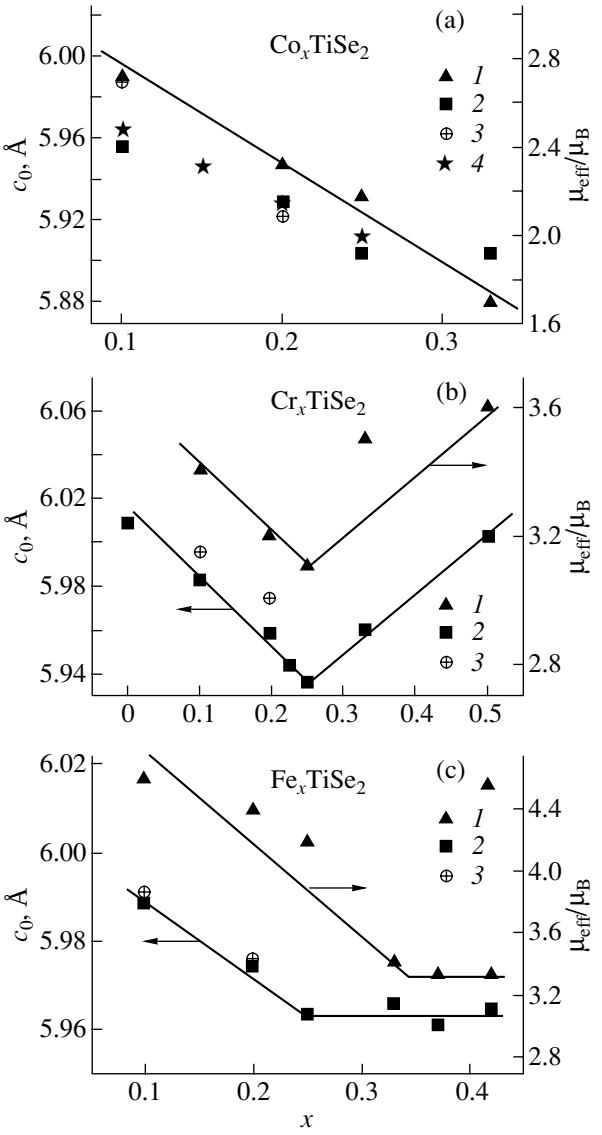

Fig. 4. Concentration dependences of (*1*) the lattice parameter c_0 and the effective magnetic moment μ_{eff} according to the data obtained in this work and data taken from (*2*) [2], (*3*) [12], and (*4*) [9].

can proceed through the mechanism of overlap of distortion fields around the Ti–Co–Ti covalent centers. No indications of the percolation mechanisms associated with the overlap of orbitals are revealed. Therefore, we can conclude that an intercalated impurity atom affects the electronic structure in the vicinity of the site occupied by the cobalt atom and this effect becomes negligible outside the unit cell.

The kink observed in the concentration dependence of the lattice parameter $c_0(x)$ for the Cr_xTiSe_2 compounds is obviously associated with the overlap of orbitals of titanium atoms coordinated by chromium atoms [mechanism (3)]. However, this mechanism is masked by the percolation due to the overlap of distor-

Effective magnetic moments μ_{eff} (in Bohr magnetons) of impurity atoms intercalated into $TiSe_2$ and theoretical spin magnetic moments μ_{sp} for charge states of intercalated atoms in the high-spin configuration (S is the spin, q is the spectroscopic splitting factor)

Compound	μ_{eff}	Charge state	$\mu_{sp} = q\sqrt{S(S+1)}$
Fe_xTiSe_2	5.11	Fe^{2+}	4.90
Co_xTiSe_2	3.18	Co^{2+}	3.87
Cr_xTiSe_2	3.6	Cr^{3+}	3.87

tion fields and, therefore, cannot be identified with certainty.

The Fe_xTiSe_2 system is intermediate between the Co_xTiSe_2 and Cr_xTiSe_2 systems. The kinks in the dependence $c_0(x)$ at contents $x = 0.25$ and 0.5 are caused by the overlap of distortion fields and orbitals of iron atoms, respectively.

The concentration dependences of the effective magnetic moment μ_{eff} and the lattice parameter $c_0(x)$ for the materials under investigation are plotted in Fig. 4. It can be clearly seen from this figure that the concentration dependences of the effective magnetic moment $\mu_{eff}(x)$ for all compounds are parallel to the concentration dependences of the lattice parameter $c_0(x)$. Consequently, the mechanism responsible for the reduction of the magnetic moments of impurity atoms is governed solely by the broadening of spin subbands due to the hybridization of impurity orbitals with orbitals of the environment according to the Anderson model [8].

On this basis, we can solve the problem regarding the determination of the charge and spin states of intercalated impurity atoms. This problem has long been discussed in the literature. The point is that the experimental dependence of the effective magnetic moment μ_{eff} on the intercalant concentration did not permit one to identify this moment with any standard state of transition metal ions [12] and could be interpreted in different ways. The true effective magnetic moment μ_{eff} can be obtained by extrapolating the concentration dependence of the effective magnetic moment $\mu_{eff}(x)$ to the impurity content $x = 0$, which corresponds to an infinitesimal concentration of intercalated metal atoms. The effective magnetic moments thus determined are presented in the table. The table also presents the magnetic moments of free ions. It can be seen that the effective magnetic moments μ_{eff} agree well with the theoretical values for Cr^{3+}, Co^{2+}, and Fe^{2+} charge states of the intercalated impurity atoms in the high-spin configuration.

ACKNOWLEDGMENTS

This work was supported by the Russian Foundation for Basic Research (project no. 01-03-32620) and the "New Materials and Structures" program of the Russian Academy of Sciences.

REFERENCES

1. A. N. Titov and A. V. Dolgoshein, Fiz. Tverd. Tela (St. Petersburg) **40** (7), 1187 (1998) [Phys. Solid State **40**, 1081 (1998)].
2. A. Titov, S. Titova, M. Neumann, V. Pleschev, Yu. Yarmoshenko, L. Krasavin, A. Dologoshein, and A. Kuranov, Mol. Cryst. Liq. Cryst. Sci. Technol., Sect. A **311**, 161 (1998).
3. A. V. Kuranov, V. G. Pleshchev, A. N. Titov, N. V. Baranov, and L. S. Krasavin, Fiz. Tverd. Tela (St. Petersburg) **42** (11), 2029 (2000) [Phys. Solid State **42**, 2089 (2000)].
4. V. G. Pleshchev, A. N. Titov, and A. V. Kuranov, Fiz. Tverd. Tela (St. Petersburg) **39** (10), 1618 (1997) [Phys. Solid State **39**, 1442 (1997)].
5. A. N. Titov, A. V. Dolgoshein, I. K. Bdikin, and S. G. Titova, Fiz. Tverd. Tela (St. Petersburg) **42** (9), 1567 (2000) [Phys. Solid State **42**, 1610 (2000)].
6. M. F. Sykes and J. W. Essam, Phys. Rev. Lett. **10**, 3 (1963); J. Math. Phys. **5**, 1117 (1964).
7. A. N. Titov, A. V. Kuranov, V. G. Pleschev, Yu. M. Yarmoshenko, M. V. Yablonskikh, A. V. Postnikov, S. Plogmann, M. Neumann, A. V. Ezhov, and E. Z. Kurmaev, Phys. Rev. B **63**, 035106 (2001).
8. P. W. Anderson, Phys. Rev. **124** (1), 41 (1961).
9. Y. Arnaud, M. Chevreton, A. Ahouanjiou, M. Danot, and J. Rouxel, J. Solid State Chem. **18**, 9 (1976).
10. V. G. Pleschov, N. V. Baranov, A. N. Titov, K. Inoue, M. I. Bartashevich, and T. Goto, J. Alloys Compd. **320**, 13 (2001).
11. A. V. Postnikov, M. Neumann, St. Plogmann, Yu. M. Yarmoshenko, A. N. Titov, and A. V. Kuranov, Comput. Mater. Sci. **17** (2–4), 450 (2000).
12. Y. Tazuke and T. Takeyama, J. Phys. Soc. Jpn. **66**, 827 (1977).

Translated by O. Borovik-Romanova

Physics of the Solid State, Vol. 46, No. 9, 2004, pp. 1686–1692. Translated from Fizika Tverdogo Tela, Vol. 46, No. 9, 2004, pp. 1633–1639.
Original Russian Text Copyright © 2004 by Kellerman, Shalaeva, Gusev.

MAGNETISM AND FERROELECTRICITY

Cluster Formation in $LiNi_{0.4}Fe_{0.6}O_2$

D. G. Kellerman, E. V. Shalaeva, and A. I. Gusev

Institute of Solid-State Chemistry, Ural Division, Russian Academy of Sciences, ul. Pervomaĭskaya 91, Yekaterinburg, 620219 Russia

Received December 2, 2003

Abstract—The structure of an $LiNi_{0.4}Fe_{0.6}O_2$ cubic solid solution is determined using magnetic measurements and electron diffraction. It is found that this solid solution has a microinhomogeneous structure due to the formation of superparamagnetic clusters. The electron diffraction analysis of $LiNi_{0.4}Fe_{0.6}O_2$ samples has revealed diffuse scattering characteristic of the substitutional short-range order in ordered solid solutions with a *B*1-type structure. It is shown that the short-range order is associated with the $LiNiO_2$-type rhombohedral superstructure (space group $R\bar{3}m$), i.e., with the redistribution of lithium and nickel atoms in the $(111)_{B1}$ alternating planes. The short-range order is observed in regions with a nickel content higher than the mean nickel content corresponding to the macroscopic composition. © *2004 MAIK "Nauka/Interperiodica".*

1. INTRODUCTION

Compounds AMO_2 (where *A* is an alkali metal and *M* is a transition metal) have been considered promising cathode materials for use in chemical current sources [1]. The capacitance of lithium ion batteries is sensitive not only to composition but also to the structure of the material. These findings have stimulated investigation into the microinhomogeneous structure of such materials [2–4] and, in particular, the $LiNiO_2$ compound, whose structure involves short-range order regions (clusters) [5]. The hexagonal (rhombohedral) structure of the $LiNiO_2$ compound is characterized by space group $R\bar{3}m$, is a derivative of the *B*1 (NaCl)-type structure, and can be represented as a result of ordering of alkali and transition metal ions in the $(111)_{B1}$ alternating planes. The disturbance of the regular structure is associated with the incorporation of nickel ions into lithium layers and the formation of short-range order regions (clusters) around these ions. It is these regions that are responsible for the unusual magnetic properties of lithium nickelite $LiNiO_2$ [6, 7].

The degree of structural ordering in $LiNiO_2$ depends on the synthesis conditions [8, 9] and doping. From this standpoint, the $LiNiO_2$–$LiFeO_2$ system is of particular interest [10–12], because, unlike $LiNiO_2$, lithium ferrite α-$LiFeO_2$ has a *B*1 cubic structure, which belongs to rare structures where two dissimilar cations occupy the same position. In [11], it was shown that there exist two concentration ranges of limited solid solutions in this system. Solid solutions $LiNi_{1-x}Fe_xO_2$ in the concentration range $0 \le x \le 0.22$ are isostructural to the hexagonal lithium nickelite $LiNiO_2$ and the degree of their ordering decreases as nickel is replaced by iron, whereas cubic solid solutions are formed in the concentration range $0.42 \le x \le 1$. Solid solutions in the intermediate range have a two-phase structure. The hexagonal solid solutions undergo a transition to a magnetically ordered phase. The magnetic ordering indicates that cations are partially disordered, i.e., the lithium layers contain transition metal ions [10].

In cubic solid solutions $LiNi_{1-x}Fe_xO_2$ ($x \ge 0.42$), no ordering of alkali and transition metal ions occurs in a way similar to that observed in the $LiNiO_2$ structure. However, these solid solutions at $T < 200$ K have a short-range magnetic order [12], which can be caused by partial aggregation of nickel ions.

In this respect, the aim of the present work was to prove the existence of magnetic clusters in the cubic solid solution $LiNi_{1-x}Fe_xO_2$ and to reveal their related short-range structural order with the use of electron diffraction. For our investigation, we chose an $LiNi_{0.4}Fe_{0.6}O_2$ solid solution with a nickel content close to the maximum content at which the cubic structure is retained. In this solid solution, the magnetic and diffraction effects should be most pronounced.

2. SAMPLE PREPARATION AND EXPERIMENTAL TECHNIQUE

The $LiNi_{0.4}Fe_{0.6}O_2$ solid solution was synthesized by the solid-phase reaction [11] from NiO and Fe_2O_3 oxides and lithium hydroxide. The primary structural characterization was performed using x-ray diffraction on a DRON-UM1 diffractometer ($CuK_{\alpha_{1,2}}$ radiation; scan mode; scan step $\Delta 2\theta = 0.1°$; exposure time per frame, 2 s). The sample contained only the cubic phase with a *B*1 structure. The unit cell parameter was equal to 0.4145 ± 0.0002 nm. Compared to the lattice of the $LiFeO_2$ compound with the unit cell parameter $a_{B1} = 0.4158 \pm 0.0002$ nm, the lattice of the solid solution synthesized is slightly contracted as a result of the

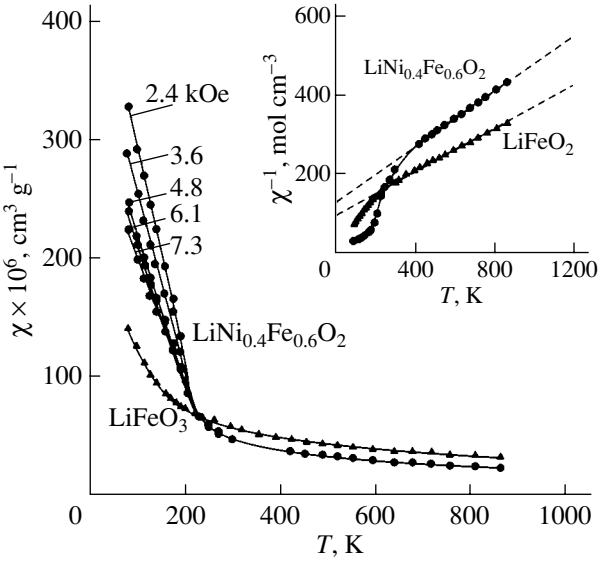

Fig. 1. Experimental temperature dependences of the magnetic susceptibility of the $LiNi_{0.4}Fe_{0.6}O_2$ and $LiFeO_2$ compounds in different magnetic fields. The inset shows the temperature dependences of the reciprocal of the magnetic susceptibility of the $LiNi_{0.4}Fe_{0.6}O_2$ and $LiFeO_2$ compounds in the field H = 2.4 kOe.

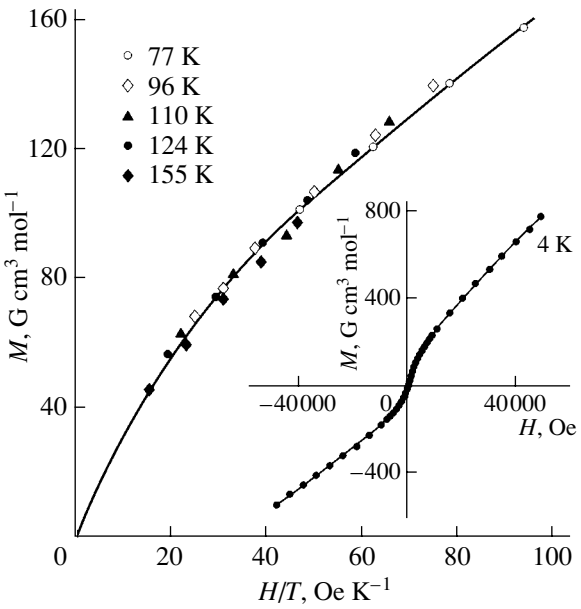

Fig. 2. Superposition of the magnetization curves for the $LiNi_{0.4}Fe_{0.6}O_2$ solid solution in the H/T–M coordinates at different temperatures. The inset shows the magnetization curve for the $LiNi_{0.4}Fe_{0.6}O_2$ solid solution at 4 K.

replacement of Fe^{3+} ions by Ni^{3+} ions with a smaller radius.

The static magnetic susceptibility was measured on an MPMS-5XL Quantum Design SQUID magnetometer at temperatures ranging from 4 to 300 K in magnetic fields up to 50 kOe and by the Faraday method in the temperature range 77–1000 K in magnetic fields up to 10 kOe.

The electron diffraction analysis was carried out with a JEM-200CX transmission electron microscope operating at a voltage of 160 keV. The microdiffraction pattern was obtained from a region ~0.5 μm in size. The samples suitable for the electron diffraction analysis were prepared through ultrasonic dispersion of an $LiNi_{0.4}Fe_{0.6}O_2$ powder in ethanol for 10 min. The smallest fraction of the $LiNi_{0.4}Fe_{0.6}O_2$ powder from an alcohol suspension was applied to a supporting amorphous carbon film on a copper grid. Judging from the results of pycnometric measurements, dispersion in the alcohol did not lead to a change in the density or, consequently, in the composition of the samples.

3. MAGNETIC PROPERTIES

The measurements revealed that the magnetic susceptibilities χ of the $LiFeO_2$ and $LiNi_{0.4}Fe_{0.6}O_2$ isostructural phases differ significantly (Fig. 1). The temperature dependence of the magnetic susceptibility $\chi^{-1}(T)$ for the $LiFeO_2$ compound exhibits a linear behavior typical of paramagnets and is adequately described by the Curie–Weiss law $\chi = A_0 + C/(T - \Theta)$, where $A_0 = -3.54$ cm^3 mol^{-1}, $C = 3.95$ cm^3 K mol^{-1}, and $\Theta = -448$ K. The deviation from linear behavior observed at $T < 200$ K is caused by the exchange interactions between Fe^{3+} ions. The magnetic susceptibility of the $LiNi_{0.4}Fe_{0.6}O_2$ solid solution obeys the Curie–Weiss law only at temperatures above 400 K ($A_0 = 90.4$ cm^3 mol^{-1}, $C = 2.86$ cm^3 K mol^{-1}, $\Theta = -386$ K). The dependence $\chi^{-1}(T)$ considerably deviates from linearity already at a temperature ~ 400 K and exhibits a kink at ~ 250 K. Below this temperature, the magnetic susceptibility depends on the magnetic field strength H (Fig. 1). The magnetizations M were measured in magnetic fields up to 50 kOe. It was found that the dependence $M(H)$ is nonlinear even at 150 K (Fig. 2). A decrease in the temperature leads to an increase in the deviation from linearity, but, even at 4 K, no saturation is observed up to a maximum field strength of 50 kOe (see inset to Fig. 2).

In order to answer the question as to whether the solid solution under investigation possesses spontaneous magnetization, we used a method based on the thermodynamic theory of ferromagnetic transformations [13]. According to Belov [13], a homogeneous system (in which magnetic ordering is possible) at $M \ll M_s$ (M_s is the saturation magnetization) obeys the following relationship between the magnetic field strength and the magnetization:

$$H/M = \alpha + \beta M^2, \quad (1)$$

where α and β are coefficients. With the use of the magnetization data, the so-called Belov–Arrott plots can be constructed in the M^2–H/M coordinates at different

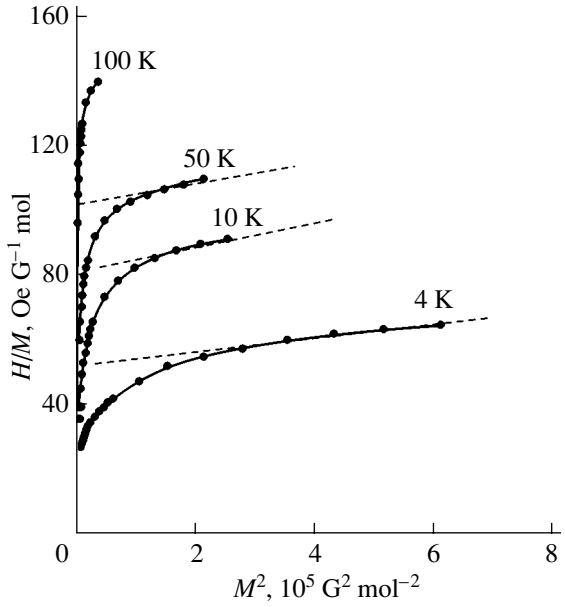

Fig. 3. Belov–Arrott plots for the $LiNi_{0.4}Fe_{0.6}O_2$ solid solution at different temperatures.

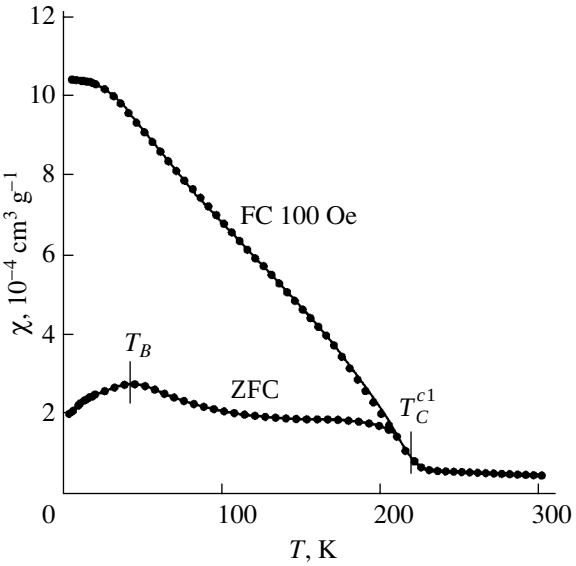

Fig. 4. Temperature dependences of the magnetic susceptibility $\chi(T)$ of the $LiNi_{0.4}Fe_{0.6}O_2$ solid solution upon heating in the field H = 100 Oe after preliminary cooling to 4 K in the field H = 100 Oe (FC) and after cooling to 4 K in zero magnetic field (ZFC). T_C^{c1} is the temperature of magnetic disordering inside clusters [11].

temperatures (Fig. 3). As follows from relationship (1), the dependences of H/M on M^2 are straight lines that intersect the ordinate axis at positive values for $T > T_C$ and at negative values for $T < T_C$. The temperature at which the coefficient α becomes zero ($\alpha = 0$) corresponds to the temperature of magnetic ordering T_C. In our case, we have $\alpha > 0$ even at 4 K (Fig. 3). This results unambiguously indicates that spontaneous magnetization and long-range magnetic order are absent in the $LiNi_{0.4}Fe_{0.6}O_2$ solid solution. Since the coefficient β in a homogeneous system does not depend on the magnetization [13, 14], the observed sharp deviation of the dependences $H/M(M^2)$ from linearity in weak fields suggests that the solid solution involves microinhomogeneities due to the formation of magnetic clusters.

Thus, the $LiNi_{0.4}Fe_{0.6}O_2$ cubic solid solution has no long-range magnetic order and the dependence of the magnetic susceptibility on the magnetic field strength is associated with the short-range magnetic order. To put it differently, the exchange interactions can occur within a limited ensemble of atoms and the conditions for percolation are absent. Such a system can be treated as a superparamagnetic system. Note that the magnetization of a superparamagnetic system is a single-valued function of the ratio H/T [15]. Therefore, the coincidence of the magnetization curves measured at different temperatures and the absence of the magnetization hysteresis with an increase and decrease in the magnetic field strength H (Fig. 2) can serve as experimental evidence of the existence of the superparamagnetic state in the $LiNi_{0.4}Fe_{0.6}O_2$ solid solution.

In superparamagnetic materials, paramagnetic centers are ferromagnetic single-domain particles rather than individual atoms (ions). Consequently, a superparamagnet possesses a high susceptibility. The magnetic moment of a superparamagnetic particle is considerably larger than that of an atom. Hence, compared to paramagnets, saturation in superparamagnetic materials can be reached in weaker magnetic fields and at sufficiently high temperatures. This manifests itself in the dependence of the susceptibility on the field strength (Fig. 1).

In the hexagonal (rhombohedral) compound $LiNiO_2$, alkali and transition metal ions are located in layers separated by oxygen planes. In the cubic compound $LiFeO_2$, ions of both metals occupy identical positions. Most likely, the formation of magnetic clusters in the $LiNi_{0.4}Fe_{0.6}O_2$ cubic solid solution is governed by the redistribution of nickel ions over the $(111)_{B1}$ planes. This leads to the formation of nickel-rich regions whose structure is similar to that of the $LiNiO_2$ compound, which is characterized by a layered structure and magnetic ordering at $T < 150$ K [16].

The microinhomogeneous structure of $LiNi_xFe_{1-x}O_2$ cubic solid solutions is also confirmed by the difference between the temperature dependences of the dc susceptibilities $\chi(T)$ (Fig. 4) measured in the magnetic field H = 100 Oe after preliminary cooling to 4 K in the same field, i.e., so-called field cooling (FC), and after cooling in zero magnetic field, i.e., so-called zero-field cooling (ZFC). The temperature of ~ 40 K, at which the dependence $\chi(T)$ measured after cooling in zero magnetic field exhibits a kink, can be interpreted as the blocking

temperature T_B. At $T \geq T_B$, the thermal energy $k_B T_B$ is comparable to (or higher than) the anisotropy energy $K_{an}V$. This leads to thermal fluctuations in the directions of the magnetic moments of the clusters and to a transition to the superparamagnetic state. Bean and Livingston [17] derived the expression for the thermal energy $k_B T_B = K_{an} V_{min}$, where V_{min} is the minimum estimate of the mean cluster volume and K_{an} is the anisotropy constant of a ferromagnetic cluster. Bajpai and Banerjee [18] estimated the anisotropy constant for $LiNiO_2$ hexagonal crystals: $K_{an} \approx 5.8 \times 10^{-4}$ J m^{-3}. From these data, the cluster radius at $T_B \sim 40$ K can be estimated as $r_{min} \geq 1.3$ nm.

It should be noted that the presence of a maximum in the temperature dependence of the static susceptibility measured after cooling in zero magnetic field and the difference between the FC and ZFC dependences often indicate a transition of the system to the spin glass state [19]. In particular, this interpretation of the experimental results for the $LiNiO_2$ compound was proposed by Shirakami *et al.* [20]. However, the presence of one more anomaly in the temperature dependence of the susceptibility at ~ 220 K (Fig. 4) due to the disturbance of magnetic order inside the clusters is inconsistent with the concept of spin glass and, in our opinion, counts in favor of the proposed model.

The mean cluster size can also be estimated from the analysis of the temperature dependence of the magnetization with the use of the expression for the superparamagnetic contribution to the susceptibility:

$$\chi_{sp} = nV\frac{M_s(T)M^*}{H\rho}L\left(\frac{VM_s(T)H}{k_B T}\right), \qquad (2)$$

where $L = [\coth(x) - 1/x]$ is the Langevin function and n is the number of superparamagnetic particles per unit volume. By assuming that clusters are spherical particles of the same size and using relationship (2), the mean radius r of magnetic clusters can be represented in the form [15, 21]

$$r = \left\{\frac{9k_B CM^*}{4\pi M_s I_0 \rho}\right\}^{1/3}. \qquad (3)$$

In formula (3), the parameters for the $LiNi_{0.4}Fe_{0.6}O_2$ solid solution are as follows: $C = 3.33$ cm^3 K mol^{-1} is the Curie constant at $H \longrightarrow 0$, $M^* = 95.93$ g mol^{-1} is the molecular weight, $\rho = 4.49$ g cm^{-3} is the density, $M_s = 1563$ G cm^3 mol^{-1} is the specific saturation magnetization per mole [the magnetization M_s was obtained through linear extrapolation of the dependence $M(T/H)$ to $T/H = 0$, i.e., to an infinite field], and $I_0 = 4000$ G cm^3 mol^{-1} is the specific saturation magnetization of the cluster material (this value corresponds to the experimental saturation magnetization of the $LiNi_{0.8}Fe_{0.2}O_2$ hexagonal solid solution with the highest iron content and long-range magnetic order [16]). For these parameters, the mean radius r of magnetic clusters is approximately equal to 1.4 nm. This radius is in good agreement with the estimate made from the blocking temperature.

4. ELECTRON DIFFRACTION

In order to reveal the short-range structural order, which was assumed from analyzing the magnetic properties and could arise from the redistribution of lithium and nickel atoms, the $LiNi_{0.4}Fe_{0.6}O_2$ solid solution was studied using electron diffraction. Indeed, when the arrangement of Li and Ni atoms is characterized by a short-range order, the electron diffraction patterns should contain both Bragg reflections and periodic features of diffuse scattering, because the distribution function of the diffuse intensity $I_D(\mathbf{g})$ in the reciprocal space is uniquely related to the short-range order parameters. Therefore, knowing the geometry of the diffuse scattering distribution in particular planes of the reciprocal lattice and reconstructing the three-dimensional pattern of diffuse scattering in the reciprocal space, we can analyze the short-range order in the $LiNi_{0.4}Fe_{0.6}O_2$ solid solution in the framework of the approximate cluster model [22, 23].

The $LiNi_{0.4}Fe_{0.6}O_2$ solid solution was examined with the use of an electron microscope. As a result, we obtain a number of microdiffraction patterns corresponding to different cross sections of the reciprocal lattice of the $LiNi_{0.4}Fe_{0.6}O_2$ cubic phase (with the $B1$ structure). Figures 5 and 6 show the diffraction patterns and their schemes for the $(111)^*_{B1}$ and $(110)^*_{B1}$ planes of the reciprocal lattice of the solid solution under investigation. These diffraction patterns contain Bragg reflections of the $B1$ lattice and a set of diffuse features. The observed periodic diffuse features do not pass through the points of the reciprocal lattice of the cubic solid solution. This implies that the diffuse features are associated with the substitutional short-range order [24]. Furthermore, the diffuse scattering observed for the $LiNi_{0.4}Fe_{0.6}O_2$ cubic solid solution is also characteristic of the substitutional short-range order in ordered binary solid solutions with a $B1$-type lattice [23, 25, 26].

Brunel *et al.* [23] demonstrated that, in ABX_2 ionic compounds ($LiFeO_2$, $NaFeO_2$), which have a $B1$ structure and are ordered in the AB sublattice, a similar diffuse scattering distribution is determined by the A_3B_3 octahedral cluster. For this cluster, the diffuse intensity contours are described by the relationship $\cos(\pi h) + \cos(\pi k) + \cos(\pi l) = 0$, where h, k, and l are the coordinates in the reciprocal space. The schematic drawing of the diffuse intensity contours in the reciprocal lattice of a $B1$-type solid solution is given in Fig. 7. The A_3B_3 octahedral cluster is characterized by different types of substitutional short-range order. The diffuse scattering geometry under consideration is equally characteristic of two types of short-range order that correspond to two

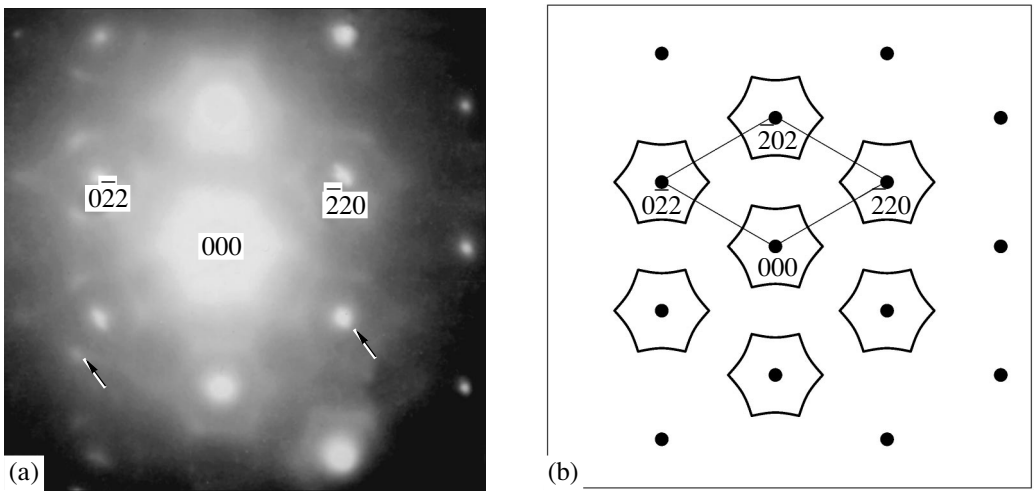

Fig. 5. (a) Diffraction pattern of the cubic solid solution crystals $LiNi_{0.4}Fe_{0.6}O_2$ (structure *B*1) and (b) schemes of the $(111)^*_{B1}$ cross section of the reciprocal lattice.

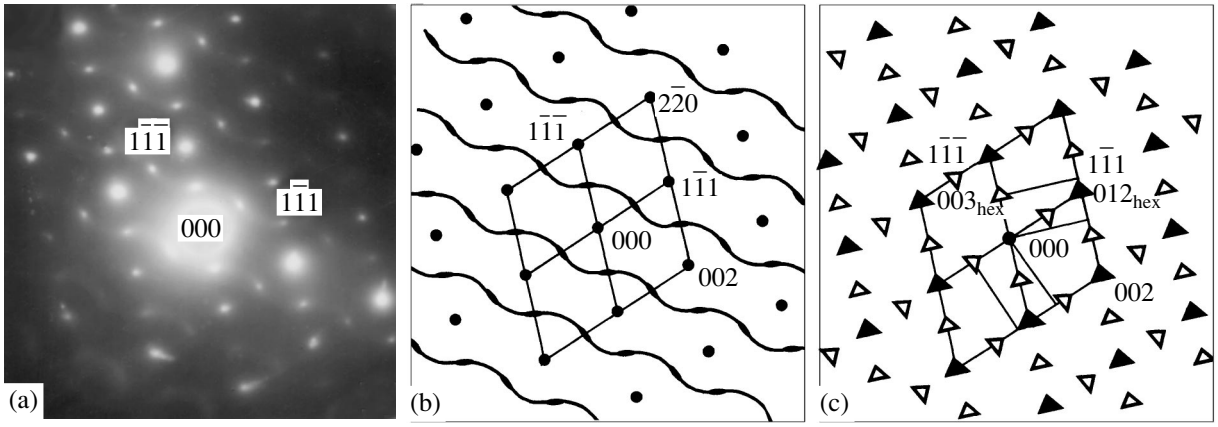

Fig. 6. (a) Diffraction pattern of the cubic solid solution crystals $LiNi_{0.4}Fe_{0.6}O_2$ (structure *B*1) and (b, c) schemes of the $(110)^*_{B1}$ cross section of the reciprocal lattice. Panel (c) shows the sets of reflections for two equivalent cross sections $(100)^*_{hex} \parallel (100)^*_{B1}$ of the reciprocal lattice of the $LiNiO_2$-type rhombohedral superstructure (space group $R\bar{3}m$) with two possible orientations of the $[001]^*_{hex}$ axis: $[001]^*_{hex} \parallel [1\bar{1}\bar{1}]^*_{B1}$ and $[001]^*_{hex} \parallel [1\bar{1}1]^*_{B1}$.

different superstructures ordered on the basis of the ABX_2 compound with the *B*1 lattice [23]. These are the tetragonal superstructure ABX_2 with space group D^{19}_{4h} (for example, γ-$LiFeO_2$), where each $(111)_{B1}$ plane contains equal fractions of *A* and *B* atoms, and the rhombohedral (hexagonal)[1] superstructure ABX_2 with space group $R\bar{3}m$ (for example, $NaFeO_2$, $LiNiO_2$), in which *A* and *B* atoms occupy positions in $(111)_{B1}$ alternating planes. The experimental diffuse scattering patterns were measured using transmission electron microscopy for both types of ordered solid solutions: (i) $LiFeO_2$ quenched samples, which are ordered following the γ superstructure type (space group D^{19}_{4h}) [26], and (ii) $TiC_{0.65}\square_{0.35}$ quenched samples (□ is a structural vacancy), which are ordered following the $TiC_{0.5}\square_{0.5}$ (Ti_2C) rhombohedral superstructure (space group $R\bar{3}m$) [27].

The analysis of the redistribution of the diffuse intensity in the contours with due regard for the possible types of short-range order enables us to draw sufficiently conclusive inferences regarding the observed short-range order. It is established that the diffuse inten-

[1] Hereinafter, the diffraction patterns and the short-range order corresponding to the rhombohedral superstructure will be analyzed in the hexagonal setting.

sity increases in the vicinity of the reciprocal lattice points with coordinates $\pm(1/2, 1/2, 1/2)_{B1}$. This increase is observed in the $(110)^*_{B1}$ and $(111)^*_{B1}$ cross sections. The $(111)^*_{B1}$ cross section does not pass exactly through reciprocal lattice points of the $(1/2, 1/2, 1/2)_{B1}$ type, but a noticeable enhancement of the segments of diffuse intensity (shown by the arrow in Fig. 5a) occurs at intersections with the diffuse intensity contours at the $(1, 1/2, 1/2)_{B1}$ positions. In a number of cases, in the $(110)^*_{B1}$ cross section of the reciprocal lattice, the intensity increases substantially and superstructure reflections are observed at positions of the $\pm(1/2, 1/2, 1/2)_{B1}$ type (Figs. 6a, 6b). The set of these diffuse maxima is completely identified by two equivalent $(100)^*_{\text{hex}}$ cross sections of the reciprocal lattice of the $LiNiO_2$-type rhombohedral superstructure (Figs. 6b, 6c) with two possible orientations of the $[001]^*_{\text{hex}}$ axis: $[001]^*_{\text{hex}} \parallel [1\bar{1}\bar{1}]^*_{B1}$ and $[001]^*_{\text{hex}} \parallel [1\bar{1}1]^*_{B1}$. We failed to reveal rhombohedral distortions in the interplanar spacings and angles, which are inherent in the $LiNiO_2$-type superstructure. For example, the $(111)_{B1}$ reflection for the $LiNiO_2$ compound is split into the $(006)_{\text{hex}}$ and $(012)_{\text{hex}}$ reflections with a difference between the interplanar distances $\Delta d = 0.0015$ nm. The corresponding angle between the vectors $[1\bar{1}\bar{1}]^*_{B1}$ and $[1\bar{1}1]^*_{B1}$ in the cubic reciprocal lattice is equal to 70.53°. The analogous angle between the rhombohedral vectors $[006]^*_{\text{hex}}$ and $[012]^*_{\text{hex}}$ is 70.65°; i.e., these angles coincide to within experimental error. The absence of rhombohedral distortions implies that the solid solution does not contain particles with a rhombohedral superstructure but exhibits a superstructural rhombohedral short-range order [28, 29], which is responsible for the redistribution of the diffuse intensity and the appearance of diffuse reflections [30].

The results obtained unambiguously indicate that the structure of the $LiNi_{0.4}Fe_{0.6}O_2$ cubic solid solution is characterized by the short-range order corresponding to a rhombohedral superstructure. The radius of short-range order regions was estimated at ~ ~$3a_{B1}$ from the magnetic data. This means that the correlations in the mutual arrangement of Li and Ni atoms cover more than 15 coordination shells [28]. A question arises as to the composition of short-range order regions, i.e., the composition of the main octahedral cluster in the framework of the cluster model proposed by Shirakami *et al.* [20]. This composition does not correspond to the macroscopic composition $LiNi_{0.4}Fe_{0.6}O_2$, because the concentration of nickel atoms in the $LiNi_{0.4}Fe_{0.6}O_2$–$LiNiO_2$ region is several times higher than the concentrations at which the short-range order manifests itself in ordered solid solutions. The observed diffraction features, which are associated with the short-range order attributed to a rhombohedral superstructure of the $LiNiO_2$ type, suggest a local compositional inhomogeneity of the $LiNi_{0.4}Fe_{0.6}O_2$ solid solution. There should exist nickel-rich regions in which the short-range order in the arrangement of Li and Ni atoms coincides with the short-range order inherent in the rhombohedral superstructure. It can be assumed that the composition of ordered clusters lies in the $LiNi_{0.8}Fe_{0.2}O_2$–$LiNiO_2$ region, because solid solutions in this region have a hexagonal structure.

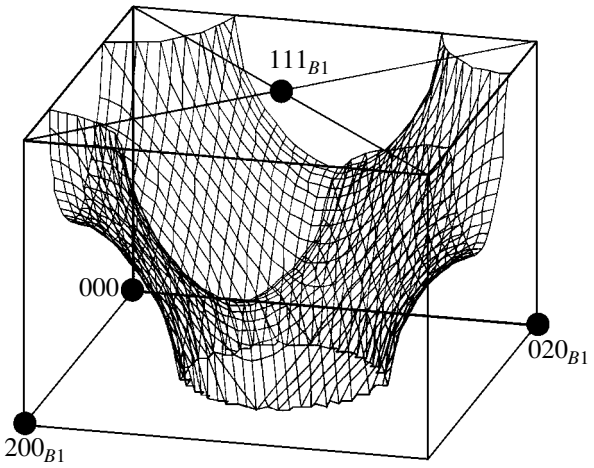

Fig. 7. Schematic drawing of the diffuse intensity contours in the reciprocal lattice of the $LiNi_{0.4}Fe_{0.6}O_2$ cubic solid solution (structure $B1$) according to the model $\cos(\pi h) + \cos(\pi k) + \cos(\pi l) = 0$ (the reciprocal lattice segment with $0 \le h \le 2$, $0 \le k \le 2$, $0 \le h \le 1$ is shown).

5. CONCLUSIONS

Thus, the above analysis of the magnetic properties of the $LiNi_{0.4}Fe_{0.6}O_2$ solid solution demonstrated that this solution is characterized by a short-range magnetic order, which can be described within the concept of superparamagnetism. The occurrence of short-range order was confirmed by the electron diffraction data. The electron diffraction patterns of the $LiNi_{0.4}Fe_{0.6}O_2$ cubic solid solution exhibit the diffuse scattering typical of the substitutional short-range order in ordered solid solutions with a $B1$ structure. The observed short-range order is associated with the $LiNiO_2$-type rhombohedral superstructure (space group $R\bar{3}m$), i.e., with the redistribution of lithium and nickel atoms in $(111)_{B1}$ alternating planes. This short-range order occurs in regions in which the Ni content is higher than the mean Ni content corresponding to the macroscopic composition of the $LiNi_{0.4}Fe_{0.6}O_2$ solid solution.

In the near future, the geometry of the diffuse intensity for ordered cubic solid solutions $LiNi_{1-x}Fe_xO_2$ can be analytically described using the refined cluster model [31, 32] within the approach proposed for

numerical estimation of the order parameters in nonstoichiometric carbides [27, 31]. This will make it possible to determine the dependence of the parameters of the analytical description of diffuse scattering and the short-range order parameters on the composition of $LiNi_{1-x}Fe_xO_2$ solid solutions. It can be expected that the weakening of short-range order effects with a decrease in the Ni content in $LiNi_{1-x}Fe_xO_2$ cubic solid solutions will correlate with the change in the magnetic properties.

ACKNOWLEDGMENTS

This work was supported by the Russian Foundation for Basic Research, project nos. 03-03-32031a and 04-03-32198a.

REFERENCES

1. C. Delmas, in *Industrial Chemistry Library*, Ed. by G. Pistoia (Elsevier, Amsterdam, 1994), Vol. 5, p. 457.
2. L. Croguennec, P. Deniard, R. Brec, and A. Lecerf, J. Mater. Chem. **7** (3), 511 (1997).
3. L. Croguennec, P. Deniard, R. Brec, P. Biensan, and M. Broussely, Solid State Ionics **89** (1–2), 127 (1996).
4. V. Berbenni, V. Massarotti, D. Capsoni, R. Riccardi, A. Marini, and E. Antolini, Solid State Ionics **48** (1–2), 101 (1991).
5. A.-L. Barra, G. Chouteau, A. Stepanov, and C. Delmas, J. Magn. Magn. Mater. **177** (2), 783 (1998).
6. A.-L. Barra, G. Chouteau, A. Stepanov, A. Rougier, and C. Delmas, Eur. Phys. J. B **7** (4), 551 (1999).
7. D. G. Kellerman, Usp. Khim. **70** (9), 874 (2001).
8. V. S. Gorshkov, D. G. Kellerman, V. A. Perelyaev, and G. P. Shveĭkin, Zh. Neorg. Khim. **41** (10), 1621 (1996).
9. H. Arai, S. Okada, H. Ohtsuka, M. Ichimura, and J. Yamaki, Solid State Ionics **80** (3–4), 261 (1995).
10. J. N. Reimers, E. Rossen, C. D. Jones, and J. R. Dahn, Solid State Ionics **61** (4), 335 (1993).
11. D. G. Kellerman, V. S. Gorshkov, V. A. Perelyaev, and G. P. Shveĭkin, Zh. Neorg. Khim. **35** (5), 1267 (1990).
12. D. G. Kellerman, V. S. Gorshkov, and V. V. Karelina, Zh. Neorg. Khim. **44** (7), 1078 (1999).
13. K. P. Belov, *Magnetic Transitions* (GIFML, Moscow, 1959; Consultants Bureau, New York, 1961).
14. K. Binder and A. P. Young, Rev. Mod. Phys. **58** (4), 801 (1986).
15. C. P. Bean, J. Appl. Phys. **26** (8), 1381 (1955).
16. V. S. Gorshkov, D. G. Kellerman, V. A. Perelyaev, and G. P. Shveĭkin, Izv. Akad. Nauk SSSR, Neorg. Mater. **27** (6), 1274 (1991).
17. C. P. Bean and J. D. Livingston, J. Appl. Phys. Suppl. **10** (4), 120 (1959).
18. A. Bajpai and A. Banerjee, Phys. Rev. B **62** (13), 8996 (2000).
19. C. Y. Huang, J. Magn. Magn. Mater. **51** (1), 1 (1985).
20. T. Shirakami, M. Takematsu, A. Hirano, R. Kanno, K. Yamaura, M. Takano, and T. Atake, Mater. Sci. Eng. B **54** (1–2), 70 (1998).
21. A. Banerjee and S. Lahiry, Phys. Status Solidi A **76** (2), 683 (1983).
22. R. de Ridder, G. van Tendello, and S. Amelinckx, Acta Crystallogr. A **32** (2), 216 (1976).
23. M. Brunel, F. D. Bergevin, and M. Gondrand, J. Phys. Chem. Solids **33** (8), 1927 (1972).
24. J. M. Cowley, *Diffraction Physics* (Elsevier, New York, 1975; Mir, Moscow, 1979).
25. J. Billingham, P. S. Bell, and N. H. Lewis, Acta Crystallogr. A **28** (6), 602 (1972).
26. R. D. Ridder, D. V. Dyck, G. V. Tendeloo, and S. Amelinckx, Phys. Status Solidi A **40** (2), 669 (1977).
27. J. Bursik and G. C. Weatherly, Phys. Status Solidi A **174** (2), 327 (1999).
28. A. A. Rempel' and A. I. Gusev, Fiz. Tverd. Tela (Leningrad) **32** (1), 16 (1990) [Sov. Phys. Solid State **32**, 8 (1990)].
29. A. I. Gusev, A. A. Rempel, and A. J. Magerl, *Disorder and Order in Strongly Nonstoichiometric Compounds: Transition Metal Carbides, Nitrides, and Oxides* (Springer-Verlag, Berlin, 2001).
30. A. G. Christy and A. K. Larson, Solid State Ionics **140** (2), 402 (1998).
31. M. Sauvage and E. Parthe, Acta Crystallogr. A **28** (6), 607 (1972).
32. G. V. Tendeloo and S. Amelinckx, Phase Transit. **67** (1), 101 (1998).

Translated by O. Borovik-Romanova

Physics of the Solid State, Vol. 46, No. 9, 2004, pp. 1693–1703. Translated from Fizika Tverdogo Tela, Vol. 46, No. 9, 2004, pp. 1640–1649.
Original Russian Text Copyright © 2004 by Gulakov, Sazonov.

MAGNETISM AND FERROELECTRICITY

Nonlinear Acoustic Transparency for Longitudinal–Transverse Picosecond Pulses in a Paramagnetic Crystal at Low Temperatures

A. V. Gulakov and S. V. Sazonov

Kaliningrad State University, Kaliningrad, 236041 Russia

e-mail: nst@alg.kaliningrad.ru

Received December 4, 2003

Abstract—Nonlinear propagation of longitudinal–transverse acoustic pulses of duration shorter than one oscillation period (video pulses) is studied theoretically in a system of paramagnetic centers with effective spin $S = 1$. It is shown that, depending on the relationship between the magnitudes of the longitudinal and transverse strain components and on the detuning of their linear velocities, various regimes of propagation corresponding to different dynamics of the field and the medium can occur. In the case where the velocities of longitudinal and transverse hypersonic waves differ only slightly, an effect similar to self-induced transparency is analyzed. For substantial velocity detuning, propagation in the form of rational solitons is possible. If the transverse component is dominant, these solitons can produce full population inversion of Zeeman sublevels. In the opposite limit, the populations remain practically unchanged. © *2004 MAIK "Nauka/Interperiodica".*

1. INTRODUCTION

One of the basic trends in the development of modern nonlinear optics and physical acoustics is the generation of progressively shorter pulses under laboratory conditions. Today, it is possible to generate pulses of duration of about one (and even a half) period of oscillations [1–3]. In such cases, one usually speaks about extremely short pulses (ESP), or video pulses. The duration τ_p can be as short as 5–10 fs for optical ESP and about 10 ps for acoustic pulses [2].

The basic difference between ESP and quasi-monochromatic pulses is the absence of a strongly pronounced carrier frequency for ESP. Therefore, in studying the interaction of such pulses with matter theoretically, one cannot use the approximation of a slowly varying envelope function, which is traditionally applied to quasi-monochromatic pulses.

Analysis of the development of the modern physics of coherent phenomena reveals, in particular, that sooner or later acoustic analogs of optical nonstationary effects had to be discovered [4]. The corresponding historical analysis is performed in [5]. In this paper, we consider the acoustic analog of self-induced transparency (SIT) [6]. The phenomenon of acoustic SIT was predicted and detected several years after the discovery of optical SIT [7–9].

It is important to note not only the similarity but also differences between the optical and acoustic coherent phenomena. One of the basic differences can be related to the fact that an acoustic wave in a solid has longitudinal–transverse structure, with the velocities of longitudinal ($a_\parallel$) and transverse ($a_\perp$) waves being generally different. In [10], the effect of this two-component structure on the acoustic SIT was studied and different soliton propagation regimes were detected for slightly different values of $a_\parallel$ and $a_\perp$. In [11, 12], the case of $a_\parallel = a_\perp$ was considered without using the approximation of a slowly varying envelope function and problems of integrability of the corresponding system of constitutive and wave equations were investigated.

The phenomenon of SIT for optical ESP was studied in detail in [13], where similarities and differences with SIT for quasi-monochromatic pulses were demonstrated.

The interaction of acoustic ESP with substances in the regime of acoustic SIT was studied in [14], where the quantum objects interacting with elastic pulses were considered to be paramagnetic ions with effective spin $S = 1/2$. Although such a model is mathematically relatively simple, it is not quite adequate to the experimental situation. Indeed, the experiment shows that paramagnetic ions with effective spin $S = 1$ are most strongly coupled dynamically with lattice vibrations [15–17]. The Fe^{2+} and Ni^{2+} ions in a MgO crystalline matrix are examples of such ions [7]. Therefore, it is important to theoretically study the interaction of acoustic ESP with a system of spins $S = 1$ in the regime of acoustic SIT. This is the objective of the present study.

2. SEMICLASSICAL EQUATIONS OF MOTION

We consider the case where an external magnetic field **B** is directed along a fourfold axis (chosen to be the z axis) of a cubic paramagnetic crystal. In this case,

1063-7834/04/4609-1693$26.00 © 2004 MAIK "Nauka/Interperiodica"

the Hamiltonian of a spin interacting with lattice vibrations in this field is

$$\hat{H} = \hat{H}_s + \hat{V}, \tag{1}$$

where the spin Hamiltonian is

$$\hat{H}_s = g\mu_B B\hat{S}_z. \tag{2}$$

Here, g is the Lande factor, μ_B is the Bohr magneton, and the spin–phonon interaction Hamiltonian $\hat{V}$ is a quadratic form in spin operators [15–17]:

$$\hat{V} = G_{ijml}\mathscr{E}_{ml}\hat{S}_i\hat{S}_j = \frac{1}{2}G_{ijml}\mathscr{E}_{ml}(\hat{S}_i\hat{S}_j + \hat{S}_j\hat{S}_i), \tag{3}$$

where G_{ijml} are the tensor components of the spin–phonon interaction; $\hat{S}_j$ ($j = x, y, z$) are the 3×3 spin matrices, which (in the geometry considered) have the form [15]

$$\hat{S}_x = \frac{1}{\sqrt{2}}\begin{pmatrix} 0 & 1 & 0 \\ 1 & 0 & 1 \\ 0 & 1 & 0 \end{pmatrix}, \quad \hat{S}_y = \frac{i}{\sqrt{2}}\begin{pmatrix} 0 & -1 & 0 \\ 1 & 0 & -1 \\ 0 & 1 & 0 \end{pmatrix},$$
$$\hat{S}_z = \begin{pmatrix} 1 & 0 & 0 \\ 0 & 0 & 0 \\ 0 & 0 & -1 \end{pmatrix}, \tag{4}$$

and $\mathscr{E}_{ml}$ is the strain tensor, which can be expressed in terms of the Cartesian components of the local displacement vector **U** as

$$\mathscr{E}_{ml} = \frac{1}{2}\left(\frac{\partial U_m}{\partial x_l} + \frac{\partial U_l}{\partial x_m}\right), \tag{5}$$

with $m, l = x, y, z$. In Eq. (3) and in what follows, summation over repeated inferior indices is implied.

The components of the tensor $\hat{G}$ are symmetric with respect to permutations of the pairs of indices i, j and m, l and also with respect to the permutations inside these pairs.

To describe the dynamics of spins and acoustic pulses self-consistently, we add the elastic-field Hamiltonian to Eqs. (2) and (3). Further, we use the semiclassical approach, according to which spins are treated quantum-mechanically and the elastic field is described by the classical equations of mechanics of continuous media. Accordingly, the elastic-field Hamiltonian has the form of a classical functional [18],

$$H_a = \frac{1}{2}\int\left(\frac{p_i p_j}{\rho} + \lambda_{ijkl}\frac{\partial U_i}{\partial x_j}\frac{\partial U_k}{\partial x_l}\right)d^3\mathbf{r}, \tag{6}$$

where ρ is the average crystal density, p_i ($i = x, y, z$) are the components of the momentum density **p** of local displacements, and λ_{ijkl} are the components of the elastic modulus of the medium.

Using the standard semiclassical approach [16], we describe the spin evolution by the equation for the density matrix,

$$i\hbar\frac{\partial\hat{\rho}}{\partial t} = [\hat{H}_s + \hat{V}, \hat{\rho}], \tag{7}$$

and describe the dynamics of the acoustic field by the classical Hamilton equations for a continuous medium,

$$\frac{\partial\mathbf{p}}{\partial t} = -\frac{\delta}{\delta\mathbf{U}}(H_a + \langle\hat{\tilde{V}}\rangle), \quad \frac{\partial\mathbf{U}}{\partial t} = \frac{\delta}{\delta\mathbf{p}}(H_a + \langle\hat{\tilde{V}}\rangle). \tag{8}$$

Here, $\langle\hat{\tilde{V}}\rangle = \int n\langle\hat{V}\rangle d\mathbf{r}$, n is the concentration of paramagnetic centers, and $\langle\hat{V}\rangle \equiv \mathrm{Tr}(\hat{\rho}\hat{V})$ is the quantum average of the interaction Hamiltonian. In Eq. (7), we disregarded relaxation terms assuming that the pulse duration is shorter than all relaxation times.

The set of equations (7) and (8), in combination with Eqs. (1)–(6), describes the propagation of an acoustic pulse in any given direction with respect to **B**. In what follows, we consider the Faraday geometry; i.e., the pulse propagates along **B**. All dynamic variables are assumed to depend only on z and t. Therefore, there are three nonzero components of the strain tensor, namely, $\mathscr{E}_{zz} = \mathscr{E}_\parallel = \partial U_z/\partial z$, $\mathscr{E}_{xz} = 0.5\partial U_x/\partial z$ and $\mathscr{E}_{yz} = 0.5\partial U_y/\partial z$. In addition, in the case of a cubic crystal, the nonzero components of the elastic modulus are $\lambda_{xzxz} = \lambda_{yzyz} = \lambda_\perp$ and $\lambda_{zzzz} = \lambda_\parallel$. For the components of the tensor $\hat{G}$, we use the Voigt notation [15]: $xx \longrightarrow 1$, $yy \longrightarrow 2$, $zz \longrightarrow 3$, $yz \longrightarrow 4$, $xz \longrightarrow 5$, and $xy \longrightarrow 6$. Due to the cubic symmetry, we have $G_{23} = G_{13}$, $G_{33} = G_{22} = G_{11}$, and $G_{55} = G_{44}$. To simplify expressions for $\hat{V}$ in a cubic crystal, we note that, under inversion of the x and y axes, the components of the spin operator are transformed as follows [16]: $x \longrightarrow -x$, $\hat{S}_x \longrightarrow \hat{S}_x$, $\hat{S}_y \longrightarrow -\hat{S}_y$, and $\hat{S}_z \longrightarrow -\hat{S}_z$; $y \longrightarrow -y$, $\hat{S}_x \longrightarrow -\hat{S}_x$, $\hat{S}_y \longrightarrow \hat{S}_y$, and $\hat{S}_z \longrightarrow -\hat{S}_z$. Taking into account the invariance of V with respect to these transformations, we can write

$$\hat{V} = \frac{3}{2}G_{11}\hat{S}_z^2\frac{\partial u_z}{\partial z} + \frac{1}{2}G_{44}\left[\frac{\partial U_x}{\partial z}(\hat{S}_z\hat{S}_x + \hat{S}_x\hat{S}_z) + \frac{\partial U_y}{\partial z}(\hat{S}_z\hat{S}_y + \hat{S}_y\hat{S}_z)\right]. \tag{9}$$

From the foregoing, it follows that, using Eqs. (8) and (9), we can write

$$\frac{\partial^2\mathscr{E}_\perp}{\partial t^2} - a_\perp^2\frac{\partial^2\mathscr{E}_\perp}{\partial z^2} = \frac{n}{2\rho}G_{44}\frac{\partial^2}{\partial z^2}(\rho_{32}^* - \rho_{21}^*), \tag{10}$$

$$\frac{\partial^2\mathscr{E}_\parallel}{\partial t^2} - a_\parallel^2\frac{\partial^2\mathscr{E}_\parallel}{\partial z^2} = -\frac{3n}{2\rho}G_{11}\frac{\partial^2\rho_{22}}{\partial z^2}, \tag{11}$$

where the transverse strain is $\mathscr{E}_\perp \equiv (\mathscr{E}_{xz} + i\mathscr{E}_{yz})/\sqrt{2}$ and $a_\perp = \sqrt{\lambda_\perp/\rho}$ and $a_\parallel = \sqrt{\lambda_\parallel/\rho}$ are the velocities of transverse and longitudinal sonic waves, respectively, in the absence of paramagnetic impurities.

Using Eqs. (2)–(4), we can rewrite the operator $\hat{H}_a + \hat{V}$ in the matrix form as

$$\hat{H}_s + \hat{V} = \begin{pmatrix} \hbar\omega_0 + \frac{3}{2}G_{11} & \mathscr{E}_\parallel \frac{G_{44}}{2}\mathscr{E}_\perp^* & 0 \\ \frac{G_{44}}{2}\mathscr{E}_\perp & 0 & -\frac{G_{44}}{2}\mathscr{E}_\perp^* \\ 0 & -\frac{G_{44}}{2}\mathscr{E}_\perp & -\hbar\omega_0 + \frac{3}{2}G_{11}\mathscr{E}_\parallel \end{pmatrix}, \quad (12)$$

where $\omega_0 = g\mu_B B/\hbar$ is the Zeeman splitting frequency in the equidistant three-level system with spin $S = 1$. We note that we number the quantum levels in ascending order.

It is seen from Eqs. (10)–(12) that, in the Faraday geometry, the transverse component of the acoustic wave induces the cascade quantum transitions $1 \rightleftharpoons 2$ and $2 \rightleftharpoons 3$, whereas the longitudinal component causes a dynamical change in the frequencies of these transitions (Fig. 1). The physical mechanism of spin–phonon interaction in the case considered is the so-called Van Vleck mechanism [4, 15, 17]; according to this mechanism, an acoustic wave creates a crystalline electric field gradient at the positions of paramagnetic ions. This gradient, in turn, induces quadrupole transitions between Zeeman sublevels and the dynamic quadrupole Stark effect, where the levels with magnetic quantum numbers M that are equal in magnitude are displaced equally [19]. In our case, the first ($M = -1$) and third ($M = +1$) levels are displaced equally.

In zeroth approximation with respect to the right-hand sides of Eqs. (10) and (11), we have two waves propagating in different directions with velocities $a_\perp$ and $a_\parallel$ respectively. We consider only waves propagating along the z axis, and assume that the velocities $a_\perp$ and $a_\parallel$ differ only slightly, $(a_\parallel - a_\perp)/a_\parallel \ll 1$. This approximation is well justified in the bulk and yields a small error near the front surface because of partial reflection. In first approximation with respect to the right-hand sides of Eqs. (10) and (11), we write $\mathscr{E}_\parallel = \mathscr{E}_\parallel(\tau, \zeta)$ and $\mathscr{E}_\perp = \mathscr{E}_\perp(\tau, \zeta)$, where $\tau = t - z/a_\parallel$ is the local time, $\zeta = \mu z$ is a "slow coordinate" [20], and μ is a small dimensionless parameter ($\mu \ll 1$), whose meaning will be discussed below. Obviously,

$$\frac{\partial^2}{\partial t^2} \longrightarrow \frac{\partial^2}{\partial \tau^2}, \quad \frac{\partial}{\partial z} \longrightarrow -\frac{1}{a_\parallel}\frac{\partial}{\partial \tau} + \mu\frac{\partial}{\partial \zeta}.$$

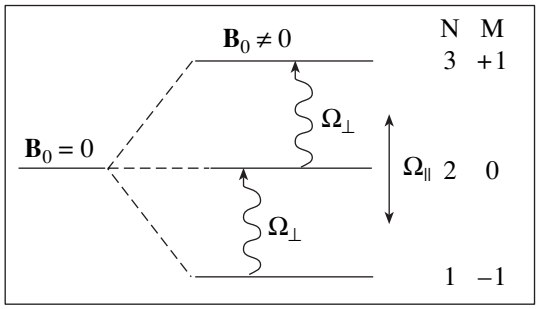

Fig. 1. Diagram of quantum transitions in a three-level system in the presence of Zeeman splitting. N is the number of the quantum level, M is the magnetic quantum number, wavy lines correspond to quantum transitions induced by the transverse component of an acoustic pulse, and the double arrow ⟷ corresponds to the dynamic frequency shift for these transitions.

Disregarding the terms of the order of $\sim\mu^2$, we write

$$\frac{\partial^2}{\partial z^2} \longrightarrow \frac{1}{a_\parallel^2}\frac{\partial^2}{\partial \tau^2} - \frac{2\mu}{a_\parallel}\frac{\partial^2}{\partial \tau \partial \zeta}.$$

Substituting these expressions into Eqs. (10) and (11), integrating with respect to τ, and taking into account that the strain and its derivatives vanish at infinity, we obtain first-order differential equations for $\mathscr{E}_\parallel$ and $\mathscr{E}_\perp$.

These equations and the corresponding constitutive equations can be written in the form

$$\frac{\partial \Omega_\perp}{\partial z} + \left(\frac{1}{a_\perp} - \frac{1}{a_\parallel}\right)\frac{\partial \Omega_\perp}{\partial \tau} = \beta_\perp \frac{\partial}{\partial \tau}(\rho_{32}^* - \rho_{21}^*), \quad (13)$$

$$\frac{\partial \Omega_\parallel}{\partial z} = -\beta_\parallel \frac{\partial \rho_{22}}{\partial \tau}, \quad (14)$$

$$\frac{\partial \hat{\rho}}{\partial \tau} = -i[\hat{\Omega}, \hat{\rho}], \quad (15)$$

where

$$\hat{\Omega} = \begin{pmatrix} \Omega_\parallel + \omega_0 & \Omega_\perp^*/2\sqrt{2} & 0 \\ \Omega_\perp/2\sqrt{2} & 0 & -\Omega_\perp^*/2\sqrt{2} \\ 0 & -\Omega_\perp/2\sqrt{2} & \Omega_\parallel - \omega_0 \end{pmatrix},$$

$$\Omega_\parallel = 3G_{11}\mathscr{E}_\parallel/2\hbar, \quad \Omega_\perp = G_{44}\mathscr{E}_\perp/2\hbar, \quad (16)$$

$$\beta_\perp = nG_{44}^0/(8\hbar\rho a_\parallel a_\perp^2), \quad \beta_\parallel = 9nG_{11}^2/(8\hbar\rho a_\parallel^3).$$

Using Eq. (15), we write the constitutive equations for the elements of the density matrix that appear on the

right-hand side of Eq. (13) in the form

$$\frac{\partial\rho_{32}^*}{\partial\tau} = i(\omega_0+\Omega_\parallel)\rho_{32}^* - \frac{i\Omega_\perp}{2\sqrt{2}}(\rho_{33}-\rho_{22}) + \frac{i\Omega_\perp^*}{2\sqrt{2}}\rho_{31}^*,$$

$$\frac{\partial\rho_{21}^*}{\partial\tau} = i(\omega_0-\Omega_\parallel)\rho_{21}^* - \frac{i\Omega_\perp}{2\sqrt{2}}(\rho_{11}-\rho_{22}) + \frac{i\Omega_\perp^*}{2\sqrt{2}}\rho_{31}^*.$$

With these equations, we can write the derivative on the right-hand side of Eq. (13) as

$$\frac{\partial}{\partial\tau}(\rho_{32}^*-\rho_{21}^*) = i\omega_0(\rho_{32}^*-\rho_{21}^*) + i\Omega_\parallel(\rho_{32}^*+\rho_{21}^*) + \frac{i\Omega_\perp}{2\sqrt{2}}(\rho_{11}-\rho_{33}). \quad (17)$$

Further study is based on the set of wave and constitutive equations (13)–(17).

3. NONLINEAR WAVE EQUATIONS

Let the pulse duration τ_p be so short that the condition of spectral overlap [14, 21] is satisfied,

$$\omega_0\tau_p \ll 1; \quad (18)$$

i.e., the pulse spectrum contains Fourier components in resonance with transitions between Zeeman sublevels. In this case, the interaction between the acoustic wave and paramagnetic impurities can be quite strong. We also assume that the spatial size l of the pulse is much greater than the interatomic spacing h and, therefore, the approximation of continuous medium is still valid. We can satisfy both these conditions if we assume that the Zeeman transition frequency $\omega_0 \sim 10^{10}$ s^{-1}. Thus, the pulse duration is $\tau_p \sim 10^{-11}$ s and $l \sim a_\perp\tau_p \sim 10^{-6}$ cm $\gg$ $h \sim 10^{-8}$ cm.

We note that, under condition (18), inhomogeneous broadening does not have an appreciable effect on the spin interaction with an acoustic pulse. Indeed, the characteristic frequency spread $\delta\omega$ in the inhomogeneously broadened lines of Zeeman transitions is about ~10^8–10^9 s^{-1} [7], whereas the spectral pulse width is $\delta\omega_p \sim 1/\tau_p \sim 10^{11}$ s^{-1}. Therefore, even in the case of inhomogeneous broadening, the pulse spectrum effectively covers all quantum transitions.

We eliminate material variables from Eqs. (13)–(15) using an operator version of the Wentzel–Kramers–Brillouin asymptotic method [10, 22, 23]. It is seen from Eq. (16) that the matrix $\hat\Omega$ does not commute with itself at different times. However, if the pulse excitation is sufficiently weak, then the variation in $\hat\Omega$ in the time of this excitation $\Delta\tau$ is small and the matrix is approximately self-commuting. Then, we have [10]

$$\hat\rho(\tau) = \hat U\hat\rho(t_0)\hat U^+, \quad (19)$$

where

$$\hat U = \lim_{\Delta\tau\to 0}[\exp(i\hat\theta)], \quad (20)$$

is the evolution operator, $\int_{t_0}^{t_0+\Delta\tau}\hat\Omega d\tau'$ is the area operator, and t_0 is the instant of time at which the pulse excitation begins.

The exponential operator can be calculated using the Silvester formula [24]:

$$\exp(i\hat\theta) = \sum_j\prod_{q\neq j}\frac{\hat\theta-\lambda_q\hat I}{\lambda_j-\lambda_q}\exp(i\lambda_j), \quad (21)$$

where $\hat I$ is the unit matrix and $\{\lambda_q\}$ is the set of eigenvalues of the operator $\hat\theta$.

We resolve the indeterminacies of the 0/0 type in the preexponential factors by using L'Hôspital's rule and assuming that, in the limit $\Delta\tau \longrightarrow 0$, we have $\lambda_j \approx p_j\Delta\tau \approx \int_{t_0}^{t_0+\Delta\tau}p_j d\tau$, where $\{p_j\}$ is the spectrum of the eigenvalues of the matrix $\hat\Omega$.

Then, using Eqs. (20) and (21), we obtain

$$\hat U = \sum_j\prod_{q\neq j}\frac{\hat\Omega-p_q\hat I}{p_j-p_q}\exp\left(i\int_{-\infty}^{\tau}p_j d\tau'\right). \quad (22)$$

Here, formally we let t_0 tend to $-\infty$.

Using Eq. (16), we find

$$p_1 = \Omega_\parallel, \quad p_{2,3} = (\Omega_\parallel \pm \Omega)/2, \quad \Omega = \sqrt{\Omega_\parallel^2 + |\Omega_\perp|^2}. \quad (23)$$

We assume that, before the pulse excitation, we have

$$\hat\rho(t_0) = \hat\rho(-\infty) = \begin{pmatrix} W_3 & 0 & 0 \\ 0 & W_2 & 0 \\ 0 & 0 & W_1 \end{pmatrix},$$

where W_j (j = 1, 2, 3) are the initial Zeeman sublevel populations satisfying the condition $W_1 + W_2 + W_3 = 1$; then, we obtain from Eqs. (16), (19), (22), and (23)

$$\rho_{32}^*+\rho_{21}^* = -\frac{\Omega_\perp}{\sqrt{2}\Omega}\left[(W_1-W_3)\sin\frac{\theta_\parallel}{2} + i(1-3W_2)\cos\frac{\theta}{2}\right]\sin\frac{\theta}{2}, \quad (24)$$

$$\rho_{32}^*-\rho_{21}^* = \frac{\Omega_\perp}{\sqrt{2}\Omega}\left[(1-3W_2)\frac{\Omega_\parallel}{\Omega}\sin\frac{\theta}{2} + i(W_1-W_3)\cos\frac{\theta_\parallel}{2}\right]\sin\frac{\theta}{2}, \quad (25)$$

$$\rho_{11} - \rho_{33} = (W_1 - W_3) \times \left(\cos\frac{\theta_\parallel}{2}\cos\frac{\theta}{2} + \frac{\Omega_\parallel}{\Omega}\sin\frac{\theta_\parallel}{2}\sin\frac{\theta}{2}\right). \quad (26)$$

Here, $\theta_\parallel = \int_{-\infty}^{\tau} \Omega_\parallel d\tau'$ and $\theta = \int_{-\infty}^{\tau} \Omega d\tau'$.

The general property of the solutions obtained by using the WKB method is that the coefficients of the periodic functions vary much more slowly [22, 23] than these functions. Therefore, we can approximately write

$$\frac{\partial \rho_{22}}{\partial \tau} = \frac{1-3W_2}{2}\frac{\partial}{\partial\tau}\left(\frac{|\Omega_\perp|}{\Omega}\right)^2 \sin^2\frac{\theta}{2}$$

$$\approx \frac{1-3W_2}{2}\left(\frac{|\Omega_\perp|}{\Omega}\right)^2 \frac{\partial}{\partial\tau}\left(\sin^2\frac{\theta}{2}\right) = \frac{1-3W_2}{4}\frac{|\Omega_\perp|^2}{\Omega}\sin\theta.$$

Using this expression and Eqs. (13), (14), and (24)–(26) and making the change of variable $\Omega_\perp = |\Omega_\perp| e^{i\varphi}$, we arrive at the following system of integrodifferential wave equations:

$$\frac{\partial|\Omega_\perp|}{\partial z} + \left(\frac{1}{a_\perp} - \frac{1}{a_\parallel}\right)\frac{\partial|\Omega_\perp|}{\partial\tau} = -\alpha_\perp \frac{\omega_0|\Omega_\perp|}{\Omega}\cos\frac{\theta_\parallel}{2}\sin\frac{\theta}{2} + \sigma_\perp\frac{\Omega_\parallel|\Omega_\perp|}{\Omega}\sin\theta, \quad (27)$$

$$\frac{\partial\varphi}{\partial z} + \left(\frac{1}{a_\perp} - \frac{1}{a_\parallel}\right)\frac{\partial\varphi}{\partial\tau} = \frac{\alpha_\perp}{2}\cos\frac{\theta_\parallel}{2}\cos\frac{\theta}{2} + \frac{\Omega_\parallel}{\Omega}\left(2\sigma_\perp\frac{\omega_0}{\Omega}\sin\frac{\theta}{2} + \frac{3\alpha_\perp}{2}\sin\frac{\theta_\parallel}{2}\right)\sin\frac{\theta}{2}, \quad (28)$$

$$\frac{\partial\Omega_\parallel}{\partial z} = -\alpha_\parallel\frac{|\Omega_\perp|^2}{\Omega}\sin\theta, \quad (29)$$

where $\alpha_\perp = \beta_\perp(W_1 - W_3)/\sqrt{2}$, $\sigma_\perp = \beta_\perp(1 - 3W_2)/2\sqrt{2}$, and $\alpha_\parallel = \beta_\parallel(1 - 3W_2)/4$.

The set of equations (27)–(29) describes nonlinear interaction between the longitudinal and transverse components of the elastic wave via resonant paramagnetic impurities. It is seen from Eq. (29) that the transverse component can generate a longitudinal component, whereas the opposite is impossible. This can easily be seen if we set $|\Omega_\perp| = 0$ and $\Omega_\parallel \neq 0$ on the right-hand side of Eq. (27), in accordance with the incidence conditions. Then, we will have $\Omega_\perp = 0$ in the bulk.

Equation (28) characterizes the phase of the transverse component of the elastic-strain pulse, i.e., the rate of rotation of its polarization plane. In analyzing Eq. (28), we can reveal two mechanisms. The first term on the right-hand side does not vanish at $|\Omega_\parallel| = 0$ and describes the dynamics of rotation of the polarization plane due to the variation in the angular momentum of the elastic wave caused by its interaction with paramagnetic impurities. We note that this effect is linear in field, i.e., occurs at arbitrarily small values of $|\Omega_\perp|$. The remaining terms on the right-hand side of Eq. (28) describe the effect of the longitudinal component on the rotation of the polarization plane of the transverse component. As noted above, the longitudinal component dynamically changes the frequencies of quantum transitions and, therefore, affects the efficiency of interaction of these transitions with the transverse component and thus the efficiency of the angular-momentum exchange between the field and the medium. The mechanism of rotation of the polarization plane related to the presence of the longitudinal component is essentially nonlinear [see Eqs. (28), (29)] and vanishes in the limit of low fields. In what follows, these two mechanisms of rotation of the polarization plane are called linear and nonlinear, respectively.

We note again that, in deriving Eqs. (27)–(29), we did not use the approximation of a slowly varying envelope function. They are derived from the original second-order differential wave equation under the assumption of small right-hand sides in Eqs. (10) and (11). Now, we can specify the parameter μ used in the derivation and given by the ratio of the right-hand sides to one of the terms on the left-hand side. It follows from Eq. (27) that

$$\mu \sim \max\left(\eta\frac{\omega_0^2\tau_p}{\Omega}, \eta\frac{\omega_0\tau_p\Omega_\parallel}{\Omega}\right) \sim \eta\omega_0\tau_p,$$

where the dimensionless parameter $\eta \sim nG_{44}^2/(\hbar\omega_0\rho a_\perp^2)$. Taking $n \sim 10^{17}$ cm^{-3}, $G_{44} \sim 10^{-13}$ erg, $\rho \sim 5$ g/cm^3, and $a_\perp \sim 3 \times 10^5$ cm/s [7, 15, 16], we find $\eta \sim 10^{-3}$. Using this value and Eq. (18), we find that $\mu \ll 1$ by a large margin. A similar result is obtained from Eq. (29).

4. SELF-INDUCED TRANSPARENCY FOR ACOUSTIC VIDEO PULSES

Let the longitudinal component be relatively small, so that $\Omega_\parallel^2 \ll |\Omega_\perp|^2$. In this case, we have $\Omega \simeq |\Omega_\perp|$. Introducing a new variable $\theta_\perp = \theta/2 = \int_{-\infty}^{\tau}\Omega_\perp d\tau'/2$, we obtain from Eq. (27) the sine–Gordon equation

$$\frac{\partial^2\theta_\perp}{\partial z\partial\tau_\perp} = -\frac{\alpha_\perp\omega_0}{2}\sin\theta_\perp, \quad (30)$$

where $\tau_\perp = t - z/a_\perp$.

A single-soliton solution to Eq. (30) has the form

$$\theta_\perp = 4\arctan\left[\exp\left(\frac{t - z/v}{\tau_p}\right)\right], \quad (31)$$

where the propagation velocity in the laboratory frame of reference is given by

$$\frac{1}{v} = \frac{1}{a_\perp} + \frac{\alpha_\perp \omega_0}{2}\tau_p^2, \tag{32}$$

and τ_p is the duration of the transverse-component soliton having the form

$$|\Omega_\perp| = 2\frac{\partial\theta_\perp}{\partial\tau} = \frac{4}{\tau_p}\operatorname{sech}\left(\frac{t-z/v}{\tau_p}\right). \tag{33}$$

Expressions for the populations ρ_{11} and ρ_{33} following from Eqs. (19), (22), and (23) are generally rather lengthy. To simplify them, we assume that the temperature T of the paramagnetic crystal is so low that $T < \hbar\omega_0/k_B$, where k_B is the Boltzmann constant. For $\omega_0 \sim 10^{10}$ s^{-1}, we have $T < 0.1$ K. In this case, we can take $W_1 = 1$ and $W_2 = W_3 = 0$ and, using Eqs. (19), (22), and (23), find that

$$\rho_{11} = \frac{1}{4}\left(1 + \cos^2\frac{\theta}{2} + 2\cos\frac{\theta_\parallel}{2}\cos\frac{\theta}{2} + 2\frac{\Omega_\parallel}{\Omega}\sin\frac{\theta_\parallel}{2}\sin\frac{\theta}{2} + \frac{\Omega_\parallel^2}{\Omega^2}\sin^2\frac{\theta}{2}\right), \tag{34}$$

$$\rho_{22} = W_2 + \frac{1-3W_2}{2}\left(\frac{|\Omega_\perp|}{\Omega}\right)^2\sin^2\frac{\theta}{2}. \tag{35}$$

We can find ρ_{33} from the relation $\rho_{33} = 1 - \rho_{11} - \rho_{22}$. Using this relation together with Eqs. (34), (35), and (31), we obtain

$$\rho_{11} = \tanh^4\left(\frac{t-z/v}{\tau_p}\right),$$
$$\rho_{22} = 2\tanh^2\left(\frac{t-z/v}{\tau_p}\right)\operatorname{sech}^2\left(\frac{t-z/v}{\tau_p}\right), \tag{36}$$
$$\rho_{33} = \operatorname{sech}^4\left(\frac{t-z/v}{\tau_p}\right).$$

The longitudinal component can be included by setting $\Omega = |\Omega_\perp|$ and $\theta = 2\theta_\perp$ in Eq. (29). Then, using Eqs. (31) and (33), we find

$$\Omega_\parallel = \frac{16\alpha_\parallel}{\alpha_\perp\tau_p^2}\tanh^2\left(\frac{t-z/v}{\tau_p}\right)\operatorname{sech}^2\left(\frac{t-z/v}{\tau_p}\right). \tag{37}$$

This expression for $\Omega_\parallel$ is valid in the case of $|\Omega_\perp|^2 \gg \Omega_\parallel^2$.

In the limit considered, using Eqs. (28) and (31) and taking into account that [see Eq. (32)]

$$\frac{\partial\varphi}{\partial z} = -\left(\frac{1}{v} - \frac{1}{a_\perp}\right)\frac{\partial\varphi}{\partial\tau_\perp} = -\frac{\alpha_\perp\omega_0}{2}\tau_p^2\frac{\partial\varphi}{\partial\tau_\perp},$$

we find the local rate of rotation of the polarization plane for the transverse component $\omega_{rot} = \partial\varphi/\partial\tau_\perp$ to be

$$\omega_{rot} = -\frac{1}{\omega_0\tau_p^2}\left(1 - 2\operatorname{sech}^2\left(\frac{t-z/v}{\tau_p}\right)\right). \tag{38}$$

In this case, the rotation of the polarization plane is caused by the linear mechanism. During pulse propagation, the spins of paramagnetic ions first perform successive transitions $1 \longrightarrow 2 \longrightarrow 3$ and then come back to the initial state in reverse order, $3 \longrightarrow 2 \longrightarrow 1$. In the $1 \longrightarrow 2$ transition, the transverse pulse component transfers the projection of its angular momentum to the medium ($\Delta M = +1$), with the consequence that the rotation of the polarization plane slows down. The same process also occurs in the $2 \longrightarrow 3$ transition. As a result, the polarization plane rotates in the direction opposite to the initial one (see Eq. (38) at $t = z/v$). Then, the acoustic pulse recovers the initial value of the projection of the angular momentum by causing cascade transitions of spins from the excited to the ground state.

Figure 2 shows the propagating profiles of $|\Omega_\perp|$, $\Omega_\parallel$, and ω_{rot} and the populations of quantum levels corresponding to the limit $|\Omega_\perp|^2 \gg \Omega_\parallel^2$.

We note that, due to the three-level structure of the medium, the area of the pulse corresponding to this solution is equal to 4π. It follows from Eq. (34) that only pulses with an area that is a multiple of 4π return the medium to the initial state.

Let us show that, in the opposite limiting case, where $\Omega_\parallel^2 \gg |\Omega_\perp|^2$ and $a_\parallel = a_\perp$, the soliton regime of propagation with zero strain at infinity is impossible. Putting $\theta = \theta_\parallel$ in Eq. (27) in this limit, then using Eq. (29), and integrating, we obtain

$$|\Omega_\perp|^2 = \frac{1}{\alpha_\parallel}(\alpha_\perp\omega_0\Omega_\parallel - \sigma_\perp\Omega_\parallel^2).$$

The quantities $\alpha_\perp$ and $\sigma_\perp$ are of the same order of magnitude, whereas $\Omega \approx |\Omega_\parallel| \gg \omega_0$. It follows that the right-hand side of this expression is negative and, therefore, the expression has no sense.

5. RATIONAL SOLITONS

In this section, we assume that the condition $|\Omega_\parallel| \gg \omega_0$ is satisfied. In this case, we have $\mathscr{E}_\parallel \gg \hbar\omega_0/G_{11} \sim 10^{-4}$. Since values of the strain $\mathscr{E}_\parallel \sim 10^{-3}$ still correspond to elastic deformation, we can neglect the first term in the right-hand side of Eq. (27). We search for a solution to Eqs. (27)–(29) satisfying the condition $\Omega_\parallel = q\Omega_\perp$, where q is a constant. For this solution, we have

$$\Omega_\perp = \frac{1}{\sqrt{1+q^2}}\frac{\partial\theta}{\partial\tau}.$$

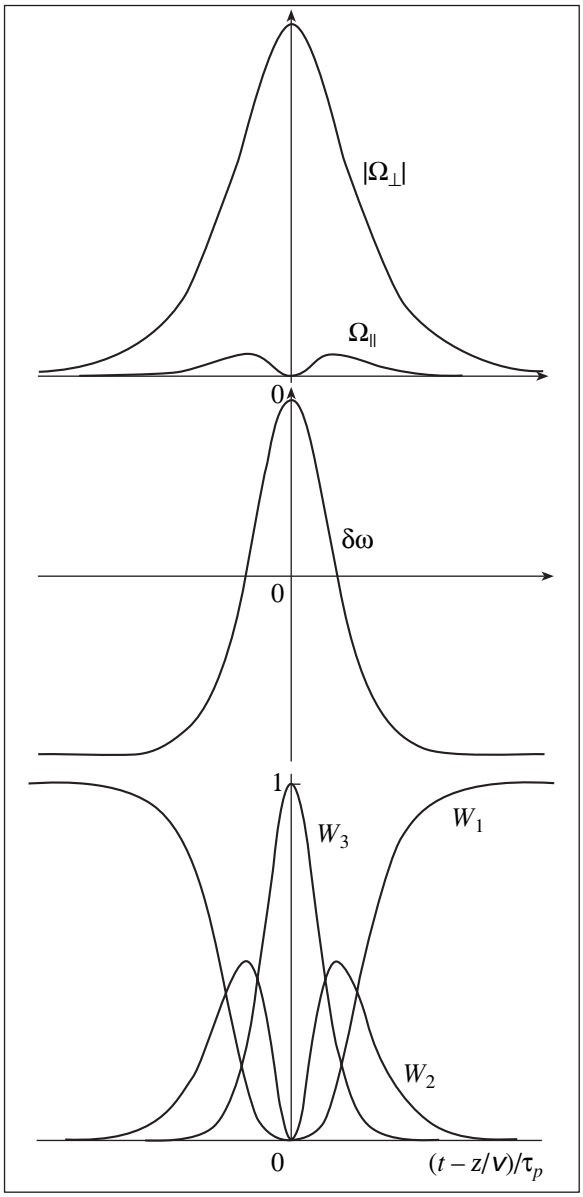

Fig. 2. The profiles of $|\Omega_\perp|$, $\Omega_\parallel$, $\delta\omega$, and quantum level populations in the case of $|\Omega_\perp|^2 \gg \Omega_\parallel^2$ (the acoustic-SIT regime).

From the foregoing, it follows that we can write Eqs. (27) and (29) in the form

$$\frac{\partial\theta}{\partial\tau} = \frac{2(\alpha_\parallel + \sigma_\perp q^2)}{\delta q\sqrt{1+q^2}}\sin^2\frac{\theta}{2},$$
$$\frac{\partial\theta}{\partial z} = -\frac{2\alpha_\parallel}{q\sqrt{1+q^2}}\sin^2\frac{\theta}{2}, \quad (39)$$

where $\delta = 1/a_\perp - 1/a_\parallel$.

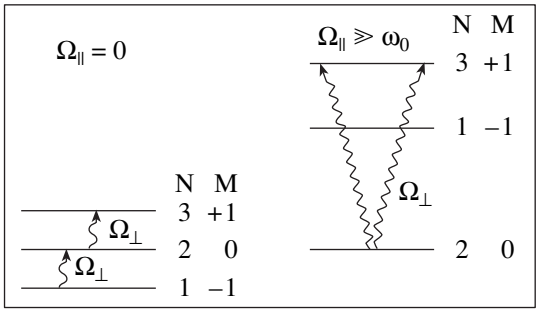

Fig. 3. Deformation of the quantum spectrum of the $S = 1$ spin caused by an intense longitudinal component of an acoustic pulse. The notation is the same as in Fig. 1.

The single-soliton solution to this set of equations in the laboratory frame of reference is

$$\theta = -2\arctan\left(\frac{t - z/v}{\tau_p}\right), \quad (40)$$

where $\tau_p = \delta q\sqrt{1+q^2}/(\alpha_\parallel + \sigma_\perp q^2)$ is the pulse duration and its velocity v is given by

$$\frac{1}{v} = \frac{1}{a_\parallel + \sigma_\perp q^2}\left(\frac{\alpha_\parallel}{a_\perp} + \frac{\sigma_\perp q^2}{a_\parallel}\right). \quad (41)$$

With allowance for Eq. (40), we have

$$|\Omega_\perp| = \frac{2(\alpha_\parallel + \sigma_\perp q^2)}{\delta q(1+q^2)(1+\xi^2)},$$
$$\Omega_\parallel = \frac{2(\alpha_\parallel + \sigma_\perp q^2)}{\delta(1+q^2)(1+\xi^2)}, \quad (42)$$

where $\xi = (t - z/v)/\tau_p$.

In contrast to Eqs. (33) and (37), pulses (42) are localized according to a power law rather than exponentially. For this reason, we call them rational solitons. Since $a_\parallel > a_\perp$, we have $\delta, \Omega_\parallel > 0$ [see Eq. (42)]. Therefore, the first and third quantum levels are dynamically displaced upwards with respect to the central level. Since $\Omega_\parallel \gg \omega_0$, the effective frequencies of the $1 \rightleftharpoons 2$ and $2 \rightleftharpoons 3$ transitions are much greater than the frequency $2\omega_0$ of the $1 \rightleftharpoons 3$ transition (Fig. 3). Thus, the longitudinal component effectively creates a medium with an inverted population with respect to the middle level. The transverse component, which induces quantum transitions under such conditions, has a velocity $v > a_\perp$ (but $v < a_\parallel$) according to Eq. (41). Here, we see an analogy with light pulses in inverted media [25–27]; however, in our case, the velocity of transverse sound $a_\perp$ plays the role of the velocity of light. A nonequilibrium population is not formed initially but instead arises due to the atomic energy spectrum reconstructed effectively by the longitudinal component of the elastic

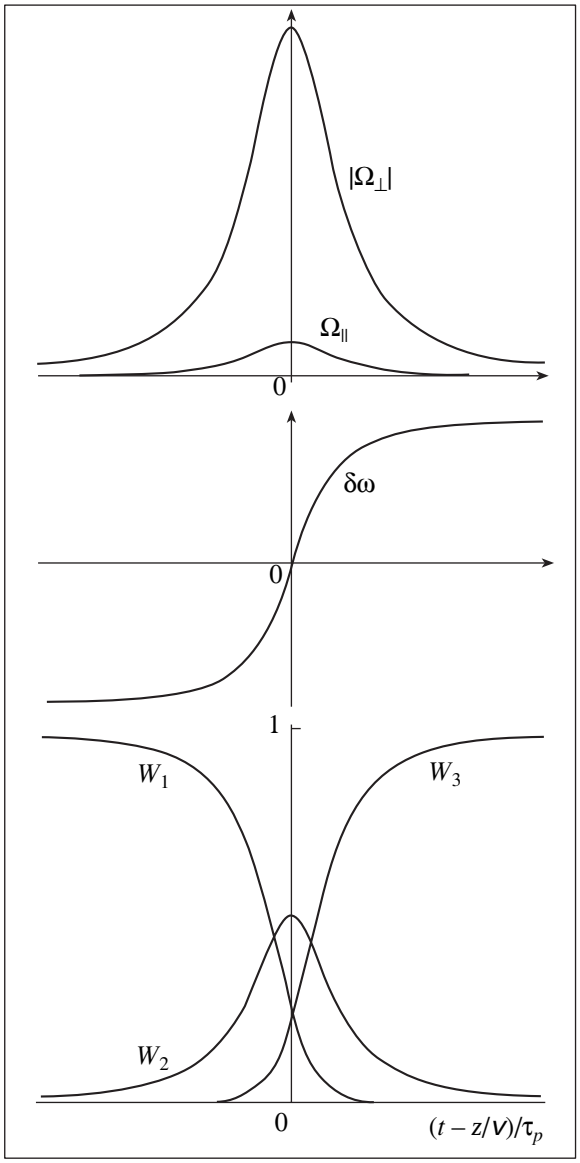

Fig. 4. Profiles of $|\Omega_\perp|$, $\Omega_\parallel$, $\delta\omega$, and quantum level populations in the case of $|\Omega_\perp|^2 \gg \Omega_\parallel^2$ for rational inverting solitons.

field propagating together with the transverse component.

To analyze the population dynamics and ω_{rot}, we now consider the limiting cases. Let us assume that $q \ll 1$ and, hence, the transverse component predominates. Then,

$$|\Omega_\perp| = \frac{2\alpha_\parallel}{\delta q(1+\xi^2)}, \quad \Omega_\parallel = \frac{2\alpha_\parallel}{\delta(1+\xi^2)}, \qquad (43)$$

where $\tau_p = \delta q/\alpha_\parallel$ and $v = a_\perp$. In this case, the populations are given by

$$\rho_{11} = \frac{1}{4}\left(1 - \frac{\xi}{\sqrt{1+\xi^2}}\right)^2, \quad \rho_{22} = \frac{1}{2(1+\xi^2)},$$

$$\rho_{33} = 1 - \rho_{11} - \rho_{22}.$$

In this limit, the rate of rotation of the polarization plane is

$$\omega_{rot} = -\frac{\xi}{\omega_0\tau_p^2\sqrt{1+\xi^2}}.$$

It is seen from Fig. 4 that, after a pulse of the form of (43) has passed, the medium becomes fully inverted; for this reason, we call rational solitons for $q \ll 1$ inverting.

We can also explain this effect in terms of reconstructing the scheme of quantum transitions for the longitudinal component. In the approximation $\Omega_\parallel \gg \omega_0$ made above, there is practically no difference between the first and third levels and the system is, in effect, two-level with a doubly degenerate upper level. The transverse component induces $1 \longrightarrow 2$ and $2 \longrightarrow 3$ quantum transitions and propagates in the SIT regime. We can say that the disappearance of distinctions between the first and third levels for $\Omega_\parallel \gg \omega_0$ corresponds to the undepleted-field approximation for the longitudinal component. Therefore, the violation of the law of energy conservation in the case where the steady-state pulse (42) passes through a medium and fully inverts it is only apparent. Keeping the first term on the right-hand side in Eq. (27) should result in a gradual decay of the pulse.

A strong change in the population of the medium is related here to the inequality $|\Omega_\perp| \gg \Omega_\parallel$, which implies that the condition of spectral overlap of quantum transitions and the pulse field also remains valid for the rearranged spectrum of spin states.

We note that, in the case of $S = 1/2$ spin, no inversion effect appears [14], since the displacements of both levels (with $M = \pm 1/2$) caused by the longitudinal component are the same and the spectrum remains unchanged.

In this case, the mechanism of rotation of the polarization plane is linear and is related to sequential transfer of the angular momentum from the field to the medium as a result of transitions $1 \longrightarrow 2 \longrightarrow 3$. Therefore, the direction of rotation is reversed as one goes from the front to the end of the pulse.

Here, we also have an analogy with the well-known effect of adiabatic inversion in optics and radiospectroscopy; this effect consists in a full excitation of a medium that occurs when the detuning of the field frequency is dynamically changed from a negative to a positive value [28]. In our case, ω_{rot} plays the role of the carrier frequency, whose asymptotic values (as $\xi \longrightarrow$

$\pm\infty$) are much greater in magnitude than the frequency $2\omega_0$ of the $1 \rightleftharpoons 3$ transition.

The above regime of propagation in which $\omega_0 \ll \Omega_\parallel \ll |\Omega_\perp|$ can be used to create population inversion in a system of Zeeman sublevels. After the passage of such a pulse, the medium must relax to the equilibrium state. It is possible that the relaxation occurs in the regime of acoustic superradiation. This problem requires additional analysis, which lies beyond the scope of the present study.

Now, we consider the opposite case $q \gg 1$, where the longitudinal component predominates. Here, the corresponding solutions for the longitudinal and transverse components of the pulse are

$$\Omega_\perp = \frac{2\sigma_\perp}{\delta q(1+\xi^2)}, \quad \Omega_\parallel = \frac{2\sigma_\perp}{\delta(1+\xi^2)}, \qquad (44)$$

where $\tau_p = \delta/\sigma_\perp$ and $v = a_\parallel$. In this limit, the populations remain practically unchanged (Fig. 5),

$$\rho_{11} = 1, \quad \rho_{22} = 0, \quad \rho_{33} = 0.$$

This result is due to the fact that, for $\Omega_\parallel \gg |\Omega_\perp| \gg \omega_0$, the spectrum of the transverse component does not contain practically any Fourier components in resonance with quantum transitions. Accordingly, we call the rational solitons (44) capturing.

Soliton propagation regimes under the conditions of population capture were earlier studied in acoustics [10] and optics of anisotropic media [29] for pulses consisting of quasi-monochromatic and extremely short components. In optics, the corresponding regime is called extraordinary transparency [29]. The case $q \gg 1$ can, to a certain extent, be considered an analog of extraordinary transparency for acoustic video pulses.

For $q \gg 1$, we can write ω_{rot} in the form

$$\omega_{\text{rot}} = -\frac{1}{\omega_0\tau_p^2}\left(1 + \frac{1}{1+\xi^2}\right).$$

In this case, the dominant contribution to the rotation of the polarization plane comes from the longitudinal component; i.e., the corresponding mechanism is essentially nonlinear. The transverse component tends to transfer the projection of the angular momentum to the $1 \rightleftharpoons 2$ transition. However, since there are no resonant Fourier components, the transition is excited very weakly and, therefore, the polarization plane of the transverse component does not rotate.

We should note an interesting feature. In both limiting cases, the amplitude of the longitudinal component of the pulse is practically the same; only the amplitude of the transverse component appreciably varies.

Passing to the limit $\tau \longrightarrow +\infty$ in the second equation in set (39), we obtain

$$\frac{dA}{dz} = -\frac{1}{l_{\text{eff}}}\sin^2\frac{A}{2}, \qquad (45)$$

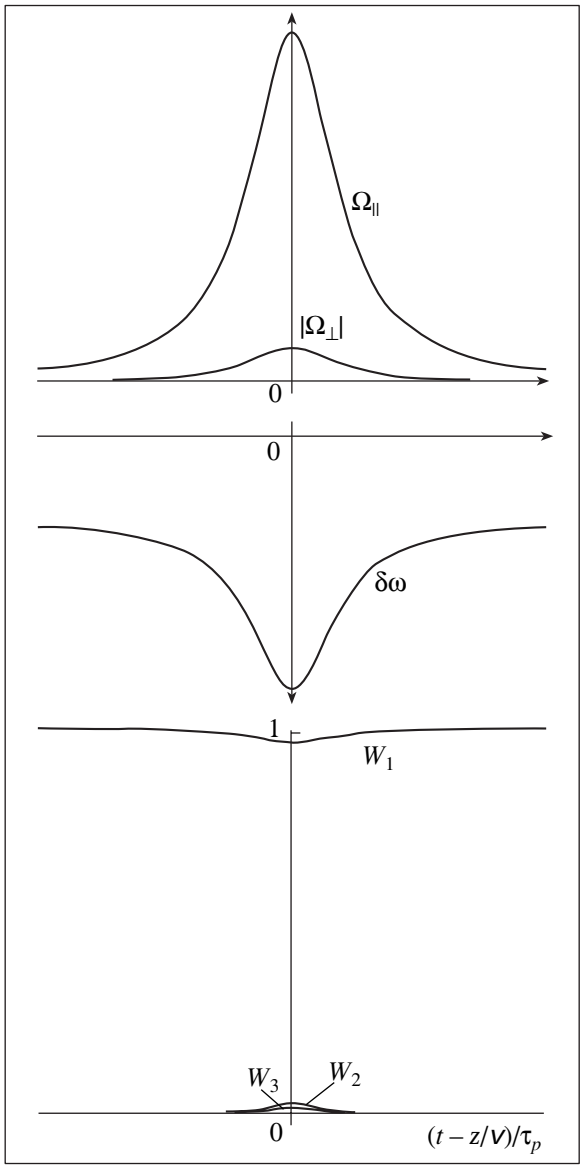

Fig. 5. Profiles of $|\Omega_\perp|$, $\Omega_\parallel$, $\delta\omega$, and quantum level populations in the case of $|\Omega_\perp|^2 \ll \Omega_\parallel^2$ for rational capturing solitons.

where $l_{\text{eff}} = q\sqrt{1+q^2}/2\alpha_\parallel$ and $A = \int_{-\infty}^{+\infty}\Omega dt'$ is the total pulse area.

Equation (45) can be considered the area theorem for rational solitons. It follows from Eq. (45) that these solitons have a one-sided stability (Fig. 6). Indeed, to form a rational 2π pulse of the type of (42), the area A_0 of the incident pulse must lie in the interval $2\pi < A_0 < 4\pi$. For $A_0 < 2\pi$, the soliton cannot form and the pulse must irreversibly decay in the medium. If $A_0 = 2\pi N + \varepsilon$, where N is an integer and $0 < \varepsilon < 2\pi$, then $A \longrightarrow 2\pi N$ as $z \gg l_{\text{eff}}$. Most likely, this means that, in the medium, the incident pulse is split into N rational solitons.

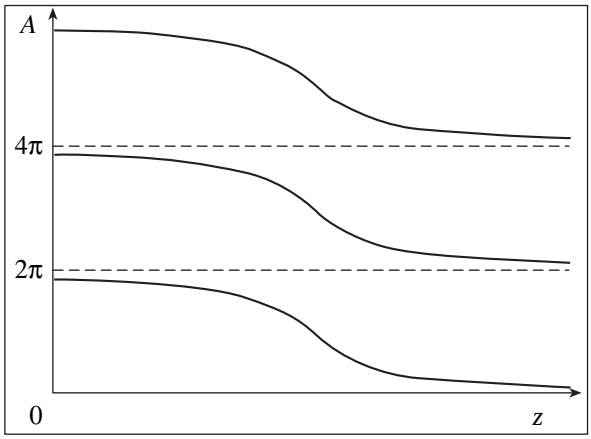

Fig. 6. Schematic analysis of the dynamics of the total rational-soliton area.

We note that the effective length l_{eff} for the formation of inverting solitons is q times shorter than the corresponding length for capturing solitons. We estimate the values of l_{eff} in both cases. For the above values of the parameters of the medium, we have $\alpha_{\|} \sim 1$ cm^{-1}. Then, for $q \sim 0.1$ (inverting solitons), we have $l_{\text{eff}} \sim 0.1$ cm, and for $q \sim 10$ (capturing solitons), $l_{\text{eff}} \sim 10$ cm.

6. CONCLUSIONS

Our study has revealed different propagation regimes of acoustic video pulses of picosecond duration in a crystal containing paramagnetic centers with effective spin $S = 1$. In the Faraday geometry, the role of transverse and longitudinal components of the pulse are strictly different: the former induces quantum transitions in the system of Zeeman sublevels, and the latter dynamically displaces the frequencies of these transitions. Due to this fact, the longitudinal component of the pulse can, under certain conditions, appreciably change the spectrum of quantum states of the effective spin, thereby bringing about the occurrence of qualitatively different soliton propagation regimes. It is possible that SIT video solitons, inverted solitons (that cannot exist in the case $S = 1/2$), and capturing solitons describe only part of the propagation regimes in the system $S = 1$ and, in geometries different from the Faraday geometry, new soliton regimes can occur.

In this study, we described the elastic field in the framework of the mechanics of continuous media; i.e., we neglected spatial dispersion. As shown above, this approximation imposes substantial restrictions on the magnitude of the external magnetic field and the temperature of the paramagnetic sample ($T < 0.1$ K). An increase in T up to 1 K necessitates ten times higher fields B (or frequencies ω_0) in order to produce an appreciable difference in the population of Zeeman sublevels. Otherwise, spin–phonon interaction will be hardly noticeable. For $\omega_0 \sim 10^{11}$ s^{-1}, the pulse duration should be $\tau_p \sim 1$ ps, since the condition of spectral overlap, Eq. (18), must be satisfied. In this case, the spatial size of the video pulse is $l \sim a_{\perp}\tau_p \sim 10^{-7}$ cm and we must go beyond the continuous medium approximation [16, 30–32]. Furthermore, the effects of nonlocality of spin–phonon interaction can be important under such conditions [16]. As video pulses become shorter, their amplitude grows. Under these conditions, it may appear to be necessary to take into account the anharmonicity of crystal lattice vibrations [16, 31, 32]. Lattice anharmonicity and spatial dispersion themselves facilitate soliton formation even in the absence of paramagnetic impurities. It is possible that, with inclusion of the spin–phonon interaction, new soliton regimes will appear.

ACKNOWLEDGMENTS

This study was supported by the Russian Foundation for Basic Research, project no. 02-02-17710a.

REFERENCES

1. J. T. Darrow, B. B. Hu, X. C. Chang, and D. H. Auston, Opt. Lett. **15** (5), 323 (1990).
2. S. A. Akhmanov, V. A. Vysloukh, and A. S. Chirkin, *The Optics of Femtosecond Laser Pulses* (Nauka, Moscow, 1988) [in Russian].
3. A. V. Kim, M. Yu. Ryabikin, and A. M. Sergeev, Usp. Fiz. Nauk **169** (1), 58 (1999) [Phys. Usp. **42**, 54 (1999)].
4. V. A. Golenishchev-Kutuzov, V. V. Samartsev, N. K. Solovarov, and B. M. Khabibulin, *Magnetic Quantum Acoustics* (Nauka, Moscow, 1977) [in Russian].
5. S. V. Sazonov, Izv. Vyssh. Uchebn. Zaved., Fiz. **36** (7), 94 (1993).
6. S. L. McCall and E. L. Hahn, Phys. Rev. Lett. **18**, 908 (1967).
7. N. S. Shiren, Phys. Rev. B **2** (7), 2471 (1970).
8. G. A. Denisenko, Zh. Éksp. Teor. Fiz. **60**, 2269 (1971) [Sov. Phys. JETP **33**, 1220 (1971)].
9. V. V. Samartsev, B. P. Smolyakov, and R. Z. Sharipov, Pisma Zh. Éksp. Teor. Fiz. **20** (10), 644 (1974) [Sov. Phys. JETP **20**, 296 (1974)].
10. S. V. Voronkov and S. V. Sazonov, Zh. Éksp. Teor. Fiz. **120** (2), 269 (2001) [JETP **93**, 236 (2001)].
11. A. A. Zabolotskiĭ, Pis'ma Zh. Éksp. Teor. Fiz. **76** (10), 709 (2002) [JETP Lett. **76**, 607 (2002)].
12. A. A. Zabolotskiĭ, Zh. Éksp. Teor. Fiz. **123** (6), 560 (2003) [JETP **96**, 496 (2003)].
13. A. Yu. Parkhomenko and S. V. Sazonov, Zh. Éksp. Teor. Fiz. **114** (11), 1595 (1998) [JETP **87**, 864 (1998)].
14. S. V. Voronkov and S. V. Sazonov, Fiz. Tverd. Tela (Leningrad) **43** (11), 1969 (2001) [Phys. Solid State **43**, 2051 (2001)].
15. J. W. Tucker and V. W. Rampton, *Microwave Ultrasonics in Solid State Physics* (North-Holland, Amsterdam, 1972; Mir, Moscow, 1975).
16. S. V. Sazonov, Zh. Éksp. Teor. Fiz. **118** (1), 20 (2000) [JETP **91**, 16 (2000)].

17. S. A. Altshuler and B. M. Kozyrev, *Electron Paramagnetic Resonance in Compounds of Transition Elements* (Nauka, Moscow, 1972; Halsted, New York, 1975).
18. L. D. Landau and E. M. Lifshitz, *Course of Theoretical Physics*, Vol. 7: *Theory of Elasticity*, 4th ed. (Pergamon, New York, 1986; Nauka, Moscow, 1987).
19. L. D. Landau and E. M. Lifshitz, *Course of Theoretical Physics*, Vol. 3: *Quantum Mechanics: Non-Relativistic Theory*, 4th ed. (Pergamon, New York, 1977; Nauka, Moscow, 1989).
20. M. B. Vinogradova, O. V. Rudenko, and A. P. Sukhorukov, *Theory of Waves* (Nauka, Moscow, 1990) [in Russian].
21. É. M. Belenov and A. V. Nazarkin, Pis'ma Zh. Éksp. Teor. Fiz. **51** (5), 252 (1990) [JETP Lett. **51**, 288 (1990)].
22. N. N. Moiseev, *Asymptotic Methods of Nonlinear Mechanics* (Nauka, Moscow, 1981) [in Russian].
23. A. H. Nayfeh, *Introduction to Perturbation Techniques* (Wiley, New York, 1981; Mir, Moscow, 1984).
24. F. R. Gantmacher, *Theory of Matrices*, 3rd ed. (Chelsea, New York, 1959; Fizmatgiz, Moscow, 1967).
25. N. G. Basov, R. V. Ambartsumyan, V. S. Zuev, P. G. Kryukov, and V. S. Letokhov, Zh. Éksp. Teor. Fiz. **50** (1), 23 (1966) [JETP **23**, 16 (1966)].
26. A. N. Oraevskiĭ, Usp. Fiz. Nauk **168** (12), 1311 (1998) [Phys. Usp. **41**, 1199 (1998)].
27. S. V. Sazonov, Usp. Fiz. Nauk **171** (6), 663 (2001) [Phys. Usp. **44**, 631 (2001)].
28. L. Allen and J. H. Eberly, *Optical Resonance and Two-Level Atoms* (Wiley, New York, 1975; Mir, Moscow, 1978).
29. S. V. Sazonov, Zh. Éksp. Teor. Fiz. **124** (4), 803 (2003) [JETP **97**, 722 (2003)].
30. S. A. Akhmanov and V. É. Gusev, Usp. Fiz. Nauk **162** (3), 3 (1992) [Sov. Phys. Usp. **35**, 153 (1992)].
31. S. V. Sazonov, J. Phys.: Condens. Matter **4** (30), 6485 (1992).
32. S. V. Sazonov, J. Phys.: Condens. Matter **6** (31), 6295 (1994).

Translated by I. Zvyagin

Physics of the Solid State, Vol. 46, No. 9, 2004, pp. 1704–1710. Translated from Fizika Tverdogo Tela, Vol. 46, No. 9, 2004, pp. 1650–1656.
Original Russian Text Copyright © 2004 by Kurbakov, Trounov, Balagurov, Pomyakushin, Sheptyakov, Gorbenko, Kaul.

MAGNETISM AND FERROELECTRICITY

Crystal and Magnetic Structure of the $Sm_{0.55}Sr_{0.45}MnO_3$ and $(Nd_{0.545}Tb_{0.455})_{0.55}Sr_{0.45}MnO_3$ Manganites

A. I. Kurbakov*, V. A. Trounov*, A. M. Balagurov, V. Yu. Pomyakushin***, D. V. Sheptyakov***, O. Yu. Gorbenko****, and A. R. Kaul******

**Konstantinov St. Petersburg Nuclear Physics Institute, Russian Academy of Sciences, Gatchina, Leningrad oblast, 188300 Russia*

e-mail: KURBAKOV@pnpi.spb.ru

***Joint Institute for Nuclear Research, Dubna, Moscow oblast, 141980 Russia*

****Paul Scherrer Institute, ETH Zürich, Willigen, 5232 Switzerland*

***** Moscow State University, Vorob'evy gory, Moscow, 119992 Russia*

Received January 15, 2004

Abstract—Neutron diffraction data are presented for the $^{152}Sm_{0.55}Sr_{0.45}MnO_3$ (SSM) and $(Nd_{0.545}Tb_{0.455})_{0.55}Sr_{0.45}MnO_3$ (NTSM) manganites. The Nd and Tb contents in the latter composition are such that the average radius of the *A* cation $\langle r_A \rangle$ in these two compounds is the same. The difference in local tolerance factor fluctuations was about 10%. It was found that replacement of a rare-earth cation with leaving $\langle r_A \rangle$ unchanged has practically no effect on the structural and transport properties; indeed, both compounds are metals at low temperatures, have the same crystal structure from liquid-helium to room temperature, and exhibit the same pattern of structural distortions at the onset of magnetic ordering. Magnetic moments of Mn ions in both compositions are ferromagnetically ordered at low temperatures, with T_C = 122 and 90 K for the SSM and NTSM, respectively. Below 80 K, the rare-earth cation moments in NTSM undergo additional ordering. In contrast to compositions that are close in Sr concentration (x_{Sr} = 0.4, 0.5), which feature a phase-separated state with a mixture of the ferromagnetic metallic and antiferromagnetic insulator phases, the ground state of both studied compositions with x_{Sr} = 0.45 is uniformly ferromagnetic and metallic. © *2004 MAIK "Nauka/Interperiodica".*

1. INTRODUCTION

We report on a continuation of our systematic investigation of the $Sm_{1-x}Sr_xMnO_3$ perovskite manganites (Sm–Sr subsequently), which have recently been enjoying considerable interest because of their nontrivial physical properties. For instance, the composition with x = 0.45 revealed a strong decrease in electrical resistivity [1] and a sharp change in the coefficients of volume expansion and volume magnetostriction near the Curie temperature T_C [2], as well as some features in the temperature dependence of heat capacity [3]. A detailed phase diagram for the $Sm_{1-x}Sr_xMnO_3$ system established from measurements of the electrical resistivity and magnetization and from electron diffraction data can be found in [4]. In contrast to the Sm–Ca compositions, the Sm–Sr phase diagram was found to have a broad region of a prevailing ferromagnetic (FM) metallic state for $0.3 < x \le 0.52$, whose formation is believed to be associated with the larger average *A* cation radius $\langle r_A \rangle$ in the Sm–Sr compositions. Another feature of the Sm–Sr system is the comparatively large scatter in the size of *A* cations (r_{Sm} = 1.132 Å, r_{Sr} = 1.310 Å), which brings about strong local fluctuations of the e_g electron hopping amplitude and lowers T_C. Finally, recent measurements [5] revealed a strong isotopic effect in Sm–Sr compositions near x = 0.45; indeed, substitution of ^{18}O for ^{16}O results in a substantial decrease in T_C (by 40 K for x = 0.45 in a cooling run and 25 K in the sample heating mode) or even in a transition to the insulating state (for x = 0.475, 0.5). The colossal magnetoresistance was found to exist in the Sm–Sr system only in the hole doping region for $0.3 \le x \le 0.5$ [6].

Because of the high absorption cross section of natural Sm, neutron diffraction was almost not used at all in the studies of the crystal and magnetic structure of the Sm-based manganite. Only the x = 0.4 composition has been investigated in detail [7, 8], and, in particular, unusually large Jahn–Teller distortions of the oxygen octahedra and the coexistence of FM and antiferromagnetic (AFM) ordering within a certain temperature interval were revealed it. The first neutron diffraction data for the x = 0.45 composition were published in [9] for several temperatures. Attention was focused on the paramagnetic phase, in which FM clusters with a characteristic size of ≈8 Å were found embedded in an orbital- and charge-ordered insulator phase (but without long-range order). At low temperatures (4 K), only FM ordering of Mn ions with a magnetic moment $\approx 3.4\mu_B$ was detected. The structural characteristics of this compound were not analyzed in [9].

1063-7834/04/4609-1704$26.00 © 2004 MAIK "Nauka/Interperiodica"

We report here on a comprehensive neutron diffraction study of the $Sm_{0.55}Sr_{0.45}MnO_3$ composition. To refine the specific part played by Sm in the unusual physical properties of the compound, the $(Nd_{1-y}Tb_y)_{0.55}Sr_{0.45}MnO_3$ composition was also studied, with the Nd and Tb concentrations chosen such that the average radius of the *A* cation in these compounds will be the same. The parameter $\sigma^2 = \sum x_i r_i^2 - \langle r \rangle^2$ (where x_i is the cation concentration and r_i is the cation ionic radius) characterizes local fluctuations of the tolerance factor and governs, to a considerable extent, the transport and magnetic properties of the manganites [10]; the difference in this parameter between the two compounds mentioned above is ~10%. We established that replacement of a rare-earth cation has practically no effect on the structural and magnetic properties of the compound, provided $\langle r \rangle$ remains unchanged.

2. EXPERIMENTAL

We prepared two samples for neutron diffraction measurements, $^{152}Sm_{0.55}Sr_{0.45}MnO_3$ (SSM) and $(Nd_{0.545}Tb_{0.455})_{0.55}Sr_{0.45}MnO_3$ (NTSM). Using the ^{152}Sm isotope (neutron absorption cross section $\sigma_a \approx 200$ b) instead of a natural mixture of samarium isotopes ($\sigma_a \approx 5920$ b) permitted us to substantially improve the quality of neutron spectra and simplify the treatment of the data. One SSM sample was prepared at the CRISMAT laboratory (Caen, France) from a mixture of Sm_2O_3, $SrCO_3$, CaO, and MnO_2 taken in appropriate ratio. The mixture was first calcined in air for 12 h for decarbonization, next ground thoroughly, and then pelletized at a pressure of 10^3 kg/cm^2. Subsequent synthesis was conducted at 1400°C for 12 h. The other SSM sample was fabricated at Moscow State University (MSU) using "paper synthesis," a procedure in which ashless filters were impregnated with a water solution of metal nitrates of stoichiometric composition with a total concentration of about 1 mol/l; the residue remaining after these filters were burned was first calcined at 700°C for 30 min, then pressed into pellets, and finally sintered at 1200°C for 12 h. The NTSM sample was prepared at MSU using the same technology as for the second SSM sample. The phase composition of the samples thus obtained was studied by x-ray diffraction and Raman spectroscopy. Both methods showed them to be single-phase. EPR measurements did not detect any magnetic impurities in the samples.

The Nd to Tb ratio in NTSM was chosen using the following data on ionic radii taken from Shannon's tables [11] for ninefold coordination of the *A* cation, which is accepted for the manganites: $r_{Sm} = 1.132$ Å, $r_{Sr} = 1.310$ Å, $r_{Nd} = 1.163$ Å, and $r_{Tb} = 1.095$ Å. The average radius of the *A* cation is 1.212 Å for both compositions; $\sigma^2 = 0.0081$ Å^2 for SSM, and 0.0091 Å^2 for NTSM.

The samples were characterized by measuring the temperature dependences of the electrical resistivity, magnetization, and magnetic susceptibility. Their characteristics were compared with the available data on samples prepared by the same research groups following the same technology but using Sm with a natural isotopic abundance [2, 4, 6]. It was found that the data for the two SSM samples are practically identical and are in good agreement with earlier publications. Small discrepancies in the absolute value of the parameters (for instance, the values of T_C differ by 3 K), but not in the character of the dependences, can be traced to a slight difference in oxygen stoichiometry. The stoichiometry was determined by iodometric titration, which revealed that the oxygen index is 3.00(1) and 3.02(1) for the first and second SSM samples, respectively.

The crystal and magnetic structures of the samples were determined on the following powder neutron diffractometers: G4.2 (ORPHEE reactor, Saclay, France; $\lambda_0 = 2.343$ Å, $3° \le 2\theta \le 174°$, $\Delta d/d_{min} = 0.2\%$) [12], HRFD (IBR-2 pulsed reactor, Dubna, Russia; $0.7 \le d_{hkl} \le 4$ Å, $\Delta d/d = 0.1\%$) [13], and DMC (SINQ source, PSI, Switzerland; $\lambda_0 = 2.56$ Å, $5° \le 2\theta \le 85°$, $\Delta d/d_{min} = 1\%$) [14]. The neutron diffraction patterns were measured over a broad temperature interval (1.4–300 K for SSM and 10–293 K for NTSM) in the sample heating mode. The crystal and magnetic structures were refined using the Rietveld technique with the MRIA [15] and FullProf [16] codes. Figure 1 illustrates the treatment of the neutron diffraction patterns obtained on G4.2 and HRFD.

3. CRYSTAL STRUCTURE

The SSM samples prepared at CRISMAT and MSU were found to be practically identical from the standpoint not only of their macroscopic properties but also in terms of crystal structure. Only a slight discrepancy in the unit cell parameters was observed, which could be assigned to a small difference in oxygen concentration. Further, we present the data only for the second sample (fabricated at MSU), because its temperature behavior was studied in more detail and because it was prepared by the same technology as the NTSM sample.

The crystal structure of both SSM and NTSM samples can be described well by the orthorhombic space group *Pnma* (N 62) typical of manganites with $\langle r_A \rangle \approx 1.2$ Å. No structural transitions were detected within the temperature interval covered. Anisotropic broadening of the diffraction lines, which was found in [8] in a $Sm_{0.6}Sr_{0.4}MnO_3$ sample close in composition to our samples, was not observed in SSM and NTSM. Figure 2a displays temperature dependences of the SSM cell parameters (obtained on G4.2). The analogous relations for NTSM follow the same pattern. At all temperatures, the sample structure is characterized by the parameter relation $c > a > b/\sqrt{2}$ and the $a^-b^+a^-$ perovskite cubic lattice distortion system typical of manganites with tol-

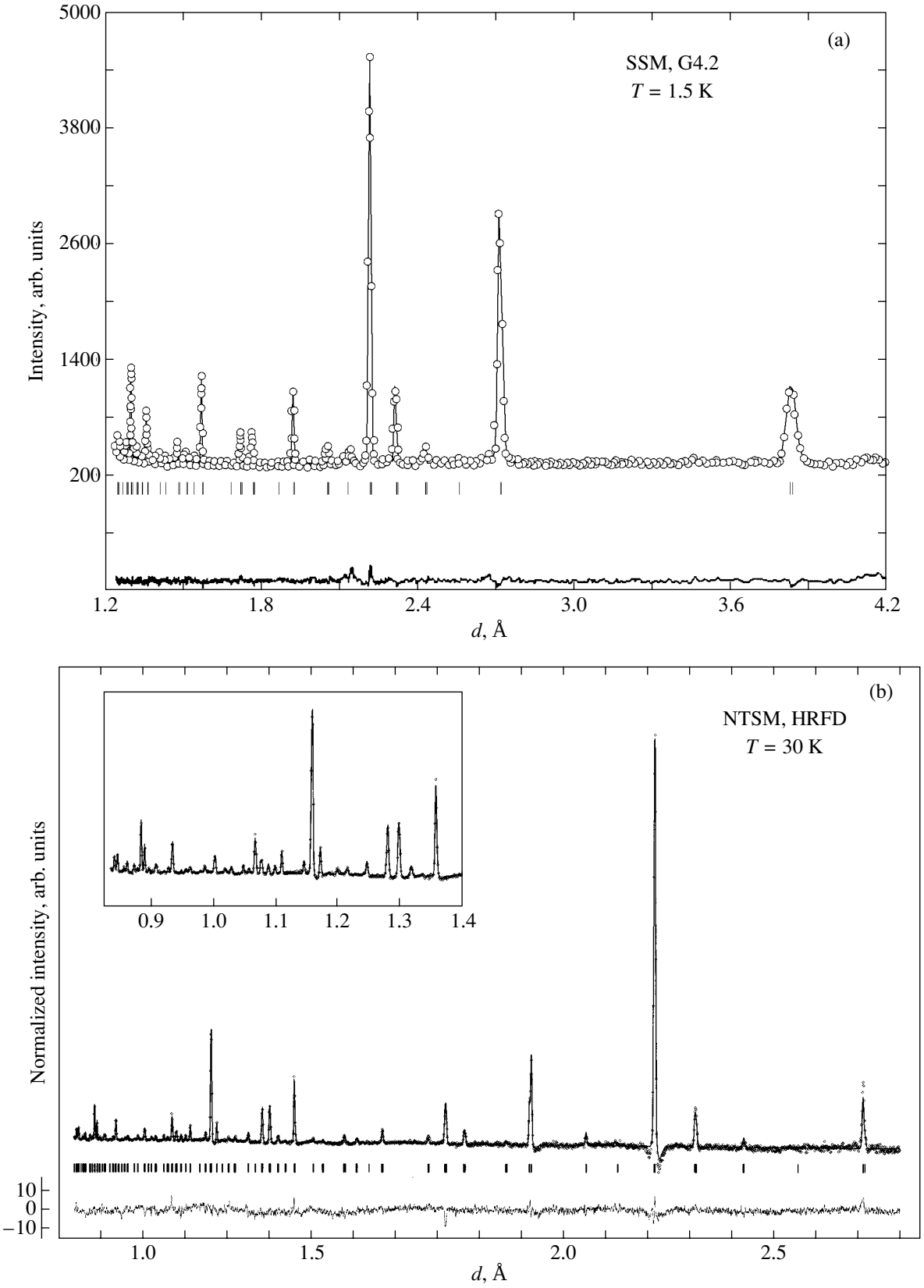

Fig. 1. Diffraction patterns of (a) $^{152}Sm_{0.55}Sr_{0.45}MnO_3$ (G4.2 diffractometer, $T = 1.5$ K) and (b) $(Nd_{0.545}Tb_{0.455})_{0.55}Sr_{0.45}MnO_3$ (HRFD, $T = 30$ K). Experimental points and calculated and difference curves are presented. Bragg reflection positions are specified by vertical bars. The difference curve for the spectrum obtained on HRFD is normalized to standard deviations.

erance factors $t < 0.94$ [17]. Because $\langle r_A \rangle$ is the same for the samples under study, the lattice parameters of SSM and NTSM are very similar; indeed, the difference in the volume of their unit cells does not exceed 0.2% throughout the temperature interval covered (Fig. 2b). Near the transition temperature to the FM phase (T_C), an abrupt decrease in the cell volume ($\Delta V_c/V_c \approx 0.1\%$) is observed, which is similar to the one found for some other manganites at the transition to the metallic FM phase. The change in cell volume is largely associated with contraction of the rhombic base; indeed, a jump in the temperature dependence of the parameters a and c is observed, whereas the parameter b remains practically constant. The orthorhombic lattice distortion $\delta = (a - c)/(a + c)$ is comparatively large ($\delta \approx 0.15\%$).

The observed hysteresis of the lattice constants in the vicinity of T_C correlates well with the hysteresis data obtained in measurements of the electrical resistivity [3, 18], magnetization [6], thermal expansion, magnetostriction [2], heat capacity, thermal conductivity, and thermopower [18]. The temperature hysteresis near the phase transition was also observed for the lattice constants of the $Sm_{0.6}Sr_{0.4}MnO_3$ composition [7, 8], but within a broader temperature interval. By contrast, no hysteresis was found to exist in $Sm_{0.5}Sr_{0.5}MnO_3$ [19].

Superstructural diffraction maxima indicative of the existence of charge long-range order (observed ordinarily at $x \approx 0.5$ in La and Pr manganites) were not detected in [9] throughout the temperature interval covered.

Neutron diffraction patterns measured on high resolution diffractometers (HRFD, G4.2) yielded detailed data on coherent Jahn–Teller distortions of the MnO_6 octahedra for both SSM and NTSM samples. As in the case of unit cell parameters, the pattern of the temperature dependences and the magnitude of the Jahn–Teller distortions turned out to be practically the same for both samples. On the whole, the cooperative Jahn–Teller effect is small in the temperature interval covered. The parameter $\sigma_{JT} = (1/3\Sigma[(Mn–O)_i - \langle Mn–O \rangle]^2)^{1/2}$ characterizing the magnitude of the distortions does not exceed 0.01 Å, which is substantially smaller than that for the $x = 0.4$ composition, where $\sigma_{JT} \approx 0.09$ Å at low temperatures [8]. The magnitude and the temperature dependences of the Mn–O_i–Mn valence angles in SSM and NTSM are likewise similar; at room temperature, we have φ(Mn–O1–Mn) ≈ 159° and φ(Mn–O2–Mn) ≈ 162.5°; near the transition to the FM phase, these angles become approximately equal to ≈161° and part slightly again as the temperature is lowered still further. The variations in the average values ⟨Mn–O⟩ and ⟨Mn–O–Mn⟩ with temperature for SSM and NTSM are small and do not exceed 0.005 Å and 1° for the bond lengths and valence angles, respectively. These features in the temperature dependence of the structural parameters are illustrated in Fig. 3 for the SSM composition.

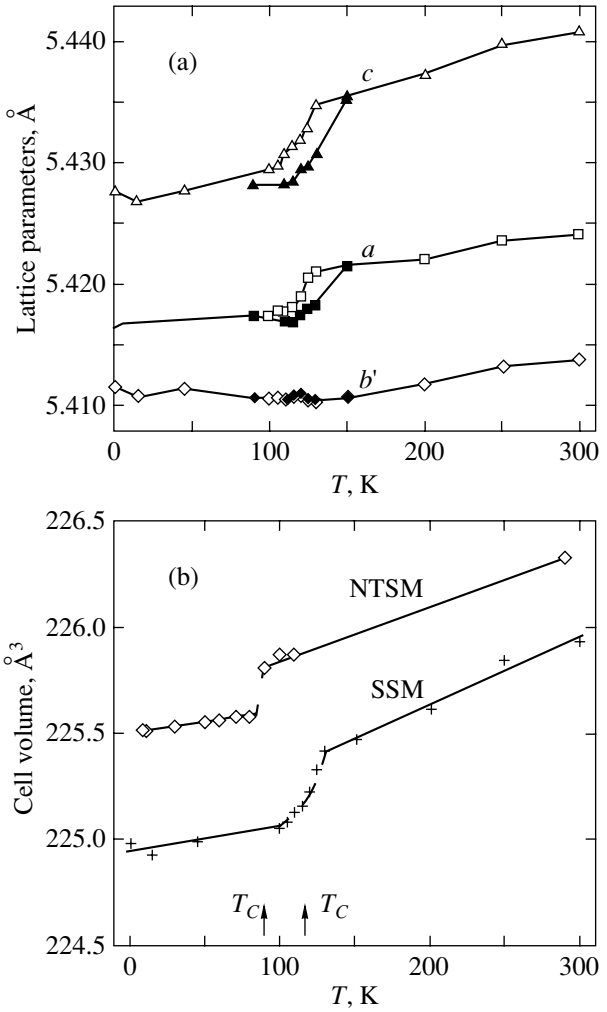

Fig. 2. (a) Temperature dependences of unit cell parameters for SSM derived from G4.2 measurements. Open symbols on the curves refer to the heating mode, and the filled symbols, to the cooling mode of the sample. The parameter b is specified by $b' = b/\sqrt{2}$. (b) Temperature dependences of the SSM and NTSM unit cell volumes. The arrows identify the FM transition temperatures for SSM (122 K) and NTSM (90 K).

4. MAGNETIC STRUCTURE

The Mn magnetic moments become ordered ferromagnetically in both SSM and NTSM compositions at T_C = 122 and 90 K, respectively. At low temperatures, the averaged ordered moments of Mn in the SSM and NTSM samples are similar and equal to $3.36(5)\mu_B$ and $3.6(1)\mu_B$, respectively. These values practically coincide with the expected average value calculated under the assumption that the structure contains 55% Mn^{3+} ions ($\mu = 4\mu_B$) and 45% Mn^{4+} ions ($\mu = 3\mu_B$). The FM ordering temperature exhibits hysteresis, as is the case with the temperature dependences of the SSM cell parameters: T_C = 122 K in the heating mode, and T_C = 115 K under cooling.

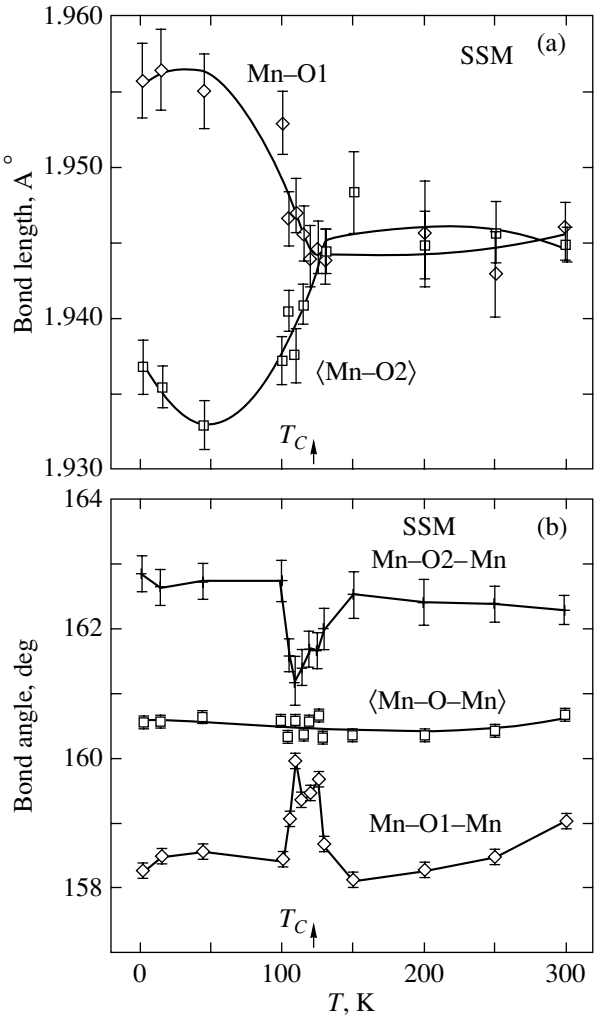

Fig. 3. Temperature dependences (a) of the Mn–O1 bond length and the average value ⟨Mn–O2⟩ and (b) of the Mn–O1–Mn and Mn–O2–Mn valence angles and the average value ⟨Mn–O–Mn⟩ for SSM.

SSM did not show any indications of Sm magnetic moment ordering. In NTSM, the magnetic moments of rare-earth (RE) cations undergo ordering below $T \approx 80$ K. This process culminates in the formation of a noncollinear magnetic structure with the FM component of the RE cation moments oriented in the direction of the Mn moment and with a *G*-type ordered AFM component (antiparallel ordering of the nearest neighbor moments along all three basic directions). Note that the contributions to the magnetic peak intensity deriving from the FM components of the Mn and RE cation moments allow unambiguous separation, because for certain peaks their magnetic structural factors are added (for instance, for (121)/(002)) while for others they are subtracted (for example, (101)/(020)). By contrast, the *G*-type AFM peaks can, in principle, be accounted for by canting of either the RE-cation or Mn magnetic moments. The first case (noncollinearity of the RE-cation magnetic moments) is chosen because otherwise

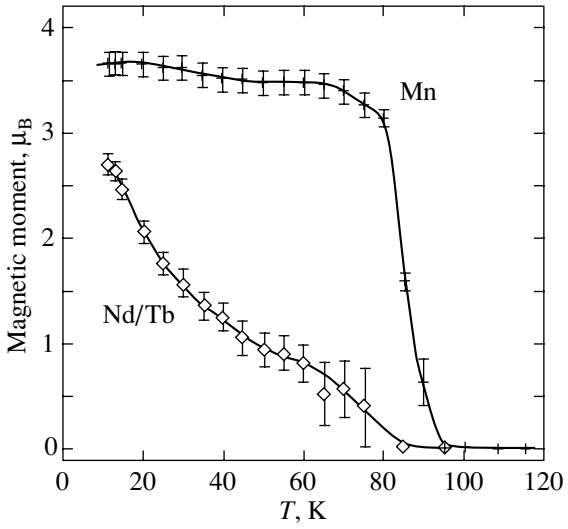

Fig. 4. Temperature dependences of the Mn-ion magnetic moment and of the total Nd/Tb moment derived from measurements made on the DMC diffractometer for $(Nd_{0.545}Tb_{0.455})_{0.55}Sr_{0.45}MnO_3$.

the total Mn moment would be larger than 4 μ_B. The absence of AFM peaks in SSM may be considered an additional argument for the chosen version. The temperature dependences of the ordered magnetic moments of Mn and the RE cation in NTSM are shown in Fig. 4. The total magnetic moment of the RE cation was calculated as an average over Nd and Tb. For definiteness, we used the magnetic formfactor of Nd^{3+} in the calculation.

An analysis of the intensities of diffraction patterns showed that the Mn magnetic moment is most probably aligned with the *c* axis of the unit cell. The FM component of the RE-cation moment is oriented in the same way, and its AFM component is directed along the *a* axis. The resolution of the DMC diffractometer is, however, not high enough to totally exclude the ordering model with the moments changing directions along the *a* and *c* axes.

To check the effect of a small compositional variation on magnetic ordering, a $^{152}Sm_{0.525}Sr_{0.475}MnO_3$ sample was prepared and studied. This sample exhibited the same features as $^{152}Sm_{0.55}Sr_{0.45}MnO_3$. This suggests that in the Sm–Sr manganite system there exists a narrow concentration region near $x = 0.45$ with a purely ferromagnetic ordering of the Mn ions.

4. DISCUSSION OF THE RESULTS

In the $Sm_{1-x}Sr_xMnO_3$ system, the concentration interval $0.4 \le x \le 0.5$ is of particular interest, because a number of remarkable properties are observed in this range. The $x = 0.4$ composition exhibits an incoherent mixture of phases, namely, one FM metallic (major) and two AFM insulating phases (*A* type and a small

amount of *CE* type) [8]. Both magnetic phases have very similar structural parameters corresponding to the orthorhombic *Pnma* group. Having a comparatively low temperature $T_C \approx 120$ K, the $x = 0.4$ composition reveals unusual magnetic behavior above T_C, which is associated with the formation of AFM domains in the paramagnetic matrix. This feature originates primarily from strong coherent Jahn–Teller distortions, which develop below $T_{JT} \approx 180$ K and persist to some extent in the FM phase. The ground state of the $x = 0.5$ compound is metallic, with the *A*-type AFM phase dominant and some inclusions of the FM phase [19]. Thus, the concentrations $x = 0.4$ and 0.5 are characterized by the coexistence of FM and AFM ordering, which is interpreted as the formation of a two-phase state at low temperatures.

We established in this work that the ground state of the $x = 0.45$ composition, which is intermediate between 0.4 and 0.5, is uniformly ferromagnetic and metallic. Thus, we discovered a fairly unexpected feature in the phase diagram of the Sm–Sr manganites, more specifically, that the inhomogeneous states with similar values of x are separated by a narrow region of a homogeneous state. It is in this interval that the colossal magnetoresistance reaches its maximum value. The fact that the ground ferromagnetic states in both compositions, SSM and NTSM, are identical indicates that the nature of magnetic ordering of the Mn ions is independent of the type of RE element and of the presence or absence of its magnetic ordering.

The existence of a homogeneous FM state below the Curie temperature is an unexpected finding also because the paramagnetic state in these samples has been found to be magnetically inhomogeneous and to exhibit a complex temperature behavior [20]. In this case, small *CE*-type AFM regions with a weak Dzyaloshinsky–Moriya ferromagnetism and FM domains form in the paramagnetic matrix. Nucleation of such AFM regions in compositions with Sr concentrations $x = 0.4$ and 0.5 at high temperatures brings about the formation of a mixed FM + AFM magnetic state at low temperatures. For the case where $x = 0.45$, the AFM fluctuations completely vanish with decreasing temperature.

When considering the transition temperatures to the FM state in SSM and NTSM, which differ by about 30 K, one should take into account the following two factors: the degree of deviation of the average structure of these compounds from that of an ideal perovskite and the level of local disorder, which is associated with the scatter of the *A* cations in size. For perovskites, the conduction band width W, which determines the FM transition temperature ($T_C \sim W$), is directly related to the deviation of the average Mn–O–Mn valence angle from 180°: $W \sim \cos[(\pi - \langle \text{Mn–O–Mn} \rangle)/2]$ (cf., e.g., [21]). According to this criterion, T_C for NTSM should be higher by ≈10 K than that for SSM. The empirical dependence of W on the average bond length $d = \langle \text{Mn–O} \rangle$ ($W \sim d^{-3.5}$), which is sometimes taken into account, does not change the situation significantly, because the $\langle \text{Mn–O} \rangle$ distances in SSM and NTSM are the same. The effect of scatter in the ionic radii of *A* cations on T_C can be estimated from the empirical relation between T_C and σ^2 proposed [10] for compositions with a doping level $x = 0.3$ and $\langle r_A \rangle = 1.23$ Å. The $T_C(\sigma^2)$ relation [10] suggests that T_C for NTSM should be ≈20 K smaller than that for SSM. Obviously enough, inclusion of the above factors does not result in agreement with the experimental value of T_C variation, although the smaller value of T_C for NTSM is predicted correctly.

6. CONCLUSIONS

Thus, replacement of Sm by a mixture of Nd/Tb with the same average cation radius did not produce any noticeable changes in the structural or magnetic properties; indeed, the SSM and NTSM compounds have the same crystal structure over a broad temperature interval, the same character of structural distortions at the FM ordering temperature, and the same magnetic structure of the Mn sublattice. The observed difference in the RE-cation ordering is a natural consequence of the Nd/Tb mixture having a substantially larger magnetic moment than Sm (the calculated effective spin moments are $0.84\mu_B$ for Sm, $3.64\mu_B$ for Nd, and $9.7\mu_B$ for Tb [22]). The alignment of the Mn and RE-cation FM-component moments suggests that the RE-cation moment ordering is induced by the ferromagnetic Mn sublattice. Accordingly, the ordering temperature of the RE-cation moments is determined by their magnitude, and in NTSM this temperature almost coincides with that of the manganese sublattice.

In contrast to replacement of the RE element, a comparatively small change in the doping level by the divalent cation, i.e., a change in the Mn^{3+}/Mn^{4+} ratio, brings about a radical modification of magnetic ordering. Both a decrease in the Sr concentration (down to $x = 0.4$) and an increase (up to $x = 0.5$) give rise to the formation of an inhomogeneous state with a mixture of the FM and AFM (primarily of the *A* type) phases.

ACKNOWLEDGMENTS

The authors (A.I.K, V.A.T.) express their sincere gratitude to C. Martin (CRISMAT, France) for preparation and characterization of the $^{152}Sm_{0.55}Sr_{0.45}MnO_3$ sample.

Part of the experiments were carried out on the SINQ neutron source at the Paul Scherrer Institute (Willigen, Switzerland).

This study was supported by the Russian Foundation for Basic Research (project no. 03-02-16954) and the state program "Neutron Studies in the Physics of Condensed Media" (project no. 40.012.1.1.1149).

REFERENCES

1. Y. Tomioka, H. Kuwahara, A. Asamitsu, M. Kasai, and Y. Tokura, Appl. Phys. Lett. **70**, 3609 (1997).
2. A. Abramovich, L. Koroleva, A. Michurin, O. Gorbenko, and A. Kaul, Physica B (Amsterdam) **293**, 38 (2000).
3. A. M. Aliev, Sh. B. Abdulvagidov, A. B. Batdatlov, I. K. Kamilov, O. Yu. Gorbenko, and V. A. Amelichev, Pis'ma Zh. Éksp. Teor. Fiz. **72**, 1451 (2000) [JETP Lett. **72**, 464 (2000)].
4. C. Martin, A. Maignan, M. Hervieu, and B. Raveau, Phys. Rev. B **60**, 12191 (1999).
5. N. A. Babushkina, E. A. Chistotina, O. Yu. Gorbenko, A. R. Kaul, D. I. Khomskii, and K. I. Kugel, Phys. Rev. B **67**, R100 410 (2003).
6. F. Damay, N. Nguyen, A. Maignan, M. Hervieu, and B. Raveau, Solid State Commun. **98**, 997 (1996).
7. V. V. Runov, D. Yu. Chernyshov, A. I. Kurbakov, M. K. Runova, V. A. Trounov, and A. I. Okorokov, Zh. Éksp. Teor. Fiz. **118**, 1174 (2000) [JETP **91**, 1017 (2000)].
8. I. D. Luzyanin, V. A. Ryzhov, D. Yu. Chernyshov, A. I. Kurbakov, V. A. Trounov, A. V. Lazuta, V. P. Khavronin, I. I. Larionov, and S. M. Dunaevsky, Phys. Rev. B **64**, 094432 (2001).
9. J. M. De Teresa, M. R. Ibarra, P. Algarabel, L. Morellon, B. Garcia-Landa, C. Marquina, C. Ritter, A. Maignan, C. Martin, B. Raveau, A. Kurbakov, and V. Trounov, Phys. Rev. B **65**, 100403 (2002).
10. L. M. Rodriguez-Martinez and J. P. Attfield, Phys. Rev. B **54**, R15622 (1996).
11. C. R. D. Shannon, Acta Crystallogr. A **32**, 751 (1976).
12. A. I. Kurbakov, V. A. Trounov, T. K. Baranova, A. P. Bulkin, R. P. Dmitriev, Ya. A. Kasman, J. Rodriguez-Carvajal, and T. Roisnel, Mater. Sci. Forum **321–324**, 308 (2000).
13. V. L. Aksenov, A. M. Balagurov, V. G. Simkin, A. P. Bulkin, V. A. Kudriashev, V. A. Trounov, O. Antson, P. Hiismaki, and A. Tiitta, J. Neutron Res. **5**, 181 (1997).
14. P. Fischer, L. Keller, J. Scheffer, and J. Kohlbrecher, Neutron News **11**, 19 (2000).
15. V. B. Zlokazov and V. V. Chernyshev, J. Appl. Crystallogr. **25**, 447 (1992).
16. J. Rodriguez-Carvajal, Physica B (Amsterdam) **192**, 55 (1993); http://www-llb.cea.fr/fullweb/powder.htm.
17. P. M. Woodward, T. Vogt, D. E. Cox, A. Arulraj, C. N. R. Rao, P. Karen, and A. K. Cheetham, Chem. Mater. **10**, 3652 (1998).
18. A. M. Aliev, Sh. B. Abdulvagidov, A. B. Batdatlov, I. K. Kamilov, O. Yu. Gorbenko, V. A. Amelichev, A. R. Kaul, A. I. Kurbakov, and V. A. Trunov, Fiz. Tverd. Tela (St. Petersburg) **45**, 124 (2003) [Phys. Solid State **45**, 130 (2003)].
19. A. I. Kurbakov, A. V. Lazuta, V. A. Ryzhov, V. A. Trounov, I. I. Larionov, C. Martin, M. Hervieu, and B. Raveau (in press).
20. A. V. Lazuta, V. A. Ryzhov, A. I. Kurbakov, V. A. Trounov, I. I. Larionov, O. Yu. Gorbenko, and A. R. Kaul, J. Magn. Magn. Mater. **258–259**, 315 (2003).
21. J. B. Goodenough, J. Appl. Phys. **81**, 5330 (1997).
22. G. S. Krinchik, *Physics of Magnetic Phenomena* (Mosk. Gos. Univ., Moscow, 1985), p. 29 [in Russian].

Translated by G. Skrebtsov

Physics of the Solid State, Vol. 46, No. 9, 2004, pp. 1711–1716. Translated from Fizika Tverdogo Tela, Vol. 46, No. 9, 2004, pp. 1657–1662.
Original Russian Text Copyright © 2004 by Abramovich, Gorbenko, Kaul, Koroleva, Michurin.

MAGNETISM AND FERROELECTRICITY

Peculiarities of Magnetic, Galvanomagnetic, Elastic, and Magnetoelastic Properties of $Eu_{0.55}Sr_{0.45}MnO_3$

A. I. Abramovich, O. Yu. Gorbenko, A. R. Kaul, L. I. Koroleva, and A. V. Michurin

Moscow State University, Vorob'evy gory, Moscow, 119992 Russia

e-mail: koroleva@ofef343.phys.msu.su

Received February 11, 2004

Abstract—Magnetic, elastic, magnetoelastic, transport, and magnetotransport properties of the $Eu_{0.55}Sr_{0.45}MnO_3$ ceramics have been studied. A break was detected in the temperature dependence of electrical resistivity $\rho(T)$ near the temperature of the magnetic phase transformation (41 K), with the material remaining an insulator down to the lowest measurement temperature reached ($\rho = 10^6$ Ω cm at 4.2 K). In the interval $4.2 \le T \le 50$ K, the isotherms of the magnetization, volume magnetostriction, and ρ were observed to undergo jumps at the critical field H_{C1}, which decreases with increasing T. For $50 \le T \le 120$ K, the jumps in the above curves persist, but the pattern of the curves changes and H_{C1} grows with increasing T. The magnetoresistance $\Delta\rho/\rho = (\rho_H - \rho_{H=0})/\rho_H$ is positive for $H < H_{C1}$ and passes through a maximum at 41 K, where $\Delta\rho/\rho = 6\%$. For $H > H_{C1}$, the magnetoresistance is negative, passes through a minimum near 41 K, and reaches a colossal value of 3×10^5 % at $H = 45$ kOe. The volume magnetostriction is negative and attains a giant value of 4.5×10^{-4} at $H = 45$ kOe. The observed properties are assigned to the existence of three phases in $Eu_{0.55}Sr_{0.45}MnO_3$, namely, a ferromagnetic (FM) phase, in which carriers are concentrated because of the gain in *s–d* exchange energy, and two antiferromagnetic (AFM) phases of the *A* and *CE* types. Their fractional volumes at low temperatures were estimated to be as follows: ~3% of the sample volume is occupied by the FM phase; ~67%, by the *CE*-type AFM phase; and ~30%, by the *A*-type AFM phase. © *2004 MAIK "Nauka/Interperiodica"*.

1. INTRODUCTION

Until recently, the interest expressed in manganites was mainly associated with the colossal magnetoresistance (CMR) observed in some compositions near room temperature. Our studies [1–4] revealed that, in the systems $La_{1-x}Sr_xMnO_3$ ($0.1 \le x \le 0.3$), $Nd_{1-x}Sr_xMnO_3$ ($x = 0.33$, 0.45), and $Sm_{1-x}Sr_xMnO_3$ ($x = 0.33$, 0.4, 0.45), in addition to the CMR, giant negative volume magnetostriction ω takes place, with its temperature, $\omega(T)$, and field, $\omega(H)$, dependences found to closely resemble those of the magnetoresistance, $\{\Delta\rho/\rho\}(T)$ and $\{\Delta\rho/\rho\}(H)$. These properties were assigned to the fact that, in these systems, there exists a magnetic two-phase state, ferromagnetic (FM) and antiferromagnetic (AFM), caused by strong *s–d* exchange, with the carriers (holes in this case) being concentrated in the FM part of the crystal [5]. It should be stressed that the concept of the Curie point is largely conventional here; in fact, it is the Curie temperature of the FM part of the crystal.

It is known that the $Sm_{1-x}Sr_xMnO_3$ system with $x = 0.5$ undergoes charge–orbital (CO) ordering that results in the onset of a *CE*-type AFM order. Neutron diffraction and electrical resistivity measurements showed that the $^{154}Sm_{0.6}Sr_{0.4}MnO_3$ compound contains *A*- and *CE*-type AFM clusters, with CO order setting in the latter. These clusters are embedded in a conducting FM matrix [6]. There are no CO-ordered clusters in the $x = 0.25$ composition [6]. As the temperature is increased, the FM order at $T = T_C$ is the first to break down in the $x = 0.4$ composition, the *A*-type AFM order at $T_N \ge T_C$ is next, and the *CE*-type AFM order at $T = T_{CO}$ is last. This behavior is in full agreement with the theoretical predictions of Dagotto *et al.* [7], who showed, using numerical modeling, that the concentration-driven transformation occurring in manganites at $x = 0.5$ from the FM to the CO state is a first-order phase transition and that compositions close to $x = 0.5$ contain various types of magnetic clusters, namely, FM, *A*-type AFM, and charge–orbital *CE*-type AFM ordering.

Our earlier study covered the magnetic, electrical, and galvanomagnetic properties of the $Eu_{0.7}Sr_{0.3}MnO_3$ composition ($x = 0.3$), which was semiconducting and exhibited giant maxima in the $\rho(T)$ and $\{\Delta\rho/\rho\}(T)$ curves [8, 9]. We furnished the following experimental evidence of the existence of an insulating state with two coexisting magnetic phases in this compound. The magnetization isotherms measured at low temperatures were the sums of a small spontaneous magnetization and a linear-in-field magnetization characteristic of an antiferromagnet. There was a difference between the magnetizations of a sample cooled with no field applied and in a field, which persisted up to the maximum field reached, 45 kOe; furthermore, the magnetization hysteresis loops of a field-cooled sample were found to be shifted along the *H* axis. The contribution due to the FM clusters noticeably enhanced the paramagnetic

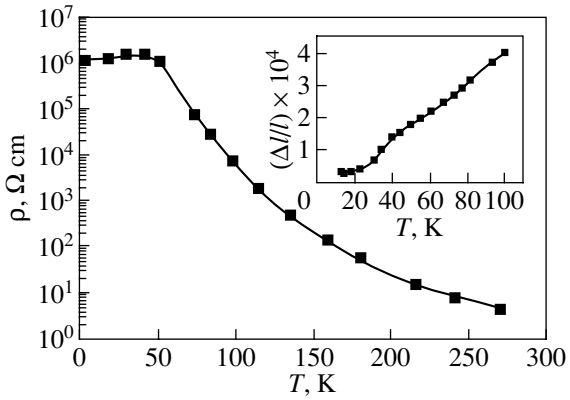

Fig. 1. Temperature dependence of electrical resistivity. Inset shows the temperature dependence of linear thermal expansion.

Curie point Θ, from –100 K for an undoped $EuMnO_3$ sample to 175 K for $Eu_{0.7}Sr_{0.3}MnO_3$. The Curie temperature of the FM part of the composition was almost impossible to measure. For instance, the value of T_C in a field of 45 kOe derived by extrapolating the steepest part of the $M(T)$ curve to the T axis was found to be equal to 90 K, which is threefold higher than the value $T_C = 30$ K determined in a field $H = 0.5$ kOe.

In this work, we study the magnetic, electrical, galvanomagnetic, and magnetoelastic properties of $Eu_{0.55}Sr_{0.45}MnO_3$, which should contain clusters of three types, namely, FM, *A*-type AFM, and *CE*-type AFM [7], and determine their differences from the properties of the compositions $Sm_{1-x}Sr_xMnO_3$ (x = 0.33, 0.4, 0.45) and $Eu_{0.7}Sr_{0.3}MnO_3$. As follows from the magnetic and galvanomagnetic properties of the latter composition [8, 9], it does not contain CO clusters. Therefore, investigation of the above properties of the $Eu_{0.55}Sr_{0.45}MnO_3$ composition should offer new information on the effect of the CO-ordered phase on these properties and, hopefully, shed light on the nature of their anomalies.

2. PREPARATION OF SAMPLES AND EXPERIMENTAL TECHNIQUES

The $Eu_{1-x}Sr_xMnO_3$ sample under study was prepared using standard ceramic technology. The phase composition and the lattice parameters were monitored with a Siemens D5000 diffractometer. The ceramic obtained was established to be a single-phase perovskite with orthorhombic structure (*Pnma* group). The orthorhombicity parameter derived from the lattice constants is 0.2%, which indicates closeness to cubic structure. The tolerance factor $\tau = 0.924$, and the degree of disorder $d^2 = 0.00893$. The single-phase state of the ceramics was corroborated by Raman spectrometric measurements performed on a Jobin-Yvon T64000 triple monochromator; in fact, the only phonon modes observed were those characteristic of orthorhombic manganites with *Pnma* symmetry.

The magnetization was measured with a vibrating-sample magnetometer at the Strong Magnetic Field Laboratory (Wroclaw) in magnetic fields of up to 130 kOe and in the temperature interval from 1.5 to 150 K. The initial magnetic susceptibility in an ac magnetic field of 1 Oe (at frequencies of 0.8 to 8 kHz) was measured with an F-5063 ferrometer. The electrical resistivity was determined by the four-probe method. The magnetostriction and thermal expansion in the temperature interval 4.2–150 K were derived from data obtained with strain gauges having a resistance of 92.30 ± 0.01 Ω and a tensometric sensitivity of 2.26. One of the gauges was attached to the sample, and the other, to quartz. In the course of measurements, the strain gauges on the sample and on the quartz were oriented identically with respect to the orientation of the magnetic field. The longitudinal ($\lambda_\parallel$) and transverse ($\lambda_\perp$) magnetostriction components were measured and were subsequently used to calculate the bulk and anisotropic parts of the magnetostriction, $\omega = \lambda_\parallel + 2\lambda_\perp$ and $\lambda_t = \lambda_\parallel - \lambda_\perp$, respectively.

3. EXPERIMENTAL RESULTS AND DISCUSSION

The temperature dependence of the initial magnetic susceptibility measured in an ac magnetic field of 1 Oe at a frequency of 8 kHz exhibited a maximum at a temperature $T_N = 41$ K, which is very close to the Néel point for the $EuMnO_3$ composition. Near this temperature, a jump in the temperature dependence of linear thermal expansion (see inset to Fig. 1) and a break in the $\rho(T)$ curve were found (Fig. 1). In the absence of a magnetic field, as seen from this figure, the sample remains insulating down to the lowest temperatures covered ($\rho = 10^6$ Ω cm at 4.2 K). The isotherms of magnetization, magnetostriction, and magnetoresistance have two temperature intervals, 4.2–50 K and 60–120 K, which exhibit similar behavior. Figure 2 presents isotherms of the magnetization $\sigma(H)$, magnetostriction $\omega(H)$, and electrical resistivity $\rho(H)$ for a temperature of 20 K from the first interval and for 60 K from the second interval. In the first temperature interval, one sees an abrupt rise in the magnetization and in the absolute magnitude of magnetostriction and a decrease in electrical resistivity occurring within the field interval $H_{C1} < H < H_{C2}$. Judging from the magnitude of magnetization in fields $H > H_{C2}$, the larger part of the sample transfers to the FM state in this interval. For $H > H_{C2}$, these parameters grow linearly with H, with no saturation being reached up to the highest fields covered (80 kOe for the magnetization and 50 kOe for the magnetostriction and magnetoresistance). The magnetization at 4.2 K in a magnetic field of 80 kOe is 2.50 μ_B/mol, which is noticeably less than 3.55 μ_B/mol, a figure corresponding to FM ordering of the Mn^{3+} and Mn^{4+} ions (the former is 70% of the latter). At the jump,

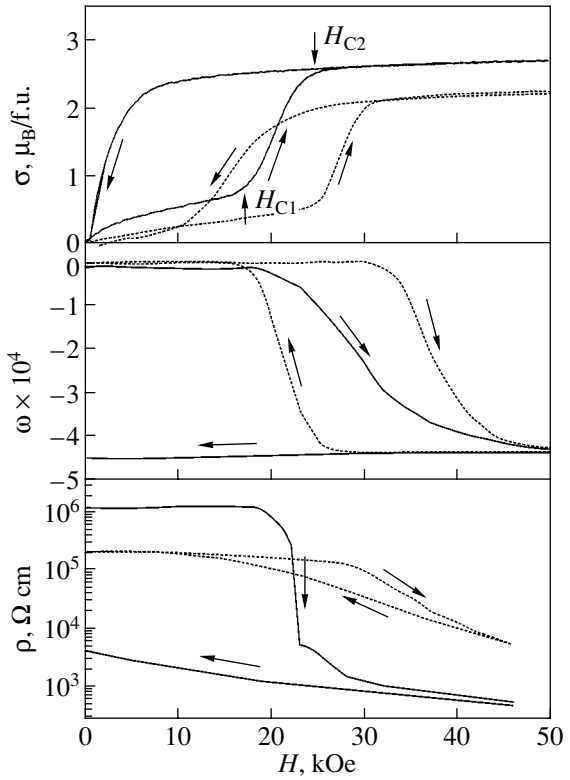

Fig. 2. Isotherms of magnetization σ(*H*), magnetostriction ω(*H*), and electrical resistivity ρ(*H*) for temperatures of 20 (solid lines) and 60 K (dashed lines).

the σ(*H*), ω(*H*), and ρ(*H*) curves exhibit hysteresis, which decreases with increasing temperature. After the magnetic field is switched off at low temperatures, the volume magnetostriction and electrical resistivity do not recover their initial values, at least not in the 1800-s period used in carrying out the measurements. These quantities could be restored to the initial level only after heating the sample to about 100 K and subsequent cooling.

In the temperature interval 60–120 K, the jumps in the σ(*H*), ω(*H*), and ρ(*H*) curves are retained, but their patterns change and, after removal of the magnetic field, the sample recovers its initial state (Fig. 2). Note that, in this temperature interval, the above curves behave exactly like those obtained on the $Sm_{0.55}Sr_{0.45}MnO_3$ ceramics studied by us earlier [1, 10]. The temperature dependence of the fields H_{C1} derived from measurements of the magnetization, magnetostriction, and electrical resistivity is presented in graphical form in Fig. 3. We see immediately that these fields coincide for each temperature and then decrease with increasing temperature in the first interval and increase in the second, with a broad minimum located near 41 K. Figure 4 plots temperature dependences of the magnetization, magnetostriction, and magnetoresistance obtained in different magnetic fields. The σ(*T*) curve passes through a maximum near 41 K, and the ω(*T*) and

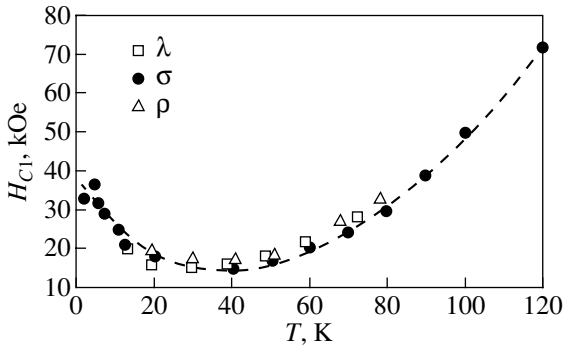

Fig. 3. Temperature dependence of the critical field H_{C1} derived from measurements of the magnetization σ, volume magnetostriction ω, and magnetoresistance Δρ/ρ.

{Δρ/ρ}(*T*) curves pass through a minimum. The magnetic transition is strongly diffused by the magnetic field. The volume magnetostriction reaches a giant value of 4.5×10^{-4} in a magnetic field of 45 kOe in the temperature interval 10–75 K. The magnetoresistance of this composition behaves in an unusual way. For $H < H_{C1}$, it is positive and passes through a maximum of 6% near 41 K (Fig. 5). For $H > H_{C1}$, it becomes negative and passes through a minimum slightly below 41 K, to reach a colossal value of 3×10^5 % in a magnetic field of 50 kOe (Fig. 4).

As already mentioned, for $T \geq 60$ K, the magnetization, magnetostriction, and magnetoresistance of the sample studied in this work behave similarly to those of the $Sm_{1-x}Sr_xMnO_3$ ceramic samples (x = 0.4, 0.45) studied by us earlier at $T > T_C$ [1, 10]. Our recent study of these properties of a $Sm_{0.55}Sr_{0.45}MnO_3$ single crystal showed them to be identical to those of ceramics of the same composition. As pointed out in the introduction, the $Sm_{0.6}Sr_{0.4}MnO_3$ composition at $1.5 \leq T \leq T_C$ is a singly connected FM matrix containing *A*-type AFM clusters and *CE*-type AFM CO-ordered clusters, with $T_C < T_N < T_{CO}$ [6]. Here, T_{CO} is the temperature of thermally induced breakdown of CO ordering, which coincides with the temperature at which AFM order breaks down in CO-ordered clusters. The behavior of the magnetization, magnetoresistance, and magnetostriction for $T > T_N$ was explained in [1, 10] as being due to the magnetic field–induced transition of the AFM CO clusters to the FM state. Because the magnetic moments of most of the nearest neighbor Mn ions are antiferromagnetically ordered in the case of *CE*-type AFM ordering, there need to be threshold fields to transfer this AFM to the FM state. In this case, the CO-ordered clusters transfer entirely to the FM state on reaching the H_{C2} field. Because the isotherms of σ, ω, and Δρ/ρ of the $Eu_{0.55}Sr_{0.45}MnO_3$ compound in the range $1.5 \leq T \leq 120$ K are very close to those observed by us earlier in the $Sm_{0.55}Sr_{0.45}MnO_3$ and $Sm_{0.6}Sr_{0.4}MnO_3$ compositions [1] for $T > T_C$, one may suggest that the

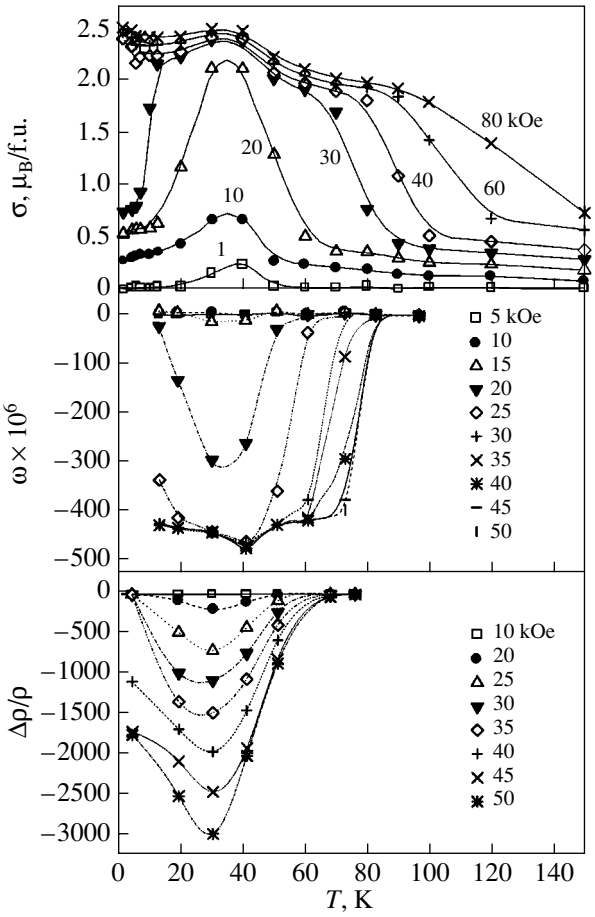

Fig. 4. Temperature dependences of the magnetization σ, volume magnetostriction ω, and magnetoresistance Δρ/ρ obtained in different magnetic fields.

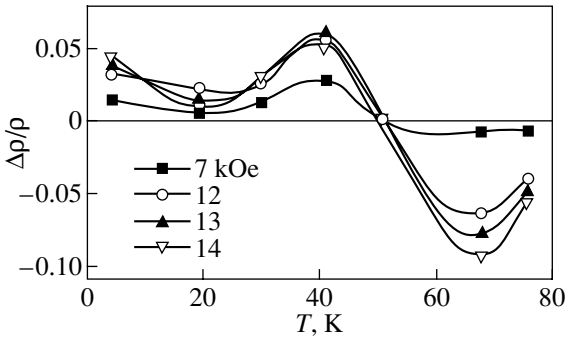

Fig. 5. Temperature dependence of magnetoresistance for $H < H_{C1}$.

$Eu_{0.55}Sr_{0.45}MnO_3$ composition likewise consists of the FM, *A*-type AFM, and *CE*-type AFM phases. The fractional volumes of these phases are, however, different from those in $Sm_{0.55}Sr_{0.45}MnO_3$ and $Sm_{0.6}Sr_{0.4}MnO_3$. As seen from Fig. 1, the temperature dependence of electrical resistivity of the $Eu_{0.55}Sr_{0.45}MnO_3$ composition is of semiconducting character and ρ at 4.2 K is very large, ~10^6 Ω cm, unlike the $Sm_{0.55}Sr_{0.45}MnO_3$ composition, which has metallic conduction. One may therefore conjecture that the FM phase in this composition is multiply connected, in contrast to the $Sm_{0.55}Sr_{0.45}MnO_3$ compound, where this phase is singly connected. The reason for this lies in fact that the tolerance factor for $Eu_{0.55}Sr_{0.45}MnO_3$, $\tau = 0.924$, is smaller than that for $Sm_{0.55}Sr_{0.45}MnO_3$ ($\tau = 0.927$), while the extent of disorder, $d^2 = 0.00893$, is larger than that in $Sm_{0.55}Sr_{0.45}MnO_3$, where it is 0.00784.

It is known that, depending on the carrier concentration, an AFM semiconductor may be either in the insulating or in the conducting FM–AFM magnetic two-phase state (MTPS), with carriers concentrated in the FM part of the crystal and with no carriers in the AFM part because the *s–d* exchange energy makes this carrier distribution preferable [11, 12]. It was shown in [13] that the fractional volume of the FM phase in a sample residing in the insulating MTPS is substantially smaller than that in a sample in the conducting state with the two coexisting magnetic phases. For instance, the fractional volume of the FM phase in a doped EuSe sample in the conducting MTPS is about an order of magnitude larger than that in the sample in the insulating TPS [14]. It may be presumed that $Eu_{0.55}Sr_{0.45}MnO_3$ is in the insulating MTPS and $Sm_{0.55}Sr_{0.45}MnO_3$ is in the conducting TPS. In this case, the magnetization process in $Sm_{0.55}Sr_{0.45}MnO_3$ at $T < T_C$ will occur through an increase in the fractional volume of the FM phase, which occupies the larger part of the sample, by intergrowth over FM planes in the *A*-type AFM phase; the abrupt rise in magnetization caused by *CE*-type AFM clusters would not be noticeable against the background of this growth, because these clusters occupy a considerably smaller volume than the FM phase. Jumps in the $\sigma(H)$ curves appear here only at high temperatures, where the FM and *A*-type AFM phases are thermally destroyed and only *CE*-type AFM clusters remain.

The $Eu_{0.55}Sr_{0.45}MnO_3$ composition exhibits jumps in the magnetization isotherms both below and above the Néel temperature $T_N = 41$ K, which was derived from the maximum of initial susceptibility in an ac magnetic field. The *A*-type AFM phase breaks down at this temperature, because this temperature coincides with the T_N of $EuMnO_3$, which exhibits *A*-type AFM order. As seen from Fig. 6, these jumps are still observed at $T = 120$ K but are absent already at $T = 150$ K; i.e., the Néel temperature of the *CE*-type AFM phase lies between 120 and 150 K. Figure 6 also shows that, in the ranges $1.4 \le T \le 40$ K and $0 \le H < H_{C1}$, the $\sigma(H)$ curves actually represent the sum of a small spontaneous magnetization $\sigma \sim 0.1\mu_B$ and a linear-in-*H* magnetization characteristic of the AFM state. Thus, the volume of the FM phase is small, only ~3% of that of the sample, as seen from the ratio of the FM-phase magnetization to the saturation magnetization that would exist under

complete FM ordering of the sample ($3.55\mu_B$). As is evident from Fig. 6, in the region $50 < T < 60$ K, this spontaneous part of the magnetization disappears, which implies that it is in this temperature region that the Curie point T_C is located. After the jump in the isotherms, as already mentioned, the magnetization constitutes ~70% of the saturation level. Assuming this jump to be caused by the *CE*-type AFM phase, the fractional volume of this phase should be about 67% of the sample volume, which makes this phase singly connected; therefore, the remaining ~30% of the sample volume is occupied by the *A*-type AFM phase. After the jump, the magnetization grows slowly and linearly with the field because of the growth in the magnetic-field-induced FM phase over the FM layers of the *A*-type AFM phase.

It is known that the *CE*-type AFM phase with CO ordering is the most stable at low temperatures, while at higher temperatures it is less stable than the FM or the *A*-type AFM phase [7]. Therefore, the critical field H_{C1} decreases with increasing T in the low-temperature range up to 40 K inclusive (Fig. 3), in which the FM and *A*-type AFM phases coexist with the *CE*-type AFM phase. Starting from $T = 50$ K and up to 120 K, H_{C1} increases. The reason for this lies apparently in the fact that for $T > T_C$ the magnetic fields needed to maintain the FM order formed in the magnetic field–induced transition of the *CE*-type AFM phase to the FM state are higher than those for $T < T_C$. As already mentioned, the *CE*-type AFM phase supports orbital ordering and the related charge ordering. If the magnetic field–induced transition from this state were to be associated only with charge order, one would expect the transition to give rise to a paramagnetic state for $T > T_C$. As follows from our experiment, however, the *CE*-type AFM phase transfers to the FM state. This is due to the fact that the carriers that are disordered by the field $H > H_{C1}$ support the FM order because of the energy gained in the *s*–*d* exchange.

It is seen from Figs. 6 and 2 that, for $T < T_C$, the $\sigma(H)$, $\rho(H)$, and $\omega(H)$ curves obtained in the increasing and decreasing field modes are different and that there are no jumps in the curves measured with decreasing field. In other words, the FM state formed under increasing H above H_{C1} in the transition of the *CE*-type AFM phase to the FM state exists under decreasing field down to fields that are negligible in comparison with H_{C1}. The giant magnitude of ω and the sharply decreased ρ caused by this transition persist after removal of the field. The sample can be restored to the original state only by heating it to $T > 100$ K followed by cooling to the desired temperature. This suggests that the free energies of the FM and *CE*-type AFM phases are similar in magnitude and that the magnetic field–induced transition of the *CE*-type AFM phase to the FM state is first-order. Starting from $T = 60$ K and up, i.e., above T_C, after the field is turned off, we have $\omega = 0$ and ρ recovers its initial value (before application of the field), though the difference in the $\rho(H)$ and $\omega(H)$ curves obtained under increasing and decreasing field is retained (Fig. 2).

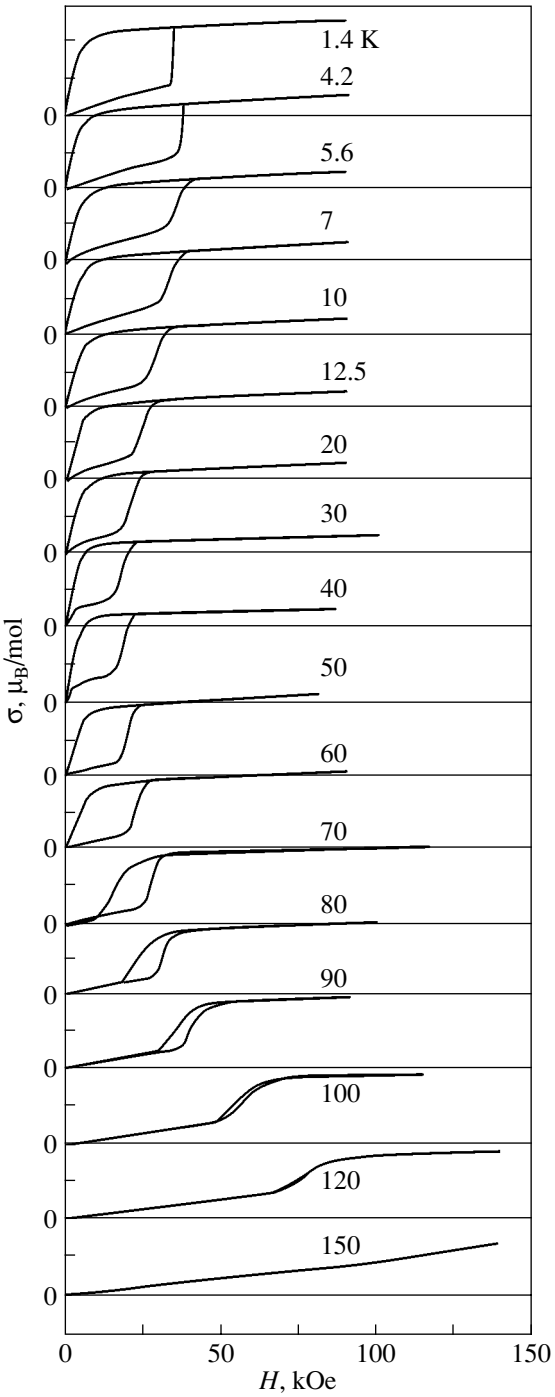

Fig. 6. Isotherms of the magnetization obtained at different temperatures. The value of division along the y axis is $1\mu_B$.

The colossal negative magnetoresistance of this composition is related only to the FM phase that formed in the magnetic field–induced transition of the *CE*-type AFM phase to the FM state. Since the compound retains its semiconducting character after this transi-

tion, the FM phase is actually given by FM clusters embedded in an *A* type AFM insulating matrix, with the carriers (holes) concentrated in these clusters because of the gain in *s–d* exchange energy. The CMR can be interpreted in the following way. An external magnetic field increases the radii of the FM clusters, thus facilitating carrier tunneling between them. Furthermore, the magnetic moments of the FM clusters become ordered by the external field, which likewise favors carrier tunneling. Finally, the external magnetic field tends to destroy FM clusters, which increases the energy of the holes inside the clusters and, thus, makes their transition to the delocalized state easier [5, 13]. The high positive magnetoresistance observed for $H < H_{C1}$ and $T < T_C$ is apparently associated with the FM phase and can be interpreted in the same way as the situation in nondegenerate FM semiconductors [15].

The giant volume magnetostriction is also intimately connected with the FM phase formed in the field-induced transition of the *CE*-type AFM phase to the FM state. Yanase and Kasuya [16] showed that within FM clusters the lattice constants are reduced because of the new charge distribution, which brings about a decrease in the energy inside the clusters through increasing the overlap of the charge clouds between the central impurity ion and its nearest neighbors (magnetic ions). Obviously enough, thermal destruction of the MTPS should give rise to an excess thermal expansion of the sample in comparison with the linear-in-temperature quantity, an effect which we observed (see inset to Fig. 1). It is known that the temperature dependence of thermal expansion of diamagnetic and paramagnetic materials is nearly linear in *T*. The excess thermal expansion can be suppressed by using an external magnetic field to restore the MTPS; i.e., the sample should exhibit negative volume magnetostriction.

4. CONCLUSIONS

Thus, the CMR, the high volume magnetostriction, and the excess thermal expansion observed to occur in $Eu_{0.55}Sr_{0.45}MnO_3$ in the vicinity of T_C are accounted for by electronic phase separation in the sample stimulated by strong *s–d* exchange, with the carriers concentrated in the FM phase. The presence of the *CE*-type AFM CO phase introduces specific features into the behavior of the magnetoresistance and volume magnetostriction; these features manifest themselves in the fact that the isotherms of these quantities as a function of the field exhibit jumps associated with the magnetic field–induced transition of this phase to the FM state.

ACKNOWLEDGMENTS

This study was supported by the Russian Foundation for Basic Research, project no. 03-02-16100.

REFERENCES

1. A. I. Abramovich, L. I. Koroleva, and A. V. Michurin, Zh. Éksp. Teor. Fiz. **122** (5), 1063 (2002) [JETP **95**, 917 (2002)].
2. R. V. Demin, L. I. Koroleva, R. Szymczak, and G. Szymczak, Pis'ma Zh. Éksp. Teor. Fiz. **75** (7), 402 (2002) [JETP Lett. **75**, 331 (2002)].
3. A. I. Abramovich and A. V. Michurin, Fiz. Nizk. Temp. **27**, 379 (2001) [Low Temp. Phys. **27**, 278 (2001)].
4. A. I. Abramovich, A. V. Michurin, O. Yu. Gorbenko, and A. R. Kaul, J. Phys.: Condens. Matter **12** (39), L627 (2000).
5. É. L. Nagaev, Usp. Fiz. Nauk **166**, 833 (1996) [Phys. Usp. **39**, 781 (1996)]; E. L. Nagaev, Phys. Rep. **346** (6), 387 (2001).
6. V. V. Runov, D. Yu. Chernyshov, A. I. Kurbakov, M. K. Runova, V. A. Trunov, and A. I. Okorokov, Zh. Éksp. Teor. Fiz. **118** (5), 1174 (2000) [JETP **91**, 1017 (2000)].
7. E. Dagotto, T. Hotta, and A. Moreo, Phys. Rep. **344** (1), 1 (2001).
8. A. I. Abramovich, R. V. Demin, L. I. Koroleva, A. V. Michurin, and A. G. Smirnitskaya, Pis'ma Zh. Éksp. Teor. Fiz. **69** (5), 375 (1999) [JETP Lett. **69**, 404 (1999)].
9. A. Abramovich, R. Demin, L. Koroleva, A. Michurin, K. A. Maslov, and Ya. M. Mukovskii, Phys. Lett. A **259** (1), 57 (1999).
10. A. I. Abramovich, L. I. Koroleva, A. V. Michurin, O. Yu. Gorbenko, A. R. Kaul, M. Kh. Mashaev, R. Szymczak, and B. Krzhymanska, Fiz. Tverd. Tela (St. Petersburg) **44** (5), 888 (2002) [Phys. Solid State **44**, 927 (2002)].
11. S. Nakamura, Y. Todokodo, Y. J. Shan, and T. Nakamura, J. Phys. Soc. Jpn. **68** (3), 1485 (1999).
12. É. L. Nagaev, *Physics of Magnetic Semiconductors* (Nauka, Moscow, 1979) [in Russian].
13. E. L. Nagaev, *Colossal Magnetoresistance and Phase Separation in Magnetic Semiconductors* (Imperial College Press, London, 2002).
14. Y. Shapira, S. Foner, and N. Jr. Oliveira, Phys. Rev. B **10** (11), 4765 (1974).
15. L. I. Koroleva, *Magnetic Semiconductors* (Mosk. Gos. Univ., Moscow, 2003) [in Russian].
16. A. Yanase and T. Kasuya, J. Phys. Soc. Jpn. **25** (4), 1025 (1968).

Translated by G. Skrebtsov

Physics of the Solid State, Vol. 46, No. 9, 2004, pp. 1717–1721. From Fizika Tverdogo Tela, Vol. 46, No. 9, 2004, pp. 1663–1667.
Original English Text Copyright © 2004 by Kvyatkovskii, Karadag, Mamedov, Zakharov.

MAGNETISM AND FERROELECTRICITY

Cluster *ab initio* Modeling of Local Lattice Instability in Relaxor Ferroelectrics*

O. E. Kvyatkovskii[1, 2], F. Karadag[1], A. Mamedov[1], and G. A. Zakharov[3]

[1] *Cukurova University, Adana, Turkey*

[2] *Ioffe Physicotechnical Institute, Russian Academy of Sciences, St. Petersburg, 194021 Russia*

[3] *St. Petersburg State Polytechnic University, St. Petersburg, 195220 Russia*

e-mail: Kvyatkovskii@mail.ioffe.ru

Received December 29, 2003

Abstract—The possibility of a zigzag-type instability occurring for oxygen atoms in *B*–O–*B*, *B*–O–Nb, and Nb–O–Nb linear chains is examined in disordered mixed perovskite compounds Pb($B_{1/3}$, $Nb_{2/3}$)O_3 (*B* = Mg, Zn, Cd). Local adiabatic potentials for oxygen atoms are studied using total energy calculations by the *ab initio* Hartree–Fock + MP2 method for many-atomic clusters with different oxygen surroundings of lead atoms. The effect of lattice relaxation along the chain on the shape of the local potential in the transverse direction for the central oxygen atom is considered. © *2004 MAIK "Nauka/Interperiodica".*

1. INTRODUCTION

The disordered perovskite compounds of complex composition Pb($Mg_{1/3}$, $Nb_{2/3}$)O_3 (PMN), Pb($Zn_{1/3}$, $Nb_{2/3}$)O_3 (PZN), and Pb($Cd_{1/3}$, $Nb_{2/3}$)O_3 (PCN) belong to the class of relaxor ferroelectrics. They have a broad, strongly frequency-dependent maximum in the temperature dependence of the dielectric permittivity and retain average cubic symmetry down to 5 K [1–5]. To explain the unusual properties of relaxor ferroelectrics, a number of models have been proposed. For instance, the diffuse ferroelectric phase transition model proposed by Smolenskii and Isupov [1, 2, 6], the dipolar glass model proposed by Cross [7], and the random field induced domain state model proposed by Westphal *et al*. [8] can be mentioned.

One of the main structural features of mixed perovskites is the random occupation of the positions *B* in an ideal perovskite lattice by chemically different ions. This disorder gives rise to local distortions of the cubic perovskite structure, that is, to random displacements of ions from the pseudocubic sites. Two types of such displacements are possible. Displacements of the first type are determined simply by the difference in the ionic radii and valences and are frozen when random distribution of the ions is quenched. Such displacements of ions produce a set of random local dipoles, which are, in turn, the source of the random local electric field. In addition to this type of local distortions, one can infer also the possibility of atomic displacements concerned with local lattice instabilities produced by peculiarities in the chemical bonding in mixed perovskites [9, 10]. These local polar distortions would be reversible and could play an important role in the formation of the ferroelectric microregions in PMN, PZN, and PCN along with the correlated displacements of polar optical type [11, 12] frozen in the random local electric field.

I can be expected that in mixed perovskites oxygen ions can be unstable relative to off-center shifts in the plane parallel to the pseudocubic face (the local zigzag instability in the *B*–O–*B*' linear chain) [9, 10]. The standard crystallographic analysis based on x-ray or neutron diffraction data [13, 14] and pair-density function (PDF) analysis of pulsed neutron and synchrotron x-ray powder diffraction data [15] show that, in PMN, the oxygen off-center shifts in the planes parallel to the cube faces are equal to ≈0.17–0.19 Å according to [13, 14] and to ≈0.4 Å according to [15]. However, these methods cannot identify the origin of the observed oxygen shifts. Thus in [9, 10] cluster *ab initio* calculations of the potential well for the oxygen atom and of the equilibrium oxygen position in the *B*–O–Nb, *B*–O–*B* (*B* = Mg, Zn, Cd), and Nb–O–Nb chains in PMN, PZN, and PCN were performed. It was found that in *B*–O–Nb chains in PMN, PZN, and PCN and in *B*–O–*B* chains in PZN and PCN oxygen atoms move in multiwell potentials with four minima shifted transversely to the fourfold [001] axis, whereas the oxygen atom in the Nb–O–Nb chain in PMN, PZN, and PCN and all oxygen atoms in BCN move in single-well potentials. This raises the question as to whether the solutions found in [9, 10] are stable relative to the cluster size, extensions of the atomic basis sets, or structural relaxation of the oxygen surroundings. These problems are studied in the present paper.

* This article was submitted by the authors in English.

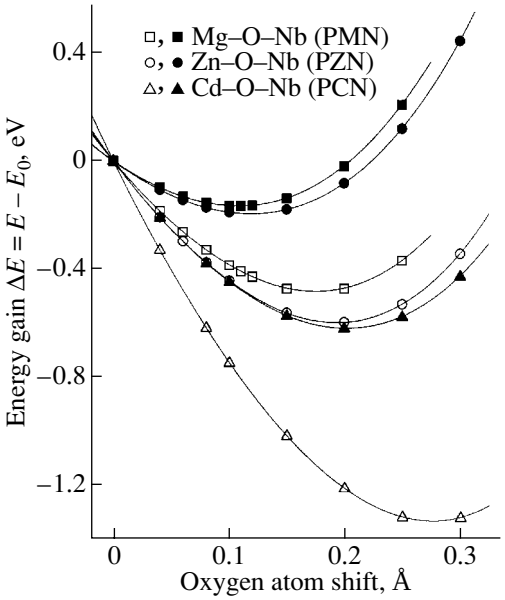

Fig. 1. Local adiabatic potentials $\Delta E(0, 0, z)$ for the oxygen atom in a *B*–O–Nb chain along the chain in PMN, PZN, and PCN calculated by the RHF method (open symbols) and by the RHF + MP2 method (solid symbols). The oxygen shift from the midpoint is positive in the direction of the Nb atom.

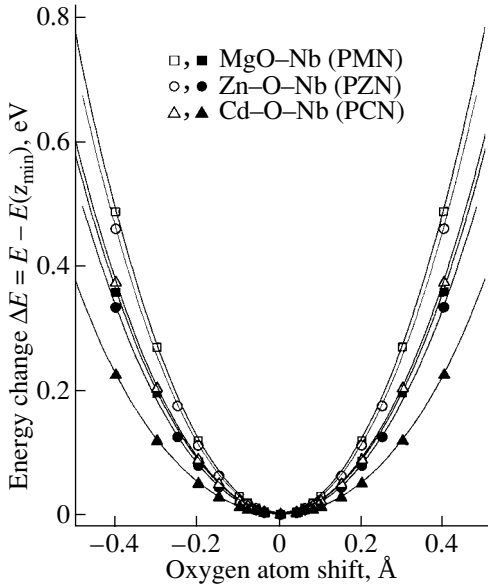

Fig. 2. Local adiabatic potentials $\Delta E(x, 0, z_{min})$ for oxygen atoms in *B*–O–Nb chains in the transverse [100] and [010] directions in PMN, PZN, and PCN calculated by the RHF method (open symbols) and by the RHF + MP2 method (solid symbols).

2. CALCULATION METHOD

Taking into account the aperiodic structure of disordered relaxor ferroelectrics, we used for calculations of the local potential wells the quasi-molecular cluster *ab initio* method described in [16–18]. In a cubic perovskite structure, oxygen atoms are situated at the center of cubic faces, at the midpoint between neighboring *B* cations forming in PMN, PZN, and PCN Nb–O–Nb, *B*–Nb–*B*, and *B*–O–Nb chains with *B*–O and Nb–O bonds of equal length. Therefore, the crystalline surroundings of the oxygen atoms is modeled by one of the extended two-octahedron clusters $[OB\mathrm{NbPb_4(OH)_{10}(OH_2)_8}]^{3+}$, $OB_2\mathrm{Pb_4(OH)_{10}(OH_2)_8}$, or $[\mathrm{ONb_2Pb_4(OH)_{10}(OH_2)_8}]^{6+}$ instead of the simple two-octahedron clusters $[OB\mathrm{NbPb_4(OH)_{10}}]^{3+}$, $OB_2\mathrm{Pb_4(OH)_{10}(OH_2)_8}$, or $[\mathrm{ONb_2Pb_4(OH)_{10}}]^{6+}$ used in [9, 10]. The clusters consist of corner-shared octahedrons (NbO_6, BO_6) and involve four Pb atoms (around the central oxygen) and eight additional oxygen atoms (around the lead atoms) arranged in the "mirror" plane. In addition, hydrogen atoms are placed on broken bonds of surface oxygen atoms at a distance of 1 Å to reduce the net charge of the cluster. All interatomic distances are equal to the corresponding values in an ideal perovskite structure PMN with lattice constants $a_0 = 4.0278$ Å (PMN) [10], $a_0 = 4.04$ Å (PZN) [19], and $a_0 = 4.135$ Å (PCN) [20].

To find the local adiabatic potential for an atom in a crystal, one has to calculate the total energy of the crystal as a function of atomic displacement from the position of the cubic perovskite lattice site, assuming that the remaining atoms occupy equilibrium positions in the crystal. A local adiabatic potential is defined as $\Delta E(\boldsymbol{\eta}) = E(\boldsymbol{\eta}) - E_0$, where E is the total crystal energy and $\boldsymbol{\eta}$ is a shift of the oxygen atom. A cluster approximation is used for the total energy: $\Delta E(\boldsymbol{\eta}) \cong \Delta E^{c1}(\boldsymbol{\eta})$, where $E^{c1}(\boldsymbol{\eta})$ is the total energy of a given cluster.

Calculations of the electronic structure and total energy of the cluster are performed using the *ab initio* restricted Hartree–Fock (RHF) MO LCAO method with second-order Møller–Plesset perturbation theory electron correlation corrections (MP2) to the total energy using the PC GAMESS version [21] of the GAMESS (US) QC package [22]. The following atomic Gaussian basis sets were used: WTBS basis sets (27*s*, 20*p*, 17*d*)/[5*s*, 3*p*, 2*d*] for Nb, (23*s*, 13*p*)/[3*s*, 1*p*] for Mg, (27*s*, 20*p*, 17*d*)/[5*s*, 3*p*, 2*d*] for Zn, and (28*s*, 20*p*, 17*d*)/[5*s*, 3*p*, 2*d*] for Cd [23]; TZV basis set (10*s*, 6*p*)/[5*s*, 3*p*] for an oxygen atom [24] with Pople (2*df*, 2*pd*) polarization functions [25] for the central oxygen atom and with the DHMS polarization function [26] for other oxygen atoms; basis set (4*s*)/[2*s*] for H [20]; and basis set SBKJC ECP for Pb (Ba) [27].

3. RESULTS AND DISCUSSION

The results of cluster *ab initio* calculations of local adiabatic potentials for oxygen atoms in disordered relaxor ferroelectrics are presented in Figs. 1–5.

In Fig. 1, local potentials for the oxygen atoms along *B*–O–Nb (*B* = Mg, Zn, Cd) chains in PMN, PZN, and PCN are presented. The equilibrium oxygen posi-

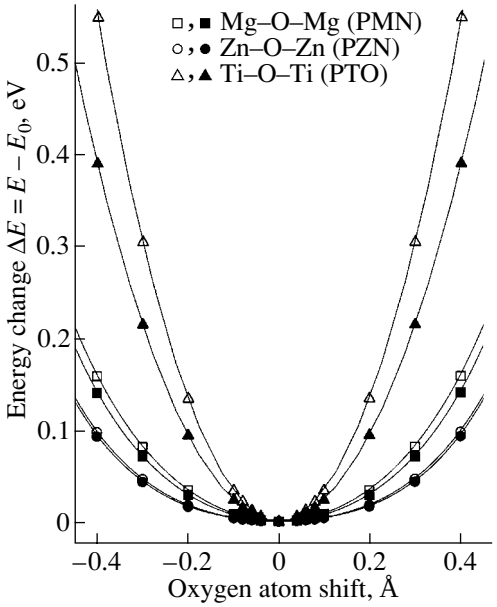

Fig. 3. Local adiabatic potentials $\Delta E(x, 0, 0)$ for oxygen atoms in Mg–O–Mg and Zn–O–Zn chains in PMN and PZN and in the Ti–O–Ti chain in PTO in the transverse [100] and [010] directions calculated by the RHF method (open symbols) and by the RHF + MP2 method (solid symbols).

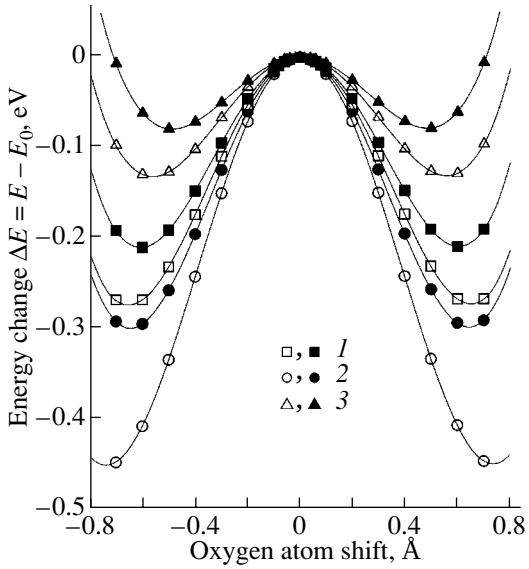

Fig. 4. Local adiabatic potential $\Delta E(x, 0, 0)$ for oxygen atoms in the Cd–O–Cd chain in PCN in the transverse [100] and [010] directions calculated by the RHF method (open symbols) and by the RHF + MP2 method (solid symbols) for cases *1–3* described in the text.

tions z_{min} are shifted from the midpoint by 0.11 Å for PMN, by 0.12 Å for PZN, and by 0.2 Å for PCN towards the Nb atom. The shape of the potential well along the chain is strongly influenced by electron correlation, as in [9, 10].

In Fig. 2, local potentials for oxygen atoms in *B*–O–Nb (*B* = Mg, Zn, Cd) chains in the directions [100] and [010] transversal to the chain are presented for PMN, PZN, and PCN. As indicated in Fig. 2, the local potentials wells for oxygen in PMN, PZN, and PCN are single-well, so the central position of the oxygen in the Mg–O–Nb chain in PMN and in the Cd–O–Nb chain in PCN is stable in the transverse direction.

In Fig. 3, local potential wells for the oxygen atoms in *B*–O–*B* (*B* = Mg, Zn) chains in the directions [100] and [010] transversal to the chains are presented for both PMN and PZN and a similar local potential is presented for oxygen in the Ti–O–Ti chain for PTO. In both cases, the oxygen atom moves in the mirror plane in a soft single-well local potential with a small transverse stiffness $\kappa_\perp$ (defined as $\kappa_\perp = 2\Delta E(\boldsymbol{\eta})/\eta^2$ at $\eta \longrightarrow 0$) equal to 1.3 eV/Å^2 for PMN and to 0.65 eV/Å^2 for PZN within RHF + MP2. For comparison, the analogous stiffness for oxygen in PTO is equal to 4.7 eV/Å^2. The anharmonic constants of the forth order are nearly the same for all three compounds.

In Fig. 4, local potentials for oxygen atoms in the Cd–O–Cd chain in PCN in the directions [100] and [010] transversal to the chain are presented for three different cases, (*1*) for $OCd_2Pb_4(OH)_{10}$, (*2*) for cluster $OCd_2Pb_4(OH)_{10}(OH_2)_8$, and (*3*) for cluster $OCd_2Pb_4(OH)_{10}(OH_2)_8$, taking into account lattice relaxation for Cd–O distances along the chain. In the first two cases, all interatomic distances are equal to that for the average cubic structure. In the third case, all distances are kept equal to their average values with the exception of Cd–O distances along the chain, which are chosen equal to $(a_0 + z_{min})/2 = 2.1675$ Å, where $a_0 = 4.135$ Å is the average lattice constant and $z_{min} = 0.2$ Å is the shift of the oxygen atom in the Cd–O–Nb chain from the mirror plane towards the Nb atom. It is obvious from the curves that in all cases the oxygen atom in the Cd–O–Cd chain moves in a multiwell local potential with four minima shifted in transverse directions.

In Fig. 5, the local potentials in the mirror plane for the oxygen atom in Nb–O–Nb chains in PCN and in the Ti–O–Ti chain in PTO are presented.

Let us discuss the results. From comparing the results presented in Fig. 2 with those found in [10], one can see that inclusion of the additional eight oxygen atoms around the lead atoms dramatically changes the shape of the local potentials for oxygen atoms in the Mg–O–Nb, Zn–O–Nb, and Cd–O–Nb chains in directions transverse to the chains. We obtained single-well hard local potentials instead of the multiwell potentials found in [10]. On the other hand, when the results presented in Figs. 3 and 4 are compared with those found in [9, 10], it becomes apparent that the shapes of the local potentials for oxygen atoms in Mg–O–Mg, Zn–O–Zn, and Cd–O–Cd chains retain their qualitative

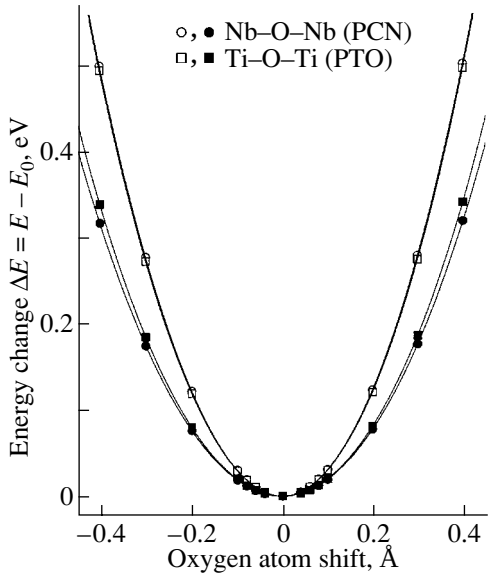

Fig. 5. Local adiabatic potential $\Delta E(x, 0, 0)$ for oxygen atoms in Nb–O–Nb chains in PCN and in the Ti–O–Ti chain in PTO in the transverse [100] and [010] directions calculated by the RHF method (open symbols) and by the RHF + MP2 method (solid symbols).

features (softness in the cases of Mg–O–Mg and Zn–O–Zn and multiwell character in the case of Cd–O–Cd) and are altered only quantitatively. We see also that extension of the cluster increases the transverse harmonic stiffness for oxygen atoms in addition to taking into account the increase in the Cd–O distance relative to the average bond length.

It should be stressed that the availability of multiwell potentials for oxygen atoms in the Cd–O–Cd chain offers a new mechanism of dipole ordering and of dielectric relaxation of order–disorder type in PCN. The softness of the transverse local potentials for oxygen atoms in the Mg–O–Mg chain in PMN and in the Zn–O–Zn chain in PZN (Fig. 3) may strongly influence the ferroelectric state observed in these compounds after cooling in an electric field [28, 29]. In addition, the small transverse local stiffness for oxygen atoms in these chains may be responsible for the large off-center shifts of the oxygen atoms in the planes parallel to cubic faces observed in [13–15]. Within classical statistics, one can write the displacement of an oxygen atom in the mirror plane due to thermal motion as $r_\perp = (\langle \mathbf{r}_\perp^2 \rangle)^{1/2} = (2T/\kappa_\perp)^{1/2}$. Taking into account the values of $\kappa_\perp$ calculated for PMN (1.3 eV/Å^2), PZN (0.65 eV/Å^2), and PTO (4.7 eV/Å^2), we find at $T = 300$ K that $r_\perp \approx 0.2$ Å in PMN (comparable with the observed values [13, 14]), $r_\perp \approx 0.3$ Å in PZN, and $r_\perp \approx 0.1$ Å in PTO. One should also take into account that the displacement $r_\perp$ induced by an electric field $E_\perp$ is proportional to $E_\perp/\kappa_\perp$. This gives rise to a larger difference in $r_\perp$ than in the case of thermal motion and ultimately results in a much larger contribution to the induced polarization in PZN than in PMN.

4. CONCLUSIONS

We have studied local lattice instabilities for oxygen atoms in PMN, PZN, and PCN employing cluster *ab initio* total energy calculations using the restricted Hartree–Fock MO LCAO method with second-order Møller–Plesset perturbation theory electron correlation corrections. The influence of the oxygen surroundings of the lead atoms in the many-atomic clusters used for the *ab initio* simulation on the shape of the local adiabatic potentials is considered. It is found that for oxygen atoms in the *B*–O–Nb chains (*B* = Mg, Zn, Cd) the use of an extended cluster with eight additional oxygen atoms around the lead atoms instead of a simple two-octahedron cluster dramatically changes the shape of the potential curves in the planes parallel to cubic faces from multiwell to single-well type. At the same time, it is found that the shape of the local potentials for oxygen atoms in Mg–O–Mg, Zn–O–Zn, and Cd–O–Cd chains is altered only quantitatively. The local potentials in directions transverse to the chain retain their softness for Mg–O–Mg and Zn–O–Zn and multiwell character for Cd–O–Cd.

ACKNOWLEDGMENTS

We are indebted to L.S. Kamzina and N.T. Krainik for many stimulating and useful discussions. This work was supported by TUBITAK (NATO PC Advanced Fellowship Program), the Russian Foundation for Basic Research (project nos. 01-02-17801 and 03-02-17557), and the Russian Academy of Sciences program for physical sciences.

REFERENCES

1. G. A. Smolenskii, V. A. Isupov, A. I. Agranovskaya, and S. N. Popov, Sov. Phys. Solid State **2**, 2584 (1961).
2. G. A. Smolenskii, J. Phys. Soc. Jpn. **28** (Suppl.), 25 (1970).
3. M. E. Lines and A. M. Glass, *Principles and Applications of Ferroelectrics and Related Materials* (Clarendon, Oxford, 1977; Mir, Moscow, 1981).
4. Z. G. Ye, Ferroelectrics **65**, 193 (1996).
5. C. A. Randall and A. S. Bhalla, Jpn. J. Appl. Phys. **29**, 327 (1990).
6. V. A. Isupov, Ferroelectrics **90**, 113 (1989); Ferroelectrics **143**, 109 (1993).
7. L. E. Cross, Ferroelectrics **76**, 241 (1987).
8. B. V. Westphal, W. Kleemann, and M. D. Glinchuk, Phys. Rev. Lett. **68**, 847 (1992).
9. F. Karadag, S. Palaz, S. Güngör, A. Mamedov, and O. E. Kvyatkovskii, Ferroelectrics **283**, 61 (2003).
10. O. E. Kvyatkovskii, Ferroelectrics **283**, 67 (2003).
11. S. Vakhrushev, S. Zhukov, G. Fetisov, and V. Chernyshov, J. Phys.: Condens. Matter **6**, 4021 (1994).

12. S. B. Vakhrushev, A. A. Naberezhnov, N. M. Okuneva, and B. N. Savenko, Fiz. Tverd. Tela (St. Petersburg) **37**, 3621 (1995) [Phys. Solid State **37**, 1993 (1995)].
13. P. Bonneau, P. Garnier, G. Calvarin, E. Husson, J. R. Gavarri, A. W. Hewat, and A. Morell, J. Solid State Chem. **91**, 350 (1991).
14. N. de Mathan, E. Husson, G. Calvarin, J. R. Gavarri, A. W. Hewat, and A. Morrell, J. Phys.: Condens. Matter **3**, 8159 (1991).
15. H. D. Rosenfeld and T. Egami, Ferroelectrics **164**, 133 (1995).
16. O. E. Kvyatkovskii and B. F. Shchegolev, Ferroelectrics **153**, 207 (1994).
17. O. E. Kvyatkovskii and B. F. Shchegolev, Izv. Ross. Akad. Nauk, Ser. Fiz. **64**, 1060 (2002).
18. O. E. Kvyatkovskii, Fiz. Tverd. Tela (St. Petersburg) **44**, 1087 (2002) [Phys. Solid State **44**, 1135 (2002)].
19. K. A. Bokov and I. E. Mylnikova, Fiz. Tverd. Tela (Leningrad) **2**, 2728 (1960) [Sov. Phys. Solid State **2**, 2428 (1960)].
20. *Landolt-Börnstein. Numerical Data and Functional Relationships in Science and Technology*, Ed. by K.-H. Hellwege and A. M. Hellwege (Springer, Berlin, 1981), Group III, Vol. 9a.
21. A. A. Granovsky, www http://classic.chem.msu.su/gran/gamess/index.html.
22. M. W. Schmidt, K. K. Baldridge, J. A. Boatz, S. T. Elbert, M. S. Gordon, J. J. Jensen, S. Koseki, N. Matsunaga, K. A. Nguyen, S. Su, T. L. Windus, M. Dupuis, and J. A. Montgomery, J. Comput. Chem. **14**, 1347 (1993).
23. S. Huzinaga and B. Miguel, Chem. Phys. Lett. **175**, 289 (1990); Chem. Phys. Lett. **212**, 260 (1993).
24. T. H. Dunning, J. Chem. Phys. **55**, 716 (1971).
25. M. J. Frisch, J. A. Pople, and J. S. Binkley, J. Chem. Phys. **80**, 3265 (1984).
26. T. H. Dunning and P. J. Hay, in *Methods of Electronic Structure Theory*, Ed. by H. F. Schaefer III (Plenum, New York, 1977).
27. W. J. Stevens, M. Krauss, H. Basch, and P. G. Jasien, Can. J. Chem. **70**, 612 (1992).
28. H. Arndt, F. Sauerbier, G. Schmidt, and L. A. Shelbanov, Ferroelectrics **79**, 145 (1988).
29. L. S. Kamzina, N. N. Krainik, L. M. Sapozhnikova, and S. V. Ivanova, Sov. Phys. Solid State **33**, 1169 (1991).

Physics of the Solid State, Vol. 46, No. 9, 2004, pp. 1722–1729. Translated from Fizika Tverdogo Tela, Vol. 46, No. 9, 2004, pp. 1668–1675.
Original Russian Text Copyright © 2004 by Bush, Kamentsev, Provotorov, Trushkova.

MAGNETISM AND FERROELECTRICITY

Low-Frequency Relaxation Processes in $Pb_5Ge_3O_{11}$ Ferroelectric Crystals

A. A. Bush*, K. E. Kamentsev*, M. V. Provotorov, and T. N. Trushkova****

**Moscow State Institute of Radioengineering, Electronics, and Automation (Technical University), pr. Vernadskogo 78, Moscow, 119454 Russia*

e-mail: abush@ranet.ru

***Mendeleev University of Chemical Technology, Miusskaya pl. 9, Moscow, 123480 Russia*

Received January 12, 2004

Abstract—Measurements and analysis of the temperature and frequency dependences of permittivity and losses and of the electrical resistivity of $Pb_5Ge_3O_{11}$ ferroelectric crystals at temperatures of 100 to 600 K and frequencies of 0.1 to 100 kHz are reported. The dielectric characteristics of the crystals exhibit, in addition to clearly pronounced anomalies near the Curie point T_C = 450 K, less distinct anomalous features of the relaxation character in the range 230–260 K. The data obtained on the effect of various factors (degree of crystal polarization, crystal annealing at different temperatures and in different environments, etc.) on the low-temperature anomalies serve as a basis for discussing the possible mechanisms responsible for these anomalies. It is concluded that the low-temperature dielectric anomalies originate from thermal carrier localization in defect levels in the band gap, which entail the formation of local polarized states. © *2004 MAIK "Nauka/Interperiodica".*

1. INTRODUCTION

$Pb_5Ge_3O_{11}$ lead germanate crystals are uniaxial ferroelectrics whose symmetry switches when cooled to the Curie point T_C = 450 K from hexagonal, $P\bar{6}$, to trigonal, $P3$ [1–4]. In view of their physical properties, which are remarkable from the standpoint of both pure and applied science, these crystals have been intensely studied over the past four decades. Numerous studies of their structure, dielectric, piezo- and pyroelectric, optical, mechanical, and other characteristics have been carried out; the main results of these works are summarized in review [4]. This compound holds considerable promise, in particular, for use as a pyroelectric material, in ferroelectric memory devices, and for hologram recording and readout [4–8].

Studies of the temperature and frequency dependences of the dielectric properties of crystals of this compound in the low-frequency domain (<1 MHz) are dealt with in [4, 9–15]. The reported data on the regions of dispersion and their interpretation are not always in agreement. The strong dispersion of the permittivity observed at sonic frequencies and temperatures slightly below T_C is attributed to relaxation processes closely linked with the motion of domain walls [10] or lattice defects [12]. Charged domain walls in thermally depolarized lead germanate crystals were found [11] to produce three partially overlapping contributions to the permittivity at temperatures of 190 to 430 K and frequencies of 0.01 to 1000.0 kHz. The lowest frequency contribution, observed in the range 290–320 K, is assigned to the difference in charge transport between the bulk of the crystal and the volume of domain walls. The other two, higher frequency contributions, which become manifest in the temperature intervals 220–290 and 190–250 K, originate from domain wall motion and redistribution of trapped charge in domain walls. As follows from measurements performed in the range 370–520 K [14], surface states and the Maxwell–Wagner relaxation provide a noticeable contribution to the low-frequency dispersion of permittivity both above and below T_C. Two relaxation mechanisms were revealed in the regions 298–873 K and 10^2–10^7 Hz: one of them involves hopping carrier transport, and the other, internal polarization of the ferroelectric crystal [15].

In all of papers [9–15], except [11], the dielectric properties of $Pb_5Ge_3O_{11}$ crystals were probed above room temperature. Studies of the dielectric properties of this compound at low temperatures [4, 16] performed at 1 kHz reveal anomalous changes in the permittivity $\varepsilon(T)$ and the loss tangent $\tan\delta(T)$ at temperatures below room temperature. The nature of these anomalies still defies explanation. The present communication reports on a more comprehensive investigation of the low-temperature dielectric anomalies aimed at determining their origin. Measurements of the pattern of the dielectric anomalies as a function of the measuring field frequency, degree of crystal polarization, details of the thermal treatment of crystals, and some other factors were carried out at temperatures of 100 to 600 K and frequencies of 0.1 to 100 kHz.

1063-7834/04/4609-1722$26.00 © 2004 MAIK "Nauka/Interperiodica"

2. PREPARATION OF CRYSTALS AND METHODS OF INVESTIGATION

Boules of $Pb_5Ge_3O_{11}$ crystals up to a few cubic centimeters in volume were Czochralski grown from a $5PbO \cdot 3GeO_2$ stoichiometric melt in air. The boule pulling rate was 2–4 mm/h, with the seed crystal growth axis oriented along either the **c** or the **a** crystallographic axis. The stripe growth structure characteristic of Czochralski-grown crystals [17] was oriented perpendicular and parallel to the direction of spontaneous polarization when pulled along the **c** and **a** axes, respectively.

The crystals were transparent, brownish in color, and exhibited the characteristic $\{10\bar{1}0\}$ growth pattern. Crystals grown from a melt that was already used once for crystal growth were dark brown. As shown by thermogravimetric measurements performed with a Q 1500D derivatograph, relative changes in crystal mass when heated to 720°C did not exceed 0.04%, which argues against the presence of inclusions of H_2O, CO_2, etc., in the sample composition.

The phase composition of the samples and their crystallographic orientation were determined with a DRON-4 x-ray diffractometer and a POLAM L-213M polarization microscope. Powder x-ray diffraction patterns of the crystals obtained and the parameters of the trigonal cell derived from them are in agreement with the data from [1–4] for $Pb_5Ge_3O_{11}$ crystals. The parameters obtained for the brownish crystals are a = 10.226(4) Å and c = 10.664(3) Å; for the dark brown samples, a = 10.214(5) Å and c = 10.649(4) Å. The darkening in color and the decrease in the size of the unit cell for the crystals grown from a used charge are apparently associated with their composition shifting toward GeO_2, an effect caused by vaporization of part of the PbO in the course of the previous boule growth.

The electrophysical properties were studied on single-crystal plates cut from boules perpendicular to the **a** and **c** axes. Silver paste electrodes were fired onto the major sides of the plates. The plate thickness was $d \sim$ 0.5–3.0 mm, and the electrode area on the major sides of the crystal was $S \sim 10$ mm^2.

The capacitance C and the loss tangent $\tan\delta$ were measured with an E7-14 meter or a P5083 ac bridge in the temperature range T = 100–600 K and frequency range f = 0.1–100 kHz in weak measuring fields. The rate of variation in the temperature was typically 5.0 K/min. The real and imaginary parts of the complex permittivity $\varepsilon^* = \varepsilon_1 - i\varepsilon_2$ and the electrical resistivity ρ were calculated from the relations $\varepsilon_1 = Cd/S\varepsilon_0$, $\varepsilon_2 = \varepsilon_1 \tan\delta$, and $\rho = 1/2\pi f \varepsilon_1 \varepsilon_0 \tan\delta$, where $\varepsilon_0 = 8.854 \times 10^{-12}$ F/m is an electric constant.

To make the crystals single-domain, they were polarized by heating to temperatures (~200°C) above the Curie point and cooled subsequently under application of a dc electric field of ~0.5 kV/cm. The degree of polarization was monitored by measuring the piezo- and pyroelectric constants of the crystals using the oscillating-load and quasistatic techniques, respectively.

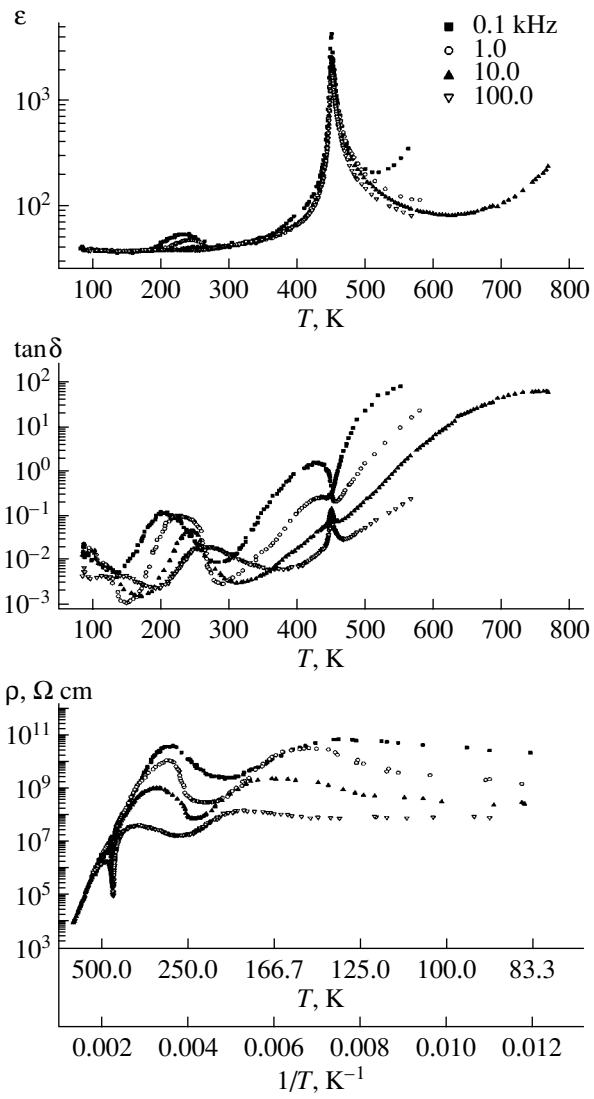

Fig. 1. Temperature dependences of permittivity ε, dielectric loss tangent tanδ, and electrical resistivity ρ of $Pb_5Ge_3O_{11}$ crystals grown along the **c** axis (measurements were performed along the **c** axis of unpolarized crystals at frequencies f = 0.1, 1.0, 10.0, and 100.0 kHz).

3. RESULTS OF DIELECTRIC MEASUREMENTS

Figures 1–4 summarize the results obtained in measurements of the permittivity ε, loss tangent $\tan\delta$, and electrical resistivity ρ along the polar axis of the crystals, which were carried out at temperatures of 100–770 K band frequencies of 0.1–100.0 kHz. According to the literature, the dependences obtained for nominally defect-free crystals exhibit distinct anomalies near the Curie point T_C = 450 K in the form of maxima in ε and $\tan\delta$ and a minimum in ρ (Fig. 1). The magnitude of

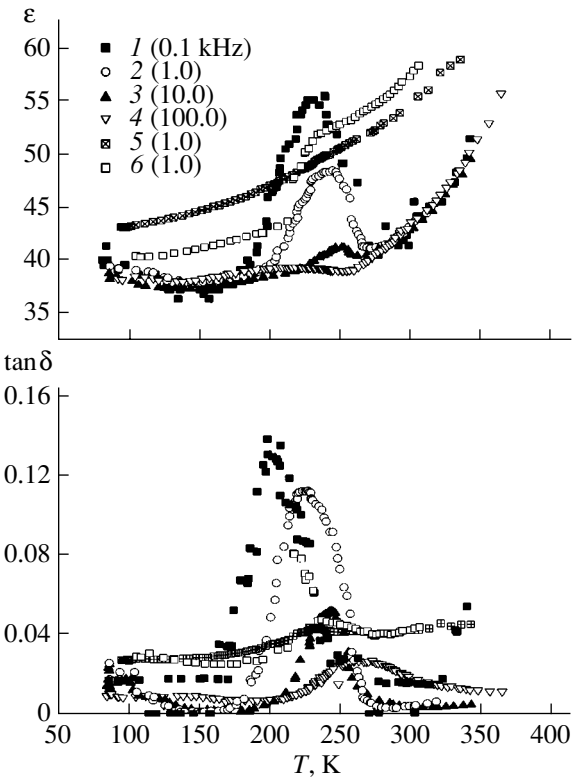

Fig. 2. Temperature dependences of permittivity ε and dielectric loss tangent tanδ measured along the **c** axis of (*1*–*4*) multidomain and (*5*, *6*) single-domain $Pb_5Ge_3O_{11}$ crystals (grown along the **c** axis) at frequencies of (*1*) 0.1, (*2*, *5*, *6*) 1.0, (*3*) 10.0, and (*4*) 100.0 kHz; the measurements on polarized crystals were carried out (*5*) immediately after and (*6*) 75 h after polarization.

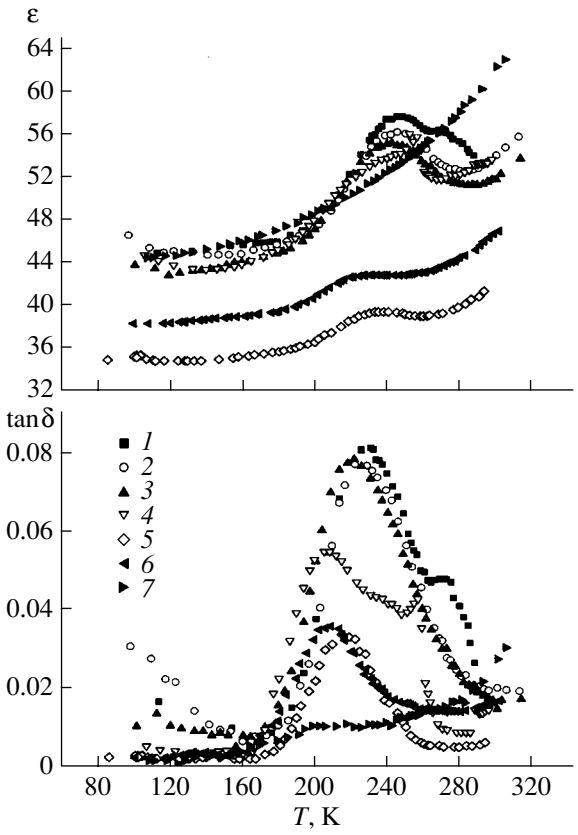

Fig. 3. Temperature dependences of ε and tanδ measured along the **c** axis of unpolarized $Pb_5Ge_3O_{11}$ crystals grown along the **a** axis. The measurements were performed sequentially on the same crystal with $d = 0.95$ mm and $S = 10$ mm^2 at a frequency of 1 kHz (*1*) in air and (*2*–*7*) at a reduced pressure $p = 10^{-2}$ atm; (*3*) after UV illumination of the crystal; (*4*–*6*) after annealing at 600°C at normal atmospheric pressure for 1.5, (1.5 + 75), and (1.5 + 75 + 1) h, respectively, and (*4*, *5*) subsequent quenching or (*6*) cooling at a rate of 40 K/h to room temperature; and (*7*) after annealing for an hour at 550°C and $p = 10^{-2}$ atm followed by quenching.

the permittivity at the maximum in crystals grown along the **c** axis noticeably exceeds that for the crystals pulled along the **a** axis, namely, ~5000 against ~1000 at 1 kHz. For $T > 300$ K, ε and $\tan\delta$ exhibit a fairly complex dispersive behavior, more specifically, a broad peak at 430 K, whose amplitude decreases rapidly with increasing frequency, and a sharp peak at 450 K, whose magnitude grows with frequency. The temperature region immediately below the Curie point has an interval within which the resistivity increases with temperature; i.e., its temperature coefficient is positive. Within broad enough temperature intervals below and above T_C, the $\varepsilon(T)$ relation follows the Curie–Weiss law. The growth in ε with deviation from the Curie–Weiss course observed in an interval slightly above the Curie point, whose width increases with frequency, is apparently associated with space charge polarization, which is noticeable at high temperatures and low frequencies.

In the low-temperature domain, multidomain crystals exhibit dielectric anomalies in the form of local maxima, ε_m and $\tan\delta_m$. At a frequency of 0.1 kHz, these maxima are seen at 230 and 200 K, respectively, and their positions shift toward higher temperatures, up to 250 and 260 K, with the frequency increasing to 100 kHz; the amplitudes of the maxima decrease fairly rapidly, making the curves smooth (Fig. 2). After the crystal polarization, the low-temperature dielectric anomalies become weaker. The temperature dependence of $\varepsilon(T)$ measured immediately after the crystal polarization becomes practically monotonic, and only one weakly pronounced maximum appears in the $\tan\delta(T)$ relation. The $\varepsilon(T)$ relation measured 75 h after the polarization has a shoulder in the above temperature interval (Fig. 2). Note that the high-temperature tails of the low-temperature anomalies in ε, tanδ, and ρ do not disappear near 300 K and considerably influence the room-temperature dielectric characteristics of the crystals.

The $\varepsilon(T)$ and $\tan\delta(T)$ relations measured along the **a** axis of the crystals do not show any anomalies at low

temperatures, with ε growing monotonically from 18 to 22 with the temperature increasing from 100 to 300 K.

Changing the amplitude of the measuring voltage within an interval 0.04–2.0 V affects the magnitude and shape of the low-temperature dielectric anomalies only weakly. Application of a dc bias of 1.5 kV/cm to the crystals shifts the maxima in ε and tanδ by ~5 K toward higher temperatures, with the maximum in ε decreasing by ~10% and the maximum in tanδ remaining practically the same.

Figure 3 covers our study of the effect exerted on the low-temperature anomalies by air pressure in the measuring cell, illumination of the crystals, and their heat treatment. Varying the partial pressure of oxygen from 0.2 to 0.002 atm does not affect the pattern of the low-temperature anomalies substantially. The additional maxima in ε and tanδ appearing at normal pressure (1 atm) at 273 K are apparently due to moisture condensing on the sample surface. Annealing the crystals at $T < 250$°C in air does not produce a noticeable effect on the shape of the low-temperature dielectric anomalies. Annealing at 600°C shifts the maximum in the $\varepsilon(T)$ and $\tan\delta(T)$ relations toward lower temperatures by ~20 K and decreases the amplitude of ε and tanδ by ~20 and ~50%, respectively. Annealing the crystals at 550°C in a chamber at a pressure reduced to 10^{-2} atm degrades the maxima. UV illumination of the crystals by a 200-W NARVA HBO200 halogen lamp for 40 min shifts the positions of the low-temperature maxima in ε and tanδ to lower temperatures by a few kelvins without noticeable change in the maxima in amplitude.

Measurements made in the range 100–350 K on crystals of various thicknesses (d = 0.4–3.2 mm) cut from a boule or thinned by etching off the basal plane of the same crystal reveal a substantial scatter in the permittivity, from 35 to 65 at 300 K. Here, the dependence of the permittivity on thickness is nonmonotonic. This suggests that the permittivity depends not only on the crystal thickness but also on other factors, for instance, on the thermal prehistory of the sample.

The Curie point of defected, dark brown crystals decreases down to 420 K, with the amplitude of ε decreasing to 900 and the maximum itself becoming diffuse (Fig. 4). The permittivity of these crystals with nonstoichiometric cation composition reaches a room temperature value of 120.

4. ANALYSIS AND DISCUSSION OF THE RESULTS

From the measurements made on the $Pb_5Ge_3O_{11}$ crystals, it follows that, in the temperature and frequency ranges covered, the crystals exhibit two anomalies in the dielectric properties, namely, (i) ferroelectric anomalies near T_C and (ii) low-temperature anomalies in the region of ~230 K. Since the low-temperature dielectric anomalies have been very poorly studied, we further focus our attention on them.

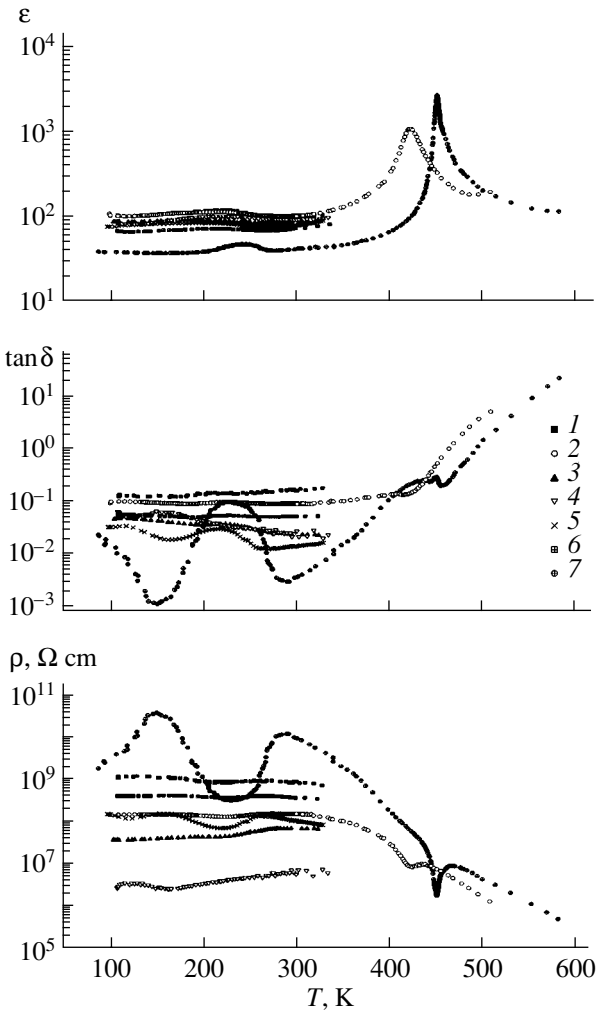

Fig. 4. Temperature dependences of permittivity ε, dielectric loss tangent tanδ, and electrical resistivity ρ measured along the **c** axis of (*1–6*) Pb-deficient $Pb_5Ge_3O_{11}$ crystals and (*7*) nominally defect-free $Pb_5Ge_3O_{11}$ crystals; (*1*) f = 0.1, (*2*, *5–7*) 1, (*3*) 10, and (*4*) 100 kHz; (*1–5*, *7*) unpolarized crystals, and (*6*) polarized crystal; (*1–4*, *6*) d = 3.2 mm, and (*5*) d = 0.67 mm (crystals grown along the **c** axis).

The shifts of the low-temperature maxima in ε and tanδ toward higher temperatures (from 200 to 260 K) with increasing frequency argue that they have a relaxation origin. Assuming that, at the point of maximum in the $\varepsilon_2(T, f_{meas})$ dependence, we have $\omega_{meas}\tau = 1$ [18, 19] ($\omega_{meas} = 2\pi f_{meas}$), we determined the characteristic relaxation times $\tau(T)$ at different temperatures. When plotted in the $\log\tau$ vs. $1/T$ coordinates, the $\tau(T)$ relation thus obtained can be fitted well by a straight line (Fig. 5), which shows that it obeys the Arrhenius law $\tau = \tau_0\exp(-U_a/k_BT)$. The activation energy U_a and the characteristic relaxation time $\tau_0 = \tau(T \longrightarrow \infty)$ derived from the $\ln\tau(1/T)$ plot are U_a = 0.58 eV and $\tau_0 = 2.2 \times 10^{-17}$ s. Thus, below T_C, $Pb_5Ge_3O_{11}$ crystals undergo Debye-type dipole relaxation with thermally activated

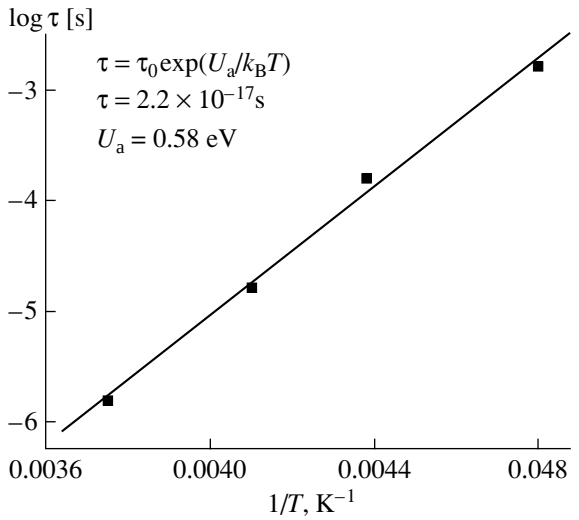

Fig. 5. Temperature dependence of characteristic relaxation time τ derived from the low-temperature maxima in $\varepsilon_2(T)$ and drawn in $\log \tau$ vs. $1/T$ coordinates.

reorientation of dipoles surmounting an energy barrier U_a.

The maxima in the temperature dependences of $\varepsilon(T)$ and $\tan\delta(T)$ at $T < 100$ K and the decrease in permittivity to 15 when the temperature is lowered to 4.2 K, which were established in [4, 16], indicate that there are other relaxation processes that operate at still lower temperatures in the crystals under study. The permittivity at frequencies above the range where the relaxation process under study operates ($\varepsilon_{\infty 1} \approx 38$) is equal to that observed at frequencies below the range of the lower temperature relaxation (ε_{s2}). The latter relaxation provides an additional contribution to the permittivity $\varepsilon = \varepsilon_{el} + \varepsilon_{ph} + \varepsilon_{rel}$ and raises it to ~40 at 300 K. As the temperature is lowered, the relaxation contribution (ε_{rel}) freezes out, with the value $\varepsilon = 15$ at 4.2 K corresponding to the sum of the contributions due to deformations of the lattice (ε_{ph}) and electronic shells (ε_{el}). Note that, in accordance with the relaxation character of the low-temperature dielectric anomalies, no clearly pronounced features are observed in the temperature dependence of heat capacity in the low-temperature domain [20].

The widths of the $\tan\delta(T)$ peaks in the region of ~230 K, which are derived from the monodisperse Debye relation $\varepsilon^* - \varepsilon_\infty = (\varepsilon_s - \varepsilon_\infty)/(1 + i\omega\tau)$ [18, 19] and the Arrhenius law with the use of the values of τ_0 and U_a found above and the values $\varepsilon_\infty = 38$ and $\varepsilon_s = 46$, are two to three times smaller than the experimentally observed peak widths in the corresponding relations. Therefore, it follows that the relaxation process revealed in our crystals is characterized by a broad set of relaxation times. The permittivity of a crystal can be represented by a superposition of Debye contributions with different relaxation times, $\varepsilon^*(\omega, T) - \varepsilon_\infty = (\varepsilon_s - \varepsilon_\infty)\int_0^\infty G(\tau, \tau_b)d\tau/(1 + i\omega\tau)$, where $G(\tau, \tau_b)$ is the distribution function of relaxation times, τ_b is the most probable relaxation time, and $\varepsilon_\infty = \varepsilon_{\infty 1} = \varepsilon_{el} + \varepsilon_{ph} + (\varepsilon_{s2} - \varepsilon_{\infty 2})$. The temperature evolution of the function $G(\tau, \tau_b)$ governs the main features in the temperature and frequency dependences of the complex permittivity. The relaxation times extracted above from the positions of the maxima in the $\varepsilon_2(T, f_{meas})$ relations are apparently the most probable relaxation times τ_b.

The manifestation of relaxation processes indicates that, in the crystals under study, there are some effective dipoles capable of reorienting in an external electric field. It would be difficult to pinpoint, at the microscopic level, the dipoles that are responsible for the relaxation processes actually observed. One could suggest a number of mechanisms that could conceivably cause low-frequency relaxation dielectric anomalies similar to those observed in our crystals:

(a) phenomena associated with the motion of ferroelectric domain walls and their freezing out;

(b) the presence of weakly bound structural blocks in the crystal structure that undergo reorientation movements;

(c) the presence of dipole defects in the crystal structure, e.g., vacancies on the Pb, Ge, or O sublattices; transition of part of the Pb^{2+} ions to the Pb^{3+} state under illumination of the crystal [21], etc.;

(d) the presence of impurity dipoles forming the orientation glass state, in which the regular crystal lattice contains a number of dipoles or quadrupoles in dynamic orientational disorder (as in crystals like KCl : OH, KBr : CN, $KTaO_3$: Li [22]);

(e) crystal inhomogeneities giving rise to interlayer polarization and relaxation of the Maxwell–Wagner type [18, 19]; and

(f) the presence of carriers responsible for the semiconducting properties of $Pb_5Ge_3O_{11}$ crystals [23, 24] and the dynamics of formation of polarization states induced by thermal localization of these charges at impurity centers [25–27].

The relaxation associated with viscous domain wall motion usually manifests itself in the temperature region immediately below T_C [28]. The domain wall dynamics probably accounts for the dispersion processes observed in $Pb_5Ge_3O_{11}$ in this temperature region, in particular, the decrease in amplitude of the broad maximum in $\tan\delta(T)$ with frequency (Fig. 1). As the temperature is lowered from T_C by ~200 K or the frequency is increased above 10 kHz, these processes freeze out and, thus, cannot be responsible for the observed low-temperature dielectric anomalies. The characteristic dispersion frequencies in the dynamics of weakly coupled structural blocks lie, as a rule, above 100 kHz [18, 19]; therefore, the existence of this

dynamics can also hardly account for the low-temperature dielectric anomalies observed in the range 0.1–100.0 kHz. Note also that a possible relation between the low-temperature dielectric anomalies and the domain structure or reorientation of weakly coupled structural blocks is at odds with the small value of τ_0. The fact that $1/\tau_0$ is higher than the lattice vibration frequencies argues rather for the electron (hole) relaxation.

While oxygen vacancies, deviations of the cation composition from stoichiometry, and the growth stripe structure do exert an influence on the dielectric properties of $Pb_5Ge_3O_{11}$ crystals, the character of the changes in the properties induced by these factors is indicative of the absence of a direct relation between these defects and the low-temperature dielectric anomalies. Indeed, annealing a crystal at a low oxygen pressure while increasing the content of oxygen vacancies brings about a rise in dielectric losses for $T > 300$ K, with an attendant degradation of the low-temperature anomalies (Fig. 3). A deviation from an ideal cation composition in crystals grown from a GeO_2-rich melt brings about a rise in ε and $\tan\delta$, but the low-temperature anomalies in $\varepsilon(T)$ and $\tan\delta(T)$ are considerably weaker than in the case of the starting crystals (Fig. 4). Rotating the growth stripe structure orientation 90° away from the direction of spontaneous polarization affects the magnitude of ε at the Curie point noticeably but does not change the pattern of the low-temperature relaxation dielectric anomalies markedly. One may thus conclude that the observed low-temperature dielectric anomalies in crystals are not related in any way to the crystal defects mentioned above. It appears appropriate to note here that the low-temperature dielectric anomalies become increasingly more pronounced as the quality of $Pb_5Ge_3O_{11}$ crystals improves; conversely, an increase in the defect concentration brings about a decrease in amplitude and increased broadening of the maxima in ε and $\tan\delta$.

When analyzing the dielectric properties of $Pb_5Ge_3O_{11}$ crystals, one should bear in mind that they belong to the class of semiconductor ferroelectrics [23, 24, 30], in which the dielectric properties are affected in a specific manner by the coupling between the electronic and lattice subsystems. These crystals are dominated for $T > 300$ K by impurity electronic (or hole) conduction due to the presence of local defect levels with an activation energy of ~0.7 eV in the band gap [13]. The impurity character of the conduction is suggested by the fact that the band gap E_g (E_g = 2.64 [23] or 3.0 eV [24]) noticeably exceeds the dc conduction activation energy (0.63 [11], 0.83 [12], or 0.62 eV [13]).

The frequency and temperature ranges within which the observed relaxation anomalies occur correlate most closely with the dynamics of thermal localization at impurity centers of carriers responsible for the semiconducting properties of $Pb_5Ge_3O_{11}$ crystals. The progressive filling of traps with decreasing temperature generates local electric fields around local centers, which, in turn, induce local polarization. The dynamics of these processes may become manifest in the form of low-frequency relaxation dielectric anomalies in the temperature region where local centers are filled due to thermal activation [25–27]. The characteristic time of variation of induced polarization and ε^* dispersion is governed by vibrational properties of the local states forming around the local centers and depends on the characteristic times of the lattice subsystem and the electron dynamics at the trapping levels. The low-frequency range of the dispersion should be assigned to the fact that the characteristic times of electron concentration variation at the traps far exceed those of the lattice.

The conclusion that the temperature region of the low-temperature dielectric anomalies is close to that of thermally activated filling of local centers is suggested by the features observed in the temperature dependence of the electrical conductivity of our crystals. Above the temperatures of the anomalies, one observes thermally activated electrical conductivity, which grows exponentially with temperature (Fig. 1). Below the temperatures at which the anomalies are observed, the conductivity is only weakly temperature-dependent. The strongly pronounced conductivity dependence on frequency and the close-to-zero activation energy of conductivity in the low-temperature domain (Fig. 1) indicate the predominance of the hopping mechanism of conduction via localized states in this temperature region.

The fact that the activation energy for the relaxation process (0.58 eV) is close to that for dc electrical conductivity in the range 300–450 K suggests that the dielectric relaxation processes and the temperature dependence of conductivity are governed by the same impurity levels.

Photorefractometric studies of $Pb_5Ge_3O_{11}$ crystals [8, 21, 31, 32] show that their characteristic defects acting as charge traps in the band gap are the Pb^{2+} lead cations transferred by optical radiation to the Pb^{3+} state. Recharging occurs due to hole trapping by Pb^{2+} ions following the generation of electron–hole pairs in interband transitions. Photoelectrons are captured by electron traps Z of, as yet, unknown origin. A comprehensive investigation of the characteristics of local centers in $Pb_5Ge_3O_{11}$ crystals would obviously provide an impetus to a deeper interpretation of the various features seen in their dielectric properties. Information on the type and structure of charge trapping centers in $Pb_5Ge_3O_{11}$ crystals can be derived from EPR spectroscopic and photoelectric studies. Our preliminary investigation of nominally pure and defect-free crystals performed in the range 100–300 K showed that defects in a single crystal manifest themselves in EPR spectra in the form of several series of absorption lines.

Doping, particularly with a nonisovalent atom, usually increases the effective charge density in semicon-

ductors. As shown in [31, 32], however, no such increase occurs in $Pb_5Ge_3O_{11}$ doped by Ba, Fe, or Rh atoms. It is believed that this doping has only a weak effect on the concentration of the Pb^{3+} defects, which are characteristic of these crystals and act as charge traps. The above features of local centers may also provide an explanation for the comparatively weak influence that the substitution of various atoms for Pb, Ge, and O in $Pb_5Ge_3O_{11}$ crystals may exert on the pattern and position of the low-temperature anomalies in $\varepsilon(T)$ and $\tan\delta(T)$ [4].

The space charge density and the character of its spatial distribution are affected considerably by the degree of polarization of crystals and their breakup into ferroelectric domains. In screening the spontaneous polarization, the charge concentrates near the boundaries of ferroelectric domains with oppositely directed spontaneous polarizations [29, 33]. As a result, an enhanced concentration of centers creating levels in the band gap arises at domain boundaries and these levels trap the carriers to form bound space charges. It follows that the polarization–depolarization processes should affect the low-temperature anomalies in $\varepsilon(T)$ and $\tan\delta(T)$, which is exactly what is observed experimentally (Fig. 2). The space charge density in multidomain crystals is obviously higher than in single-domain ones, which accounts for their more pronounced manifestation of the low-temperature dielectric anomalies. Note that the absence of any dependence of the conductivity activation energy on the degree of crystal polarization [11] provides evidence in support of the impurity center levels being independent of their position relative to the boundaries of ferroelectric domains. The change in the pattern of the low-temperature anomalies induced by crystal annealing near 600°C can be assigned to the annealing-stimulated redistribution of space charges, which is related, in particular, to the changed domain structure.

5. CONCLUSIONS

(1) $Pb_5Ge_3O_{11}$ crystals exhibit, in addition to ferroelectric anomalies in ε and $\tan\delta$ near the Curie point, less pronounced low-temperature anomalies in the vicinity of ~230 K, which are related to Debye-type dipole relaxation with thermally activated reorientation of dipoles surmounting an energy barrier U_a. The relaxation rate obeys the Arrhenius relation. The observed relaxation is characterized by a broad set of relaxation times. The most probable values of the activation energy and characteristic relaxation time are $\tau_0 = 2.2 \times 10^{-17}$ s and $U_a = 0.58$ eV. The relaxation processes exert a pronounced influence on the values of the dielectric characteristics near room temperature.

(2) The defects in $Pb_5Ge_3O_{11}$ crystals that are associated with oxygen vacancies, off-stoichiometric cation composition, and the stripe growth structure influence the dielectric properties of these crystals. The pattern of this influence does not suggest direct correlation between these defects and the low-temperature dielectric anomalies.

(3) The temperature and frequency ranges within which the above relaxation anomalies are observed correspond to the dynamics of formation of polarized states through thermally induced localization of impurity-bound carriers, which account for the semiconducting properties of $Pb_5Ge_3O_{11}$ crystals. The activation energy and the temperature region of carrier localization as derived from the temperature dependence of electrical conductivity are close to the activation energy and temperature region of the low-temperature dielectric relaxation.

(4) The polarization–depolarization processes and breakup of a crystal into ferroelectric domains are accompanied by a redistribution of the space charge involved in the screening of spontaneous polarization and noticeably affect the pattern and magnitude of the low-temperature dielectric anomalies.

(5) The dielectric characteristics of $Pb_5Ge_3O_{11}$ ferroelectric crystals depend to a considerable extent on a number of various factors, such as the degree of polarization of the crystal, its thermal prehistory, and the kind and concentration of defects in the crystal. Uncontrolled combined action of various factors brings about apparent irregular changes in the values of ε and $\tan\delta$. In particular, the observed permittivity at room temperature may range in magnitude from 30 to 120.

(6) Photorefractometric studies of $Pb_5Ge_3O_{11}$ crystals suggest that the characteristic defects inherent in $Pb_5Ge_3O_{11}$ crystals and acting as charge traps in the band gap are Pb^{2+} lead cations transferred by light to the Pb^{3+} state. The actual form and structure of the charge-trapping centers producing local levels in the $Pb_5Ge_3O_{11}$ band gap, the structure of the density of states of the defect levels, and the specific features of the dynamics of charge localization on these levels need further refinement, in particular, with the use of EPR spectroscopy and photoelectric techniques.

ACKNOWLEDGMENTS

This study was supported by the Russian Foundation for Basic Research, project no. 02-02-17798.

REFERENCES

1. H. Iwasaki, K. Sugii, T. Yamada, and N. Niizeki, Appl. Phys. Lett. **18** (10), 444 (1971).
2. S. Nanamatsu, H. Sugiyama, K. Doi, and Y. Kondo, J. Phys. Soc. Jpn. **31** (2), 616 (1971).
3. H. Iwasaki, S. Miyazawa, H. Kiyomada, K. Sugii, and N. Niizeki, J. Appl. Phys. **43** (12), 4907 (1972).
4. A. A. Bush and Yu. N. Venevtsev, *PbO–GeO_2 Single Crystals with Ferroelectric and Related Properties and*

Their Possible Application (NIITÉKhIM, Moscow, 1981) [in Russian].

5. C. R. Jones, N. Show, and A. W. Vere, Electron. Lett. **8** (14), 346 (1972).
6. R. Watton, C. Smith, and G. R. Jones, Ferroelectrics **14** (1–4), 719 (1976).
7. T. Li and S. T. Hsu, Integr. Ferroelectr. **34** (1–4), 1495 (2001).
8. S. Mendricks, X. Yue, R. Pankrath, H. Hesse, and D. Kip, Appl. Phys. B: Lasers Opt. **68** (5), 887 (1999).
9. V. V. Dem'yanov and V. D. Sal'nikov, Fiz. Tverd. Tela (Leningrad) **16** (12), 3623 (1974) [Sov. Phys. Solid State **16**, 2353 (1974)].
10. E. V. Sinyakov, E. F. Dudnik, V. G. Monya, V. G. Savchenko, and L. Ya. Sadovskaya, Izv. Akad. Nauk SSSR, Ser. Fiz. **39** (5), 1025 (1975).
11. L. E. Cross and T. W. Cline, Ferroelectrics **11** (1–4), 333 (1976).
12. M. Polomska, M. Malinowski, and H. H. Otto, Phys. Status Solidi A **56**, 335 (1979).
13. A. Mansingh, K. N. Srivastava, and B. Singh, J. Appl. Phys. **50** (6), 4319 (1979).
14. Y. Goto, J. Phys. Soc. Jpn. **50** (4), 1241 (1981).
15. J.-H. Kim, J.-B. Kim, K.-S. Lee, B.-C. Choi, and J.-N. Kim, Solid State Commun. **86** (4), 257 (1993).
16. A. A. Bush and Yu. N. Venevtsev, Kristallografiya **26** (2), 349 (1981) [Sov. Phys. Crystallogr. **26**, 198 (1981)].
17. T. V. Panchenko, M. D. Volnyanskiĭ, V. G. Monya, and V. M. Duda, Fiz. Tverd. Tela (Leningrad) **19** (8), 2238 (1977) [Sov. Phys. Solid State **19**, 1311 (1977)].
18. H. Frølich, *Theory of Dielectrics: Dielectric Constant and Dielectric Loss*, 2nd ed. (Inostrannaya Literatura, Moscow, 1960; Clarendon, Oxford, 1986).
19. V. V. Daniel, *Dielectric Relaxation* (Academic, London, 1967).
20. A. A. Bush and E. A. Popova, Fiz. Tverd. Tela (St. Petersburg) **46** (5), 875 (2004) [Phys. Solid State **46**, 902 (2004)].
21. H. J. Reyher, M. Pape, and N. Hausfeld, J. Phys.: Condens. Matter **13** (16), 3767 (2001).
22. U. T. Hochli, K. Knorr, and A. Loidl, Adv. Phys. **39** (5), 405 (1990).
23. V. T. Gabriélyan, P. V. Ionov, K. A. Mikhaĭliva, and O. A. Arikalov, Kristallografiya **19** (1), 176 (1974) [Sov. Phys. Crystallogr. **19**, 106 (1975)].
24. V. V. Mikhnevich, A. V. Mikulenok, and A. V. Myasoedov, Fiz. Tverd. Tela (Leningrad) **27** (3), 932 (1985) [Sov. Phys. Solid State **27**, 572 (1985)].
25. R. F. Mamin, Pis'ma Zh. Éksp. Teor. Fiz. **58** (7), 534 (1993) [JETP Lett. **58**, 538 (1993)].
26. R. F. Mamin, Fiz. Tverd. Tela (St. Petersburg) **43** (7), 1262 (2001) [Phys. Solid State **43**, 1314 (2001)].
27. R. F. Mamin, Izv. Akad. Nauk SSSR, Ser. Fiz. **67** (8), 1157 (2003).
28. Y. N. Huang, Y. N. Wang, and H. M. Shen, Phys. Rev. B **46** (6), 3290 (1992).
29. V. M. Fridkin, *Photoferroelectrics* (Nauka, Moscow, 1976; Springer, Berlin, 1979).
30. N. F. Mott and E. A. Davis, *Electronic Processes in Non-Crystalline Materials* (Clarendon, Oxford, 1971; Mir, Moscow, 1974).
31. X. Yue, S. Mendricks, Y. Hu, H. Hesse, and D. Kip, J. Appl. Phys. **83** (7), 3473 (1998).
32. X. Yue, S. Mendricks, T. Nikolajsen, H. Hesse, D. Kip, and E. Kratzig, J. Appl. Phys. **86** (3), 1186 (1999).
33. V. Ya. Shur, Yu. A. Popov, and N. V. Korovina, Fiz. Tverd. Tela (Leningrad) **26** (3), 781 (1984) [Sov. Phys. Solid State **26**, 471 (1984)].

Translated by G. Skrebtsov

Physics of the Solid State, Vol. 46, No. 9, 2004, pp. 1730–1736. Translated from Fizika Tverdogo Tela, Vol. 46, No. 9, 2004, pp. 1676–1681.
Original Russian Text Copyright © 2004 by Trubitsyn, Volnyanskiĭ, Kudzin.

MAGNETISM AND FERROELECTRICITY

The Influence of Chromium Impurity Centers on the Critical Properties of a Weakly Polar Ferroelectric $Li_2Ge_7O_{15}$

M. P. Trubitsyn, M. D. Volnyanskiĭ, and A. Yu. Kudzin

Dnepropetrovsk National University, Nauchnyĭ pr. 13, Dnepropetrovsk, 49050 Ukraine

Received January 29, 2004

Abstract—The Cr^{3+} EPR spectra of $Li_2Ge_7O_{15}$ (LGO) crystals are analyzed in the temperature range of the ferroelectric phase transition. The temperature dependence of the local order parameter is determined from the measured splittings of the EPR lines in the polar phase. The experimental critical exponent of the order parameter $\beta = 0.31$ in the range from the phase transition temperature T_C to $(T_C - T) \sim 40$ K corresponds to the critical exponent of the three-dimensional Ising model. Analysis of the available data demonstrates that, away from the phase transition temperature T_C, the macroscopic and local properties of LGO crystals are characterized by a crossover from the fluctuation behavior to the classical behavior described in terms of the mean-field theory. The temperature dependence of the local order parameter for LGO : Cr crystals does not exhibit a crossover from the Ising behavior ($\beta = 0.31$) to the classical behavior ($\beta = 0.5$). This is explained by the defect nature of Cr^{3+} impurity centers, which weaken the spatial correlations in the LGO host crystal. The specific features of the critical properties of LGO : Cr^{3+} crystals are discussed within a microscopic model of structural phase transitions. © *2004 MAIK "Nauka/Interperiodica".*

1. INTRODUCTION

Crystals of lithium heptagermanate $Li_2Ge_7O_{15}$ (LGO) upon cooling below the temperature T_C = 283.5 K undergo a transition from the high-temperature paraelectric phase (space group D_{2h}^{14}) to the ferroelectric phase (space group C_{2v}^{5}) with spontaneous polarization along the **c** axis [1–4]. According to the neutron diffraction data [5, 6], the structural transformations upon phase transition involve rotations of $[GeO_4]^{4-}$ tetrahedra and ordering of Li^+ ions in channels of the LGO crystal lattice. Analysis of the vibrational spectra of the LGO compound revealed that the soft mode is associated with the oscillatory dynamics of germanium–oxygen tetrahedra, whereas and the central peak is attributed to the relaxation dynamics of the lithium sublattice [7–9].

In our previous works [10–12], the phase transition in LGO crystals was investigated by Mn^{2+} EPR spectroscopy. It was demonstrated that manganese centers substitute for lithium ions in positions of the second type [5, 6] and retain the local C_2 symmetry of sites in the perfect lattice. Since the Ge–O and Li subsystems play an important role in the phase transition, it is of interest to analyze the EPR spectra of paramagnetic ions embedded in the germanium–oxygen framework of the LGO lattice. As was shown in [13, 14], Cr^{3+} ions substitute for Ge(1) atoms at the center of oxygen octahedral complexes [5, 6] and, hence, can serve as convenient model objects for EPR studies of the phase transition in LGO crystals.

Galeev *et al.* [13] analyzed the results obtained in the first EPR study of LGO : Cr crystals and proposed a model according to which Cr^{3+} ions at the Ge^{4+} positions and Li^+ interstitial ions compensating for an excess charge form Cr^{3+}–Li^+ pair centers with electric dipole moments aligned parallel to the **a** axis. More recently, Basun *et al.* [15, 16] measured the optical luminescence spectra of similar crystals and confirmed and refined the above model.

Taking into account that chromium ions are embedded in the Ge–O framework of the LGO crystal lattice, analysis of the Cr^{3+} EPR spectra measured in the vicinity of the phase transition temperature T_C can provide new information on the specific features in the temperature behavior of structural distortions in the Ge–O sublattice. Moreover, the formation of Cr^{3+}–Li^+ pair centers implies a sufficiently strong distortion of the crystal field around paramagnetic ions. In particular, this can lead to a considerable change in the phase transition temperature [17, 18]. With a fairly complete model [13, 15, 16] at our disposal, it becomes possible to elucidate how the Cr^{3+}–Li^+ centers affect the anomalies in the physical properties of lithium heptagermanate.

Earlier [14], we measured the EPR spectra of LGO : Cr^{3+} crystals and revealed that the spectral components are split into doublets upon cooling below the phase transition temperature T_C and the resonance lines are anomalously broadened at temperatures close to T_C. This behavior is typical of the EPR spectra upon phase transitions [19]. The splitting of spectral lines is associated with the local order parameter in the low-symme-

try phase, whereas their broadening reflects an enhancement of local fluctuations in the vicinity of the phase transition temperature T_C. In the present work, we investigated the temperature dependence of the local order parameter. For this purpose, we measured the temperature shift of the Cr^{3+} lines in the polar phase of LGO crystals.

2. EXPERIMENTAL TECHNIQUE AND RESULTS

For our experiments, single crystals of lithium heptagermanate were grown by the Czochralski method and doped with chromium ions (0.01 wt %).

The EPR spectra were recorded in the 3-cm band on a Radiopan SE/X 2547 radiospectrometer. The temperature of the samples was controlled by heating nitrogen vapors with the use of a standard cryostat.

From analyzing the orientational dependences of the EPR spectra of LGO : Cr crystals in the paraelectric phase [14], we obtained four spectra ($k_M = 4$) with C_1 triclinic symmetry. The directions of the principal axes of these spectra $\mathbf{Z}_i$ (i = 1–4), which were chosen in the vicinity of the **c** axis from the maximum splittings of the outer lines in the fine structure, are determined by the polar and azimuthal angles $\theta = 14°$ and $\varphi = 30°$ with respect to the crystal lattice basis [14]. In the system of the magnetic axes, the EPR spectra can be described by the orthorhombic spin Hamiltonian [20, 21]

$$\mathcal{H} = g\beta_B \mathbf{BS} + D\left(S_Z^2 - \frac{1}{3}S(S+1)\right) + E(S_X^2 - S_Y^2) \quad (1)$$

with the following parameters (T = 298 K): g = 1.978, $D = 1300 \times 10^{-4}$ cm^{-1}, and $E = -330 \times 10^{-4}$ cm^{-1}. The data obtained in [14] are in agreement with the results of the EPR studies in the Q band of the radio-frequency field (36 GHz) and confirm the model proposed by Galeev *et al.* [13] for Cr^{3+} centers in the LGO structure.

Upon cooling below the phase transition temperature T_C, an ensemble of four Cr^{3+} centers is divided into two groups of structurally nonequivalent centers with a multiplicity $k_M = 4$ for each group [13, 14]. Upon the phase transition, the local C_1 symmetry of the centers remains unchanged and the doublet splitting of the resonance lines is observed for any direction of the external magnetic field **B** with respect to the crystal axes. The temperature dependences of the EPR spectra were measured for the principal directions of the magnetic field along the crystal axes and were analyzed for **B** || **a**. For this orientation, the above spectra in the paraphase coincide with each other and the positions of the lines associated with the electronic transitions only weakly depend on the angle between the magnetic field and the **a** axis [14]. Consequently, insignificant errors in orienting the sample do not lead to a substantial distortion of the spectral contour.

The temperature dependence of the position of the low-field resonance line $M_S = -3/2 \longleftrightarrow -1/2$ measured for **B** || **a** is plotted in Fig. 1. It can be seen from this figure that, as the phase transition temperature is approached from above, the EPR line slightly shifts toward the high-field range. At temperatures below T_C = 283.4 K, the EPR line is split into two components. Upon further cooling, these components shift from the position of the signal in the high-symmetry phase.

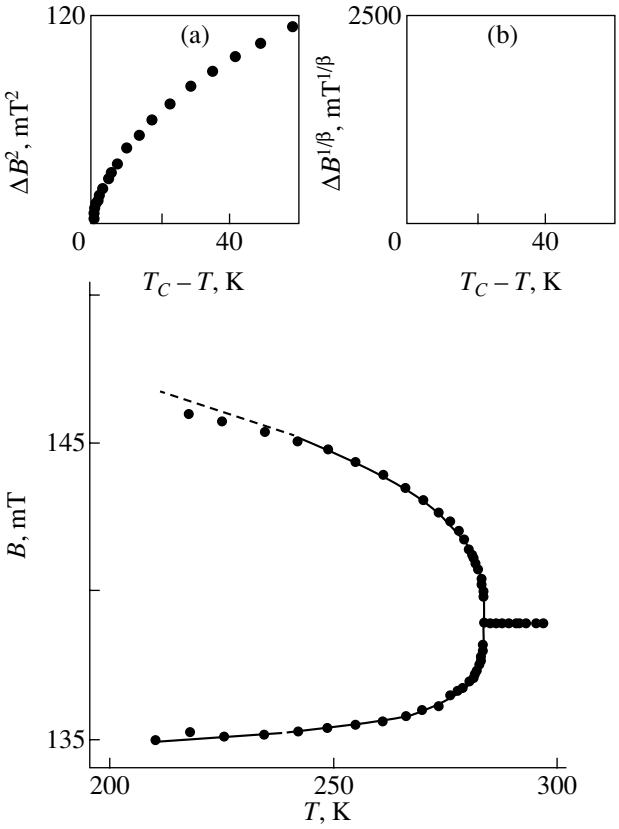

Fig. 1. Temperature dependences of the position of the EPR line $M_S = -3/2 \longleftrightarrow -1/2$ at temperatures above T_C and the split components at temperatures below T_C for LGO : Cr^{3+} crystals. Circles are experimental data. Solid and dashed lines represent the dependences calculated from relationships (3) and (5) in the temperature ranges $(T_C - 40\ \text{K}) < T < (T_C + 20\ \text{K})$ and $T < (T_C - 40\ \text{K})$, respectively. **B** || **a**. The insets show the temperature dependences of the separation between the split components of the EPR line in the (a) $(T_C - T)$–ΔB^2 and (b) $(T_C - T)$–$\Delta B^{1/\beta}$ coordinates at $\beta = 0.31$.

3. TEMPERATURE DEPENDENCE OF THE LOCAL ORDER PARAMETER

In the vicinity of the second-order phase transition, the resonance fields B at which radio-frequency radiation is absorbed can be expanded into a power series of the local order parameter:

$$B = B_0 + a_1\eta + \frac{1}{2}a_2\eta^2 + \ldots. \quad (2)$$

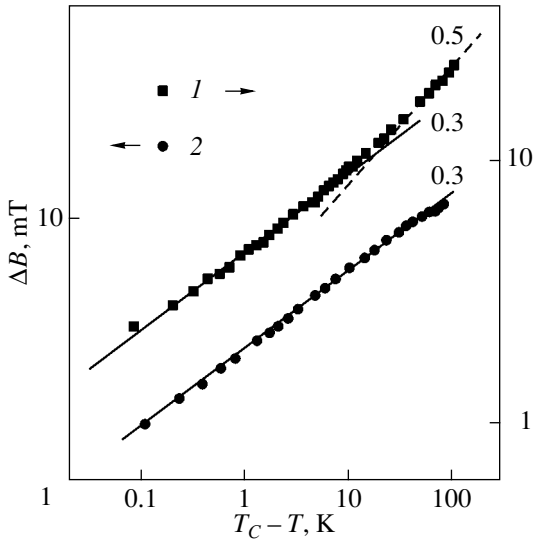

Fig. 2. Splitting ΔB of the (*1*) Mn^{2+} and (*2*) Cr^{3+} EPR lines as a function of $(T_C - T)$ on the log–log scale for LGO : Mn^{2+} [11] and LGO : Cr^{3+} crystals.

Here, η is the local order parameter corresponding to structural transformations in the environment of a magnetic ion upon the phase transition, B_0 stands for the position of the resonance line in the high-symmetry phase ($\eta = 0$), and the coefficients a_1 and a_2 are determined by the position of the magnetic ion in the unit cell and the direction of the magnetic field **B** with respect to the crystal axes.

Since the point symmetry of Cr^{3+} centers (C_1) does not change upon the phase transition, the expansion of resonance fields (2) at any direction of the magnetic field **B** involves both even and odd powers of the order parameter η. As follows from the data obtained in [10–12], the properties of the LGO compound exhibit a critical behavior over a wide temperature range around the transition point T_C. The local order parameter can be represented in the form of the power function: $\eta \sim (T_C - T)^\beta$, where β is the critical exponent. By substituting this function into relationship (2), the expressions for the positions of the EPR line components split below T_C can be written in the form

$$B_{1,2}(\pm\eta) = B_0 \pm \tilde{a}_1(T_C - T)^\beta + \frac{1}{2}\tilde{a}_2(T_C - T)^{2\beta}, \quad (3)$$

where $\tilde{a}_1 \sim a_1$ and $\tilde{a}_2 \sim a_2$. According to relationships (2) and (3), the change in the separation between the split components characterizes the temperature dependence of the local order parameter:

$$\Delta B = B_1(+\eta) - B_2(-\eta) = 2a_1\eta(T) = 2\tilde{a}_1(T_C - T)^\beta. \quad (4)$$

In order to reveal the character of the dependence of ΔB on $(T_C - T)$, the experimental data are presented in different coordinates in the insets to Fig. 1. As can be seen from this figure, the experimental data presented in the $(T_C - T)$–ΔB^2 coordinates do not fall on a straight line. Moreover, according to relationship (4), the mean-field approximation ($\beta = 0.5$) in inapplicable for describing the dependence $\eta(T)$ in any of the studied temperature ranges. By contrast, the dependence $\Delta B^{1/\beta}(T_C - T)$ constructed at $\beta = 0.31$ is linear up to $(T_C - T) \sim 40$ K (Fig. 1). At lower temperatures, the experimental dependence $\Delta B^{1/\beta}(T_C - T)$ deviates from a straight line toward smaller values. This means that the temperature dependence $\eta(T)$ becomes less steep and flattens out.

The experimental dependences of the position of the Cr^{3+} EPR line in the temperature range $(T_C - 40\text{ K}) < T < (T_C + 20\text{ K})$ are described by relationship (3) with the critical exponent β as a variable parameter. By minimizing the root-mean-square deviations of the calculated values from the experimental data, we obtained the following parameters:

$$T_C = 283.38\text{ K}, \quad \beta = 0.31,$$
$$\tilde{a}_1 = 1.60 mT/K^\beta, \quad \tilde{a}_2 = 0.25 mT/K^{2\beta}. \quad (5)$$

The variation in the position B_0 of the resonance line at temperatures above the transition point T_C (Fig. 1) due to the temperature dependence of the lattice parameters was approximated by the straight line $B_0\,[mT] = (139.78 - 0.003T)$. The dependences calculated from relationships (3) and (5) are shown by solid and dashed lines in Fig. 1. As can be seen, these relationships fit the experimental dependences fairly well and the calculation gives a phase transition point T_C [see relationship (5)] that is very close to the temperature of splitting of the resonance lines (283.4 K).

The critical exponent β (5) determined from the analysis of the Cr^{3+} EPR spectra coincides within the experimental error with the critical exponent obtained from the temperature shift of the Mn^{2+} EPR lines in [10, 11]. The occurrence of critical fluctuations in such a wide temperature range is associated with the weakly polar nature of the ferroelectric state of LGO crystals [22] and was previously discussed in greater detail in [11, 12].

It is worth noting that the temperature dependences of the local order parameter determined from the analysis of the Mn^{2+} [11] and Cr^{3+} (Fig. 1) EPR spectra differ from each other. This difference can be seen in Fig. 2, in which the dependences of the splitting of the EPR lines $\Delta B \sim \eta$ on $(T_C - T)$ are depicted on the log–log scale. As follows from the analysis of the Mn^{2+} spectra, the above dependence away from the phase transition at $T^* \approx (T_C - 10\text{ K})$ exhibits a crossover from the Ising behavior in the portion with a slope of 0.3 to the classical behavior in the portion with a slope of 0.5. On the other hand, the dependence obtained by processing the Cr^{3+} EPR spectra exhibits Ising behavior over the entire temperature range in which the temperature dependence of the local order parameter is

described by the power function $\eta \sim (T_C - T)^{\beta}$. Therefore, away from the phase transition point T_C, the crossover from the Ising behavior to the classical behavior occurs in the environment of Mn^{2+} active ions and is absent in the case of Cr^{3+} ions. Let us consider the possible origin of this discrepancy.

4. WEAKENING OF THE SPATIAL CORRELATIONS DUE TO Cr^{3+}–Li^{+} PAIR CENTERS

Making allowance for the specific features in the dynamic behavior and the important role of the Ge–O and Li sublattices in the phase transition, the results obtained can be interpreted in terms of different positions of probes, namely, Mn^{2+} centers at the Li(2) positions in structural channels and Cr^{3+} ions at the Ge(1) positions inside the oxygen octahedra. The difference between the temperature dependences $\eta(T)$ (Fig. 2) can be associated with the specific features in the critical behavior of the lattice displacements in the sublattices.

On the other hand, it should be taken into account that paramagnetic centers have a defect nature. The EPR data indicate that paramagnetic ions are differently incorporated into the lattice. Divalent manganese ions do not change the general properties (local symmetry) of the Li(2) positions in the perfect lattice. Chromium ions strongly distort the Ge–O structural framework and are embedded in the Ge(1) positions with the formation of Cr^{3+}–Li^{+} dipole pair centers. Consequently, the LGO crystals doped with Mn^{2+} and Cr^{3+} ions can exhibit different properties.

Analysis of the thermal and acoustic anomalies demonstrates that the macroscopic properties of pure LGO crystals are characterized by a crossover from the fluctuation behavior to the classical behavior away from the phase transition temperature T_C [24]. This specific feature of LGO crystals is confirmed by the EPR data for Mn^{2+} centers that are located in lattice channels and do not substantially affect the Ge–O framework of the crystal structure [11]. The fact that the mean-field approximation is not applicable to any of the portions of the dependence $\eta(T)$ determined from the splitting of the Cr^{3+} EPR lines (Figs. 1, 2) can be explained by the defect nature of paramagnetic centers distorting the Ge–O framework of the crystal structure. This inference is qualitatively supported by a quite different shift of the transition temperature T_C upon introduction of manganese ions (which is not observed upon introduction of ~ 1 wt % Mn) and chromium ions (~ –70 K/wt %) [17, 18].

Therefore, distortions of the Ge–O structural network in the environment of Cr^{3+}–Li^{+} centers are responsible for the increase in the range of the fluctuation behavior and the suppression of the crossover to the classical behavior away from the phase transition point T_C. This change in the critical properties of the LGO compound suggests a decrease in the effective interaction range and the range of spatial correlations of the order parameter in the system containing defects. Since the behavior of thermodynamic anomalies in the vicinity of the phase transition temperature T_C differs from that predicted from the Landau theory [10–12, 23, 24], we will attempt to analyze the influence of Cr^{3+}–Li^{+} centers on the properties of the LGO crystal in the framework of a simple microscopic model of structural phase transitions. Within this model, the potential energy of the crystal can be represented as the sum of the energy $\mathcal{H}_s$ of structure cells and the energy $\mathcal{H}_{\text{int}}$ of the interaction between them [25, 26]:

$$\begin{aligned}\mathcal{H} &= \mathcal{H}_s + \mathcal{H}_{\text{int}} \\ &= \sum_r \left[\frac{1}{2}\alpha_1 u_r^2 + \frac{1}{4}\alpha_2 u_r^4\right] + \frac{1}{2}\sum_{rr'} J_{rr'}(u_r - u_{r'})^2 \\ &= \left[\frac{1}{2}(\alpha_1 + 12J)\sum_r u_r^2 + \frac{1}{4}\alpha_2 \sum_r u_r^4\right] - J\sum_{rr'}^{n.n.} u_r u_{r'}.\end{aligned} \tag{6}$$

Here, u_r stands for a combination of atomic displacements upon the phase transition in a unit cell with radius vector r, $\alpha_1 < 0$, $\alpha_2 > 0$, and $J > 0$. For simplicity, relationship (6) is written under the assumption of isotropic interaction between the nearest neighbor cells in a three-dimensional lattice. As a rule, Hamiltonian (6) is analyzed for limiting cases. At $|\alpha_1| \ll J$, the single-particle potential $\mathcal{H}_s$ has one minimum, the phase transition is described by the displacement model, and the mean-field approximation is assumed to be valid. In the opposite limit $|\alpha_1| \gg J$, the potential $\mathcal{H}_s$ has two minima at equilibrium displacements $\pm u_0 = \pm(|\alpha_1|/\alpha_2)^{1/2}$ and the phase transition is governed by the different occupations of the wells. In this case, Hamiltonian (6) is reduced to the Ising Hamiltonian, structural transformations correspond to the model of ordering, and the conditions for the applicability of the mean-field approximation are not met. The classical behavior in the framework of the mean-field theory gives way to fluctuation behavior, in which the universal character of the critical phenomena manifests itself.

It is assumed that the state of the LGO host crystal can be described by Hamiltonian (6) and the Cr^{3+}–Li^{+} defect centers can be included through renormalizing the parameters of the model. Moreover, we assume that a unit cell in the lattice can contain a defect with probability n and can be free of defects with probability $(1 - n)$, where $n = N_d/N$ is the ratio of the number of defect cells to their total number. For simplicity, the displacements u_r in the defect-free and defect cells are assumed to be identical. We will analyze how the presence of the above defects affects the parameters of Hamiltonian (6).

The parameter α_1 changes as a result of the interaction between displacements and dipole moments of

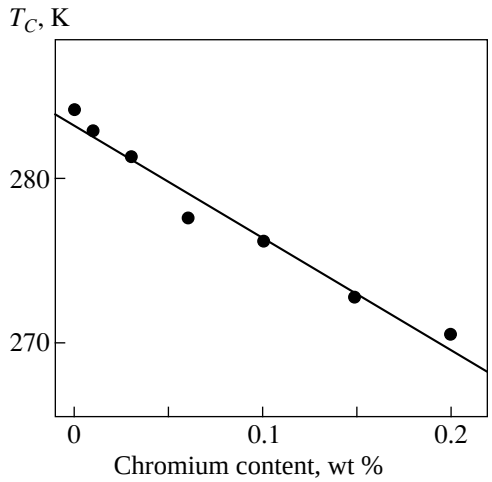

Fig. 3. Dependence of the transition temperature T_C on the chromium impurity content in LGO crystals according to the dielectric data taken from [17].

defects. Reasoning from the D_{2h} symmetry of the paraelectric phase [1] and the direction of the defect dipole **d** || **a** [13, 15, 16], the allowed lowest order invariant has the form $d^2u_r^2$. The addition of the term $(1/2)gd^2\sum_{r_d}u_r^2$ ($g > 0$, summation is performed over defect cells with radius vector r_d) to Hamiltonian (6) leads to a decrease in $|\alpha_1|$ (a decrease in the transition temperature) and improves the condition for the mean-field approximation $|\alpha_1| \ll J$. The effect of Cr^{3+}–Li^+ pair centers on the properties of the LGO host crystal has an opposite tendency. For this reason, we will not consider the change in the parameter α_1 in a defect crystal. The renormalization of the parameter α_2 is also insignificant, because it is associated with the higher order interaction and does not result in the appearance of any features.

Since the Cr^{3+}–Li^+ pair centers bring about an increase in the range of the fluctuation behavior, the change in the correlation parameter J seems to be most significant. The suppression of the classical (mean-field) behavior (the displacement limit) implies that the inequality $|\alpha_1| \gg \tilde{J}$ (where $\tilde{J}$ is the renormalized correlation parameter) is better satisfied in the defect crystal. The correlation of displacements in defect cells with displacements in adjacent cells (which are assumed to be defect free) is weaker than that in defect-free regions of the crystal. Let $J_d < J$ be a parameter describing the correlation of the defect region with the adjacent cells. By changing $\sum_{r \neq r_d} \longrightarrow (1-n)\sum_r$ and $\sum_{r_d} \longrightarrow n\sum_r$, the correlation parameter for the defect crystal can be represented in the form

$$\tilde{J}(n) = (1-n)J + nJ_d. \quad (7)$$

The weakening of elastic forces between displacements in unit cells of the defect crystal results in a decrease in the characteristic interaction length. Within the model described by Hamiltonian (6), the ratio of the correlation length to the unit cell parameter is defined as $r_0^2 = -J/\alpha_1$. This indicates that the effective interaction range decreases in the matrix due to Cr^{3+}–Li^+ pair centers: $\tilde{r}_0 < r_0$ (where $\tilde{r}_0$ is the renormalized correlation length for the defect crystal).

Now, we make a number of quantitative estimates. For this purpose, we consider the dependence of the phase transition temperature on the chromium impurity content. In terms of the model described by Hamiltonian (6), the phase transition temperature can be written as

$$T_C(n) = -C\frac{\alpha_1}{\alpha_2}\tilde{J}(n), \quad (8)$$

where the proportionality factor C takes on different values in the limits of the displacement and order–disorder transition [25, 26]. Then, the relative shift of the transition temperature can be represented in the form

$$\frac{T_C(0) - T_C(n)}{T_C(0)} = \left(1 - \frac{J_d}{J}\right)n. \quad (9)$$

This relationship is in agreement with the experimental linear dependence of the phase transition temperature T_C on the impurity content (Fig. 3). Taking into account the correction for the ratio between the molar masses of formula units of the LGO crystal and the Cr_2O_3 dopant and also the number of formula units per unit cell ($Z = 4$), we obtain $J_d \approx 0.3J$. Therefore, the interaction of the defect cell with the adjacent cells appears to be three times weaker than the elastic forces in defect-free regions. Under the above assumptions, the decrease in the correlation length in the LGO host crystal containing Cr^{3+}–Li^+ pair centers with an increase in their concentration is estimated as $\tilde{r}_0^2 \approx r_0^2(1 - 0.7n)$.

5. DISCUSSION

Now, we dwell on the following problem. The crossover from the fluctuation behavior to the classical behavior has been observed in the study of the local order parameter from the Mn^{2+} EPR spectra [10, 11] and also of the thermal and acoustical properties of LGO crystals [23, 24]. However, a similar crossover has not been revealed in the temperature dependence of the local susceptibility determined from the broadening of the Mn^{2+} EPR lines [12] and the temperature dependence of the permittivity [27]. This can be associated with the following circumstances. First, the temperature range of the fluctuation behavior differs for different properties of the physical system [25]. Second, the anomalous contributions to the width of the EPR line and the permittivity can be measured to sufficient accu-

racy only in the limited ranges $(T - T_C) \sim 10$ and ~ 20 K, respectively. By contrast, when studying the temperature dependences of the local order parameter (Figs. 1, 2), the splitting of the EPR lines and, hence, the accuracy in measurements increases away from the transition temperature T_C. Therefore, the lack of experimental evidence for the crossover in [12, 27] can stem from the relatively narrow ranges in which the anomalous contributions to the width of the EPR line and the permittivity can be separated with confidence.

It should be emphasized that relationship (7) for the correlation parameters actually implies the replacement of a discrete medium [see expression (6)] by a continuum in which defect distortions are averaged over the crystal volume. In this respect, the above analysis should be treated as a qualitative illustration of the influence of Cr^{3+}–Li^+ pair defects on the critical properties of lithium heptagermanate crystals. However, the assumptions made do not change the main inference regarding a decrease in the correlation length in the LGO host crystal with Cr^{3+}–Li^+ pair centers.

6. CONCLUSIONS

Thus, the EPR spectra of chromium ions introduced into LGO crystals were investigated in the temperature range of the ferroelectric phase transition. These ions substitute for Ge(1) atoms at the centers of octahedral oxygen complexes and form Cr^{3+}–Li^+ pair centers with Li^+ interstitial ions.

It was found that, upon cooling below the transition point T_C, the Cr^{3+} EPR spectrum is split into two structurally nonequivalent components, each with a magnetic multiplicity $k_M = 4$. The temperature dependences of the split components of the EPR lines were described using the expansion of the resonance fields in powers of the local order parameter.

The splitting of the Cr^{3+} EPR lines was measured at temperatures corresponding to the polar phase of LGO crystals. It was revealed that the power dependence of the local order parameter in the temperature range from the transition temperature T_C to $(T_C - T) \sim 40$ K is consistent with the three-dimensional Ising model ($\beta = 0.31$).

The analysis of the available experimental data demonstrated that the crossover from the fluctuation behavior to the classical behavior away from the transition temperature T_C is characteristic of thermodynamic anomalies of pure LGO crystals. The absence of the crossover in the behavior of the properties of LGO : Cr crystals was explained by the weakening of spatial correlations in the LGO host crystal with Cr^{3+}–Li^+ defect centers. The influence of Cr^{3+}–Li^+ pair centers on the critical properties of LGO crystals was discussed within the microscopic model of structural phase transitions.

REFERENCES

1. H. Volenkle, F. Wittman, and H. Nowotny, Monatsh. Chem. **101**, 46 (1970).
2. S. Haussuhl, F. Wallrafen, K. Recker, and J. Eckstein, Z. Kristallogr. **153**, 329 (1980).
3. M. Wada, A. Sawada, and Y. Ishibashi, J. Phys. Soc. Jpn. **50** (6), 1811 (1981).
4. H. Terauchi, S. Iida, Y. Nishihata, M. Wada, A. Sawada, and Y. Ishibashi, J. Phys. Soc. Jpn. **52** (7), 2312 (1983).
5. Y. Iwata, N. Koyana, and I. Shibuya, Annu. Rep. Res. React. Inst., Kyoto Univ. **19**, 11 (1986).
6. Y. Iwata, I. Shibuya, M. Wada, A. Sawada, and Y. Ishibashi, J. Phys. Soc. Jpn. **56** (7), 2420 (1987).
7. H. Orihara, M. Wada, and Y. Ishibashi, J. Phys. Soc. Jpn. **52** (4), 1478 (1983).
8. A. Volkov, G. Kozlov, Yu. Goncharov, M. Wada, A. Sawada, and Y. Ishibashi, J. Phys. Soc. Jpn. **54** (2), 818 (1985).
9. M. Horioka, A. Sawada, and M. Wada, J. Phys. Soc. Jpn. **58** (10), 3793 (1989).
10. M. P. Trubitsyn, M. D. Volnyanskiĭ, and A. Yu. Kudzin, Kristallografiya **36** (6), 1472 (1991) [Sov. Phys. Crystallogr. **36**, 835 (1991)].
11. M. P. Trubitsyn, Fiz. Tverd. Tela (St. Petersburg) **40** (1), 114 (1998) [Phys. Solid State **40**, 101 (1998)].
12. M. P. Trubitsyn, M. D. Volnyanskiĭ, A. Yu. Kudzin, and T. L. Kuz'menko, Fiz. Tverd. Tela (St. Petersburg) **40** (1), 111 (1998) [Phys. Solid State **40**, 98 (1998)].
13. A. A. Galeev, N. M. Khasanova, A. V. Bykov, V. M. Vinokurov, N. M. Nizamutdinov, and G. R. Bulka, in *Spectroscopy, Crystal Chemistry, and Real Structure of Minerals and Their Analogs* (Kazan. Gos. Univ., Kazan, 1990), p. 77 [in Russian].
14. M. P. Trubitsyn, M. D. Volnyanskiĭ, and I. A. Busoul, Fiz. Tverd. Tela (St. Petersburg) **40** (6), 1102 (1998) [Phys. Solid State **40**, 1006 (1998)].
15. S. A. Basun, A. A. Kaplyanskiĭ, and S. P. Feofilov, Fiz. Tverd. Tela (St. Petersburg) **34** (11), 3377 (1992) [Sov. Phys. Solid State **34**, 1807 (1992)].
16. S. A. Basun, A. A. Kaplyanskiĭ, and S. P. Feofilov, Fiz. Tverd. Tela (St. Petersburg) **36** (11), 3429 (1994) [Phys. Solid State **36**, 1821 (1994)].
17. M. D. Volnyanskiĭ and A. Yu. Kudzin, Fiz. Tverd. Tela (Leningrad) **33** (7), 2228 (1991) [Sov. Phys. Solid State **33**, 1257 (1991)].
18. M. D. Volnyanskiĭ, Doctoral Dissertation (Dnepropetrovsk State Univ., Dnepropetrovsk, 1993).
19. K. A. Muller and J. C. Fayet, in *Structural Phase Transitions II*, Ed. by K. A. Muller and H. Thomas (Springer-Verlag, Berlin, 1991), Topics in Current Physics, Vol. 45, p. 1.
20. A. Abragam and B. Bleaney, *Electron Paramagnetic Resonance of Transition Ions* (Clarendon, Oxford, 1970; Mir, Moscow, 1972), Vol. 1.

21. M. L. Meĭl'man and M. I. Samoĭlovich, *Introduction to EPR Spectroscopy of Activated Single Crystals* (Atomizdat, Moscow, 1977) [in Russian].

22. A. K. Tagantsev, Pis'ma Zh. Éksp. Teor. Fiz. **45** (7), 352 (1987) [JETP Lett. **45**, 447 (1987)].

23. B. A. Strukov, M. Yu. Kozhevnikov, E. L. Sorkin, and M. D. Volnyanskiĭ, Fiz. Tverd. Tela (Leningrad) **32** (9), 2823 (1990) [Sov. Phys. Solid State **32**, 1639 (1990)].

24. B. A. Strukov, M. Yu. Kozhevnikov, M. D. Volnyanskiĭ, and Kh. A. Nizomov, Kristallografiya **36** (4), 942 (1991) [Sov. Phys. Crystallogr. **36**, 529 (1991)].

25. A. D. Bruce and R. A. Cowley, *Structural Phase Transitions* (Taylor and Francis, Philadelphia, 1981; Mir, Moscow, 1984).

26. B. A. Strukov and A. P. Livanyuk, *Physical Principles of Ferroelectric Phenomena in Crystals* (Nauka, Moscow, 1983) [in Russian].

27. A. Yu. Kudzin, M. D. Volnyanskiĭ, M. P. Trubitsyn, and I. A. Busoul, Fiz. Tverd. Tela (St. Petersburg) **40** (9), 1698 (1998) [Phys. Solid State **40**, 1544 (1998)].

Translated by O. Borovik-Romanova

Physics of the Solid State, Vol. 46, No. 9, 2004, pp. 1737–1740. Translated from Fizika Tverdogo Tela, Vol. 46, No. 9, 2004, pp. 1682–1685.
Original Russian Text Copyright © 2004 by Shpilevaya, Kabirov, Kupriyanov.

MAGNETISM AND FERROELECTRICITY

Structure of Cadmium Titanate

N. V. Shpilevaya, Yu. V. Kabirov, and M. F. Kupriyanov

Research Institute of Physics, Rostov State University, pr. Stachki 194, Rostov-on-Don, 344090 Russia

e-mail: shpilevay@mail.ru

Received February 16, 2004

Abstract—The structure of the ilmenite phase of cadmium titanate is determined and the structure of the perovskite phase of this compound is refined using x-ray powder diffraction. The effect of gamma radiation on the structure and properties of the perovskite phase is investigated. The nature of relaxation of the dielectric parameters for the perovskite phase of cadmium titanate is discussed. © *2004 MAIK "Nauka/Interperiodica"*.

1. INTRODUCTION

Investigations into the structure and properties of $A\mathrm{TiO_3}$ double oxides (A = Ba, Pb, Sr, Ca, Cd, Mg, Mn, Zn, Co) with a perovskite structure have demonstrated that these compounds are characterized by a wide variety of structural configurations and physical properties. These variations in the structure and properties of $A\mathrm{TiO_3}$ double oxides can be caused by the following factors: (i) deviations from the $A\mathrm{TiO_3}$ stoichiometry (changes in the occupancies of the A and O sites), (ii) the formation of other (non-perovskite) phases, and (iii) the manifestation of different types and degrees of structural ordering on a scale of a unit cell, a crystallite (crystal block), or a crystal.

Earlier structural studies have established that, depending on the crystallization conditions, cadmium titanate $\mathrm{CdTiO_3}$ can have either an ilmenite-like [1, 2] or perovskite structure [3]. Upon high-temperature annealing, the $\mathrm{CdTiO_3}$ compound undergoes a transition from the ilmenite phase to the perovskite phase [4, 5]. In [6, 7] and [2, 8], the unit cell parameters of the perovskite (P) phase of the $\mathrm{CdTiO_3}$ compound under normal conditions differ from each other. According to [6, 7], the orthorhombic cell (which is fourfold superstructural with respect to the perovskite unit cell) is characterized by the following parameters: $\mathbf{A}_O = \mathbf{a}_p + \mathbf{c}_p$, $\mathbf{B}_O = 2\mathbf{b}_p$, and $\mathbf{C}_O = \mathbf{a}_p - \mathbf{c}_p$ (A_O = 5.348 Å, B_O = 7.615 Å, C_O = 5.417 Å), where a_p, b_p, and c_p are the parameters of the perovskite monoclinic subcell with two possible space groups (*Pnma* or $Pc2_1n$). In [2, 8], the perovskite phase of the $\mathrm{CdTiO_3}$ compound is characterized by an orthorhombic unit cell with the following parameters: $\mathbf{A}_O = 2(\mathbf{a}_p + \mathbf{c}_p)$, $\mathbf{B}_O = 2\mathbf{b}_p$, and $\mathbf{C}_O = 2(\mathbf{a}_p - \mathbf{c}_p)$ (A_O = 10.607 Å, B_O = 7.606 Å, C_O = 10.831 Å) and space groups *Cmca* and *Cmma*. It is known that, at low temperatures, the perovskite modification of the $\mathrm{CdTiO_3}$ compound undergoes a transition to a ferroelectric state [9, 10]. However, the ilmenite (I) phase of the $\mathrm{CdTiO_3}$ compound does not exhibit ferroelectric properties. Earlier [8], we examined the temperature and frequency dependences of the permittivity of $\mathrm{CdTiO_3}$ crystals with a perovskite structure before and after alpha and gamma irradiation and observed strong dielectric relaxation at temperatures $T \sim 200$–300°C. More recent studies of the electrical conductivity of $\mathrm{CdTiO_3}$ single crystals with a perovskite structure [5] revealed that the electrical conductivity exhibits anomalies in the same temperature range. Note that the structure of the ilmenite modification of the $\mathrm{CdTiO_3}$ compound was first studied by Posnjak and Barth [1].

The objectives of the present work were as follows: (1) to determine the structure of the ilmenite-like $\mathrm{CdTiO_3}$ modification, which is of interest as a ferroelectric structural analog of the $\mathrm{LiNbO_3}$ compound [11]; (2) to refine the structure of the perovskite $\mathrm{CdTiO_3}$ modification; (3) to investigate how the radiation-induced defects (gamma radiation) affect the structure and properties of the perovskite $\mathrm{CdTiO_3}$ modification with the aim of verifying the hypothesis regarding the role played by the nanosize effects in the ilmenite–perovskite phase transition of the $\mathrm{CdTiO_3}$ compound; and (4) to discuss the nature of relaxation of the dielectric parameters for the perovskite $\mathrm{CdTiO_3}$ modification [8].

2. SAMPLE PREPARATION AND EXPERIMENTAL TECHNIQUE

Polycrystalline samples of the ilmenite-like $\mathrm{CdTiO_3}$ (I) and perovskite $\mathrm{CdTiO_3}$ (P) modifications were prepared from a stoichiometric mixture of CdO and $\mathrm{TiO_2}$ (rutile phase) according to the standard procedure of solid-phase synthesis. The x-ray powder diffraction analysis of the $\mathrm{CdTiO_3}$ samples revealed that the ilmenite-like $\mathrm{CdTiO_3}$ modification is formed at synthesis temperatures in the range 600–850°C [12]. Upon annealing at a temperature $T \geq 900$°C, the ilmenite-like $\mathrm{CdTiO_3}$ modification undergoes a transition to the perovskite $\mathrm{CdTiO_3}$ modification.

Table 1. Atomic parameters and lengths of the Cd–O and Ti–O bonds in the ilmenite-like $CdTiO_3$ modification (the atomic coordinates *x*, *y*, and *z* are given in fractions of the perovskite cell)

Atom	*x*	*y*	*z*	*B*, Å^2
Cd	0.000	0.000	0.346	1.6
Ti	0.000	0.000	0.150	1.0
O	0.333	0.050	0.237	1.1
Atom 1	Atom 2	Cd–O, Ti–O, Å		
Cd	O(1)	2.269		
Cd	O(2)	2.483		
Ti	O(1)	1.804		
Ti	O(2)	2.068		

Note: The Cd and Ti atoms are located in the octahedral environment of oxygen atoms and form Cd–O(1), Cd–O(2) and Ti–O(1), Ti–O(2) bonds of different length, respectively. *B* is the atomic thermal parameter.

X-ray structural investigations of $CdTiO_3$ polycrystals in the ilmenite-like and perovskite modifications under normal conditions were performed at the University of Aveiro (Portugal). The x-ray diffraction patterns were recorded in the Bragg–Brentano geometry on a Rigaku diffractometer (CuK_α radiation; graphite monochromator; 2 range $16° < 2\theta < 116°$; scan step, 0.02°; exposure time per frame, 2 s). The total number of unique reflections was 113 for the ilmenite-like $CdTiO_3$ modification and 166 for the perovskite $CdTiO_3$ modification. The x-ray diffraction patterns of the powder samples prepared in the two $CdTiO_3$ modifications were processed with the PowderCell 2.2 program.

3. RESULTS AND DISCUSSION

When determining the structure of the ilmenite-like $CdTiO_3$ modification, we considered a number of possible structural models of the rhombohedral phase. The unit cell of the ilmenite-like $CdTiO_3$ modification in the hexagonal system is characterized by the parameters $A_H = 5.2403$ Å and $C_H = 14.8380$ Å [1] and contains six formula units. In order to determine the space group of symmetry, we chose the space groups $R3c$, $R\bar{3}c$, $R\bar{3}$, $R32$, and $R3m$ for our analysis, because they have 6- and 18-fold regular systems of points and, hence, the number of parameters refined can be decreased significantly. For each space group, we determined the possible variants of the arrangement of atoms in the unit cell in accordance with the crystal chemistry rules and the results of a comparison with related structures. In the analysis, we varied the atomic parameters over a rather wide range and used the refinement procedure. It was established that the minimum *R* factor (R_p = 14%) is achieved in the model with space group $R\bar{3}$ and the atomic coordinates *x*, *y*, and *z* presented in Table 1. This table also lists lengths of the Cd–O and Ti–O bonds in the ilmenite-like $CdTiO_3$ modification. Figure 1 shows the fragments of the x-ray diffraction patterns for models of the ilmenite-like $CdTiO_3$ modification with space groups $R3c$ and $R\bar{3}$ and the experimental diffraction curve. It should be noted that the data obtained in [1] do

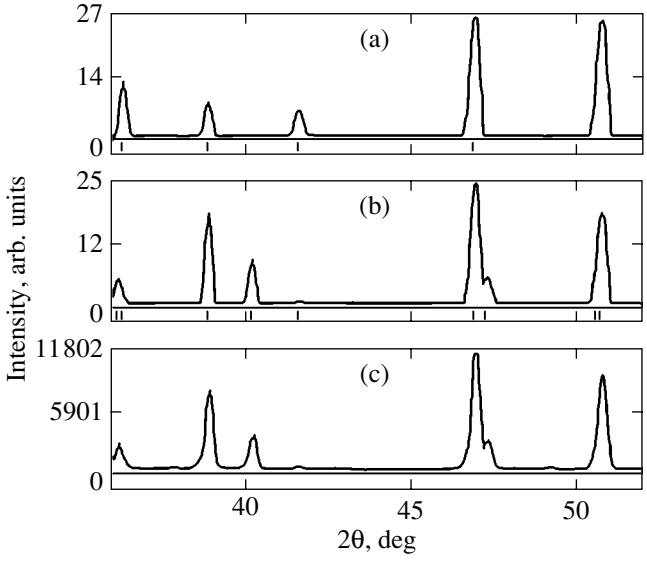

Fig. 1. Fragments of the x-ray diffraction patterns of the ilmenite-like $CdTiO_3$ modification: (a) model with space group *R3c*, (b) model with space group $R\bar{3}$, and (c) experimental data.

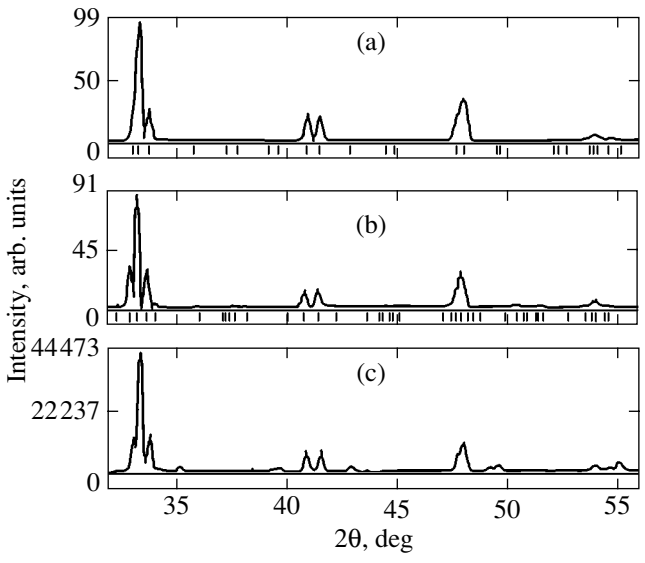

Fig. 2. Fragments of the x-ray diffraction patterns of the perovskite $CdTiO_3$ modifications: (a) model of the *P*1 modification, (b) model of the *P*2 modification, and (c) experimental data.

Table 2. Atomic parameters and lengths of the Cd–O and Ti–O bonds in the perovskite $CdTiO_3$ (*P*1, *P*2) modifications

$CdTiO_3$ (*P*1) (space group *Pnma*)					$CdTiO_3$ (*P*2) (space group *Cmca*)				
A_0 = 5.348 Å B_0 = 7.615 Å C_0 = 5.417 Å		$a_p = c_p$ = 3.806 Å b_p = 3.807 Å β_p = 90.73°			A_0 = 10.607 Å B_0 = 7.606 Å C_0 = 10.831 Å		$a_p = c_p$ = 3.790 Å b_p = 3.803 Å β_p = 91.0(3)°		
Atom	*x*	*y*	*z*	*B*, Å^2	Atom	*x*	*y*	*z*	*B*, Å^2
Cd	0.020	0.250	0.022	2.0	Cd(1)	0.250	0.251	0.250	4.0
Ti	0.500	0.000	0.000	1.2	Cd(2)	0.000	0.248	0.010	4.0
O(1)	0.255	0.030	0.253	1.4	Ti(1)	0.270	0.000	0.000	1.1
O(2)	0.520	0.250	0.015	1.4	Ti(2)	0.000	0.510	0.240	1.1
					O(1)	0.250	0.250	0.000	1.4
					O(2)	0.000	0.720	0.220	1.4
					O(3)	0.121	0.070	0.124	1.4
					O(4)	0.127	0.550	0.123	1.4
Atom 1	Atom 2	Cd–O, Ti–O, Å			Atom 1	Atom 2	Cd–O, Ti–O, Å		
Cd	O(1)	2.687			Cd(1)	O(1)	2.710		
Cd	O(2)	2.654			Cd(1)	O(2)	2.652		
Ti	O(1)	1.895			Cd(1)	O(3)	2.339		
Ti	O(2)	1.906			Cd(1)	O(4)	2.432		
					Cd(2)	O(4)	2.432		
					Ti(1)	O(1)	1.904		
					Ti(1)	O(3)	1.969		
					Ti(1)	O(4)	1.934		
					Ti(2)	O(2)	1.904		
					Ti(2)	O(4)	1.934		

not seem reliable, because, in this case, the Cd–O bonds should be shorter than the Ti–O bonds. However, in the ilmenite-like structure, the Cd^{2+} and Ti^{4+} ions are located in oxygen octahedra. Since the ionic radius of Cd^{2+} is larger than that of Ti^{4+}, the Cd–O bonds should be longer than the Ti–O bonds, as was determined in our experiments.

In processing of the experimental x-ray diffraction pattern of the perovskite $CdTiO_3$ modification (Fig. 2c), we analyzed the variants of the unit cells determined in [6, 7] and [2, 8] and the variants of the orthorhombic space groups and positional atomic parameters. It was found that the powder sample of the perovskite-like $CdTiO_3$ compound under investigation has a two-phase composition. This compound consists of the perovskite $CdTiO_3$ (*P*1) modification with unit cell parameters close to those determined in [6, 7] and the perovskite $CdTiO_3$ (*P*2) modification with unit cell parameters close to those obtained in [2, 8]. The minimum R_p factor corresponds to the sample with a composition containing 22.4% *P*1 and 77.6% *P*2 and the atomic parameters presented in Table 2.

The positional and thermal parameters were determined accurate to within ±0.001 Å and ±0.1 Å^2, respectively. Figure 2 presents the fragments of the x-ray diffraction patterns of the *P*1 and *P*2 perovskite modifications of cadmium titanate and the experimental diffraction curve.

Polycrystalline samples of the perovskite $CdTiO_3$ modification were exposed to bremsstrahlung gamma radiation with an electron energy of ~20 MeV and a dose of 10^7 R on an ST microtron. After this irradiation, we revealed the following structural changes: (1) an increase in the parameters of the monoclinic subcell (at room temperature) $a_p = c_p$ (from 3.8015 to 3.8107 Å) and b_p (from 3.8212 to 3.8256 Å) and a decrease in the angle β_p (from 91.22° to 91.09°); (2) the appearance of new reflections corresponding to the cubic phase with unit cell parameter a_k = 3.850 Å; and (3) the disappearance of some superstructure reflections (in particular, the superstructure reflections with parameter d = 1.5217 Å).

Thus, in our experiment, we failed to induce a phase transition from the perovskite $CdTiO_3$ modification to the ilmenite-like $CdTiO_3$ modification under irradia-

tion, as was assumed earlier in [8]. It is obvious that gamma irradiation at this dose leads to an increase in the linear unit cell parameters of the perovskite $CdTiO_3$ modification and partial breaking of the long-range order (the disappearance of several superstructure reflections) due to the formation of defects. Annealing of the samples at $T = 700°C$ for 2 h results in a decrease in the unit cell parameters a_p, c_p, and b_p.

The measured lengths of the metal–oxygen bonds in the ilmenite-like $CdTiO_3$ modification (Table 1) differ significantly, even though both the Cd and Ti atoms are in the octahedral oxygen environment. Once the difference between the Cd–O and Ti–O bond lengths is associated with the difference between the ionic radii of Cd^{2+} and Ti^{4+}, the two different lengths of the Cd–O and Ti–O bonds can be explained in terms of strong distortion of oxygen layers in the hexagonal closest packing, i.e., the displacement of part of the oxygen ions from the packing layers. This situation can correspond to a relatively low temperature of the phase transition from the ilmenite-like $CdTiO_3$ modification to the perovskite $CdTiO_3$ modification (with a transformation of the hexagonal packing of the layers into a cubic packing), in which the Cd ions are located in layers of the closest packing with a large coordination number (12) and the Cd–O bond lengths are considerably increased (Table 2).

The ilmenite phase of the $CdTiO_3$ compound, like the *P*1 and *P*2 perovskite phases, are characterized by relatively high values of the Debye–Waller defects for heavier Cd atoms. This suggests that, apart from thermal motion, static disordered displacements of these atoms can contribute noticeably to the aforementioned parameters.

The analysis of the lengths of interatomic bonds in the *P*1 and *P*2 perovskite $CdTiO_3$ modifications showed that the Cd–O bond lengths in the *P*1 modification differ only slightly (Table 2), whereas the difference between these lengths in the *P*2 modification is more significant and can be of the order of 0.3–0.4 Å.

The previously revealed effects of relaxation of the permittivity (similar to those observed in [13]) can be explained in terms of the relaxation of space charges induced by structural defects.

ACKNOWLEDGMENTS

The authors are grateful to M. Avdeev for his assistance in performing the experiment.

REFERENCES

1. E. Posnjak and T. F. W. Barth, Z. Kristallogr. **88**, 1971 (1934).
2. H. D. Megaw, Proc. Phys. Soc. London **58** (328), 133 (1946).
3. W. H. Zachariasen, Math. Naturwiss. Kl. **1**, 165 (1928).
4. M. L. Sholokhovich, O. P. Kramarov, B. F. Proskuryakov, and E. I. Éknadiosyants, Kristallografiya **13**, 1102 (1968) [Sov. Phys. Crystallogr. **13**, 967 (1968)].
5. Yu. V. Kabirov, B. S. Kul'buzhev, and M. F. Kupriyanov, Fiz. Tverd. Tela (St. Petersburg) **43** (10), 1890 (2001) [Phys. Solid State **43**, 1968 (2001)].
6. H. F. Kay and J. L. Miles, Acta Crystallogr. **10**, 213 (1957).
7. S. Sasaki, Ch. T. Prewitt, J. L. Bass, and W. A. Schulze, Acta Crystallogr. **43**, 1668 (1987).
8. Yu. V. Kabirov, M. F. Kupriyanov, Ya. Dets, and P. Wawzala, Fiz. Tverd. Tela (St. Petersburg) **42** (7), 1291 (2000) [Phys. Solid State **42**, 1329 (2000)].
9. G. A. Smolenskiĭ, Dokl. Akad. Nauk SSSR **70**, 405 (1950).
10. H. Y. Sun, T. Nakamura, Y. J. Sun, Y. Inaguma, and M. Iton, Ferroelectrics **217**, 137 (1998).
11. B. T. Mattias and J. R. Remeika, Phys. Rev. **76** (12), 1886 (1949).
12. Yu. V. Kabirov, B. S. Kul'buzhev, and M. F. Kupriyanov, Zh. Strukt. Khim. **42** (5), 972 (2001).
13. O. Bidault, P. Goux, M. Kchikech, M. Belkaoumi, and M. Maglione, Phys. Rev. B **49** (12), 7868 (1994).

Translated by I. Volkov

Physics of the Solid State, Vol. 46, No. 9, 2004, pp. 1741–1749. Translated from Fizika Tverdogo Tela, Vol. 46, No. 9, 2004, pp. 1686–1694.
Original Russian Text Copyright © 2004 by Misochko, Hase, Kitajima.

LATTICE DYNAMICS AND PHASE TRANSITIONS

On the Nature of Coherent Phonons Generated by Ultrashort Laser Pulses in Single-Crystal Antimony

O. V. Misochko*, M. Hase, and M. Kitajima****

**Institute of Solid State Physics, Russian Academy of Sciences, Chernogolovka, Moscow oblast, 142432 Russia*

***National Institute for Materials Science, Tsukuba, 305-0047 Japan*

Received June 3, 2003; in final form, November 20, 2003

Abstract—Reflectivity oscillations generated by A_{1g} coherent phonons in an antimony single crystal have been studied by a method involving pumping and probing by femtosecond laser pulses, which was complemented by spectral filtration of the signal. An analysis of the spectrally resolved signal showed that not only the integrated intensity but also the spectrum of the probe pulse are functions of the delay time between the pumping and probing and oscillate between the Stokes and anti-Stokes components at the optical-phonon frequency. A comparison of the integrated lattice excitation relaxation dynamics with the spectrally resolved lattice excitation relaxation dynamics revealed new facets in the nature and generation mechanism of coherent phonons. © *2004 MAIK "Nauka/Interperiodica".*

1. INTRODUCTION

Progress in laser technologies, which have made it possible to shorten the laser pulse duration down to the subpicosecond range, opened the way for studying excitation dynamics in solids on a real-time scale. At present, this is apparently one of the most intensely pursued subjects in the physics of condensed state and studies involving pumping with subsequent probing by ultrashort laser pulses are being increasingly used with materials that have application potential [1–4]. Understanding the way in which the equilibrium violated by a pump pulse is restored sheds light on the dynamics of elementary excitations and their interaction and, thus, provides information that cannot be obtained using other methods.

Numerous studies of the dynamics of condensed media acted upon by ultrashort laser pulses revealed a subpicosecond-scale oscillatory behavior of the relaxation of the excited state created by a pump pulse [1–4]. The oscillation period coincides, as a rule, with the reciprocal frequency of Raman-active phonons, although the decay of oscillations differs from the phonon energy relaxation as derived from the linewidth of a spontaneous Raman spectrum [4]. These oscillations are identified with coherent lattice excitations (phonons), and the adjective "coherent" is employed because the oscillations have a definite phase. Obtaining a stable phase is made possible by the pump pulse length Δt being less than the reciprocal phonon mode frequency $\Omega^{-1}(\Delta t < \Omega^{-1})$.

2. QUALITATIVE CONSIDERATION OF THE MECHANISM OF COHERENT PHONON GENERATION

To reveal the way in which ultrashort laser pulses give rise to an oscillatory optical response of a system, we consider a harmonic oscillator. This oscillator, presented in Fig. 1 in the form of a pendulum, should be identified with a phonon mode of the crystal, and we shall be interested in how to change the pendulum state. The state can be changed in two different ways. First, one can translate the point of suspension of the pendulum horizontally to change its potential energy. This type of action does not require that work be done on the pendulum; in other words, the applied force is purely imaginary. Second, we can strike the pendulum to change its kinetic energy. Because in this case an external force brings about a change in the pendulum velocity, this force is real. These two types of action (a change in the potential or kinetic energy) are displayed schematically in Fig. 1, which shows that in both cases an external action transfers the pendulum to a new (excited) state and that its response to this action reduces to oscillations with respect to a new or the old equilibrium position.

To cross over now to the optical method of initiating oscillations, we need to bear in mind that direct coupling of photons of the visible range to phonons is impossible because the light-field quanta and lattice excitations differ strongly in energy. Their interaction should be considered only on an effective basis and is realized in some form of electron–phonon coupling. In

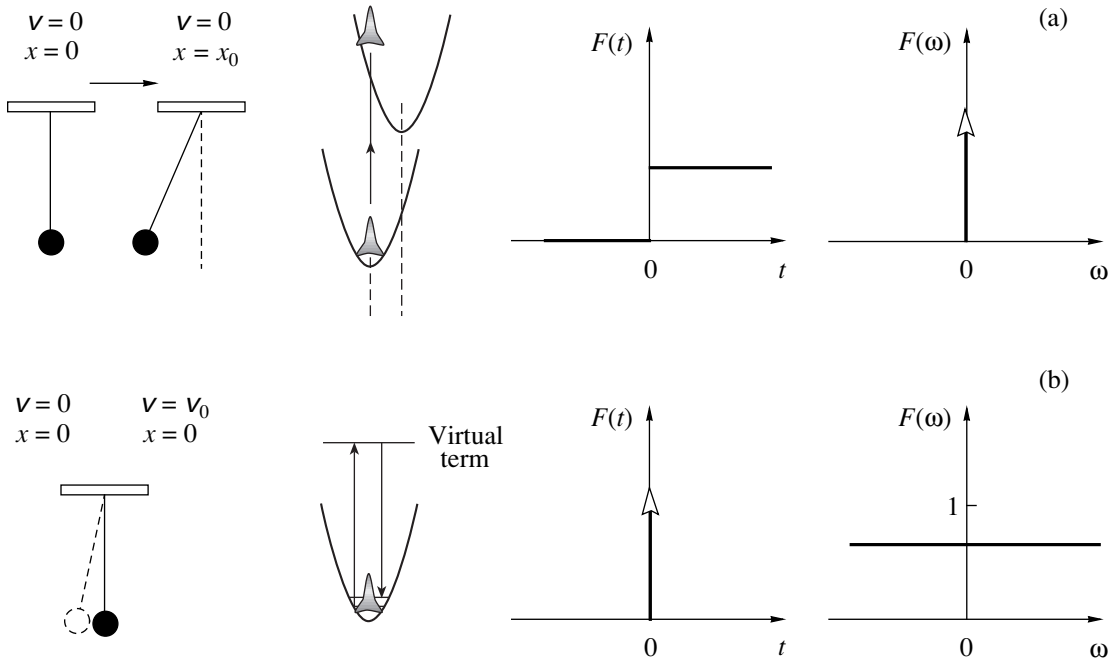

Fig. 1. Schemes of harmonic-oscillator excitation by varying (a) the potential energy (DECP) and (b) kinetic energy (TSRS). The graphs to the right of each scheme display the temporal and frequency dependences of the driving force.

the case where linear absorption is negligibly low (transparent media), the generation of coherent phonons is identified with impulsive stimulated Raman scattering [1]. The driving force is real in this case, and the lattice coherence is realized in the ground electronic state. A steady-state analog of impulsive stimulated Raman scattering is given by coherent anti-Stokes light scattering, in which the frequencies of two laser beams are chosen so that their difference coincides with the Raman-active mode frequency of the material medium. For opaque media, however, where linear absorption may no longer be disregarded, there is still no clear understanding of how lattice excitations become coherent. This is partially due to the fact that lattice coherence can be created in this case in both the ground and an excited electronic state, a factor that considerably complicates theoretical consideration. Nevertheless, the onset of oscillations in opaque media can be described phenomenologically, with equal measure of success, in terms of a model of displacive excitation of coherent phonons (DECP) [5] and a mechanism resembling, in many aspects, inelastic scattering of light [2]. The first model predicts the generation of only fully symmetric phonons in an excited electronic state that can be reached in both one- and two-photon absorption. The phonon phase is described in this case by a cosine relation; i.e., oscillations start with their maximum amplitude (Fig. 1). The evolution of the driving force in DECP is fitted by a Heaviside step function $F(t) = (1/2)[1 + \mathrm{sgn}(t)]$. Because the Fourier transform of the Heaviside function, $F(\omega) = (1/2)[\delta(\omega) - i/\pi\omega]$, has no real component, the driving force is an imaginary quantity; i.e., the oscillator energy is modified through a change in potential energy. The second model, proposed in [2], accounts for the onset of oscillations and was called transient stimulated Raman scattering (TSRS). This model is capable of accounting for any of the Raman-active phonons generated in either the ground (nonresonant case) or an excited (resonant case) electronic state. The initial phase of oscillations in TSRS depends on the actual resonance conditions and varies from the sine (in the first case) to cosine (in the second) relation. The driving force in nonresonant TSRS is real ($F(t) = \delta(t)$ and $F(\nu) = 1$), and the energy is transferred to the oscillator through a change in its kinetic energy.

Note that both phenomenological models describe energy transfer between the external force and the lattice rather than the onset of coherence in the phonon subsystem. The coherence is determined by the off-diagonal elements of the density matrix, which do not depend, as a rule, on the populations described by the diagonal elements and are responsible for the energy state of the material system [4]. In actual fact, oscillations arise because of the light-induced lattice coherence (onset of certain phase relations among the various phonon states) and not only as a result of a change in the phonon mode populations. Moreover, the difference between the phenomenological models as regards the symmetry of excited phonon modes is fairly conventional. For instance, the fairly common statement that the DECP can excite only fully symmetric modes ignores the fact that, if an electronic subsystem does not thermalize instantaneously, its symmetry does not coin-

cide with that of the lattice. Hence, in this nonequilibrium case, phonon modes of a lower symmetry can be excited. At the same time, stating that any Raman-active mode can be generated by TSRS would be too strong, because the two-band Raman mechanism underlying TSRS is responsible for the scattering by fully symmetric phonons, whereas scattering by lower symmetry modes is allowed only in the case of resonance and degenerate electronic states. The fundamental difference between the DECP and TSRS lies in the part played by the electromagnetic field in the creation of coherent phonons. While in the first case this field provides only the energy needed for excitation of the system, in the second case the phase characteristics and lattice excitation symmetry are determined by the parameters of the Fourier components of the electromagnetic pulse.

Attempts at gaining a deeper understanding of the physics of coherent lattice excitations made by invoking microscopic descriptions led to contradictory conclusions concerning the nature of the coherent phonon. The onset of coherence when considered in reciprocal (momentum) space was explained as being due to many-phonon processes within the same mode [6], which reduces to macroscopic population of only onephonon state, $\mathbf{q} = 0$, and makes the situation similar to the case of Bose–Einstein condensation. Another approach, which is based on a two-point representation of excitation in real space, attributes the coherence to a locking of phonon modes with different wave vectors [7, 8]. Although both microscopic approaches made recourse to the DECP, the first of them (if the wave-vector selection rules are limited to long-wavelength phonons) can also be applied to the TSRS model. This can hardly be done for the second approach, because, in view of the high velocity of light, optical processes do not allow photons to interact with phonons far from the Γ point of the Brillouin zone.

A comparison of the phenomenological models suggests that, in the case of the DECP, the initial oscillation phase is determined by the position of the excited-state potential minimum. If this minimum lies to the left of that of the ground state, i.e., if the total energy of the system in an excited state reaches a minimum at a smaller separation between ions, the initial lattice response will be compression. In the reverse case, the lattice response is expansion. The response of the lattice (and, accordingly, the initial oscillation phase) will be uniquely determined by the position of the minimum of the excited-state potential. In the case of TSRS, the initial phase of oscillations is governed by resonance conditions and, depending on the actual scattering channel (Stokes or anti-Stokes), can be additionally shifted by π.

To unravel the nature of coherent lattice excitations and establish the relevant dominant mechanism of its realization in the interaction of femtosecond pulses with matter, we carried out a detailed investigation of the fast lattice relaxation dynamics of single-crystal antimony, with the time resolution technique complemented by spectral analysis of the detected light. The selection of such a semimetal as antimony as an object for study stems from the fact that for antimony the cubic nonlinear susceptibility $\chi^{(3)}$ is large and the oscillation amplitude $\Delta R/R_0$ is maximal and can be as high as 10^{-3} [4]. Furthermore, the mechanism of generation and the properties of coherent phonons in antimony have recently been a subject of heated debate in the literature [9–13].

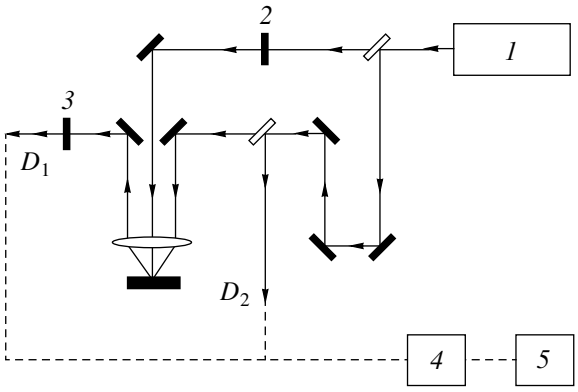

Fig. 2. Block diagram of the experiment: (*1*) laser, (*2*) modulator, (*3*) interference filter, (*4*) lock-in amplifier, and (*5*) computer; D_1 and D_2 are optical detectors.

3. EXPERIMENT

The time dependences were measured using Ti sapphire laser pulses ($\lambda = 800$ nm) with a minimum length of 50 fs and a repetition rate of 76 MHz. The pump and probe pulses were orthogonally polarized, and the optical response was studied for the [001] plane of the Sb single crystal. The pump and probe beams were focused onto the sample surface by a short-focus lens, $f = 5$ cm. The pump to probe pulse power ratio was maintained at a level of 50 : 1, with the pump pulse energy density being no greater than 1 μJ/cm^2. The pump channel was modulated with an optical chopper with a frequency of 2 kHz, and measurements were performed using synchronous detection of mixed signals of photodiodes D_2 and D_1 placed in different arms of the detection channel. The spectral response of the probe pulse was effected by interference filters (with a pass band from 1.5 to 10 nm) arranged immediately in front of detector D_1 (Fig. 2). The quantity measured in the experiment was the normalized difference between the reflectivities of the sample after and before excitation

$$\frac{\Delta R}{R_0} = \frac{R(t) - R_0(t<0)}{R_0(t<0)}$$

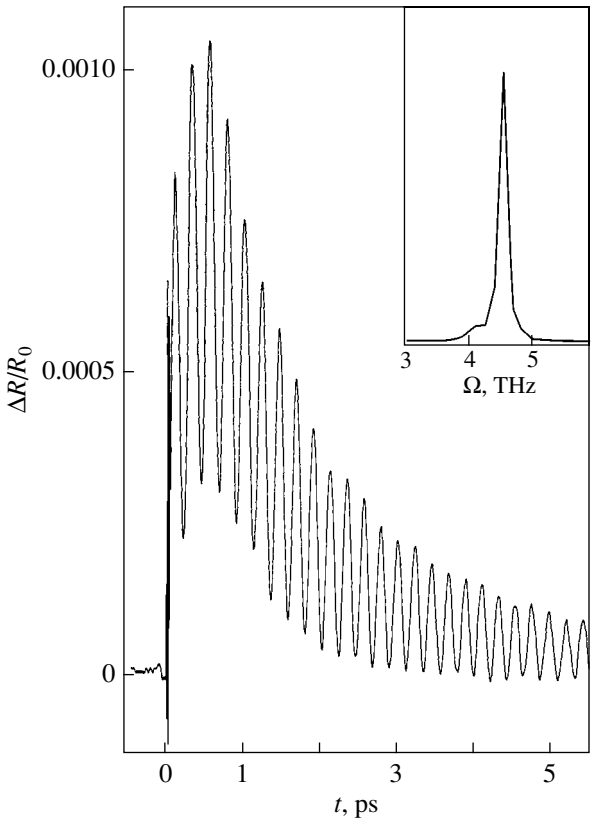

Fig. 3. Time-resolved normalized differential reflectivity, $\Delta R/R_0$, of a Sb single crystal. Inset shows the Fourier transform of the oscillating part of the signal.

as a function of time delay t between the pumping and probing. The time $t = 0$ and the pump pulse length were found from the autocorrelation function derived from two-photon absorption of light by a nonlinear crystal.

4. EXPERIMENTAL RESULTS

Figure 3 plots a typical optical response observed under excitation with subsequent probing of the antimony single crystal with femtosecond pulses. For negative delay times, when the probe pulse arrives before the pump pulse, $\Delta R/R_0 \approx 0$, which is reached by matching the intensities of the probe and reference laser beams striking the detectors D_2 and D_1, respectively. When the pump and the probe pulses coincide in time, a coherent artifact appears as a result of four-wave mixing, in which the pump and the probe pulses exchange energy. Therefore, the coherent artifact requires pulse overlap and is zero outside the limits of this overlap. For positive delay times, the excited electronic state of the system relaxes to equilibrium on a time scale on the order of a few picoseconds. Fast oscillations assigned to coherent phonons are superimposed onto this electronic relaxation [4, 9–13]. As follows from fitting the oscillations with a decaying harmonic function $A\exp(-t/\tau)\sin(\Omega t - \varphi)$ and the Fourier transform of the oscillating component (inset to Fig. 3), these oscillations are damped; they start with the minimum value, and their frequency is 4.51 THz. Comparing these data with spontaneous Raman scattering studies [4, 13] and other time-resolved measurements [9–13] enables one to identify this mode as the A_{1g} phonon, because out of the six optical phonons in antimony, which crystallizes in a structure with point symmetry D_{3d}, only one is fully symmetric at the Γ point of the Brillouin zone [4].

Knowing the magnitude of the photoinduced response, we can readily estimate the number of coherent phonons. After finding for the ion displacement that [14]

$$x_0 \approx \sqrt{\left(\frac{\Delta R}{R_0}\right)_{\text{osc}} \frac{377F}{\rho\Omega|\varepsilon|}},$$

where F is the laser pulse energy density in units of [mJ/cm^2], ρ is the sample density in units of [amu/Å^3], Ω is the frequency in THz, and ε is the dielectric constant, the change in reflectivity is calculated to be $\sim 10^{-5}$ and $x_0 \sim 10^{-3}$ Å. The square of the dimensionless coherent amplitude [6] determines the number of phonons in the interaction volume and is equal to $N \approx 10^{12}$, which indicates macroscopic filling of the phonon mode.

A more complete idea of the energy and momentum exchange between the crystal and the electromagnetic field can be gained, in addition to straightforward time-resolved measurements, from studies of the spectral properties of the time-resolved signal; said otherwise, one can obtain information not only on the spectrally integrated response but also on the evolution of the various spectral components of the light field. This can be done by analyzing the probe pulse spectrum as a function of delay time. In our experiments, spectral filtering was performed by placing an interference filter immediately in front of detector D_2 and could not affect in any way the state of the sample, which was determined by the pumping conditions. Figure 4 displays the oscillations obtained under spectral filtering of the probe pulse with interference filters having different central frequencies and the same pass band $\Delta\lambda = 10$ nm. Figure 4a illustrates the overall pattern of the $\Delta R/R_0$ signals, whereas Fig. 4b shows only the first cycles of the oscillating part obtained by fitting with a decaying harmonic function. A comparison of the oscillations detected in different wavelengths reveals that, although these oscillations always start from an extreme level, their initial phases differ by π for the Stokes and anti-Stokes parts of the spectrum (the Stokes and anti-Stokes frequencies, $\nu < \nu_0$ and $\nu > \nu_0$, respectively, are defined with respect to the central frequency ν_0 of the laser pulse spectrum). Therefore, it follows that not only the intensity of the probe pulse but also its spectrum become functions of delay time after interaction with the object under study and oscillate, at the frequency of the fully symmetric phonon mode, between the Stokes and anti-Stokes components of the spec-

trum. This situation is illustrated in Fig. 5, which gives the pump pulse spectrum and the initial phase of oscillations plotted versus the probe pulse wavelength. These data argue for the probe laser pulse being frequency-modulated around the central optical frequency.

Fourier analysis of the spectrally resolved oscillations shows that their frequency and damping (dephasing) do not depend, within experimental error, on the optical spectral range in which they are detected. This follows from Fig. 6a, which shows the frequency and the dephasing rate plotted versus the wavelength of the central interference-filter band. The coherent amplitude $(\Delta R/R_0)_{osc}$ is slightly larger for the anti-Stokes part of the spectrum than for the Stokes part, which is seen clearly from a comparison of the oscillations presented in Fig. 4 or of their amplitudes in Fig. 6b. At the same time, the magnitude of the coherent amplitude is independent of the interference filter pass band. Certainly, this conclusion does not apply to the absolute magnitude of the reflectivity change $\Delta R = R(t) - R_0$, which decreases with reduction of the pass band. In addition to the above effects, narrowing the spectral range of probing also brings about a considerable increase of noise in the oscillating signal, which is clearly seen at short time delays. This noise is damped out, however, more strongly than the oscillations themselves; therefore, the signal to noise ratio improves at long delay times (Fig. 7). It should be stressed that narrowing the filtering window also gives rise to noise at negative delay times. This questions the statement that spectrally resolved pump–probe experiments are indeed real-time measurements in the sense that they offer the possibility of following the temporal evolution of a material system under study [15].

Earlier forward-scattering experiments performed with transparent media showed that the probe pulse spectrum is a function of delay time and oscillates, at a frequency of the Raman mode, between the Stokes and anti-Stokes components [1, 2]. It was argued that a material system either donates or receives the energy of the probe pulse, depending on the delay time. For a spectrally integrated signal, however, the initial oscillation phase was shifted by $\pi/2$ with respect to the Stokes and anti-Stokes components, which was assigned to a contribution from surface effects [2].

5. DISCUSSION OF THE RESULTS

After the first time–resolved studies of Sb, which revealed A_{1g}-phonon oscillations, the generation mechanism was identified as DECP. This conclusion was drawn from the cosine pattern of the oscillations and the symmetry of the excited mode [9, 10]. Subsequent investigation showed, however, that coherent oscillations are also generated for E_g phonons, which cannot be excited by DECP [11]. This conclusion served as the basis for a model in which coherent phonons are gener-

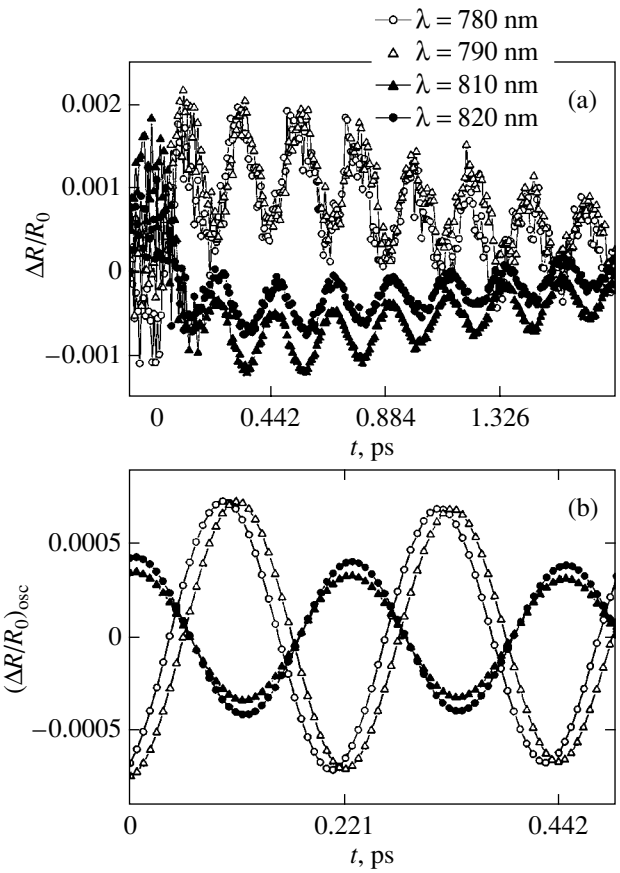

Fig. 4. (a) Spectrally resolved, normalized differential reflectivity, $\Delta R/R_0$, and (b) coherent amplitude for different probe wavelengths plotted vs. delay time. Interference filter pass bandwidth $\Delta\lambda = 10$ nm.

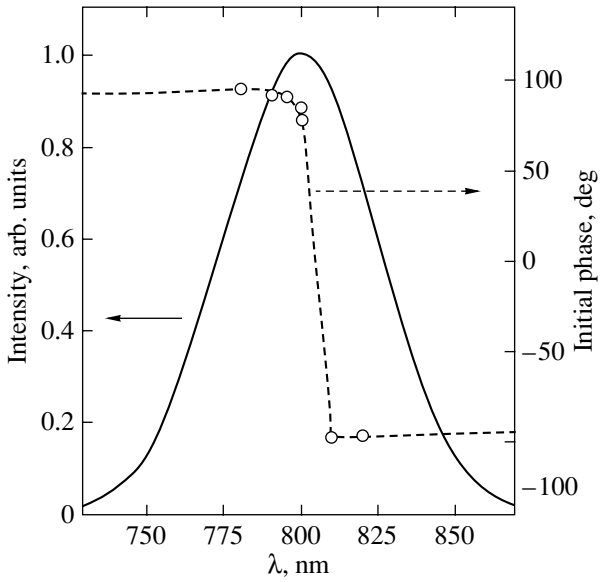

Fig. 5. Spectrum of pump pulse (solid line) and plot of the initial oscillation phase vs. probe pulse wavelength (points).

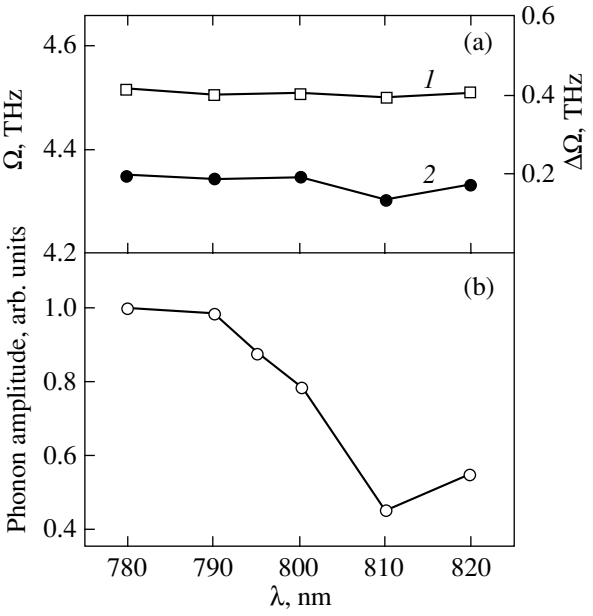

Fig. 6. (a) (*1*) Frequency (Ω) and (*2*) dephasing rate, defined as the linewidth ΔΩ of the Fourier transform of oscillations, and (b) modulus of coherent amplitude plotted vs. central wavelength of the interference filter.

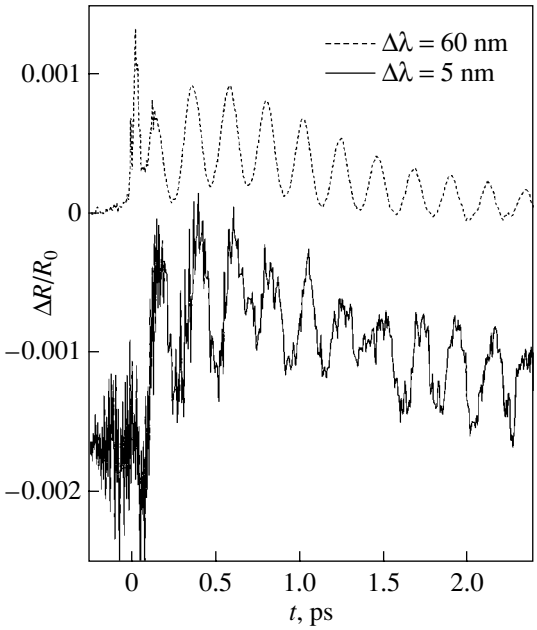

Fig. 7. Normalized differential reflectivity $\Delta R/R_0$ for two detection frequency bands centered at λ = 800 nm. The solid line corresponds to Δλ = 5 nm (translated along the vertical axis), and the dashed line corresponds to the case without a filter, Δλ ≈ 60 nm.

ated by the TSRS, and the applicability of DECP was reduced to a specific (resonant) case [2, 11]. This approach was validated by comparing the resonance behavior of spontaneous Raman scattering and coherent oscillations [13].

To understand the revealed dependence of the initial oscillation phase on the probe pulse wavelength, let us consider the process of detection of the optical signal. We first assume the pump and probe pulse interaction to be governed by the same physics, i.e., that coherence is created and detected through the same process. Being a quadratic detector, the photodiode measures the total energy of the probe pulse throughout the entire spectral range determined by the spectral sensitivity $R(t) = \int h\nu n(\nu)d\nu$, where $R(t)$ is the signal to be detected, ν is the optical frequency, and $n(\nu)$ is the number of photons of a given frequency. In the case of DECP, in which the electromagnetic field is not related to the coherent phonon, $n(\nu)$ is modulated uniformly at all frequencies; this is what accounts for the signal oscillations. Indeed, as is evident from Fig. 8, coherence of a split excited state can be realized in second order of perturbation theory for an electromagnetic field. Because of saturated absorption, reflection of the delayed probe pulse is modified by a change in the absorption rate that is proportional to the square of the projection of the probed state onto the initial coherent state and contains an oscillating term.

The TSRS case is shown schematically in Fig. 8b. In this mechanism, the reflected probe pulse $R(t)$ is additionally modulated by photon scattering into modes with different frequencies. The delayed probe signal, as in the DECP mechanism, is influenced by the absorption saturation, but, in addition to this, the signal can both donate and receive energy from the material system through inelastic light scattering. Although the total number of photons in a pulse, $\int n(\nu)d\nu$, can remain constant in this case, their spectral distribution varies, thereby modifying the total probe pulse energy.

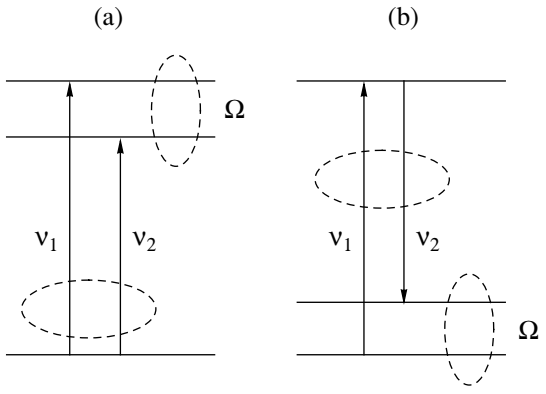

Fig. 8. Schemes illustrating (a) two-photon absorption resonance, $\nu_1 + \nu_2 = \Omega$, and (b) combination-type resonance, $\nu_1 - \nu_2 = \Omega$, which produce coherence of split levels under four-wave mixing. The ellipses shown by dashed line denote interaction.

The observed dependence of the initial oscillation phase on the probe light wavelength indicates that the spectrum of reflected light is a function of delay time. This provides supportive evidence for the mechanism of formation and detection of oscillations being dominated by a process resembling, in many respects, inelastic scattering of light. On the other hand, this dependence may indicate that, if we represent a coherent phonon in the form of a harmonic oscillator, this oscillator will be localized at the same instant of time at opposite sides of the potential curve (Fig. 1). This situation is impossible for a classical oscillator. Hence, either the oscillator is in a nonclassical state and its wave function contains components localized in different regions of the phase space or, alternatively, spectrally resolved signals cannot be considered a measure of the spatial localization of the oscillator. Most likely, both statements are correct. Using spatial filtering, we attempt to outsmart the Heisenberg uncertainty principle, according to which $\Delta E \Delta t \geq h$. In our case, $E = h\nu$, so $\Delta\nu\Delta t \geq 1$. This relation is automatically met for spectrally limited pulses (no spectral filtering); however, the use of spectral filtering to reduce $\Delta\nu$ brings about a breakdown of the inequality if we assume the temporal resolution to remain unchanged. This means that the duration of the measurement, which defines the temporal resolution for a spectrally resolved signal, is no longer determined by the duration of the laser pulse and is substantially larger. Thus, temporal resolution is lost in a spectrally resolved experiment. However, the fact itself that the object under study (in our case, a coherent phonon) obeys the uncertainty principle implies its nonclassical nature.

To be precise, the assumption of the pump and probe pulses interacting in a similar way has limited validity. The pump pulse interacts with a material medium originally residing in thermal equilibrium. The probing light pulse interacts with a coherent medium formed by the pump pulse. This parametric coupling between waves of different nature is nothing else but phase-dependent Raman scattering [16]. In this process, enhancement or attenuation of the Stokes and anti-Stokes components of the probe pulse, rather than being a result of a change in the phonon mode population, is determined by the phase relations connecting the excitations of the material medium and the field. In this case, the phase of the coherent oscillations in $\Delta R/R_0$ of frequency Ω is determined by the phase difference between the product of the Fourier components of the field and the induced polarization of the medium.

We now consider the point of how phase relations among phonons are established. We may recall that, in theoretical analysis, nonlinear optical phenomena are usually divided into two classes, depending on the actual phase relations between the interacting electromagnetic waves. Such phenomena as multiphoton absorption and stimulated Raman scattering belong to the class for which photon phase relations do not play a dominant role [17]. Therefore, it is unlikely that elementary excitations of a material medium produced by a field through these processes have the same phase. A four-wave mixing process, $\nu_1 = \nu_1 - \nu_2 + \nu_2$, however, is capable of preserving the phase of an excited phonon, provided resonances of the type of two-photon absorption, $\nu_1 + \nu_2 = \Omega$, or a combination type, $\nu_1 - \nu_2 = \Omega$, are realized in the material medium (Fig. 8). Note that here, unlike for coherent anti-Stokes scattering of light, the phase-matching conditions for the interacting Fourier components of a laser pulse are met automatically. Phase matching of phonon modes in a condensed medium interacting with ultrashort laser pulses is forced, i.e., induced by an external force. This phase matching is attained through modulation of the pump-pulse Fourier component losses at the intermode beat frequency. Since the spectrum of the pump pulse contains components differing by $\nu_1 - \nu_2 = n\Omega$ (where n is an integer), these spectral components act as a driving force. Phonon modes with $n = 1, 2, 3,\ldots$, are excited with the same phase, which is set rigorously by the driving force; therefore, the modes are phase-matched. Furthermore, because the photon wave vector is defined to within δ^{-1} in opaque media (where δ is the light penetration depth), phonon modes with wave vectors $q = -1/2\delta$ and $q = 1/2\delta$ turn out to be phase correlated. This situation is analogous in more than one respect to the case of obtaining ultrashort laser pulses by locking the laser resonator longitudinal modes. In our case, the condensed medium acts as an acoustooptical modulator with a standing ultrasonic wave used to modulate laser radiation. It should, however, be pointed out that, although light interacts with a "continuum" of phonon modes, the absolute value of the wave vector of any mode is far smaller than the width of the Brillouin zone determined by the lattice constant $|q| \ll 1/a$.

Thus, the generation of coherent phonons is determined by the nonlinear susceptibility induced by a high-power pump pulse. Coherence can set in in both the ground and excited electronic state, depending on the actual type (two-photon or combination) of resonance of the medium. Unlike for spontaneous Raman scattering of light, which involves a real change in the phonon level population, in the case of coherent phonons there may be no change in population at all, with the scattering being caused by the induced macroscopic (coherent) dipole moment of the medium. Therefore, the efficiency of scattering into the Stokes and anti-Stokes regions should be the same. Moreover, the original level of population brings about a decrease in the oscillation amplitude, which becomes manifest in an increase in the coherent amplitude with decreasing sample temperature [4]. The larger coherent amplitude for the anti-Stokes part of the spectrum in the spectrally resolved signal may originate from the fact that the conditions of spatial filtering for the Stokes and anti-Stokes components were different (which is due to the fact that the central pass band of the filters used was linear in wavelength rather than in frequency). Also, one should

not disregard the possibility that quantum beats occur in different electronic states, more specifically, in the split ground state and split excited states, which may change the relation between the Stokes and anti-Stokes components. These contributions can hopefully be identified by varying the central frequency of the pump pulse within a broader range or by using a nondegenerate version of the pump–probe method. Valuable information can also be gained by studying the temperature dependence of oscillations using the spectrally resolved pump–probe method. Additional information can be obtained using laser pulses with a linearly varied frequency ("chirps"), which will permit variation of the phase relation between the Fourier components of the light field (in this study, spectrally limited pulses were employed for which the frequency modulation rate was zero).

When a solid is acted upon by ultrashort pulses, the one-phonon states are not the only states that are excited; as a consequence, the excitation acquires the form of a wave packet. Wave packets (like coherent states) lie at the boundary between the classical and quantum-mechanical description of objects. A wave packet can be treated classically as long as the position probability function of the object under study is localized in real or phase space. The localization is a distinctive feature of a wave packet and is due to a coherent superposition of many states with large quantum numbers. In the case of a large number of states, one maximum of the wave function can become significant because of quantum interference; large quantum numbers are required in order for this maximum to have a small spatial extent. Although a wave packet does demonstrate dynamic evolution similar to that of a classical particle, it is nevertheless a quantum object and, accordingly, its behavior is much more complex. For instance, in the case of an anharmonic potential, a wave packet can localize again after delocalization [18]. We have recently succeeded in observing the collapse and rebirth of coherent phonons in semimetals, such as bismuth and antimony [19], thus furnishing convincing evidence for the lattice states being nonclassical. Furthermore, the spatial and temporal extents of a wave packet may depend periodically on its position in phase space, which is realized for the so-called squeezed states [4, 12]. All of these features of a wave packet originate from the discrete nature of the spectrum and do not have analogs in classical physics. The dependence of the initial phase on the detection wavelength revealed in this study also shows that the state created by femtosecond pulses cannot be described in terms of classical mechanics. Indeed, the coherent amplitude may have opposite signs depending on the method of detection employed, thus demonstrating that wave packet "localization" occurs simultaneously in different regions of phase space, which is impossible for a classical object. Leaving for future studies the question concerning the character of nonclassical states to which the state realized in Sb by ultrashort pulses belongs, we note only that this state seems to relate to the class of Einstein–Podolsky–Rozen tangled states. For these states, $\hat{X}_1 - \hat{X}_2 \longrightarrow 0$ and $\hat{P}_1 + \hat{P}_2 \longrightarrow 0$, where $\hat{X}_i$ and $\hat{P}_i$ are the coordinate and momentum operators, respectively, of two parts of the wave packet well separated in phase space [20]. The entanglement of phonon states may originate from their being created by correlated photons whose phases are locked within an ultrashort pulse. Note that the entanglement of vibrational states of a nonlinear molecule was studied in considerable detail in [21].

Thus, coherence appears in a phonon system as a result of multiphonon processes within a continuum of phonon modes, which is determined by the light penetration depth. This process entails phase matching for one- and two-phonon modes rather than for phonons with different wave vectors [19], while phonons with wave vectors equal in absolute magnitude but opposite in sign, within the range $\Delta q = \pm 1/2\delta$, turn out to be phase correlated. The oscillation decay time is determined by the loss of (initial-)phase memory of the process that brought about their generation.

6. CONCLUSIONS

Application of the pump–probe method complemented by spectral analysis has revealed that the initial phase of an A_{1g} coherent phonon in Sb depends on the wavelength of the probe light. This fact shows that the spectrum of the probe pulse (as well as its integrated intensity) is a function of the time delay between the pump and probe pulses. The shift of the coherent-phonon initial phase for the Stokes and anti-Stokes components of the probe pulse may be considered another argument (in addition to those presented in [4, 12, 19]) for the lattice state created by ultrashort laser pulses being of nonclassical nature. The the onset of fast temporal oscillations should be assigned to quantum beats in the split ground and excited states, which are detected in the process of phase-dependent Raman scattering of light.

ACKNOWLEDGMENTS

This study was supported in part by the Russian Foundation for Basic Research (project nos. 01-02-16480, 02-02-17074) and the Ministry of Education, Culture, Sports, Science, and Technology of Japan.

REFERENCES

1. L. Dhar, J. A. Rogers, and K. A. Nelson, Chem. Rev. **94** (1), 157 (1994).
2. R. Merlin, Solid State Commun. **102** (2–3), 207 (1997).
3. T. Dekorsy, G. C. Cho, and H. Kurz, in *Light Scattering in Solids*, Ed. by M. Cardona and G. Güntherodt (Springer, Berlin, 2000), Vol. 8, p. 169.

4. O. V. Misochko, Zh. Éksp. Teor. Fiz. **119** (2), 285 (2001) [JETP **92**, 246 (2001)].
5. H. J. Zeiger, J. Vidal, T. K. Cheng, E. P. Ippen, G. Dresselhaus, and M. S. Dresselhaus, Phys. Rev. B **45** (1), 768 (1992).
6. A. V. Kuznetzov and C. J. Stanton, Phys. Rev. Lett. **73** (24), 3243 (1994).
7. R. Scholz, T. Pfeifer, and H. Kurz, Phys. Rev. B **47** (24), 16 229 (1993).
8. W. A. Kutt, W. Albrecht, and H. Kurz, IEEE J. Quantum Electron. **28**, 2434 (1992).
9. T. K. Cheng, S. D. Brorson, S. Kazeroonian, J. S. Moodere, G. Dresselhaus, M. S. Dresselhaus, and E. P. Ippen, Appl. Phys. Lett. **57** (10), 1004 (1990).
10. T. K. Cheng, J. Vidal, H. J. Zeiger, G. Dresselhaus, M. S. Dresselhaus, and E. P. Ippen, Appl. Phys. Lett. **59** (16), 1923 (1991).
11. G. A. Garrett, T. F. Albrecht, J. F. Whitaker, and R. Merlin, Phys. Rev. Lett. **77** (17), 3661 (1996).
12. O. V. Misochko, K. Kisoda, K. Sakai, and H. Nakashima, Appl. Phys. Lett. **76** (8), 961 (2000).
13. T. E. Stevens, J. Kuhl, and R. Merlin, Phys. Rev. B **65** (14), 144304 (2002).
14. M. F. DeCamp, D. A. Reis, P. H. Bucksbaum, and R. Merlin, Phys. Rev. B **64** (9), 092301 (2001).
15. J. Stock and W. Domcke, Phys. Rev. A **45** (5), 3032 (1992).
16. B. Fain, V. Khidekel, and S. H. Lin, Phys. Rev. A **49** (2), 1498 (1994).
17. N. I. Koroteev and I. L. Shumaĭ, *Physics of High-Power Laser Radiation* (Nauka, Moscow, 1991) [in Russian].
18. M. J. J. Vrakking, D. M. Villeneuve, and A. Stolow, Phys. Rev. A **54** (1), R37 (1996).
19. O. V. Misochko, M. Hase, and M. Kitajima, Pis'ma Zh. Éksp. Teor. Fiz. **78** (2), 85 (2003) [JETP Lett. **78**, 75 (2003)].
20. B. Julsgaard, A. Kozhekin, and E. S. Polzik, Nature **413**, 400 (2001).
21. Z. Kis, J. Janszky, P. Adam, An. V. Vinogradov, and T. Kobayashi, Phys. Rev. A **54** (6), 5110 (1996).

Translated by G. Skrebtsov

Physics of the Solid State, Vol. 46, No. 9, 2004, pp. 1750–1754. Translated from Fizika Tverdogo Tela, Vol. 46, No. 9, 2004, pp. 1695–1699.
Original Russian Text Copyright © 2004 by Klyukanov, Guréu, Sandu.

LOW-DIMENSIONAL SYSTEMS AND SURFACE PHYSICS

Plasma Effects in Magnetoabsorption of D^- Centers in Quantum Wells

A. A. Klyukanov, V. Guréu, and I. Sandu

Moldova State University, ul. Mateevicha 60, Chisinau, 2009 Moldova

e-mail: klukanov@cinf.usm.md

Received November 18, 2003

Abstract—The spectrum of magnetoabsorption of D^- centers in quantum wells is calculated with allowance for their interaction with a magnetic plasma under resonance conditions, when the distance between the Landau levels is of the same order of magnitude as the quantum energy of magnetoplasma oscillations. It is shown that splitting of Landau levels results in the fine structure of absorption lines and that the relative peak heights depend on the detuning from the resonance. The calculated frequency dependence of the absorption coefficient agrees with the experimental results. © *2004 MAIK "Nauka/Interperiodica".*

Coulomb many-particle interaction of charge carriers plays an important role in semiconductor optics. In addition to renormalizing the energy spectrum and decreasing the band gap, this interaction also induces transitions with the participation of several low-frequency optical plasmons [1–5]. Plasmon emission and absorption can substantially modify the dynamics of electrons and holes [1–5]. Collective interactions manifested in multiplasmon optical transitions have been studied both theoretically and experimentally [2–5]. In [5], a generalized Bloch equation for semiconductor polarization was obtained with allowance for coherent memory effects and multiplasmon processes of light absorption and emission satisfying the energy conservation law, which is given by the argument of the δ function of the form $\omega - \omega_g \pm n\omega_p$, where ω is the photon frequency and ω_p is the frequency of a long-wavelength plasmon. In many respects, magnetic plasmas differ from a plasma in the absence of a magnetic field, and the effects of their interaction with an electromagnetic field have been an area of research for many years. In this study, we calculate the spectrum of the absorption of light by an impurity center in a quantum well in the presence of a dc homogeneous magnetic field with allowance for interaction of a bound electron with magnetoplasma waves. To calculate the density–density correlator describing a spectrum of interacting elementary excitations, we use the fluctuation–dissipation theorem, which relates the correlation function to the structure factor [6]. According to the Kubo formula [7], the light absorption coefficient due to electron transitions between discrete energy levels can be written as

$$\alpha(\omega) = \frac{4\pi e^2 N}{\omega\hbar c n(\omega)}(1 - e^{-\hbar\omega/k_0 T}) \times \sum_n \rho_i |(\hat{p}_y)_{fi}|^2 \mathrm{Re}\int_0^\infty e^{i(\omega-\omega_{fi})t} I_{fi}(t)\,dt. \quad (1)$$

Here, e and m_0 are the electron charge and mass, respectively, k_0 is the Boltzmann constant, T is the temperature of the crystal, $\hbar\omega_g = E_g$ is its band gap, N is the concentration of the centers, c is the velocity of light, and $n(\omega)$ is the refraction index. The polarization vector of light is directed along the y axis, which is parallel to the surface of the quantum well, and a dc homogeneous magnetic field of intensity $\mathbf{H}$ with a vector potential $\mathbf{A} = (-Hy, 0, 0)$ is directed normal to the surface, i.e., along the quantum confinement axis z. The indices i and j denote the set of quantum numbers of an optical electron, and the wave function of the system is written as a product of the wave functions (quasiparticle representation). We calculated the transition frequency ω_{if} and the initial-state occupation probability ρ_i in the one-particle approximation by neglecting the interaction of the electron on the center with lattice vibrations and with magnetic plasma:

$$V(r) = \sum_{\mathbf{q}} v_{\mathbf{q}} \rho_{\mathbf{q}} P_{-\mathbf{q}}, \quad \rho_{\mathbf{q}} = \exp(i\mathbf{q}\mathbf{r}), \quad (2)$$

where $v_{\mathbf{q}}$ is the Fourier transform of the Coulomb interaction of the electron with the charge density $P_{-\mathbf{q}}$ produced by lattice and magnetic-plasma vibrations. Many-particle interaction (2) was taken into account using the generating function

$$I_{fi} = \langle i(r_s)|\langle i(r_\sigma)|\langle f(r_s')| < \exp\left\{-\frac{i}{\hbar}\int_0^t (V(r_s) - V(r_s'))\,ds - \int_0^\lambda V(r_\sigma)\,d\sigma\right\} > |u(r_s)\rangle|i(r_\sigma)\rangle|f(r_s')\rangle, \quad (3)$$

where $\lambda = 1/k_0 T$ and $V(r_s)$ is the interaction operator (2) in the Heisenberg representation. In Eq. (3), the averag-

ing $\langle \ldots \rangle$ is performed over the states of the system without the electron on the center and the Feynman rule of operator ordering [8] is used. When evaluating the averages, all unprimed operators are placed on the left in descending order of the time argument from left to right (so that the latest time stands at the left end), then follows the equilibrium density matrix, the operators V_σ in descending order of σ, and all primed operators in ascending order of the time argument from left to right. If we assume that $V(r)$ in Eq. (2) is the interaction with phonons in the linear approximation and neglect the electron–phonon interaction in the equilibrium density matrix, i.e., if we set $V_\sigma = 0$, then, averaging over the phonon states in Eq. (3), we easily obtain the well-known result for the Feynman influence phase [8]. We note that it is necessary to take the correlator $\langle V_\sigma V_s \rangle$ into account, since it substantially affects the time dependence of the generating function (3). We calculate this function using the cumulant method [9] and restrict ourselves to the second cumulant $\langle e^{\hat{A}} \rangle \approx e^{\langle \hat{A} \rangle + \frac{1}{2}(\langle \hat{A}^2 \rangle - \langle \hat{A} \rangle^2)}$ (the first cumulant vanishes). In the linear harmonic approximation, this approach yields an exact result, since the higher order cumulants vanish. Thus, calculating the generating function (3) reduces to finding the density–density correlator $\langle P_{\mathbf{q}}(s) P_{-\mathbf{q}}(s_1) \rangle$, which can be expressed through the structure factor [6]. In the quasistatic approximation, we have

$$\langle P_{\mathbf{q}}(s) P_{-\mathbf{q}}(s_1) \rangle = \frac{\hbar}{\pi V_q} \int_{-\infty}^{\infty} \exp\{-i\Omega(s - s_1)\} F_q(\Omega) d\Omega,$$
$$F_q(\Omega) = (n(\Omega) + 1) \mathrm{Im} \left\{ \frac{\varepsilon_\infty q^2}{q_i \varepsilon_{ij}^*(q, \Omega) q_j} \right\}, \quad (4)$$

where $n(\Omega) = \{\exp(\lambda\hbar\Omega) - 1\}^{-1}$, ε_∞ is the high-frequency permittivity, and ε_{ij} is the permittivity tensor. We calculate the quantum-mechanical averages in Eq. (3) in the first-cumulant approximation. In this way, the generating function is found to be

$$I_{fi}(t) = \exp\left\{ -\frac{1}{\pi\hbar} \sum_{\mathbf{q}} V_q \int_{-\infty}^{\infty} F_q(\Omega) \right.$$
$$\times \left[\sum_n |\rho_{fn}(\mathbf{q})|^2 \Phi_t(\Omega - \tilde{\omega}_{fn}) + \sum_n |\rho_{in}(q)|^2 \Phi_t^*(\Omega - \tilde{\omega}_{in}) \right.$$
$$+ \sum_n |\rho_{in}(q)|^2 \Phi_{i\hbar\lambda}(\Omega - \tilde{\omega}_{in}) - 2\rho_{ii}(\mathbf{q}) \rho_{ff}^*(\mathbf{q}) \mathrm{Re}\, \Phi_t(\Omega)$$
$$\left. \left. + 2i(\rho_{ii}(\mathbf{q}) - \rho_{ff}(\mathbf{q})) \rho_{ii}^*(\mathbf{q}) \frac{\sin \Omega t}{\Omega^2} \right] d\Omega \right\}, \quad (5)$$

where

$$\Phi_t(\omega) = \{1 - i\omega t - \exp(-i\omega t)\}/\omega^2. \quad (6)$$

Formulas (1)–(5) determine the impurity absorption coefficient with allowance for multiquantum transitions. The frequencies of elementary excitations with which the bound electrons interact are determined by the zeros of the permittivity tensor of the system in a magnetic field. We apply these general results to analyze the frequency dependence of the absorption coefficient of two-dimensional D^- centers. The terms linear in time and in λ in the functions Φ determine the contributions to the energy of the optical electron of the D^- center coming from the interaction of this electron with lattice vibrations (polaron effect) and with the plasma:

$$\tilde{E}_j = E_j + \frac{1}{\pi} \sum_{\mathbf{q}} V_q \sum_n |\rho_{jn}(\mathbf{q})|^2 \int_{-\infty}^{\infty} \frac{F(\Omega)}{\tilde{\omega}_{jn} - \Omega} d\Omega. \quad (7)$$

It follows from Eq. (7) that the interaction with magnetic plasma and lattice vibrations lowers the energy levels of the bound electrons. According to the experimental data [10], the binding energy of the electron on the D^- center increases with magnetic field following approximately the square-root law. The theoretical results obtained in [11, 12] for the binding energy $E_b = \hbar\omega_b$ by neglecting interaction (2) qualitatively agree with the experimental dependence of E_b on H, although the calculated values of E_b themselves are somewhat smaller than the observed values. Quantitative agreement between the theory and the experiment can be achieved not only by improving variational functions [11] but also by taking into account the contribution from the interaction with lattice vibrations and with plasma to E_b, in accordance with Eq. (7). It follows from Eq. (6) that $\Phi_t(\omega) \cong 0.5t^2$ as $\omega \longrightarrow 0$; this results in a Gaussian shape of the absorption spectrum $\alpha(\omega)$. The contribution from the interaction of the bound electrons with acoustic phonons to the half-width of the Gaussian curve Δ is determined by

$$\Delta = 2\left(\frac{2\ln 2}{(2\pi)^{3/2}} \frac{E_1^2 k_0 T}{\rho w^2 a^2 a_0} \right)^{1/2}. \quad (8)$$

This result can easily be obtained if we take the ground-state wave function of the electron on the center in the form

$$\Psi_i(r) = \pi^{-3/2} a^{-1} a_0^{-1/2} \exp\left\{ -\frac{r^2}{2a^2} - \frac{z^2}{2a_0^2} \right\}. \quad (9)$$

In Eq. (8), w is the of velocity of sound, ρ is the density of the crystal, and E_1 is the deformation potential constant. We see from Eq. (8) that this broadening mechanism may be important for strongly bound electrons with a small localization radius a. Using the values of

the parameters of GaAs–GaAlAs quantum wells $\rho = 5.4$ g/cm^2, $w = 3 \times 10^5$ cm/s, $E_1 = 10$ eV, $T = 9$ K, and $a = a_0 = 100$ Å) [10], we find $\Delta = 0.31$ eV, which is much smaller than the experimental half-width $\Delta = 4.8$ eV used in [11, 12]. The analysis of the experimental data from [10] performed in the theoretical study in [11] showed that the absorption lines of D^- centers have a Lorentzian (rather than Gaussian) shape:

$$L(\omega - \tilde{\omega}_{if}) = \frac{\Delta_{if}/2\hbar}{(\omega - \tilde{\omega}_{if})^2 + (\Delta_{if}/2\hbar)^2}. \quad (10)$$

Here, $\hbar\tilde{\omega}_{if} = \tilde{E}_i - \tilde{E}_f$ is the transition energy, which is found with allowance for the interaction of the center with lattice vibrations and with plasma and is given by Eq. (7), and the absorption line half-width Δ_{if} is calculated in the limit $t \longrightarrow \infty$ using the relation

$$\lim_{t\to\infty} \frac{1 - \exp(-i\Omega t)}{\Omega^2} = \pi t\delta(\Omega) + i\pi\delta'(\Omega). \quad (11)$$

According to Eqs. (5) and (10), the $i \longrightarrow f$ transition is characterized by the half-width Δ_{if}, whose magnitude depends on the imaginary part of the permittivity tensor at the frequencies $\Omega = \omega_{in}$, $\Omega = \omega_{fn}$, and $\Omega \longrightarrow 0$:

$$\Delta_{if} = \sum_{\mathbf{q}} v_q \left\{ \sum_n |\rho_{fn}(\mathbf{q})|^2 F_q(\omega_{fn}) + \sum_n |\rho_{in}(\mathbf{q})|^2 F_q(\omega_{in}) - 2\rho_{ff}(\mathbf{q})\rho_{ii}(-\mathbf{q})F_q(0) \right\}. \quad (12)$$

The frequency dependence of the absorption coefficient $\alpha(\omega)$ is determined above all by the energy spectrum of the D^- center, but the spectrum of elementary excitations of the magnetic plasma and of the crystal is no less important. In the case of a quantum well where the magnetic field is normal to its surface, according to the known results for two-dimensional plasmas [6], we have

$$\frac{\varepsilon_0 q^2}{q_i \varepsilon_{ij}^*(q,\Omega) q_j} = \frac{\Omega^2 - \omega_c^2}{\Omega^2 - \omega_c^2 - \omega_p^2}, \quad \omega_c = \frac{eH}{mc}, \quad \omega_p^2 = \frac{4\pi N e^2}{\varepsilon_0 m}. \quad (13)$$

This expression has a pole at the point $\Omega = \tilde{\omega}_p = (\omega_c^2 + \omega_p^2)^{1/2}$, which determines the frequency of the so-called upper hybrid mode $\tilde{\omega}_p$. At low temperatures, only spontaneous emission of quanta of magnetoplasma waves is important. Taking multiquantum transitions into account, the absorption coefficient of the D^- center at low temperatures is found to be

$$\alpha(\omega, H) = \alpha_0 \frac{\omega_p}{\omega}(1 - e^{-\hbar\omega/k_0T}) \frac{\gamma^{5/2}}{(1+\gamma)(1+\gamma+\gamma^2)} \times \{L(\omega - \omega_b) + I_1 L(\omega - \omega_b - \omega_c) + N_0 L(\omega - \omega_b - \tilde{\omega}_p) + I_2 L(\omega - \omega_b - 2\omega_c) + I_1 N_1 L(\omega - \omega_b - \omega_c - \tilde{\omega}_p) + 0.5 N_0^2 L(\omega - \omega_b - 2\tilde{\omega}_p) + \dots\}. \quad (14)$$

The constants N_n (n enumerates the Landau levels) determine the average number of magnetoplasma quanta $\hbar\tilde{\omega}_p$ that are emitted as a photon is absorbed and an electron is transferred to the corresponding Landau level. In Eq. (14), the first and second terms in braces characterize transitions from the ground state of the center to the zeroth and first Landau levels, respectively. The third term describes a transition to the zeroth Landau level with emission of a magnetoplasma quantum. The remaining terms are interpreted likewise. The coefficients of the relative intensities of transitions from the ground state i to a Landau level n can be calculated analytically using wave function (9) for the ground state and the Landau wave functions for the excited states. For example,

$$I_1 = \frac{4}{\gamma} + \frac{3}{2}(\gamma_1 - \gamma_2), \quad I_2 = \frac{15}{8}(\gamma_1 - \gamma_2)^2 + \frac{3}{2}\gamma_1\gamma_2 + \frac{6}{\gamma}(\gamma_1 - \gamma_2) - 1, \quad \gamma_1 = \frac{1 - \gamma + \gamma^2}{1 + \gamma + \gamma^2}, \quad \gamma_2 = \frac{1-\gamma}{1+\gamma}, \quad (15)$$

where $\gamma = c\hbar/eHa^2$. We do not write out intricate expressions for $I_3, I_4, \dots$. For $\gamma = 1$, we have $I_1 = 4.5$, $I_2 = 1.24$, and $I_3 = 0.41$. The transition to the first Landau level is the strongest. We recall that, for free electrons, the 0–1 transition is the only allowed transition at low temperatures. Figure 1 shows the theoretical dependence of the absorption coefficient (14) on the magnetic field in relative units at a photon energy $\hbar\omega = 17.58$ meV. The half-widths Δ of all Lorentzians in Eq. (14), as well as the values of the parameters N, are taken to be equal. In a simple model using the pole defined by Eq. (13) and the ground-state wave function (9), we find

$$N \cong \frac{\omega_p^2}{2\hbar\tilde{\omega}_p^3} \sum_{\mathbf{q}} v_q |\rho_{ii}(\mathbf{q})|^2 = \sqrt{\frac{\pi}{8}} \frac{e^2}{\varepsilon_0 a \hbar \tilde{\omega}_p} \left(\frac{\omega_p}{\tilde{\omega}_p}\right)^2. \quad (16)$$

We disregard the magnetic field dependence of the parameters Δ and N. In numerical calculations, we used the experimental values of the binding energy from [10], the value $\hbar\omega_p = 3.67$ meV (without dispersion), and $a = 100$ Å. It is seen from Fig. 1a that, for $\Delta = 0.28$ meV, all

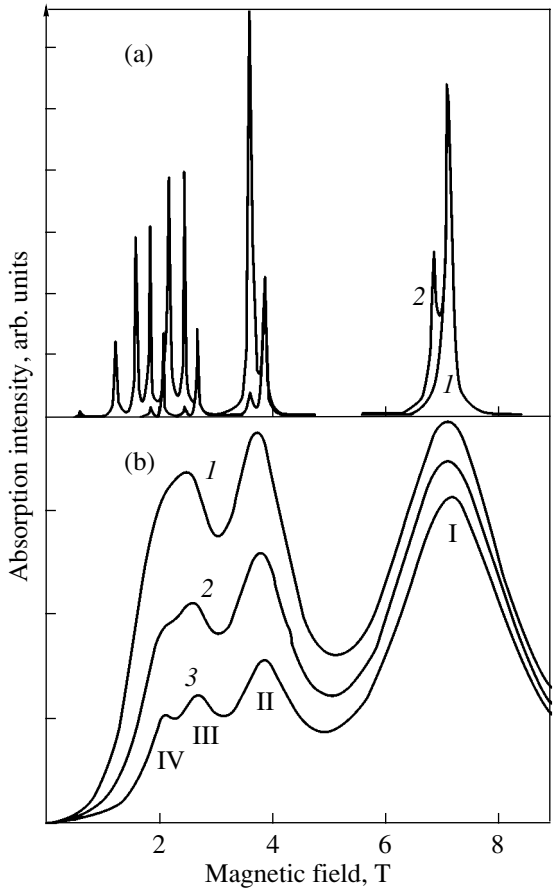

Fig. 1. Absorption spectrum of D^- centers calculated by Eq. (14) at photon energy $\hbar\omega = 17.58$ meV, $\hbar\omega_p = 3.67$ meV, and $a = 100$ Å. Roman numerals indicate the number of the Landau level to which an electron is transferred from the ground state. (*a*) Half-width $\Delta = 0.28$ meV, and (1) $N = 0.1$ and (2) 2. (*b*) Half-width $\Delta = 4.8$ meV, and (*1*) $N = 0.01$, (*2*) 0.5, and (*3*) 1.

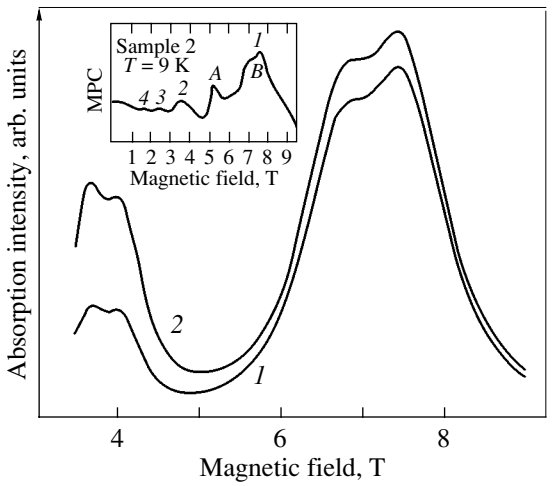

Fig. 2. Magnetic field dependence of the absorption coefficient of a D^- center calculated with allowance for interaction of the first and second Landau levels with the upper hybrid mode of magnetoplasma oscillations for photon energy $\hbar\omega = 17.58$ meV, $\hbar\omega_p = 2$ meV, $a = 100$ Å, $\hbar G_{10} = \hbar G_{21} = 1.64$ meV, and the experimental values of the binding energy from [10]. (*1*) $N = 0.01$ and (*2*) 0.5. The inset shows the experimental magnetic field dependence of the magnetophotoconductivity from [10].

absorption lines described by Eq. (14) are allowed. The light absorption accompanied by the emission of magnetoplasma quanta of frequency $\tilde{\omega}_p$ increases with N. The increase in the line half-widths smoothes the fine structure of the absorption spectrum. For $\Delta = 4.8$ meV, the results of calculations are shown in Fig. 1b. The Roman numerals near each absorption line indicate the Landau level to which the electron is excited from the ground state of the center. The absorption spectrum in Fig. 1b calculated by formula (14) correctly reflects the main experimental features [10] shown in the inset to Fig. 2. We note that the ratio of the peak heights is substantially changed even at $N = 0.5$. Huant *et al.* [10] measured the magnetophotoconductivity (MPC) due to D^- centers in GaAs–$Ga_{0.75}Al_{0.25}As$ MQW structures consisting of 150 quantum wells 100 Å wide separated by 100-Å-wide barriers. Samples were doped by silicon (10^{10} cm^{-2}) at the center of each quantum well and at a distance of 10 Å from its surface. The magnetic field dependence of MPC had an oscillating character due to ionization of D^- centers and neutral donors (peak *A* in the inset to Fig. 2). According to [10], the MPC maxima (Fig. 2) correspond to $i \longrightarrow n$ transitions from the ground state of a D^- center to the first to fourth Landau levels. The absorption line corresponding to the $i \longrightarrow 1$ transition (to the first Landau level) dominates in the spectrum. These experimental data agree with the theory.

However, some experimental features are not described by formula (14). There is a shoulder on the low-field side of the $i \longrightarrow 1$ peak and a shoulder on the high-field side of the $i \longrightarrow 2$ peak. In [10], the former shoulder is attributed to the contribution of donors lying near the boundaries of quantum wells. However, in this case, the shoulder at the $i \longrightarrow 2$ peak should also lie on the low-field side of the peak. Moreover, a similar shoulder should also appear on the low-field side of the $i \longrightarrow 0$ peak. According to the experimental data from [10], the $i \longrightarrow 0$ peaks in MPC at different photon energies $\hbar\omega$ are symmetric without indications of any structure. We believe that the shoulders at the $i \longrightarrow 1$ and $i \longrightarrow 2$ peaks are due to resonant interaction of D^- centers with magnetoplasma waves. Analogous effects appear in resonant interaction of electron and phonon subsystems [13–17]. As the cyclotron frequency coincides with the longitudinal optical phonon frequency, the Landau levels split, which manifests itself in the pinned-mode structure of the transmission minima [13]. Polaron pinned modes were observed when studying both interband magnetoabsorption [13] and intraband cyclotron–phonon and cyclotron resonances [14–16]. We note at once that it is impossible to explain the shoulders in the MPC spectra [10] in terms of emission

of real quanta $\hbar\tilde{\omega}_p$, since $N < 1$ and $I_1 > 1$. Emission of virtual magnetoplasma quanta essentially changes the energy spectrum and transition probabilities. Indeed, at low plasma concentrations ($\tilde{\omega}_p \cong \omega_c$), the electron states corresponding to the first Landau level and to the zeroth level plus one quantum $\hbar\tilde{\omega}_p$ are close in energy, $E_1 \cong E_0 + \hbar\tilde{\omega}_p$. Under resonance conditions, even in zeroth approximation, we must take into account a superposition of these states [18], since the standard perturbation theory cannot be applied here. We can find the energy spectrum of the impurity–plasma system near the first Landau level from expression (7) by taking into account the resonant terms and the pole at the point $\Omega = \tilde{\omega}_p = (\omega_c^2 + \omega_p^2)^{1/2}$ (see Eq. (13)). The result is

$$\tilde{E}_1 \cong E_0 + \frac{1}{2}\hbar(\delta \pm \tilde{\Omega}), \quad \delta = \tilde{\omega}_p - \omega_c,$$
$$\tilde{\Omega} = \{\delta^2 + G_{10}^2\}^{1/2}, \quad G_{jn}^2 = \frac{2\omega_p^2}{\hbar\tilde{\omega}_p}\sum_{\mathbf{q}} v_q |\rho_{jn}(\mathbf{q})|^2. \tag{17}$$

The magnetoplasma analog of the Rabi frequency $\tilde{\Omega}$ depends on the detuning from the resonance $\delta = \tilde{\omega}_p - \omega_c$ and on resonant interaction of the zeroth and first Landau levels (constant G). Accordingly, the second and third terms in Eq. (14) are replaced by

$$(I_1 b + N_0 d)L(\omega - \omega_b - \omega_c + 0.5(\tilde{\Omega} + \delta)) + (I_1 d + N_0 b)L(\omega - \omega_b - \omega_c - 0.5(\tilde{\Omega} + \delta)). \tag{18}$$

As before, there are two peaks, but they are of substantially different heights, which are determined by the coefficients

$$b = \frac{\tilde{\Omega} + \delta}{2\Omega}, \quad d = \frac{\tilde{\Omega} - \delta}{2\Omega}. \tag{19}$$

The ratio of the intensities of the two absorption peaks depends on b and d. If the inequalities $N_0 < 1$ and $I_1 > 1$ are satisfied, this ratio is determined by the quantity b/d, which always exceeds unity, since $\delta > 0$. Therefore, the peak on the side of higher magnetic fields is higher and the shoulder on the $I \longrightarrow 1$ peak is located on the low-field side, in accordance with the MPC spectrum shown in the inset to Fig. 2. In the region of the second Landau level, four levels interact with one another; however, the interaction between the levels with the smallest detuning from the resonance is the strongest. In Fig. 2, we show the calculated magnetic field dependence of the absorption coefficient with allowance for the splitting of the first and second Landau levels. We included the interaction of the second Landau level with the level $\tilde{E}_1 \cong E_0 + \frac{\hbar}{2}(\delta - \tilde{\Omega})$, for which the detuning from the resonance $\delta_1 = 1.5\delta - 0.5\tilde{\Omega}$ is smaller than δ and can become negative and the quantities $N_1 I_1$ and N_2 are comparable in magnitude. Accordingly, the shoulder on the $I \longrightarrow 2$ peak appears on the high-field side, in agreement with the experimental data from [10].

REFERENCES

1. R. Schepe, T. Schmelau, D. Tamme, and K. Henneberger, Phys. Status Solidi B **206** (1), 273 (1998).
2. A. A. Klyukanov, Fiz. Tverd. Tela (Leningrad) **29** (11), 1529 (1987) [Sov. Phys. Solid State **29**, 876 (1987)].
3. V. S. Vavilov, A. A. Klyukanov, K. D. Sushkevich, M. V. Chukichev, A. Z. Avavdekh, and R. Rezvanov, Fiz. Tverd. Tela (St. Petersburg) **43** (5), 776 (2001) [Phys. Solid State **43**, 808 (2001)].
4. A. A. Klyukanov, N. A. Loiko, and I. V. Babushkin, Laser Phys. **11** (3), 318 (2001).
5. A. A. Klyukanov, N. A. Loiko, I. V. Babushkin, and V. Gurau, Proc. SPIE **4748**, 301 (2002).
6. P. M. Platzman and P. A. Wolff, *Waves and Interactions in Solid State Plasmas* (Academic, New York, 1973; Mir, Moscow, 1975).
7. R. Kubo, J. Phys. Soc. Jpn. **12** (3), 570 (1957).
8. R. Feynman, R. Hellwarth, C. Iddings, and P. Platzman, Phys. Rev. **127** (4), 1004 (1962).
9. R. Kubo, J. Phys. Soc. Jpn. **17** (7), 1100 (1962).
10. M. Fujito, A. Natori, and H. Yasunaga, Phys. Rev. B **51** (7), 4637 (1995).
11. S. Huant, S. P. Najda, and B. Etienne, Phys. Rev. Lett. **65** (12), 1486 (1990).
12. É. P. Sinyavskiĭ and S. M. Sokovnich, Fiz. Tekh. Poluprovodn. (St. Petersburg) **34** (7), 844 (2000) [Semiconductors **34**, 815 (2000)].
13. E. J. Johnson and D. M. Larsen, Phys. Rev. Lett. **16** (15), 655 (1966); K. L. Ngai and E. J. Johnson, Phys. Rev. Lett. **29** (24), 1607 (1972).
14. V. I. Ivanov-Omskiĭ and E. M. Sheregiĭ, Fiz. Tverd. Tela (Leningrad) **16** (1), 238 (1974) [Sov. Phys. Solid State **16**, 153 (1974)]; V. I. Golubev, V. I. Ivanov-Omskiĭ, and E. M. Sheregiĭ, Fiz. Tverd. Tela (Leningrad) **17** (1), 185 (1975) [Sov. Phys. Solid State **17**, 108 (1975)].
15. D. H. Dickei, E. J. Johnson, and D. M. Larsen, Phys. Rev. Lett. **18** (10), 539 (1967); K. Nagasaca, Phys. Rev. B **15** (4), 2273 (1977).
16. A. A. Klyukanov, V. N. Gladilin, and T. H. Wu, Ukr. Fiz. Zh. **25** (6), 937 (1980); A. A. Klyukanov, E. P. Pokatilov, V. N. Gladilin, and T. H. Wu, Phys. Status Solidi B **87** (1), K159 (1978).
17. Yu. E. Perlin, A. A. Kaminskiĭ, V. N. Enachi, and D. N. Vylegzhanin, Pis'ma Zh. Éksp. Teor. Fiz. **30** (7), 426 (1979) [JETP Lett. **30**, 398 (1979)]; V. N. Enachi, A. Lupei, V. Lupei, C. Presura, and V. E. Ciobu, Proc. SPIE **3405**, 570 (1998).
18. A. S. Davydov, *Quantum Mechanics* (GIFML, Moscow, 1963; Pergamon, Oxford, 1976).

Translated by I. Zvyagin

Physics of the Solid State, Vol. 46, No. 9, 2004, pp. 1755–1760. Translated from Fizika Tverdogo Tela, Vol. 46, No. 9, 2004, pp. 1700–1705.
Original Russian Text Copyright © 2004 by Dneprovskiĭ, Zhukov, Lyaskovskiĭ, Ryzhkov, Tolpeĭkin, Shatalin.

LOW-DIMENSIONAL SYSTEMS AND SURFACE PHYSICS

Luminescence of $CdSe/Al_2O_3$ Quantum Wires at High Photoexcitation Levels

V. S. Dneprovskiĭ, E. A. Zhukov, V. L. Lyaskovskiĭ, M. V. Ryzhkov, I. V. Tolpeĭkin, and A. I. Shatalin

Moscow State University, Vorob'evy gory, Moscow, 119992 Russia

e-mail: scon281@phys.msu.su

Received January 12, 2004

Abstract—Nonlinear dependence of the $CdSe/Al_2O_3$ quantum wire luminescence intensity on the photoexcitation level and an asymmetric broadening of luminescence spectra accompanied by a high-frequency shift of the maximum are observed and explained in terms of the dominant filling of exciton phase space in wires with different cross sections. *© 2004 MAIK "Nauka/Interperiodica".*

1. INTRODUCTION

It has been shown theoretically [1–5] that optical absorption and luminescence spectra of quantum wires are dominated by exciton transitions, i.e., that the oscillator strength is concentrated at the wavelength of the exciton transition to the ground state. The absorption due to interband transitions of free electrons and holes in quantum wires is substantially weaker than that of excitons. Furthermore, the Sommerfeld contribution to absorption by the "exciton continuum" is considerably smaller (the Sommerfeld factor is less than unity) than that in two- and three-dimensional (bulk) semiconductors.

In a semiconducting quantum wire with a dielectric barrier, in which $\varepsilon_s \geqslant \varepsilon_d$ (ε_s and ε_d are the permittivities of the semiconductor and insulator, respectively), the exciton binding energy and oscillator strength increase with decreasing transverse size not only due to quantum confinement but also as a result of "dielectric enhancement." The origin of the dielectric enhancement lies in the fact that the electric field of the electron and the hole making up an exciton in a quantum wire becomes redistributed due to the permittivity of an insulator being considerably smaller than that of a semiconductor. In quantum wires with a small cross section, most of the electric field lines coupling the electron with the hole pass through the insulator; as a result, for the above ratio of the permittivities of a semiconductor and an insulator, the Coulomb attraction between the electron and the hole is enhanced. The phenomenon of dielectric enhancement of excitons was predicted for thin films in [6–8] and quantum wires in [5, 9–11]. The exciton binding energy in InP quantum wires with a dielectric barrier (the semiconductor was crystallized in transparent hollow nanotubes of chrysotile asbestos) was shown [12] to increase by a few times as compared to InP quantum wires with semiconducting barriers. By properly choosing (when preparing quantum wires) semiconducting and insulating materials with different permittivities, one can vary the exciton binding energy and oscillator strength in a quantum wire within a broad range, which may serve as an illustration of the possibilities of the Coulomb interaction engineering approach [5].

The present communication reports on an observation of a change in the photoluminescence spectra of $CdSe/Al_2O_3$ quantum wires and of reference CdSe single crystals with increasing excitation level. An analysis of photoluminescence spectra of $CdSe/Al_2O_3$ quantum wires obtained at high excitation levels enabled us to identify the processes occurring at high exciton concentrations.

2. VARIATION OF PHOTOLUMINESCENCE SPECTRA OF $CdSe/Al_2O_3$ QUANTUM WIRES AND OF CDSE SINGLE CRYSTALS WITH INCREASING PHOTOEXCITATION LEVEL

To prepare samples of quantum wires, hollow through channels 4–6 nm in radius were produced in a transparent dielectric Al_2O_3 matrix (a layer a few microns thick on an aluminum foil) by electrochemical etching at room temperature in a 10% solution of sulfuric acid. The transverse dimensions of the channels were measured with an atomic force microscope [13]. The CdSe semiconductor was crystallized in the matrix nanochannels by electrochemical substitution. The semiconductor crystallized apparently not only in the hollow nanochannels but also on the surface of our samples in the form of islands of bulk material. This is what may account for the features in the luminescence spectra of samples cooled to liquid-helium temperature (Fig. 1), which were recorded at various times after excitation by weak second-harmonic picosecond pulses of a Ti-sapphire laser ($h\nu$ = 3.1 eV, pulse duration 1.5 ps, pulse repetition frequency 82 MHz, pump energy den-

1063-7834/04/4609-1755$26.00 © 2004 MAIK "Nauka/Interperiodica"

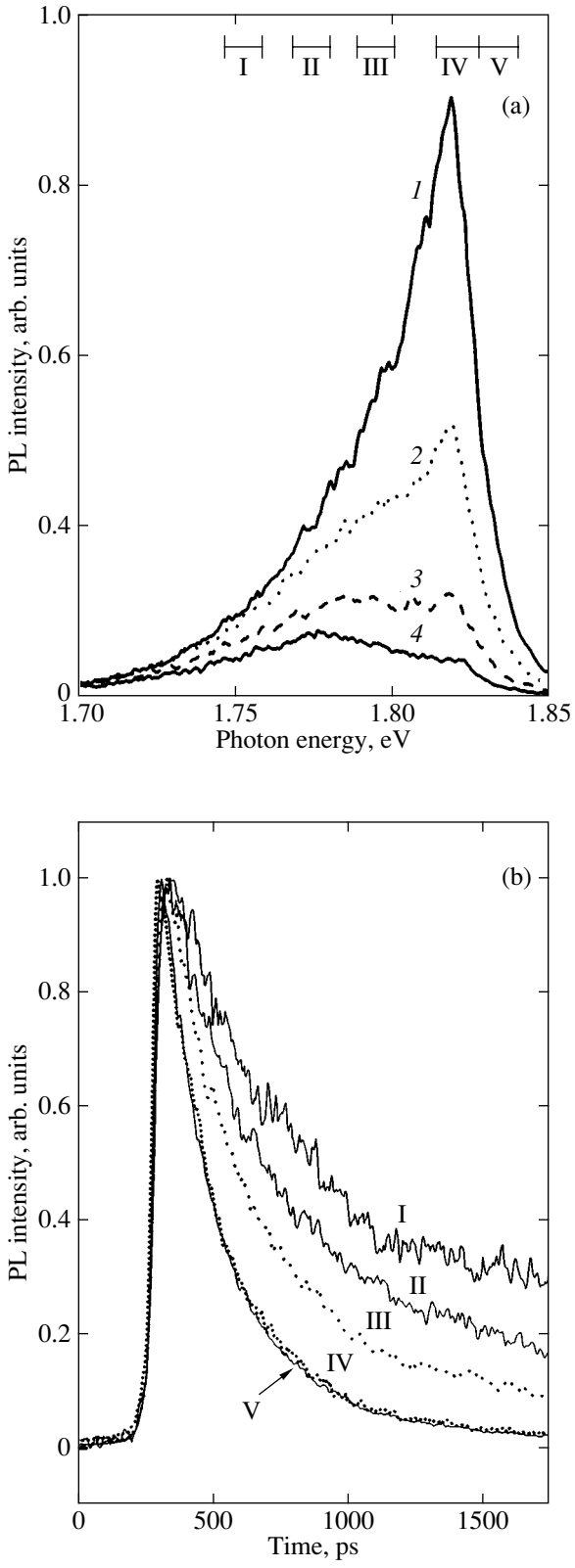

Fig. 1. (a) Photoluminescence spectra of a $CdSe/Al_2O_3$ sample (18 K) obtained at different times after termination of the pump pulse: (*1*) 0–80, (*2*) 190–270, (*3*) 460–540, and (*4*) 720–820 ps. (b) Variation in the luminescence intensity with time in various spectral intervals identified in panel (a).

sity 0.2 μJ/cm^2) pumped by an argon laser. Time-resolved luminescence spectra obtained with a polychromator equipped with a Hamamatsu C1587 synchroscan streak camera revealed two luminescence bands (Fig. 1a). The low-frequency band, which we assign to luminescence of the bulk semiconductor (luminescence at the frequency of the first exciton phonon replica, the *A-LO* band [14]), decays with a time constant of about 1 ns, which is characteristic of this recombination channel. The high-frequency band peaking near 1.82 eV, which we attribute to quantum wire luminescence, decays much faster (Fig. 1b). The intensity of this band depends on the polarization of the pump radiation. When excited by linearly polarized cw He–Cd laser radiation, the luminescence intensity in the case where the laser beam polarization was perpendicular to the axis of the semiconductor-filled nanochannels was lower [15] than that in the presence of a polarization component oriented along the nanochannel axis (for an angle of 45° between the direction of laser beam polarization and the nanochannel axis). This allows us to assume that the semiconductor crystallized in the matrix nanochannels predominantly in the form of quantum wires. The field component perpendicular to the wire axis inside thin (with a transverse size much less than the pump radiation wavelength) semiconductor wires embedded in a medium with a lower permittivity (in our case, an insulator) is weakened considerably, by a factor $(\varepsilon_d + \varepsilon_s)/2\varepsilon_d$ [12]. The decrease in absorption of the pump radiation polarized in this way may account for the drop in the luminescence intensity.

Because the luminescence bands (Fig. 1) lie close to one another and even partially overlap, we also performed measurements with plates of undoped single-crystal CdSe prepared from a gas phase, which permitted us, in particular, to reveal differences in the variation of spectra under increasing excitation levels.

Figure 2 presents luminescence spectra of samples of $CdSe/Al_2O_3$ and single-crystal CdSe measured at low excitation levels. The $CdSe/Al_2O_3$ samples were pumped by the second harmonic (2.3 eV) of a *Q*-switched Nd : $YAlO_4$ laser (lasing pulse duration 14 ns). To ensure efficient absorption of the pump radiation (the radiation should be polarized along the semiconductor-filled nanochannels), the pump beam struck the sample at 45° to the sample surface normal and was polarized in the plane of incidence.

Plates of single-crystal CdSe about 20 μm thick were excited by 30-ps second-harmonic pulses of a mode-locked neodymium laser. The pump beam was oriented at an angle of 45° to the (1210) plane.

As seen from Fig. 2, the maximum of the $CdSe/Al_2O_3$ luminescence band is shifted to high frequencies relative to the luminescence line of a weakly excited CdSe single crystal (i.e., to the *A-LO* line representing the first phonon replica of the exciton line). This high-frequency shift and the dependence of the lumi-

nescence intensity on pump polarization suggest that the luminescence band peaking at 1.82 eV derives from exciton transitions in the quantum wires. A comparison of the exciton transition energy with calculated (Fig. 3) dependences of the exciton transition energy on the semiconductor/insulator quantum-wire radius yields 3–6 nm as an estimate of the quantum wire radius. These calculations were made with due account of the large (about 130 meV) halfwidth of the exciton transition line, which should apparently be assigned to a dispersion of the quantum wires in transverse size. These data are consistent with the measured transverse dimensions of nanochannels in the Al_2O_3 matrix in which the semiconductor crystallized. As the pump level increased, the variations in the luminescence spectra of the $CdSe/Al_2O_3$ and single-crystal CdSe samples became fundamentally different. Increasing the pump intensity in single-crystal CdSe plates gave rise to new luminescence bands, which are shifted to lower frequencies with respect to the *A-LO* first phonon replica of the exciton line (Fig. 4a).

As is evident from Figs. 4b and 2, the luminescence spectrum of the $CdSe/Al_2O_3$ sample obtained at low excitation levels consists of two bands. Measurements made to verify the luminescence spectra of the Al_2O_3 matrix with no semiconductor in the nanochannels show that it is the matrix that is responsible for the high-frequency band with the maximum near 2 eV. As the excitation level increases, the 1.82-eV luminescence band of the $CdSe/Al_2O_3$ quantum wires begins to dominate, its asymmetric broadening (contributed primarily by its high-frequency wing) is accompanied by a shift of the maximum toward higher frequencies (Fig. 4c), and the dependence of the luminescence intensity on the excitation level for various spectral intervals identified in Fig. 4b becomes nonlinear (the luminescence intensity was found to saturate; see Fig. 5).

We assign the nonlinear dependence of the luminescence intensity on pump intensity in various spectral regions (Fig. 5) and the variation in spectral shape (Figs. 4b, 4c) to nonlinear absorption in the $CdSe/Al_2O_3$ quantum wires, which exhibit a noticeable dispersion in transverse dimensions. Increasing the excitation level gives rise to the onset of various nonlinear processes in quantum wires, which can coexist and compete with one another [16, 17]. For instance, exciton screening, phase-space filling by excitons, and occupation of states in electronic and hole one-dimensional bands (the dynamic Burstein–Moss effect) account for the decrease in absorption at the exciton transition frequencies, while renormalization (decrease) of the width of the one-dimensional band gap at high carrier concentrations brings about an increase in absorption. The decrease (saturation) in absorption and, hence, the nonlinear variation in the luminescence intensity at the exciton transition frequency occurring as the excitation level increases in

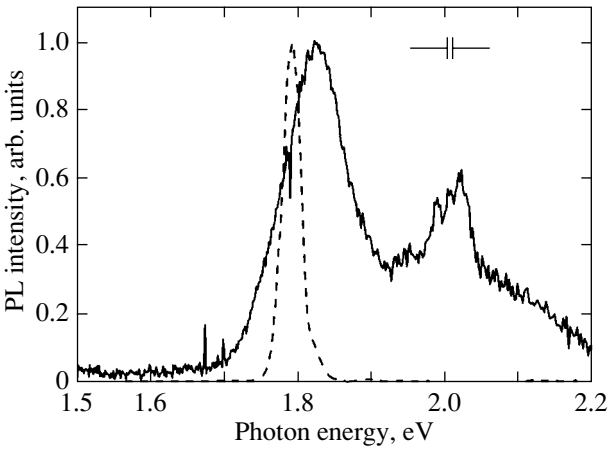

Fig. 2. Photoluminescence spectra of a $CdSe/Al_2O_3$ sample (solid line) and of a CdSe single crystal (dashed line) obtained at low photoexcitation levels. Sample temperature 80 K.

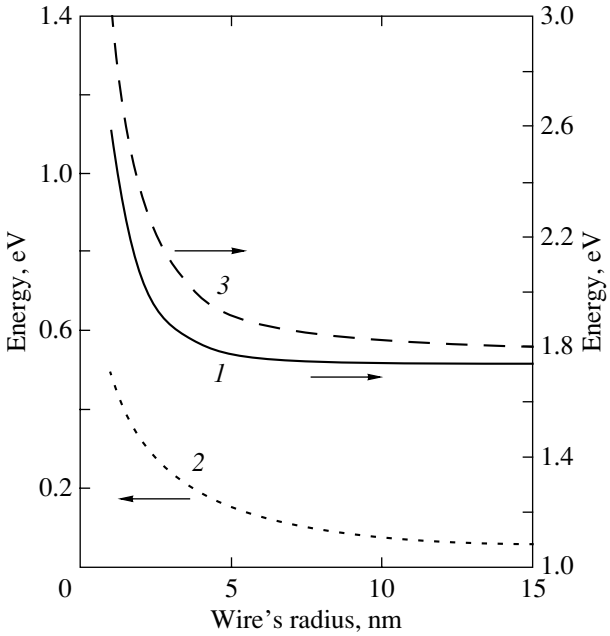

Fig. 3. Calculated dependences of (*1*) the exciton transition energy, (*2*) exciton binding energy, and (*3*) one-dimensional band-gap width on the radius of $CdSe/Al_2O_3$ quantum wires.

semiconductor/insulator quantum wires (which are characterized by a high exciton binding energy) are apparently due to the excitonic phase-space filling becoming a dominant effect. The phase-space filling is actually the result of excitons consisting of electrons and holes, which obey the Pauli exclusion principle. Only the electron–hole states that are not yet occupied by free electrons and holes can participate in exciton creation. Thus, the large number of excited electrons and holes reduces the electron–hole attraction not only

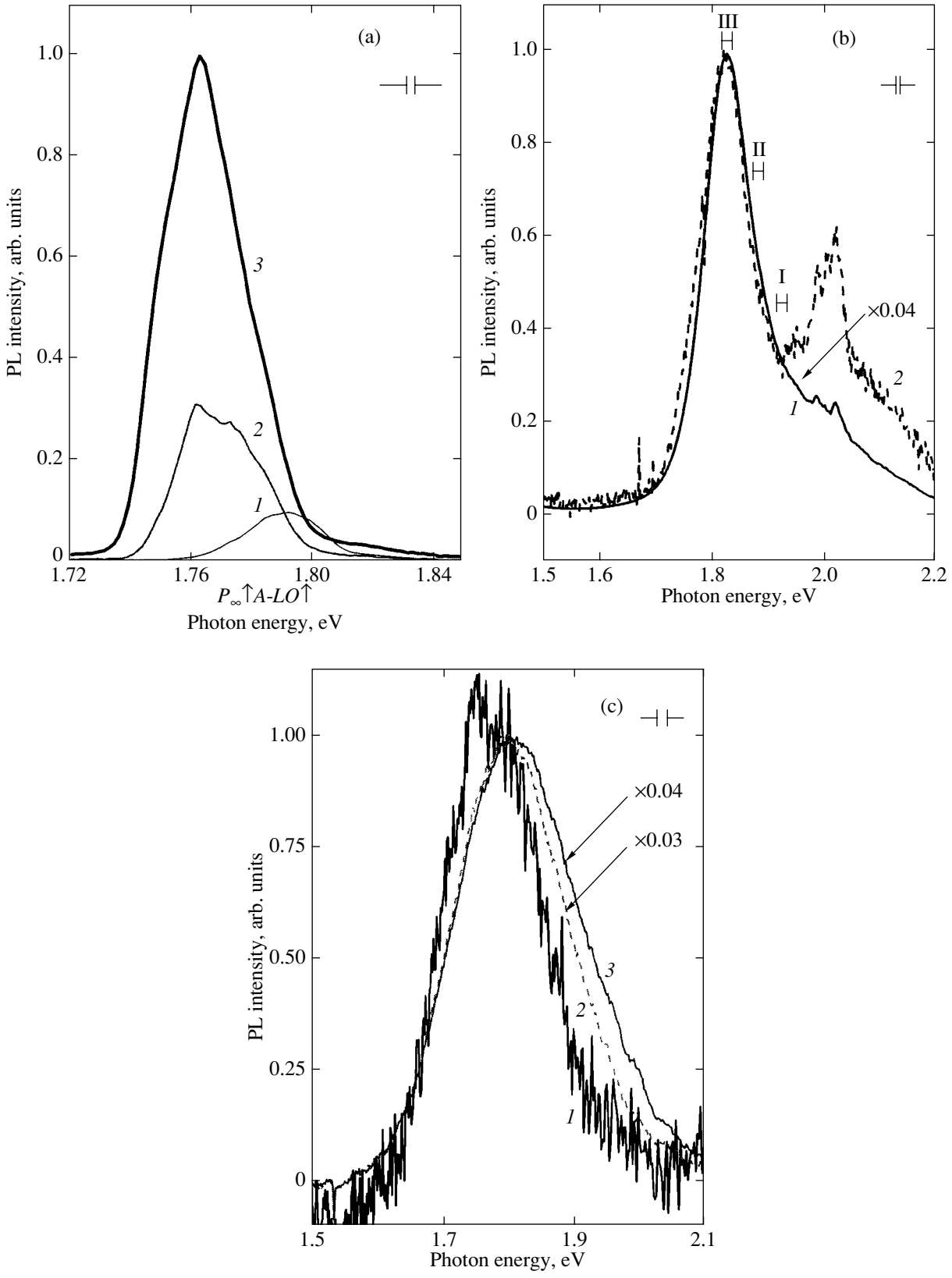

Fig. 4. Photoluminescence spectra of (a) a CdSe single crystal (80 K) and of (b) $CdSe/Al_2O_3$ (80 K) and (c) $CdSe/Al_2O_3$ (300 K) samples obtained at different excitation levels (MW/cm^2): (a) (*1*) 1, (*2*) 10, and (*3*) 100; (b) (*1*) 0.4 and (*2*) 10; and (c) (*1*) 0.4, (*2*) 5, and (*3*) 10.

because of the screening but also as a result of filling of the phase space. Here, the effect of exciton screening by free carriers is apparently weakened, because the motion of carriers in a quantum wire is confined to one direction, in which case they have almost no influence on the field lines in the barrier material. Quantum wires with large transverse dimensions are responsible for the low-frequency part of the luminescence spectrum. Phase-space filling appears primarily in quantum wires with a large cross section, i.e., with a larger exciton effective length. This fact can account for the variation in the luminescence spectral shape with increasing pump power (Figs. 4b, 4c), which is accompanied by a short-wavelength shift of the spectral maximum.

The effective exciton length (l = 5–10 nm) in semiconductor (CdSe) quantum wires with a dielectric barrier calculated for a wire diameter of 6–10 nm [12] enables one to estimate the linear concentration of excitons (the number of excitons per unit length) necessary for the phase-space filling effect to occur as $n_{ph} = l^{-1} \cong 10^6$ cm^{-1}. Estimates show that this exciton concentration was indeed reached in the experiment. The steady-state linear concentration of excited excitons (in our case, the measured exciton lifetime $\tau_{ex} \cong 10^{-10}$ s is much shorter than the laser pump pulse duration τ) is

$$n \cong \beta \frac{\tau_{ex} W}{\tau S L h\nu N} \approx 10^6 - 10^7 \text{ cm}^{-1}.$$

The values used in the estimation were as follows: the energy absorbed in a sample $L \approx 5$ μm thick under maximum pumping is W = 0.2 mJ (windows were etched out in the opaque substrate of the samples to measure the absorption of the second harmonic of the laser); the density of pores (hollow channels) filled by the semiconductor, as measured with an atomic force microscope, is $N \approx 10^{11}$ cm^{-2} [13]; the pumped area is $S = 10^{-2}$ cm^2; and the quantum yield of conversion of absorbed photons to excitons is $\beta \cong 0.5$.

The dependences of the luminescence intensity on the level of excitation for various intervals in the luminescence spectrum (Fig. 5) can be approximated in terms of the saturation model, as was done in [18]. The luminescence intensity ($I \sim n$) is

$$I = \frac{n}{1 + n/n_s},$$

where $n_s \sim P_s$ is the exciton density necessary for saturation and P_s is the corresponding saturation power (saturation parameter). Thus, the saturation power is the pump power at which the luminescence intensity decreases to one-half the value reached in the case of linear growth as the excitation level is increased. The saturation power levels are presented in Fig. 6 for various spectral intervals (for one-dimensional excitons with various effective Bohr lengths). We readily see that the saturation parameter increases with the spectral-interval energy, which may be attributed to either

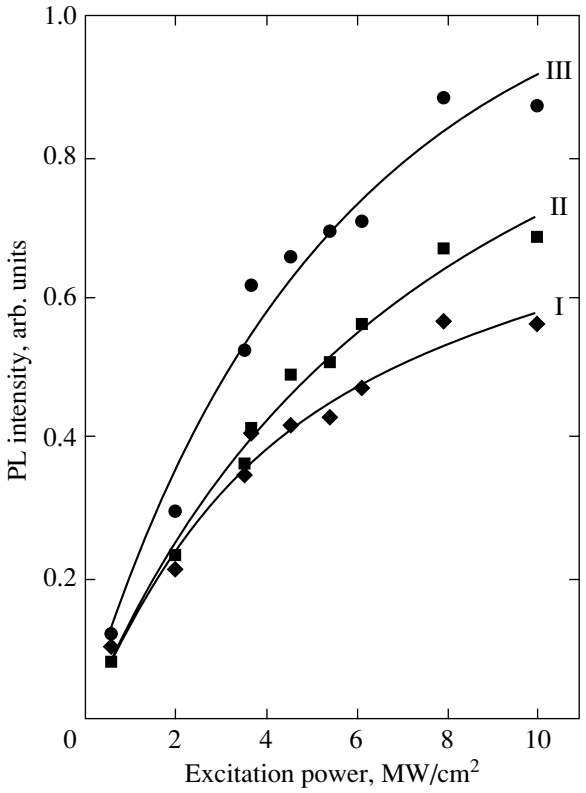

Fig. 5. Photoluminescence intensity of a $CdSe/Al_2O_3$ sample plotted vs. excitation level for various spectral intervals specified in Fig. 4b.

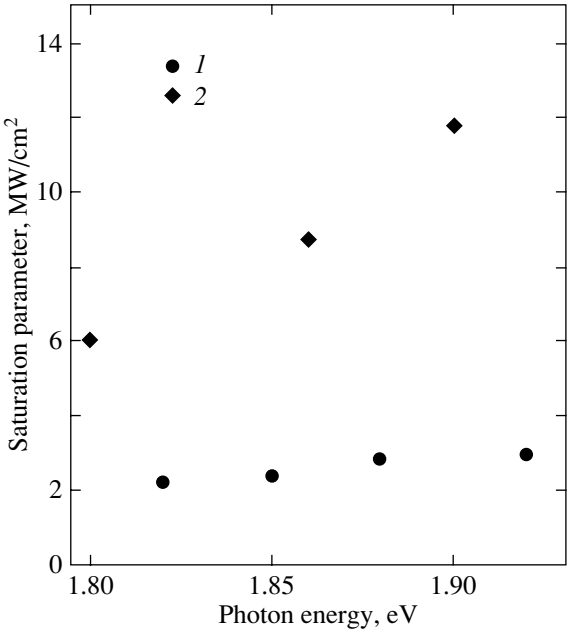

Fig. 6. Spectral dependence of the photoluminescence saturation parameter for $CdSe/Al_2O_3$ quantum wires at a sample temperature of (*1*) 80 and (*2*) 300 K.

the pump intensity increasing to the level where the concentration of excitons with a smaller effective length becomes high enough for the phase-space filling process to set in or to a decrease in the recombination time of these excitons (Fig. 1). The decrease in the saturation parameter observed in samples cooled to liquid-nitrogen temperature (Fig. 6) can be ascribed to the exciton lifetime increasing with decreasing temperature. In this case, the exciton concentration needed to fill the phase space can be produced at lower levels of pump intensity.

As follows from Figs. 4b and 4c, the broadening of the exciton luminescence line and the shift of its maximum to shorter wavelengths observed to occur in $CdSe/Al_2O_3$ quantum wires with increasing pump power manifest themselves more strongly at room temperature than at liquid-nitrogen temperatures. This fact may be due to the pronounced influence of the renormalization of the one-dimensional band-gap width, an effect countering the luminescence band shift to shorter wavelengths at low temperatures. Note that, in CdSe single crystals at high excitation levels and room temperature, the dynamic Burstein–Moss effect dominates, while at low temperatures the renormalization (decrease in the width) of the band gap becomes predominant [19].

As the excitation level increases, new bands appear in CdSe single crystals, which, unlike the luminescence spectra of $CdSe/Al_2O_3$ samples, shift toward lower energies (Fig. 4a). It may be conjectured [20] (see the calculated energies of the corresponding transitions identified by arrows in Fig. 4a) that the *A-LO* luminescence band is replaced by a P_∞ luminescence band due to inelastic exciton–exciton interaction resulting in the formation of a photon and of a free electron and a hole (ex + ex $\longrightarrow$ $h\nu + e + h$) and by an electron–hole plasma luminescence band. In our case, both luminescence bands appear apparently at the same time, because no special measures were taken to produce a spatially uniform excitation level (for instance, by isolating the central part of the excitation spot).

3. CONCLUSIONS

The changes in the luminescence spectra of $CdSe/Al_2O_3$ quantum wires observed to occur at high photoexcitation levels (asymmetric broadening accompanied by a short-wavelength shift of the maximum in the luminescence spectrum), the nonlinear dependence of the luminescence intensity on pump power (luminescence intensity saturation), and the dependence of the saturation parameter on the energy of the corresponding part in the luminescence spectrum (i.e., on the quantum-wire transverse dimensions) and on the sample temperature are explained as being due to the dominant role played by the exciton phase-space filling and the dependence of this effect (and, hence, of the saturation parameter) on the exciton Bohr length and its recombination time.

ACKNOWLEDGMENTS

The authors are indebted to S.A. Gavrilov for preparing $CdSe/Al_2O_3$ quantum wire samples and to E.A. Mulyarov for calculating the binding energy and effective Bohr length of excitons in semiconductor quantum wires embedded in an insulating matrix.

This study was supported in part by the Russian Foundation for Basic Research (project no. 02-02-16167) and the program “Integration.”

REFERENCES

1. T. Ogawa and T. Takagahara, Phys. Rev. B **43**, 14325 (1991).
2. T. Ogawa and T. Takagahara, Phys. Rev. B **43**, 8138 (1991).
3. T. Someya, H. Akiyama, and H. Sakaki, Phys. Rev. Lett. **76**, 2965 (1996).
4. R. Zimmermann, Jpn. J. Appl. Phys. **34**, 228 (1995).
5. L. V. Keldysh, Phys. Status Solidi A **164**, 3 (1997).
6. N. S. Rytova, Dokl. Akad. Nauk SSSR **163**, 1118 (1965) [Sov. Phys. Dokl. **10**, 754 (1966)].
7. A. V. Chaplik and M. V. Éntin, Zh. Éksp. Teor. Fiz. **61**, 2496 (1971) [Sov. Phys. JETP **34**, 1335 (1971)].
8. L. V. Keldysh, Pis’ma Zh. Éksp. Teor. Fiz. **29**, 716 (1979) [JETP Lett. **29**, 658 (1979)].
9. S. Glutsch, F. Bechstedt, W. Wegsheider, and G. Schedelbeck, Phys. Status Solidi A **164**, 405 (1997).
10. V. S. Babichenko, L. V. Keldysh, and A. P. Silin, Fiz. Tverd. Tela (Leningrad) **22**, 1238 (1980) [Sov. Phys. Solid State **22**, 723 (1980)].
11. E. A. Mulyarov and S. G. Tikhodeev, Zh. Éksp. Teor. Fiz. **111**, 274 (1997) [JETP **84**, 151 (1997)].
12. E. A. Muljarov, E. A. Zhukov, V. S. Dneprovskii, and Y. Masumoto, Phys. Rev. B **62**, 7420 (2000).
13. S. F. Gavrilov, V. V. Gusev, V. S. Dneprovskiĭ, E. A. Zhukov, A. N. Syrnikov, and I. V. Yaminskiĭ, Pis’ma Zh. Éksp. Teor. Fiz. **70**, 216 (1999) [JETP Lett. **70**, 216 (1999)].
14. J. I. Pankove, *Optical Processes in Semiconductors* (Prentice Hall, Englewood Cliffs, N.J., 1971; Mir, Moscow, 1973).
15. V. S. Dneprovskiĭ, E. A. Zhukov, O. A. Shalygina, V. L. Lyaskovskiĭ, E. A. Mulyarov, S. A. Gavrilov, and I. Masumoto, Zh. Éksp. Teor. Fiz. **121**, 1362 (2002) [JETP **94**, 1169 (2002)].
16. S. Benner and H. Haug, Europhys. Lett. **16**, 579 (1991).
17. S. Benner and H. Haug, Phys. Rev. B **47**, 15750 (1993).
18. *Nonlinear Photonics*, Ed. by H. M. Gibbs, G. Khitrova, and N. Peighambarian (Springer, Berlin, 1990).
19. R. Zimmermann, Phys. Status Solidi B **146**, 371 (1988).
20. G. A. Boiko, V. S. Dneprovskii, M. V. Kraevskii, K. Marinova, S. M. Oak, E. K. Silina, and V. S. Fokin, Phys. Status Solidi B **85**, 111 (1978).

Translated by G. Skrebtsov

Physics of the Solid State, Vol. 46, No. 9, 2004, pp. 1761–1775. Translated from Fizika Tverdogo Tela, Vol. 46, No. 9, 2004, pp. 1706–1718.
Original Russian Text Copyright © 2004 by Lang, Pavlov, Korovin.

LOW-DIMENSIONAL SYSTEMS AND SURFACE PHYSICS

Theory of Reflection and Absorption of Light by Low-Dimensional Semiconductor Objects in a Strong Magnetic Field under Monochromatic and Pulsed Excitations

I. G. Lang[1], S. T. Pavlov[2, 3], and L. I. Korovin[1]

[1] *Ioffe Physicotechnical Institute, Russian Academy of Sciences, Politekhnicheskaya ul. 26, St. Petersburg, 194021 Russia*

[2] *Facultad de Fisica de la UAZ, Apartado Postal C-580, Zacatecas, 8060 Mexico*

[3] *Lebedev Institute of Physics, Russian Academy of Sciences, Leninskiĭ pr. 53, Moscow, 119991 Russia*

Received January 15, 2004

Abstract—The theoretical principles of reflection and absorption of light by low-dimensional semiconductor objects (quantum wells, quantum wires, quantum dots) under monochromatic and pulsed excitations with an arbitrary pulse shape are developed. A semiconductor object can be placed in a strong constant magnetic field. The normal incidence of light on a quantum well whose width can be comparable to the light wavelength and for which the number of levels of electronic excitations can be arbitrary is considered as an example. An integral equation similar to the Dyson equation is derived for the Fourier components of the electric fields. The solutions to this equation are given for a number of special cases. © *2004 MAIK "Nauka/Interperiodica".*

1. INTRODUCTION

In recent years, great interest has been expressed by researchers in the time-dependent effects associated with the optical response of semiconductor objects [1–4]. This interest stems from the considerable advances achieved in short-pulse engineering, which, in turn, has made it possible to investigate the coherent phenomena occurring in the processes of interaction of light with elementary excitations in different systems.

When an object is irradiated by a short light pulse, there arises a secondary-radiation pulse whose shape significantly differs from the shape of the primary pulse and contains information on exited states of the object, for example, on the lifetime of electron–hole pairs, the energy splitting in magnetopolarons, etc.

In general, secondary radiation is a powerful tool for investigating the internal structure of material objects. Under both monochromatic and pulsed irradiation, there can arise two types of secondary radiation. In particular, upon irradiation of low-dimensional semiconductor objects, secondary radiation of the first type initiates reflection of light, which can be resonant if the frequency ω_l of the exciting light coincides with the frequency ω_0 of one of the discrete energy levels of the electronic system. In a bulk semiconductor, secondary radiation of the first type is responsible for the difference between the true electromagnetic fields and exciting fields, i.e., for the deviation of the permittivity ε from unity.

Secondary radiation of the second type is scattering of light, for example, Raman scattering, which cannot be described in terms of permittivity.

A question now arises as to the origin of secondary radiation of material objects. The exciting light induces alternating electric currents and charges in systems of charged particles. These currents and charge fluctuations generate first-order electromagnetic fields, which, in turn, induce second-order electric currents and charges, etc. By summing over electromagnetic fields of all orders (beginning with the first order), we can obtain exact values of induced electromagnetic fields (actually, we will solve an equation similar to the Dyson equation).

By averaging the densities of induced currents and charges (for example, at zero temperature, i.e., over the ground state of the system of charges), we obtain secondary radiation of the first type (without changing the frequency). Secondary radiation of the second type is governed by fluctuations of the induced current and charge densities and can be accompanied by a change in the frequency, as is the case with Raman scattering. In this work, we investigated only secondary radiation of the first type and light absorption.

Modern semiconductor technologies make it possible to produce high-quality quantum wells for which the radiative broadening of an absorption line can be comparable to the contribution from nonradiative relaxation mechanisms or can even exceed it. In this situation, it will not suffice to use the approximation lowest with respect to the interaction of electrons with an electromagnetic field as it is necessary to take into account all orders of this interaction [5–13].

In the present work, we develop the principles of the theory of secondary radiation of the first type as applied to low-dimensional semiconductor objects. Attention is

1063-7834/04/4609-1761$26.00 © 2004 MAIK "Nauka/Interperiodica"

focused on the situation where an object is placed in a strong constant magnetic field. The results obtained can be applied to the case of irradiation with pulses of arbitrary shape.

This paper is organized as follows. In Section 2, relationships are derived for the average densities of the current and charge induced by a weak electromagnetic field in a spatially confined system of charged particles. These relationships are applicable in the case of any stationary potential, any interaction between particles, and a constant magnetic field of arbitrary strength. The contributions containing the electric fields and the contributions involving their derivatives with respect to the coordinates are separated. Hereinafter, the latter contributions are considered to be small and, hence, are disregarded.

In Sections 3–8, the average density of the induced current in low-dimensional semiconductor objects is calculated without regard for the Coulomb interaction between electrons and holes. At the end of Section 8, the result obtained is generalized with allowance made for the excitonic effect.

In Section 9, we introduce the notion of an electrical conductivity tensor $\sigma_{\alpha\beta}(\mathbf{k}, \omega|\mathbf{r})$, which depends on the spatial coordinates in the case of low-dimensional semiconductor objects due to the spatial inhomogeneity. The general formula derived for the tensor $\sigma_{\alpha\beta}(\mathbf{k}, \omega|\mathbf{r})$ is applicable to any object, for example, quantum wells, wires, or dots.

In Section 10, the electrical conductivity tensor is calculated for quantum wells in both zero and strong magnetic fields. In Section 11, the average density of the induced current is determined for the special case of normal incidence of light on the surface of a quantum well.

In Section 12, we describe a model that corresponds to two degenerate valence bands and simplify the expressions for the average density of the induced current. It is demonstrated that, within this model, the density of the induced charge is zero.

In Section 13, the vector potential is expressed through the integral containing the average density of the induced current with the use of a formula for the retarded potential. The vector potential obtained is used to calculate the induced electric field. Since the induced current density depends on the electric field, we derive an integral equation for this field.

In Section 14, the integral equation is transformed to be applicable to the case of an infinitely deep quantum well.

In Sections 15–17, the integral equation for the electric field is solved for a number of special cases. In Section 15, analysis is performed for a system with many levels of electronic excitations in a narrow quantum well whose width is considerably less than the wavelength of the exciting light. In Section 16, the integral equation is solved for a system with many levels in a wide quantum well, to the lowest order in the interaction of the electromagnetic field with electrons. In Section 17, the electric fields are exactly determined in the case of one excitation level in a wide quantum well.

Finally, in Section 18, it is demonstrated how the expressions for the induced fields are related to the shape of the exciting pulse.

2. EXACT RELATIONSHIPS FOR THE AVERAGE INDUCED CURRENT AND CHARGE DENSITIES

Earlier [14], we showed that the average current and charge densities induced by an external weak electromagnetic field can be expressed through the electric fields and their derivatives with respect to the coordinates as follows:

$$\langle 0|j_{1\alpha}(\mathbf{r}, t)|0\rangle = \langle 0|j_{1\alpha}(\mathbf{r}, t)|0\rangle_{\mathrm{I}} + \langle 0|j_{1\alpha}(\mathbf{r}, t)|0\rangle_{\mathrm{II}}, \quad (1)$$

$$\langle 0|\rho_1(\mathbf{r}, t)|0\rangle = \langle 0|\rho_1(\mathbf{r}, t)|0\rangle_{\mathrm{I}} + \langle 0|\rho_1(\mathbf{r}, t)|0\rangle_{\mathrm{II}}, \quad (2)$$

where the subscript 1 refers to the approximation linear in fields, the subscript I indicates the contributions involving the electric fields, and the subscript II denotes the contribution containing the derivatives of the electric fields with respect to the coordinates, respectively. We obtained the following expressions:

$$\langle 0|j_{1\alpha}(\mathbf{r}, t)|0\rangle_{\mathrm{I}} = \frac{i}{\hbar}\int d\mathbf{r}' \int_{-\infty}^{t} dt' \langle 0|[j_\alpha(\mathbf{r}, t), \bar{d}_\beta(\mathbf{r}', t')]|0\rangle E_\beta(\mathbf{r}', t'), \quad (3)$$

$$\langle 0|j_{1\alpha}(\mathbf{r}, t)|0\rangle_{\mathrm{II}} = \frac{e}{mc}\langle 0|\bar{d}_\beta(\mathbf{r})|0\rangle \frac{\partial a_\beta(\mathbf{r}, t)}{\partial r_\alpha} - \frac{i}{\hbar c}\int d\mathbf{r}' \int_{-\infty}^{t} dt' \langle 0|[j_\alpha(\mathbf{r}, t)\bar{Y}_{\beta\gamma}(\mathbf{r}', t')]|0\rangle \frac{\partial a_\beta(\mathbf{r}', t')}{\partial r'_\gamma}, \quad (4)$$

$$\langle 0|\rho_1(\mathbf{r}, t)|0\rangle_{\mathrm{I}} = \frac{i}{\hbar}\int d\mathbf{r}' \int_{-\infty}^{t} dt' \langle 0|[\rho(\mathbf{r}, t), \bar{d}_\beta(\mathbf{r}', t')]|0\rangle E_\beta(\mathbf{r}', t'), \quad (5)$$

$$\langle 0|\rho_1(\mathbf{r}, t)|0\rangle_{\mathrm{II}} = -\frac{i}{\hbar c}\int d\mathbf{r}' \int_{-\infty}^{t} dt' \langle 0|[\rho(\mathbf{r}, t)\bar{Y}_{\beta\gamma}(\mathbf{r}', t')]|0\rangle \frac{\partial a_\beta(\mathbf{r}', t')}{\partial r'_\gamma}. \quad (6)$$

Here, we used the following designations: $\langle 0|\ldots|0\rangle$ is the averaging over the ground state of the system, $[\ldots]$ is a commutator of two operators, and $\mathbf{j}(\mathbf{r}, t)$ and $\rho(\mathbf{r}, t)$

are the current and charge density operators in the interaction representation:

$$\mathbf{j}(\mathbf{r}, t) = \exp(i\mathcal{H}t/\hbar)\mathbf{j}(\mathbf{r})\exp(-i\mathcal{H}t/\hbar),$$
$$\rho(\mathbf{r}, t) = \exp(i\mathcal{H}t/\hbar)\rho(\mathbf{r})\exp(-i\mathcal{H}t/\hbar),$$

where $\mathcal{H}$ is the Hamiltonian of the system, which is defined by the expressions

$$\mathcal{H} = \frac{1}{2m}\sum_i p_i^2 + V(\mathbf{r}_1, \ldots, \mathbf{r}_N),$$
$$\mathbf{p}_i = \mathbf{P}_i - (e/c)\mathbf{A}_c(\mathbf{r}_i), \quad \mathbf{P}_i = -i\hbar\frac{\partial}{\partial \mathbf{r}_i}. \tag{7}$$

Here, $\mathbf{A}_c(\mathbf{r})$ is the vector potential corresponding to the constant magnetic field $\mathbf{H}_c = \mathrm{curl}\mathbf{A}_c(\mathbf{r})$, in which the system can be placed and which can be rather strong; and $V(\mathbf{r}_1, \ldots, \mathbf{r}_N)$ is the potential energy, including the interaction between particles and an external potential. Hamiltonian (7) describes a system consisting of N particles with charge e and mass m.

The operators $\mathbf{j}(\mathbf{r})$ and $\rho(\mathbf{r})$ are defined as

$$\mathbf{j}(\mathbf{r}) = \sum_i \mathbf{j}_i(\mathbf{r}), \quad \rho(\mathbf{r}) = \sum_i \rho_i(\mathbf{r}),$$
$$\rho_i(\mathbf{r}) = e\delta(\mathbf{r} - \mathbf{r}_i),$$
$$\mathbf{j}_i(\mathbf{r}) = (e/2)\{\delta(\mathbf{r} - \mathbf{r}_i)\mathbf{v}_i + \mathbf{v}_i\delta(\mathbf{r} - \mathbf{r}_i)\}, \tag{8}$$
$$\mathbf{v}_i = \mathbf{p}_i/m,$$

where $\mathbf{r}_i$ is the coordinate of the ith particle. We also introduced the designations

$$\bar{\mathbf{d}}(\mathbf{r}) = \sum_i \bar{\mathbf{r}}_i\rho_i(\mathbf{r}), \quad \bar{Y}_{\beta\gamma}(\mathbf{r}) = \sum_i (j_{j\gamma}\bar{r}_{i\beta} + \bar{r}_{i\beta}j_{i\gamma})/2,$$
$$\bar{\mathbf{r}}_i = \mathbf{r}_i - \langle 0|\mathbf{r}_i|0\rangle, \tag{9}$$

and

$$\mathbf{a}(\mathbf{r}, t) = -c\int_{-\infty}^{\infty} dt'\mathbf{E}(\mathbf{r}, t').$$

The fields are assumed to be classical, and the temperature is taken equal to zero. When deriving expressions (1)–(6), we assumed that charges and currents are absent at infinity and that the fields $\mathbf{E}(\mathbf{r}, t)$ and $\mathbf{H}(\mathbf{r}, t)$ are equal to zero at $t \longrightarrow -\infty$. This corresponds to the adiabatic switching-on of the fields.

3. THE SECOND-QUANTIZATION REPRESENTATION

In this analysis, the contributions with subscript II, which contain the derivatives of the electric fields with respect to the coordinates, are ignored under the assumption that these contributions are small compared to the main contributions with subscript I. This problem was discussed in our previous work [15].

Now, we consider the second-quantization representation with the use of a set of particle wave functions Ψ_m that satisfy the orthogonality and normalizing condition:

$$\int d\mathbf{r}\Psi^*_{m'}(\mathbf{r})\Psi_m(\mathbf{r}) = \delta_{mm'}.$$

In this representation, the current and charge density operators defined by formulas (8) have the form

$$j_\alpha(\mathbf{r}) = \frac{e}{2m}\sum_{m, m'}\{\Psi^*_{m'}(\mathbf{r})p_\alpha\Psi_m(\mathbf{r}) - \Psi_m(\mathbf{r})p_\alpha\Psi^*_{m'}(\mathbf{r})\}a^+_{m'}a_m,$$
$$\rho(\mathbf{r}) = e\sum_{m, m'}\Psi^*_{m'}(\mathbf{r})\Psi_m(\mathbf{r})a^+_{m'}a_m.$$

In turn, within the second-quantization representation, the operator $\bar{\mathbf{d}}(\mathbf{r})$ given by expression (9) takes the form

$$\bar{d}_\alpha(\mathbf{r}) = e(r_\alpha - r_{0\alpha})\sum_{m, m'}\Psi^*_{m'}(\mathbf{r})\Psi_m(\mathbf{r})a^+_{m'}a_m, \tag{10}$$

where

$$r_{0\alpha} = \frac{1}{N}\sum_{m_0}\int d\mathbf{r}\Psi^*_m(\mathbf{r})r_\alpha\Psi_m(\mathbf{r})$$

and m_0 is the set of N states occupied by particles in the ground state $|0\rangle$. Note that the quantity $r_\alpha - r_{0\alpha}$ on the right-hand side of relationship (10) is invariant with respect to the shift in the origin of the coordinates, i.e., with respect to the change $\mathbf{r}$ by $\mathbf{r} + \mathbf{R}$, where $\mathbf{R}$ is an arbitrary vector.

4. ANALYSIS OF SEMICONDUCTOR OBJECTS

Let us consider a semiconductor quantum well (quantum wire, quantum dot) with valence bands and a conduction band. In the set of indices m, the subscripts v and c indicate the valence and conduction bands, respectively (there can be several valence bands). The transitions to higher bands are disregarded. The other indices are designated as ζ.

We calculate the average induced current density from the initial expression (3). The right-hand side of this expression involves only off-diagonal matrix elements of the operators $j_\alpha(\mathbf{r})$ and $\bar{d}_\beta(\mathbf{r})$, because the

operators are under the commutator sign. Therefore, the relationships

$$j_\alpha^{\rm nd}(\mathbf{r}) = \frac{e}{2m}\sum_{v,\zeta,\zeta'}\{\Psi^*_{c\zeta'}(\mathbf{r})p_\alpha\Psi_{v\zeta}(\mathbf{r}) - \Psi_{v\zeta}(\mathbf{r})p_\alpha\Psi^*_{c\zeta'}(\mathbf{r})\}a^+_{c\zeta'}a_{v\zeta} + \text{h.c.}, \quad (11)$$

$$\bar{d}_\alpha^{\rm nd}(\mathbf{r}) = e\sum_{v,\zeta,\zeta'}\Psi^*_{c\zeta'}(\mathbf{r})(r_\alpha - r_{0\alpha})\Psi_{v\zeta}(\mathbf{r})a^+_{c\zeta'}a_{v\zeta} + \text{h.c.}$$

should be substituted into the right-hand side of expression (3).

In relationships (11) and below, we deal with electrons. Hence, we have $e = -|e|$ and $m = m_0$, where m_0 is the mass of a free electron. The superscript nd refers to the part of the operator that contains only off-diagonal matrix elements.

5. THE EFFECTIVE-MASS APPROXIMATION

It is assumed that the sizes of an object, namely, the quantum-well width d or the wire or dot sizes, are considerably larger than the lattice constant a and the slowly varying factor in the wave function changes over distances significantly larger than a. In this case, it is possible to use the effective-mass approximation, according to which

$$\Psi_{\mu\zeta}(\mathbf{r}) = u_{0\mu}(\mathbf{r})\psi_{\mu\zeta}(\mathbf{r}), \quad (12)$$

where $u_{0\mu}(\mathbf{r})$ is a rapidly varying dimensionless factor, $\psi_{\mu\zeta}(\mathbf{r})$ is a slowly varying factor, and $\mu = c$ or v.

In relationships (11), we ignore the action of the operators P_α on the slowly varying factors in the wave functions (12). Then, we obtain the approximate expressions

$$j_\alpha^{\rm nd}(\mathbf{r}) \simeq \frac{e}{2m_0}\sum_v\{u^*_{0c}(\mathbf{r})p_\alpha u_{0v}(\mathbf{r}) - u_{0v}(\mathbf{r})p_\alpha u^*_{0c}(\mathbf{r})\} \times\sum_{\zeta,\zeta'}\psi^*_{c\zeta'}(\mathbf{r})\psi_{v\zeta}(\mathbf{r})a^+_{c\zeta'}a_{v\zeta} + \text{h.c.}, \quad (13)$$

$$\bar{d}_\alpha^{\rm nd}(\mathbf{r}) \simeq e\sum_v u^*_{0c}(\mathbf{r})u_{0v}(\mathbf{r})(r_\alpha - r_{0\alpha}) \times\sum_{\zeta,\zeta'}\psi^*_{c\zeta'}(\mathbf{r})\psi_{v\zeta}(\mathbf{r})a^+_{c\zeta'}a_{v\zeta} + \text{h.c.} \quad (14)$$

Next, we eliminate the rapidly varying factors on the right-hand sides of expressions (13) and (14). For this purpose, we introduce the Fourier components

$$j_\alpha(\boldsymbol{\kappa}) = \int d\mathbf{r}\, j_\alpha(\mathbf{r})\exp(-i\boldsymbol{\kappa}\mathbf{r}),$$

$$\bar{d}_\alpha(\boldsymbol{\kappa}) = \int d\mathbf{r}\,\bar{d}_\alpha(\mathbf{r})\exp(-i\boldsymbol{\kappa}\mathbf{r}).$$

For $\kappa a \ll 1$, we approximately obtain

$$\mathbf{j}^{\rm nd}(\boldsymbol{\kappa}) = \frac{e}{m_0}\sum_v\mathbf{p}_{cv} \times\sum_{\zeta,\zeta'}\{\int d\mathbf{r}\psi^*_{c\zeta'}(\mathbf{r})\psi_{v\zeta}(\mathbf{r})e^{-i\boldsymbol{\kappa}\mathbf{r}}\}a^+_{c\zeta'}a_{v\zeta} + \text{h.c.},$$

$$\bar{\mathbf{d}}^{\rm nd}(\boldsymbol{\kappa}) = \sum_v\mathbf{d}_{cv} \times\sum_{\zeta,\zeta'}\{\int d\mathbf{r}\psi^*_{c\zeta'}(\mathbf{r})\psi_{v\zeta}(\mathbf{r})e^{-i\boldsymbol{\kappa}\mathbf{r}}\}a^+_{c\zeta'}a_{v\zeta} + \text{h.c.},$$

where

$$\mathbf{p}_{cv} = \frac{1}{\Omega}\int_\Omega d\mathbf{r}u^*_{0c}(\mathbf{r})\mathbf{P}u_{0v}(\mathbf{r}),$$

$$\mathbf{d}_{cv} = \frac{e}{\Omega}\int_\Omega d\mathbf{r}u^*_{0c}(\mathbf{r})\mathbf{r}u_{0v}(\mathbf{r}), \quad (15)$$

and Ω is the volume of the crystal unit cell over which integration is performed.

In the first equality (15), we replaced the operator $\mathbf{p}$ [see expression (7)] by the operator $\mathbf{P}$. When the system is in a strong magnetic field $\mathbf{H}_c = \text{curl}\,\mathbf{A}_c(\mathbf{r})$ and operator $\mathbf{p}$ contains the term $-(e/c)\mathbf{A}_c(\mathbf{r})$, this term makes a small contribution to the quantity $\mathbf{p}_{cv}$ and can be omitted in the effective-mass approximation.

By assuming that our interest will be only in the long-wavelength components $\mathbf{j}^{\rm nd}(\mathbf{r})$ and $\bar{\mathbf{d}}^{\rm nd}(\mathbf{r})$, we change over from the $\boldsymbol{\kappa}$ representation to the $\mathbf{r}$ representation and obtain

$$\mathbf{j}^{\rm nd}(\mathbf{r}) = \frac{e}{m_0}\sum_v\mathbf{p}_{cv}\sum_{\zeta,\zeta'}\psi^*_{c\zeta'}(\mathbf{r})\psi_{v\zeta}(\mathbf{r})a^+_{c\zeta'}a_{v\zeta} + \text{h.c.}, \quad (16)$$

$$\bar{\mathbf{d}}^{\rm nd}(\mathbf{r}) = \sum_v\mathbf{d}_{cv}\sum_{\zeta,\zeta'}\psi^*_{c\zeta'}(\mathbf{r})\psi_{v\zeta}(\mathbf{r})a^+_{c\zeta'}a_{v\zeta} + \text{h.c.} \quad (17)$$

6. WAVE FUNCTIONS OF ELECTRONS IN A QUANTUM WELL

Now, we consider two specific examples of electron wave functions in a quantum well within the effective-mass approximation. For free electrons, we have

$$\psi_{\mathbf{k}_\perp,l}(\mathbf{r}) = S_0^{-1/2}\exp(i\mathbf{k}_\perp\mathbf{r}_\perp)\varphi_l(z),$$

where S_0 is the normalization area, the z axis is perpendicular to the quantum-well plane, and the real function $\varphi_l(z)$ corresponds to the levels $l = 1, 2, \ldots$ of the quantum confinement of electrons. For quantum wells with

a finite depth, the functions $\varphi_l(z)$ and the corresponding energy levels were determined, for example, in our earlier work [16].

The second example is provided by electrons in a quantum well in a strong magnetic field $\mathbf{H}_c$ perpendicular to the quantum-well plane. The z axis is aligned parallel to the magnetic field. The gauge of the vector potential can be chosen in the form

$$\mathbf{A}_c(\mathbf{r}) = \mathbf{A}_c(0, xH_c, 0).$$

Then, the electron wave functions can be written as follows:

$$\varphi_{nk_yl}(\mathbf{r}) = \Phi_n(x + a_H^2 k_y)\exp(ik_y y)\varphi_l(z)/\sqrt{L_y},$$

$$\Phi_n(x) = \frac{1}{\sqrt{\pi^{1/2}2^n n! a_H}} H_n(x/a_H)\exp(-x^2/2a_H^2),$$

where $a_H = \sqrt{c\hbar/|e|H_c}$, $H_n(t)$ are the Hermitian polynomials, and L_y is the normalization length.

7. THE NOTION OF A HOLE IN THE VALENCE BAND

It is assumed that the components of the hole quasimomentum obey the equalities $\mathbf{k}_{h\perp} = -\mathbf{k}_\perp$ and $k_{hy} = -k_y$ (in a strong magnetic field H_c) and the annihilation operator $a_{v\zeta}$ for an electron in the valence band is equal to the creation operator for a hole. We introduce a set of indices η describing the quantum numbers of an electron–hole pair and its creation (annihilation) operator a_η^+ (a_η). Then, from relationships (16) and (17), we find

$$\mathbf{j}^{\mathrm{nd}}(\mathbf{r}) = (e/m_0)\sum_\eta \{\mathbf{p}_{cv}F_\eta^*(\mathbf{r})a_\eta^+ + \mathbf{p}_{cv}^* F_\eta(\mathbf{r})a_\eta\}, \quad (18)$$

$$\bar{\mathbf{d}}^{\mathrm{nd}}(\mathbf{r}) = \sum_\eta \{\mathbf{d}_{cv}F_\eta^*(\mathbf{r})a_\eta^+ + \mathbf{d}_{cv}^* F_\eta(\mathbf{r})a_\eta\}, \quad (19)$$

where $F_\eta(\mathbf{r})$ is the wave function of the electron–hole pair at $\mathbf{r}_e = \mathbf{r}_h = \mathbf{r}$ and $\mathbf{r}_e(\mathbf{r}_h)$ is the radius vector of the electron (hole).

For free electron–hole pairs in a quantum well, we have

$$F_\eta(\mathbf{r}) = \exp[i(\mathbf{k}_{e\perp} + \mathbf{k}_{v\perp})\mathbf{r}_\perp]\varphi_{l_e}^e(z)\varphi_{l_v}^v(z)/S_0, \quad (20)$$

where the set η involves the indices v, $\mathbf{k}_{e\perp}$, $\mathbf{k}_{v\perp}$, l_e, and l_v. The energy of the electron–hole pair is reckoned from the ground-state energy and can be represented in the form

$$E_\eta = \hbar\omega_\eta = \hbar\omega_g + \varepsilon_{l_e}^e + \varepsilon_{l_v}^v + \frac{\hbar^2 k_{e\perp}^2}{2m_e} + \frac{\hbar^2 k_{v\perp}^2}{2m_v}, \quad (21)$$

where $\hbar\omega_g$ is the band gap and $m_e(m_v)$ is the effective mass of the electron (hole).

For pairs in a quantum well in a strong magnetic field, we obtain

$$F_\eta(\mathbf{r}) = \Phi_{n_e}(x + a_H^2 k_{ey})\Phi_{n_v}(x - a_H^2 k_{vy}) \times \exp(i(k_{ey} + k_{vy})y)\varphi_{l_e}^e(z)\varphi_{l_v}^v(z)/L_y, \quad (22)$$

where the set η includes the indices v, n_e, n_v, k_{ey}, k_{vy}, l_e, and l_v. The corresponding energy can be written in the form

$$E_\eta = \hbar\omega_g + \varepsilon_{l_e}^e + \varepsilon_{l_v}^v + \hbar\Omega_{eH}(n_e + 1/2) + \hbar\Omega_{vH}(n_v + 1/2), \quad (23)$$

where $\Omega_{e(v)H} = |e|H_c/(m_{e(v)}c)$ is the cyclotron frequency of the electron (hole). It can be shown that formulas (18) and (19) are also applicable to the case where the Coulomb interaction between electrons and holes makes a significant contribution. For example, at $H_c = 0$, the discrete energy levels in the quantum well correspond to exciton states. Then, $F_\eta(\mathbf{r})$ is the exciton wave function at $\mathbf{r}_c = \mathbf{r}_h = \mathbf{r}$ and η is the set of indices characterizing the exciton. In a strong magnetic field, the Coulomb forces can change the positions of the energy levels and affect the function $F_\eta(\mathbf{r})$.

8. THE AVERAGE INDUCED CURRENT DENSITY IN SEMICONDUCTOR OBJECTS

The relationship between the matrix elements $\mathbf{p}_{cv}$ and $\mathbf{d}_{cv}$ defined by expressions (15) can be easily found from the formula $v_\alpha = (i/\hbar)[\mathcal{H}, r_\alpha]$. According to this expression, we can write the relationship

$$\mathbf{d}_{cv} = -(ie/(m_0\omega_g))\mathbf{p}_{cv}. \quad (24)$$

Substituting relationship (24) into formula (19) and then formulas (18) and (19) into relationship (3) gives

$$\langle 0|j_{1\alpha}(\mathbf{r}, t)|0\rangle = \frac{e^2}{\hbar\omega_g m_0^2}\int d\mathbf{r}' \int_{-\infty}^{\infty} dt'\Theta(t - t') \times \sum_{\eta,\eta'} \{p_{cv'\alpha}^* p_{cv\beta} F_{\eta'}(\mathbf{r})F_\eta^*(\mathbf{r}')\langle 0|a_{\eta'}(t)a_\eta^+(t')|0\rangle + p_{cv'\alpha}p_{cv\beta}^* F_{\eta'}^*(\mathbf{r})F_\eta(\mathbf{r}')\langle 0|a_\eta(t')a_{\eta'}^+(t)|0\rangle\}E_\beta(\mathbf{r}', t'), \quad (25)$$

where $\Theta(\tau) = 1$ at $\tau > 0$ and $\Theta(\tau) = 0$ at $\tau < 0$.

As follows from [(7.35), 17], averaging over the ground state leads to the following expression:

$$\langle 0|a_{\eta'}(t)a_\eta^+(t')|0\rangle = \delta_{\eta,\eta'}\exp[i\omega_\eta(t' - t) - (\gamma_\eta/2)|t - t'|], \quad (26)$$

where γ_η is the reciprocal nonradiative lifetime of the state with the set of indices η.

Substituting relationship (26) into formula (25) and changing the variable $t' \longrightarrow t + t'$, we obtain

$$\langle 0|j_{1\alpha}(\mathbf{r}, t)|0\rangle = \frac{e^2}{\hbar\omega_g m_0^2}\sum_\eta \Bigg\{ p^*_{cv\alpha}p_{cv\beta}F_\eta(\mathbf{r}) \times \int d\mathbf{r}' F^*_\eta(\mathbf{r}') \int_{-\infty}^{0} dt' e^{i\omega_\eta t' + (\gamma_\eta/2)t'} + p_{cv\alpha}p^*_{cv\beta}F^*_\eta(\mathbf{r}) \times \int d\mathbf{r}' F_\eta(\mathbf{r}') \int_{-\infty}^{0} dt' e^{-i\omega_\eta t' + (\gamma_\eta/2)t'} \Bigg\} E_\beta(\mathbf{r}', t + t'). \quad (27)$$

Expression (27) is applicable over a wide range, for example, for exciton states in zero and strong magnetic fields, i.e., with allowance made for the Coulomb interaction between electrons and holes in the cases where this interaction is significant. Undeniably, the form of the functions $F_\eta(\mathbf{r})$ with inclusion of the Coulomb interaction should differ from those described by relationships (20) and (22). Moreover, expression (27) is valid for other low-dimensional semiconductor objects, such as quantum wires or dots.

9. ELECTRICAL CONDUCTIVITY TENSOR

Expression (27) can be rewritten in the following form:

$$\langle 0|j_{1\alpha}(\mathbf{r}, t)|0\rangle = \int d\mathbf{r}' \int_{-\infty}^{\infty} dt' \sigma_{\alpha\beta}(\mathbf{r}', t'|\mathbf{r}, t) E_\beta(\mathbf{r} - \mathbf{r}', t - t'), \quad (28)$$

where $\sigma_{\alpha\beta}(\mathbf{r}', t'|\mathbf{r}, t)$ is the electrical conductivity tensor. From expression (27), we find

$$\sigma_{\alpha\beta}(\mathbf{r}', t'|\mathbf{r}, t) = \frac{e^2}{\hbar\omega_g m_0^2}\Theta(t') \times \sum_\eta \{ p^*_{cv\alpha}p_{cv\beta}F_\eta(\mathbf{r}) + F^*_\eta(\mathbf{r} - \mathbf{r}')e^{-i\omega_\eta t' - (\gamma_\eta/2)t'} + \text{c.c.}\}. \quad (29)$$

It can be seen from formula (29) that the tensor $\sigma_{\alpha\beta}(\mathbf{r}', t'|\mathbf{r}, t)$ does not depend on the time t if the potential energy $V(\mathbf{r}_1, \ldots, \mathbf{r}_N)$ in Hamiltonian (7) is independent of the time t, which is assumed. This fact follows from the time homogeneity. Therefore, hereafter, we will use the designation

$$\sigma_{\alpha\beta}(\mathbf{r}', t'|\mathbf{r}) = \sigma_{\alpha\beta}(\mathbf{r}', t'|\mathbf{r}, t).$$

Next, we take the Fourier transform. The electric field can be written in the form

$$E_\alpha(\mathbf{r}, t) = E^{(+)}_\alpha(\mathbf{r}, t) + E^{(-)}_\alpha(\mathbf{r}, t), \quad (30)$$

where

$$E^{(+)}_\alpha(\mathbf{r}, t) = \frac{1}{(2\pi)^4}\int d\mathbf{k}\int_0^\infty d\omega E_\alpha(\mathbf{k}, \omega)e^{i(\mathbf{kr} - \omega t)}, \quad (31)$$

$$E^{(-)}_\alpha(\mathbf{r}, t) = (E^{(+)}_\alpha(\mathbf{r}, t))^*,$$
$$E_\alpha(\mathbf{k}, \omega) = \int d\mathbf{r}\int_{-\infty}^{\infty} dt E_\alpha(\mathbf{r}, t)e^{i(-\mathbf{kr} + \omega t)}. \quad (32)$$

Separation is usually carried out in formula (30) in order to avoid the use of negative frequencies ω.

Let us introduce the Fourier transform of the tensor $\sigma_{\alpha\beta}(\mathbf{r}', t'|\mathbf{r})$ with respect to the variables $\mathbf{r}'$ and t':

$$\sigma_{\alpha\beta}(\mathbf{k}, \omega|\mathbf{r}) = \int d\mathbf{r}' \int_{-\infty}^{\infty} dt' \sigma_{\alpha\beta}(\mathbf{r}', t'|\mathbf{r})e^{i(-\mathbf{kr}' + \omega t')}. \quad (33)$$

Then, from relationships (28), (31), and (32), we find

$$\langle 0|j_{1\alpha}(\mathbf{r}, t)|0\rangle = \frac{1}{(2\pi)^4}\int d\mathbf{k} \times \int_0^\infty d\omega \sigma_{\alpha\beta}(\mathbf{k}, \omega|\mathbf{r})E_\beta(\mathbf{k}, \omega)e^{i\mathbf{kr} - i\omega t} + \text{c.c.} \quad (34)$$

For spatially homogeneous systems, such as bulk semiconductor crystals, we have

$$\sigma_{\alpha\beta}(\mathbf{k}, \omega|\mathbf{r}) = \sigma_{\alpha\beta}(\mathbf{k}, \omega).$$

By using formula (29), taking the Fourier transform (33), and integrating over t', we obtain

$$\sigma_{\alpha\beta}(\mathbf{k}, \omega|\mathbf{r}) = \frac{ie^2}{\hbar\omega_g m_0^2} \times \sum_\eta \Bigg\{ p^*_{cv\alpha}p_{cv\beta}F_\eta(\mathbf{r})\frac{\int d\mathbf{r}' e^{-i\mathbf{kr}'}F^*_\eta(\mathbf{r} - \mathbf{r}')}{\omega - \omega_\eta + i\gamma_\eta/2} + p_{cv\alpha}p^*_{cv\beta}F^*_\eta(\mathbf{r})\frac{\int d\mathbf{r}' e^{-i\mathbf{kr}'}F_\eta(\mathbf{r} - \mathbf{r}')}{\omega + \omega_\eta + i\gamma_\eta/2} \Bigg\}. \quad (35)$$

Note that the electrical conductivity tensor possesses the following property:

$$\sigma^*_{\alpha\beta}(\mathbf{k}, \omega|\mathbf{r}) = \sigma_{\alpha\beta}(-\mathbf{k}, -\omega|\mathbf{r}).$$

It should be emphasized that expressions (34) and (36), in principle, enable one to calculate the average induced current density under monochromatic and pulsed light excitation at an arbitrary direction of the incident light, i.e., not only for normal incidence but also for oblique incidence of light on the quantum-well plane.

10. ELECTRICAL CONDUCTIVITY TENSOR IN A QUANTUM WELL

It follows from formulas (20) and (22) that, for free electron–hole pairs in zero and strong magnetic fields, the function $F_\eta(\mathbf{r})$ can be represented as the product

$$F_\eta(\mathbf{r}) = Q_\pi(\mathbf{r}_\perp)\phi_\chi(z), \tag{36}$$

where π is the set of indices v, $\mathbf{k}_{e\perp}$, and $\mathbf{k}_{v\perp}$ at $H_c = 0$ and v, n_e, n_v, k_{cy}, and k_{vy} in a strong magnetic field; χ is the set of indices v, l_e, and l_v; and

$$\phi_\chi(z) = \varphi^e_{l_e}(z)\varphi^v_{l_v}(z). \tag{37}$$

Separation (36) is also applicable to the case where the Coulomb interaction of electrons and holes can substantially affect only the motion of particles along the z axis. This situation occurs under the condition [18] $a_{\text{exc}}^2 \gg a_H^2$ (i.e., in sufficiently strong magnetic fields), where $a_{\text{exc}} = \hbar^2\varepsilon_0/(\mu e^2)$ is the Wannier–Mott exciton radius in the absence of the magnetic field, ε_0 is the static permittivity, and $\mu = m_e m_v/(m_e + m_v)$ is the effective mass. At $a_{\text{exc}} \gg d$ (i.e., for sufficiently narrow quantum wells), the Coulomb forces weakly affect the motion of particles along the z axis and the functions $\phi_\chi(z)$ have the form of formula (37). In the opposite case, at $a_{\text{exc}} \ll d$, formula (37) is inapplicable. For GaAs, we obtain $a_{\text{exc}} = 146$ Å and $a_H^{\text{res}} = 57.2$ Å, where a_H^{res} corresponds to the magnetic field H_{res} in which the magnetophonon resonance $\Omega_{eH} = \omega_{LO}$ takes place. From relationships (36) and (35), we find

$$\begin{aligned}\sigma_{\alpha\beta}(\mathbf{k}, \omega|\mathbf{r}) &= \frac{ie^2}{\hbar\omega_g m_0^2} e^{-i\mathbf{kr}} \sum_\eta \phi_\chi(z) \\ &\times \int_{-\infty}^{\infty} dz' \phi_\chi(z') \exp(ik_z z') \left\{ p^*_{cv\alpha} p_{cv\beta} Q_\pi(\mathbf{r}_\perp) \right. \\ &\times \int d\mathbf{r}'_\perp Q^*_\pi(\mathbf{r}'_\perp) \frac{\exp(i\mathbf{k}_\perp \mathbf{r}'_\perp)}{\omega - \omega_\eta + i\gamma_\eta/2} + p_{cv\alpha} p^*_{cv\beta} Q^*_\pi(\mathbf{r}_\perp) \\ &\left. \times \int d\mathbf{r}'_\perp Q_\pi(\mathbf{r}'_\perp) \frac{\exp(i\mathbf{k}_\perp \mathbf{r}'_\perp)}{\omega + \omega_\eta + i\gamma_\eta/2} \right\}.\end{aligned} \tag{38}$$

For free electron–hole pairs at $H_c = 0$, we have

$$Q_\pi(\mathbf{r}_\perp) = S_0^{-1} \exp[i(\mathbf{k}_{e\perp} + \mathbf{k}_{v\perp})\mathbf{r}_\perp].$$

By substituting this expression into formula (38) and performing integration over $\mathbf{r}'_\perp$, we obtain

$$\begin{aligned}\sigma_{\alpha\beta}(\mathbf{k}, \omega|\mathbf{r}) &= \frac{ie^2}{\hbar\omega_g m_0^2 S_0} \exp(-ik_z z) \\ &\times \sum_\eta \phi_\chi(z) R^*_\chi(k_z) \left\{ \frac{p^*_{cv\alpha} p_{cv\beta} \delta_{\mathbf{K}_\perp, \mathbf{k}_\perp}}{\omega - \omega_\eta + i\gamma_\eta/2} \right. \\ &\left. + \frac{p_{cv\alpha} p^*_{cv\beta} \delta_{\mathbf{K}_\perp, -\mathbf{k}_\perp}}{\omega + \omega_\eta + i\gamma_\eta/2} \right\},\end{aligned} \tag{39}$$

where $\mathbf{K}_\perp = \mathbf{k}_{e\perp} + \mathbf{k}_{v\perp}$,

$$R_\chi(k_z) = \int_{-\infty}^{\infty} dz \exp(-ik_z z)\phi_\chi(z),$$

and the energy $\hbar\omega_\eta$ is determined from formula (21). For electron–hole pairs in a strong magnetic field, we derive

$$\begin{aligned}Q_\pi(\mathbf{r}_\perp) &= \Phi_{ne}(x + a_H^2 k_{ey}) \Phi_{nv}(x - a_H^2 k_{vy}) \\ &\times \exp[i(k_{ey} + k_{vy})y]/L_y.\end{aligned} \tag{40}$$

Now, we substitute expression (40) into relationship (38), integrate over the variable y', and sum over indices k_{ey} and k_{vy}, which do not affect the energies $\hbar\omega_\eta$ given by formula (23). As a result, we find

$$\begin{aligned}&\sigma_{\alpha\beta}(\mathbf{k}, \omega|\mathbf{r}) \\ &= \frac{ie^2}{2\pi\hbar\omega_g m_0^2 a_H^2} \exp(-ik_z z) \sum_\xi \phi_\chi(z) R^*_\chi(k_z) \\ &\times \left\{ \frac{p^*_{cv\alpha} p_{cv\beta} \Xi_{n_c, n_v}(k_x, k_y)}{\omega - \omega_\xi + i\gamma_\xi/2} \right. \\ &\left. + \frac{p_{cv\alpha} p^*_{cv\beta} \Xi_{n_c, n_v}(-k_x, -k_y)}{\omega + \omega_\xi + i\gamma_\xi/2} \right\},\end{aligned} \tag{41}$$

$$\Xi_{n_e, n_v}(k_x, k_y) = \left| \int_{-\infty}^{\infty} dt \Phi_{n_e}(t) \Phi_{n_v}(t - a_H^2 k_y) e^{ik_x t} \right|^2,$$

where ξ is the set of indices χ, n_e, and n_v and the energy $\hbar\omega_\xi = \hbar\omega_\eta$.

It is worth noting that, as follows from expressions (39) and (41), the quantities $\sigma_{\alpha\beta}(\mathbf{k}, \omega|\mathbf{r})$ in the case of the quantum well at $H_c = 0$ or if the vector $\mathbf{H}_c$ is aligned parallel to the z axis depend only on z. This is associated with the fact that the system is inhomoge-

neous only along the z axis perpendicular to the quantum-well plane. Consequently, we can write

$$\sigma_{\alpha\beta}(\mathbf{k}, \omega|\mathbf{r}) = \sigma_{\alpha\beta}(\mathbf{k}, \omega|z).$$

After substituting formula (39) or (41) into expression (34), it can be applied to the case where the light is incident on the quantum well at an arbitrary angle with respect to the z axis under monochromatic and pulsed irradiation.

11. NORMAL INCIDENCE OF LIGHT ON THE SURFACE OF THE QUANTUM WELL

For normal incidence of light, the electric field $\mathbf{E}(\mathbf{r}, t)$ depends only on the variables z and t. We introduce the Fourier component of the field with respect to the variable t:

$$E_\beta(z, \omega) = \int_{-\infty}^{\infty} dt e^{i\omega t} E_\beta(z, t). \tag{42}$$

With the use of formulas (34) and (39), it is possible to show that the average induced current density at $H_c = 0$ is described by the expression

$$\begin{aligned}\langle 0|j_{1\alpha}(\mathbf{r}, t)|0\rangle &= \frac{i}{2\pi}\left(\frac{e}{m_0}\right)^2 \frac{1}{\hbar\omega_g S_0} \\ &\times \sum_\chi \phi_\chi(z) \int_{-\infty}^{\infty} d\omega e^{-i\omega t} \int_{-\infty}^{\infty} dz' \phi_\chi(z') E_\beta(z', \omega) \\ &\times \left\{ p^*_{cv\alpha} p_{cv\beta} \sum_{\mathbf{k}_\perp} (\omega - \omega_\kappa + i\gamma_\kappa/2)^{-1} \right. \\ &\left. + p_{cv\alpha} p^*_{cv\beta} \sum_{\mathbf{k}_\perp} (\omega + \omega_\kappa + i\gamma_\kappa/2)^{-1} \right\},\end{aligned} \tag{43}$$

where κ is the set of indexes χ, $\mathbf{k}_\perp = \mathbf{k}_{e\perp} = -\mathbf{k}_{v\perp}$, and

$$\omega_\kappa = \omega_g + \varepsilon^e_{l_e}/\hbar + \varepsilon^v_{l_v}/\hbar + \hbar k^2_\perp/2\mu.$$

In relationship (43), we change over from integration over ω from 0 to ∞ to integration from $-\infty$ to ∞. This is more convenient for specific calculations, because the integration contour can be closed in the upper or lower half-plane.

In a strong magnetic field, from relationships (34) and (41), we obtain

$$\begin{aligned}\langle 0|j_{1\alpha}(\mathbf{r}, t)|0\rangle &= \frac{i}{(2\pi)^2}\left(\frac{e}{m_0}\right)^2 \frac{1}{\hbar\omega_g a_H^2} \\ &\times \sum_\chi \phi_\chi(z) \int_{-\infty}^{\infty} d\omega e^{-i\omega t} \int_{-\infty}^{\infty} dz' \phi_\chi(z') E_\beta(z', \omega) \\ &\times \left\{ p^*_{cv\alpha} p_{cv\beta} \sum_n (\omega - \omega_\lambda + i\gamma_\lambda/2)^{-1} \right. \\ &\left. + p_{cv\alpha} p^*_{cv\beta} \sum_n (\omega + \omega_\lambda + i\gamma_\lambda/2)^{-1} \right\},\end{aligned} \tag{44}$$

where

$$\omega_\lambda = \omega_g + \varepsilon^e_{l_e}/\hbar + \varepsilon^v_{l_v}/\hbar + \Omega_{\mu H}(n + 1/2),$$
$$\Omega_{\mu H} = |e|H_c/(\mu c).$$

In deriving expression (44), we used the relationship

$$\Xi_{n_e, n_v}(k_x = 0, k_y = 0) = \left| \int_{-\infty}^{\infty} dt \Phi_{n_e}(t) \Phi_{n_v}(t) \right|^2 = \delta_{n_e, n_v},$$

This relationship corresponds to the following selection rule: for normal incidence of light, electron–hole pairs in which electrons and holes have identical Landau quantum numbers are excited.

Since the electron–hole pairs with zero quasi-momentum in the quantum-well plane are excited at $H_c = 0$ with normal incidence of light, it follows from the law of conservation of quasi-momentum in the xy plane that $\mathbf{k}_{e\perp} = -\mathbf{k}_{h\perp}$.

Note that expression (44) for the strong magnetic field differs from expression (43) for $H_c = 0$ only in that the normalization area S_0 is replaced by $2\pi a_H^2$ and the index $\mathbf{k}_\perp$ is replaced by the index n.

12. THE MODEL SIMPLIFYING THE EXPRESSIONS FOR THE AVERAGE CURRENT DENSITIES

Let us now consider the model used earlier in [19–27]. The $\mathbf{p}_{cv}$ vectors for the two degenerate valence bands I and II have the form

$$\begin{aligned}\mathbf{p}_{cv\mathrm{I}} &= \frac{p_{cv}}{\sqrt{2}}(\mathbf{e}_x - i\mathbf{e}_y), \\ \mathbf{p}_{cv\mathrm{II}} &= \frac{p_{cv}}{\sqrt{2}}(\mathbf{e}_x + i\mathbf{e}_y),\end{aligned} \tag{45}$$

where $\mathbf{e}_x$ and $\mathbf{e}_y$ are the unit vectors along the x and y axes and p_{cv} is the real quantity. This model corresponds to heavy holes in a semiconductor with a zinc blende structure when the z axis is aligned along the

fourfold symmetry axis [28, 29]. For the circular polarization vectors of the exciting light,

$$\mathbf{e}_l = \frac{1}{\sqrt{2}}(\mathbf{e}_x \pm i\mathbf{e}_y),$$

the following condition of conservation of the polarization vector is satisfied:

$$\sum_{v = \mathrm{I, II}} \mathbf{p}^*_{cv}(\mathbf{e}_l\mathbf{p}_{cv}) = \sum_{v = \mathrm{I, II}} \mathbf{p}_{cv}(\mathbf{e}_l\mathbf{p}^*_{cv}) = \mathbf{e}_l p^2_{cv}.$$

Note that both the functions $\varphi^v_{l_v}$ and the energy levels $\varepsilon^v_{l_v}$ do not depend on the numbers of valence bands I and II.

With the use of model (45) and expressions (43) and (44), the relationship for the average induced current density at $H_c = 0$ in a strong magnetic field can be written in a unified form:

$$\langle 0|j_{1\alpha}(\mathbf{r}, t)|0\rangle = \frac{ic\nu}{8\pi^2}\sum_\rho \gamma_{r\rho}\phi_\rho(z) \times \int_{-\infty}^{\infty} d\omega e^{-i\omega t}\int_{-\infty}^{\infty} dz'\phi_\rho(z')E_\alpha(z', \omega) \times \{(\omega - \omega_\rho + i\gamma_\rho/2)^{-1} + (\omega + \omega_\rho + i\gamma_\rho/2)^{-1}\}, \quad (46)$$

where ν is the refractive index for light. For $H_c = 0$, we obtain

$$\gamma_{r\rho} = \gamma_r = 4\pi\frac{e^2}{\hbar c\nu}\frac{p^2_{cv}}{m_0^2}\frac{1}{S_0\omega_g} \quad (47)$$

and the set ρ of indices l_e, l_h, and $\mathbf{k}_\perp$, where l_h is the quantum number of the quantum confinement in valence bands I and II. In the case of a strong magnetic field, we have

$$\gamma_{r\rho} = \gamma_r = 2\frac{e^2}{\hbar c\nu}\frac{p^2_{cv}}{m_0^2}\frac{1}{a_H^2\omega_g} = 2\frac{e^2}{\hbar c\nu}\frac{p^2_{cv}}{m_0}\frac{\Omega_{0H}}{\hbar\omega_g}, \quad (48)$$

$\Omega_{0H} = |e|H_c/m_0c$, and the set ρ of indices l_e, l_h, and n. On the right-hand side of formula (46), the quantity γ_r has the index ρ, even though the right-hand sides of formulas (47) and (48) do not involve this index. The reason is that, in this form, relationship (46) is also applicable to other situations, for example, to the magnetopolaron resonance in a strong magnetic field. The physical meaning of the quantity $\gamma_{r\rho}$ will be explained below.

It should be noted that, for model (45), the following important expression is satisfied:

$$\mathrm{div}\langle 0|\mathbf{j}_1(\mathbf{r}, t)|0\rangle = 0.$$

Therefore, as follows from the continuity equation, the average induced charge density is equal to zero.

13. CALCULATION OF THE VECTOR POTENTIAL AND ELECTRIC FIELD

Knowing the distribution of the average current density inside the quantum well, we can determine the vector potential from the standard formula for the retarded potentials (see, for example, [30]); that is,

$$\mathbf{A}(\mathbf{r}, t) = \frac{1}{c}\int d\mathbf{r}'\frac{\mathbf{j}(\mathbf{r}', t - \nu|\mathbf{r} - \mathbf{r}'|/c)}{|\mathbf{r} - \mathbf{r}'|} + \mathbf{A}_0(\mathbf{r}, t). \quad (49)$$

It follows from relationship (46) that the dependence of the current density on the coordinates is governed only by the factor $\phi_\rho(z)$ under the sign of the sum over ρ.

The integral

$$I_\rho(\omega, z) = \int d\mathbf{r}'\frac{\phi_\rho(z')\exp(i\omega\nu)|\mathbf{r} - \mathbf{r}'|/c}{|\mathbf{r} - \mathbf{r}'|}$$

can be rewritten in the form

$$I_\rho(\omega, z) = \frac{2\pi ic}{\omega\nu} \times \left\{\int_{-\infty}^{z} dz'\phi_\rho(z')e^{i\kappa(z - z')} + \int_z^{\infty} dz'\phi_\rho(z')e^{-i\kappa(z - z')}\right\}, \quad (50)$$

where $\kappa = \omega\nu/c$. From expressions (46), (49), and (50), we obtain the following relationship for the vector potential:

$$A_\alpha(z, t) = A_{0\alpha}(z, t) - \frac{c}{4\pi}\int_{-\infty}^{\infty}\frac{d\omega}{\omega}e^{-i\omega t} \times \sum_\rho \gamma_{r\rho}\int_{-\infty}^{\infty} dz'\phi_\rho(z')E_\alpha(z', \omega) \times \left\{\int_{-\infty}^{z} dz'\phi_\rho(z')e^{i\kappa(z - z')} + \int_z^{\infty} dz'\phi_\rho(z')e^{-i\kappa(z - z')}\right\} \times \{(\omega - \omega_\rho + i\gamma_\rho/2)^{-1} + (\omega + \omega_\rho + i\gamma_\rho/2)^{-1}\}.$$

As was noted above, the average charge density for model (45) is equal to zero. Therefore, the scalar potential φ also goes to zero. As a result, we have

$$\mathbf{E}(z, t) = -\frac{1}{c}\frac{\partial\mathbf{A}(z, t)}{\partial t}.$$

Correspondingly, we obtain

$$E_\alpha(z,t) = E_{0\alpha}(z,t) - \frac{i}{4\pi}\int_{-\infty}^{\infty} d\omega e^{-i\omega t} \times \sum_\rho \gamma_{r\rho} \int_{-\infty}^{\infty} dz' \phi_\rho(z') E_\alpha(z',\omega) \times \left\{ \int_{-\infty}^{z} dz' \phi_\rho(z') e^{i\kappa(z-z')} + \int_{z}^{\infty} dz' \phi_\rho(z') e^{-i\kappa(z-z')} \right\} \times \{(\omega - \omega_\rho + i\gamma_\rho/2)^{-1} + (\omega + \omega_\rho + i\gamma_\rho/2)^{-1}\}, \quad (51)$$

where $E_{0\alpha}(z, t)$ is the exciting field. By taking the Fourier transform of the left-hand and right-hand sides of expression (51) with due regard for formula (42), we find

$$E_\alpha(z,\omega) = E_{0\alpha}(z,\omega) - \frac{i}{2}\sum_\rho \gamma_{r\rho} \int_{-\infty}^{\infty} dz' \phi_\rho(z') E_\alpha(z',\omega) \times \left\{ \int_{-\infty}^{z} dz' \phi_\rho(z') e^{i\kappa(z-z')} + \int_{z}^{\infty} dz' \phi_\rho(z') e^{-i\kappa(z-z')} \right\}.$$

Therefore, we derived the integral equation for the Fourier components of the electric field. The exciting field can be represented as follows:

$$\mathbf{E}_0(z,t) = E_0 \mathbf{e}_l \int_{-\infty}^{\infty} d\omega e^{-i\omega p} D_0(\omega) + \text{c.c.}, \quad (52)$$

where $p = t - \omega\nu z/c$. For monochromatic excitation at the frequency ω_l, we have

$$D_0(\omega) = \delta(\omega - \omega_l).$$

The quantity $D_0(\omega)$ can correspond to pulses with an arbitrary duration and shape. From formula (52), we can write

$$\mathbf{B}_{0\alpha}(z,\omega) = 2\pi E_0 e^{i\omega\nu z/c} \{\mathbf{e}_l D_0(\omega) + \mathbf{e}_l^* D_0(-\omega)\}.$$

The sought solution can be represented in the form

$$\mathbf{E}(z,t) = (\mathbf{e}_l/2\pi) \int_{-\infty}^{\infty} d\omega \exp(-i\omega t) \mathscr{E}(z,\omega) + \text{c.c.} \quad (53)$$

Then, for the quantity $\mathscr{E}(z, \omega)$, we obtain the equation

$$\mathscr{E}(z,\omega) = 2\pi E_0 e^{i\kappa z} D_0(\omega) - \frac{i}{2}\sum_\rho \gamma_{r\rho} \int_{-\infty}^{\infty} dz' \phi_\rho(z') \mathscr{E}(z',\omega) \times \left\{ \int_{-\infty}^{z} dz' \phi_\rho(z') e^{i\kappa(z-z')} + \int_{z}^{\infty} dz' \phi_\rho(z') e^{-i\kappa(z-z')} \right\} \times \{(\omega - \omega_\rho + i\gamma_\rho/2)^{-1} + (\omega + \omega_\rho + i\gamma_\rho/2)^{-1}\}. \quad (54)$$

14. APPROXIMATION OF AN INFINITELY DEEP QUANTUM WELL

For simplicity and clarity in the solutions, let us consider the case of an infinitely deep quantum well where the wave functions $\varphi_l(z)$ of electrons and holes are rigidly confined within the quantum well and do not penetrate into the barrier. This means that the wave functions for free pairs can be written in the form

$$\varphi_l(z) = \begin{cases} \frac{2}{\sqrt{d}} \sin\left(\frac{\pi l z}{d} + \frac{\pi l}{2}\right), & l = 1, 2, \ldots; \\ & -\frac{d}{2} \le z \le \frac{d}{2}, \\ 0; \quad z \le -\frac{d}{2}, z \ge \frac{d}{2}. \end{cases} \quad (55)$$

$$\varepsilon_l^e = \frac{\hbar^2\pi^2 l^2}{2m_e d^2}, \quad \varepsilon_l^h = \frac{\hbar^2\pi^2 l^2}{2m_h d^2}.$$

Then, with the use of Eq. (54), we obtain the expression

$$\mathscr{E}(z,\omega) = 2\pi E_0 e^{i\kappa z} D_0(\omega) - \frac{i}{2}\sum_\rho \gamma_{r\rho} \int_{-d/2}^{d/2} dz' \phi_\rho(z') \mathscr{E}(z',\omega) \times \left\{ e^{i\kappa z} \int_{-d/2}^{z} dz' \phi_\rho(z') e^{-i\kappa z'} + e^{-i\kappa z} \int_{z}^{d/2} dz' \phi_\rho(z') e^{i\kappa z'} \right\} \times \{(\omega - \omega_\rho + i\gamma_\rho/2)^{-1} + (\omega + \omega_\rho + i\gamma_\rho/2)^{-1}\}. \quad (56)$$

15. SOLUTIONS FOR A QUANTUM WELL WHOSE WIDTH IS CONSIDERABLY LESS THAN THE LIGHT WAVELENGTH

Now, we analyze the solution to Eq. (56) at $\kappa d \ll 1$. For monochromatic irradiation, we have $\kappa_l = \omega_l \nu/c$. In the case of pulsed irradiation, the frequencies in the range $\pm\Delta\omega$ around the carrier frequency ω_l of an exciting pulse are significant. The quantity $\Delta\omega$ is of the order of $(\Delta t)^{-1}$, where Δt is the pulse duration. In all cases, the

frequency ω is of the order of ω_g, where $\hbar\omega_g$ is the band gap of the semiconductor. The solution $\mathscr{E}(z, \omega)$ will be sought to the left and the right of the quantum well, where only plane waves with frequencies $\omega = c\kappa/\nu$ can propagate. The solutions are sought in the following form:

$$\begin{aligned}\mathscr{E}_1(z, \omega) &= \mathscr{E}_0(z, \omega) + \Delta\mathscr{E}_1(z, \omega),\\ \mathscr{E}_r(z, \omega) &= \mathscr{E}_0(z, \omega) + \Delta\mathscr{E}_r(z, \omega),\\ \Delta\mathscr{E}_1(z, \omega) &= 2\pi E_0 e^{-i\kappa z} D(\omega), \quad z \le -d/2,\\ \Delta\mathscr{E}_r(z, \omega) &= 2\pi E_0 e^{i\kappa z} D(\omega), \quad z \ge d/2.\end{aligned} \tag{57}$$

The field inside the quantum well is denoted by the subscript *QW* and can represented in the form

$$\mathscr{E}_{\mathrm{QW}}(z, \omega) = \mathscr{E}_0(z, \omega) + \Delta\mathscr{E}_{\mathrm{QW}}(z, \omega). \tag{58}$$

Now, we calculate the integral

$$\int_{-d/2}^{d/2} dz\phi_\rho(z)\mathscr{E}_{\mathrm{QW}}(z, \omega)$$

on the right-hand side of relationship (56) at $\kappa d \ll 1$. Substituting formula (58) into the integrand gives

$$\begin{aligned}&\int_{-d/2}^{d/2} dz\phi_\rho(z)\mathscr{E}_{\mathrm{QW}}(z, \omega)\\ &= \int_{-d/2}^{d/2} dz\phi_\rho(z)\Delta\mathscr{E}_{\mathrm{QW}}(z, \omega) + 2\pi E_0 D_0(\omega) C_\rho,\end{aligned} \tag{59}$$

where

$$C_\rho = \int_{-d/2}^{d/2} dz\phi_\rho(z).$$

The function $\Delta\mathscr{E}_{\mathrm{QW}}(z)$ is unknown. However, at the quantum-well boundaries, we have

$$\begin{aligned}\Delta\mathscr{E}_{\mathrm{QW}}(-d/2, \omega) &= \Delta\mathscr{E}_1(-d/2, \omega) = 2\pi E_0 e^{i\kappa d/2} D(\omega),\\ \Delta\mathscr{E}_{\mathrm{QW}}(d/2, \omega) &= \Delta\mathscr{E}_r(d/2, \omega) = 2\pi E_0 e^{i\kappa d/2} D(\omega).\end{aligned} \tag{60}$$

It is obvious from formulas (60) that, at $\kappa d \ll 1$, the following approximate equality should be satisfied:

$$\Delta\mathscr{E}_{\mathrm{QW}}(z, \omega) \simeq 2\pi E_0 D(\omega). \tag{61}$$

Substituting relationship (61) into integral (59) gives

$$\int_{-d/2}^{d/2} dz\phi_\rho(z)\mathscr{E}_{\mathrm{QW}}(z, \omega) = 2\pi E_0 (D_0(\omega) + D(\omega)) C_\rho.$$

With the use of the first expression (57), we write Eq. (56) for the range $z < -d/2$. In this range, the integral

$$\int_{-d/2}^{z} dz' e^{-i\kappa z'} \phi_\rho(z')$$

on the right-hand side of relationship (56) is equal to zero and the other integral is written as

$$\int_{z}^{d/2} dz' e^{i\kappa z'} \phi_\rho(z') = \int_{-d/2}^{d/2} dz'\phi_\rho(z') = C_\rho.$$

We obtain an equation for $D(\omega)$ whose solution is given by the expression

$$\begin{aligned}D(\omega) &= -\frac{4\pi\chi(\omega) D_0(\omega)}{1 + 4\pi\chi(\omega)},\\ \chi(\omega) &= \frac{i}{8\pi}\sum_\rho \gamma_{r\rho} C_\rho^2 \{(\omega - \omega_\rho + i\gamma_\rho/2)^{-1}\\ &\quad + (\omega + \omega_\rho + i\gamma_\rho/2)^{-1}\}.\end{aligned} \tag{62}$$

Equation (56) in the range $z > d/2$ also leads to a solution in the form of expression (62). In the case of free traveling electrons and holes along the z axis, when condition (37) is satisfied, we find that $C_\rho = \delta_{l_e, l_h}$ and

$$\begin{aligned}\chi(\omega) &= \frac{i}{8\pi}\sum_{\rho_0} \gamma_{r\rho_0} \{(\omega - \omega_{\rho_0} + i\gamma_{\rho_0}/2)^{-1}\\ &\quad + (\omega + \omega_{\rho_0} + i\gamma_{\rho_0}/2)^{-1}\}.\end{aligned}$$

Here, ρ_0 is the set of indices at $l_e = l_h = l$, i.e., the set of indices l and $\mathbf{k}_\perp$ at $H_c = 0$ and indices l and n in a strong magnetic field.

The energy levels are given by the formulas

$$\omega_{\rho_0} = \bar{\omega}_{gl} + \frac{\hbar^2 k_\perp^2}{2\mu}, \quad \omega_{\rho_0} = \bar{\omega}_{gl} + \Omega_\mu(n + 1/2),$$

where

$$\bar{\omega}_{gl} = \omega_g + \frac{\hbar^2\pi^2 l^2}{2\mu d^2}.$$

The electric fields to the left and the right of the quantum well are described by the relationships

$$\mathbf{E}_{l(r)}(z, t) = \mathbf{E}_0(z, t) + \Delta\mathbf{E}_{l(r)}(z, t), \tag{63}$$

$$\Delta\mathbf{E}_{l(r)}(z, t) = E_0\mathbf{e}_l \int_{-\infty}^{\infty} d\omega e^{-i\omega(t \pm z\nu/c)} D(\omega) + \text{c.c.}, \tag{64}$$

where the upper and lower signs refer to indices l and r, respectively. The use of expressions (63) and (64) makes it possible to derive formulas for the transmitted, reflected, and absorbed light fluxes for a quantum well

with an arbitrary number of energy levels in the quantum well, any shape of the exciting pulse (including monochromatic irradiation), and an arbitrary ratio between the parameters γ_r and γ (reciprocal radiative and nonradiative excited-state lifetimes). As follows from relationship (64), the induced fields $\Delta\mathbf{E}_l(z, t)$ and $\Delta\mathbf{E}_r(z, t)$ differ only in the direction of propagation.

16. SOLUTIONS FOR QUANTUM WELLS WHOSE WIDTH IS COMPARABLE TO THE LIGHT WAVELENGTH: FIRST ORDER IN THE LIGHT–ELECTRON INTERACTION

The electric field $\mathbf{E}(z, t)$ can be expanded into a series in the interaction of the field with electrons, that is,

$$\mathbf{E}(z, t) = \mathbf{E}_0(z, t) + \mathbf{E}_1(z, t) + \mathbf{E}_2(z, t) + \ldots, \quad (65)$$

where $\mathbf{E}_0(z, t)$ is the exciting field and terms of subsequent orders can be obtained by the iteration method from Eq. (56).

In the first order, we obtain

$$\mathbf{E}_1(z, t) = (\mathbf{e}_l/2\pi)\int_{-\infty}^{\infty} d\omega e^{-i\omega t}\mathscr{E}_1(z, \omega) + \text{c.c.}, \quad (66)$$

$$\mathscr{E}_1(z, \omega) = -\frac{i}{2}\sum_\rho \gamma_{r\rho}\int_{-d/2}^{d/2} dz'\phi_\rho(z')\mathscr{E}_0(z', \omega)$$
$$\times\left\{e^{i\kappa z}\int_{-d/2}^{z} dz' e^{-i\kappa z'}\phi_\rho(z') + e^{-i\kappa z}\int_{z}^{d/2} dz' e^{i\kappa z'}\phi_\rho(z')\right\} \quad (67)$$
$$\times\{(\omega - \omega_\rho + i\gamma_\rho/2)^{-1} + (\omega + \omega_\rho + i\gamma_\rho/2)^{-1}\}.$$

From the definition

$$\mathscr{E}_0(z, \omega) = 2\pi E_0 e^{i\kappa z} D_0(\omega)$$

and relationship (66), we find

$$\mathbf{E}_1(z, t) = -iE_0\mathbf{e}_l\int_{-\infty}^{\infty} d\omega e^{-i\omega t} D_0(\omega)\sum_\rho(\gamma_{r\rho}/2)R_\rho^*(\kappa)$$
$$\times\left\{e^{i\kappa z}\int_{-d/2}^{z} dz' e^{-i\kappa z'}\phi_\rho(z') + e^{-i\kappa z}\int_{z}^{d/2} dz' e^{i\kappa z'}\phi_\rho(z')\right\} \quad (68)$$
$$\times\{(\omega - \omega_\rho + i\gamma_\rho/2)^{-1} + (\omega + \omega_\rho + i\gamma_\rho/2)^{-1}\} + \text{c.c.}$$

Here, we introduced the designation

$$R_\rho(\kappa) = \int_{-d/2}^{d/2} dz\phi_\rho(z)\exp(-i\kappa z). \quad (69)$$

For free electrons and holes in an infinitely deep quantum well, we have

$$R_\rho(\kappa) = \int_{-d/2}^{d/2} dz\phi_{l_e}(z)\varphi_{l_h}(z)\exp(-i\kappa z), \quad (70)$$

where the functions $\varphi_l(z)$ are given by formulas (55). From expression (68), we obtain the relationships for the fields to the left and the right of the quantum well in the following form:

$$\mathbf{E}_{1l}(z, t) = -iE_0\mathbf{e}_l$$
$$\times\int_{-\infty}^{\infty} d\omega e^{-i\kappa z - i\omega t} D_0(\omega)\sum_\rho(\gamma_{r\rho}/2)(R_\rho^*(\kappa))^2 \quad (71)$$
$$\times\{(\omega - \omega_\rho + i\gamma_\rho/2)^{-1} + (\omega + \omega_\rho + i\gamma_\rho/2)^{-1}\} + \text{c.c.},$$

$$\mathbf{E}_{1r}(z, t) = -iE_0\mathbf{e}_l$$
$$\times\int_{-\infty}^{\infty} d\omega e^{i\kappa z - i\omega t} D_0(\omega)\sum_\rho(\gamma_{r\rho}/2)|R_\rho(\kappa)|^2 \quad (72)$$
$$\times\{(\omega - \omega_\rho + i\gamma_\rho/2)^{-1} + (\omega + \omega_\rho + i\gamma_\rho/2)^{-1}\} + \text{c.c.}$$

Formula (68) should be used for the field $\mathbf{E}_{1QW}(z, t)$ inside the quantum well. From expressions (68)–(72), it follows that, for sufficiently wide quantum wells, there can arise electron–hole pairs with quantum numbers $l_e \neq l_h$ and the fields depend on the quantum-well width d. This dependence is included in the coefficients $R_\rho(\kappa)$. It can be demonstrated that, for the wave functions (55), the factor $R_\rho^*(\kappa)/R_\rho(\kappa)$ entering into the ratio $\mathbf{E}_{1l}(z, t)/\mathbf{E}_{1r}(z, t)$ depends on the indices l_e and l_h as follows: $R_\rho^*(\kappa)/R_\rho(\kappa) = 1$ for the indices l_e and l_h of the same parity and $R_\rho^*(\kappa)/R_\rho(\kappa) = -1$ for the indices l_e and l_h of different parities.

Substituting solution (67) of the first order into the right-hand side of relationship (56) gives a solution of the second order, etc. In such a manner, series (65), in principle, can be obtained. However, we will use one more method for calculating the fields for wide quantum wells at $\kappa d \geq 1$.

17. SOLUTION FOR WIDE QUANTUM WELLS WITH ONE ENERGY LEVEL

In the case where one energy level is significant, Eq. (56) can be solved exactly. By introducing the designations

$$\omega_\rho = \omega_0, \quad \gamma_\rho = \gamma, \quad \phi_\rho(z) = \phi(z), \quad \gamma_{r\rho} = \gamma_r,$$

Eq. (56) can be rewritten in the form

$$\mathcal{E}(z,\omega) = 2\pi E_0 e^{i\kappa z} D_0(\omega) - (i/2)\gamma_r M(\omega) \times \left\{ e^{i\kappa z} \int_{-d/2}^{z} dz' e^{-i\kappa z}\phi(z') + e^{-i\kappa z} \int_{z}^{d/2} dz' e^{i\kappa z'}\phi(z') \right\} \times \{(\omega-\omega_0+i\gamma/2)^{-1} + (\omega+\omega_0+i\gamma/2)^{-1}\}, \quad (73)$$

where we used one more designation,

$$M(\omega) = \int_{-d/2}^{d/2} dz'\phi(z')\mathcal{E}(z',\omega).$$

Now, we multiply both sides of equality (73) into $\phi(z)$ and integrate over z from $-d/2$ to $d/2$. As a result, we derive an equation for the quantity $M(\omega)$ whose solution has the form

$$M(\omega) = 2\pi E_0 D_0(\omega) R^*(\kappa)\{1 + (i/2)\gamma_r J(\kappa) \times [(\omega-\omega_0+i\gamma/2)^{-1} + (\omega+\omega_0+i\gamma/2)^{-1}]\}^{-1}, \quad (74)$$

where

$$J(\kappa) = \int_{-d/2}^{d/2} dz\phi(z) \times \left\{ e^{i\kappa z} \int_{-d/2}^{z} dz' e^{-i\kappa z'}\phi(z') + e^{-i\kappa z} \int_{z}^{d/2} dz' e^{i\kappa z'}\phi(z') \right\}.$$

It is possible to show that the following equality is satisfied:

$$J(\kappa) = |R(\kappa)|^2 + iQ(\kappa).$$

Substituting expression (74) into formula (73) gives the solution of the problem. From expression (53), we obtain the relationships for the induced fields to the left and the right of the quantum well in the following form:

$$\Delta\mathbf{E}_l(z,t) = -i\mathbf{e}_l E_0(\gamma_r/2)\int_{-\infty}^{\infty} d\omega e^{-i\kappa z - i\omega t} D_0(\omega)(R^*(\kappa))^2 \times [(\omega-\omega_0+i\gamma/2)^{-1} + (\omega+\omega_0+i\gamma/2)^{-1}] \times \{1 + i(\gamma_r/2)(|R(\kappa)|^2 + iQ(\kappa))[(\omega-\omega_0+i\gamma/2)^{-1} + (\omega+\omega_0+i\gamma/2)^{-1}]\}^{-1} + \text{c.c.}, \quad (75)$$

$$\Delta\mathbf{E}_r(z,t) = -i\mathbf{e}_l E_0(\gamma_r/2)\int_{-\infty}^{\infty} d\omega e^{i\kappa z - i\omega t} D_0(\omega)|R^*(\kappa)|^2 \times [(\omega-\omega_0+i\gamma/2)^{-1} + (\omega+\omega_0+i\gamma/2)^{-1}] \times \{1 + i(\gamma_r/2)(|R(\kappa)|^2 + iQ(\kappa))[(\omega-\omega_0+i\gamma/2)^{-1} + (\omega+\omega_0+i\gamma/2)^{-1}]\}^{-1} + \text{c.c.} \quad (76)$$

The quantity

$$\tilde{\gamma}_r(\omega) = \gamma_r|R(\kappa)|^2$$

at $\omega = \omega_0$ with allowance made for expression (48) coincides with the reciprocal radiative lifetime calculated in [26] for electron–hole pairs in a strong magnetic field for $n_e = n_h = n$, $\mathbf{K}_\perp = 0$, and an arbitrary quantity $\omega_0 v d/c$.

By ignoring the nonresonant contribution $(\omega + \omega_0 + i\gamma/2)^{-1}$, from relationships (75) and (76), we can derive formulas identical to those obtained in our earlier work [25]:[1]

$$\Delta\mathbf{E}_l(z,t) = -i\mathbf{e}_l E_0 \times \int_{-\infty}^{\infty} d\omega \frac{\exp(-i\kappa z - i\omega t + i\alpha)(\tilde{\gamma}_r(\omega)/2)D_0(\omega)}{\omega - (\omega_0+\Delta) + i(\gamma+\tilde{\gamma}_r(\omega))/2} + \text{c.c.},$$

$$\Delta\mathbf{E}_r(z,t) = -i\mathbf{e}_l E_0 \times \int_{-\infty}^{\infty} d\omega \frac{\exp(i\kappa z - i\omega t)(\tilde{\gamma}_r(\omega)/2)D_0(\omega)}{\omega - (\omega_0+\Delta) + i(\gamma+\tilde{\gamma}_r(\omega))/2} + \text{c.c.},$$

where

$$\exp(i\alpha) = R^*(\kappa)/R(\kappa), \quad \Delta = (\gamma_r/2)Q(\kappa).$$

Note that, in this section, we did not use expression (37), which is valid only for free motion of electrons and holes along the z axis, and assumed that only relationship (36) was applicable.

By using expression (37) with wave functions (55) substituted into it, the relationships for the coefficients $R(\kappa)$ and $R^*(\kappa)$ can be rearranged to the form

$$R(\kappa) = \frac{1}{2}\int_{-d/2}^{d/2} dz e^{-i\kappa z}\{\cos[(\pi/d)(l_e - l_h)z + (\pi/2)(l_e - l_h)] - \cos[(\pi/d)(l_e + l_h)z + (\pi/2)(l_e + l_h)]\},$$

$$R^*(\kappa) = \frac{1}{2}\int_{-d/2}^{d/2} dz e^{-i\kappa z}\{\cos[(\pi/d)(l_e - l_h)z - (\pi/2)(l_e - l_h)] - \cos[(\pi/d)(l_e + l_h)z - (\pi/2)(l_e + l_h)]\}.$$

For narrow quantum wells at $\kappa d \ll 1$, we have

$$R(\kappa) = R^*(\kappa) = \delta_{l_e l_h}.$$

This implies that the light gives rise only to pairs with identical numbers of the quantum confinement of electrons and holes (in the limit of infinitely deep quantum

[1] In [25], the parameter $\tilde{\gamma}_r$ in formulas (47) and (48) should be replaced by the expression $\tilde{\gamma}_r \exp(-i\kappa d/2)$.

wells). At $\kappa d \geq 1$, there arise pairs with different numbers l_e and l_h; i.e., a substantially larger number of energy levels can be excited under irradiation.

18. MONOCHROMATIC AND PULSED EXCITATION

In [7–15], the exciting light pulse was described by the relationship

$$\mathbf{E}_0(z, t) = E_0(\mathbf{e}_l e^{-i\omega_l p} + \mathbf{e}_l^* e^{i\omega_l p}) \times \{\Theta(p) e^{-\gamma_{l1} p/2} + [1 - \Theta(p)] e^{\gamma_{l2} p/2}\},$$

where ω_l is the carrier frequency, $p = t - z\nu/c$, and $\Theta(p)$ is the Heaviside function. By expanding the pulse in terms of frequencies, we obtain

$$\mathbf{E}(z, t) = E_0 \mathbf{e}_l \int_{-\infty}^{\infty} d\omega e^{-i\omega p} D_0(\omega) + \text{c.c.},$$

where

$$D_0(\omega) = \frac{i}{2\pi}[(\omega - \omega_l + i\gamma_{l1}/2)^{-1} - (\omega - \omega_l - i\gamma_{l2}/2)^{-1}].$$

Under the condition $\gamma_{l1} = \gamma_{l2} = \gamma_l$, the pulse is symmetric and the pulse duration is of the order of γ_l^{-1}. At $\gamma_l \longrightarrow 0$, we have

$$D_0(\omega) = \delta(\omega - \omega_l).$$

This corresponds to monochromatic irradiation. At $\gamma_{l2} \longrightarrow \infty$, the pulse is asymmetric and has a very steep front.

In a number of our previous works, we analyzed different variants of irradiation, such as monochromatic irradiation in [25, 26], pulsed irradiation with asymmetric pulses in [19–21], pulsed irradiation with symmetric pulses in [22, 23, 27], and pulsed irradiation with symmetric and asymmetric pulses in [24].

19. CONCLUSIONS

The two most important results obtained in the present work are as follows.

The first result is the derivation of expressions (34) and (35) for the average induced current density. These expressions can be applied to any semiconductor object with an arbitrary number of levels of electronic excitations with any exiting pulse shape for an arbitrary direction of the light with respect to the crystallographic axes.

The second result is the integral equation (54) for the Fourier components of the electric field at normal incidence of light on a quantum well whose width can be comparable to the light wavelength and for which the number of levels of electronic excitations can be arbitrary. In particular, this situation is typical of a quantum well in a strong magnetic field. Equation (54) is applicable to cases of both monochromatic and pulsed irradiation. The results obtained can be used for solving a large number of problems in the optics of low-dimensional semiconductor objects.

REFERENCES

1. H. Stolz, *Time Resolved Light Scattering from Excitons* (Springer-Verlag, Berlin, 1994).
2. J. Shah, *Ultrafast Spectroscopy of Semiconductors and Semiconductor Nanostructures* (Springer-Verlag, Berlin, 1996).
3. H. Hang and S. W. Koch, *Quantum Theory of the Optical and Electronic Properties of Semiconductors* (World Sci., Singapore, 1993).
4. L. E. Vorob'ev, E. L. Ivchenko, D. A. Firsov, and V. A. Shaligin, *Optical Properties of Nanostructures* (Nauka, St. Petersburg, 2001) [in Russian].
5. L. C. Andreani, F. Tassone, and F. Bassani, Solid State Commun. **77** (9), 641 (1991).
6. E. L. Ivchenko, Fiz. Tverd. Tela (Leningrad) **33** (8), 2388 (1991) [Sov. Phys. Solid State **33**, 1344 (1991)].
7. E. L. Ivchenko and A. V. Kavokin, Fiz. Tverd. Tela (St. Petersburg) **34** (6), 1815 (1992) [Sov. Phys. Solid State **34**, 968 (1992)].
8. F. Tassone, F. Bassani, and L. C. Andreani, Phys. Rev. B **45** (11), 6023 (1992).
9. L. C. Andreani, in *Confined Electrons and Photons*, Ed. by E. Burstein and C. Weinsbuch (Plenum, New York, 1995), p. 57.
10. T. Stroucken, A. Knorr, C. Anthony, P. Thomas, S. W. Koch, M. Koch, S. T. Cungiff, Y. Felgman, and E. Göbel, Phys. Rev. Lett. **74** (9), 2391 (1995).
11. T. Stroucken, A. Knorr, P. Thomas, and S. W. Koch, Phys. Rev. B **53** (4), 2026 (1996).
12. M. Hubner, T. Kuhl, S. Haas, T. Stroucken, S. W. Koch, R. Hey, and K. Ploog, Solid State Commun. **105** (2), 105 (1998).
13. L. C. Andreani, G. Pansarini, A. V. Kavokin, and M. R. Vladimirova, Phys. Rev. B **57**, 4670 (1998).
14. I. G. Lang, L. I. Korovin, J. A. de la Cruz-Alcaz, and S. T. Pavlov, Zh. Éksp. Teor. Fiz. **123** (2), 305 (2003) [JETP **96**, 268 (2003)]; cond-mat/0212549.
15. S. T. Pavlov, I. G. Lang, and L. I. Korovin, Fiz. Tverd. Tela (St. Petersburg) **45** (10), 1903 (2003) [Phys. Solid State **45**, 2001 (2003)]; cond-mat/0304304.
16. I. G. Lang, V. I. Belitsky, A. Cantarero, L. I. Korovin, S. T. Pavlov, and M. Cardona, Phys. Rev. B **54** (24), 17768 (1996).
17. A. A. Abrikosov, L. P. Gor'kov, and I. E. Dzyaloshinskiĭ, *Methods of Quantum Field Theory in Statistical Physics*, 2nd ed. (Dover, New York, 1975); Dobrosvet, Moscow, 1998).
18. I. V. Lerner and Yu. E. Lozovik, Zh. Éksp. Teor. Fiz. **78** (3), 1167 (1980) [Sov. Phys. JETP **51**, 588 (1980)].
19. I. G. Lang, V. I. Belitsky, and M. Cardona, Phys. Status Solidi A **164** (1), 307 (1997).

20. I. G. Lang and V. I. Belitsky, Solid State Commun. **107** (13), 577 (1998).

21. I. G. Lang and V. I. Belitsky, Phys. Lett. A **245** (3–4), 329 (1998).

22. L. I. Korovin, I. G. Lang, D. A. Contreras-Solorio, and S. T. Pavlov, Fiz. Tverd. Tela (St. Petersburg) **42** (12), 2230 (2000) [Phys. Solid State **42**, 2300 (2000)]; cond-mat/0006364.

23. D. A. Contreras-Solorio, S. T. Pavlov, L. I. Korovin, and I. G. Lang, Phys. Rev. B **62** (23), 16815 (2000); cond-mat/0002229.

24. I. G. Lang, L. I. Korovin, D. A. Contreras-Solorio, and S. T. Pavlov, Fiz. Tverd. Tela (St. Petersburg) **43** (6), 1117 (2001) [Phys. Solid State **43**, 1159 (2001)]; cond-mat/0004178.

25. L. I. Korovin, I. G. Lang, D. A. Contreras-Solorio, and S. T. Pavlov, Fiz. Tverd. Tela (St. Petersburg) **43** (11), 2091 (2001) [Phys. Solid State **43**, 2182 (2001)]; cond-mat/0104262.

26. I. G. Lang, L. I. Korovin, D. A. Contreras-Solorio, and S. T. Pavlov, Fiz. Tverd. Tela (St. Petersburg) **44** (11), 2084 (2002) [Phys. Solid State **44**, 2181 (2002)]; cond-mat/0001248.

27. L. I. Korovin, I. G. Lang, V. A. Contreras-Solorio, and S. T. Pavlov, Fiz. Tverd. Tela (St. Petersburg) **44** (9), 1681 (2002) [Phys. Solid State **44**, 1759 (2002)]; cond-mat/0203390.

28. J. M. Luttinger and W. Kohn, Phys. Rev. **97**, 869 (1955).

29. I. M. Tsidil'kovskiĭ, *Band Structure of Semiconductors* (Nauka, Moscow, 1978) [in Russian].

30. L. D. Landau and E. M. Lifshitz, *The Classical Theory of Fields*, 6th ed. (Nauka, Moscow, 1973; Pergamon, Oxford, 1975).

Translated by O. Borovik-Romanova

Physics of the Solid State, Vol. 46, No. 9, 2004, pp. 1776–1780. Translated from Fizika Tverdogo Tela, Vol. 46, No. 9, 2004, pp. 1719–1722.
Original Russian Text Copyright © 2004 by Agekyan, Vasil'ev, Serov, Filosofov, Karczewski.

LOW-DIMENSIONAL SYSTEMS AND SURFACE PHYSICS

Optical Properties of $Cd_{0.6}Mn_{0.4}Te/Cd_{0.5}Mg_{0.5}Te$ Quantum-Well Structures

V. F. Agekyan*, N. N. Vasil'ev*, A. Yu. Serov*, N. G. Filosofov*, and G. Karczewski**

**Fock Institute of Physics, St. Petersburg State University, Petrodvorets, St. Petersburg, 198504 Russia*

e-mail: avf@VA4678.spb.edu

***Institute of Physics, Polish Academy of Sciences, Warsaw, 02-668 Poland*

Received February 5, 2004

Abstract—Emission spectra of three $Cd_{0.6}Mn_{0.4}Te/Cd_{0.5}Mg_{0.5}Te$ superlattices with $Cd_{0.6}Mn_{0.4}Te$ quantum-well (QW) widths of 7, 13, and 26 monolayers, respectively, and the same thickness (46 monolayers) of the $Cd_{0.5}Mg_{0.5}Te$ barriers have been studied. The QW width affects the shape and spectral position of the Mn^{2+} intracenter luminescence (IL) band as a result of the crystal field being dependent on the position of the manganese ion with respect to the interface. Measured in identical experimental conditions, the exciton luminescence as compared to the IL is substantially higher in intensity in a QW than in a bulk CdMnTe crystal. Some samples of superlattices and bulk crystals exhibit, in addition to the conventional IL band near 2.0 eV, a weaker band at about 1.45 eV. This band apparently derives from intracenter transitions in the Mn^{2+} ions in the regions where the crystal lattice has the rock-salt rather than the conventional zinc blende structure. © *2004 MAIK "Nauka/Interperiodica".*

1. INTRODUCTION

II–VI compound crystals doped by iron group elements form the major family of dilute magnetic semiconductors (DMS). These compounds combine conventional semiconducting properties with strong magnetism, which accounts for the appearance of new characteristics, in particular, the giant Zeeman and Faraday effects and the magnetic polaron effect. Bulk DMSs and nanostructures containing II–VI compound DMSs have been a subject of intense study over the past three decades, with particular emphasis placed on $Cd_{1-x}Mn_xTe$, the $CdTe/Cd_xMn_{1-x}Te$ quasi-two-dimensional structures, and manganese-doped nanocrystals. The optical properties of DMSs, which are governed by interband excitons and intracenter transitions in unfilled 3*d* shells of magnetic ions, are treated in a number of review papers [1–4]. The broad band-gap manganese-doped II–VI compound crystals enjoy wide use as luminophors due to the bright Mn^{2+} 3*d*-shell intracenter luminescence (IL) they produce near 2 eV (the $^6A_1$–$^4T_1$ transition) [5]. The spectral and kinetic properties of the Mn^{2+} IL in bulk II–VI compound crystals were reported on in a number of publications [6–10].

It is known that the position of the $^6A_1$ level is practically independent of the crystal field, whereas the $^4T_1$ level energy decreases with increasing field, so the IL band shifts toward lower energies. The manganese IL decay time τ is of the order of 10^{-5} s; at high manganese concentrations, τ varies over the emission band profile. Of particular interest for investigating the relative contributions of the conventional exciton and the intracenter emission mechanisms are $Cd_{1-x}Mn_xTe$ solid solutions, in which the lowest exciton level crosses the Mn^{2+} intracenter absorption threshold at a concentration near $x = 0.4$, so that for $x < 0.4$ one observes only the exciton emission, while for $x > 0.4$ both the exciton and intracenter emissions occur. The Mn^{2+} IL Stokes shift in $Cd_{1-x}Mn_xTe$ is quite large, with the distance between the IL maximum and the Mn^{2+} excitation threshold being about 0.15 eV.

The interest that has arisen in recent years in doped nanostructures is partially related to theoretical substantiation of the quantum confinement effect on transitions in unfilled 3*d* and 4*f* shells [11, 12] and to experimental evidence of an increase in the manganese IL quantum yield in II–VI compound nanocrystals [13–16]. The transformation of the Mn^{2+} IL properties in a nanomatrix may be caused by two factors. First, the contraction of the band electron and hole wave functions is capable of substantially affecting the *sp–d* coupling. Second, the migration of intracenter excitation in a nanomatrix is partially or completely suppressed and the crystal field and the interaction of 3*d* electrons with phonons change. In nanomatrices, the oscillator strength of the $^6A_1$–$^4T_1$ intercombination intracenter transition and the IL decay rate should increase and the nonradiative relaxation of intracenter excitation should weaken. Studies of wide band-gap ZnS : Mn/ZnS quasi-two-dimensional structures have provided evi-

dence of an enhancement of the IL quantum yield at high temperatures [17]. As for CdTe- and $Cd_xMn_{1-x}Te$-based 2D structures, either nonmagnetic quantum wells (QWs) or QWs with a low manganese content, where IL is not observed and there is insufficient data on the IL of Mn^{2+} ions in wide magnetic barriers of $CdTe/Cd_xMn_{1-x}Te$ structures [18], have been studied. Unlike the case of doped nanocrystals, quasi-two-dimensional II–VI compound systems in which IL of iron group ions is observed have only been investigated in a few publications.

This communication deals with the luminescence of $Cd_{0.6}Mn_{0.4}Te$ quantum wells of various thickness separated by nonmagnetic barriers.

2. EXPERIMENTAL

A set of superlattices consisting of 100 $Cd_{1-x}Mn_xTe/Cd_{0.5}Mg_{0.5}Te$ periods were MBE grown under identical conditions. In samples *1*, *2*, and *3*, the width of the $Cd_{1-x}Mn_xTe$ ($x = 0.4$) QWs is 7, 13, and 26 monolayers (ML), respectively; in sample *4*, with a QW width of 13 ML, the manganese concentration is slightly lower. The thickness of the $Cd_{0.5}Mg_{0.5}Te$ barrier layers is 46 ML in all samples. For the chosen manganese and magnesium concentrations, the barrier height in a QW is 100 meV for electrons and 60 meV for holes. The structures were grown by sequentially depositing [on a (100)-oriented substrate] CdTe (4.2 μm) and $Cd_{0.5}Mg_{0.5}Te$ (0.4 μm) layers, a superlattice, and a $Cd_{0.5}Mg_{0.5}Te$ cap layer (40 nm).

Experiments were performed at temperatures of 4 K and higher, with luminescence excited by a cw argon-ion laser and a pulsed nitrogen laser.

3. RESULTS AND THEIR INTERPRETATION

All samples exhibit exciton emission bands from the $Cd_{0.6}Mn_{0.4}Te$ QW and the $Cd_{0.5}Mg_{0.5}Te$ barrier, and their halfwidths and intensity ratios depend only weakly on temperature in the range 4–77 K. As seen from Fig. 1, in structures *2*, *3*, and *4* (13- and 26-ML wide QWs), exciton emission from QWs is predominant, whereas in structure *1* with narrower QWs the situation is reversed, because under above-barrier excitation the lifetime of the exciton is too short for it to relax in the QW. In sample *4*, the exciton level lies close to the Mn^{2+}excitation threshold, which accounts for the weak manganese IL.

The maxima of the Mn^{2+} IL bands are located in the 2.0-eV region, which corresponds in position to the IL band in bulk $Cd_{1-x}Mn_xTe$ samples with $x > 0.4$. The accurate position of the maximum and the shape of the IL band depend, however, as is evident from Fig. 2, on the QW width. Note that, in the multilayer structures studied, the broad IL band located in the region of transparency of all the constituent layers is superposed by the bands due to light interference in the compara-

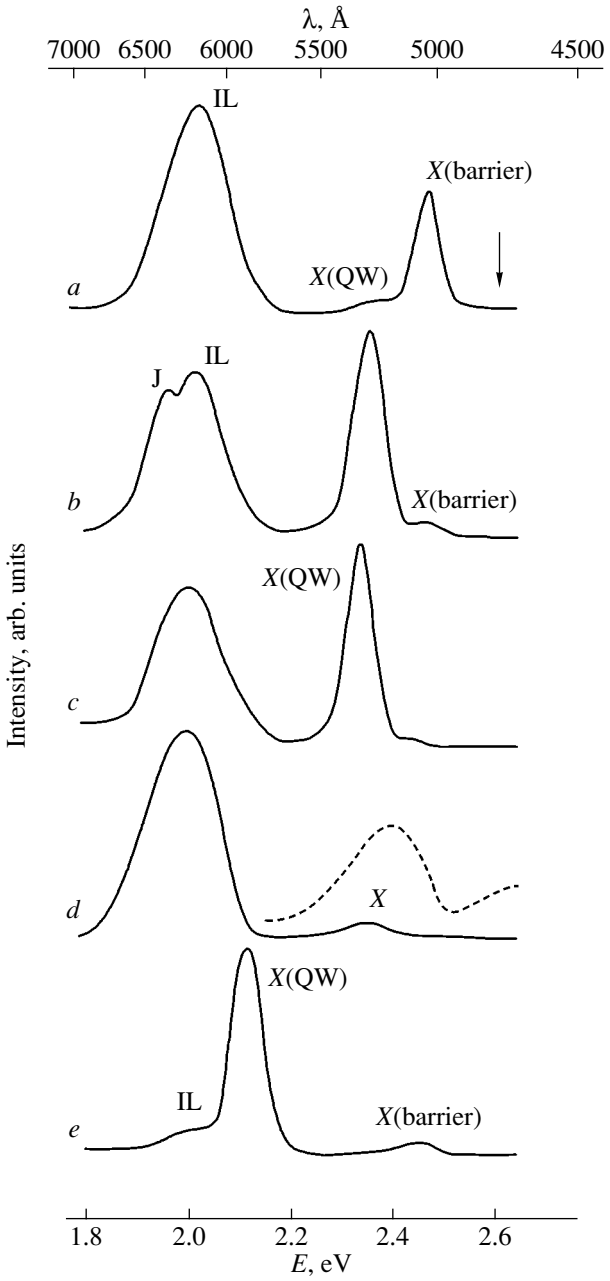

Fig. 1. Luminescence spectra of $Cd_{1-x}Mn_xTe/Cd_{0.5}Mg_{0.5}Te$ structures (*a*–*c*) with $x = 0.5$ and a QW width equal to 7 (sample *1*), 13 (*2*), and 26 ML (*3*); (*e*) with an x value of about 0.35 and a QW width of 13 ML (sample *4*); and (*d*) luminescence spectrum of bulk $Cd_{0.5}Mn_{0.5}Te$. IL is intracenter luminescence of the Mn^{2+} 3*d* shell; *X*(QW), *X*(barrier), and *X* stand for excitons in the QWs and barriers of the superlattices and in a bulk crystal, respectively; and the dashed line is Mn^{2+} intracenter absorption (relative to the band *J*; see text). CW excitation by 2.60-eV photons is used (indicated by the arrow), the excitation level is 30 W/cm^2, and $T = 77$ K.

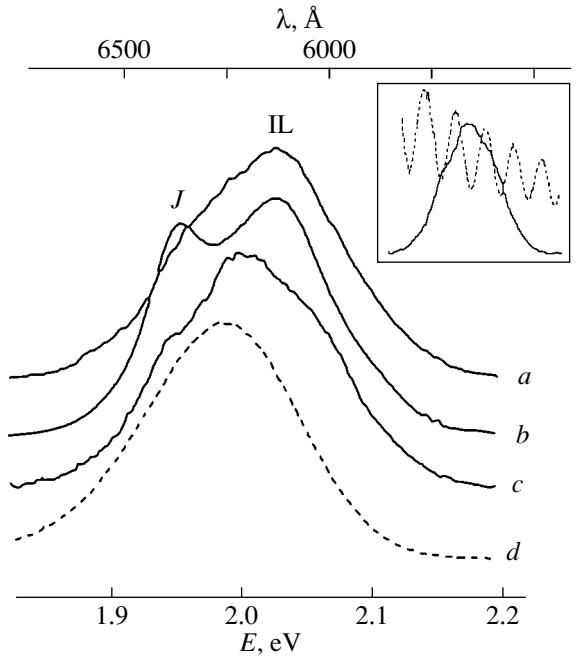

Fig. 2. Mn^{2+} intracenter luminescence bands (*a–c*) in samples *1–3* and (*d*) in a bulk $Cd_{0.5}Mn_{0.5}Te$ crystal; $T = 77$ K. Profiles *a–c* are deformed by interference; the band *J* is discussed in the text. The inset shows the Mn^{2+} IL band profile of sample *3* superposed by an interference pattern seen in reflection under normal incidence of light.

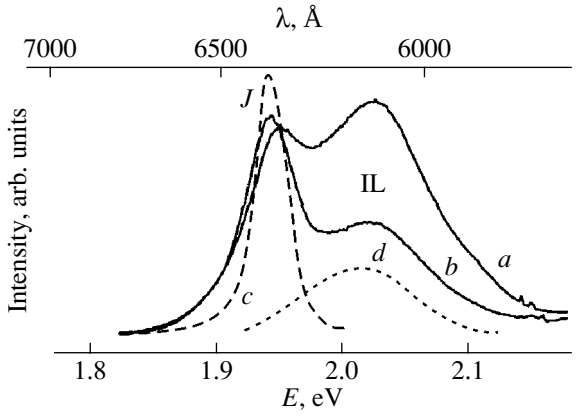

Fig. 3. Mn^{2+} intracenter luminescence band and band *J* in the spectrum of sample *2* obtained under excitation by 10-ns-long pulses. (*a*, *b*) Normalized spectra measured continuously at pumping levels of 10^2 and 10^4 W/cm^2 and (*c*, *d*) spectra obtained 0.1 and 5 μs after the completion of excitation; $T = 77$ K.

tively thick CdTe and $Cd_{0.5}Mg_{0.5}Te$ layers on which the superlattice was grown (see inset to Fig. 1). This consideration should be taken into account in analyzing the IL band profiles, because the distance between the interference maxima forming in this region under normal incidence is about 10 nm.

The QWs studied here are specific in that they contain layers of manganese ions located at different distances from the interfaces. The crystal field acting on the interface ions is weaker than the field in which the Mn^{2+} ions in the QW are located. This follows from the well-known dependence of the IL maximum energy on the cation concentration ratio in bulk $Cd_{1-x-y}Mn_xMg_yTe$ crystals [6]. Thus, the ions located close to the interfaces are responsible for the short-wavelength wing of the IL profile due to Mn^{2+} ions in the QW. The high-energy IL shift should be the largest in structure *1* with narrow QWs, in full agreement with experiment. While the crystal field acting on cations in the structures studied generally has a lower symmetry than that in a bulk crystal, this change is the most pronounced for the ions near the interfaces. As already pointed out, the optical transition in the Mn^{2+} 3*d* shell is of the intercombination type and, thus, is forbidden in the dipole approximation (the corresponding absorption coefficient does not exceed 10^3 cm^{-1}). This forbiddenness is weakened by various factors, one of them being the asymmetric crystal-field component, which should relatively enhance the interface ion contribution to the IL.

The homogeneous and inhomogeneous broadenings of the 2.0-eV IL band for $Cd_{0.4}Mn_{0.6}Te$ solid solutions are 85 and 70 meV, respectively, at $T = 15$ K [8]. The main factors responsible for these broadenings are the electron–phonon coupling and the crystal field fluctuations, respectively. Crystal field fluctuations in a bulk crystal originate from random concentration inhomogeneities of the solid solutions, as well as from impurities and structural defects. MBE-grown QWs are higher in quality than bulk solid solutions, which are usually prepared using the Bridgman method, but the major contribution to inhomogeneous broadening is due to the inherent properties of a solid solution. The calculated dependence of the crystal field on the Mn^{2+} ion location in a QW with respect to the interface and the influence of this dependence on the energy of the radiating $^4T_1$ level correlate well, on the whole, with the experimentally observed shift and broadening of the IL band in QWs as compared to that from a bulk crystal.

There is a difference in the intensity ratio of the exciton luminescence and the Mn^{2+} IL between the bulk crystal and QW structures. Comparison of a bulk crystal with a $Cd_{1-x}Mn_xTe$ QW with the same energy spacings between the Mn^{2+} 3*d*-shell excitation threshold and the exciton level reveals that the relative exciton intensity in a QW is considerably higher than that in a bulk crystal.[1] This difference may be due to either an

[1] The intensities should be compared for the same excitation levels of about 10 W/cm^2, because, in contrast to exciton luminescence, the Mn^{2+} IL saturates rapidly.

increase in the exciton oscillator strength or the specific features of exciton excitation transfer to the 3*d* shell in a quasi-two-dimensional system. Two cases should be considered in the structures under study, namely, excitation of the manganese 3*d* shell by the barrier exciton and excitation preceded by relaxation of the QW exciton. Measurements of the dependence of the exciton-to-IL intensity ratio on the QW width at different excitation levels using different methods of optical excitation would permit one to refine the mechanisms of electronic excitation in two-dimensional systems via excitons and 3*d* shells of magnetic ions, including the part played by spin effects; this dependence requires additional investigation.

Sample *2* exhibits a new band *J* with a decay time of less than 0.1 μs on the low-energy wing of the IL profile. In contrast to the IL, this band saturates only weakly at high excitation levels (Fig. 3). The band *J* may have a bearing on defects forming at the interfaces of the $Cd_{0.6}Mn_{0.4}Te/Cd_{0.5}Mg_{0.5}Te$ heterostructure. Note that the band *J* is not seen in samples *1*, *3*, and *4*, grown in the same conditions.

The radiation from sample *3* measured at long detection delay times, when the exciton luminescence of the $Cd_{0.6}Mn_{0.4}Te/Cd_{0.5}Mg_{0.5}Te$ superlattice and of the GaAs substrate is no longer present in the spectrum, still contains the conventional 2.0-eV manganese IL band and a band near 1.45 eV (Fig. 4). The intensity of the 1.45-eV band varies from one sample to another; indeed, in sample *2* it is weak, while in samples *1* and *4* it is almost completely absent. We studied a number of bulk $Cd_{1-x}Mn_xTe$ crystals and found that this band is also seen in some of them (Fig. 4). CdTe is known to undergo a phase transition (at a hydrostatic pressure of 3.5 kbar) from the zinc blende to the rock-salt structure through a cinnabar-type lattice, which is stable within a narrow pressure interval [19–21]. We believe that the 1.45-eV band originates from the IL of manganese ions that are located in crystal regions with rock-salt symmetry (octahedral anion environment), where the crystal field is substantially stronger than in the case of zinc blende symmetry (tetrahedral anion environment). This interpretation is supported by the change the luminescence spectrum of $Zn_{0.93}Mn_{0.07}S$ undergoes at the structural phase transition induced by hydrostatic pressure; during this transition, the 2.1-eV band vanishes and a broad band near 1.4 eV sharply increases in intensity [22]. The energy shift of the IL band from 2.0 to 1.45 eV is due to the crystal field *Dq* acting on the Mn^{2+} ion in $Cd_{1-x}Mn_xTe$ and changing from 800 to 1300 cm^{-1}, respectively. As already mentioned, while samples *1–4* were grown using the same technology, the 1.45-eV band in samples *1*, *2*, and *4* is either weak or altogether lacking. It may be conjectured that the probability of formation of regions with a rock-salt structure in thin $Cd_{0.6}Mn_{0.4}Te$ layers is very low.

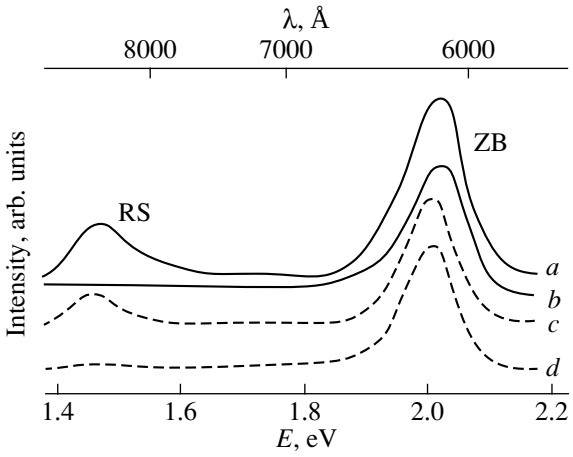

Fig. 4. Mn^{2+} intracenter luminescence (*a*, *b*) in $Cd_{1-x}Mn_xTe/Cd_{0.5}Mg_{0.5}Te$ superlattices [(*a*) sample *3*, (*b*) sample *1*] and (*c*, *d*) in two bulk $Cd_{0.5}Mn_{0.5}Te$ crystals. The bands ZB and RS relate to manganese ions located in regions with zinc blende and rock-salt lattices, respectively. The luminescence was measured 5 μs after pulse termination; $T = 77$ K.

ACKNOWLEDGMENTS

The authors are indebted to Yu.A. Stepanov for assistance in the experiments.

This study was supported by the Ministry of Education of the Russian Federation, project no. E02-3.4-426.

REFERENCES

1. O. Goede and W. Heimbrodt, Phys. Status Solidi B **146**, 11 (1988).
2. J. K. Furdyna, J. Appl. Phys. **64**, R29 (1988).
3. P. A. Wolff, in *Semiconductors and Semimetals*, Ed. by J. K. Furdyna and J. Kossut (Academic, London, 1988), Vol. 25.
4. V. F. Agekyan, Phys. Solid State **44**, 2013 (2002).
5. J. S. Lewis, M. R. Davidson, and P. H. Holloway, J. Appl. Phys. **92**, 6646 (2002).
6. V. F. Agekyan, N. N. Vasil'ev, A. Yu. Serov, and N. G. Filosofov, Phys. Solid State **42**, 836 (2000).
7. J. D. Park, S. Yamamoto, J. Watanabe, K. Takamura, and J. Nakahara, J. Phys. Soc. Jpn. **66**, 3289 (1997).
8. J. Gregus, J. Watanabe, and J. Nakahara, J. Phys. Soc. Jpn. **66**, 1810 (1997).
9. V. F. Agekyan, N. N. Vasil'ev, and A. Yu. Serov, Phys. Solid State **41**, 41 (1999).
10. V. F. Agekyan, N. N. Vasil'ev, A. Yu. Serov, and N. G. Filosofov, J. Cryst. Growth **214/215**, 391 (2000).
11. R. N. Bhargava, D. Gallagher, X. Hong, and A. Nurmikko, Phys. Rev. Lett. **72**, 416 (1994).
12. R. N. Bhargava, J. Cryst. Growth **214/215**, 926 (2000).

13. D. Adachi, S. Hasui, T. Toyama, and H. Okamoto, Appl. Phys. Lett. **77**, 1301 (2000).
14. J. Zhou, Yu. Zhou, S. Buddhudu, S. L. Ng, Y. L. Lam, and H. Kam, Appl. Phys. Lett. **76**, 3513 (2000).
15. L. M. Gan, B. Liu, C. H. Chew, S. J. Xu, S. J. Chua, G. L. Loy, and G. Q. Xu, Langmuir **13**, 6427 (1997).
16. W. Chen, F. Su, G. Li, A. L. Jolly, J.-O. Malm, and J.-O. Bovin, J. Appl. Phys. **92**, 1950 (2002).
17. W. Park, T. C. Jones, W. Tong, S. Schon, M. Chaichimansour, B. K. Wagner, and C. J. Summers, J. Appl. Phys. **84**, 6852 (1998).
18. J. Nakahara, K. Takamura, and S. Yamamoto, Phys. Status Solidi B **211**, 223 (1999).
19. A. Mujica, A. Rubio, A. Munoz, and R. J. Needs, Rev. Mod. Phys. **75**, 863 (2003).
20. A. N. Mariano and E. P. Warekois, Science **142**, 672 (1963).
21. M. I. McMahon and R. J. Nelmes, Phys. Rev. B **47**, 8337 (1993).
22. M. Kobayashi, Y. Nakamura, S. Endo, and W. Giriat, Phys. Status Solidi B **211**, 359 (1999).

Translated by G. Skrebtsov

Physics of the Solid State, Vol. 46, No. 9, 2004, pp. 1781–1784. Translated from Fizika Tverdogo Tela, Vol. 46, No. 9, 2004, pp. 1723–1726.
Original Russian Text Copyright © 2004 by Evteev, Kosilov, Solyanik.

LOW-DIMENSIONAL SYSTEMS AND SURFACE PHYSICS

Atomic Mechanisms and Kinetics of Self-Diffusion on the Pd(001) Surface

A. V. Evteev, A. T. Kosilov, and S. A. Solyanik

Voronezh State Technical University, Moskovskiĭ pr. 14, Voronezh, 394026 Russia

e-mail: mfm@fm.vorstu.ac.ru

Received January 22, 2004

Abstract—The atomic mechanisms and kinetics of self-diffusion of Pd adatoms on a single-crystal Pd(001) surface are investigated using molecular dynamics simulation. It is shown that the migration of Pd adatoms on the Pd(001) surface predominantly occurs through the relay-race mechanism with the participation of substrate atoms. The activation energy for an elementary event of relay-race self-diffusion is calculated from the kinetic equation describing the change in the concentration of surface adatoms labeled at the initial instant of time. © *2004 MAIK "Nauka/Interperiodica".*

1. INTRODUCTION

It is known that, at the early stages of formation of films from a gas phase on crystal substrates, the surface diffusion of adatoms is one of the controlling factors in the nucleation and subsequent growth of the condensate [1–12].

At present, it is generally believed that the diffusion of adatoms on a metal surface predominantly occurs according to the rolling-stone mechanism, i.e., through a sequence of thermally activated transitions of adatoms from one stable state to another [1–4]. This scheme of migration of adatoms over an atomically smooth surface is so obvious that, up to now, other (alternative) mechanisms of diffusion of adatoms had been considered unlikely. Direct experimental methods for observing diffusion on a solid surface enable one to "see" single atoms; however, when the positions of atoms are fixed prior to and after a self-diffusion event, it is impossible to determine the particular processes due to which an atom is brought into a new position and to establish whether it is this atom that was located in the initial position. The motion of each atom in a system (including adatoms) at all stages of the diffusion can be traced in a computer experiment based on the molecular dynamics method. In particular, Garofalini and Halicioglu [13] carried out a molecular dynamics simulation of the diffusion of Au, Ir, and Pt adatoms on the Pt(110) surface with the use of the Lennard-Jones pair potential of the interatomic interaction. It was shown that the Ir and Pt atoms can diffuse according to the exchange mechanism through the displacement of a substrate atom by a diffusing adatom. This process is favorable for mutual mixing of atoms of the condensed material and the substrate. Circumstantial evidence in support of the above mechanism of diffusion is given by the experimentally observed escape of Cu atoms onto the surface of Pd, Rh, and Pt growing films [9], which has defied explanation within the model of bulk heterodiffusion.

In this work, the atomic mechanisms and kinetics of self-diffusion of Pd adatoms on the surface of a single-crystal Pd(001) substrate were investigated using molecular dynamics simulation.

2. COMPUTER EXPERIMENT

The substrate was simulated using a computational cell made up of eight (001) planes that were cut in the form of a square lattice 48×48 atoms in size and contained 2304 atoms each. Periodic boundary conditions were imposed on the system in the directions [110] and $[1\bar{1}0]$. In the computational cell, the three lower layers at the bottom were static and the five subsequent layers were dynamic. For the computer experiment, 64 adatoms were regularly arranged on the surface of the substrate in such a way that they formed a square lattice 8×8 adatoms in size. Then, the system was subjected to static relaxation. The interaction between the atoms was governed by the many-particle potential, which was calculated in the framework of the embedded-atom method [14]. Thereafter, velocities specified by a Maxwell distribution at a given temperature were imparted to the adatoms and substrate atoms arranged in the dynamic layers and isothermal annealing of the substrate was simulated by the molecular dynamics method. The molecular dynamics calculation involved numerical integration of the equations of motion of the atoms with a time step $\Delta t = 1.5 \times 10^{-15}$ s according to the Verlet algorithm [15].

3. RESULTS AND DISCUSSION

It was established that, during isothermal annealing, the diffusion of Pd adatoms on the Pd(001) surface pre-

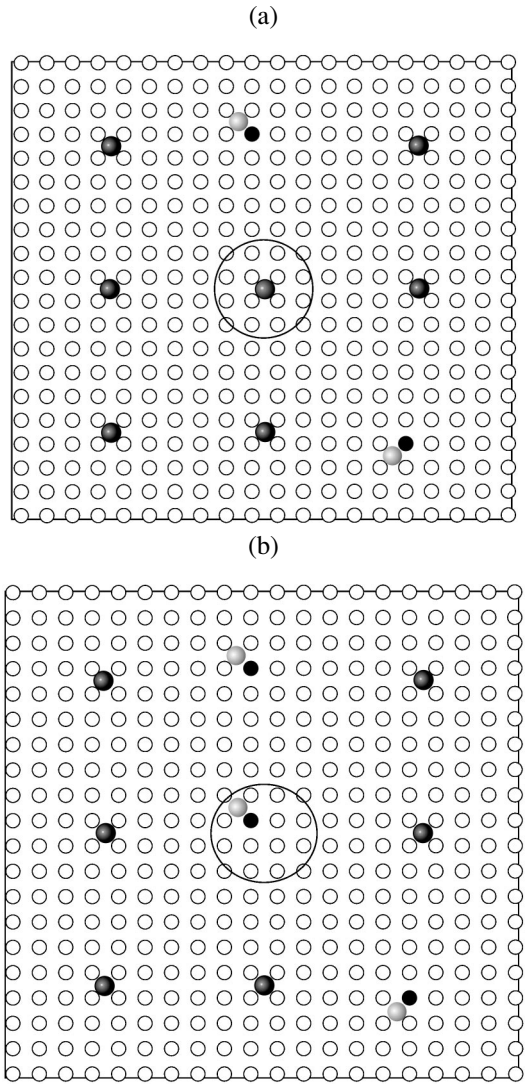

Fig. 1. Fragment of the Pd(001) surface after annealing at 700 K for (a) 1.5×10^{-11} and (b) 3×10^{-11} s. An elementary event of the surface diffusion occurring through the relay-race mechanism is illustrated in the bounded region. Circles with a large diameter are adatoms, and circles with a small diameter are substrate atoms. Black circles are the adatoms labeled at the initial instant.

dominantly occurs not from one stable position to another stable position through the rolling-stone mechanism but through the transfer of an atom from the first layer of the substrate to the adatom position followed by the migration of this atom to the nearest stable surface position situated at the longest distance from the initial position of the adatom (see Fig. 1).

In a single-component system, an adatom involved in a similar relay-race diffusion event is displaced in the ⟨100⟩ direction over a distance equal to the lattice constant. For example, the computer experiment performed at 800 K demonstrated that, among the 64 initial labeled Pd adatoms, 37 adatoms turn out to be in the first layer of the Pd(001) substrate in 3×10^{-11} s. It

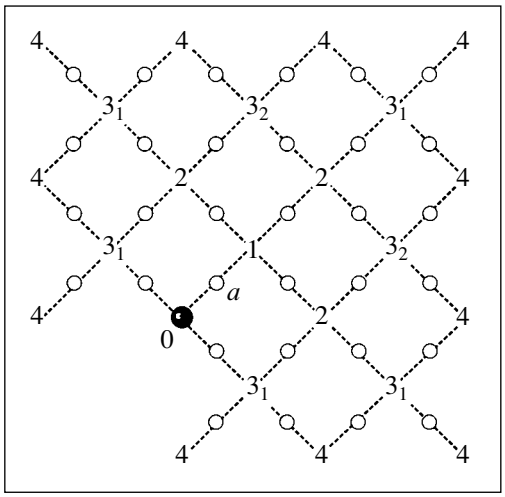

Fig. 2. Schematic diagram of the mutual arrangement of substrate atoms (small circles) and the possible paths of migration of adatoms to positions 1, 2, 3_1, 3_2, and 4 (dashed lines). The large circle is a labeled adatom in the initial position.

should be noted that, in this case, no labeled atom was observed in the second or subsequent layers of the substrate and no atom from the nearest environment of the adatom escaped from the first layer of the substrate onto the surface.

Therefore, during annealing, the number of labeled atoms in the first layer of the substrate increases, whereas the number of labeled atoms on the surface of the sample decreases. The total number of adatoms remains constant due to the escape of atoms from the first layer of the substrate onto the surface. However, an increase in the number of labeled atoms in the first layer of the substrate leads to an increase in the probability of their back transfer to the surface of the sample. With time, the counter flows of labeled atoms balance and the concentration of these atoms at the surface becomes close to equilibrium.

The obtained data on the atomic mechanism of the surface self-diffusion allowed us to describe the kinetics of the decrease in the number n_0 of adatoms (labeled at the initial instant of time) with a low coverage $\theta = n_0/N$, where N is the total number of adsorption positions on the surface. Using the schematic diagram of the mutual arrangement of substrate atoms as an illustration (Fig. 2), we consider the possible paths of the motion of adatoms through the mechanism of relay-race self-diffusion. Let us assume that a labeled adatom is displaced from the initial position 0 to the position *a* of the substrate due to the relay-race diffusion, whereas the substrate atom is displaced from the position *a* to the adatom position 1. The probability of this process in a unit time is defined as $\nu = \nu_0 \exp(-W/kT)$, where ν_0 is the frequency factor, W is the activation energy for an elementary event of the relay-race diffusion, k is the

Boltzmann constant, and T is the temperature. In this case, there are two possibilities for the adatom located in position 1; namely, it either can "pass on the baton" to the substrate atom for occupying one of the three positions 2 or can displace the labeled adatom from the position a and again return to the initial position 1 with a probability of 1/4 for each of these events. If the adatom turns out to be in one of the positions 2 with a probability of 1/3, it either can occupy one of the five positions 3_1 and one of the two positions 3_2 with a probability of

$$\frac{1}{3}\left(5\cdot\frac{1}{4}+2\cdot\frac{1}{4}\cdot 2\right) = 3/4$$

or can come back to the initial position 1 with a probability of 1/4. Since the probability of the transfer of the adatom from position 2 to position 3_2 is two times higher than that to position 3_1, the probabilities of the adatom occupying one of the five positions 3_1 and one of the two positions 3_2 are equal to 5/9 and 4/9, respectively. Consequently, the probability of the transfer of the adatom from position 3 to position 2 is determined to be

$$\frac{5}{9}\cdot\frac{1}{4}+\frac{4}{9}\cdot\frac{1}{2} = \frac{13}{36}.$$

The above variants of the relay-race transfer of adatoms between the positions at small coverages ($\theta \ll 1$) were used to construct a system of kinetic equations for adatoms located in different positions. By assuming that the numbers of atoms in positions 0, 1, 2, and 3 at the instant of time t are equal to n, n_1, n_2, and n_3, respectively, the kinetic equations take the form

$$\begin{aligned}
\frac{dn}{dt} &= -\nu n+\frac{1}{4}\nu n_1,\\
\frac{dn_1}{dt} &= \nu n-\nu n_1+\frac{1}{4}\nu n_2,\\
\frac{dn_2}{dt} &= \frac{3}{4}\nu n_1-\nu n_2+\frac{13}{36}\nu n_3,\\
\frac{dn_3}{dt} &= \frac{3}{4}\nu n_2-\nu n_3.
\end{aligned} \qquad (1)$$

Here, we assume that the number of atoms in positions 4 is so small that their diffusion into positions 3 can be disregarded. Therefore, the system of equations (1) describes the time dependences of the concentration of adatoms arranged in four positions (0, 1, 2, 3). It follows from the system of equations (1) that, if all adatoms at the initial instant of time are arranged in positions 0 [$n(0) = n_0$] and are labeled, the decrease in the concentration of labeled adatoms as a function of time $c(t) = n/n_0$ can be described by the expression

$$\begin{aligned}
c(t) &= \frac{1}{2}\exp(-\nu t)\\
&\times\left[\left(1-\frac{5\sqrt{133}}{133}\right)\cosh\left(\frac{\sqrt{51}}{12}\sqrt{1+\frac{\sqrt{133}}{17}}\nu t\right)\right.\\
&\left.+\left(1+\frac{5\sqrt{133}}{133}\right)\cosh\left(\frac{\sqrt{51}}{12}\sqrt{1-\frac{\sqrt{133}}{17}}\nu t\right)\right].
\end{aligned} \qquad (2)$$

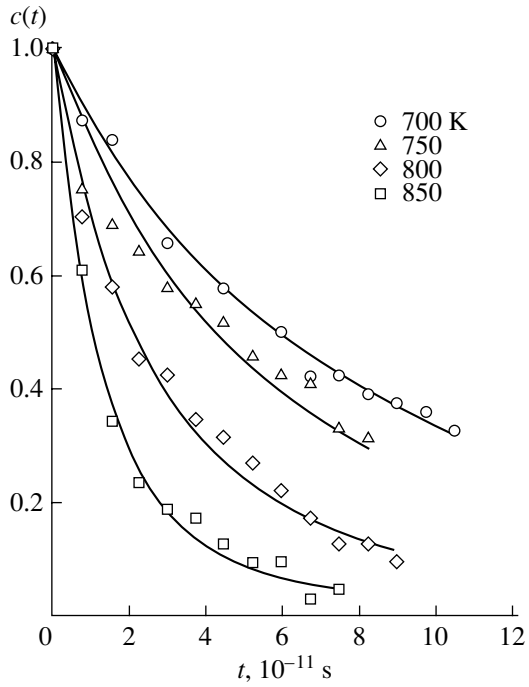

Fig. 3. Variation in the concentration of labeled adatoms during annealing at different temperatures and the results of approximation by formula (2).

Figure 3 presents the results of a computer simulation of the surface diffusion at temperatures of 700, 750, 800, and 850 K. The values of the parameter ν at different temperatures were found by approximating the results of the computer experiment according to expression (2). The data obtained were used to determine the activation energy for an elementary event of the relay-race diffusion of adatoms from the slope of the dependence of $\ln(\nu)$ on $1/T$ (Fig. 4). As a result, the activation energy was estimated to be 0.62 ± 0.04 eV/atom. Liu *et al.* [4] found that the activation energy for rolling-stone diffusion falls in the range 0.71–0.74 eV/atom; i.e., it is higher than the activation energy obtained in our experiment. This is an additional argument in support of the dominant role played by the relay-race mecha-

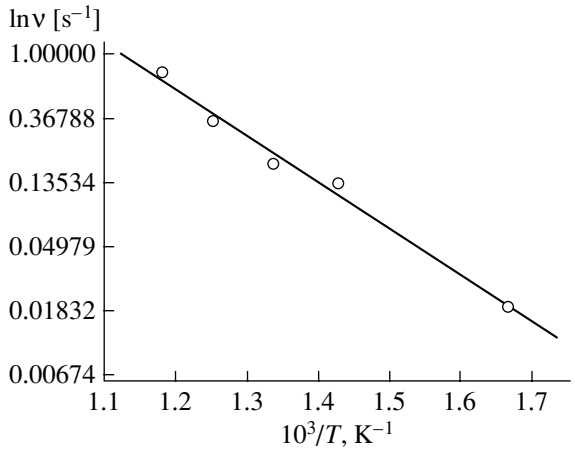

Fig. 4. Temperature dependence of the number of elementary events of the relay-race surface diffusion in a unit time in the $1/T$–lnν coordinates.

nism in the self-diffusion of adatoms on the Pd(001) surface.

In conclusion, we note that the relay-race mechanism of the diffusion of adatoms on the Pd(001) surface does not exclude the occurrence of other mechanisms of the surface self-diffusion. However, as follows from our molecular dynamics experiments, the probability of these mechanisms is considerably lower. For example, for the entire computer experiment, only at a temperature of 850 K did the molecular dynamics simulation performed in this work reveal an elementary event of self-diffusion occurring through the rolling-stone mechanism.

REFERENCES

1. L. N. Larikov and V. I. Isaĭchev, *Diffusion in Metals and Alloys: A Handbook on Structure and Properties of Metals and Alloys* (Naukova Dumka, Kiev, 1987) [in Russian].
2. V. P. Zhdanov, *Elementary Physicochemical Processes on the Surface* (Nauka, Novosibirsk, 1988) [in Russian].
3. S. Yu. Davydov, Fiz. Tverd. Tela (St. Petersburg) **41**, 11 (1999) [Phys. Solid State **41**, 8 (1999)].
4. C. L. Liu, J. M. Cohen, J. B. Adams, and A. F. Voter, Surf. Sci. **253**, 334 (1991).
5. S. S. Chao, E. A. Knabbe, and R. W. Vook, Surf. Sci. **100**, 581 (1980).
6. H. Asonen, C. Barnes, A. Salokatve, and A. Vuoristo, Appl. Surf. Sci. **22/23**, 556 (1985).
7. C. Boeglin, B. Carriere, J. P. Deville, O. Heckman, C. Leroux, and P. Panissod, Surf. Sci. **211/212**, 767 (1989).
8. H. Li, S. C. Wu, D. Tian, J. Quinn, Y. S. Li, and F. Jona, Phys. Rev. B **40** (8), 5841 (1989).
9. G. W. Graham, P. J. Sshmitz, and P. A. Thiel, Phys. Rev. B **41** (6), 3353 (1990).
10. J. A. Bernard and J. J. Ehrhardt, J. Vac. Sci. Technol. A **8** (6), 4061 (1990).
11. Y. S. Li, J. Quinn, H. Li, D. Tian, and F. Jona, Phys. Rev. B **44** (15), 8261 (1991).
12. H. Zeng and G. Vidali, Phys. Rev. Lett. **74** (4), 582 (1995).
13. S. H. Garofalini and T. Halicioglu, Surf. Sci. **104**, 199 (1981).
14. S. M. Folies, Phys. Rev. B **32** (6), 3409 (1985).
15. L. Verlet, Phys. Rev. **159**, 98 (1967).

Translated by N. Korovin